BOARDS OF ADVISORS, ENGINEERING

A. H-S. ANG University of Illinois	Civil Engineering—Systems and Probability
DONALD S. BERRY Northwestern University	Transportation Engineering
JAMES GERE Stanford University	Civil Engineering and Applied Mechanics
J. STUART HUNTER Princeton University	Engineering Statistics
T. WILLIAM LAMBE R. V. WHITMAN Massachusetts Institute of Technology	Civil Engineering—Soil Mechanics
PERRY L. McCARTY Stanford University	Environmental Engineering
DON T. PHILLIPS Texas A & M	Industrial Engineering
DALE RUDD University of Wisconsin	Chemical Engineering
ROBERT F. STEIDEL, JR. University of California—Berkeley	Mechanical Engineering
R. N. WHITE Cornell University	Civil Engineering—Structures

AERODYNAMICS, AERONAUTICS, AND FLIGHT MECHANICS

BARNES W. McCORMICK
The Pennsylvania State University

JOHN WILEY & SONS
New York • Chichester • Brisbane • Toronto • Singapore

To my family and to a great university, The Pennsylvania State University; they have truly shaped my life

Library of Congress Cataloging in Publication Data

McCormick, Barnes Warnock, 1926–
Aerodynamics, aeronautics, and flight mechanics.

Includes index.
1. Aerodynamics. 2. Airplanes. I. Title.
TL570.M22 629.132'3 79–11073
ISBN 0-471-03032-5

Printed in the United States of America

10 9

PREFACE

An airplane, whether it is a sleek, modern jet or a Piper Cub, is a thing of beauty, supported almost miraculously by the invisible medium through which it travels. As an aeronautical engineer and a pilot, the beauty of flight is a pleasure I hope always to enjoy. One of my favourite poems is "High Flight," by John Gillespie Magee, Jr., a young RAF pilot killed during World War II. Although it is unusual to include a poem in a preface, I must break convention because this poem expresses my thoughts better than I can.

Oh, I have slipped the surly bonds of earth
And danced the skies on laughter-silvered
wings;
Sunward I've climbed, and joined the tumbling
mirth
Of sun-split clouds—and done a hundred
things
You have not dreamed of—wheeled and
soared and swung
High in the sunlit silence. Hov'ring there,
I've chased the shouting wind along, and flung
My eager craft through footless halls of air.
Up, up the long, delirious, burning blue
I've topped the windswept heights with
easy grace
Where never lark, or even eagle flew.
And, while with silent, lifting mind I've trod
The high untrespassed sanctity of space,
Put out my hand, and touched the face of
God.

This book explains the many technical aspects of flight; the title reflects its contents. Beginning with the fundamentals of incompressible and compressible flows, aerodynamic principles relating to lift, drag, and thrust are developed. Two-dimensional airfoils and three-dimensional wings with high and low aspect ratios are treated for subsonic and supersonic flows.

The operating characteristics of different types of aircraft power plants, including normally aspirated and supercharged-piston engines, turboprops, turbojets, and turbofans, are presented in some detail. Typical operating curves are given for specific engines within these classes. A fairly complete treatment of propellers is also included.

This information, which is necessary for estimating the aerodynamic characteristics of an airplane, is followed by a presentation of methods for calculating airplane performance; items such as takeoff distance, climb rates and times, range payload curves, and landing distances, are discussed.

Finally, the subjects of longitudinal and lateral-directional stability and control, both static and dynamic, are introduced. Because this book is intended for use in a first course in these subjects, it covers only open-loop control.

Features of this textbook include material on the prop-fan, winglets, high lift devices, cooling and trim drag, the latest NASA airfoils, criteria for providing satisfactory open-loop flying qualities, and the use of the SI and English systems of units. Practical examples are given for most developments and, in many cases, are applied to currently operating airplane-engine combinations. Some numerical treatments of aerodynamic problems and the use of the analog computer for examining longitudinal and lateral dynamic behavior are also introduced. Considerable data are provided relating to lift, drag, and thrust predictions. Stability and control data and performance data on a number of presently operating aircraft are found throughout the book.

Since each subject is developed from first principles, it can be used as a text for a first course in aerodynamics at the junior level. It also can be used in successive courses in compressible flow, airplane performance, and stability and control as either the primary text or as a reference. At least half of the material in the book is at the senior level of most aerospace engineering programs.

Obviously a book of this nature could not have been written without the help and cooperation of many individuals and organizations. I especially thank Pratt & Whitney and Pratt & Whitney of Canada for the performance curves on their engines; Avco-Lycoming for information on cooling drag and reciprocating engines; Cessna for the data pertaining to the performance of the Citation I; and Piper for their support of this effort in many ways. My friends and acquaintances with these fine companies who helped personally are too numerous to mention. They know who they are, and I am grateful to them.

I am indebted to my secretaries, Charlotte Weldon, and Sharon Symanovich, who typed the manuscript, for a job well done. Their correction of mistakes and their patience with my penmanship and the other trying aspects of preparing the manuscript are sincerely appreciated.

I prepared the manuscript on evenings, weekends and, when I could find the time, during the day at The Pennsylvania State University. This meant many lonely evenings and weekends for my wife, Emily, so I offer my appreciation for her indulgence, patience, and understanding.

Barnes W. McCormick, Jr.

CONTENTS

ONE *INTRODUCTION*	1
A Brief History	1
A Brief Introduction to the Technology of Aeronautics	9
TWO *FLUID MECHANICS*	16
Fluid Statics and the Atmosphere	16
Fluid Dynamics	22
Conservation of Mass	26
The Momentum Theorem	29
Euler's Equation of Motion	31
Bernoulli's Equation	33
Determination of Free-Stream Velocity	35
Determination of True Airspeed	36
Potential Flow	38
Velocity Potential and Stream Function	39
Elementary Flow Functions	42
Vortex	43
Source	44
Biot-Savart Law	45
The Calculation of Flows for Well-Defined Body Shapes	47
The Circular Cylinder	51
The Numerical Calculation of Potential Flow Around Arbitrary Body Shapes	54
THREE *THE GENERATION OF LIFT*	61
Wing Geometry	61
Airfoils	63
Airfoil Families	72
NACA Four-Digit Series	72
NACA Five-Digit Series	72
NACA 1-Series (Series 16)	74
NACA 6-Series	74
Modern Airfoil Developments	76
Prediction of Airfoil Behavior	82
Maximum Lift	93
Flaps	95
Plain Flaps	99
Split Flaps	99
Slotted Flaps	100

Flap Effectiveness in the Linear Range 109
Leading Edge Devices 113
The Optimum Airfoil for High Lift 117
Powered-Lift Systems 120
The Lifting Characteristics of a Finite Wing 130
The Vortex System for a Wing 131
The Maximum Lift of a Finite Wing 140
Effect of Fuselage on $C_{L_{max}}$ 144
Effect of Trim on $C_{L_{max}}$ 146
Estimation of $C_{L_{max}}$ for a Complete Airplane Configuration 148
Airfoil Characteristics at Low Reynolds Numbers 151

FOUR *DRAG* 162
Skin Friction Drag 163
Form Drag 168
Drag of Streamlined Shapes 176
Interference Drag 181
Induced Drag 185
Calculation of Induced Drag 186
Effective Aspect Ratio 194
Drag Breakdown and Equivalent Flat-Plate Area 196
Drag Counts 196
Average Skin Friction Coefficients 197
Example Estimates of Drag Breakdown 199
Trim Drag 203
Cooling Drag 206
Drag Reduction 214
Winglets 215
Reduction of Skin Friction Drag 221
Drag Cleanup 231
Total Airplane Drag 232

FIVE *LIFT AND DRAG AT HIGH MACH NUMBERS* 237
Qualitative Behavior of Airfoils as a Function of Mach Number 237
Subsonic Flow at High Mach Numbers 238
Fundamentals of Gas Dynamics 244
One-Dimensional Isentropic Flow 244
Normal Shock Waves 248
Oblique Shock Waves 253
Expansion Waves 258
Transonic Airfoils 261
Supersonic Airfoils 266
Linearized Compressible Potential Flow 271
Subsonic Flow 272
Supersonic Flow (Ackeret Theory) 274
Three-Dimensional Wings 279
Characteristics of Sweptback Wings 281
Delta Wings 294

Supersonic Wings 303
Subsonic Leading Edges 304
Supersonic Leading Edges 309
Effect of Mach Number on the Zero Lift Drag of Two- and Three-Dimensional Shapes 315
Area Rule for Transonic Flow 321

SIX *THE PRODUCTION OF THRUST* 332
A Brief History of the Piston Engine 332
Piston Engine Characteristics 333
Supercharged Engines 339
Propeller Analysis 343
Momentum Theory 343
Blade Element Theories 347
Momentum-Blade Element Theory 349
Vortex Theory 351
Practical Use of Propeller Charts 359
Approximate Useful Relationships for Propellers 364
Propeller Selection 366
Design of a New Propeller 368
A Brief History of the Turbojet 370
Description of the Gas Turbine Engine 371
Engine Ratings 377
Flat Rating 378
Some Considerations Relating to Gas Turbine Performance 378
Qualitative Comparison of the Performance of Turbojet, Turbofan, and Turboprop Engines 382
Specific Engine Characteristics and Performance 385
Turbojet 385
Turbofan 398
Turboprop 405
Installation Losses 411
Trends in Aircraft Propulsion 411

SEVEN *AIRPLANE PERFORMANCE* 418
Takeoff 418
Ground Roll 419
Effect of Wind 425
Airborne Distance 427
Balanced Field Length 431
Rate of Climb, Time to Climb, and Ceilings 432
Generalized Power-Required Curve 438
Time to Climb 439
Range 440
Maximum Endurance 446
Descent 447
Landing 448

Airborne Distance 450
Ground Roll 451
Range Payload 452
Operating Limitations 460
Flight Envelope 460
Maneuvering Envelope (V–n Diagram) 463
Gust Load Factors 466
Energy Methods for Optimal Trajectories 468
The Art of Estimating and Scaling 471

EIGHT *STATIC STABILITY AND CONTROL* 477
Introduction 477
Coordinate System—Forces, Moments, and Velocities 478
Longitudinal Static Stability 479
Stick-Fixed Stability 479
Stick-Fixed Neutral Point and Static Margin 481
$C_{M_{ac}}$ and Aerodynamic Center Location for a Finite Wing 484
Downwash Angle 486
Longitudinal Control 488
Control Position as a Function of Lift Coefficient 488
All-Movable Tail 489
Stabilizer-Elevator 489
Stabilator 491
Control Forces 491
Gearing 492
Stick Force for A Stabilator 493
Stick Force for a Horizontal Stabilizer-Elevator Combination 494
Estimation of Aerodynamic Hinge Moments 495
Example Calculation of Stick Force 502
Stick-Free Longitudinal Static Stability 505
Elevator-Stabilizer Configuration 505
Stabilator Configuration 506
Stick-Free Static Margin 508
Steady Maneuvering 508
Horizontal Stabilizer-Elevator Configuration: Elevator Angle per g 509
Stabilator Angle per g 512
Stick Force per g 512
Stabilizer-Elevator Configuration 512
Stabilator 513
Effect of Fuselage and Nacelles 513
Effects of Propulsion System 515
Propellers 515
Jets 521
Ground Effect 523
Lateral and Directional Static Stability and Control 524

Directional Static Stability 524
Directional Control 526
Lateral Control 528
Adverse Yaw 534
Roll Control by the Use of Spoilers 534
Aileron Reversal 537
Steady Rolling Motion 538
Coupling Effects 541
Rolling Moment with Rudder 541
Rolling Moment with Yaw Rate 542
Yawing Moment with Roll Rate 543
Rolling Moment with Sideslip Angle—Dihedral Effect 543

NINE *LONGITUDINAL DYNAMIC STABILITY AND CONTROL* 552
Equations of Motion 552
Linearization of the Equations 556
A Summary Look at the Stability Derivatives and Other Parameters Affecting Longitudinal Dynamic Motion 561
X Derivatives and Parameters 561
Z Derivatives and Parameters 563
M Derivatives and Parameters 564
Examination and Reduction of Equations of Longitudinal Motion 565
Solution of nth-Order Linear Differential Equations with Constant Coefficients 565
Mode Shapes 569
Phugoid (Long-Period Mode) 574
Short-Period Mode 576
Solution of the Longitudinal Equations of Motion Using an Analog Computer 576
Longitudinal Flying Qualities 585
Phugoid Mode 586
Flight Path Stability 587
Short Period Mode 587

TEN *LATERAL-DIRECTIONAL DYNAMIC STABILITY AND CONTROL* 591
Equations of Motion 591
Euler Angles 594
Reduction of the Lateral-Directional Equations of Motion 595
A Summary Look at the Stability Derivatives and Other Parameters Affecting Lateral-Directional Dynamic Motion 596
Y Derivatives 596
C_{Y_β} 597
$C_{Y_{\hat{p}}}$ 597
$C_{Y_{\hat{r}}}$ 598
$C_{Y_{\delta_r}}$ 600

l Derivatives 600
C_{l_β} 600
$C_{l_{\dot{\beta}}}$ 601
C_{l_F} 602
$C_{l_{\delta_a}}$ 603
$C_{l_{\delta_r}}$ 603
N Derivatives 604
C_{N_β} 604
$C_{N_{\dot{\beta}}}$ 604
C_{N_F} 604
$C_{N_{\delta_a}}$ 605
$C_{N_{\delta_r}}$ 605
Lateral-Directional Equations for the Cherokee 180 605
Mode Shapes 606
Roll Mode 606
Spiral Mode 607
Oscillatory or "Dutch Roll" Mode 609
Lateral Directional Flying Qualities 610
Roll Mode 611
Dutch Roll Mode 612
Spiral Stability 612
Spinning 613

APPENDIX A.1 *THE SI SYSTEM* 621

APPENDIX A.2 *STANDARD ATMOSPHERE* 624

APPENDIX A.3 *AIRPLANE DATA* 629

APPENDIX A.4 *NOMENCLATURE AND ABBREVIATIONS* 640

INDEX 649

AERODYNAMICS, AERONAUTICS, AND FLIGHT MECHANICS

ONE
INTRODUCTION

Aeronautics is defined as "the science that treats of the operation of aircraft; also, the art or science of operating aircraft." Basically, with aeronautics, one is concerned with predicting and controlling the forces and moments on an aircraft that is traveling through the atmosphere.

A BRIEF HISTORY

Thursday, December 17, 1903

"When we got up a wind of between 20 and 25 miles was blowing from the north. We got the machine out early and put out the signal for the men at the station. Before we were quite ready, John T. Daniels, W. S. Dough, A. D. Etheridge, W. C. Brinkly of Manteo, and Johnny Moore of Nags Head arrived. After running the engine and propellers a few minutes to get them in working order, I got on the machine at 10:35 for the first trial. The wind, according to our anemometers at this time, was blowing a little over 20 miles (corrected) 27 miles according to the government anemometer at Kitty Hawk. On slipping the rope the machine started off increasing in speed to probably 7 or 8 miles. The machine lifted from the truck just as it was entering the fourth rail. Mr. Daniels took a picture just as it left the tracks. I found the control of the front rudder quite difficult on account of its being balanced too near the center and thus had a tendency to turn itself when started so that the rudder was turned too far on one side and then too far on the other. As a result the machine would rise suddenly to about 10 ft. and then as suddenly, on turning the rudder, dart for the ground. A sudden dart when out about 100 feet from the end of the tracks ended the flight. Time about 12 seconds (not known exactly as watch was not promptly stopped). The level for throwing off the engine was broken, and the skid under the rudder cracked. After repairs, at 20 min. after 11 o'clock Will made the second trial."

The above, taken from Orville Wright's diary, as reported in Reference 1.1, describes mankind's first sustained, controlled, powered flight in a

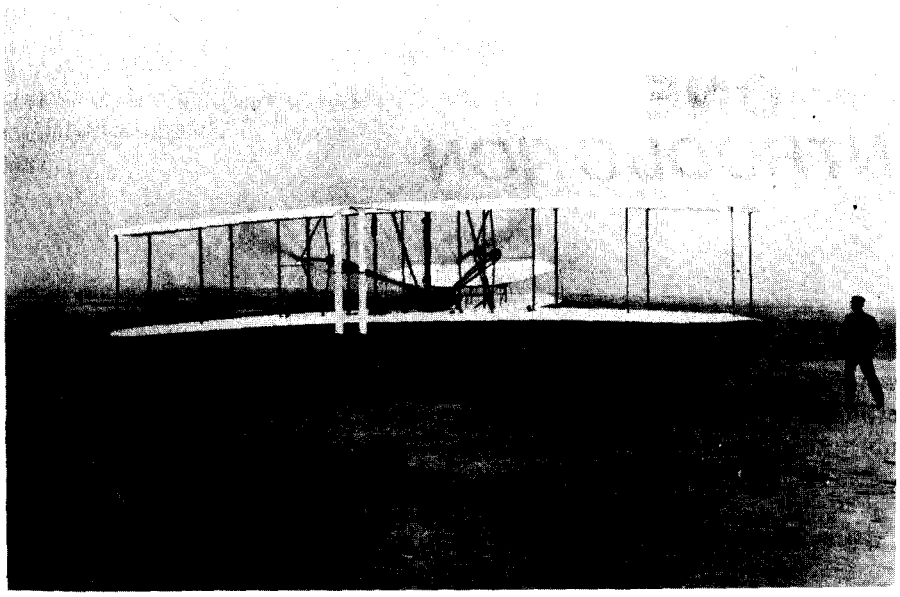

Figure 1.1 The first flight, December 17, 1903. (Courtesy of the National Air and Space Museum, Smithsonian Institution.)

heavier-than-air machine. The photograph, mentioned by Orville Wright, is shown here as Figure 1.1. Three more flights were made that morning. The last one, by Wilbur Wright, began just at 12 o'clock and covered 260 m in 59 s. Shortly after this flight, a strong gust of wind struck the airplane, turning it over and over. Although the machine was severely damaged and never flew again, the Wright Brothers achieved their goal, begun approximately 4 yr earlier.

Their success was no stroke of luck. The Wright Brothers were painstaking in their research and confident of their own results. They built their own wind tunnel and tested, in a methodical manner, hundreds of different airfoil and wing planform shapes. They were anything but a "couple of bicycle mechanics." Their letters to Octave Chanute, a respected civil engineer and aviation enthusiast of the day, reveal the Wright Brothers to have been learned men well versed in basic concepts such as work, energy, statics, and dynamics. A three-view drawing of their first airplane is presented in Figure 1.2.

On September 18, 1901, Wilbur Wright was invited to deliver a lecture before the Western Society of Engineers at a meeting in Chicago, Illinois. Among the conclusions reached by him in that paper were:

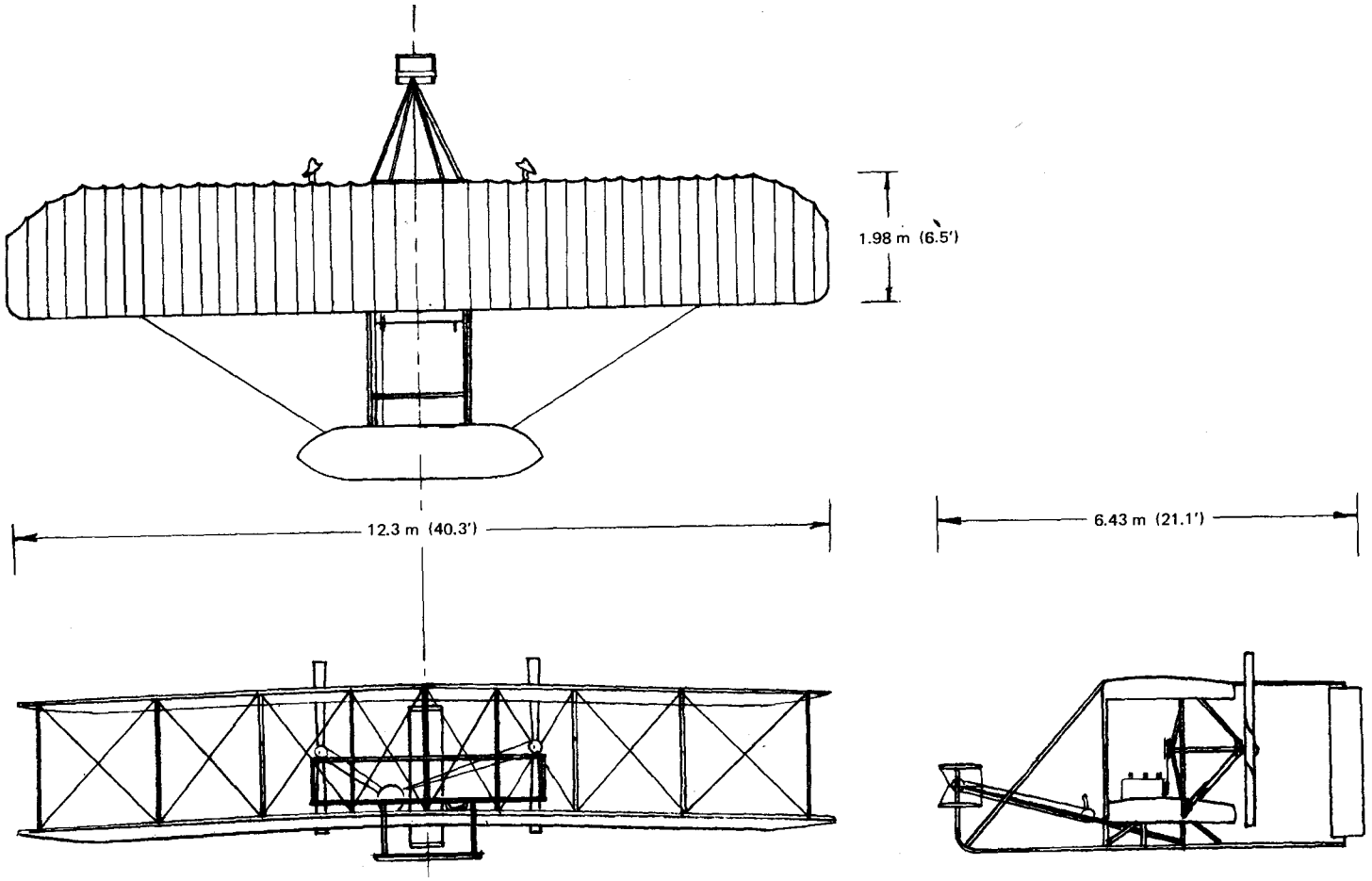

Figure 1.2 Three views of the Wright Brothers' flyer.

1. *"That the ratio of drift to lift in well-shaped surfaces is less at angles of incidence of five degrees to 12 degrees than at an angle of three degrees." ("Drift" is what we now call "drag.")*
2. *"That in arched surfaces the center of pressure at 90 degrees is near the center of the surface, but moves slowly forward as the angle becomes less, till a critical angle varying with the shape and depth of the curve is reached, after which it moves rapidly toward the rear till the angle of no lift is found."*
3. *"That a pair of superposed, or tandem surfaces, has less lift in proportion to drift than either surface separately, even after making allowance for weight and head resistance of the connections."*

These statements and other remarks (see Ref. 1.1) show that the Wright Brothers had a good understanding of wing and airfoil behavior well beyond that of other experimenters of the time.

Following their first successful flights at Kitty Hawk, North Carolina, in 1903, the Wright Brothers returned to their home in Dayton, Ohio. Two years later they were making flights there, almost routinely, in excess of 30 km and 30 min while others were still trying to get off the ground.

Most of the success of the Wright Brothers must be attributed to their own research, which utilized their wind tunnel and numerous experiments with controlled kites and gliders. However, their work was built, to some degree, on the gliding experiments of Otto Lilienthal and Octave Chanute. Beginning in 1891, Lilienthal, working near Berlin, Germany, made approximately 2000 gliding flights over a 5-yr period. Based on measurements obtained from these experiments, he published tables of lift and drag measurements on which the Wright Brothers based their early designs. Unfortunately, Lilienthal had no means of providing direct aerodynamic control to his gliders and relied instead on kinesthetic control, whereby he shifted his weight fore and aft and side to side. On August 9, 1896, as the result of a gust, Otto Lilienthal lost control and crashed from an altitude of approximately 15 m. He died the next day. During 1896 and 1897, Octave Chanute, inspired by Lilienthal's work, designed and built several gliders that were flown by others near Miller, Indiana. Chanute recognized Lilienthal's control problems and was attempting to achieve an "automatic" stability in his designs. Chanute's principal contribution was the addition of both vertical and horizontal stabilizing tail surfaces. In addition, he went to the "box," or biplane, configuration for added strength. Unfortunately, he also relied on kinesthetic control.

When the Wright Brothers began their gliding experiments in the fall of 1900, they realized that adequate control about all three axes was one of the major prerequisites to successful flight. To provide pitch control (i.e., nose up or down), they resorted to an all-movable horizontal tail mounted in front of

the wing. Yaw control (i.e., turning to the left or right) was accomplished by means of an all-movable vertical tail mounted behind the wing. Their method of roll control (i.e., lowering one side of the wing and raising the other) was not as obvious from photographs as the controls about the other two axes. Here, the Wright Brothers devised a means of warping their "box" wing so that the angle of incidence was increased on one side and decreased on the other. The vertical tail, or rudder, was connected to the wing-warping wires so as to produce what pilots refer to today as a coordinated turn.

The Wright Brothers were well ahead of all other aviation enthusiasts of their era. In fact, it was not until 3 yr after their first flight that a similar capability was demonstrated, this by Charles and Gabriel Voisin in Paris, France (Ref. 1.2). On March 30, 1907, Charles Voisin made a controlled flight of approximately 100 m in an airplane similar in appearance to the Wright flyer. A second machine built by the Voisin Brothers for Henri Farman, a bicycle and automobile racer, was flown by Farman later that year on flights that exceeded 2000 m. By the end of that year at least five others succeeded in following the Wright Brothers' lead, and aviation was on its way.

Today we are able to explain the results of the early experimenters in a very rational way by applying well-established aerodynamic principles that have evolved over the years from both analysis and experimentation. These developments have their beginnings with Sir Isaac Newton, who has been called the first real fluid mechanician (Ref. 1.3). In 1687 Newton, who is probably best known for his work in solid mechanics, reasoned that the resistance of a body moving through a fluid is proportional to the fluid density, the velocity squared, and the area of the body.

Newton also postulated the shear force in a viscous fluid to be proportional to the velocity gradient. Today, any fluid obeying this relationship is referred to as a Newtonian fluid.

In 1738, Daniel Bernoulli, a Swiss mathematician, published his treatise, "Hydrodynamics," which was followed in 1743 by a similar work produced by his father, John Bernoulli. The Bernoullis made important contributions to understanding the behavior of fluids. In particular, John introduced the concept of internal pressure, and he was probably the first to apply momentum principles to infinitesimal fluid elements.

Leonhard Euler, another Swiss mathematician, first put the science of hydrodynamics on a firm mathematical base. Around 1755, Euler properly formulated the equations of motion based on Newtonian mechanics and the works of John and Daniel Bernoulli. It was he who first derived along a streamline the relationship that we refer to today as "Bernoulli's equation."

The aerodynamic theories of the 1800s and early 1900s developed from the early works of these mathematicians. In 1894 the English engineer, Frederick William Lanchester, developed a theory to predict the aerodynamic behavior of wings. Unfortunately, this work was not made generally known

Table 1.1 (continued)

Designer or Manufacturer a. Model Number b. Model Name	First Flight Date	Span, ft	Length, ft	Wing Area, ft^2	Gross Weight, 1000 lb	Empty Weight, 1000 lb	Useful Load, 1000 lb	Power Plant, no. × hp/eng.	Loadings: Wing lb/ft^2	Loadings: Power, lb/hp or lb	Number[a] Flown	Passenger Capacity	Range, ST.M.	Comment
Kalinin a. K-7	8/33	173.9	91.9	4,887	83.78	53.79	29.99	7 × 750 hp	17.14	15.96	1	...	620	Bomber; projected 120-passenger transport version not built.
Tupolev a. ANT-20 b. Maxim Gorki	5/34	206.7	106.5	5,233	116.84	92.58	24.26	8 × 875 hp	22.33	16.69	2[e]	64[e]	1,240	Equipped with printing press and propaganda aerial loudspeaker system.
Douglas a. XB-19	6/41	212	132.3	4,285	162	75	65	4 × 2,000 hp	32.67	17.50	1	...	7,700	Bomber.
Lockheed a. 89 b. Constitution	11/46	189.1	156.1	3,610	184	114	70	4 × 3,000 hp	50.97	15.33	2	168	4,700	Full double-deck accommodations.
Hughes a. H-4(HK-1)	11/47	320.5	218.5	11,450	400	248	152	8 × 3,000 hp	34.93	16.67	1[k]	700	5,900	Flying boat; all wood.
Convair a. XC-99	11/47	230	182.5	4,772	265	140	125	6 × 3,000 hp	55.53	14.72	1	400	...	6 wing-buried engines with pusher propellers; full double-deck accommodations.
Bristol a. 167 b. Brabazon I	9/49	230	177	5,317	290	145	145	8 × 2,500 hp	54.54	14.50	1	100	5,500	8 wing-buried engines coupled in pairs to 4 tractor propellers.

Table 1.1 Largest Aircraft Examples Starting with the Wright Brothers

Designer or Manufacturer a. Model Number b. Model Name	First Flight Date	Span, ft	Length, ft	Wing Area, ft^2	Gross Weight, 1000 lb	Empty Weight, 1000 lb	Useful Load, 1000 lb	Power Plant, no. × hp/eng.	Loadings: Wing lb/ft^2	Loadings: Power, lb/hp or lb	Number[a] Flown	Passenger Capacity	Range, ST.M.	Comment
Wright b. Flyer	12/03	40.3	21.1	510	0.75	0.6	0.15[b]	1 × 12 hp	1.47	62.50	1	0	...	Canard biplane and single engines driving two pusher propellers.
Sikorsky/RBVZ b. Ilya Mourometz	4/13	113	67.2	1,615	10.58	7.28	3.3	4 × 100 hp	6.55	26.45	80	16	300	Biplane with tractor engines on lower wing; used effectively as a bomber in W.W.I.
Zeppelin-Staaken a. VGO.1	4/15	138.5	78.7	3,572	20.99	14.38	6.61	3 × 240 hp	5.9	29.2	44	...	...	Biplane with one nose mounted engine and two wing-mounted pushers.
Handley Page a. H.P. 15(V/1500)	4/18	126	64	3,000	30	15	15	4 × 275 hp	10.00	27.27	10	40	1,300	Built to bomb Berlin in W.W.1; biplane with 2 × 2 tractor/pusher arrangement.
Caproni a. Ca 60 b. Transaero	1921[c]	98.4	76.9	7,696	55.12	30.86	24.26	8 × 400 hp	7.16	19.69	0[c]	100	410	Flying boat: triple triplane.
Junkers a. G-38	11/29	144.3	76.1	3,229	44.09	28.66	15.33	2 × 400 hp 2 × 800 hp	13.63	18.33	8[j]	30	746	Engines wing-buried; DLH line service from 1932 to 1944.
Dornier a. Do X	7/29	157.5	131.4	4,736	105.8	72.2	33.6	12 × 500 hp	22.34	17.63	3	100[d]	850	Flying boat.

Table 1.1 (continued)

Designer or Manufacturer a. Model Number b. Model Name	First Flight Date	Span, ft	Length, ft	Wing Area, ft^2	Gross Weight, 1000 lb	Empty Weight, 1000 lb	Useful Load, 1000 lb	Power Plant, no. × hp/eng.	Loadings: Wing lb/ft^2	Loadings: Power, lb/hp or lb	Number[a] Flown	Passenger Capacity	Range, ST.M.	Comment
Boeing a. YB-52 b. Stratofortress	4/52	185	153	4,000	390	166	224	8 × 10,000 lb	97.50	3.00[f]	744	...	7,000	Bomber.
Boeing a. B-52G b. Stratofortress	3/61	185	157.6	4,000	488	...	...	8 × 13,750 lb	122.00	2.85[f]		...	10,000	Bomber.
Antonov a. An-22 b. Antheus	2/65	211.3	189.6	3,713	551.2	251.4	299.8	4 × 15,000 hp	148.45	9.19	SP[g]	350[h]	6,800	High-wing, tail-loading cargo transport; contra-rotating propellers.
Lockheed a. C-5A b. Galaxy	6/68	222.7	247.7	6,200	764.5	320	444.5	4 × 41,000 lb	123.31	4.78[f]	SP[g]	1,000[i]	7,500	High-wing, nose and tail-loading cargo transport; T-tail.

Source. From F. A. Cleveland, "Size Effects in Conventional Aircraft," *J. of Aircraft*, 7(6), November–December 1970 (33rd Wright Brothers Lecture). Reproduced with permission.

[a] Counting original(s), subsequent series production, and derivatives—if any.

[b] Counting pilot (Orville Wright) and 5 lb of fuel.

[c] Destroyed in taxi-test which resulted in unintended liftoff.

[d] Set world record 21 Oct. 1929 with 169 onboard.

[e] One ANT-20 is built with six 1100-hp engines.

[f] Turbine energy expressed in terms of gas-hp with 0.8 efficiency.

[g] SP = in series production.

[h] Used mainly as freighter: 724-seat stretched version projected.

[i] Triple deck version.

[j] Two in Germany; six in Japan.

[k] Flew only once on high-speed taxi test.

until 1907 in a book published by Lanchester. By then the Wright Brothers had been flying for 3 yr. Much of the knowledge that they had laboriously deduced from experiment could have been reasoned from Lanchester's theory. In 1894, Lanchester completed an analysis of airplane stability that could also have been of value to the Wrights. Again, this work was not published until 1908.

Lanchester's wing theory was somewhat intuitive in its development. In 1918 Ludwig Prandtl, a German professor of mechanics, presented a mathematical formulation of three-dimensional wing theory; today both men are credited with this accomplishment. Prandtl also made another important contribution to the science with his formalized boundary layer concept.

Around 1917 Nikolai Ergorovich Joukowski (the spelling has been anglicized), a Russian professor of rational mechanics and aerodynamics in Moscow, published a series of lectures on hydrodynamics in which the behavior of a family of airfoils was investigated analytically.

The work of these early hydro- and aerodynamicists contributed little, if any, to the progress and ultimate success of those struggling to fly. However, it was the analytical base laid by Euler and those who followed him on which the rapid progress in aviation was built.

After 1908, the list of aviators, engineers, and scientists contributing to the development of aviation grew rapidly. Quantum improvements were accomplished with the use of flaps, retractable gear, the cantilevered wing, all-metal construction, and the turbojet engine. This impressive growth is documented in Table 1.1. Note that in less than 10 yr from the Wright Brothers' first flight, the useful load increased from 667 N (150 lb) to more than 13,300 N (3000 lb). In the next 10 yr, the useful load increased by a factor of 10 and today is more than 1.78×10^6 N (400,000 lb) for the Lockheed C-5A.

Our state of knowledge is now such that one can predict with some certainty the performance of an airplane before it is ever flown. Where analytical or numerical techniques are insufficient, sophisticated experimental facilities are utilized to investigate areas such as high-lift devices, complicated three-dimensional flows in turbomachinery, and aerothermodynamics.

A BRIEF INTRODUCTION TO THE TECHNOLOGY OF AERONAUTICS

Consider the airplane in steady, climbing flight shown in Figure 1.3. The term *steady* means that the airplane is not accelerating; hence, all forces and moments on the aircraft must be in balance. To be more precise, one states that the vector sum of all forces and moments on the airplane must be zero. To depict the angles more clearly, all forces are shown acting through the center of gravity (cg). Although the resultant of all the forces must pass

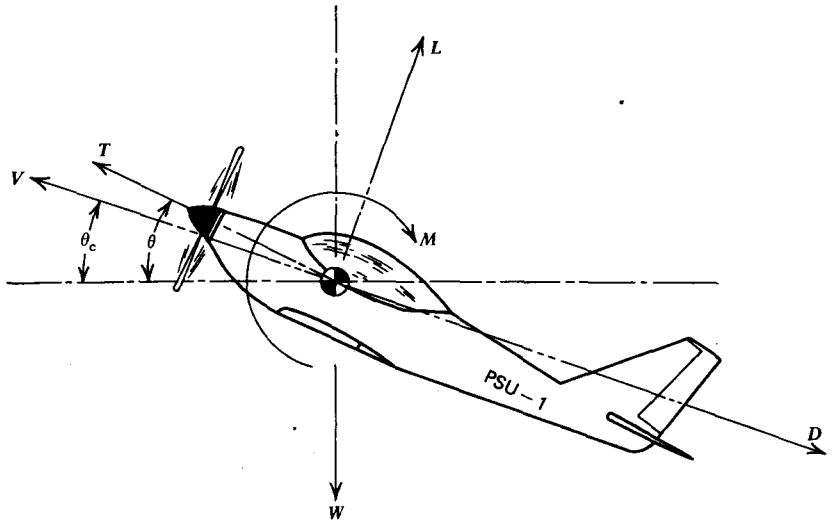

Figure 1.3 Forces and moments on an airplane in a steady climb.

through the center of gravity, it is not generally true that any one of the forces, with the exception of W, must satisfy this condition.

In this figure V represents the velocity vector of the airplane's center of gravity. This vector is shown inclined upward from the horizontal through the angle of climb, θ_c. The angle between the horizontal and the thrust line is denoted as θ. If this line is taken to be the reference line of the airplane, then one states that the airplane is pitched up through this angle. The angle between the reference line and the velocity vector, $\theta - \theta_c$, is referred to as the angle of attack of the airplane. Later we will use other angles of attack referenced to the wing geometry; thus, one must be careful in interpreting lift and drag data presented as a function of the angle of attack.

The thrust, T, is the propelling force that balances mainly the aerodynamic drag on the airplane. T can be produced by a propeller, a turbojet, or a rocket engine.

The lift, L, is defined as the component of all aerodynamic forces generated by the aircraft in the direction normal to the velocity vector, V. In level flight this means principally the upward vertical force produced by the wing. Generally, however, it includes the tail and fuselage forces. For example, in landing many aircraft require a downward force on the horizontal tail in order to trim out the nose-down pitching moment produced by the wing flaps. This trimming force can be significant, requiring a wing lift noticeably in excess of the airplane's weight.

Similar to the lift, the drag, D, is defined as the component of all aerodynamic forces generated by the airplane in the direction opposite to the

velocity vector, V. This force is composed of two principal parts, the parasite drag and the induced drag. The induced drag is generated as a result of producing lift; the parasite drag is the drag of the fuselage, landing gear, struts, and other surfaces exposed to the air. There is a fine point concerning the drag of the wing to be mentioned here that will be elaborated on later. Part of the wing drag contributes to the parasite drag and is sometimes referred to as profile drag. The profile drag is closely equal to the drag of the wing at zero lift; however, it does increase with increasing lift. This increase is therefore usually included as part of the induced drag. In a strict sense this is incorrect, as will become clearer later on.

W is the gross weight of the airplane and, by definition, acts at the center of gravity of the airplane and is directed vertically downward. It is composed of the empty weight of the airplane and its useful load. This latter weight includes the payload (passengers and cargo) and the fuel weight.

The pitching moment, M, is defined as positive in the nose-up direction (clockwise in Figure 1.3) and results from the distribution of aerodynamic forces on the wing, tail, fuselage, engine nacelles, and other surfaces exposed to the flow. Obviously, if the airplane is in trim, the sum of these moments about the center of gravity must be zero.

We know today that the aerodynamic forces on an airplane are the same whether we move the airplane through still air or fix the airplane and move the air past it. In other words, it is the relative motion between the air and airplane and not the absolute motion of either that determines the aerodynamic forces. This statement was not always so obvious. When he learned of the Wright Brothers' wind tunnel tests, Octave Chanute wrote to them on October 12, 1901 (Ref. 1.1) and referred to "natural wind." Chanute conjectured in his letter:

"It seems to me that there may be a difference in the result whether the air is impinged upon by a moving body or whether the wind impinges upon the same body at rest. In the latter case each molecule, being driven from behind, tends to transfer more of its energy to the body than in the former case when the body meets each molecule successively before it has time to react on its neighbors."

Fortunately, Wilbur and Orville Wright chose to believe their own wind tunnel results.

Returning to Figure 1.3, we may equate the vector sum of all forces to zero, since the airplane is in equilibrium. Hence, in the direction of flight,

$$T \cos(\theta - \theta_c) - D - W \sin \theta_c = 0 \tag{1.1}$$

Normal to this direction,

$$W \cos \theta_c - L - T \sin(\theta - \theta_c) = 0 \tag{1.2}$$

These equations can be solved for the angle of climb to give

$$\theta_c = \tan^{-1} \frac{T \cos(\theta - \theta_c) - D}{L + T \sin(\theta - \theta_c)} \tag{1.3}$$

In this form, θ_c appears on both sides of the equation. However, let us assume *a priori* that θ_c and $(\theta - \theta_c)$ are small angles. Also, except for very high performance and V/STOL (vertical or short takeoff and landing) airplanes, the thrust for most airplanes is only a fraction of the weight. Thus, Equation 1.3 becomes

$$\theta_c \simeq \frac{T - D}{W} \tag{1.4}$$

For airplanes propelled by turbojets or rockets, Equation 1.4 is in the form that one would normally use for calculating the angle of climb. However, in the case of airplanes with shaft engines, this equation is modified so that we can deal with power instead of thrust.

First, consider a thrusting propeller that moves a distance S in time t at a constant velocity, V. The work that the propeller performs during this time is, obviously,

$$\text{work} = TS$$

Power is the rate at which work is performed; hence,

$$\text{power} = T \frac{S}{t}$$

But S/t is equal to the velocity of advance of the propeller. Hence the power available from the propeller is given by

$$P_{\text{avail}} = TV \tag{1.5}$$

Similarly, the power required by a body traveling through the air with a velocity of V and having a drag of D will be

$$P_{\text{req'd}} = DV$$

Thus, returning to Equation 1.4, by multiplying through by WV, we get

$$W(V\theta_c) = P_{\text{avail}} - P_{\text{req'd}} \tag{1.6}$$

The quantity $V\theta_c$ is the vertical rate of climb, V_c. The difference between the power that is required and that available is referred to as the excess power, P_{XS}. Thus Equation 1.6 shows that the vertical rate of climb can be obtained by equating the excess power to the power required to lift the airplane's weight at the rate V_c. In operating an airplane this means the following. A pilot is flying at a given speed in steady, level flight with the engine throttle only partially open. If the pilot advances the throttle while maintaining a

constant airspeed, the power from the engine will then be in excess of that required for level flight, and the airplane will climb.

Suppose, instead of keeping it constant, the pilot, while opening the throttle, allows the airspeed to increase in such a manner as to maintain a constant altitude. When a wide open throttle (WOT) condition is reached the maximum power available is equal to the power required. This is the condition for maximum airspeed, "straight and level."

From this brief introduction into airplane performance, it is obvious that we must be able to estimate the aerodynamic forces on the airplane before we can predict its performance. Also, a knowledge of the characteristics of its power plant-propulsor combination is essential.

In addition to performance, the area of "flying qualities" is very important to the acceptance of an airplane by the customer. Flying qualities refers primarily to stability and control, but it also encompasses airplane response to atmospheric disturbances.

Let us briefly consider the pitching moment M, shown in Figure 1.3. This moment, which must be zero for steady, trimmed flight, results mainly from the lift on the wing and tail. In addition, contributions arise from the fuselage, nacelles, propulsor, and distribution of pressure over the wing. Suppose now that the airplane is trimmed in steady, level flight when it is suddenly disturbed (possibly by a gust or an input from the pilot) such that it pitches up by some amount. Before it can respond, the airplane's path is still essentially horizontal, so that the angle between the velocity vector and the plane's axis is momentarily increased. It will be shown later that, at a given airspeed, the moment, M, is dependent on this angle, defined previously as the angle of attack. Since the moment was initially zero before the airplane was disturbed, it follows that, in general, it will have some value other than zero due to the increase in angle of attack. Suppose this increment in M is positive. In this case the tendency would then be for the angle of attack to increase even further. This is an unstable situation where the airplane, when disturbed, tends to move even further from its steady-state condition. Thus, for the airplane to exhibit a more favorable, stable response, we desire that the increment in M caused by an angle of attack change be negative.

This is about as far as we can go without considering in detail the generation of aerodynamic forces and moments on an airplane and its components. The preceding discussion has shown the importance of being able to predict these quantities from both performance and flying qualities viewpoints. The following chapters will present detailed analytical and experimental material sufficient to determine the performance and stability and control characteristics of an airplane.

As you study the material to follow, keep in mind that it took the early aviation pioneers a lifetime to accumulate only a fraction of the knowledge that is yours to gain with a few months of study.

The primary system of units to be used in this text is the SI (Systems Internationale) system. Since this system is just now being adopted in the United States, a comparison to the English system is presented in Appendix A.1. Also, to assure familiarity with both systems, a limited number of exercises are given in the English system. For a more complete explanation of the SI system, see Reference 1.4.

PROBLEMS

1.1 Calculate the rate of climb of an airplane having a thrust-to-weight ratio of 0.25 and a lift-to-drag ratio of 15.0 at a forward velocity of 70 m/s (230 fps). Express V_c in meters per second. Current practice is to express rate of climb in feet per minute. What would be your answer in these units?

1.2 Which of the systems (ball and track) pictured below are in equilibrium? Which are stable?

1.3 An aircraft weighs 45,000 N (10,117 lb) and requires 397 kW (800 hp) to fly straight and level at a speed of 80 m/s (179 mph). If the available power is 895 kW (1200 hp), how fast will the airplane climb when the throttle is advanced to the wide open position?

1.4 For an aircraft with a high thrust-to-weight ratio, the angle of climb is not necessarily small. In addition, for certain V/STOL aircraft, the thrust vector can be inclined upward significantly with respect to the direction of flight. If this angle is denoted as θ_T, show that

$$\theta_c = \tan^{-1} \frac{T \cos \theta_T - D}{L + T \sin \theta_T}$$

1.5 A student pushes against the side of a building with a force of 6 N for a period of 4 hr. How much work was done?

1.6 An aircraft has a lift-to-drag ratio of 15. It is at an altitude of 1500 m (4921 ft) when the engine fails. An airport is 16 km (9.94 miles) ahead. Will the pilot be able to reach it?

REFERENCES

1.1 McFarland, Marvin W., editor, *The Papers of Wilbur and Orville Wright, Including the Chanute-Wright Letters*, McGraw-Hill, New York, 1953.

1.2 Harris, Sherwood, *The First to Fly, Aviation's Pioneer Days*, Simon and Schuster, New York, 1970.

1.3 Robertson, James M., *Hydrodynamics in Theory and Application*, Prentice-Hall, Englewood Cliffs, N.J., 1965.

1.4 Mechtly, E. A., *The International System of Units, Physical Constants and Conversion Factors*, NASA SP-7012, U.S. Government Printing Office, Washington, D.C., 1969.

1.5 Cleveland, F. A., "Size Effects in Conventional Aircraft Design," *J. of Aircraft*, 7(6), November–December 1970 (33rd Wright Brothers Lecture).

TWO
FLUID MECHANICS

This chapter will stress the principles in fluid mechanics that are especially important to the study of aerodynamics. For the reader whose preparation does not include fluid mechanics, the material in this chapter should be sufficient to understand the developments in succeeding chapters. For a more complete treatment, see any of the many available texts on fluid mechanics (e.g., Refs. 2.1 and 2.2).

Unlike solid mechanics, one normally deals with a continuous medium in the study of fluid mechanics. An airplane in flight does not experience a sudden change in the properties of the air surrounding it. The stream of water from a firehose exerts a steady force on the side of a burning building, unlike the impulse on a swinging bat as it connects with the discrete mass of the baseball.

In solid mechanics, one is concerned with the behavior of a given, finite system of solid masses under the influence of force and moment vectors acting on the system. In fluid mechanics one generally deals not with a finite system, but with the flow of a continuous fluid mass under the influence of distributed pressures and shear stresses.

The term *fluid* should not be confused with the term *liquid*, since the former includes not only the latter, but gases as well. Generally a fluid is defined as any substance that will readily deform under the influence of shearing forces. Thus a fluid is the antonym of a solid. Since both liquids and gases satisfy this definition, they are both known as fluids. A liquid is distinguished from a gas by the fact that the former is nearly incompressible. Unlike a gas, the volume of a given mass of liquid remains nearly constant, independent of the pressure imposed on the mass.

FLUID STATICS AND THE ATMOSPHERE

Before treating the more difficult case of a fluid in motion, let us consider a fluid at rest in static equilibrium. The mass per unit volume of a fluid is defined as the mass density, usually denoted by ρ. The mass density is a

constant for liquids, but it is a function of temperature, T, and pressure, p, for gases. Indeed, for a gas, p, ρ, and T are related by the equation of state

$$p = \rho RT \tag{2.1}$$

R is referred to as the gas constant and has a value of 287.3 $m^2/°K\text{-}sec^2$ for air at normal temperatures. In Equation 2.1, T is the thermodynamic or absolute temperature in degrees Kelvin. T and the Celsius temperature, t, are related by

$$T = t + 273.15 \tag{2.2}$$

A container filled with a liquid is pictured in Figure 2.1*a*. A free-body diagram of a small slug of the fluid is shown in Figure 2.1*b*. This slug has a

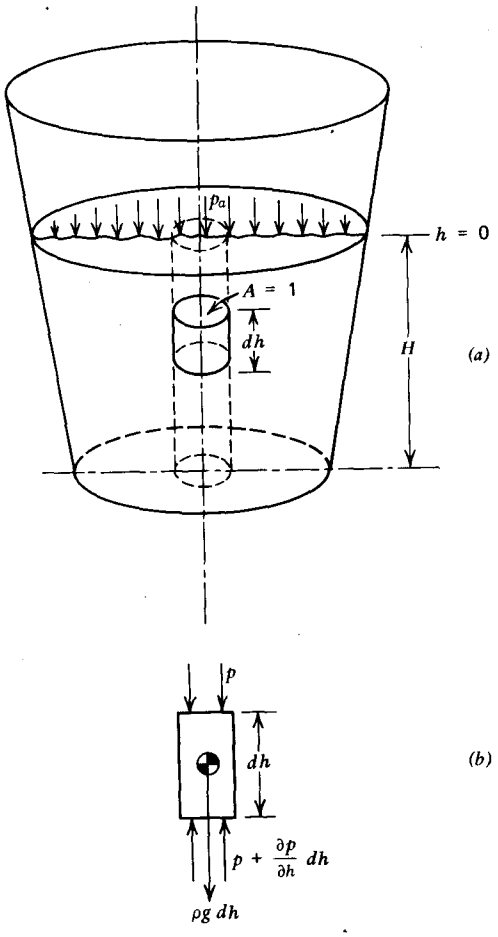

Figure 2.1 The variation of pressure with depth in a liquid.

unit cross-sectional area and a differential length of dh. Acting downward over the upper surface is the static pressure, p, while acting upward over the lower face is this same pressure plus the rate of increase of p with depth multiplied by the change in depth, dh. The static pressure also acts inward around the sides of the element, but this contributes nothing to the balance of forces in the vertical direction. In addition to the pressure forces, the weight of the fluid element, $\rho g\, dh$, acts vertically downward; g is the gravitational constant.

Summing forces on the element in the vertical direction leads to

$$\frac{dp}{dh} = \rho g \tag{2.3}$$

Integrating Equation 2.3 from $h = 0$ at the surface to any depth, h, results in the static pressure as a function of the depth.

$$p = p_a + \rho g h \tag{2.4}$$

where p_a is the atmospheric pressure at the free surface.

A manometer is a device frequently used to measure pressures. It is based on Equation 2.4. Consider the experimental setup pictured in Figure 2.2. Here, a device known as a pitot-static tube is immersed in and aligned with a gas flow. The impact of the gas being brought to rest at the nose of the tube produces a pressure higher than that along the sides of the tube. This pressure, known as the total pressure, is transmitted through a tube to one side of a U-shaped glass tube partially filled with a liquid. Some distance back from the nose of the pitot-static tube the pressure is sampled through a small opening that is flush with the sides of the tube. This opening, if it is far enough back from the nose, does not disturb the flow so that the pressure sampled by it is the same as the static pressure of the undisturbed flow. This static pressure is transmitted to the right side of the glass U-tube manometer. The total pressure, being higher than the static pressure, causes the liquid in the right side of the U-tube to drop while the level on the left side rises.

If we denote p as the static pressure and $p + \Delta p$ as the total pressure, the pressure at the bottom of the U-tube can be calculated by Equation 2.4 using either the right or left side of the tube. Equating the results from the two sides gives

$$p + \Delta p + \rho g h_0 = p + \rho g(\Delta h + h_0)$$

or

$$\Delta p = \rho g\, \Delta h \tag{2.5}$$

Hence, the difference of the liquid levels in the two sides of the manometer is a direct measure of the pressure difference applied across the manometer. In this case we could then determine the difference between the total pressure

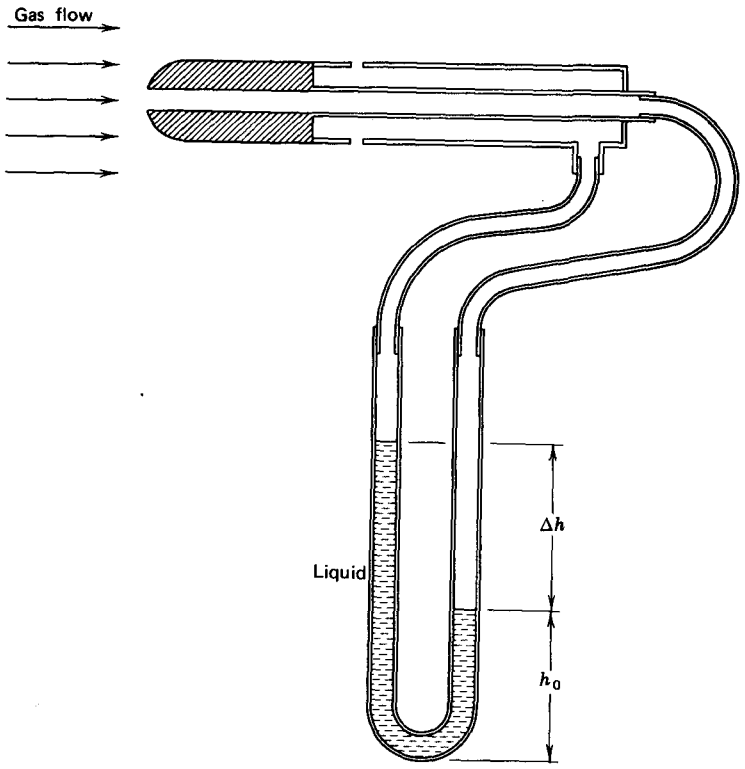

Figure 2.2 Pitot-static tube connected to a U-tube liquid manometer.

and static pressure in the gas flow from which, as we will see later, the velocity of the gas can be calculated.

Now consider the variation of static pressure through the atmosphere. Again the forces acting on a differential mass of gas will be treated in a manner similar to the development of Equation 2.3 for a liquid. However, h will be taken to be the altitude above the ground and, since the gravitational attraction is now opposite to the direction of increasing h, the sign of Equation 2.3 changes. For the atmosphere,

$$\frac{dp}{dh} = -\rho g \tag{2.6}$$

The mass density, ρ, is not a constant in this case, so that Equation 2.6 cannot be integrated immediately. In order to perform the integration the equation of state, Equation 2.1, is substituted for ρ, which leads to

$$\frac{dp}{p} = -\frac{g\,dh}{RT} \tag{2.7}$$

From experimental observation, the variation of temperature with altitude is known or, at least, a standard variation has been agreed on. Up to an altitude of 11 km, the temperature is taken to decrease linearly with altitude at a rate, known as the lapse rate, of 6.51 °C/km. Thus, Equation 2.7 becomes

$$\frac{dp}{p} = -\frac{dT}{T}\frac{g}{R(dT/dh)}$$

or

$$\delta = \theta^{5.2561} \tag{2.8}$$

where δ is the ratio of the static pressure at altitude to the pressure at sea level and θ is the corresponding absolute temperature ratio.

Using the equation of state, the corresponding density ratio, σ, is obtained immediately from Equation 2.8.

$$\sigma = \frac{\delta}{\theta}$$

or

$$\sigma = \theta^{4.2561} \tag{2.9}$$

Using the standard lapse rate and a sea level temperature of 288.15 °K, θ as a function of altitude is given by

$$\theta = 1 - 0.02256\,h \tag{2.10}$$

where h is the altitude in kilometers.

The lower region of the atmosphere up to an altitude for which Equations 2.8 to 2.10 hold is referred to as the troposphere. This is the region in which most of today's flying is done. Above 11 km and up to an altitude of approximately 23 km, the temperature is nearly constant. This region forms the lower part of the stratosphere. Through the remainder of the stratosphere, the temperature increases, reaching approximately 270 °K at an altitude of around 50 km.

Figure 2.3 presents graphs (taken from Ref. 2.3) of the various properties of the standard atmosphere as a function of altitude. Each property is presented as a ratio to its standard sea level value denoted by the subscript "0." In addition to p, ρ, and T, the acoustic velocity and kinematic viscosity are presented. These two properties will be defined later.

One normally thinks of altitude as the vertical distance of an airplane above the earth's surface. However, the operation of an airplane depends on the properties of the air through which it is flying, not on the geometric height. Thus the altitude is frequently specified in terms of the *standard atmosphere.* Specifically, one refers to the *pressure altitude* or the *density altitude* as the height in the standard atmosphere corresponding to the pressure or density, respectively, of the atmosphere in which the airplane is operating. An airplane's altimeter is simply an absolute pressure gage calibrated according to

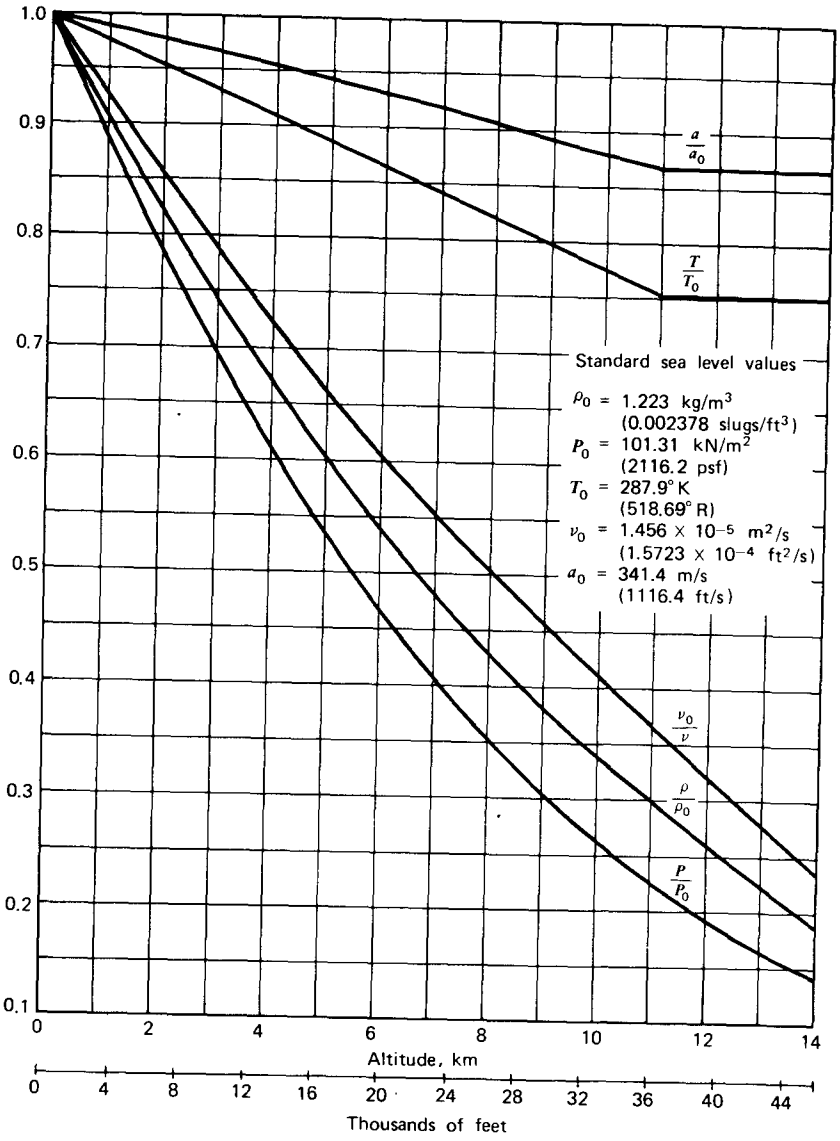

Figure 2.3 The standard atmosphere.

the standard atmosphere. It has a manual adjustment to allow for variations in sea level barometric pressure. When set to standard sea level pressure (760 mm Hg, 29.92 in. Hg), assuming the instrument and static pressure source to be free of errors, the altimeter will read the pressure altitude. When set to the local sea level barometric pressure (which the pilot can obtain over the

radio while in flight), the altimeter will read closely the true altitude above sea level. A pilot must refer to a chart prescribing the ground elevation above sea level in order to determine the height above the ground.

FLUID DYNAMICS

We will now treat a fluid that is moving so that, in addition to gravitational forces, inertial and shearing forces must be considered.

A typical flow around a streamlined shape is pictured in Figure 2.4. Note that this figure is labled "two-dimensional flow"; this means simply that the flow field is a function only of two coordinates (x and y, in the case of Figure 2.4) and does not depend on the third coordinate. For example, the flow of wind around a tall, cylindrical smokestack is essentially two-dimensional except near the top. Here the wind goes over as well as around the stack, and the flow is three-dimensional. As another example, Figure 2.4 might represent the flow around a long, streamlined strut such as the one that supports the wing of a high-wing airplane. The three-dimensional counterpart of this shape might be the blimp.

Several features of flow around a body in general are noted in Figure 2.4. First, observe that the flow is illustrated by means of streamlines. A streamline is an imaginary line characterizing the flow such that, at every point along the line, the velocity vector is tangent to the line. Thus, in two-dimensional

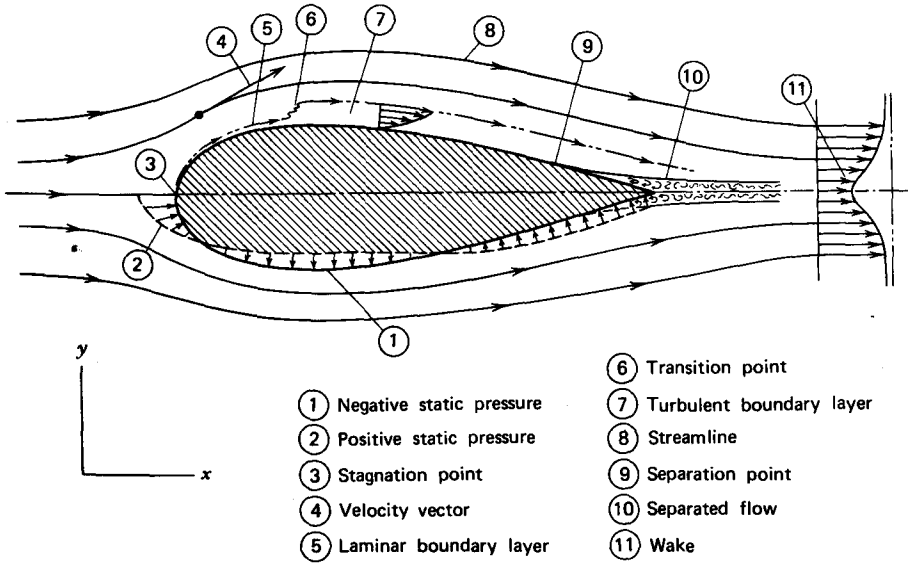

Figure 2.4 Two-dimensional flow around a streamlined shape.

flow, if $y(x)$ defines the position of a streamline, $y(x)$ is related to the x and y components of the velocity, $u(x)$ and $v(x)$, by

$$\frac{dy}{dx} = \frac{v(x)}{u(x)} \tag{2.11}$$

Note that the body surface itself is a streamline.

In three-dimensional flow a surface swept by streamlines is known as a stream surface. If such a surface is closed, it is known as a stream tube.

The mass flow accelerates around the body as the result of a continuous distribution of pressure exerted on the fluid by the body. An equal and opposite reaction must occur on the body. This static pressure distribution, acting everywhere normal to the body's surface, is pictured on the lower half of the body in Figure 2.4. The small arrows represent the local static pressure, p, relative to the static pressure, p_0, in the fluid far removed from the body. Near the nose p is greater than p_0; further aft the pressure becomes negative relative to p_0. If this static pressure distribution, acting normal to the surface, is known, forces on the body can be determined by integrating this pressure over its surface.

In addition to the local static pressure, shearing stresses resulting from the fluid's viscosity also give rise to body forces. As fluid passes over a solid surface, the fluid particles immediately in contact with the surface are brought to rest. Moving away from the surface, successive layers of fluid are slowed by the shearing stresses produced by the inner layers. (The term "layers" is used only as a convenience in describing the fluid behavior. The fluid shears in a continuous manner and not in discrete layers.) The result is a thin layer of slower moving fluid, known as the boundary layer, adjacent to the surface. Near the front of the body this layer is very thin, and the flow within it is smooth without any random or turbulent fluctuations. Here the fluid particles might be described as moving along in the layer on parallel planes, or laminae; hence the flow is referred to as laminar.

At some distance back from the nose of the body, disturbances to the flow (e.g., from surface roughnesses) are no longer damped out. These disturbances suddenly amplify, and the laminar boundary layer undergoes transition to a turbulent boundary layer. This layer is considerably thicker than the laminar one and is characterized by a mean velocity profile on which small, randomly fluctuating velocity components are superimposed. These flow regions are shown in Figure 2.4. The boundary layers are pictured considerably thicker than they actually are for purposes of illustration. For example, on the wing of an airplane flying at 100 m/s at low altitude, the turbulent boundary 1.0 m back from the leading edge would be only approximately 1.6 cm thick. If the layer were still laminar at this point, its thickness would be approximately 0.2 cm.

Returning to Figure 2.4, the turbulent boundary layer continues to thicken toward the rear of the body. Over this portion of the surface the fluid

is moving into a region of increasing static pressure that is tending to oppose the flow. The slower moving fluid in the boundary layer may be unable to overcome this adverse pressure gradient, so that at some point the flow actually separates from the body surface. Downstream of this separation point, reverse flow will be found along the surface with the static pressure nearly constant and equal to that at the point of separation.

At some distance downstream of the body the separated flow closes, and a wake is formed. Here, a velocity deficiency representing a momentum loss by the fluid is found near the center of the wake. This decrement of momentum (more precisely, momentum flux) is a direct measure of the body drag (i.e., the force on the body in the direction of the free-stream velocity).

The general flow pattern described thus far can vary, depending on the size and shape of the body, the magnitude of the free-stream velocity, and the properties of the fluid. Variations in these parameters can eliminate transition or separation or both.

One might reasonably assume that the forces on a body moving through a fluid depend in some way on the mass density of the fluid, ρ, the size of the body, l, and the body's velocity, V. If we assume that any one force, F, is proportional to the product of these parameters each raised to an unknown power, then

$$F \propto \rho^a V^b l^c$$

In order for the basic units of mass, length, and time to be consistent, it follows that

$$\frac{ML}{T^2} = \left(\frac{M}{L^3}\right)^a \left(\frac{L}{T}\right)^b L^c$$

Considering M, L, and T in order leads to three equations for the unknown exponents a, b, and c from which it is found that $a = 1$, $b = 2$, and $c = 2$. Hence,

$$F \propto \rho V^2 l^2 \tag{2.12}$$

For a particular force the constant of proportionality in Equation 2.12 is referred to as a coefficient and is modified by the name of the force, for example, the lift coefficient. Thus the lift and drag forces, L and D, can be expressed as

$$L = \tfrac{1}{2}\rho V^2 S C_L \tag{2.13a}$$

$$D = \tfrac{1}{2}\rho V^2 S C_D \tag{2.13b}$$

Note that the square of the characteristic length, l^2, has been replaced by a reference area, S. Also, a factor of 1/2 has been introduced. This can be done, since the lift and drag coefficients, C_L and C_D, are arbitrary at this point. The quantity $\rho V^2/2$ is referred to as the dynamic pressure, the significance of which will be made clear shortly.

For many applications, the coefficients C_L and C_D remain constant for a given geometric shape over a wide range of operating conditions or body size. For example, a two-dimensional airfoil at a 1° angle of attack will have a lift coefficient of approximately 0.1 for velocities from a few meters per second up to 100 m/s or more. In addition, C_L will be almost independent of the size of the airfoil. However, a more rigorous application of dimensional analysis [see Buckingham's π theorem (Ref. 2.1)] will result in the constant of proportionality in Equation 2.12 possibly being dependent on a number of dimensionless parameters. Two of the most important of these are known as the Reynolds number, R, and the Mach number, M, defined by,

$$R = \frac{Vl\rho}{\mu} \tag{2.14a}$$

$$M = \frac{V}{a} \tag{2.14b}$$

where l is a characteristic length, V is the free-stream velocity, μ is the coefficient of viscosity, and a is the velocity of sound. The velocity of sound is the speed at which a small pressure disturbance is propagated through the fluid; at this point, it requires no further explanation. The coefficient of viscosity, however, is not as well known and will be elaborated on by reference to Figure 2.5. Here, the velocity profile is pictured in the boundary layer of a laminar, viscous flow over a surface. The viscous shearing produces a shearing stress of τ_w on the wall. This force per unit area is related to the gradient of the velocity $u(y)$ at the wall by

$$\tau_w = \mu \left(\frac{du}{dy}\right)_{y=0} \tag{2.15}$$

Actually, Equation 2.15 is applicable to calculating the shear stresses between fluid elements and is not restricted simply to the wall. Generally, the viscous shearing stress in the fluid in any plane parallel to the flow and away

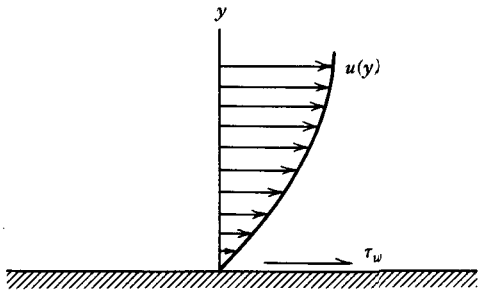

Figure 2.5 Viscous flow adjacent to a surface.

from the wall is given by the product of μ and the velocity gradient normal to the direction of flow.

The kinematic viscosity, ν, is defined as the ratio of μ to ρ.

$$\nu = \frac{\mu}{\rho}$$

ν is defined as a matter of convenience, since it is the ratio of μ to ρ that governs the Reynolds number. The kinematic viscosity for the standard atmosphere is included in Figure 2.3 as an *inverse fraction* of the standard sea level value.

A physical significance can be given to the Reynolds number by multiplying numerator and denominator by V and dividing by l.

$$R = \frac{\rho V^2}{(\mu V/l)}$$

In the following material (see Equation 2.28) the normal pressure will be shown to be proportional to ρV^2 whereas, from Equation 2.15, $\mu V/l$ is proportional to the shearing stress. Hence for a given flow the Reynolds number is proportional to the ratio of normal pressures (inertia forces) to viscous shearing stresses. Thus, relatively speaking, a flow is less viscous than another flow if its Reynolds number is higher than that of the second flow.

The Mach number determines to what extent fluid compressibility can be neglected (i.e., the variation of mass density with pressure). Current jet transports, for example, can cruise at Mach numbers up to approximately 0.8 before significant compressibility effects are encountered.

At lower Mach numbers, two flows are geometrically and dynamically similar if the Reynolds numbers are the same for both flows. Hence, for example, for a given shape, C_D for a body 10 m long at 100 m/s will be the same as C_D for a 100-m long body at 10 m/s. As another example, suppose transition occurs 2 m back from the leading edge of a flat plate aligned with a flow having a velocity of 50 m/s. Then, at 25 m/s transition would occur at a distance of 4 m from the leading edge. Obviously the effects of R and M on dimensionless aerodynamic coefficients must be considered when interpreting test results obtained with the use of small models.

For many cases of interest to aerodynamics the pressure field around a shape can be calculated assuming the air to be inviscid and incompressible. Small corrections can then be made to the resulting solutions to account for these "real fluid" effects. Corrections for viscosity or compressibility will be considered as needed in the following chapters.

Conservation of Mass

Fluid passing through an area at a velocity of V has a mass flow rate equal to ρAV. This is easily seen by reference to Figure 2.6. Here flow is

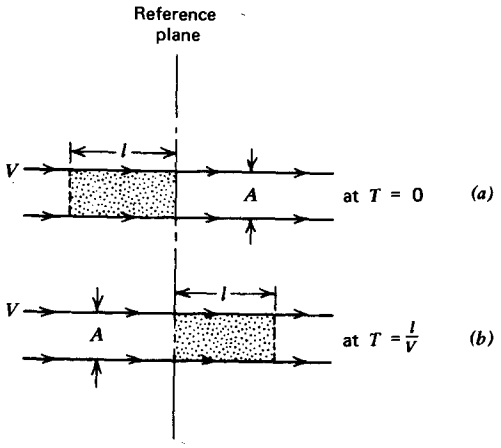

Figure 2.6 Mass flow through a surface.

pictured along a streamtube of cross-sectional area A. The fluid velocity is equal to V. At time $t = 0$, picture a small slug of fluid of length, l, about to cross a reference plane. At time l/V, this entire slug will have passed through the reference plane. The volume of the slug is Al, so that a mass of ρAl was transported across the reference plane during the time l/V. Hence the mass rate of flow, m, is given by

$$m = \frac{\rho Al}{(l/V)}$$
$$= \rho AV \tag{2.16}$$

Along a streamtube (which may be a conduit with solid walls) the quantity ρAV must be a constant if mass is not to accumulate in the system. For incompressible flow, ρ is a constant, so that the conservation of mass leads to the continuity principle

$$AV = \text{constant}$$

AV is the volume flow rate and is sometimes referred to as the flux. Similarly, ρAV is the mass flux. The mass flux through a surface multiplied by the velocity vector at the surface is defined as the momentum flux. Generally, if the velocity vector is not normal to the surface, the mass flux will be

$$\rho A\mathbf{V} \cdot \mathbf{n}$$

with the momentum flux written as

$$(\rho A\mathbf{V} \cdot \mathbf{n})\mathbf{V}$$

here $\mathbf{n}$ is the unit vector normal to the surface and in the direction in which the flux is defined to be positive. For example, if the surface encloses a volume and the net mass flux out of the volume is to be calculated, $\mathbf{n}$ would

be directed outward from the volume, and the following integral would be evaluated over the entire surface.

$$\int_S \int \rho \mathbf{V} \cdot \mathbf{n}\, dS$$

Consider the conservation of mass applied to a differential control surface. For simplicity, a two-dimensional flow will be treated. A rectangular contour is shown in Figure 2.7. The flow passing through this element has velocity components of u and v in the center of the element in the x and y directions, respectively. The corresponding components on the right face of the element are found by expanding them in a Taylor series in x and y and dropping second-order and higher terms in Δx. Hence the mass flux out through the right face will be

$$\left[\rho u + \frac{\partial(\rho u)}{\partial x}\frac{\Delta x}{2}\right]\Delta y$$

Writing similar expressions for the other three faces leads to the net mass flux out being

$$\left[\frac{\partial(\rho u)}{\partial x} + \frac{\partial(\rho v)}{\partial y}\right]\Delta x\, \Delta y$$

The net mass flux out of the differential element must equal the rate at which the mass of the fluid contained within the element is decreasing, given by

$$-\frac{\partial}{\partial t}(\rho\, \Delta x\, \Delta y)$$

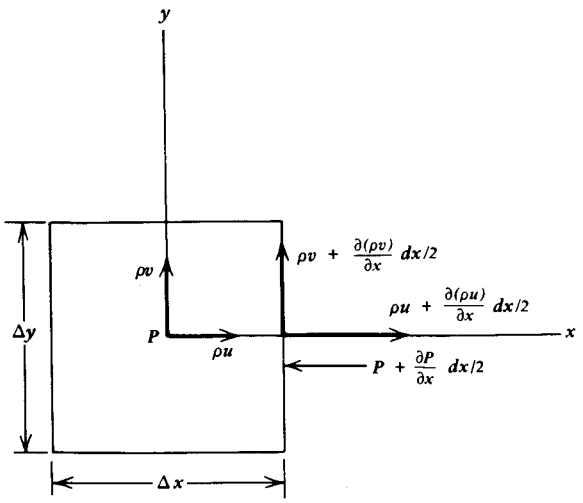

Figure 2.7 A rectangular differential control surface.

Since Δx and Δy are arbitrary, it follows that, in general,

$$\frac{\partial \rho}{\partial t} + \frac{\partial (\rho u)}{\partial x} + \frac{\partial (\rho v)}{\partial y} = 0$$

In three dimensions the preceding equation can be written in vector notation as

$$\frac{\partial \rho}{\partial t} + \nabla \cdot (\rho \mathbf{V}) = 0 \tag{2.17}$$

where ∇ is the vector operator, del, defined by

$$\nabla = \mathbf{i}\frac{\partial}{\partial x} + \mathbf{j}\frac{\partial}{\partial y} + \mathbf{k}\frac{\partial}{\partial z}$$

Any physically possible flow must satisfy Equation 2.17 at every point in the flow.

For an incompressible flow, the mass density is a constant, so Equation 2.17 reduces to

$$\nabla \cdot \mathbf{V} = 0 \tag{2.18}$$

The above is known as the divergence of the velocity vector, div **V**.

The Momentum Theorem

The momentum theorem in fluid mechanics is the counterpart of Newton's second law of motion in solid mechanics, which states that a force imposed on a system produces a rate of change in the momentum of the system. The theorem can be easily derived by treating the fluid as a collection of fluid particles and applying the second law. The details of the derivation can be found in several texts (e.g., Ref. 2.1) and will not be repeated here.

Defining a control surface as an imaginary closed surface through which a flow is passing, the momentum theorem states:

"*The sum of external forces (or moments) acting on a control surface and internal forces (or moments) acting on the fluid within the control surface produces a change in the flux of momentum (or angular momentum) through the surface and an instantaneous rate of change of momentum (or angular momentum) of the fluid particles within the control surface.*"

Mathematically, for linear motion of an inviscid fluid, the theorem can be expressed in vector notation by

$$-\int_S \int p\mathbf{n}\, dS + \mathbf{B} = \int_S \int \rho \mathbf{V}(\mathbf{V} \cdot \mathbf{n})\, dS + \frac{\partial}{\partial t} \int \int_V \int \rho \mathbf{V}\, d\tau \tag{2.19}$$

In Equation 2.19, **n** is the unit normal directed outward from the surface,

S, enclosing the volume, V. $\mathbf{V}$ is the velocity vector, which generally depends on position and time. $\mathbf{B}$ represents the vector sum of all body forces within the control surface *acting on the fluid.* ρ is the mass density of the fluid defined as the mass per unit volume.

For the angular momentum,

$$\mathbf{Q} = \int_S \int \rho(\mathbf{V} \times \mathbf{r})(\mathbf{V} \cdot \mathbf{n})\, dS + \frac{\partial}{\partial t} \int_V \int \int \rho(\mathbf{V} \times \mathbf{r})\, d\tau \tag{2.20}$$

Here, $\mathbf{Q}$ is the vector sum of all moments, both internal and external, acting on the control surface or the fluid within the surface. $\mathbf{r}$ is the radius vector to a fluid particle.

As an example of the use of the momentum theorem, consider the force on the burning building produced by the firehose mentioned at the beginning of this chapter. Figure 2.8 illustrates a possible flow pattern, admittedly simplified. Suppose the nozzle has a diameter of 10 cm and water is issuing from the nozzle with a velocity of 60 m/s. The mass density of water is approximately 1000 kg/m^3. The control surface is shown dotted. Equation 2.19 will now be written for this system in the x direction. Since the flow is steady, the partial derivative with respect to time of the volume integral given by the last term on the right side of the equation vanishes. Also, $\mathbf{B}$ is zero, since the control surface does not enclose any

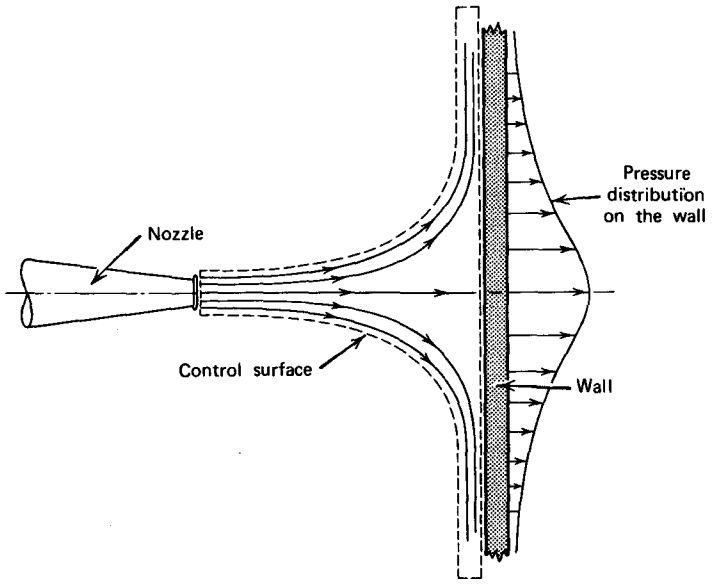

Figure 2.8 A jet of water impacting on a wall.

bodies. Thus Equation 2.19 becomes

$$-\int_S \int p\mathbf{n}\, dS = \int_S \int \rho \mathbf{V}(\mathbf{V}\cdot\mathbf{n})\, dS$$

Measuring p relative to the atmospheric static pressure, p is zero everywhere along the control surface except at the wall. Here $\mathbf{n}$ is directed to the right so that the surface integral on the left becomes the total force exerted on the fluid by the pressure on the wall. If F represents the magnitude of the total force on the wall,

$$-\mathbf{i}F = \int_S \int \rho \mathbf{V}(\mathbf{V}\cdot\mathbf{n})\, dS$$

For the fluid entering the control surface on the left,

$$\mathbf{V} = 60\mathbf{i}$$
$$\mathbf{n} = -\mathbf{i}$$

For the fluid leaving the control surface, the unit normal to this cylindrical surface has no component in the x direction. Hence,

$$-\mathbf{i}F = -\int_S \int (1000)60\mathbf{i}(-60)\, dS$$
$$= -36\times 10^5 \mathbf{i} \int_S \int dS$$

The surface integral reduces to the nozzle area of $7.85\times 10^{-3}\,\mathrm{m}^2$. Thus, without actually determining the pressure distribution on the wall, the total force on the wall is found from the momentum theorem to equal 28.3 kN.

Euler's Equation of Motion

The principle of conservation of mass, applied to an elemental control surface, led to Equation 2.17, which must be satisfied everywhere in the flow. Similarly, the momentum theorem applied to the same element leads to another set of equations that must hold everywhere.

Referring again to Figure 2.7, if p is the static pressure at the center of the element then, on the center of the right face, the static pressure will be

$$p + \frac{\partial p}{\partial x}\frac{\Delta x}{2}$$

This pressure and a similar pressure on the left face produce a net force in the x direction equal to

$$-\frac{\partial p}{\partial x}\Delta x\, \Delta y$$

Since there are no body forces present and the fluid is assumed inviscid, the above force must equal the net momentum flux out plus the instantaneous change of fluid momentum contained within the element.

The momentum flux out of the right face in the x direction will be

$$\left[\rho u + \frac{\partial(\rho u)}{\partial x}\frac{\Delta x}{2}\right]\left(u + \frac{\partial u}{\partial x}\frac{\Delta x}{2}\right)\Delta y$$

Out of the upper face the corresponding momentum flux will be

$$\left[\rho v + \frac{\partial(\rho v)}{\partial y}\frac{\Delta y}{2}\right]\left(u + \frac{\partial u}{\partial y}\frac{\Delta y}{2}\right)\Delta x$$

Similar expressions can be written for the momentum flux in through the left and bottom faces.

The instantaneous change of the fluid momentum contained within the element in the x direction is simply

$$\frac{\partial}{\partial t}(\rho u\,\Delta x\,\Delta y)$$

Thus, equating the net forces in the x direction to the change in momentum and momentum flux and using Equation 2.17 leads to

$$\frac{\partial u}{\partial t} + u\frac{\partial u}{\partial x} + v\frac{\partial u}{\partial y} = -\frac{1}{\rho}\frac{\partial p}{\partial x} \tag{2.21}$$

Generalizing this to three dimensions results in a set of equations known as Euler's equations of motion.

$$\frac{\partial u}{\partial t} + u\frac{\partial u}{\partial x} + v\frac{\partial u}{\partial y} + w\frac{\partial u}{\partial z} = -\frac{1}{\rho}\frac{\partial p}{\partial x} \tag{2.22a}$$

$$\frac{\partial v}{\partial t} + u\frac{\partial v}{\partial x} + v\frac{\partial v}{\partial y} + w\frac{\partial v}{\partial z} = -\frac{1}{\rho}\frac{\partial p}{\partial y} \tag{2.22b}$$

$$\frac{\partial w}{\partial t} + u\frac{\partial w}{\partial x} + v\frac{\partial w}{\partial y} + w\frac{\partial w}{\partial z} = -\frac{1}{\rho}\frac{\partial p}{\partial z} \tag{2.22c}$$

Notice that if u is written as $u(x, y, z, t)$, the left side of Equation 2.22 is the total derivative of u. The operator, $\partial(\ )/\partial t$, is the local acceleration and exists only if the flow is unsteady.

In vector notation Euler's equation can be written

$$\frac{\partial \mathbf{V}}{\partial t} + (\mathbf{V}\cdot\nabla)\mathbf{V} = -\frac{1}{\rho}\nabla p \tag{2.23}$$

If the vector product of the operator ∇ is taken with each term in Equation 2.23, Equation 2.24 results.

$$\frac{\partial \boldsymbol{\omega}}{\partial t} + (\mathbf{V} \cdot \nabla)\boldsymbol{\omega} = 0 \tag{2.24}$$

$\boldsymbol{\omega}$ is the curl of the velocity vector, $\nabla \times \mathbf{V}$, and is known as the vorticity.

$$\nabla \times \mathbf{V} = \begin{vmatrix} \mathbf{i} & \mathbf{j} & \mathbf{k} \\ \dfrac{\partial}{\partial x} & \dfrac{\partial}{\partial y} & \dfrac{\partial}{\partial z} \\ u & v & w \end{vmatrix} \tag{2.25}$$

One can conclude from Equation 2.24 that, for an inviscid fluid, the vorticity is constant along a streamline. Since, far removed from a body, the flow is usually taken to be uniform, the vorticity at that location is zero; hence, it is zero everywhere.

Bernoulli's Equation

Bernoulli's equation is well known in fluid mechanics and relates the pressure to the velocity *along a streamline* in an inviscid, incompressible flow. It was first formulated by Euler in the middle 1700s. The derivation of this equation follows from Euler's equations using the fact that along a streamline the velocity vector is tangential to the streamline.

$$\frac{dx}{u} = \frac{dy}{v} = \frac{dz}{w} \tag{2.26}$$

First, multiply Equation 2.22*a* through by dx and then substitute Equation 2.26 for $v\,dx$ and $w\,dx$. Also, the first term of the equation will be set equal to zero; that is, at this time only steady flow will be considered.

$$u\frac{\partial u}{\partial x}dx + u\frac{\partial u}{\partial y}dy + u\frac{\partial u}{\partial z}dz = -\frac{1}{\rho}\frac{\partial p}{\partial x}dx$$

Similarly, multiply Equation 2.22*b* by dy, Equation 2.22*c* by dz, and substitute Equation 2.26 for $u\,dy$, $w\,dy$ and $u\,dz$, $v\,dz$, respectively. Adding the three equations results in perfect differentials for p and V^2, V being the magnitude of the resultant velocity along the streamline. This last term results from the fact that

$$u\frac{\partial u}{\partial x} = \frac{1}{2}\frac{\partial u^2}{\partial x}$$

and

$$V^2 = u^2 + v^2 + w^2$$

Thus, along a streamline, Euler's equations become

$$V\,dV + \frac{dp}{\rho} = 0 \tag{2.27}$$

If ρ is not a function of p (i.e., the flow is incompressible), Equation 2.27 can be integrated immediately to give

$$p + \tfrac{1}{2}\rho V^2 = \text{constant} \tag{2.28}$$

If the flow is uniform at infinity, Equation 2.28 becomes

$$p + \tfrac{1}{2}\rho V^2 = \text{constant} = p_\infty + \tfrac{1}{2}\rho V_\infty^2 \tag{2.29}$$

Here V is the magnitude of the local velocity and p is the local static pressure. V_∞ and p_∞ are the corresponding free-stream values. Equation 2.29 is known as Bernoulli's equation.

The counterpart to Equation 2.29 for compressible flow is obtained by assuming pressure and density changes to follow an isentropic process. For such a process,

$$p/\rho^\gamma = \text{constant} \tag{2.30}$$

γ is the ratio of the specific heat at constant pressure to the specific heat at constant volume and is equal approximately to 1.4 for air. Substituting Equation 2.30 into Equation 2.27 and integrating leads to an equation sometimes referred to as the compressible Bernoulli's equation.

$$\frac{V^2}{2} + \frac{\gamma}{\gamma - 1}\frac{p}{\rho} = \text{constant} \tag{2.31}$$

This equation can be written in terms of the acoustic velocity. First it is necessary to derive the acoustic velocity, which can be done by the use of the momentum theorem and continuity. Figure 2.9 assumes the possibility of a stationary disturbance in a steady flow across which the pressure, density, and velocity change by small increments. In the absence of body forces and viscosity, the momentum theorem gives

$$-dp = (\rho + d\rho)(u + du)^2 - \rho u^2$$

But, from continuity,

$$(\rho + d\rho)(u + du) = \rho u$$

or

$$u\,d\rho = -\rho\,du$$

Thus

$$u^2 = \frac{dp}{d\rho} \tag{2.32}$$

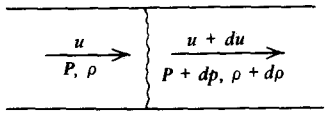

Figure 2.9 A stationary small disturbance in a steady compressible flow.

If the small disturbance is stationary in the steady flow having a velocity of u, then obviously u is the velocity of the disturbance relative to the fluid. By definition, it follows that u, given by Equation 2.32, is the acoustic velocity.

By the use of Equation 2.30, the acoustic velocity is obtained as

$$a = \left(\frac{\gamma p}{\rho}\right)^{1/2} \tag{2.33}$$

An alternate form, using the equation of state (Equation 2.1), is

$$a = (\gamma RT)^{1/2} \tag{2.34}$$

Thus Equation 2.31 can be written

$$\frac{V^2}{2} + \frac{a^2}{\gamma - 1} = \text{constant} \tag{2.35}$$

The acoustic velocity is also included in Figure 2.3 for the standard atmosphere.

Determination of Free-Stream Velocity

At low speeds (compared to the acoustic velocity) a gas flow is essentially incompressible. In this case, and for that of a liquid, Equation 2.29 applies. If the fluid is brought to rest so that the local velocity is zero then, from Equation 2.29, the local pressure, referred to in this case as the stagnation or total pressure, is equal to the sum of the free-stream static pressure, p_∞, and $\rho V_\infty^2/2$. This latter term is called the dynamic pressure and is frequently denoted by the symbol q. Thus,

$$V_\infty = \left[\frac{2(p_0 - p_\infty)}{\rho}\right]^{1/2} \tag{2.36}$$

where p_0 is the total pressure, also referred to as the stagnation or reservoir pressure. The pitot-static tube shown in Figure 2.2 measures $(p_0 - p_\infty)$ and is probably the most common means used to determine airspeed. However, notice that Equation 2.36 contains the mass density that must be determined before the airspeed can be calculated. This is most readily achieved by measuring, in addition to the difference between the stagnation pressure and the static pressure, the static pressure itself and the temperature. The density is then determined from the equation of state (Equation 2.1).

At higher speeds (and we will now examine what is high) Equation 2.29 no longer holds, so that V_∞ must be determined from Equation 2.31.

$$\frac{V^2}{2} + \frac{\gamma}{\gamma - 1}\frac{p}{\rho} = \frac{\gamma}{\gamma - 1}\frac{p_0}{\rho_0}$$

At this point the subscript ∞ has been dropped, so that p, ρ, and V without a subscript may be local or free-stream values.

Remembering that $\gamma p/\rho$ is the square of the acoustic velocity, the preceding equation becomes

$$\frac{M^2}{2}+\frac{1}{\gamma-1}=\frac{1}{\gamma-1}\frac{p_0}{p}\frac{\rho}{\rho_0}$$

Using Equation 2.30, this can be written as

$$\frac{p_0}{p}=\left[1+\frac{\gamma-1}{2}M^2\right]^{\gamma/(\gamma-1)} \tag{2.37}$$

The dynamic pressure, q, is defined as

$$q=\tfrac{1}{2}\rho V^2 \tag{2.38}$$

which can be written in terms of the Mach number as

$$q=\tfrac{1}{2}\gamma p M^2$$

Combining this with Equation 2.37 gives

$$\frac{p_0-p}{q}=\frac{2}{\gamma M^2}\left[\left(1+\frac{\gamma-1}{2}M^2\right)^{\gamma/(\gamma-1)}-1\right] \tag{2.39}$$

The square root of Equation 2.39 is presented graphically in Figure 2.10. The departure of this function from unity is a measure of the error to be incurred in calculating the airspeed from the incompressible Bernoulli equation. Below a Mach number of 0.5 the error is seen to be less than 3%.

Determination of True Airspeed

During training, a pilot soon learns that the airspeed that appears on the airspeed indicator is not the true airspeed. Instead, in order to determine the true airspeed, the pilot must also read the altimeter and outside air temperature. The pilot then resorts to a small hand calculator or, in some instances, adjusts the dial on the airspeed indicator accordingly to allow for the atmospheric properties.

The airspeed indicator is nothing more than an accurate differential pressure gage calibrated according to Equation 2.31. This equation can be put in the form

$$V^2=\frac{2a^2}{\gamma-1}\left[\left(\frac{p_0-p}{p}+1\right)^{(\gamma-1)/\gamma}-1\right]$$

The airspeed indicator measures the difference, p_0-p (sometimes called the compressible dynamic pressure), but then is calibrated to obtain V by assuming standard sea level values for the acoustic velocity and the free-

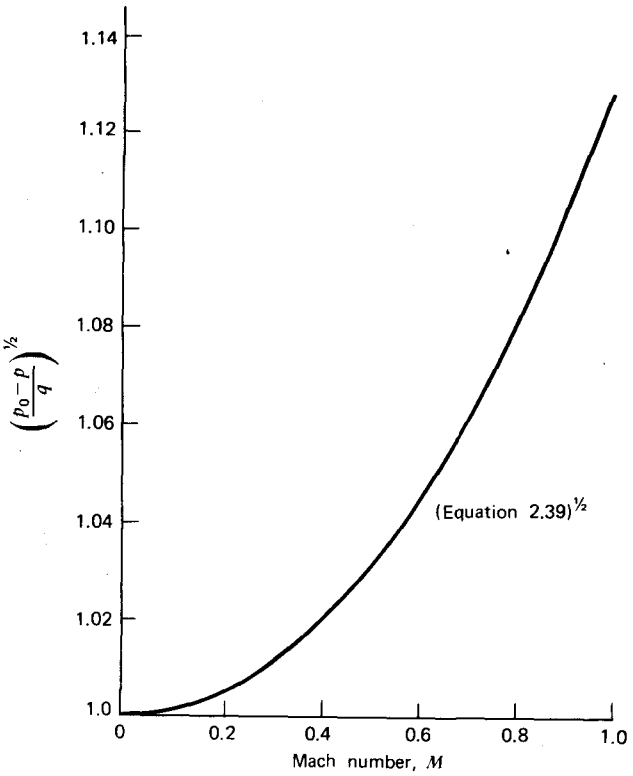

Figure 2.10 Relationship between reservoir pressure and dynamic pressure as a function of Mach number.

stream static pressure. Thus the calibrated airspeed is defined by

$$v_{cal} = \left[\frac{2a_{SL}^2}{(\gamma-1)}\left[\left(\frac{p_0-p}{p_{SL}}+1\right)^{(\gamma-1)/\gamma}-1\right]\right]^{1/2} \tag{2.40}$$

where a subscript SL is used to denote standard sea level values.

As a ratio to V_{cal}, the true airspeed can be written

$$\frac{V}{V_{cal}} = \left\{\theta\left[\frac{[f(V_{cal})/\delta+1]^{(\gamma-1)/\gamma}-1}{[f(V_{cal})+1]^{(\gamma-1)/\gamma}-1}\right]\right\}^{1/2} \tag{2.41}$$

where

$$\frac{p_0-p}{P_{SL}} = f(V_{cal})$$

and can be obtained from Equation 2.40. θ and δ are the temperature and pressure ratios, respectively.

If compressibility can be neglected, the airspeed will be given by Equa-

tion 2.36. In this case, using the standard sea level value of ρ to calibrate the airspeed indicator dial leads to the equivalent airspeed.

$$V_e = \left[\frac{2(p_0 - p)}{\rho_{SL}}\right]^{1/2}$$

or

$$\frac{V}{V_e} = \sigma^{-1/2} \tag{2.42}$$

where σ is the density ratio.

Finally, the indicated airspeed, V_i, is defined simply as the airspeed that the pilot reads from the airspeed indicator. If the indicator has no mechanical error (*instrument error*) and if the static source is located so that it samples the true free-stream static pressure (otherwise a *position* error incurs), $V_i = V_{cal}$. Furthermore, if the Mach number is not too high, $V_i = V_{cal} = V_e$.

As an example in determining true airspeed, suppose a pilot reads an indicated airspeed of 180 m/s for an OAT of 239 °K and an altimeter reading of 6000 m. This altitude, according to Equations 2.8 and 2.10, corresponds to a pressure ratio δ of 0.466. The measured temperature ratio, θ, is equal to 0.826. Hence $\sigma = 0.564$. According to Equation 2.42, the true airspeed will be 239.7 m/s. From Equation 2.41, the true airspeed is calculated to be 231.6 m/s. Thus, using the incompressible relationship to estimate the true airspeed from the indicated airspeed results in a speed a few percent higher than that obtained from the calibrated airspeed relationship.

To be precise one calculates the true airspeed from the calibrated airspeed and then determines the equivalent airspeed from its definition, Equation 2.42. In the previous example, this results in a V_e of 173.9 m/s, a value 3.4% less than the calibrated airspeed.

POTENTIAL FLOW

For a steady, inviscid, incompressible flow, Euler's equations of fluid motion reduce to two relatively simple relationships that govern the velocity vector.

$$\text{div } \mathbf{V} = \nabla \cdot \mathbf{V} = 0 \tag{2.43a}$$

$$\text{curl } \mathbf{V} = \nabla \times \mathbf{V} = 0 \tag{2.43b}$$

The first equation satisfies conservation of mass; the second one assures that the dynamics of the flow is treated correctly.

In addition to satisfying Equation 2.43 one must assure that any mathematical description of the flow field around a given body shape satisfies the boundary condition that there be no velocity normal to the body at all points

on its surface. If **n** is the unit vector normal to the surface, the following must hold.

$$\mathbf{V} \cdot \mathbf{n} = 0 \tag{2.44}$$

Velocity Potential and Stream Function

To assist in the solution of Equation 2.43, two functions are introduced. The first of these is known as the velocity potential, ϕ, and is defined such that

$$u = \frac{\partial \phi}{\partial x}$$

$$v = \frac{\partial \phi}{\partial y}$$

$$w = \frac{\partial \phi}{\partial z}$$

or, generally,

$$\mathbf{V} = \nabla \phi \tag{2.45}$$

Equation 2.45 satisfies identically Equation 2.43*b*. However, in order to satisfy Equation 2.43*a*, it follows that ϕ must be a harmonic function; that is,

$$\nabla^2 \phi = 0 \tag{2.46}$$

The operator, ∇^2, known as the Laplacian, is defined as

$$\nabla^2 = \frac{\partial^2}{\partial x^2} + \frac{\partial^2}{\partial y^2} + \frac{\partial^2}{\partial z^2}$$

A flow for which Equation 2.45 is satisfied, and hence ϕ can be defined, is known as a potential flow. The resulting fluid motion is described as being irrotational. This follows since, in the limit at a point, the curl of the velocity vector, which is zero, is equal to twice the rotational or angular velocity.

The stream function, ψ, is related to the velocity components by

$$u = \frac{\partial \psi}{\partial y}$$

$$v = -\frac{\partial \psi}{\partial x} \tag{2.47}$$

ψ can only be defined for two-dimensional, or axisymmetric, flow. To obtain a particular component, the partial derivative of ψ is taken in the direction normal to the velocity and to the left as one looks in the direction of the velocity.

A line element is pictured in Figure 2.11 with flow passing through it. This element is a segment of an arbitrary line connecting two points *A* and *B*. The

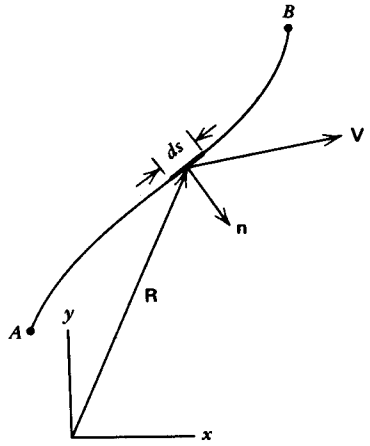

Figure 2.11 Two-dimensional flow through a line element.

differential flux through this element will be

$$dQ = \mathbf{V} \cdot \mathbf{n}\, ds$$

But

$$\mathbf{n} = (\mathbf{i}\, dy - \mathbf{j}\, dx)/ds$$
$$\mathbf{V} = \mathbf{i}\, u + \mathbf{j}\, v$$

Substituting **n** and **V** into dQ and using Equation 2.47 results in

$$dQ = \frac{\partial \psi}{\partial x}\, dx + \frac{\partial \psi}{\partial y}\, dy$$

or

$$dQ = d\psi$$

Thus

$$\psi(B) - \psi(A) = \int_A^B \mathbf{V} \cdot \mathbf{n}\, ds \tag{2.48}$$

That is, the change in the stream function between two points is equal to the flux between the points. It follows that ψ is a constant along a streamline. This can be shown by noting that along a streamline

$$\frac{v}{u} = \frac{dy}{dx}$$

and

$$d\psi = dQ = u\, dy - v\, dx$$

Combined, the two relationships give

$$d\psi = 0$$

or

$$\psi = \text{constant (along a streamline)}$$

The stream function, as a measure of the flux, satisfies identically Equation 2.43*a*. For an irrotational flow, however, in order to meet Equation 2.43*b* it follows that ψ must also be harmonic.

$$\nabla^2\psi = 0 \tag{2.49}$$

In a manner similar to the derivation of Equation 2.48, the change in ϕ between two points can also be easily obtained. If

$$\phi = \phi(x, y)$$

then

$$d\phi = \frac{\partial\phi}{\partial x}\,dx + \frac{\partial\phi}{\partial y}\,dy$$
$$= u\,dx + v\,dy$$

or, using vector notation,

$$\phi(B) - \phi(A) = \int_A^B \mathbf{V} \cdot \mathbf{dR} \tag{2.50}$$

where **R** is the radius vector to the curve along which the integration is being performed, as shown in Figure 2.11. **dR** is then the differential vector along the curve, directed positively, with a magnitude of ds.

As an example in the use of ϕ and ψ, consider the uniform flow pictured in Figure 2.12. For this flow,

$$u = U = \text{constant}$$
$$v = 0$$

ψ will be taken to be zero along the x-axis. This choice is arbitrary, since the values of both ϕ and ψ can be changed by a constant amount without affecting the velocity field obtained from their derivatives. Equation 2.48 will be zero if the integral is performed along a line for which y is a constant.

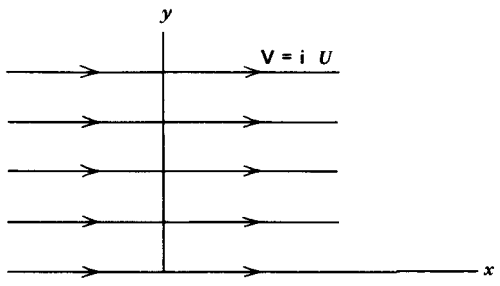

Figure 2.12 Uniform flow in the x direction.

Thus ψ changes only in the y direction. Integrating Equation 2.48 in this direction gives

$$\psi(y) - \psi(0) = \int_0^y (\mathbf{i}\, U) \cdot \mathbf{i}\, dy$$

or

$$\psi = Uy$$

If the uniform flow contains, in addition to U, a constant velocity component V in the y direction, ψ becomes

$$\psi = Uy - Vx \tag{2.51}$$

The minus sign in Equation 2.51 is in accordance with the positive direction of **n**, as shown in figure 2.11. **n** is directed to the right as one looks in the direction of point B from point A. In this case the integration for the second term is in the positive x direction, so **n** equals $-\mathbf{j}$.

In a more formal manner, ϕ will be derived for this same flow using Equation 2.50.

$$\mathbf{V} = \mathbf{i}\, U + \mathbf{j}\, V$$

$$\mathbf{R} = \mathbf{i}\, x + \mathbf{j}\, y$$

Hence

$$d\mathbf{R} = \mathbf{i}\, dx + \mathbf{j}\, dy$$

so that, taking $\phi = 0$ at $x, y = 0$,

$$\phi(x, y) = \int_0^{x,y} U\, dx + V\, dy$$

$$= Ux + Vy \tag{2.52}$$

Elementary Flow Functions

If ϕ_1 and ϕ_2 are functions satisfying Equation 2.46 then, because this equation is linear, their sum will also satisfy Equation 2.46. In general, both the velocity potential and stream function can be constructed by summing less complicated functions.

$$\phi(x, y) = \sum_{i=1}^{n} \phi_i(x, y) \tag{2.53a}$$

$$\psi(x, y) = \sum_{i=1}^{n} \psi_i(x, y) \tag{2.53b}$$

Equation 2.53 represents the real benefit to be gained in describing a flow in terms of ϕ and ψ. This statement will become obvious as the developments proceed.

The simple flows from which more complicated patterns can be

developed are referred to as elementary flow functions. There are three of them: uniform rectilinear flow, vortex, and source. The first of these has already been covered with ϕ and ψ given by Equations 2.52 and 2.51, respectively.

Vortex

A vortex is pictured in Figure 2.13. This flow in two dimensions is purely circular around a point with no radial velocity component. Denoting the tangential velocity component by v_θ, the problem is to find v_θ as a function of r that will satisfy the set of Equations 2.43*a* and 2.43*b*. v_θ is to be independent of θ.

In polar coordinates,

$$\nabla \times \mathbf{V} = \frac{\partial v_\theta}{\partial r} + \frac{v_\theta}{r} - \frac{1}{r}\frac{\partial v_r}{\partial \theta} \tag{2.54a}$$

$$\nabla \cdot \mathbf{V} = \frac{1}{r}\frac{\partial v_\theta}{\partial \theta} + \frac{\partial v_r}{\partial r} + \frac{v_r}{r} \tag{2.54b}$$

where r and θ are the polar coordinates, with v_r being the radial component of velocity and v_θ the tangential component.

Since v_r is zero in Figure 2.13 and v_θ is independent of θ, Equation 2.54*b* is satisfied identically and, from Equation 2.54*a*

$$\frac{dv_\theta}{dr} + \frac{v_\theta}{r} = 0$$

or, after integrating,

$$rv_\theta = \text{constant}$$

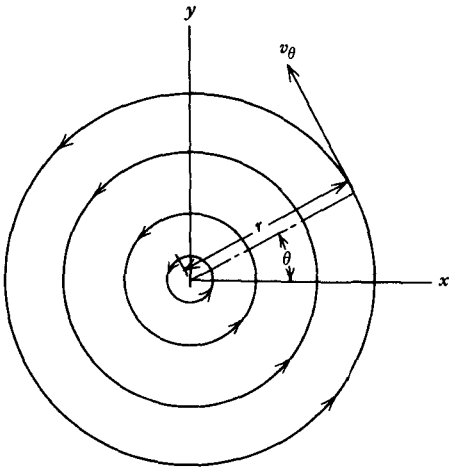

Figure 2.13 Flow field around a vortex.

Thus, for potential flow, the tangential velocity around a vortex must vary inversely with the radial distance from the center of the vortex.

The strength of a vortex, denoted by γ, is measured by integrating the tangential velocity completely around the vortex. The value of this integral is independent of the path providing it encloses the singular point at the center of the vortex.

$$\gamma = \oint \mathbf{V} \cdot \mathbf{dR} \tag{2.55}$$

This closed-line integral of the velocity is known as the *circulation.* Evaluating Equation 2.55 on a constant radius leads to the relationship between the tangential velocity around a vortex, the radius, and the vortex strength.

$$v_\theta = \frac{\gamma}{2\pi r} \tag{2.56}$$

Equation 2.55 is a well-known relationship and can be easily remembered from the definition of γ.

ϕ and ψ for a vortex follow immediately from Equations 2.50, 2.48, and 2.56.

$$\phi(B) - \phi(A) = \int_A^B \frac{\gamma}{2\pi r}(r\, d\theta)$$

$$= \frac{\gamma}{2\pi}[\theta(B) - \theta(A)]$$

If θ is measured relative to zero and $\theta(B)$ is taken to be any value of θ,

$$\phi \doteq \frac{\gamma\theta}{2\pi} \tag{2.57}$$

The stream function for a vortex is found from

$$\psi(B) - \psi(A) = -\int_A^B \frac{\gamma}{2\pi r}\, dr$$

$$= -\frac{\gamma}{2\pi} \ln \frac{r(B)}{r(A)}$$

Letting $\psi(A)$ be zero and $r(A)$ be an arbitrary radius, a, leads to

$$\psi = -\frac{\gamma}{2\pi} \ln \frac{r}{a} \tag{2.58}$$

The minus sign results from the choice of positive coordinate directions.

Source

The source is the counterpart of a vortex. Here the flow, pictured in Figure 2.14, is again symmetrical about the center, but it is entirely radial with no tangential velocity component.

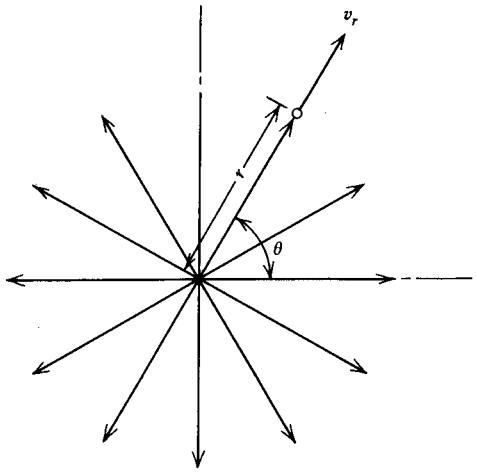

Figure 2.14 Flow from a source.

The strength of a source, q, is measured by the total flux emanating from the center. From Figure 2.14, q is obviously given by

$$q = 2\pi r v_r$$

or

$$v_r = \frac{q}{2\pi r} \tag{2.59}$$

In a manner similar to that followed for the vortex, one may verify that for the source

$$\phi = \frac{q}{2\pi} \ln r \tag{2.60}$$

$$\psi = \frac{q\theta}{2\pi} \tag{2.61}$$

Equations 2.56 and 2.59, which define the velocities around vortices and sources, can be extended to three dimensions. If Q is the strength of a three-dimensional source, this flux will equal the product of the radial velocity and the surface area through which the velocity is passing. Thus, one can write v_r immediately as

$$v_r = \frac{Q}{4\pi r^2} \tag{2.62}$$

Biot–Savart Law

The three-dimensional velocity field associated with a vortex line is considerably more complicated and is given by the Biot–Savart law. The derivation of this law is beyond the scope of this text. Figure 2.15*a* illustrates

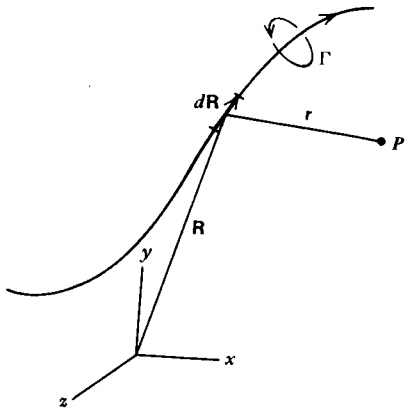

Figure 2.15a Definition of quantities used in the Biot–Savart law.

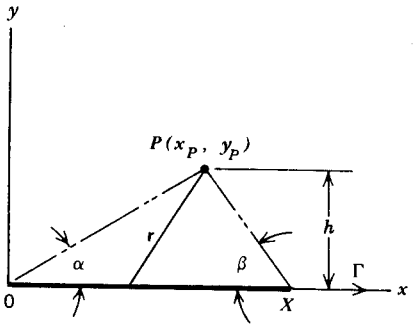

Figure 2.15b The Biot–Savart law for a straight-line vortex.

a portion of a vortex line about which at any point the circulation, Γ, is constant. If $\mathbf{v}_i$ is the velocity vector induced at any point, P, in the field by the vortex line, the Biot–Savart law states

$$d\mathbf{v}_i = \frac{\Gamma}{4\pi} \frac{\mathbf{r} \times \mathbf{dR}}{|\mathbf{r}|^3} \tag{2.63}$$

This is the most general form of the Biot–Savart law. **dR** is the derivative of the radius vector from the origin to the vortex line and is thus the directed differential distance along the line. **r** is the radius vector from the point P to the line element **dR**. The positive direction of the circulatory strength, Γ, is defined according to the right-hand rule. The x, y, z orthogonal coordinate system is also right-handed.

A special form of the Biot–Savart law for a straight-line vortex segment found in many texts can be obtained by integrating Equation 2.63. Referring

to Figure 2.15*b*, for convenience the line vortex is placed on the x-axis and lies between 0 and x. The z-axis will project out of the paper according to the right-hand rule. The circulation Γ is taken to be positive in the x direction which means it will be clockwise when viewed in that direction. For this figure,

$$\mathbf{R} = \mathbf{i}\,x$$

$$\mathbf{OP} + \mathbf{r} = \mathbf{R}$$

$$\mathbf{OP} = \mathbf{i}\,x_p + \mathbf{j}\,y_p$$

Thus

$$\mathbf{r} = \mathbf{i}(x - x_P) - \mathbf{j}\,y_P$$

$$d\mathbf{R} = \mathbf{i}\,dx$$

so that

$$\mathbf{r} \times d\mathbf{R} = \begin{vmatrix} \mathbf{i} & \mathbf{j} & \mathbf{k} \\ (x - x_P) & -y_P & 0 \\ dx & 0 & 0 \end{vmatrix}$$

$$= \mathbf{k}\,y_P\,dx$$

$$|\mathbf{r}| = [(x - x_P)^2 + y_P^2]^{1/2}$$

Equation 2.63 then becomes

$$\mathbf{v}_i = \frac{k\Gamma y_P}{4\pi} \int_0^x \frac{dx}{[(x - x_P)^2 + y_P^2]^{3/2}}$$

This reduces to

$$\mathbf{v}_i = \mathbf{k}\,\frac{\Gamma}{4\pi h}(\cos\alpha + \cos\beta) \tag{2.64}$$

α, β, and h are defined in Figure 2.15*b*. Notice that the velocity has only a z component. As the line becomes infinite in length, the angles α and β approach zero, and Equation 2.64 reduces to the expression for the velocity around a two-dimensional point vortex given by Equation 2.56.

The Calculation of Flows for Well-Defined Body Shapes

The flow functions described thus far are basic functions. By combining these functions a multitude of more complicated flows can be described. When combining these functions, the velocities will add vectorially. This is obvious from Equation 2.53*a*, since

$$\text{grad}\,\phi = \text{grad}\,\phi_1 + \text{grad}\,\phi_2 + \cdots$$

or

$$\mathbf{V} = \mathbf{V}_1 + \mathbf{V}_2 + \cdots$$

As an example of the use of these functions, consider the classic

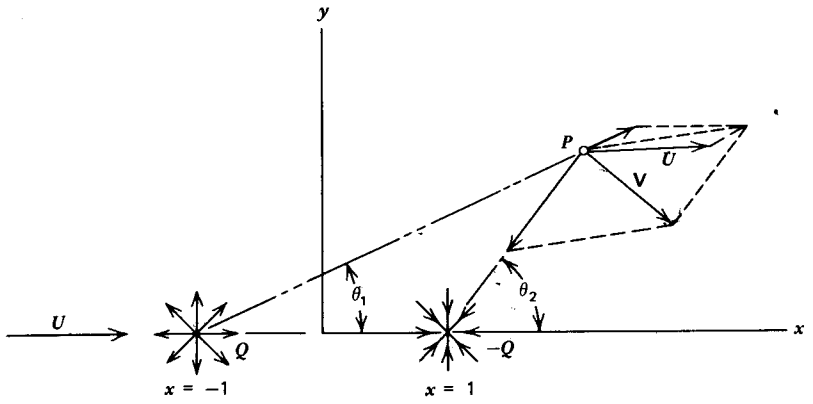

Figure 2.16 Source-sink combination in a uniform flow.

two-dimensional case illustrated in Figure 2.16. Here a source and a sink (a negative source) of equal strength are placed a unit distance from either side of the origin in a uniform flow. Three velocities from the source, sink, and uniform flow are shown added vectorially at P giving the resultant velocity, **V**.

It is easily verified that the entire resulting flow is symmetrical about both the x- and y-axes. To the left of the source along the x-axis a distance of x_0 from the origin a stagnation point exists where the resultant velocity is zero. The location of this point can be found from Equation 2.59 for the velocity from a source (or sink).

$$0 = U - \frac{q}{2\pi(x_0 - 1)} + \frac{q}{2\pi(x_0 + 1)}$$

or

$$x_0^2 = 1 + \frac{q}{\pi U} \tag{2.65}$$

It will be seen that this point lies on a dividing streamline that is closed and that separates the flow leaving the source and entering the sink from the uniform flow. The resultant streamline pattern can be constructed by calculating the velocity at many points in the field and fairing streamlines tangent to these vectors. However, a more direct way is to form the stream function and then solve for $y(x)$ for constant values of ψ. Adding the ψ functions for the uniform flow, source, and sink, one obtains

$$\psi = \frac{q}{2\pi}(\theta_1 - \theta_2) + Uy \tag{2.66}$$

where θ_1 and θ_2 are shown in Figure 2.16. Because of the multivaluedness of the tangent function, one must be careful in evaluating this expression.

At the stagnation point, $\theta_1 = \theta_2$ and $y = 0$, so that $\psi = 0$. Since this point lies on the dividing streamline, a value of $\psi = 0$ will define this streamline. Hence

$$\theta_2 - \theta_1 = \frac{2\pi U y}{q} \tag{2.67}$$

Since the flow is symmetrical, we only need to calculate the streamline shapes in one quadrant, say the one for which x and y are both positive. In this quadrant,

$$\theta_1 = \tan^{-1}\frac{y}{1+x}$$

$$\theta_2 = \pi - \tan^{-1}\frac{y}{1-x}$$

Hence x and y along the dividing streamline are related by

$$\tan^{-1}\frac{2y}{1-x^2-y^2} = \pi\left(1 - 2\frac{U}{q}y\right) \tag{2.68}$$

This can be solved explicitly for x.

$$x^2 = 1 - y^2 - \frac{2y}{\tan\{\pi[1-(2Uy/q)]\}} \tag{2.69}$$

Notice that as y approaches zero in Equation 2.68, x approaches the value given by Equation 2.65.

Since any streamline can be replaced by a solid boundary, the dividing streamline represents a closed body. If it is assumed that the body's fineness ratio (i.e., thickness to length) is small, then at its maximum thickness point ($x = 0$), Equation 2.68 can be written approximately as

$$2y_0 = \pi\left(1 - 2\frac{U}{q}y_0\right)$$

or

$$y_0 = \frac{\pi}{2[1+(\pi U/q)]} \tag{2.70}$$

y_0 is the semithickness of the body corresponding to x_0, the semilength. Hence the fineness ratio of the body, t/l, is related to q/U by

$$\frac{t}{l} = \frac{q/U}{2[1+(q/\pi U)]^{3/2}} \tag{2.71}$$

This classical body shape is referred to as the Rankine oval. The streamline pattern can be determined as a function of the streamline position far from the body. If y_∞ is the location of a particular streamline away from the body

then, for this particular streamline,

$$\psi = y_\infty U$$

Equating this to Equation 2.66, one obtains a relationship between x and y along the streamline as a function of y_∞ and q/U that can be solved explicitly for x.

$$x = \left\{1 - y^2 - \frac{2y}{\tan \pi[1 - 2(U/q)(y - y_\infty)]}\right\}^{1/2} \tag{2.72}$$

This relation was used to calculate the streamline patterns of Figure 2.17. Only the flow external to the dividing streamline is shown.

For comparison, this figure presents the streamline patterns (in one quadrant only) for 20% and 50% thick ovals. For each thickness, q/U was chosen on the basis of Equation 2.69. Because this equation assumes t/l to be small, the thickness ratio of the one shape is slightly greater than 50%.

Having defined the shape of a body and the velocity field around it, the next obvious point of interest is the pressure distribution over the body's surface. In order to remove the dependence of the predicted pressure distribution on the free-stream pressure and velocity, the pressure distribution is normally presented in coefficient form, C_p, where C_p is defined according to

$$C_p = \frac{p - p_0}{(1/2)\rho V_0^2} \tag{2.73}$$

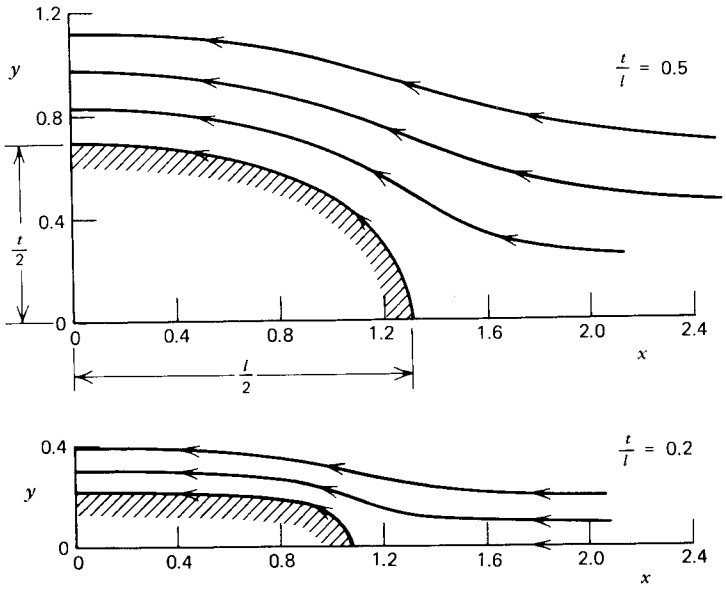

Figure 2.17 Calculated streamlines for 20 and 50% thick Rankine ovals.

From Equation 2.29, C_p is found from the ratio of local velocity to free-stream velocity.

$$C_p = 1 - \left(\frac{V}{V_0}\right)^2 \tag{2.74}$$

Returning now to the Rankine oval, note first that $C_p = 1$ at the stagnation point where V is zero. Moving away from the nose along the $\psi = 0$ streamline, the velocity increases to a maximum at some location. Depending on the fineness ratio, this point of maximum velocity may or may not be at the maximum thickness of the body; that is, $x = 0$.

Although one could work with ψ, knowing the source (and sink) strength the easiest approach is to calculate the u and v components directly by adding the components attributed to each elementary flow function. In this case it will be found that

$$\frac{u}{U_0} = 1 + \frac{q}{2\pi U_0}\left[\frac{x+1}{(x+1)^2+y^2} - \frac{x-1}{(x-1)^2+y^2}\right]$$

$$\frac{v}{U_0} = \frac{q}{2\pi U_0}\left[\frac{y}{(x+1)^2+y^2} - \frac{y}{(x-1)^2+y^2}\right]$$

The pressure coefficient is then calculated from

$$C_p = 1 - \left[\left(\frac{u}{U_0}\right)^2 + \left(\frac{v}{U_0}\right)^2\right] \tag{2.75}$$

The pressure distribution along the surfaces of 20 and 50% thick Rankine ovals have been calculated using the preceding equations, and the results are presented in Figure 2.18. It is not too surprising to find that, for the 20% oval, the minimum pressure occurs near the nose, where the curvature is the greatest. For the 50% thick oval the minimum pressure occurs approximately halfway from the center of the body to the nose, but it is nearly flat over the middle 70% of the body's length.

The Circular Cylinder

The flow field around a circular cylinder and resulting pressure distribution can be determined as a limiting case of the Rankine oval. In Figure 2.16 the source and sink were placed at $x = -1.0$ and $x = 1.0$, respectively. We will now move them instead toward the origin, but increase their strengths in inverse proportion to the distance between them. In the limit as the distance between the source and sink goes to zero, a so-called source-sink doublet is obtained.

Letting 2ϵ equal the distance between the source and sink and m the

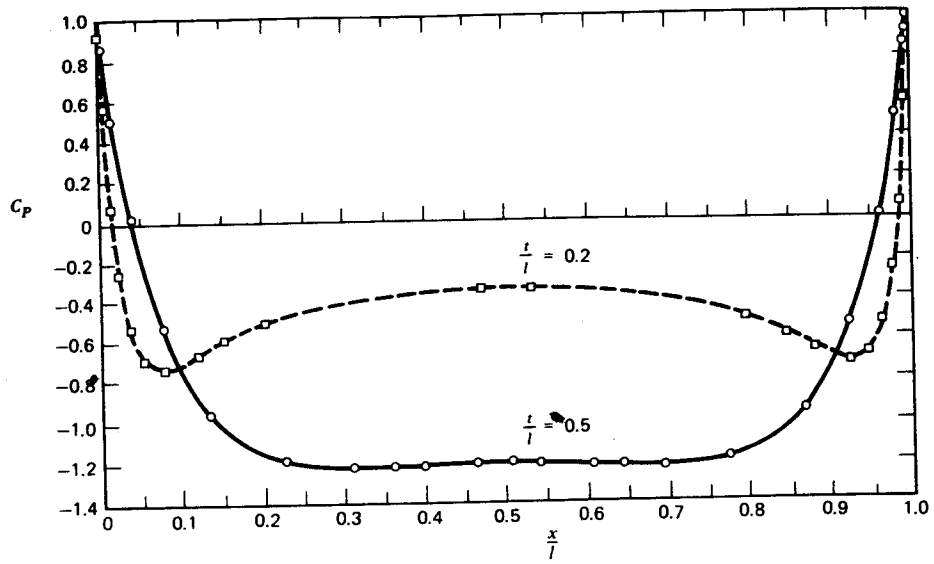

Figure 2.18 Predicted pressure distributions for 20 and 50% thick Rankine ovals.

constant doublet strength equal to $2\epsilon Q$, Equation 2.66 can be written as

$$\psi = \frac{m}{4\pi\epsilon}\left(\tan^{-1}\frac{y}{\epsilon + x} + \tan^{-1}\frac{y}{\epsilon - x} - \pi\right) + U_y$$

$$\lim\ \epsilon \to 0$$

In the limit, this becomes

$$\psi = -\frac{m}{2\pi}\frac{y}{x^2 + y^2} + Uy$$

For $\psi = 0$, since y is not generally zero, it follows that

$$x^2 + y^2 = \frac{m}{2\pi U}$$

This is the equation of a circle of radius

$$R = (m/2\pi U)^{1/2}$$

Thus ψ can be written in polar coordinates as

$$\psi = Ur \sin\theta\left[1 - \left(\frac{R}{r}\right)^2\right] \tag{2.76}$$

where $r^2 = x^2 + y^2$

$$\theta = \tan^{-1}\left(\frac{y}{x}\right)$$

The tangential velocity along the surface of the cylinder is found from Equation 2.47 by differentiating ψ with respect to r and evaluating the result at $r = R$. In this way v_θ is found to be

$$v_\theta = 2U \sin \theta \tag{2.77}$$

The pressure coefficient distribution, from Equation 2.75, is thus predicted to be

$$C_p = 1 - 4 \sin^2 \theta \tag{2.78}$$

In Chapter Four it will be seen that Equation 2.78 agrees fairly well with experimental results over the front half of the cylinder, but departs from actual measurements over the rear portion as the result of viscosity.

A point vortex of strength γ can be placed at the origin without altering the streamline representing the surface of the cylinder. If this is done, Equation 2.77 becomes

$$v_\theta = 2U \sin \theta + \frac{\gamma}{2\pi R} \tag{2.79}$$

Relative to p_0 the pressure on the surface of the cylinder will be

$$p - p_0 = \frac{1}{2}\rho U^2 - \frac{1}{2}\rho \left| 2U \sin \theta + \frac{\gamma}{2\pi R} \right|^2 \tag{2.80}$$

Referring to Figure 2.19, the net vertical force, or lift, on the cylinder resulting from the pressure distribution will be

$$L = -\int_0^{2\pi} pR \sin \theta \, d\theta$$

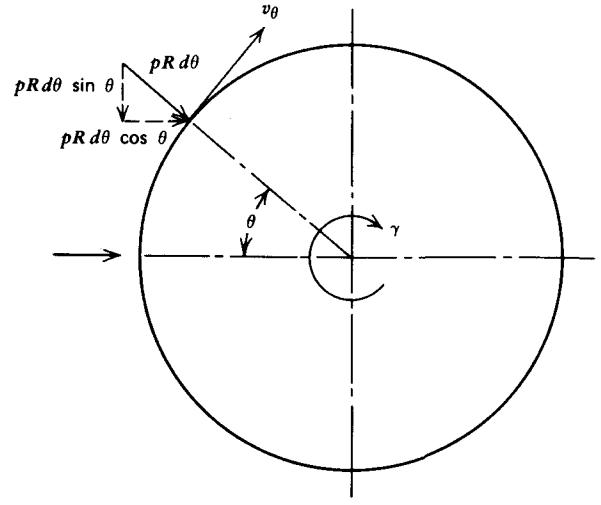

Figure 2.19 Circular cylinder with circulation.

or, from Equation 2.78, this reduces to

$$L = \rho U \gamma \tag{2.81}$$

This is referred to as the Kutta–Joukowski law. Although derived here specifically for a circular cylinder, it can be applied to other shapes where γ represents generally the circulation around the shape. This will be amplified further in Chapter Three.

The net horizontal force, or drag, on the cylinder is found from

$$D = \int_0^{2\pi} pR \cos\theta \, d\theta$$

Using Equation 2.80, the drag is found to be zero, a result that is true in general for a closed body in steady potential flow. This result is known as D'Alembert's paradox, after Jean le Rond D'Alembert, a French mathematician who first reached this conclusion around 1743.

The Numerical Calculation of Potential Flow Around Arbitrary Body Shapes

The preceding has demonstrated how particular body shapes can be generated by the superposition of elementary flow functions. This procedure can be generalized and the inverse problem can be solved where the body shape is prescribed and the elementary flow functions that will generate the body shape are found.

The concept of a point source or a point vortex can be extended to a continuous distribution of these functions. Consider first the two-dimensional source distribution shown in Figure 2.20. Here q is the source strength per unit length.

Consider the closed contour shown dashed in Figure 2.20, having a length of Δx and a vanishing small height. The total flux through this surface must equal $q\,\Delta x$. Close to the surface the u velocity components from the elemental sources will cancel so that only a v component remains. Thus

$$2v\,\Delta x = q\,\Delta x$$

or

$$v = \frac{q}{2} \tag{2.82}$$

In Reference 2.4 this relationship is used to determine the flow about arbitrary shapes. Thus, unlike the Rankine oval, the body shape is specified, and the problem is to find the distribution of singularities to satisfy the condition that the velocity everywhere normal to the body surface to be zero. This particular problem is referred to as the Neumann problem. Essentially the numerical solution of the problem proceeds by segmenting the body

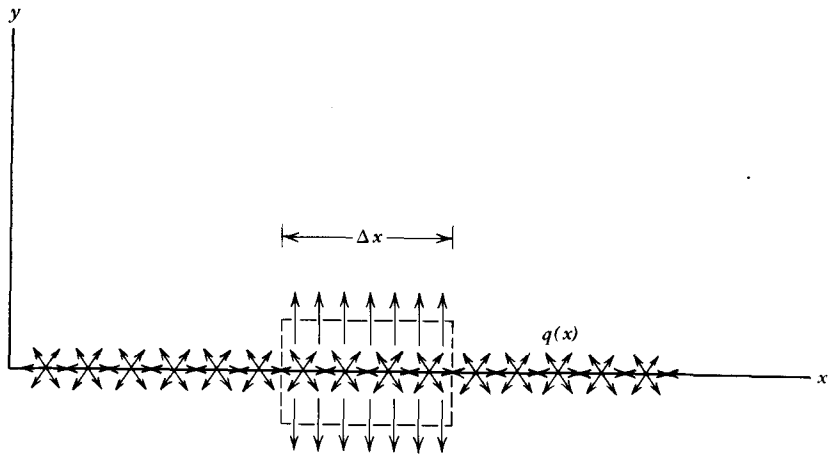

Figure 2.20 Distributed sources in two-dimensional flow.

surface and distributing a unit source strength, q_i, over the ith element. The normal velocity induced at the middle of the ith element by q_i is obtained immediately from Equation 2.82. The contribution to the velocity at the ith element from another element is calculated by assuming the total source strength at the second element to be a point source located at the middle of that element. Taking n elements and letting $i = 1, 2, 3, \ldots, n$ leads to a set of n linear simultaneous algebraic equations for the unknowns, $q_1, q_2, q_3, \ldots, q_n$.

Consider in more detail this approach for two-dimensional flow. Figure 2.21 shows two elements along the surface of a body. The ith element is the control element over which the unit source strength q_i is distributed. At the jth element a point source is located having a strength equal to $q_j \Delta S_j$, ΔS_j being the length of the jth element. The free-stream velocity U_0 is shown relative to the body x-axis at an angle of attack of α.

At the center of the ith element the normal velocity components from each source and the free stream must vanish. Hence

$$U_0 \sin(\theta_i - \alpha) = \frac{q_i}{2} + \sum_{j=1}^{N} q_j c_{ij} \qquad j \neq i \tag{2.83}$$

c_{ij} is an influence coefficient, which accounts for the geometry of the body shape in determining the normal velocity induced at the ith element by the source at the jth element.

If ζ_i and η_i correspond to the midpoints of the ith element then, for Figure 2.21:

$$c_{ij} = \frac{\sin(\theta_i - \phi_{ij})}{2\pi r_{ij}} \tag{2.84a}$$

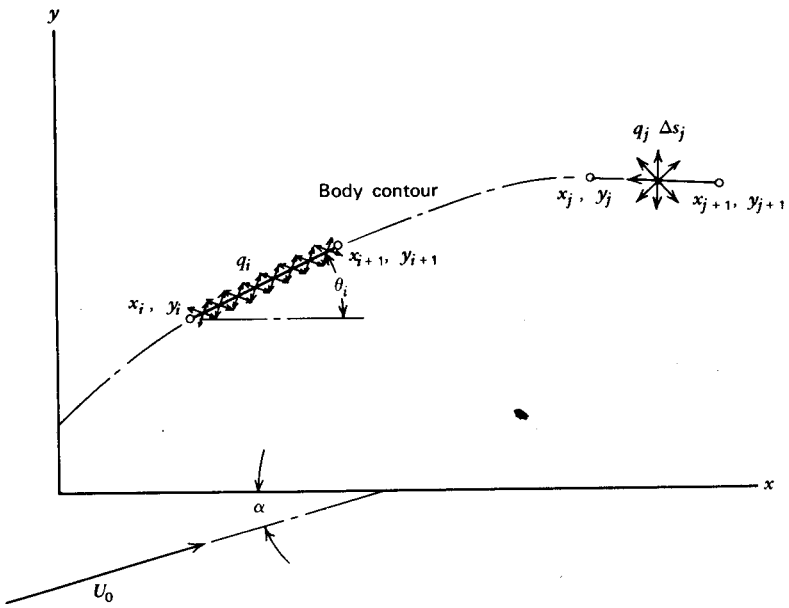

Figure 2.21 Numerical solution of the Neumann problem by a distribution of sources.

$$r_{ij} = [(\zeta_i - \zeta_j)^2 + (\eta_i - \eta_j)^2]^{1/2} \tag{2.84b}$$

$$\phi_{ij} = \tan^{-1} \frac{\eta_j - \eta_i}{\zeta_j - \zeta_i} \tag{2.84c}$$

$$\theta_i = \tan^{-1} \frac{y_{i+1} - y_i}{x_{i+1} - x_i} \tag{2.84d}$$

$$\zeta_i = \frac{1}{2}(x_i + x_{i+1}) \tag{2.84e}$$

$$\eta_i = \frac{1}{2}(y_i + y_{i+1}) \tag{2.84f}$$

Having thus determined the source strengths, q_i, the resultant velocity at any location can be determined by adding vectorially the free-stream velocity to the contributions from all of the sources. Finally, the pressure distribution can be determined from Equation 2.74.

This numerical procedure applied to a circular cylinder with a unit radius is illustrated in Figure 2.22. Here, only eight elements are shown. For this case,

$$x_i = \cos \theta_i$$

$$y_i = \sin \theta_i$$

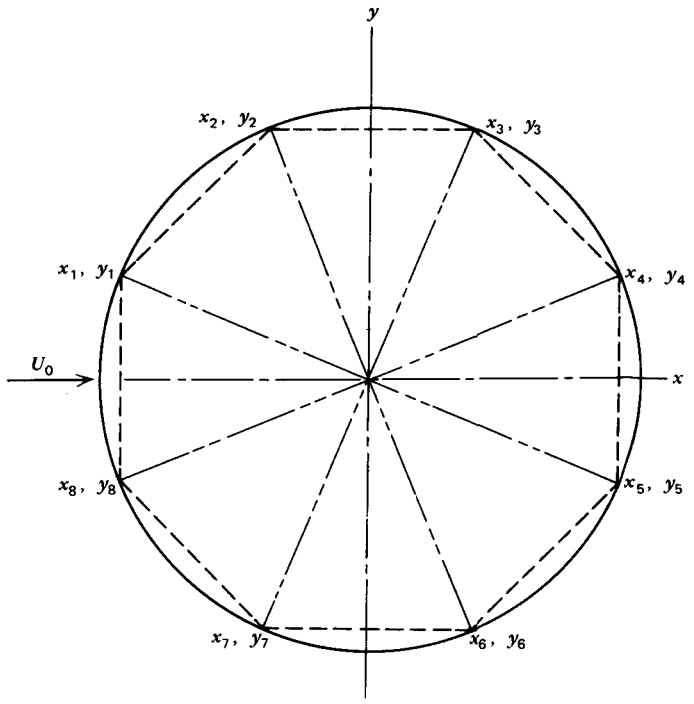

Figure 2.22 Approximation to a circular cylinder with straight-line segments.

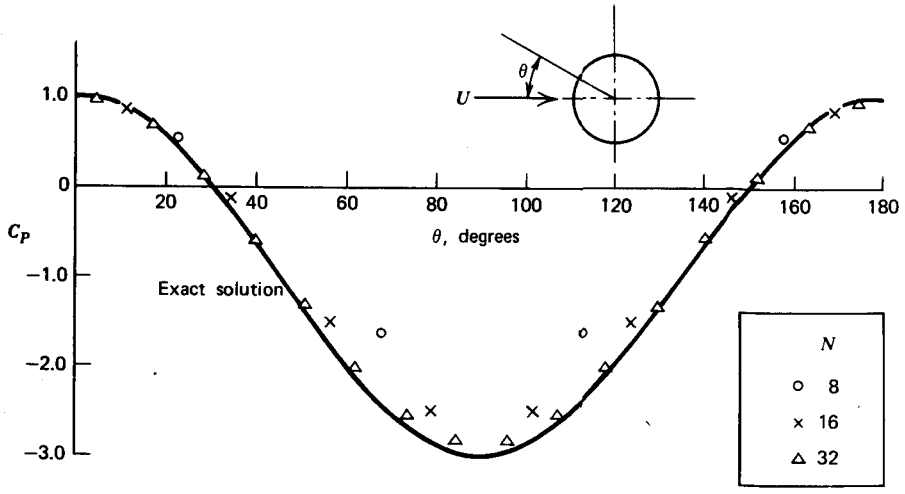

Figure 2.23 Convergence of the numerical result to the exact solution for a circular cylinder.

where

$$\theta_i = \pi - \frac{2\pi}{n}\left(i - \frac{1}{2}\right)$$

$$n = 8$$

The numerical calculation of the pressure distribution around a circular cylinder is compared in Figure 2.23 with the exact solution given by Equation 2.78. As the number of segments increases, the approximate solution is seen to approach the exact solution rapidly. In Chapter Three this numerical method will be extended to include distributed vortices in addition to sources. In this way the lift of an arbitrary airfoil can be predicted.

SUMMARY

This chapter has introduced some fundamental concepts in fluid mechanics that will be expanded on and applied to explaining the aerodynamic behavior of airplane components in succeeding chapters. Potential flow methods will be used extensively with corrections given for Reynolds and Mach numbers.

PROBLEMS

2.1 How should the thickness of a dam of constant width vary with depth to insure a constant shearing stress in the dam's material?

2.2 Show that the incompressible Bernoulli's equation (Equation 2.28) becomes $p + \rho gh + \frac{1}{2}\rho V^2 = \text{constant}$ for a liquid, the weight of which is significant in comparison to the static pressure forces. (h is the depth of the streamline relative to an arbitrary horizontal reference plane.)

2.3 A pilot is making an instrument approach into the University Park Airport, State College, Pennsylvania, for which the field elevation is listed at 378 m (1241 ft) above sea level. The sea level barometric pressure is 763.3 mm Hg (30.05 in. Hg), but the pilot incorrectly sets the altimeter to 758.2 mm Hg (29.85 in. Hg). Will the pilot be flying too high or too low and by how much? [*Note.* Standard sea level pressure is equal to 760 mm Hg (29.92 in. Hg)].

2.4 Set to standard sea level pressure, an altimeter reads 2500 m (8200 ft). The outside air temperature (OAT) reads −15 °C (5 °F). What is the pressure altitude? What is the density altitude?

2.5 By integrating the pressure over a body's surface, prove that the buoyant force on the body when immersed in a liquid is equal to the product of the volume of the displaced liquid, the liquid's mass density, and the acceleration due to gravity.

2.6 The hypothetical wake downstream of a two-dimensional shape is pictured below. This wake is far enough away from the body so that the static pressure through the wake is essentially constant and equal to the free-stream static pressure. Calculate the drag coefficient of the shape based on its projected frontal area.

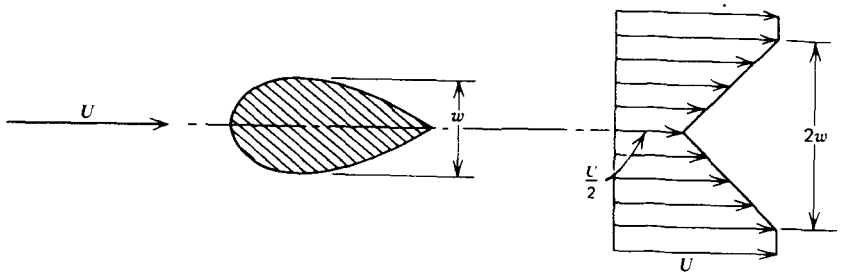

2.7 An incompressible flow has velocity components given by $u = -\omega y$ and $v = \omega x$, where ω is a constant. Is such a flow physically possible? Can a velocity potential be defined? How is ω related to the vorticity? Sketch the streamlines.

2.8 Derive Bernoulli's equation directly by applying the momentum theorem to a differential control surface formed by the walls of a small streamtube and two closely spaced parallel planes perpendicular to the velocity.

2.9 A jet of air exits from a tank having an absolute pressure of 152,000 Pa (22 psi). The tank is at standard sea level (SSL) temperature. Calculate the jet velocity if it expands isentropically to SSL pressure.

2.10 A light aircraft indicates an airspeed of 266 km/hr (165.2 mph) at a pressure altitude of 2400 m (7874 ft). If the outside air temperature is −10 °C, what is the true airspeed?

2.11 Prove that the velocity induced at the center of a ring vortex (like a smoke ring) of strength Γ and radius R is normal to the plane of the ring and has a magnitude of $\Gamma/2R$.

2.12 Write a computer program to solve the Biot–Savart equations numerically. This can be done by dividing a line vortex into finite, small straight-line elements. At a desired location the velocities induced by all of the elements can then be added vectorially to give the total resultant velocity. Check your program by using it to solve Problem 2.11.

REFERENCES

2.1 Streeter, Victor L., and Wylie, E. Benjamin, *Fluid Mechanics*, 6th edition, McGraw-Hill, New York, 1975.

2.2 Roberson, John A., and Crowe, Clayton T., *Engineering Fluid Mechanics*, Houghton Mifflin, Boston, 1975.

2.3 Minzner, R. A., Champion, K. S. W., and Pond, H. L., "The ARDC Model Atmosphere," AF CRC-TR-59-267, 1959.

2.4 Smith, A. M. O., "Incompressible Flow About Bodies of Arbitrary Shape," IAS Paper No. 62–143, presented at the IAS National Sciences Meeting, Los Angeles, June 1962.

THREE
THE GENERATION OF LIFT

Lift is the component of the resultant aerodynamic forces on an airplane normal to the airplane's velocity vector. Mostly, the lift is directed vertically upward and sustains the weight of the airplane. There are exceptions however. A jet fighter with a thrust-to-weight ratio close to unity in a steep climb may be generating very little lift with its weight being opposed mainly by the engine thrust.

The component that is the major lift producer on an airplane and on which this chapter will concentrate is the wing. Depending on the airplane's geometry, other components can contribute to or significantly affect the lift, including the fuselage, engine nacelles, and horizontal tail. These latter components will be considered, but to a lesser extent than the wing.

WING GEOMETRY

The top view, or planform, of a wing is shown in Figure 3.1. The length, b, from one wing tip to the other is defined as the wingspan. The chord, c, at some spanwise station, y, is the distance from the wing's leading edge to its trailing edge measured parallel to the plane of symmetry in which the centerline chord, c_0, lies. The chord generally varies with y so that, for purposes of characterizing wing geometry, a mean chord, $\bar{c}$, is defined as the value that, when multiplied by the span, results in the planform area, S.

$$\bar{c} = \frac{S}{b} \tag{3.1}$$

The aspect ratio of a wing, A, is a measure of how long the span is with respect to the mean chord. Thus

$$A = \frac{b^2}{S} \tag{3.2}$$

For a rectangular planform where the chord is constant, this reduces to

$$A = \frac{b}{c} \tag{3.3}$$

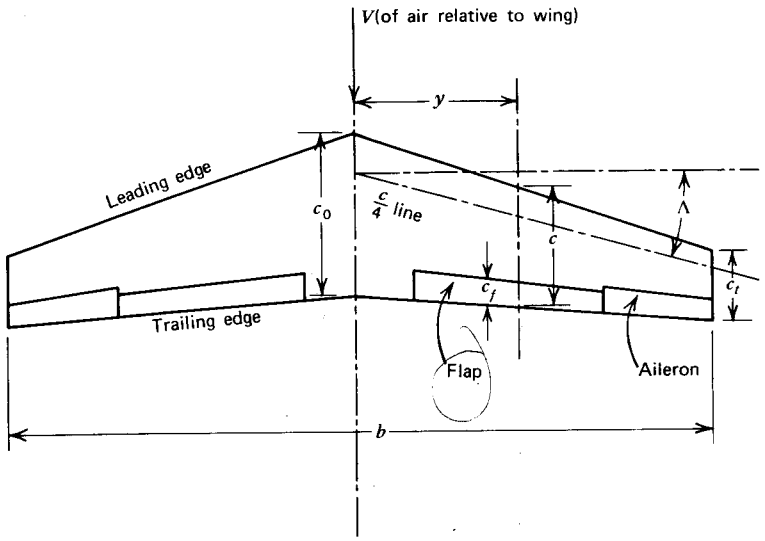

Figure 3.1 Top view of a wing (planform).

As shown in Figure 3.1, a wing planform may be tapered and swept back. The taper ratio, λ, is defined as the ratio of the tip chord, c_t, to the midspan chord, c_0.

$$\lambda = \frac{c_t}{c_0} \tag{3.4}$$

The sweep angle, Λ, is frequently measured relative to the quarter-chord line of the wing, that is, a line defined by the locus of points a quarter of the distance from the leading edge to the trailing edge. Λ, on occasion, is also measured relative to the leading edge.

Usually the center portion of a wing is enclosed by the fuselage. In such an instance the wing's aspect ratio and taper ratio are determined by ignoring the fuselage and extrapolating the planform shape into the centerline. The midspan chord in this instance is thus somewhat fictitious. The wing root is defined as the wing section at the juncture of the wing and fuselage. Occasionally, in the literature, one will find wing geometry characterized in terms of the wing root chord instead of the midspan chord.

Approximately the aft 25 to 30% of a wing's trailing edge is movable. On the outer one-third or so of the span the trailing edge on one side of the wing deflects opposite to that on the other. These oppositely moving surfaces are called ailerons; ailerons provide a rolling moment about the airplane's longitudinal axis. For example, when the aileron on the left wing moves down and the one on the right moves up, a moment is produced that tends to lift the

left wing and lower the right one; this is a maneuver necessary in making a coordinated turn to the right.

The inner movable portions of the wing's trailing edge on both sides of the wing are known as the flaps. For takeoff and landing the flaps are lowered the same on both sides. There is no differential movement of the flaps on the left and right sides of the wing. The purpose of the flaps is to allow the wing to develop a higher lift coefficient than it would otherwise. Thus, for a given weight, the airplane can fly slower with the flaps down than with them up. Flaps, including leading edge flaps and the many different types of trailing edge flaps, will be discussed in more detail later.

For some applications both ailerons are lowered to serve as an extension to the flaps. In such a case they are referred to as drooped ailerons, or flaperons. When flaperons are employed, additional roll control is usually provided by spoilers. These are panels that project into the flow near the trailing edge to cause separation with an attendant loss of lift.

In order to understand and predict the aerodynamic behavior of a wing, it is expedient to consider first the behavior of two-dimensional airfoils. An airfoil can be thought of as a constant chord wing of infinite aspect ratio.

AIRFOILS

A considerable amount of experimental and analytical effort has been devoted to the development of airfoils. Much of this work was done by the National Advisory Committee for Aeronautics (NACA), the predecessor of the National Aeronautics and Space Administration (NASA). Reference 3.1 is an excellent summary of this effort prior to 1948. More recently NASA and others have shown a renewed interest in airfoil development, particularly for application to helicopter rotor blades, general aviation aircraft, and aircraft operating at transonic speeds of Mach 0.7 or higher.

The development of an unflapped airfoil shape is illustrated in Figure 3.2. First, in Figure 3.2*a*, the chord line, c, is drawn. Next in Figure 3.2*b*, the camber line is plotted up from the chord a small distance z, which is a function of the distance from the leading edge. Next, as shown in Figure 3.2*c*, the semithickness is added to either side of the camber line. Also, the nose circle is centered on a tangent to the camber line at the leading edge and passes through the leading edge. Finally, an outer contour is faired around the skeleton to form the airfoil shape. Observe that the chord line is the line joining the ends of the mean camber line.

The early NACA families of airfoils were described in this way, with the camber and thickness distributions given as algebraic functions of the chordwise position. However, for certain combinations of maximum thickness-to-chord ratios, maximum camber-to-chord ratios, and chordwise posi-

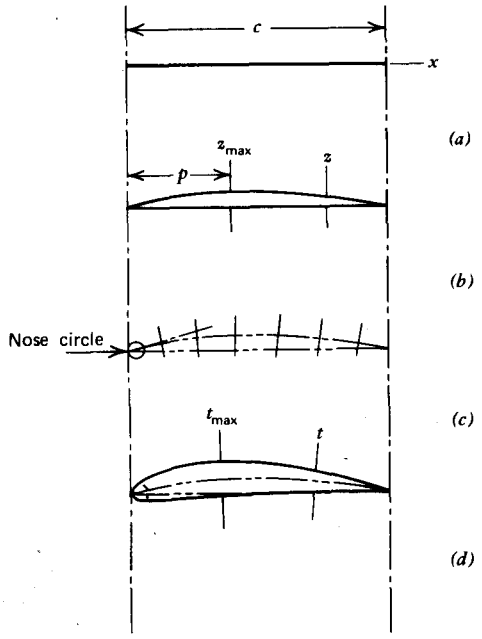

Figure 3.2 The construction of an airfoil contour.

tion of maximum camber, tabulated ordinates for the upper and lower surfaces are available (Ref. 3.1).

Before discussing the various families of airfoils in detail, we will generally consider the aerodynamic characteristics for airfoils, all of which can be influenced by airfoil geometry.

To begin, an airfoil derives its lift from the pressure being higher on the lower surface of the airfoil than on the upper surface. If a subscript l denotes lower surface and "u" denotes upper surface, then the total lift (per unit span) on the airfoil will be

$$L = \int_0^c (p_l - p_u)\, dx \tag{3.5}$$

The moment about the leading edge, defined positive nose up, will be

$$M_{LE} = -\int_0^c x(p_l - p_u)\, dx \tag{3.6}$$

In accord with Equation 2.12, the lift and moment can be expressed in terms of dimensionless coefficients.

$$C_l = \frac{L}{(1/2)\rho V^2 c} \tag{3.7}$$

$$C_{m_{LE}} = \frac{M_{LE}}{(1/2)\rho V^2 c^2} \tag{3.8}$$

Note that lowercase subscripts are used to denote coefficients for a two-dimensional airfoil, whereas uppercase subscripts are used for the three-dimensional wing.

Writing

$$\frac{p_l - p_u}{(1/2)\rho V^2} = \frac{p_l - p_0}{(1/2)\rho V^2} - \frac{p_u - p_0}{(1/2)\rho V^2}$$

and redefining x as the distance in chord lengths from the leading edge, Equations 3.5 and 3.6 become

$$C_l = \int_0^1 (C_{p_l} - C_{p_u})\, dx \tag{3.9}$$

and

$$C_{m_{LE}} = -\int_0^1 x(C_{p_l} - C_{p_u})\, dx \tag{3.10}$$

where the upper and lower pressure coefficients are defined according to Equation 2.73.

The moment calculated from Equation 3.10 can be visualized as being produced by the resultant lift acting at a particular distance back from the leading edge. As a fraction of the chord, the distance x_{cp} to this point, known as the center of pressure, can be calculated from

$$-x_{cp} C_l = C_{m_{LE}} \tag{3.11}$$

Knowing x_{cp}, the moment coefficient about any other point, x, along the airfoil can be written, referring to Figure 3.3, as

$$C_m = -(x_{cp} - x)\, C_l \tag{3.12}$$

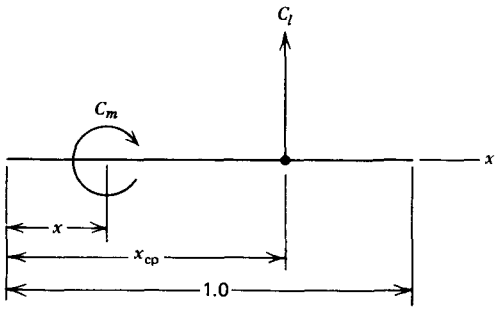

Figure 3.3 Dimensionless moment at x produced by dimensionless lift acting at

It will be shown later that a point exists on an airfoil called the *aerodynamic center* about which the moment coefficient is constant and does not depend on C_l. Denoting the location of the aerodynamic center by x_{ac}, Equation 3.12 can be solved for the location of the center of pressure.

$$x_{cp} = x_{ac} - \frac{C_{m_{ac}}}{C_l} \tag{3.13}$$

Do not confuse the aerodynamic center with the center of pressure. Again, the aerodynamic center is the location about which the moment is constant, the center of pressure is the point at which the resultant lift acts.

The progressive development of an airfoil shape is illustrated by reference to Figure 3.4*a* and 3.4*b*. Historically airfoils developed approximately in this manner. Consider first the simple shape of a thin, flat plate.

Beginning with Figure 3.4*a* if the angle of attack of a thin, flat plate is suddenly increased from zero, the flow will appear for a moment as shown. Because of near-symmetry, there is practically no lift produced on the plate. However, because of viscosity, the flow at the trailing edge cannot continue to turn the sharp edge to flow upstream. Instead, it quickly adjusts to the pattern shown in Figure 3.4*b*. Here the flow leaves nearly tangent to the trailing edge. This condition is known as the *Kutta* condition after the German scientist, W. M. Kutta, who in 1902 first imposed the trailing edge condition in order to predict the lift of an airfoil theoretically. In Figure 3.4*b* observe that there is one streamline that divides the flow that passes over the plate from that below. Along this "dividing streamline," the flow comes to rest at the stagnation point, where it joins perpendicular to the lower surface of the plate near the leading edge. As the flow progresses forward along this line, it is unable to adhere to the surface around the sharp leading edge and separates from the plate. However, it is turned backward by the main flow and reattaches to the upper surface a short distance from the leading edge. The resulting nonsymmetrical flow pattern causes the fluid particles to accelerate over the upper surface and decelerate over the lower surface. Hence, from Bernoulli's equation, there is a decrease in air pressure above the plate and an increase below it. This pressure difference acting on the airfoil produces a lift.

If the angle of attack of the plate is too great, the separated flow at the leading edge will not reattach to the upper surface, as shown in Figure 3.4*c*. When this occurs, the large separated region of unordered flow on the upper surface produces an increase in pressure on that surface and hence a loss in lift. This behavior of the airfoil is known as stall. Thus the limit in C_l, that is, $C_{l_{max}}$, is the result of flow separation on the upper surface of the airfoil.

To improve this condition, one can curve the leading edge portion of the flat plate, as shown in Figure 3.4*d*, to be more nearly aligned with the flow in

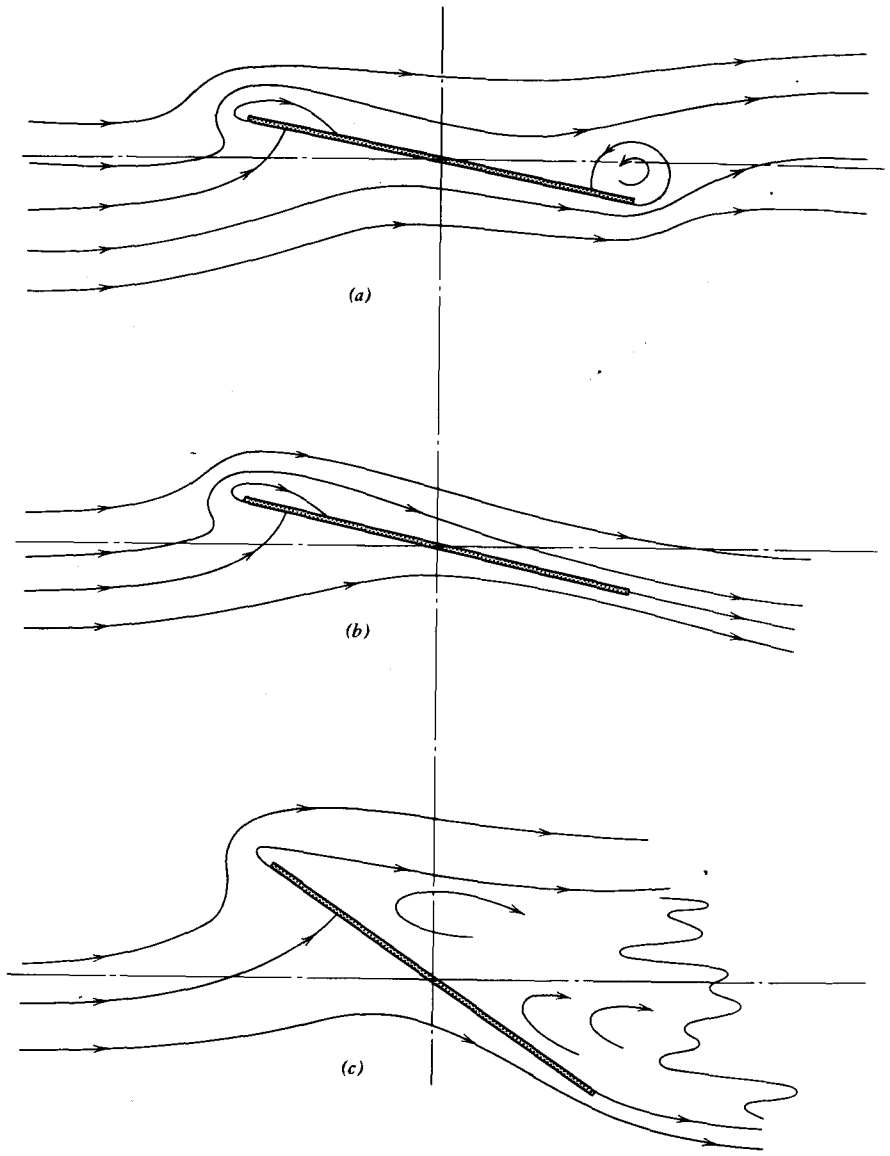

Figure 3.4 Progressive development of airfoil shapes. (*a*) Flat plate at sudden angle of attack—no lift. (*b*) Flat plate at angle of attack in steady flow and generating lift. (*c*) Flat plate experiencing leading edge separation and loss of lift (stall). (*d*) Flat plate with curved leading edge to prevent leading edge separation. (*e*) Airfoil with thickness and camber to delay stall. (*f*) Airfoil with trailing edge separation.

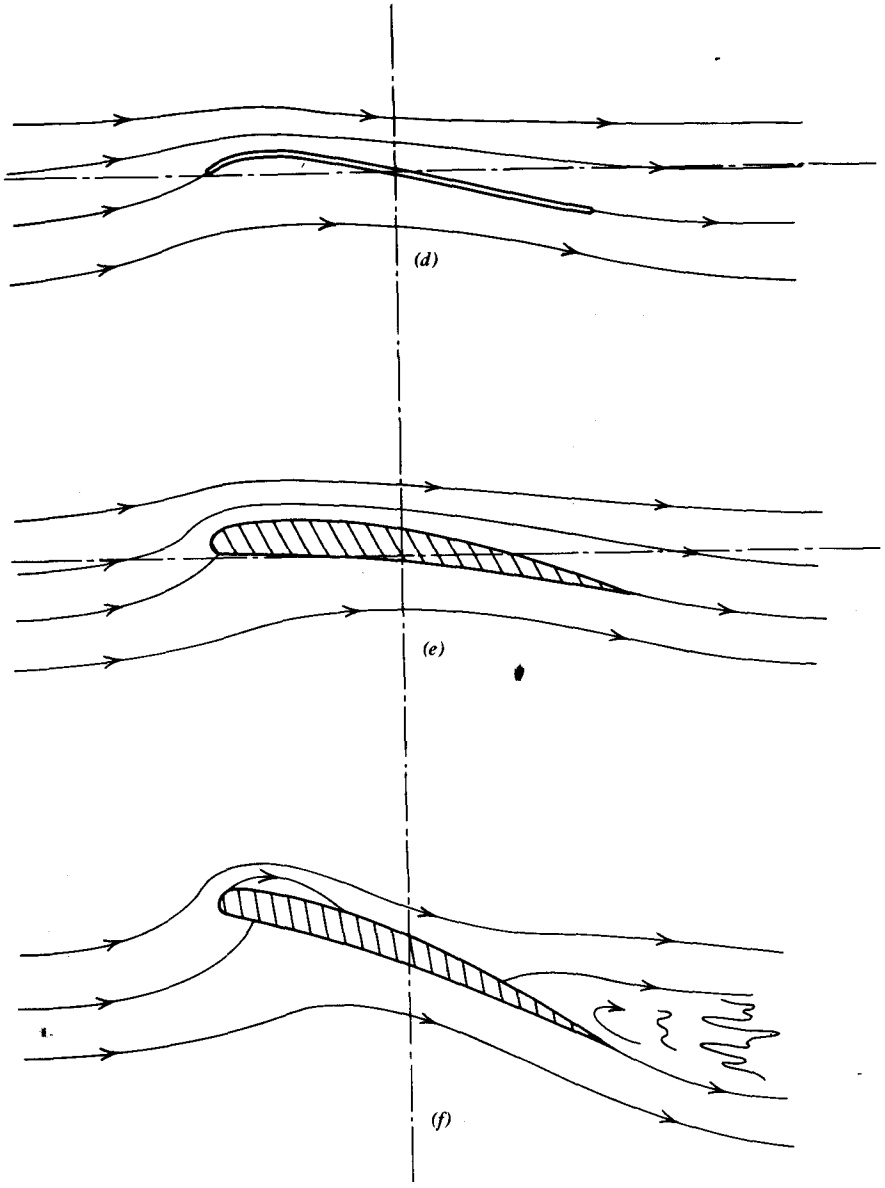

Figure 3.4 (Continued)

that region. Such a shape is similar to that used by the Wright Brothers. This solution to the separation problem, as one might expect, is sensitive to angle of attack and only holds near a particular design angle. However, by adding thickness to the thin, cambered plate and providing a rounded leading edge, the performance of the airfoil is improved over a range of angles, with the leading edge separation being avoided altogether. Thus, in a qualitative sense, we have defined a typical airfoil shape. Camber and thickness are not needed to produce lift (lift can be produced with a flat plate) but, instead, to increase the maximum lift that a given wing area can deliver.

Even a cambered airfoil of finite thickness has its limitations, as shown in Figure 3.4*f*. As the angle of attack is increased, the flow can separate initially near the trailing edge, with the *separation point* progressively moving forward as the angle of attack continues to increase.

The degree to which the flow separates from the leading or trailing edge depends on the Reynolds number and the airfoil geometry. Thicker airfoils with more rounded leading edges tend to delay leading edge separation. This separation also improves with increasing values of the Reynolds number.

Leading edge separation results in flow separation over the entire airfoil and a sudden loss in lift. On the other hand, trailing edge separation is progressive with angle of attack and results in a more gradual stalling. The situation is illustrated in Figures 3.5 and 3.6 (taken from Ref. 3.1). In Figure 3.5 note the sharp drop in C_l at an α of 12° for $R = 3 \times 10^6$, whereas for $R = 9 \times 10^6$, the lift curve is more rounded, with a gradual decrease in C_l beyond an α of 14°. In Figure 3.6, for a thicker airfoil with the same camber, the lift increases up to an angle of approximately 16° for all R values tested. At this higher angle, even for $R = 9 \times 10^6$, it appears that leading edge separation occurs because of the sharp drop in C_l for α values greater than 16°. From a flying qualities standpoint, an airfoil with a well-rounded lift curve is desirable in order to avoid a sudden loss in lift as a pilot slows down the airplane. However, other factors such as drag and Mach number effects must also be considered in selecting an airfoil. Hence, as is true with most design decisions, the aerodynamicist chooses an airfoil that represents the best compromise to conflicting requirements, including nonaerodynamic considerations such as structural efficiency.

Figures 3.5 and 3.6 illustrate other characteristics of airfoil behavior that will be considered in more detail later. Observe that the lift curve, C_l versus α, is nearly linear over a range of angles of attack. Notice also that the slope, $dC_l/d\alpha$, of the lift curve over the linear portion is unchanged by deflecting the split flap. The effect of lowering the flap or, generally, of increasing camber is to increase C_l by a constant increment for each α in the linear range. Thus the angle of attack for zero lift, α_{0l}, is negative for a cambered airfoil. In the case of the 1408 airfoil pictured in Figure 3.5, α_{0l} equals −12.5°, with the split flap deflected 60°.

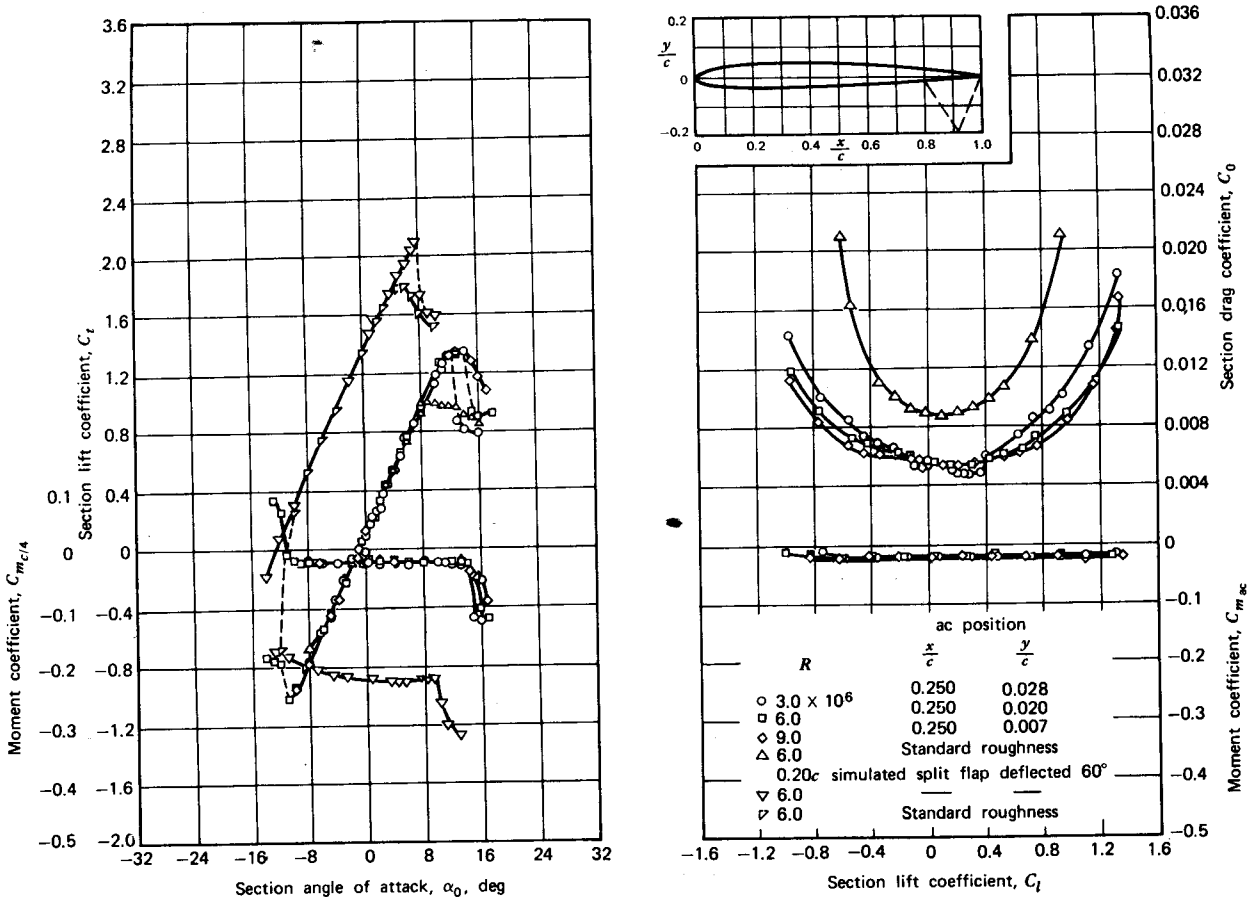

Figure 3.5 Characteristics of the NACA 1408 airfoil.

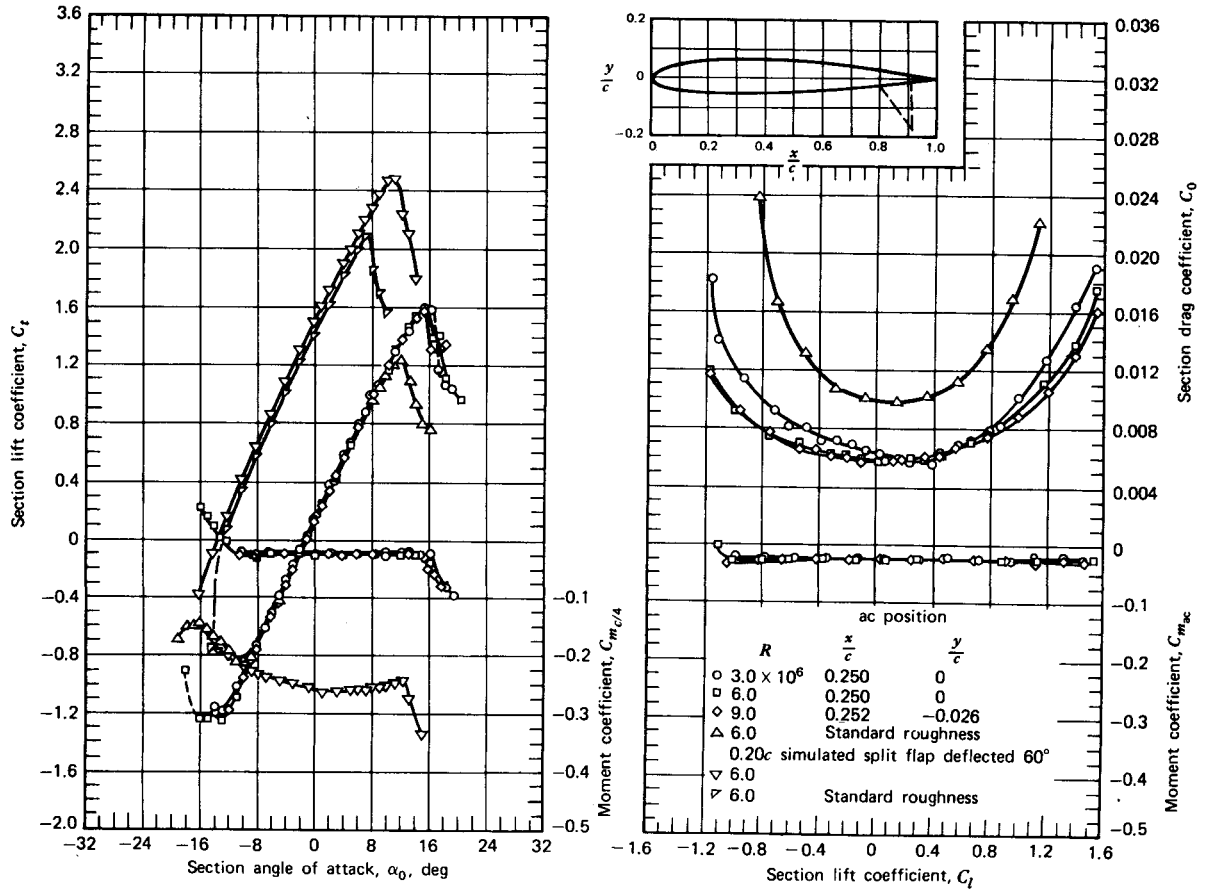

Figure 3.6 Characteristics of the NACA 1412 airfoil.

If α is increased beyond the stall C_l will again begin to increase before dropping off to zero at an α of approximately 90°. The second peak in C_l is generally not as high as that which occurs just before the airfoil stalls. S. P. Langley, in his early experiments, noted these two peaks in the C_l versus α curve but chose to fair a smooth curve through them. Later, the Wright Brothers observed the same characteristics and were troubled by Langley's smooth curve. After searching Langley's original data and finding that he, too, had a "bump" in the data, Wilbur Wright wrote to Octave Chanute on December 1, 1901.

"If he (Langley) had followed his observations, his line would probably have been nearer the truth. I have myself sometimes found it difficult to let the lines run where they will, instead of running them where I think they ought to go. My conclusion is that it is safest to follow the observations exactly and let others do their own correcting if they wish" (*Ref.* 1.1).

To paraphrase the immortal Wilbur Wright, "Do not 'fudge' your data—it may be right."

AIRFOIL FAMILIES

NACA Four-Digit Series

Around 1932, NACA tested a series of airfoil shapes known as the four-digit sections. The camber and thickness distributions for these sections are given by equations to be found in Reference 3.1. These distributions were not selected on any theoretical basis, but were formulated to approximate efficient wing sections in use at that time, such as the well-known Clark-Y section.

The four-digit airfoil geometry is defined, as the name implies, by four digits; the first gives the maximum camber in percent of chord, the second the location of the maximum camber in tenths of chord, and the last two the maximum thickness in percent of chord. For example, the 2412 airfoil is a 12% thick airfoil having a 2% camber located 0.4c from the leading edge. The 2412 airfoil is pictured in Figure 3.7 along with other airfoils yet to be described.

NACA Five-Digit Series

The NACA five-digit series developed around 1935 uses the same thickness distribution as the four-digit series. The mean camber line is defined differently, however, in order to move the position of maximum camber

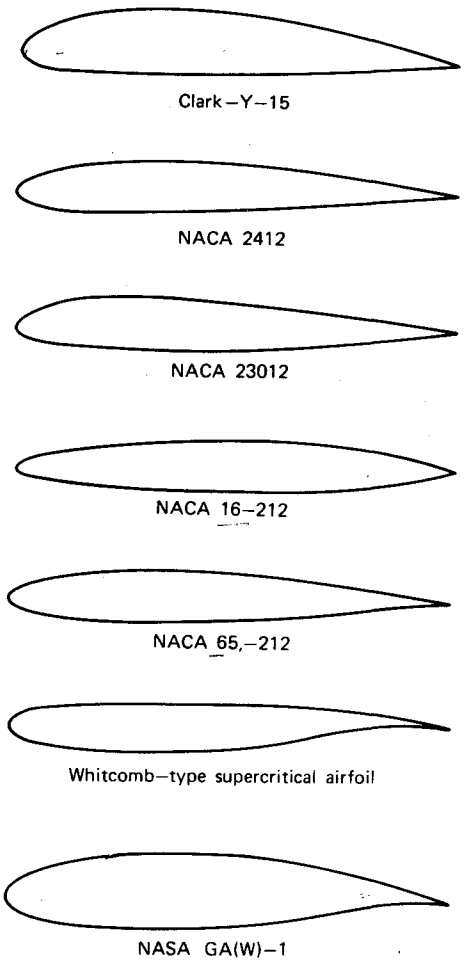

Figure 3.7 Comparison of various airfoil shapes.

forward in an effort to increase $C_{l_{max}}$. Indeed, for comparable thicknesses and cambers, the $C_{l_{max}}$ values for the five-digit series are 0.1 to 0.2 higher than those for the four-digit airfoils. The numbering system for the five-digit series is not as straightforward as for the four-digit series. The first digit multiplied by 3/2 gives the design lift coefficient in tenths of the airfoil. The next two digits are twice the position of maximum camber in percent of chord. The last two digits give the percent thickness. For example, the 23012 airfoil is a 12% thick airfoil having a design C_l of 0.3 and a maximum camber located 15% of c back from the leading edge. This airfoil is also pictured in Figure 3.7.

NACA 1-Series (Series 16)

The NACA 1-series of wing sections developed around 1939 was the first series based on theoretical considerations. The most commonly used 1-series airfoils have the minimum pressure located at the $0.6c$ point and are referred to as series-16 airfoils. The camber line for these airfoils is designed to produce a uniform chordwise pressure difference across it. In the thin airfoil theory to follow, this corresponds to a constant chordwise distribution of vorticity.

Operated at its design C_l, the series-16 airfoil produces its lift while avoiding low-pressure peaks corresponding to regions of high local velocities. Thus the airfoil has been applied extensively to both marine and aircraft propellers. In the former application, low-pressure regions are undesirable from the standpoint of cavitation (the formation of vaporous cavities in a flowing liquid). In the latter, the use of series-16 airfoils delays the onset of deleterious effects resulting from shock waves being formed locally in regions of high velocities.

Series-1 airfoils are also identified by five digits as, for example, the NACA 16–212 section. The first digit designates the series; the second digit designates the location of the minimum pressure in tenths of chord. Following the dash, the first number gives the design C_l in tenths. As for the other airfoils, the last two digits designate the maximum thickness in percent of chord. The 16–212 airfoil is shown in Figure 3.7.

NACA 6-Series

The 6-series airfoils were designed to achieve desirable drag, compressibility, and $C_{l_{max}}$ performance. These requirements are somewhat conflicting, and it appears that the motivation for these airfoils was primarily the achievement of low drag. The chordwise pressure distribution resulting from the combination of thickness and camber is conducive to maintaining extensive laminar flow over the leading portion of the airfoil over a limited range of C_l values. Outside of this range, C_d and $C_{l_{max}}$ values are not too much different from other airfoils.

The mean lines used with the 6-series airfoils have a uniform loading back to a distance of $x/c = 2$. Aft of this location the load decreases linearly. The $a = 1$ mean line corresponds to the uniform loading for the series-16 airfoils.

There are many perturbations on the numbering system for the 6-series airfoils. The later series is identified, for example, as

$$\text{NACA } 65_1\text{-}212 \qquad a = 0.6$$

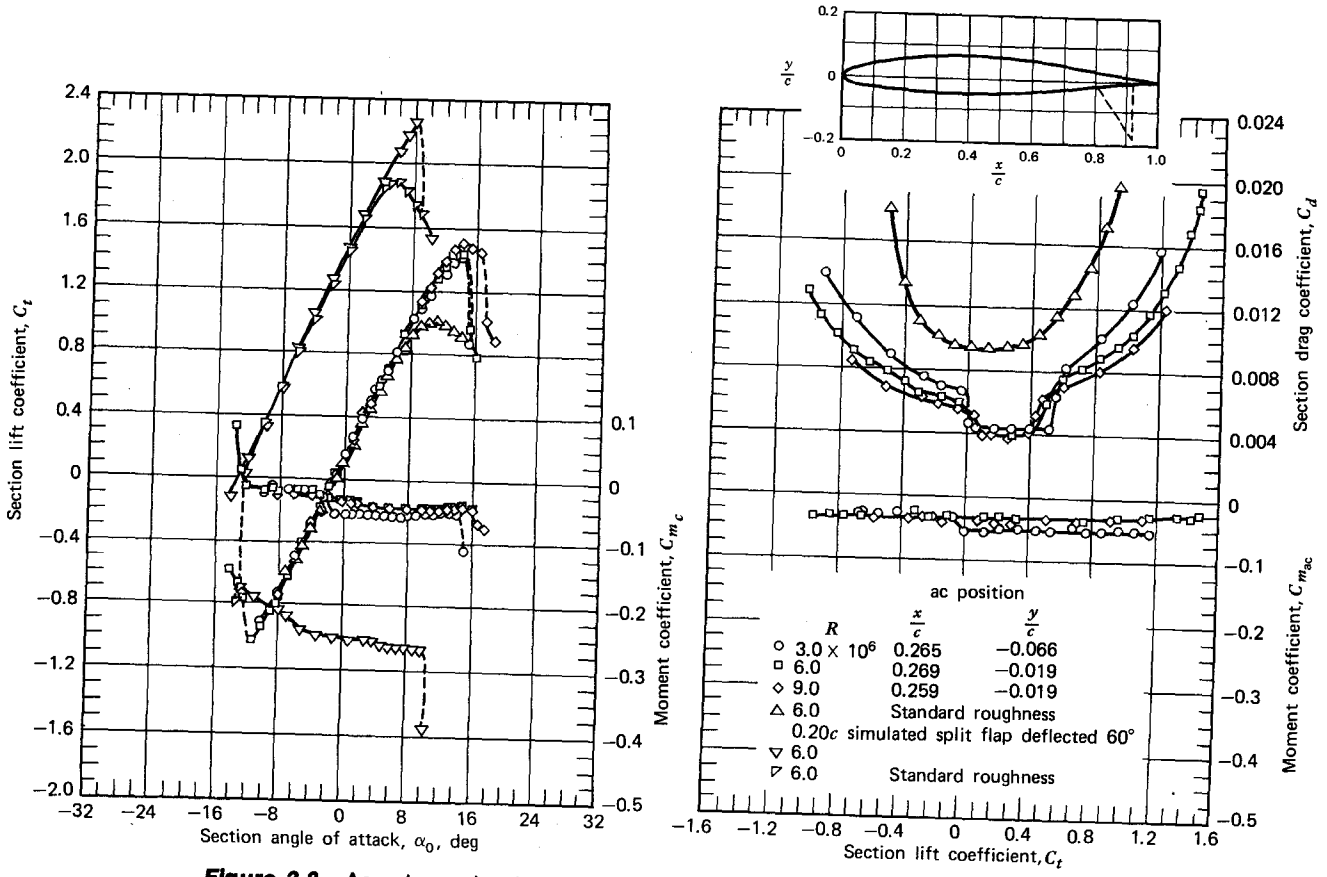

Figure 3.8 Aerodynamic characteristics of the NACA 65, −212, a = 0.6 airfoil.

Here 6 denotes the series; the numeral 5 is the location of the minimum pressure in tenths of chord for the basic thickness and distribution; and the subscript 1 indicates that low drag is maintained at C_l values of 0.1 above and below the design C_l of the 0.2, denoted by the 2 following the dash. Again, the last two digits specify the percentage thickness. If the fraction, a, is not specified, it is understood to equal unity. The 65_1-212 airfoil is shown in Figure 3.7.

Lift and drag curves for the 65_1-212 airfoil are presented in Figure 3.8. Notice the unusual shape of C_d versus C_l, where the drag is significantly lower between C_l values of approximately 0 to 0.3. In this region, for very smooth surfaces and for Reynolds numbers less than 9×10^6, extensive laminar flow is maintained over the surface of the foil with an attendent decrease in the skin friction drag. This region, for obvious reasons, is known as the "drag bucket." In practice this laminar flow, and resulting low drag, is difficult to achieve because of contamination by bugs or by structurally transmitted vibration that perturbs the laminar boundary layer, causing transition. Chapter Four will discuss the drag of these airfoils in more detail.

MODERN AIRFOIL DEVELOPMENTS

Systematic series of airfoils have given way, at least in part, to specialized airfoils designed to satisfy particular requirements. These airfoils are synthesized with the use of sophisticated computer programs such as the one described in Reference 3.5, which will be discussed in more detail later. One such special purpose airfoil is the so-called supercritical airfoil reported on in References 3.6 and 3.7. This airfoil has a well-rounded leading edge and is relatively flat on top with a drooped trailing edge. For a constant thickness of 12%, wind tunnel studies indicate a possible increase of approximately 15% in the drag-divergence Mach number for a supercritical airfoil as compared to a more conventional 6-series airfoil. In addition, the well-rounded leading edge provides an improvement in $C_{l_{max}}$ at low speeds over the 6-series, which has sharper leading edges.

A qualitative explanation for the superior performance of the supercritical airfoil is found by reference to Figure 3.9. At a free-stream Mach number as low as 0.7 or so depending on the shape and C_l, a conventional airfoil will accelerate the flow to velocities that are locally supersonic over the forward or middle portion of its upper surface. The flow then decelerates rapidly through a relatively strong shock wave to subsonic conditions. This compression wave, with its steep positive pressure gradient, causes the boundary layer to thicken and, depending on the strength of the shock, to separate. This, in turn, causes a significant increase in the drag. The minimum value of the free-stream Mach number for which the local flow becomes

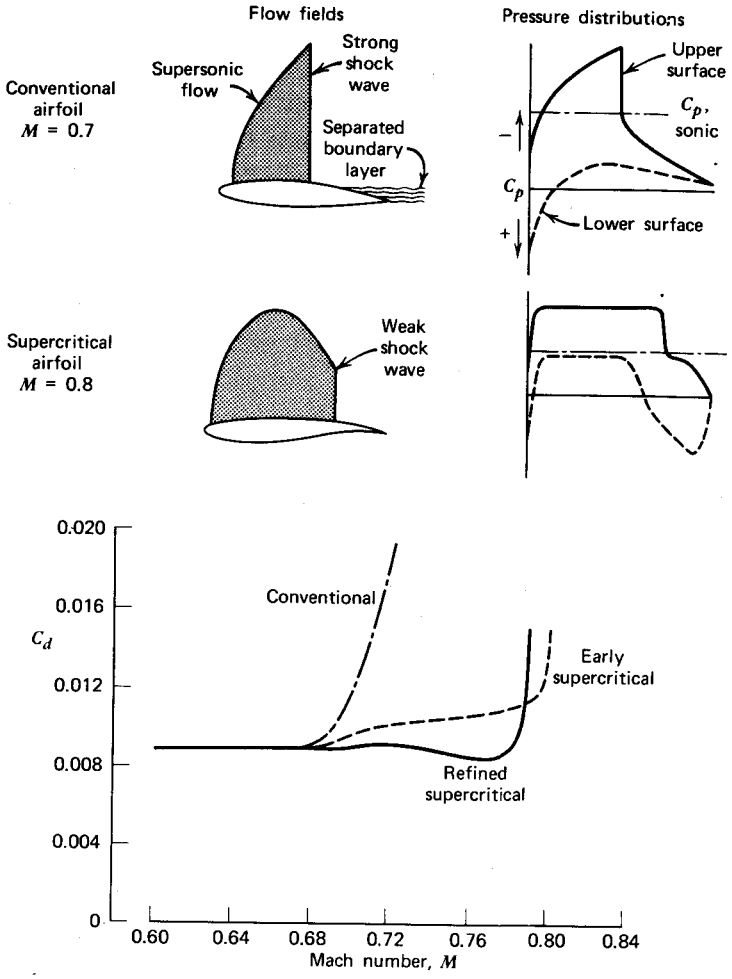

Figure 3.9 Supercritical flow phenomena.

supersonic is referred to as the critical Mach number. As this value is exceeded by a few hundredths, the shock wave strengthens sufficiently to cause the drag to rise suddenly. This free-stream Mach number is known as the drag-divergence Mach number.

The supercritical airfoil also accelerates the flow to locally supersonic conditions at free-stream Mach numbers comparable to the 1- or 6-series airfoils. However, the supercritical airfoil is shaped, so that around its design lift coefficient, the flow decelerates to subsonic conditions through a distribution of weak compression waves instead of one strong one. In this way the drag-divergence Mach number is increased substantially.

Although the possibility of such airfoils was known for some time, their successful development in modern times is attributed to R. T. Whitcomb. A Whitcomb-type supercritical airfoil is pictured in Figure 3.7.

Tested at low speeds, the supercritical airfoils were found to have good $C_{l_{max}}$ values as well as low C_d values at moderate lift coefficients. As a result, another family of airfoils evolved from the supercritical airfoils, but for low-speed applications. These are the "general aviation" airfoils, designated GA(W) for general aviation (Whitcomb). The GA(W)-1 airfoil is the last of the

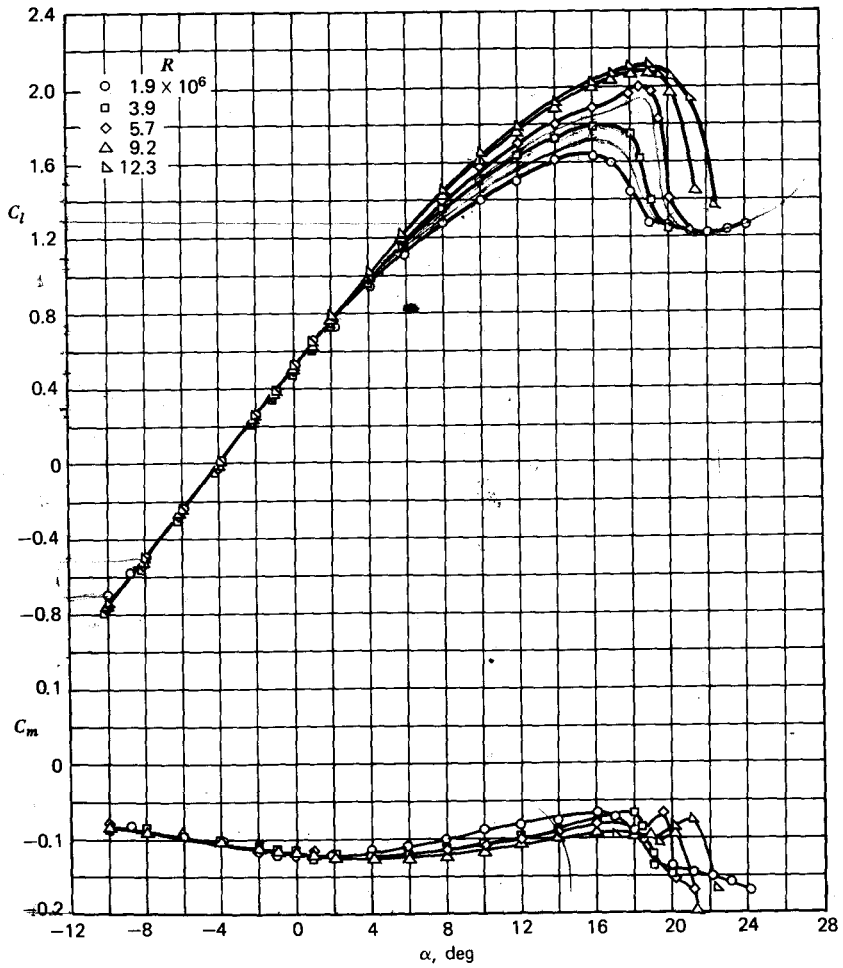

Figure 3.10a Effect of Reynolds number on section characteristics of the GA(W)-1 airfoil Model smooth, $M = 0.15$.

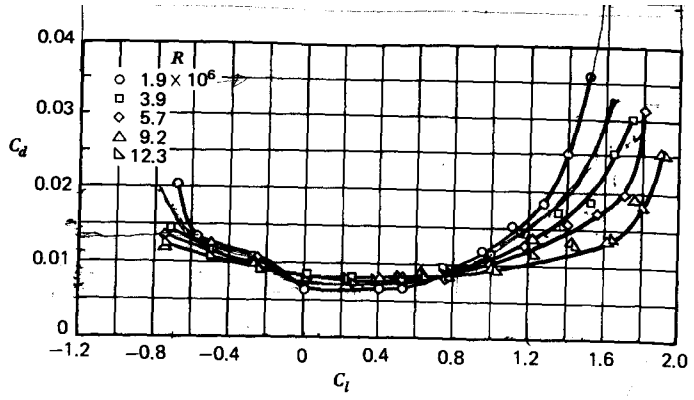

Figure 3.10b Conditions same as Figure 3.10*a*.

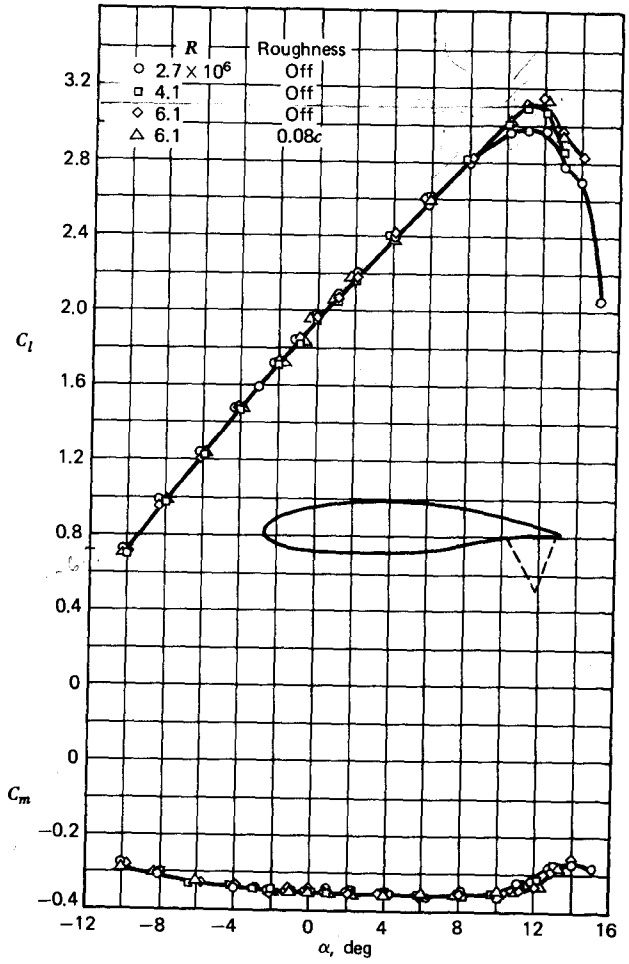

Figure 3.10c GA(W)-1 airfoil section characteristics for 0.20*c* simulated split flap deflected 60° ($M = 0.20$).

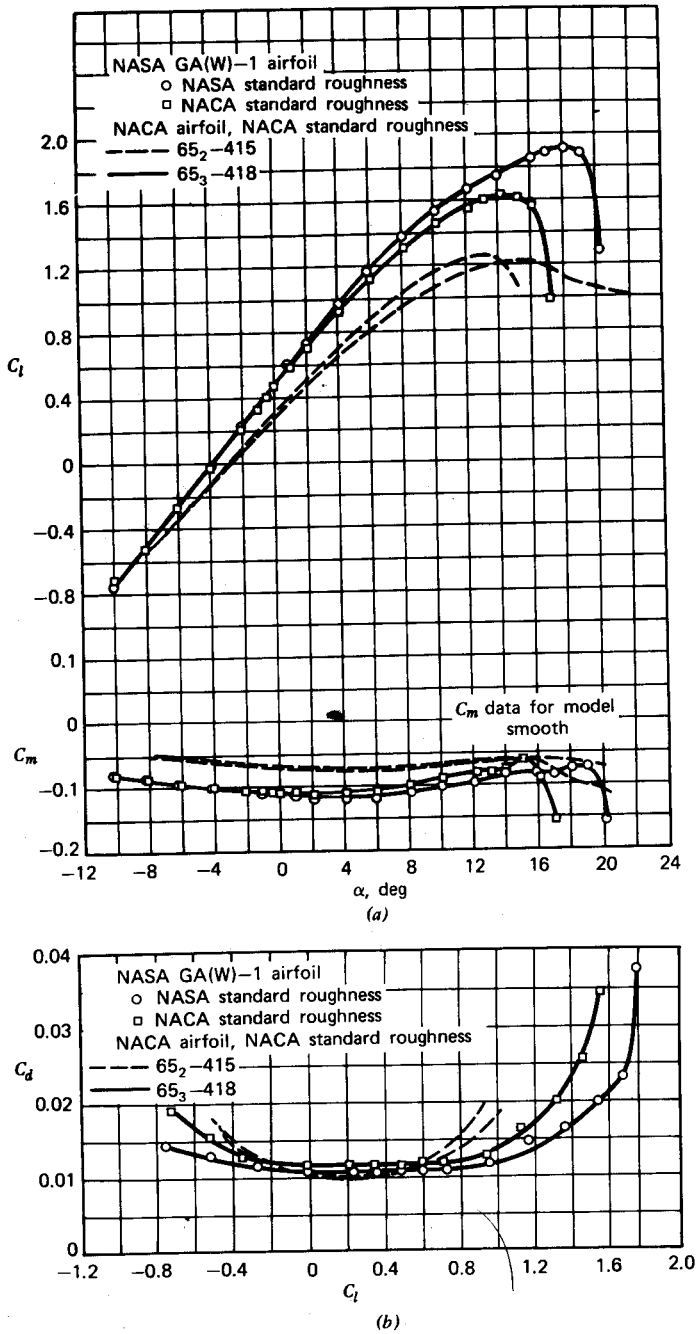

Figure 3.11 Comparison of section characteristics of NASA GA(W)-1 airfoil and NACA 65_2–415 and 65_3–418 airfoils. $M = 0.20$; $R \approx 6 \times 10^6$. (*a*) Variation of C_l and C_m with α. (*b*) Variation of C_d with C_l.

airfoils pictured in Figure 3.7. Test results for this airfoil are reported in Reference 3.8, where its $C_{l_{max}}$ values are shown to be about 30% higher than those for the older NACA 65-series airfoils. In addition, above C_l values of around 0.6, its drag is lower than the older laminar flow series with standard roughness. These data are presented in Figure 3.10 for the GA(W)-1 airfoil. Comparisons of $C_{l_{max}}$ and C_d for this airfoil with similar coefficients for other airfoils are presented in Figures 3.11 and 3.12.

Observe that the performance of the GA(W)-1 airfoil is very Reynolds number-dependent, particularly $C_{l_{max}}$, which increases rapidly with Reynolds number from 2 to 6 million. At the time of this writing, the GA(W) airfoil is beginning to be employed on production aircraft. The same is true of the supercritical airfoil. Indeed, the supercritical airfoil is being used on both the Boeing YC-14 and McDonnell-Douglas YC-15 prototypes currently being tested for the advanced medium STOL transport (AMST) competition. At the time of this writing, NASA is adopting a new nomenclature for the GA(W) airfoils. They will be designated by LS (low speed) or MS (medium speed) followed by four digits. For example, the GA(W)-1 airfoil becomes LS(1)-0417. The (1) designates a family. The 04 refers to a design lift coefficient of 0.4, and 17 is the maximum

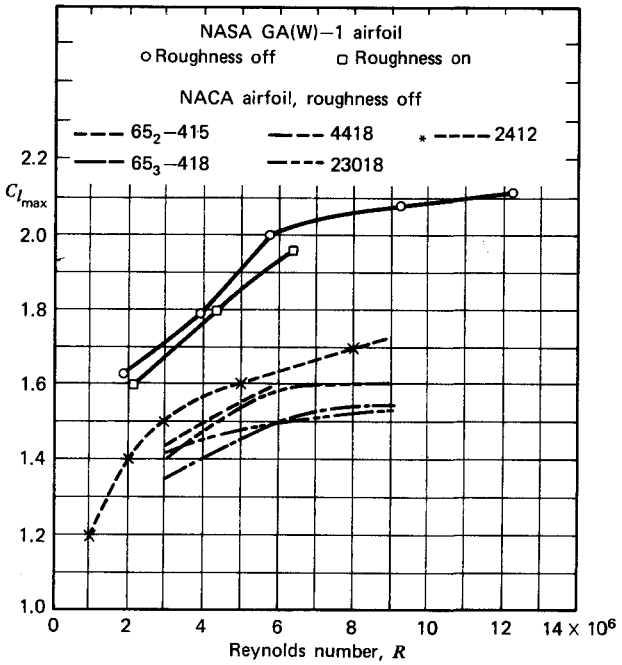

Figure 3.12 Comparison of maximum lift coefficient of the GA(W)-1 airfoil with other NACA airfoils $M = 0.15$.

thickness in percent of chord. For more information on modern airfoils, consult Reference 3.36.

PREDICTION OF AIRFOIL BEHAVIOR

In Chapter Two it was noted that the concepts of a point vortex and a point source could be extended to a continuous distribution of the elementary flow functions. In that chapter a distribution of sources in a uniform flow was found to produce a nonlifting body of finite thickness. In the case of the circular cylinder, the addition of a vortex also produced lift.

Comparable to the continuous distribution of sources pictured in Figure 2.20, consider a similar distribution of vortices as illustrated in Figure 3.13. Such a distribution is referred to as a vortex sheet. If γ is the strength per unit length of the sheet, $\gamma\,\Delta x$ will be the total strength enclosed by the dashed contour shown in the figure. The contour is taken to lie just above and below the sheet. Δx is sufficiently small so that the velocity tangent to the sheet, v, can be assumed to be constant. Because of the symmetry to the flow provided by any one segment of the sheet, the tangential velocity just below the sheet is equal in magnitude but opposite in direction to that just above the sheet. From Equation 2.55, relating circulation to the strength of a vortex, it follows that

$$\gamma\,\Delta x = 2v\,\Delta x$$

or

$$v = \frac{\gamma}{2} \tag{3.14}$$

Note the similarity of this relationship to that expressed by Equation 2.82. However, in the case of Equation 3.14, the velocity is tangent to the vortex sheet whereas, for Equation 2.82, the velocity is normal to the line on which the sources lie.

Consider now the thin airfoil pictured in Figure 3.14. If the airfoil is producing a lift, the pressure on the lower surface is greater than that on the upper. Hence, from Bernoulli's equation, the velocity on the upper surface is greater than the velocity on the lower surface. Letting this difference in

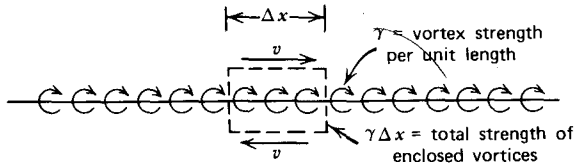

Figure 3.13 Distributed vortices in a two-dimensional flow (vortex sheet).

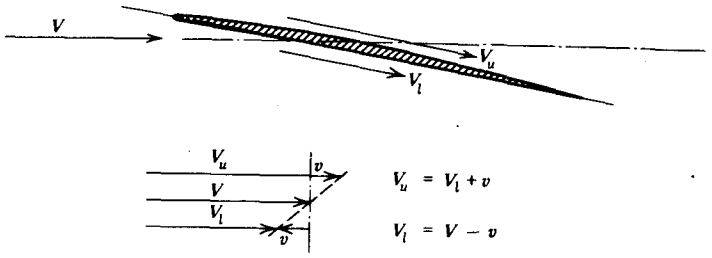

Figure 3.14 The velocity difference across a lifting thin airfoil.

velocity across the airfoil equal $2v$, the upper and lower velocities can be written as

$$V_u = V + v$$

and

$$V_l = V - v$$

Thus the flow field around the airfoil is the same as that which would be produced by placing, in a uniform flow of velocity V, a vortex sheet of unit strength $2v$ along the airfoil.

The contribution to the lift of a differential length of the airfoil will be

$$dl = (p_l - p_u)\,dx$$

Or, using Bernoulli's equation, this becomes,

$$dl = \rho V(2v)\,dx$$

Since $2v$ is the unit vortex strength, the Kutta–Joukowski law (Equation 2.81) is found to hold for the airfoil element.

$$dl = \rho V\gamma\,dx$$

or, integrating the above equation over the entire chord,

$$l = \rho V\Gamma \tag{3.15}$$

where Γ is the total circulation around the airfoil given by

$$\Gamma = \int_0^c \gamma\,dx \tag{3.16}$$

In order to predict the lift and moment on the airfoil, one must find the chordwise distribution of $\gamma(x)$ that will produce a resultant flow everywhere tangent to the mean camber line (thin airfoil approximation). In addition, the *Kutta* condition is applied at the trailing edge to assure that the flow *leaves* the trailing edge tangent to the mean camber line at that point. This is a

necessary condition; otherwise, the resulting flow will appear similar to Figure 3.4*a* with the lift being equal to zero.

An analytical solution to the thin airfoil will be obtained later but, first, let us consider a numerical approach to predicting the lift and moment of an airfoil.

As a gross approximation to the distributed vorticity along the airfoil, the distribution will be replaced by only one vortex of unknown strength, Γ. However, Γ will be placed at a particular point on the airfoil, at the quarter-chord point. The boundary condition and the Kutta condition will be satisfied at only one point, the three-quarter-chord point. This approximation, known as Weissinger's approximation, is illustrated in Figure 3.15 for a flat-plate airfoil.

The velocity induced at $3c/4$ *by* Γ placed at $c/4$ will be

$$v_i = \frac{\Gamma}{\pi c}$$

Assuming α to be a small angle, it follows that

$$v_i = V\alpha \tag{3.17}$$

or

$$\Gamma = \pi c V \alpha \tag{3.18}$$

From the Kutta–Joukowski relationship, $L = \rho V \Gamma$, so that

$$L = \rho \pi c V^2 \alpha \tag{3.19}$$

Expressing lift in terms of the lift coefficient and using Equation 3.19 leads to

$$C_l = 2\pi\alpha \tag{3.20}$$

where α is the angle of attack in radians.

The expression agrees identically with the theoretical solution of this problem that follows. Notice that the result predicts the slope of the lift curve, $dC_l/d\alpha$, to be 2π/rad. Experimentally this figure is usually found to be

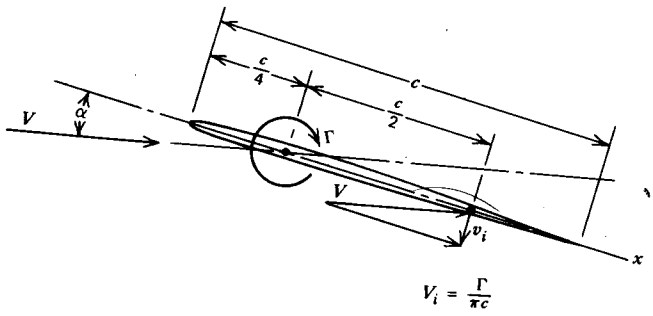

Figure 3.15 Weissinger's approximation to a thin airfoil.

somewhat less. Figures 3.5 and 3.6, for example, show a value of around 0.105/deg or 6.02/rad.

The approximation of Figure 3.15 can be improved on by dividing the airfoil chord into a number of equal segments and placing a vortex of unknown strength at the *quarter-chord point of each segment.* The unknown strengths are determined by assuring that the normal velocity vanishes at the *three-quarter-chord point of each segment.* With the last control point downstream of the last vortex singularity, the Kutta condition is assured.

To illustrate this numerical solution of the thin airfoil, consider Figure 3.16. Here, a circular arc airfoil having a unit chord length with a maximum camber ratio of z is operating at an angle of attack α.

If it is assumed that

$$z \ll 1 \tag{3.21}$$

the radius of curvature, R, of the airfoil will be related to z approximately by

$$R = \frac{1}{8z}$$

The slope of the camber line relative to the chord line (the angle ϕ in Figure 3.16) at any distance x can be determined from the geometry of the figure.

$$\phi = (4 - 8x)z \tag{3.22}$$

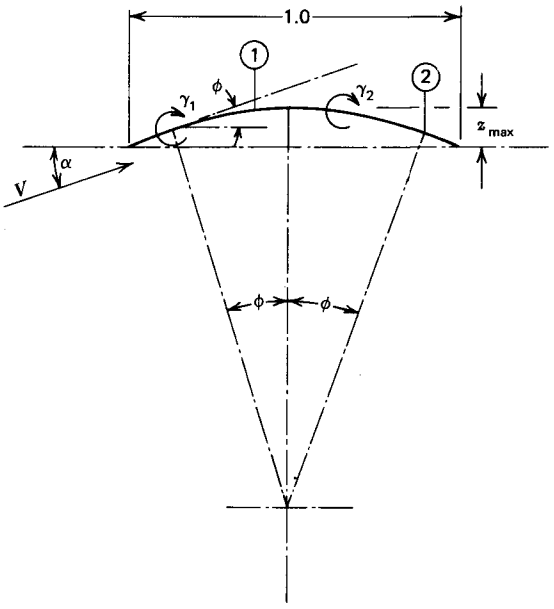

Figure 3.16 A circular arc airfoil approximated by two vortices.

The component of V normal to the mean camber line and directed upward is thus

$$v_n = V(\alpha - \phi)$$

It follows that at control points 1 and 2 located at x values of $3c/8$ and $7c/8$, respectively, the two vortices similating the airfoil must induce velocities downward given by

$$v_i = V(\alpha - z) \quad \text{at} \quad 1 \tag{3.23a}$$

$$v_i = V(\alpha + 3z) \quad \text{at} \quad 2 \tag{3.23b}$$

The problem is linearized by Equation 3.21 so that the vortices, γ_1 and γ_2, are taken to lie on the chord line. Thus, according to Equation 2.56, the total velocities induced at the two control points by the two vortices will be

$$v_i = \frac{1}{\pi}(2\gamma_1 - 2\gamma_2) \quad \text{at } 1 \tag{3.24a}$$

$$v_i = \frac{1}{\pi}\left(\frac{2}{3}\gamma_1 + 2\gamma_2\right) \quad \text{at } 2 \tag{3.24b}$$

Equating Equations 3.23 and 3.24 results in

$$\gamma_1 = \frac{3\pi V}{4}(\alpha + z) \tag{3.25a}$$

$$\gamma_2 = \frac{\pi V}{4}(\alpha + 5z) \tag{3.25b}$$

Applying the Kutta–Joukowski law to each vortex results not only in a predicted total lift, but also in a moment. In coefficient form the lift and moment (about the leading edge) become

$$C_l = 2\pi(\alpha + 2z) \tag{3.26a}$$

$$C_{m_{LE}} = -\pi\left(\frac{\alpha}{2} + \frac{7z}{4}\right) \tag{3.26b}$$

The moment coefficient about the leading edge can be transferred to the quarter-chord point by using

$$C_{m_{1/4}} = c_{m_{LE}} + \frac{1}{4}C_L$$

Thus,

$$C_{m_{1/4}} = -\frac{3\pi z}{4} \tag{3.27}$$

This simple, two-point model results in several important observations that are in agreement with more exact solutions. First, note that Equation 3.26*a* shows the lift coefficient to be a linear combination of α and z. Thus,

cambering an airfoil will not change the slope of the lift curve. Second, it is predicted that the moment about the quarter chord will be independent of α. Hence, this point is predicted to be the aerodynamic center.

As one divides the airfoil into a greater and greater number of elements, the resulting γ distributions will approach the theoretical pressure distribution predicted on the basis of continuous γ distributions. The strength, γ, of a vortex placed at the $c/4$ point of an element of length Δx will be related to the pressure jump, Δp, across the element by

$$\Delta p = \frac{\rho V \gamma}{\Delta x} \tag{3.28}$$

Figure 3.17 presents a comparison, for the flat-plate airfoil, between the pressure distribution obtained using the foregoing numerical procedure with that based on a continuous distribution of γ along the chord. It is seen that the numerical results rapidly converge to the continuous solution as the number of elements increases. In preparing this figure it should be noted that Δp, given by Equation 3.28, has been expressed in coefficient form and plotted at the location of each point vortex. Figure 3.18 presents a similar comparison for the circular arc airfoil. In this case α is taken to be zero, avoiding the infinitely negative C_p at the leading edge.

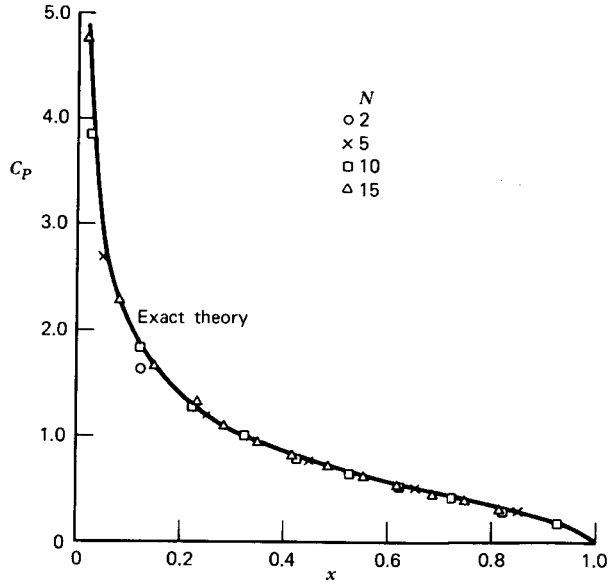

Figure 3.17 Comparison of numerical calculation of chordwise lift distribution with analytical prediction for a flat-plate airfoil at 10° angle of attack.

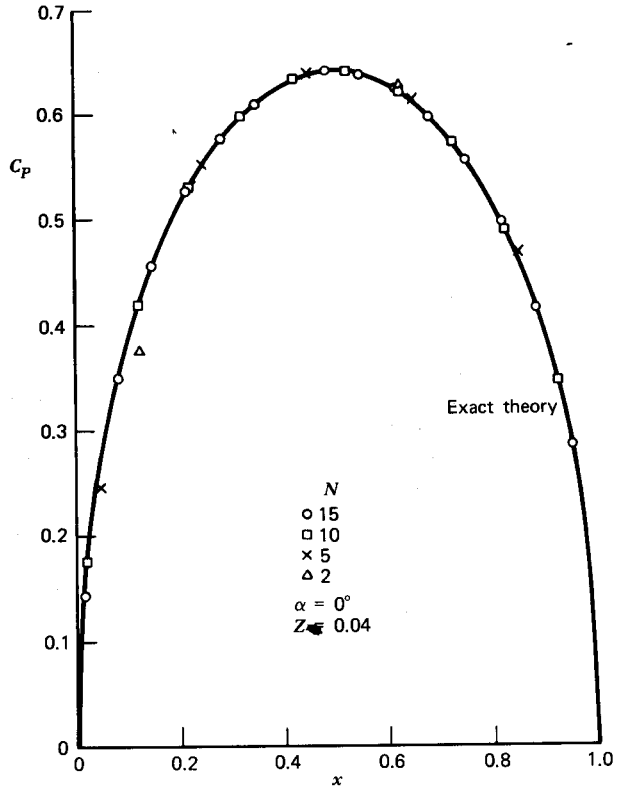

Figure 3.18 Comparison of numerical calculation of chordwise lift distribution with analytical prediction for a 4% cambered, circular arc airfoil.

The numerical model predicts the lift in exact agreement with more precise analytical models. However, the moment coefficient, given by Equation 3.27, is only three-quarters of that obtained by analytical means. Figure 3.19 shows that the exact value is approached rapidly, however, as the number of segments increases.

As indicated by Figure 3.19, the exact value of the moment coefficient about the aerodynamic center ($c/4$) for the circular arc airfoil is given by

$$C_{m_{ac}} = -\pi z \tag{3.29}$$

Using Equation 3.13, the location of the center of pressure can be found as

$$X_{cp} = \frac{1}{4} + \frac{\pi z}{C_l} \tag{3.30}$$

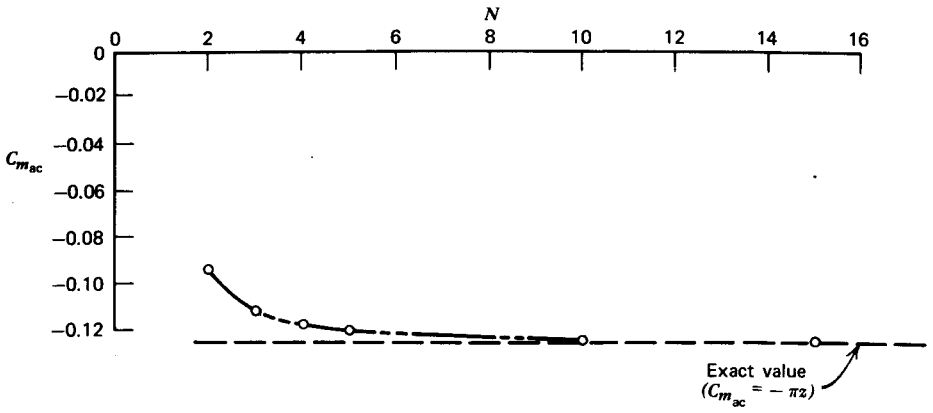

Figure 3.19 Numerical calculation of moment coefficient compared with analytical prediction for 4% cambered, circular arc airfoil.

Observe that as C_l decreases, the center of pressure moves aft, approaching infinity as C_l goes to zero. This movement of the center of pressure is opposite to what was believed to be true by the early pioneers in aviation. The Wright Brothers were probably the first to recognize the true nature of the center-of-pressure movement as a result of their meticulous wind tunnel tests.

Analytical solutions to the thin airfoil can be found in several texts (e.g., Ref. 3.2 and 3.3). Here, the airfoil is replaced by a continuous distribution of vortices instead of discrete point vortices, as used with the numerical solution.

Referring to Figure 3.20, without any loss of generality, the airfoil is taken to have a unit chord lying along the x-axis with the origin at the leading

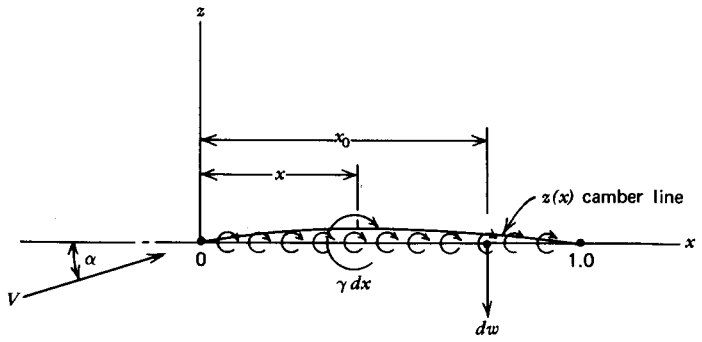

Figure 3.20 The modeling of a thin airfoil by a vortex sheet.

edge. The shape of the camber line is given by $z(x)$, and it is assumed that

$$z(x) \ll 1$$

With this assumption the problem is linearized and made tractable by replacing the airfoil with a vortex sheet of unit strength $\gamma(x)$ lying along the chord line instead of along the camber line.

At the point x_0, the downward velocity induced by an elemental vortex of strength $\gamma(x)\,dx$ located at x, according to Equation 2.56, will be given by

$$dw(x_0) = \frac{\gamma(x)\,dx}{2\pi(x_0 - x)}$$

or, integrating over the chord,

$$w(x_0) = \frac{1}{2\pi}\int_0^1 \frac{\gamma(x)\,dx}{x_0 - x} \tag{3.31}$$

In order to satisfy the boundary condition that the flow be tangent everywhere to the mean camber line, it follows that, to a small angle approximation,

$$\frac{w(x_0)}{V} = \alpha - \left(\frac{dz}{dx}\right)_{x_0} \tag{3.32}$$

Thus, given α and $z(x)$, the following integral equation must be solved for $\gamma(x)$.

$$\frac{1}{2\pi V}\int_0^1 \frac{\gamma(x)\,dx}{x_0 - x} = \alpha - \left(\frac{dz}{dx}\right)_{x_0} \tag{3.33}$$

In addition, $\gamma(x)$ must vanish at the trailing edge in order to satisfy the Kutta condition. Otherwise, the induced velocity will be infinite just downstream of this point.

Equation 3.33 is solved by first transforming to polar coordinates.

Letting

$$x = \frac{1}{2}(1 - \cos\theta) \tag{3.34}$$

Equation 3.33 becomes

$$\frac{1}{2\pi V}\int_0^\pi \frac{\gamma(\theta)\,d\theta}{\cos\theta - \cos\theta_0} = \alpha - \left(\frac{dz}{dx_{x_0}}\right) \tag{3.35}$$

On the basis of the more sophisticated method of conformal mapping (e.g., see Ref. 3.4), it is known that $\gamma(x)$ is generally singular at the leading edge approaching infinity as $1/x$. Thus we will assume a priori that Equation 3.35 can be satisfied by a $\gamma(\theta)$ distribution of the form

$$\gamma = 2V\left[A_0\frac{(1+\cos\theta)}{\sin\theta} + \sum_{n=1}^{\infty} A_n \sin n\theta\right] \tag{3.36}$$

Using the relationships

$$\frac{1}{2}\left[\cos(n-1)\theta - \cos(n+1)\theta\right] = \sin n\theta \sin\theta$$

and

$$\int_0^{\pi} \frac{\cos n\theta \, d\theta}{\cos\theta - \cos\theta_0} = \pi \frac{\sin n\theta_0}{\sin\theta_0} \tag{3.37}$$

Equation 3.35 becomes

$$A_0 - \sum_{n=1}^{\infty} A_n \cos n\theta = \alpha - \frac{dz}{dx}$$

Multiplying both sides of the preceding equation by $\cos m\theta$ ($m = 0, 1, 2, \ldots, n, \ldots$) and integrating from 0 to π leads to

$$A_0 = \alpha - \frac{1}{\pi}\int_0^{\pi} \frac{dz}{dx} d\theta \tag{3.38a}$$

$$A_n = \frac{2}{\pi}\int_0^{\pi} \frac{dz}{dx} \cos n\theta \, d\theta \tag{3.38b}$$

Thus, knowing the shape of the mean camber line, the coefficients A_0, A_1, $A_2, \ldots$ can be determined either in closed form or by graphical or numerical means (see Ref. 3.1). Having these coefficients, C_l and C_m can then be easily determined from the Kutta–Joukowski relationship.

The lift and moment about the leading edge are given by

$$L = \int_0^1 \rho V \gamma(x) \, dx$$

$$M_{LE} = -\int_0^1 \rho V \gamma(x) \, x \, dx$$

From these and using Equation 3.36,

$$C_l = 2\pi A_0 + \pi A_1 \tag{3.39}$$

$$C_{m_{LE}} = -\frac{\pi}{2}\left(A_0 + A_1 - \frac{A_2}{2}\right) \tag{3.40}$$

It follows that C_m about the quarter-chord point is independent of α, so that this point is the aerodynamic center, with the moment coefficient being given by

$$C_{m_{ac}} = -\frac{\pi}{4}(A_1 - A_2) \tag{3.41}$$

Since α is contained only in the A_0 coefficient, it can be concluded immediately without considering the actual form of $z(x)$ that C_l is given by a

linear combination of α and a function of z. Thus, camber changes can be expected to affect the angle of zero lift but not the slope of the lift curve.

Reference to airfoil data, such as that presented in Figures 3.5 and 3.6, will show that the predictions of thin airfoil theory are essentially correct. There is a range of angles of attack over which the lift coefficient varies linearly with α. The slope of this lift curve is usually not as high as the theory predicts, being approximately 4 to 8% less than the theoretical value. For many purposes an assumed value of 0.1 C_l/deg is sufficiently accurate and is a useful number to remember. Experimental data also show the aerodynamic center to be close to the quarter-chord point. The effects of camber on C_l, $dC_l/d\alpha$, and $C_{m_{ac}}$ are also predicted well.

Recently large numerical programs have been developed to predict the performance of airfoils that incorporate Reynolds number and Mach number effects. These are typified by Reference 3.5, which will be described briefly. This program begins by calculating the potential flow around the airfoil. In order to allow for both finite thickness and circulation, the airfoil contour is approximated by a closed polygon, as shown in Figure 3.21. A continuous distribution of vortices is then placed on each side of the polygon, with the vortex strength per unit length, γ, varying linearly from one corner to the next and continuous across the corner. Figure 3.22 illustrates this model for two sides connecting corners 3, 4, and 5. Control points are chosen midway between the corners. The values of the vortex unit strengths at the corners are then found that will induce velocities at each control point tangent to the polygon side at that point. Note, however, that if there are n corners and hence $n + 1$ unknown γ values at the corners, the n control points provide one less equation than unknowns. This situation is remedied by applying the Kutta condition at the trailing edge. This requires that $\gamma_{n+1} = -\gamma_1$, assuring that the velocities induced at the trailing edge are finite.

Having determined the vortex strengths, the velocity field and, hence, the

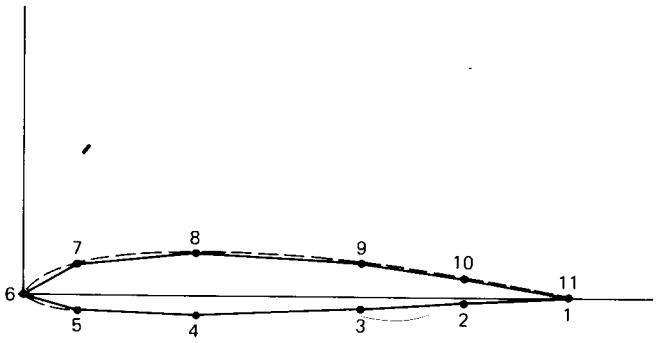

Figure 3.21 Approximation of airfoil contour by closed polygon.

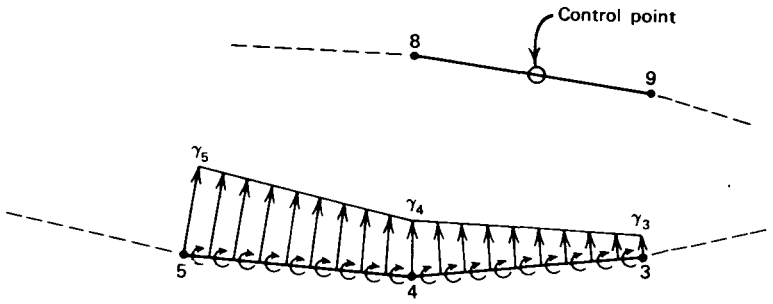

Figure 3.22 Vortex distributions representing airfoil contour.

pressure distribution around the airfoil can be calculated. This result is then used to calculate the boundary layer development over the airfoil, including the growth of the laminar layer, transition, the growth of the turbulent layer, and possible boundary layer separation. The airfoil shape is then enlarged slightly to allow for the boundary layer thickness and the potential flow solutions are repeated. The details of this iterative procedure are beyond the scope of this text.

MAXIMUM LIFT

Airfoil theory based on potential flow methods predicts the lift of an airfoil in its linear range but does not provide any information concerning maximum lift capability. As discussed previously, $C_{l_{max}}$, is determined by flow separation, which is a "real fluid" effect. Separation is difficult to predict analytically, so the following material on $C_{l_{max}}$ is mainly empirical.

Typically, conventional airfoils without any special high-lift devices will deliver $C_{l_{max}}$ values of approximately 1.3 to 1.7, depending on Reynolds number, camber, and thickness distribution. The appreciable dependence of $C_{l_{max}}$ on R shown in Figure 3.12 for the GA(W)-1 airfoil is typical of other airfoils. Figure 3.23 presents $C_{l_{max}}$ as a function of R and thickness ratio for NACA four-digit airfoils having a maximum camber of 2%, located 40% of the chord back from the leading edge. At intermediate thickness ratios of around 0.12, the variation of $C_{l_{max}}$ with R parallels that of the 17% thick GA(W)-1 airfoil. Note, at least for this camber function, that a thickness ratio of 12% is about optimum. This figure is taken from Reference 3.14. This same reference presents the following empirical formula for $C_{l_{max}}$ for NACA four-digit airfoils at an R of 8×10^6.

$$C_{l_{max}} = 1.67 + 7.8\,pz - 2.6\,\frac{(0.123 + 0.022p - 0.5z - t)^2}{t^{3/2}} \tag{3.42}$$

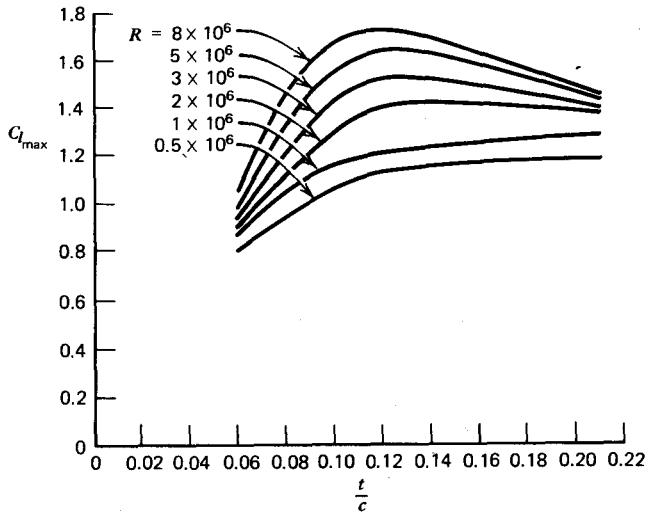

Figure 3.23 Variation of $C_{l_{max}}$ with thickness ratio of NACA 24xx airfoils for various Reynolds numbers. (B. W. McCormick, *Aerodynamics of V/STOL Flight*, Academic Press, Inc, 1967. Reprinted by permission of Academic Press, Inc.)

t, z, and p are thickness, maximum camber, and position of maximum camber, respectively, expressed as a fraction of the chord. For example, for a 2415 airfoil,

$$t = 0.15$$
$$z = 0.02$$
$$p = 0.40$$

so that according to Equation 3.42,

$$C_{l_{max}} = 1.70$$

For a plain wing (unflapped), there is little effect of aspect ratio or taper ratio on $C_{L_{max}}$. Even the presence of a fuselage does not seem to have much effect. As the angle of attack of a wing increases, $C_{L_{max}}$ is reached and any further increase in α will result in a loss of lift. Beyond $C_{L_{max}}$ the wing is said to be stalled. Although taper ratio does not significantly affect the overall wing $C_{L_{max}}$, it (and wing twist) significantly affect what portion of the wing stalls first. As the taper ratio is decreased, the spanwise position of initial stall moves progressively outboard. This tendency is undesirable and can be compensated for by "washing out" (negative twist) the tips. One usually wants a wing to stall inboard initially for two reasons. First, with inboard stall, the turbulence shed from the stalled region can shake the tail, providing a built-in stall warning device. Second, the outboard region being unstalled will still provide

aileron roll control even though the wing has begun to stall. The lift characteristics of three-dimensional wings will be treated in more detail later.

Flaps

An examination of all of the airfoil data presented in Reference 3.1 discloses that the greatest value of $C_{l_{max}}$ one can expect at a high Reynolds number from an ordinary airfoil is around 1.8. This maximum value is achieved by the NACA 23012 airfoil. Another 12% thick airfoil, the 2412, delivers the second highest value, 1.7.

In order to achieve higher $C_{l_{max}}$ values for takeoff and landing without unduly penalizing an airplane's cruising performance, one resorts to the use of mechanical devices to alter temporarily the geometry of the airfoil. These devices, known as flaps, exist in many different configurations, the most common of which are illustrated in Figure 3.24. In addition to the purely mechanical flaps, this figure depicts flaps that can be formed by sheets of air exiting at the trailing edge. These "jet flaps" can produce $C_{l_{max}}$ values in excess of those from mechanical flaps, provided sufficient energy and momentum are contained in the jet. Frequently one uses the terms "powered" and "unpowered" to distinguish between jet and mechanical flaps.

The effect of a mechanical flap can be seen by referring once again to Figure 3.6. Deflecting the flap, in this case a split flap, is seen to shift the lift curve upward without changing the slope. This is as one might expect from Equation 3.26, since deflecting the flap is comparable to adding camber to the airfoil.

Some flap configurations appear to be significantly better than others simply because, when deflected, they extend the original chord on which the lift coefficient is based. One can determine if the flap is extensible, such as the Fowler or Zap flaps in Figure 3.24, by noting whether or not the slope of the lift curve is increased with the flap deflected. Consider a flap that, when deflected, extends the original chord by the fraction x. The physical lift curve would have a slope given by

$$\frac{dL}{d\alpha} = \frac{1}{2}\rho V^2(1+x)cC_{l_\alpha} \tag{3.43}$$

since $(1+x)c$ is the actual chord. C_{l_α} does not depend significantly on thickness or camber; hence, the lift curve slope of the flapped airfoil based on the unflapped chord, c, would be

$$C_{l_\alpha}\text{ (flapped)} = (1+x)C_{l_\alpha}\text{ (unflapped)}$$

Now the maximum lift, expressed in terms of the extended chord and $C_{l_{max_e}}$

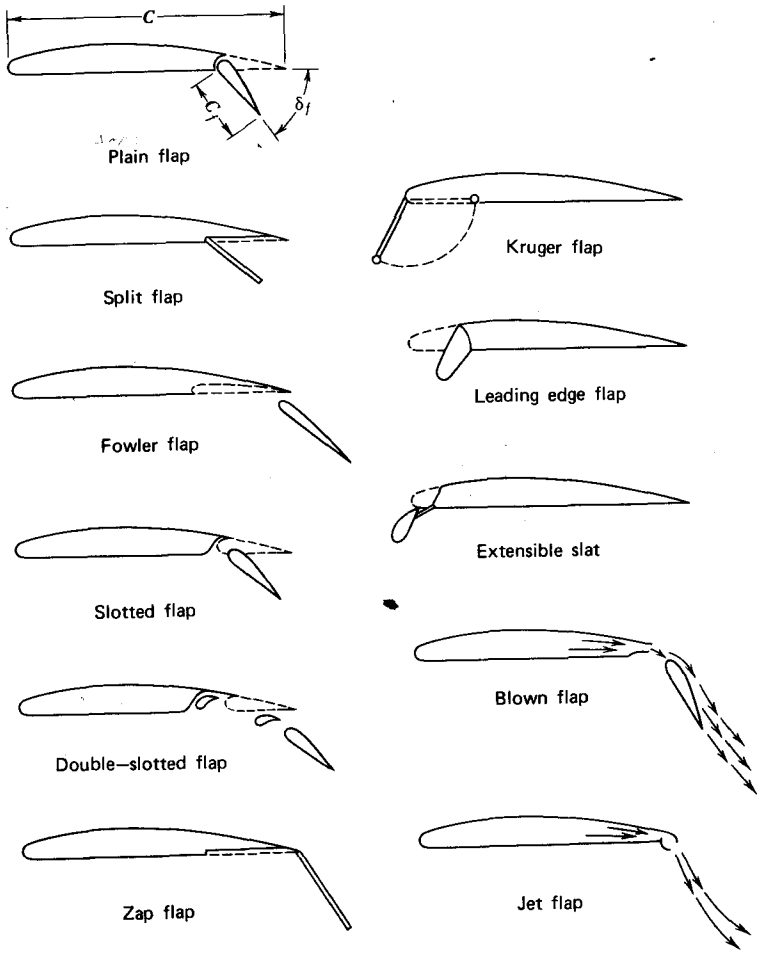

Figure 3.24 Flap configurations.

(based on that chord) would be,

$$L_{\max} = \frac{1}{2}\rho V^2(1+x)cC_{l_{\max_e}}$$

Thus $C_{l_{\max}}$ based on the original chord becomes

$$C_{l_{\max}} = (1+x)C_{l_{\max_e}}$$

or

$$C_{L_{\max_e}} = C_{l_{\max}}/(1+x)$$

$$= C_{l_{\max}} \frac{C_{l_\alpha}\ \text{(unflapped)}}{C_{l\alpha}\ \text{(flapped)}} \qquad (3.44)$$

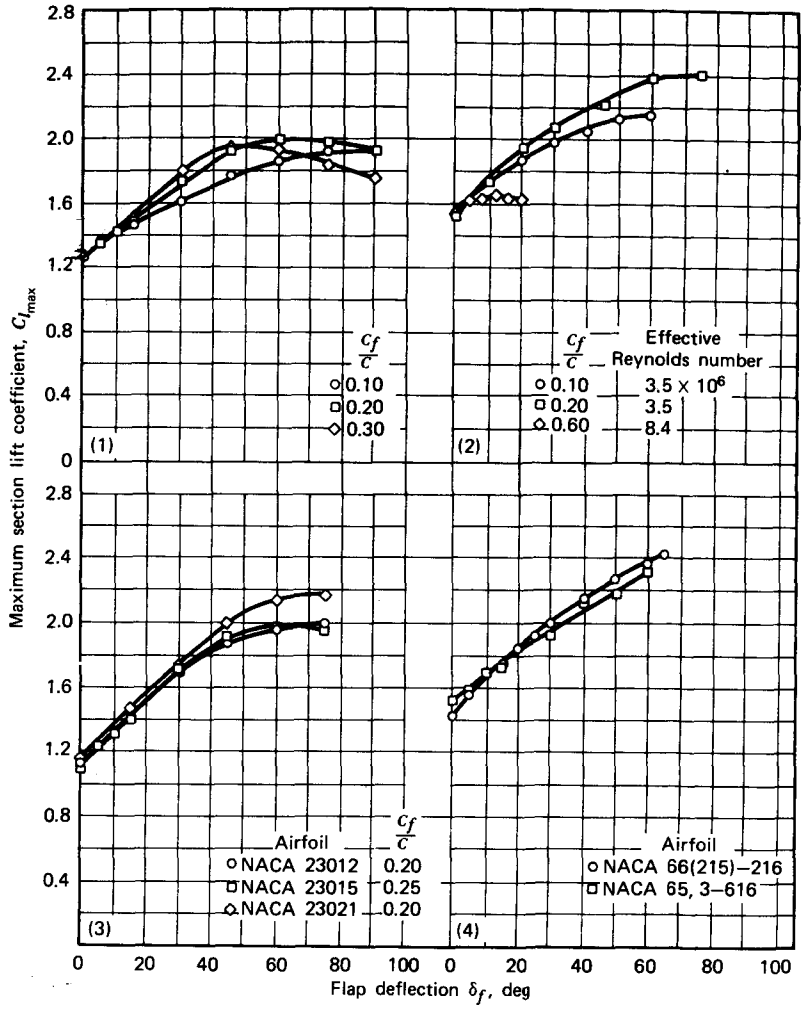

(1) Clark–Y airfoil; $R = 0.609 \times 10^6$.

(2) NACA 230–series airfoils; $R = 0.609 \times 10^6$.

(3) NACA 23012 airfoil.

(4) NACA 6–series airfoils; $R = 6.0 \times 10^6$, $\frac{c_f}{c} = 0.20$.

(a)

Figure 3.25 Performance of plain flaps. (*a*) Variation of maximum section lift coefficient with flap deflection for several airfoil sections equipped with plain flaps. (*b*) Variation of optimum increment of maximum section lift coefficient with flap chord ratio for several airfoil sections equipped with plain flaps. (*c*) Effect of gap seal on maximum lift coefficient of a rectangular Clark-Y wing equipped with a full-span 0.20*c* plain flap. $A = 6$, $R = 0.6 \times 10^4$.

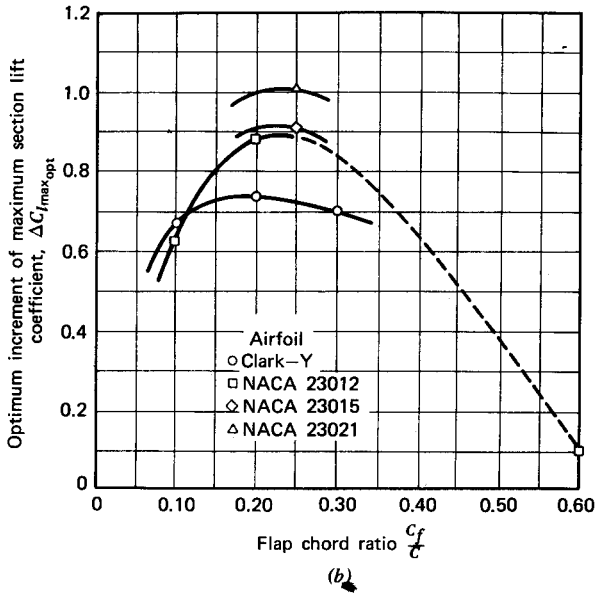

(b)

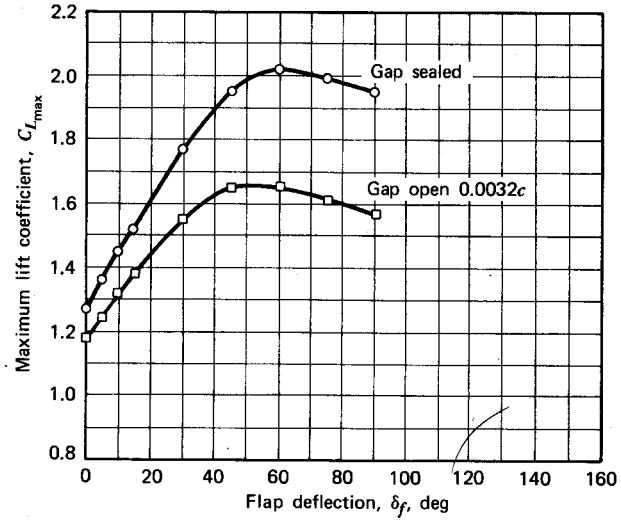

(c)

Figure 3.25 (Continued)

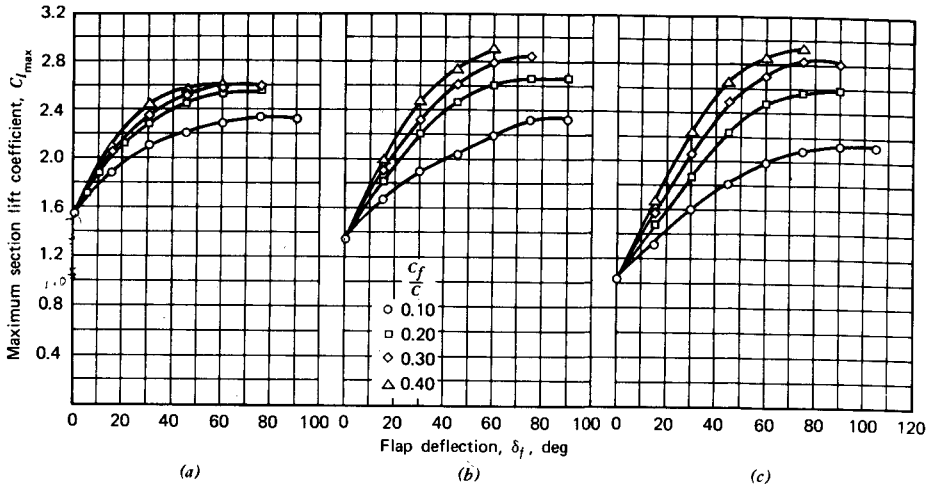

Figure 3.26 Variation of maximum section lift coefficient with flap deflection for three NACA 230-series airfoils equipped with split flaps of various sizes. $R = 3.5 \times 10^6$. (*a*) NACA 23012 airfoil section. (*b*) NACA 23021 airfoil section. (*c*) NACA 23030 airfoil section.

Figures 3.25 to 3.30 and Tables 3.1 and 3.2 present section data on plain, split, and slotted flaps as reported in Reference 3.15. With these data one should be able to estimate reasonably accurately the characteristics of an airfoil section equipped with flaps.

A study of this data suggests the following:

Plain Flaps

1. The optimum flap chord ratio is approximately 0.25.
2. The optimum flap angle is approximately 60°.
3. Leakage through gap at flap nose can decrease $C_{l_{max}}$ by approximately 0.4.
4. The maximum achievable increment in $C_{l_{max}}$ is approximately 0.9.

Split Flaps

1. The optimum flap chord ratio is approximately 0.3 for 12% thick airfoils, increasing to 0.4 or higher for thicker airfoils.
2. The optimum flap angle is approximately 70°.
3. The maximum achievable increment in $C_{l_{max}}$ is approximately 0.9.
4. $C_{l_{max}}$ increases nearly linearly with log R for $0.7 \times 10^6 < R < 6 \times 10^6$.
5. The optimum thickness ratio is approximately 18%.

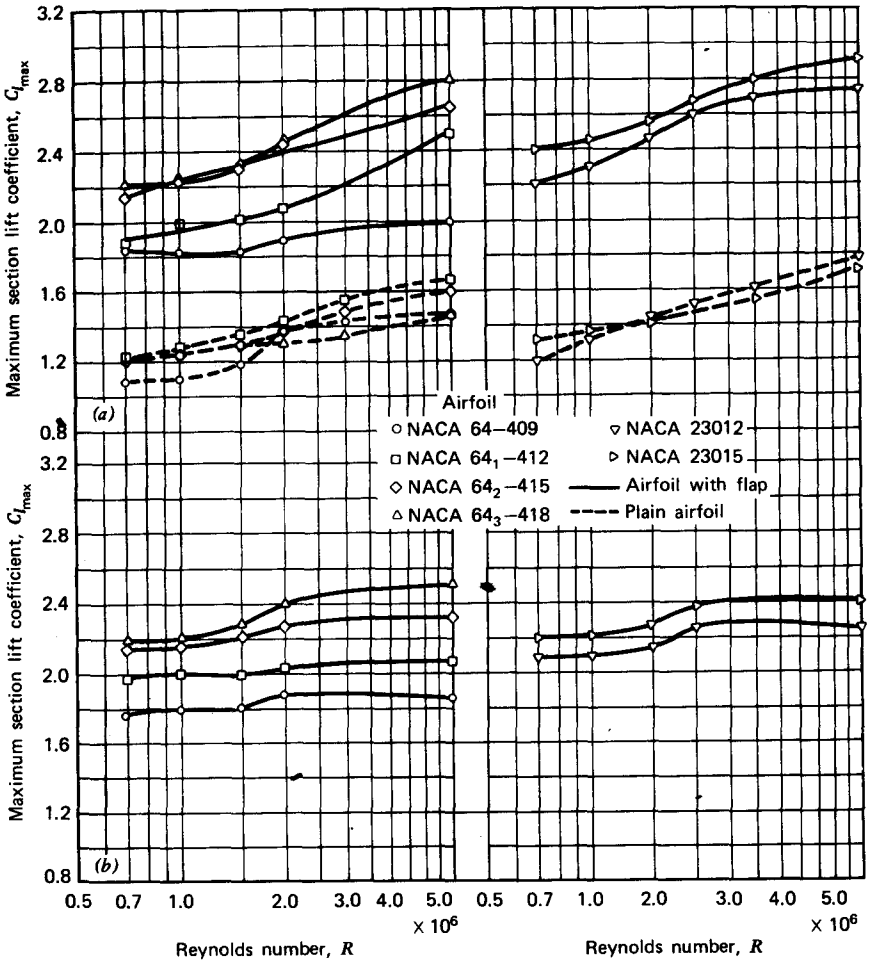

Figure 3.27 Variation of maximum section lift coefficient with Reynolds number for several NACA airfoil sections with and without 0.20*c* split flaps deflected 60°. (*a*) Smooth airfoil. (*b*) Airfoil with leading edge roughness.

Slotted Flaps

1. The optimum flap chord ratio is approximately 0.3.
2. The optimum flap angle is approximately 40° for single slots and 70° for double-slotted flaps.
3. The optimum thickness ratio is approximately 16%.
4. $C_{l_{max}}$ is sensitive to flap (and vane) position.
5. The maximum achievable increment in $C_{l_{max}}$ is approximately 1.5 for single slots and 1.9 for double slotted flaps.

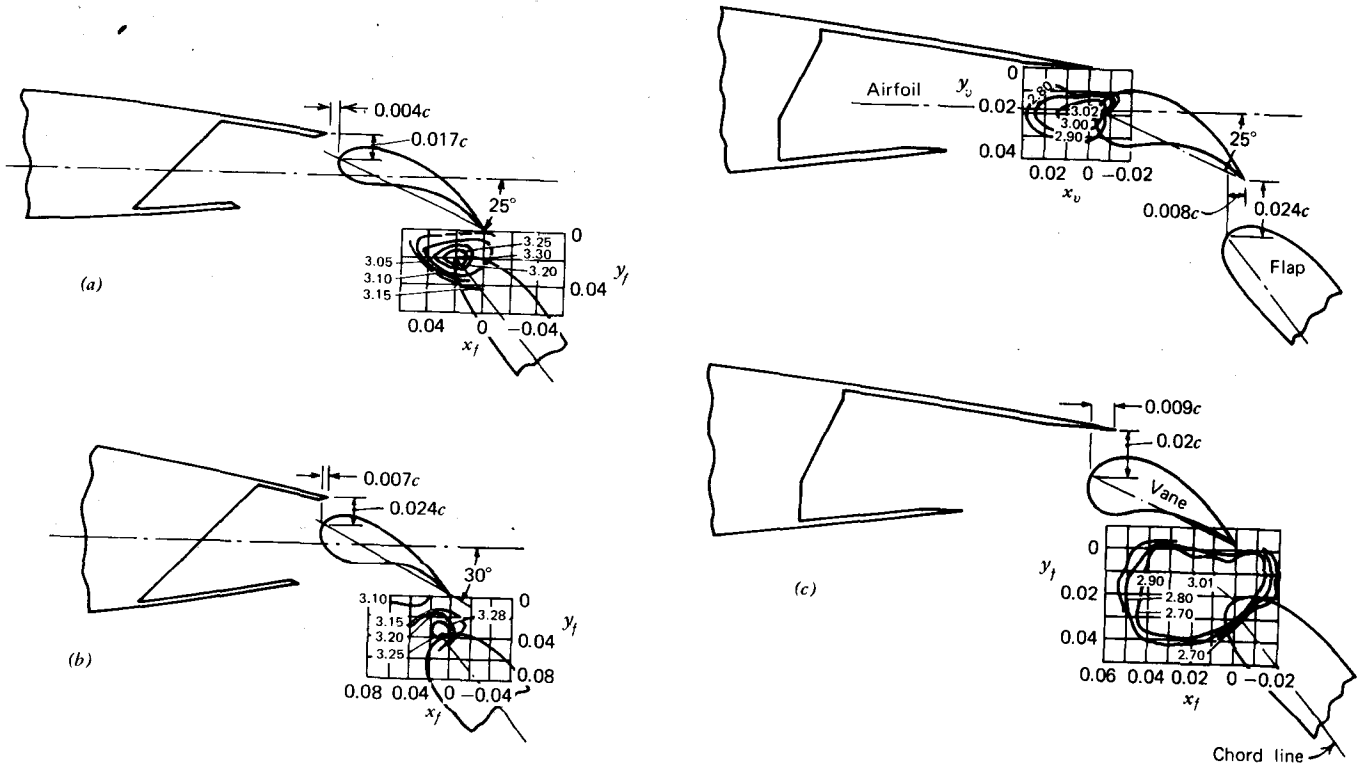

Figure 3.28 Contours of flap and vane positions for maximum section lift coefficient for several airfoil sections equipped with double-slotted flaps. (*a*) NACA 23012 airfoil section; $\delta_f = 60°$. (*b*) NACA 23021 airfoil section; $\delta_f = 60°$. (*c*) NACA 61_1–212 airfoil section.

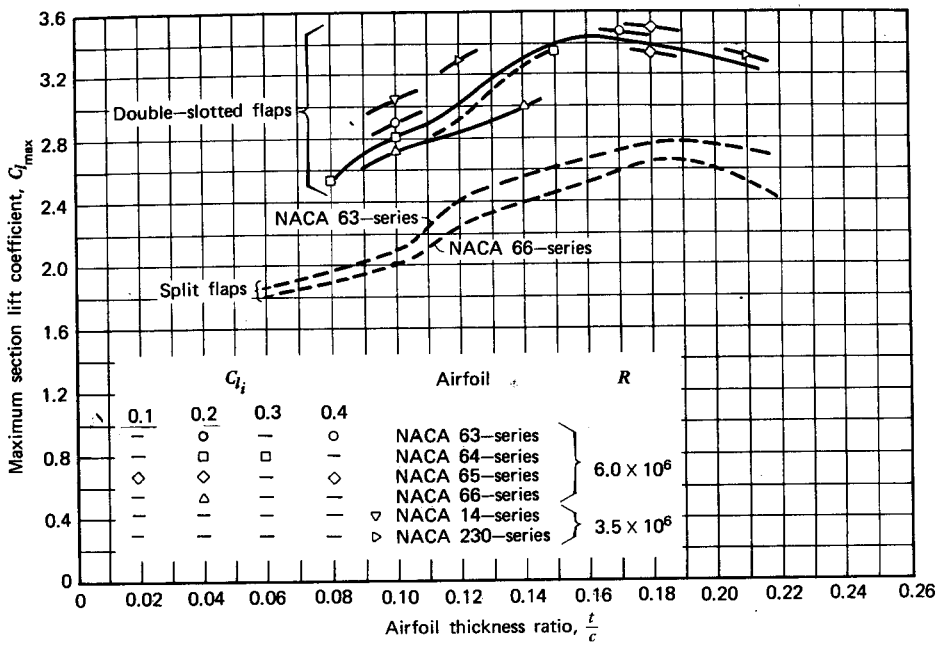

Figure 3.29 Maximum section lift coefficients for several NACA airfoil sections with double-slotted and split flaps.

Referring to Equation 3.44 and Figure 3.30, it is obvious that some of the superior performance of the double-slotted flap results from the extension of the chord. From the figure, C_{l_a} (flapped) is equal to 0.12 C_l/deg as compared to the expected unflapped value of approximately 0.1. Hence, based on the actual chord, the increment in $C_{l_{max}}$ for the double-slotted flap is only 1.6. However, this is still almost twice that afforded by plain or split flaps and points to the beneficial effect of the slot in delaying separation.

Figure 3.31 (taken from Ref. 3.15) presents pitching moment data for flapped airfoil sections. The lift and moment are taken to act at the aerodynamic center of the airfoil, located approximately 25% of the chord back from the leading edge. The moment is positive if it tends to increase the angle of attack.

From Figure 3.31, the lowering of a flap results in an incremental pitching moment. In order to trim the airplane a download must be produced on the horizontal tail. The wing must now support this download in addition to the aircraft's weight. Hence the effective increment in lift due to the flap is less than that which the wing-flap combination produces alone. This correction can typically reduce $\Delta C_{L_{max}}$ by 0.1 to 0.3.

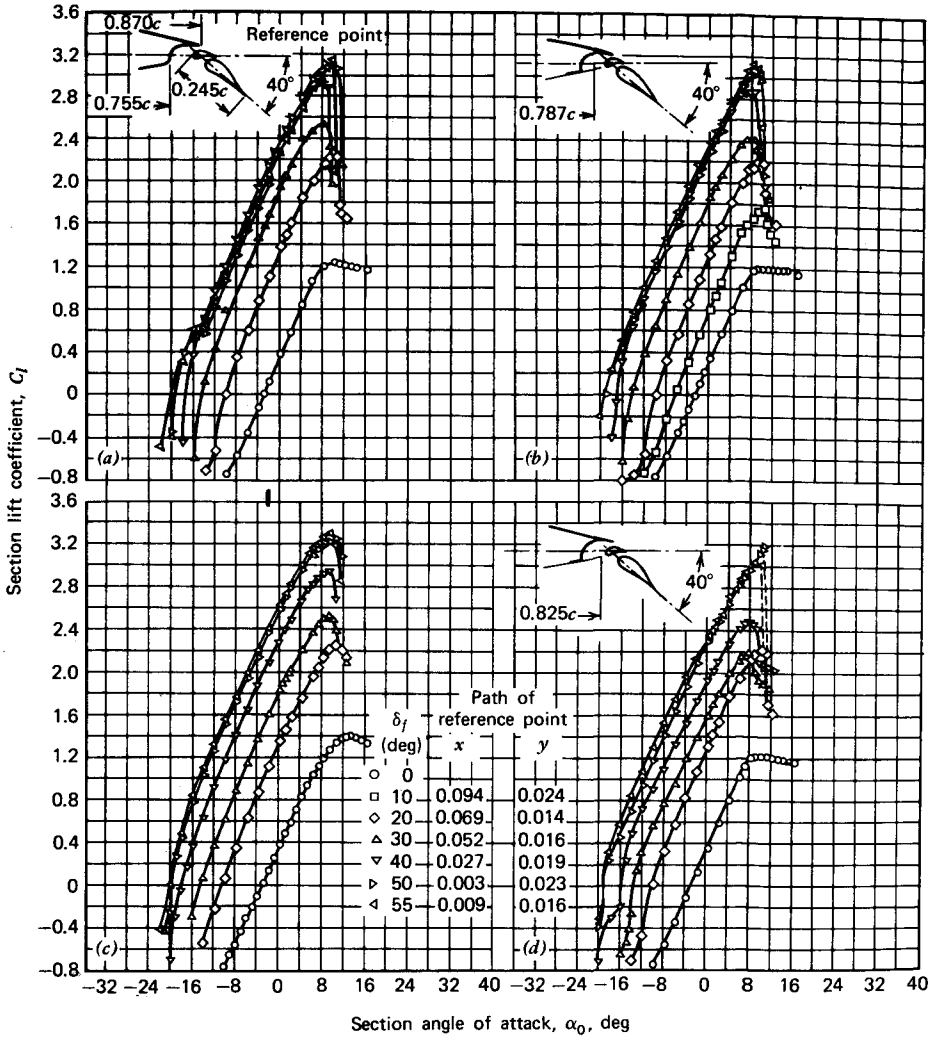

Figure 3.30 Section lift characteristics of an NACA 63, 4–421 (approximately) airfoil equipped with a double-slotted flap and several slot-entry-skirt extensions. (*a*) No skirt extension; $R = 2.4 \times 10^4$. (*b*) Partial skirt extension; $R = 2.4 \times 10^6$. (*c*) Partial skirt extension; $R = 6.0 \times 10^6$. (*d*) Full skirt extension; $R = 2.4 \times 10^6$.

Table 3.1 Maximum Lift Coefficients of Airfoil Sections Equipped with Single-Slotted Flaps

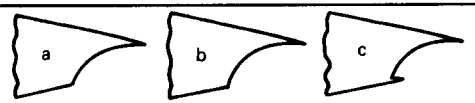

Slot–entry configuration

Flap nose shapes

Airfoil Section	c_f/c	c_a	Slot-Entry configuration	Flap Nose Shape	$C_{l_{max}}$	δf (deg)	x_f	y_f	Optimum Position	R
Clark Y	0.20	1.00	b	A	2.44	30	0	−0.025	Yes	0.61×10
Clark Y	0.30	1.00	b	A	2.83	40	0	−0.025	Yes	0.61
Clark Y	0.40	1.00	b	A	3.10	40	0	−0.025	Yes	0.61
23012	0.10	0.93	a	A	2.25	50	0.004	0.005	Yes	3.5
23012	0.15	1.00	b	A	2.68	30	0	0.015	Yes	3.5
23012	0.25	1.00	b	A	3.22	40	0	0.015	Yes	3.5
23012	0.256	0.800	a	B	2.76	50	0.005	0.018	Yes	3.5
23012	0.257	0.83	a	A	2.81	50	0.005	0.016	Yes	3.5
23012	0.257	0.83	a	A	2.83	40	0.013	0.024	Yes	3.5
23012	0.267	1.00	b	A	2.90	30	0	0.025	No	3.5
23012	0.30	0.90	c	A	2.92	50	0.002	0.010	No	3.5
23012	0.30	0.90	c	A	2.92	40	0.002	0.020	No	3.5
23012	0.30	0.90	c	A	2.93	30	0.002	0.030	No	3.5
23012	0.30	0.90	b	A	2.88	40	0.002	0.020	No	3.5
23012	0.30	1.00	b	A	3.29	40	0	0.015	No	3.5
23012	0.40	0.715	b	A	2.87	50	0.015	0.015	Yes	3.5
23012	0.40	0.715	a	A	2.90	50	0.015	0.015	Yes	3.5
23012	0.15	1.00	b	A	2.59	60	0	0.015	No	3.5
23021	0.15	1.00	b	A	2.66	60	0.050	0.030	Yes	3.5
23021	0.25	1.00	b	A	3.17	40	0.025	0.015	Yes	3.5
23021	0.257	0.827	b	B	2.69	60	0	0.015	Yes	3.5
23021	0.257	0.827	a	B	2.74	60	0	0.015	Yes	3.5
23021	0.257	0.827	b	A	2.71	60	0.005	0.020	Yes	3.5
23021	0.257	0.827	a	A	2.82	50	0	0.025	Yes	3.5

23021	0.40	0.715	b	A	2.79	50	0.015	0.025	Yes	3.5
23021	0.40	0.715	a	A	2.88	50	0.015	0.045	Yes	3.5
23030	0.257	0.860	b	B	2.59	60	0.025	0.040	Yes	3.5
23030	0.257	0.860	a	B	2.68	60	−0.005	0.040	Yes	3.5
23030	0.40	0.775	b	B	2.82	50	0.025	0.060	Yes	3.5
23030	0.40	0.775	a	B	2.90	50	0.025	0.060	Yes	3.5
63,4–420	0.25	0.88	b	B	3.00	35	0.018	0.045	No	6.0
3,4–421 (approximately)	0.243	0.835	a	A	3.21	40	0	0.027	Yes	9.0
65–210	0.25	0.84	c	A	2.47	45	0.009	0.010	Yes	6.0
65–210	0.25	0.90	c	A	2.48	41.3	0.014	0.009	Yes	6.0
65–210	0.25	0.975	c	A	2.45	35	0.004	0.020	Yes	6.0
$5_{(112)}$A111 (approximately)	0.35	0.839	c	A	2.69	35	−0.020	0.032	Yes	9.0
5_1-213 (approximately)	0.336	0.889	c	A	2.63	40	0.019	0.046	No	9.0
$5_{(215)}$-114	0.259	0.915	c	A	2.80	40	0.019	0.038	No	9.0
5,2–221 (approximately)	0.263	0.832	a	B	2.83	30	0.025	0.046	Yes	9.95
6(215)-116, $a = 0.6$	0.25	0.824	c	B	2.70	55	0	0.028	No	6.0
6,2–116, $a = 0.6$	0.25	0.827	a	A	2.69	45	0.017	0.038	No	6.0
6,2–216, $a = 0.6$	0.30	0.90	c	A	2.92	37	0	0.016	No	6.0
6,2–216, $a = 0.6$	0.25	0.824	a	A	2.89	40	0.023	0.040	Yes	5.1
6,2–216, $a = 0.6$	0.25	0.834	c	A	2.88	45	0.011	0.031	Yes	5.1
6,2–118	0.25	0.90			2.68	32.5	--------	--------	No	6.0

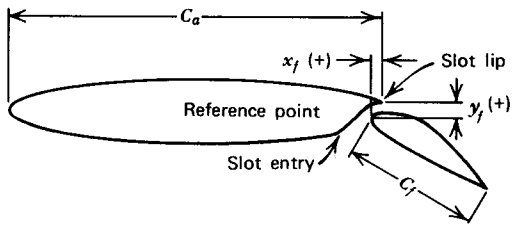

Typical single–slotted flap configuration.
(All dimensions are given in fractions of airfoil chord.)

Table 3.2 Maximum Lift Coefficients of Airfoil Sections Equipped with Double-Slotted Flaps

Airfoil Section	c_f/c	c_v/c	C_a	$C_{l_{max}}$	δ_f deg	δ_s deg	x_f	y_f	x_v	y_v	Optimum Position	R
23012	0.10	0.189	0.83	2.99	70	40	0.009	0.009	0.014	0.024	Yes	3.5×10^6
23012	0.257	0.227	0.715	3.47	70	30	0.014	0.012	0.015	0.035	No	3.5
23021	0.257	0.227	0.715	3.56	60	30	0.019	0.024	0.025	0.065	No	3.5
23030	0.257	0.260	0.715	3.71	80	40	0.049	0.050	0.045	0.040	No	3.5
23012	0.257	0.117	0.826	3.30	60	25	−0.016	0.010	−0.004	0.017	Yes	3.5
23021	0.257	0.147	0.827	3.32	70	30	0.017	0.027	0.007	0.024	Yes	3.5
63–210	0.25	0.075	0.84	2.91	50	25	0.022	0.024	0.024	0.018	Yes	6.0
63,4–421 (approximately)	0.195	0.083	0.87	3.30	55	14	0.038	0.012	0.009	0.016	No	6.0
64–208	0.25	0.075	0.84	2.51	45	30	0.015	0.015	0.015	0.019	Yes	6.0
64–208	0.25	0.056	0.84	2.40	50	25	0.018	0.014	0.015	0.024	Yes	6.0
64–210	0.25	0.075	0.84	2.82	55	30	0.023	0.006	0.012	0.018	Yes	6.0
64_1–212	0.25	0.075	0.84	3.03	50	30	0.021	0.020	0.010	0.019	Yes	6.0
64_1A212	0.229	0.083	0.833	2.83	55	26	0.044	0.005	0.004	0.014	Yes	6.0
65–210	0.25	0.075	0.84	2.72	50	25	0.025	0.011	0.009	0.024	Yes	6.0
65(216)–215, $a = 0.8$	0.248	0.096	0.82	3.38	70	12	0.024	0.010	0.025	0.032	No	6.3
65_3–118	0.244	0.10	0.864	3.35	65	23	0.038	0.007	0.009	0.025	Yes	6.0
65_3–418	0.236	0.106	0.851	3.50	65	21	0.027	0.007	0.012	0.028	Yes	6.0
65_4–421	0.236	0.109	0.85	3.08	51	20	0.029	0.017	0.012	0.024	Yes	2.2
66–210	0.25	0.075	0.84	2.64	55	25	0.029	0.023	0.012	0.022	Yes	6.0
66–210	0.25	0.100	0.84	2.72	60	25	0.027	0.039	0.024	0.021	Yes	6.0
66_2–214 (approximately)	0.227	0.085	0.854	3.00	55	20	0.044	0.009	0.004	0.025	Yes	9.0
1410	0.25	0.075	0.84	3.06	50	25	0.026	0.016	0.012	0.019	Yes	6.0

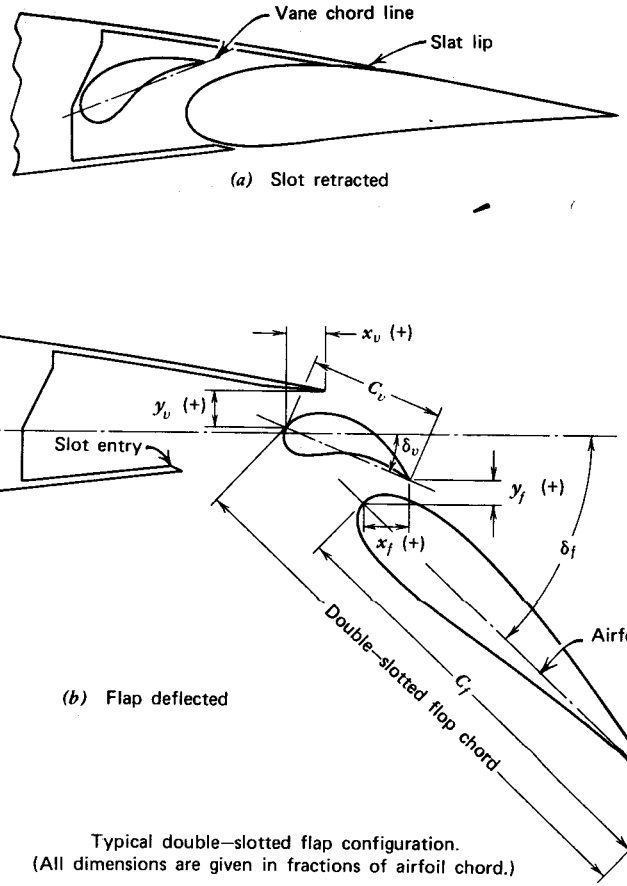

Typical double–slotted flap configuration.
(All dimensions are given in fractions of airfoil chord.)

Definition of Flap Geometry given in Table 3.2

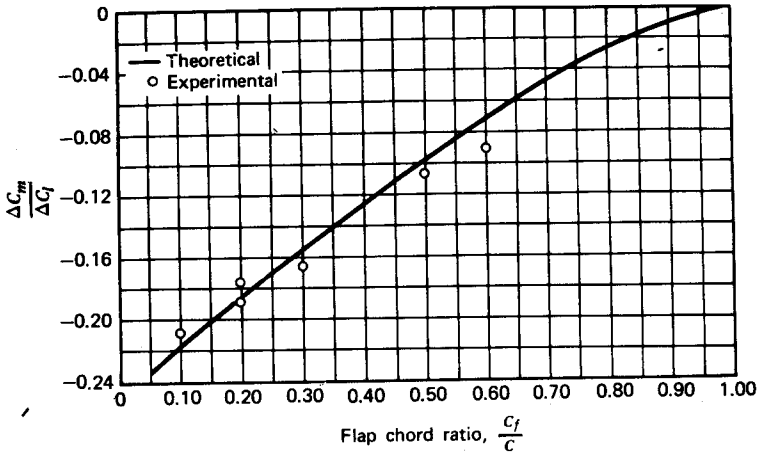

(a)

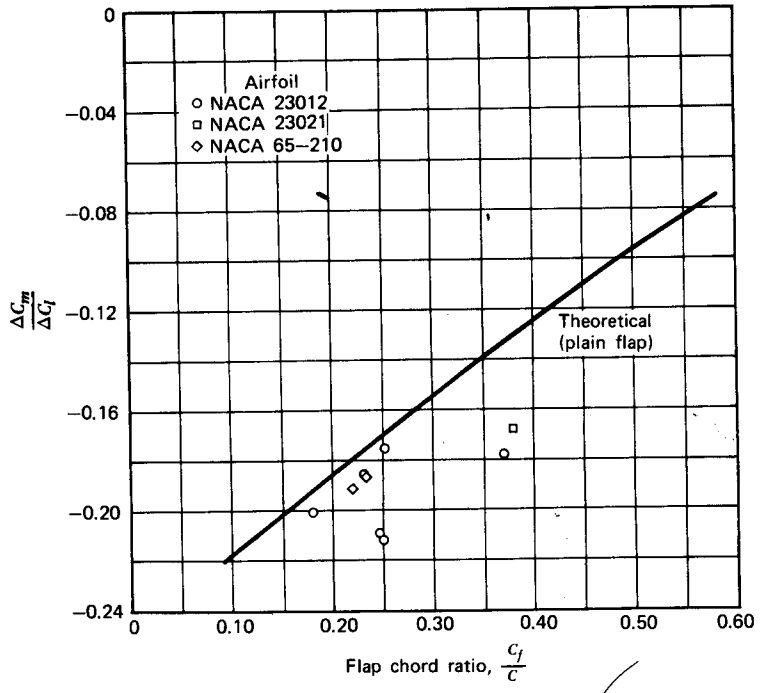

(b)

Figure 3.31 Influence of flap configuration on pitching moment coefficient. (a) Plain flaps. (*b*) Split flaps. (*c*) Slotted flaps.

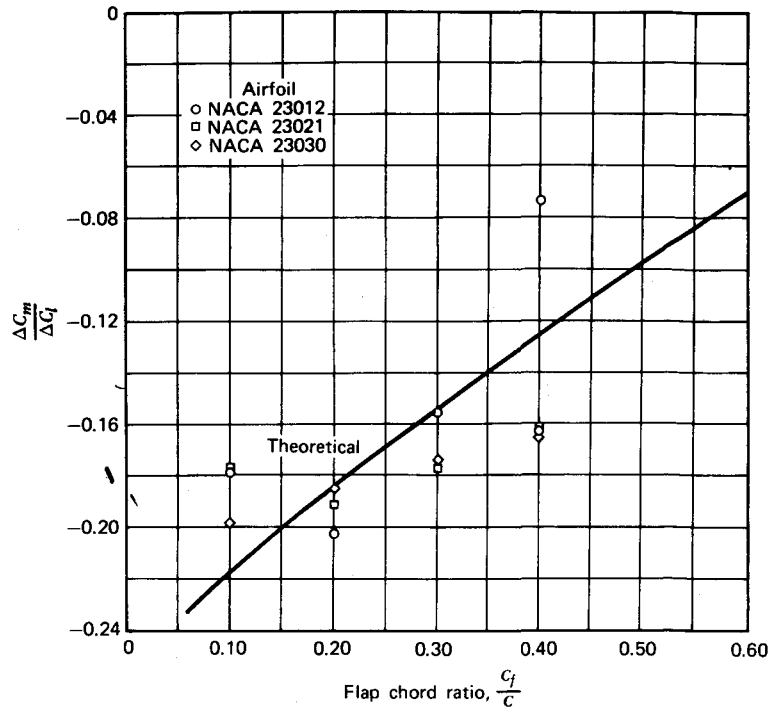

(c)

Figure 3.31 (Continued)

In a high-wing airplane, lowering the flaps can cause the nose to pitch up. This is due to the moment produced about the center of gravity from the increase in wing drag because of the flaps. Based on the wing area, the increment in wing drag coefficient, ΔC_D, due to the flaps is given approximately by,

$$\Delta C_D = 1.7(c_f/c)^{1.38}(S_f/S)\sin^2\delta_f \qquad \text{(plain and split)} \qquad (3.45)$$

$$= 0.9(c_f/c)^{1.38}(S_f/S)\sin^2\delta_f \qquad \text{(slotted)} \qquad (3.46)$$

If the wing is located a height of h above the center of gravity, a balancing upload is required on the tail. The effect of trim on $C_{L_{max}}$ for a complete airplane will be discussed in more detail later.

Flap Effectiveness in the Linear Range

Frequently one needs to estimate the increment in C_l below stall, ΔC_l, produced by a flap deflection. Not only is this needed in connection with the

wing lift, but ΔC_l is required also in analyzing the effectiveness of movable control surfaces, which frequently resemble plain flaps.

If an airfoil section has a lift curve slope of C_{l_α} and lowering its flap produces an increment of ΔC_l, the angle of zero lift, α_{0l}, is decreased by

$$\Delta\alpha_{0l} = \frac{\Delta C_l}{C_{l_\alpha}} \tag{3.47}$$

The rate of decrease of α_{0l} per unit increase in the flap angle δ_f is referred to as the flap effectiveness factor, τ. Thus, for a flapped airfoil, the lift coefficient can be written as

$$C_l = C_{l_\alpha}(\alpha + \tau\,\delta_f) \tag{3.48}$$

where α is the angle of attack of the airfoil's zero lift line with the flap undeflected.

Theoretically τ is a constant for a given flap geometry but, unfortunately, flap behavior with δ_f is rather nonlinear and hence τ must be empirically corrected by a factor η to account for the effects of viscosity. Including η, Equation 3.48 becomes,

$$C_l = C_{l_\alpha}(\alpha + \tau\eta\,\delta_f) \tag{3.49}$$

The functions τ and η can be obtained from Figures 3.32 and 3.33. Figure 3.33 is empirical and is based on data from References 3.15, 3.17, 3.19, and 3.20. Although there is some scatter in the data, as faired, the comparisons between the various types of flaps are consistent. The double-slotted flap delays separation on the upper surface, so that the decrease in flap effectiveness occurs at higher flap angles than for the other flap types. The same can be said of the slotted flap relative to the plain and split flaps. The plain flap is fairly good out to about 20° and then apparently the flow separates from the upper surface and the effectiveness drops rapidly, approaching the curve for split flaps at the higher flap angles. In a sense the flow is always separated on the upper surface of a split flap. Thus, even for small flap angles, the effective angular movement of the mean camber line at the trailing edge of an airfoil with a split flap would only be about half of the flap displacement.

In the case of the double-slotted flap it should be emphasized that this curve in Figure 3.33 is for an optimum flap geometry. The trailing segment of the flap is referred to as the main flap and the leading segment is called the vane. In applying Equation 3.49 and Figures 3.32 and 3.33 to the double-slotted flap, the total flap chord should be used together with the flap angle of the main flap. Usually, the deflection angle of the vane is less than that for the main flap for maximum lift performance.

Figure 3.32 is based on the thin airfoil theory represented by Equation 3.39. As an exercise, derive the expression for τ given on the figure. τ can also be obtained using the numerical methods that led to Figures 3.17 and

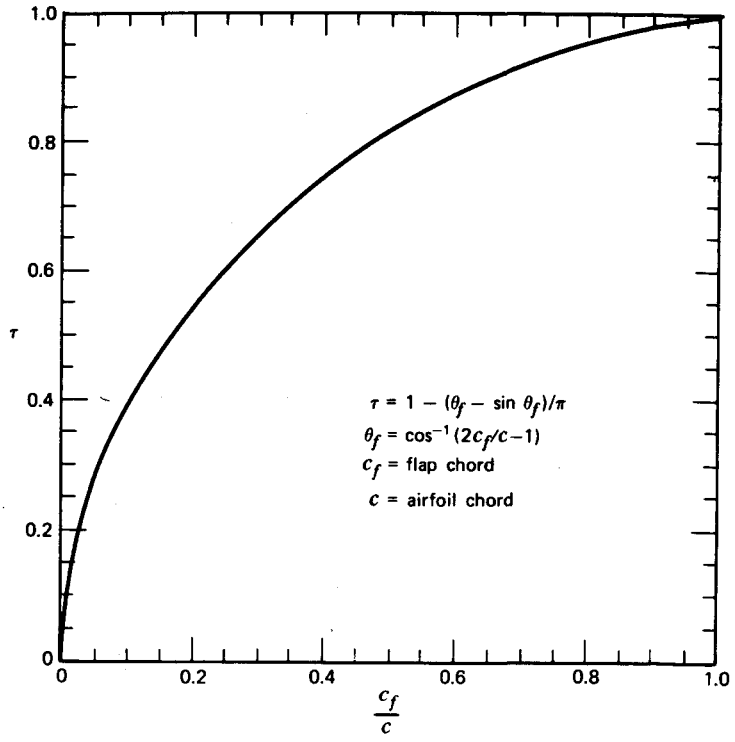

Figure 3.32 .Flap effectiveness factor.

3.18. As another exercise, apply Weissinger's approximation to the flapped airfoil using only two point vortices to represent the airfoil. Placing one vortex on the quarter chord of the flap and the other on the quarter chord of the remainder of the airfoil leads to

$$\tau = \frac{3(3-2c_f)c_f}{4(1-c_f)c_f + 3} \tag{3.50}$$

where c_f is the fraction of chord that is flapped. Equation 3.50 is approximately 10% lower than Figure 3.32 for c_f/c values of around 0.25.

The angle of attack at which the flapped airfoil stalls is generally less than that for the plain airfoil. Hence, the increment in $C_{l_{max}}$ because of the flap is not as great as the increment in C_l at an angle below the stall. Denoting these increments by $\Delta C_{l_{max}}$ and ΔC_l, respectively, it is obvious that the ratio $\Delta C_{l_{max}}/\Delta C_l$ must depend on c_f/c. If c_f/c, for example, is equal to 1.0, in a sense the entire airfoil is the flap and $\Delta C_{l_{max}}$ must be zero. Systematic data on $\Delta C_{l_{max}}/\Delta C_l$ are sparse. Figure 3.34 has been drawn based on a limited number of data points and should be used with discretion.

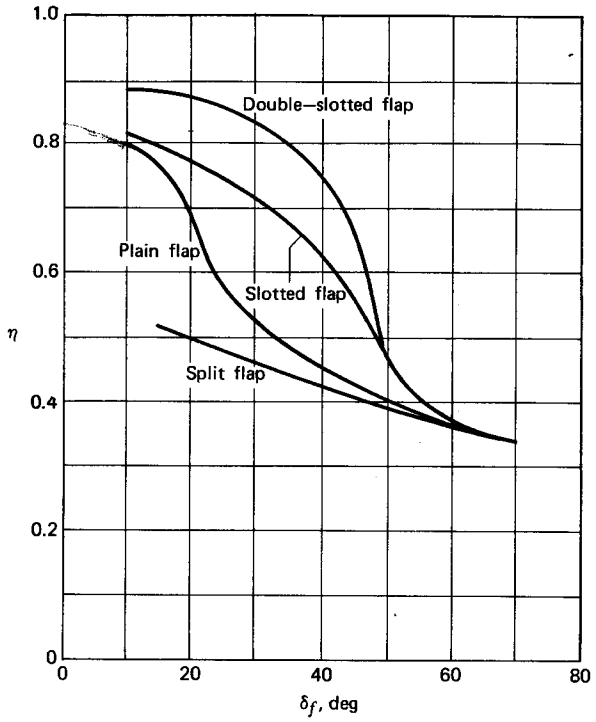

Figure 3.33 Correction factor to flap effectiveness factor τ. Note that curves apply for thickness ratios of approximately 12% and flap chord fractions of 40% or less.

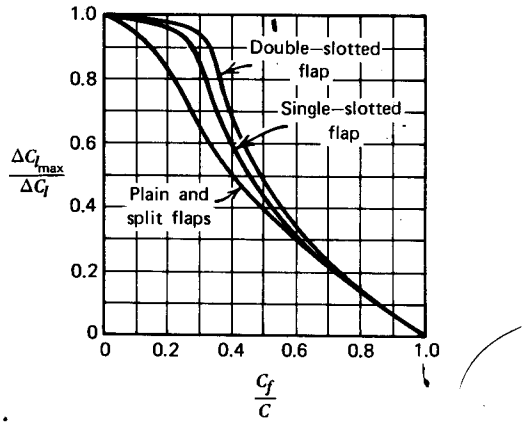

Figure 3.34 $C_{l_{max}}$ increment ratio as a function of flap chord ratio.

As an example, in using Figures 3.32, 3.33, and 3.34, consider the prediction of $C_{l_{max}}$ for a 23012 airfoil equipped with a 30% chord split flap deflected 60° and operating at a Reynold's number of 3.5×10^6. From Figure 3.32, $\tau = 0.66$ for $c_f/c = 0.3$ and from Figure 3.33, $\eta = 0.35$ for a split flap deflected 60°. Hence from Equation 3.49, ΔC_l is equal to

$$\begin{aligned} \Delta C_l &= C_{l_\alpha} \tau \eta \, \delta \\ &= (0.105)(0.66)(0.35)(60) \\ &= 1.46 \end{aligned} \tag{3.51}$$

In Equation 3.51, C_{l_α} of 0.105 is obtained from Reference 3.1. Using Figure 3.34, the ratio of $\Delta C_{l_{max}}$ to ΔC_l is obtained as 0.66. Hence,

$$\Delta C_{l_{max}} = 0.96$$

According to Figure 3.27, $C_{l_{max}}$ for a plain 23012 airfoil equals 1.65 at $R = 3.5 \times 10^6$. Thus, for the flapped airfoil, $C_{l_{max}}$ is predicted to be 1.65 + 0.96, or 2.61. This result compares closely with Figure 3.26*a*. If the procedure is repeated for other flap angles, close agreement is also obtained with the figure. However for a flap chord ratio of 0.1, the predicted values of $C_{l_{max}}$ based on Figures 3.32 to 3.34 are higher than those shown in Figure 3.26*a*.

Leading Edge Devices

In order to avoid leading edge separation, particularly at low Reynolds numbers or for airfoils with relatively sharp leading edges, special high-lift devices can also be incorporated into the leading edge to supplement the benefits of trailing edge flaps. These are illustrated in Figure 3.35. The fixed slot and extensible slat have been in use for some time, whereas the Kruger-type nose flap was first employed on the turbojet transport.

As the name implies, the fixed slot is just that—a narrow channel through which the air can flow from the lower surface to the upper surface. This channeling of the flow allows the airfoil to operate at higher angles of attack before the upper surface of the leading edge separates than otherwise would be the case. Increments in $C_{l_{max}}$ of approximately 0.1 or 0.2 are achieved by the fixed slot. It is a moot question as to why this delay in the separation occurs. As in the case of slots with trailing edge flaps, the explanation has been offered in the past that the flow through the slot feeds energy into the slower moving boundary layer, thereby decreasing its tendency to separate. More recently, however, in a Wright Brothers' Lecture (Ref. 3.16) Smith, in examining numerical results on multielement airfoils, concluded that improved stall performance from slots is most likely the result of more favorable pressure gradients being produced on one airfoil element by the other.

The extensible slat is similar in its performance to the slot, but it is

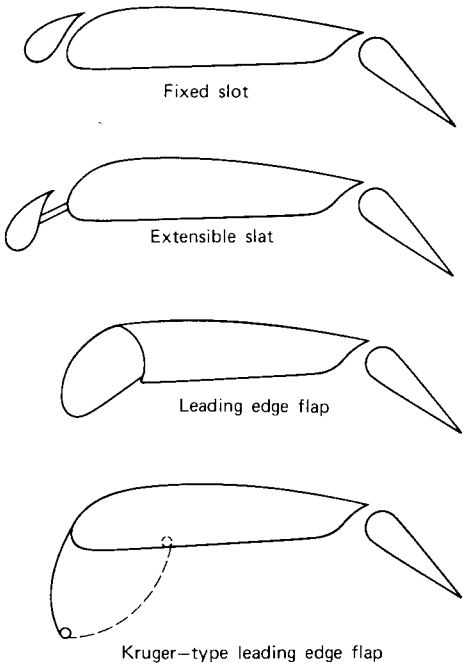

Figure 3.35 Various methods for delaying leading edge separation.

considerably more efficient because it can be positioned to optimize its contribution to $C_{l_{max}}$. The mechanically extended slat is finding increased application, particularly with the use of thinner airfoil sections for high-speed applications. Figure 3.36 presents some data on slats taken from Reference 3.17. Here a NACA 64A010 airfoil was tested using a slat in combination with split and double-slotted trailing edge flaps. The slat is seen to improve $C_{l_{max}}$ significantly, producing increments in $C_{l_{max}}$ of approximately 0.9, 0.8, and 0.6 for the no-flap, split-flap, and double-slotted flap configurations, respectively. Unlike the trailing edge flap, the primary effect of the slat is seen to be an extension of the lift curve without the slat; that is, opening the slat does not change C_l by a large increment at a fixed angle of attack. The same is true of leading edge flaps and is not unexpected in view of Figure 3.32.

The performance of a leading edge flap is presented in Figure 3.37 for the same airfoil as for Figure 3.36. Comparing the two figures, it is obvious that the two leading edge devices are nearly comparable in performance.

Figure 3.38 shows a section of a sophisticated Kruger-type flap. As this flap swings down and forward, it assumes the curved shape that is shown. With this optimum shaping, its performance probably exceeds to some extent

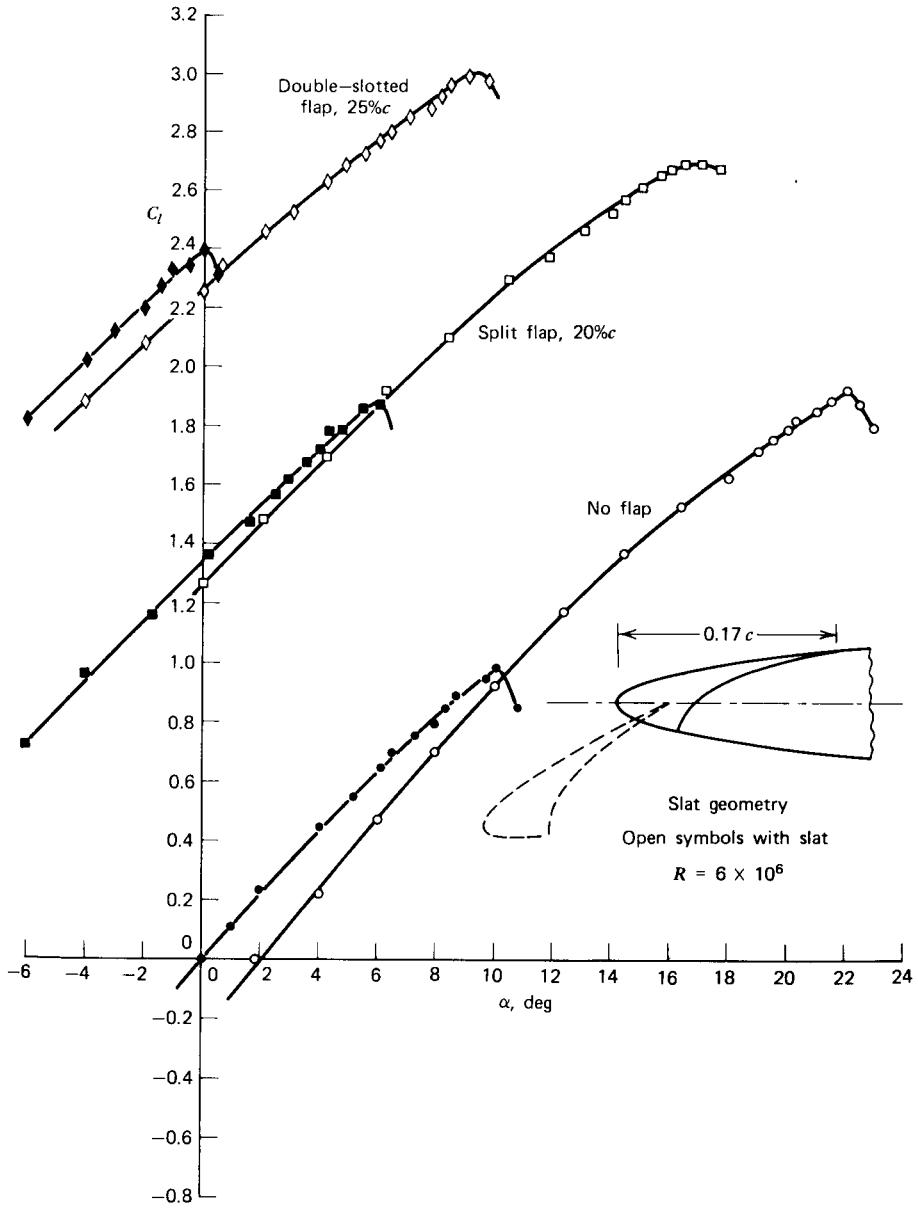

Figure 3.36 Effect of leading edge slat on NACA 64A010 airfoil with and without flaps.

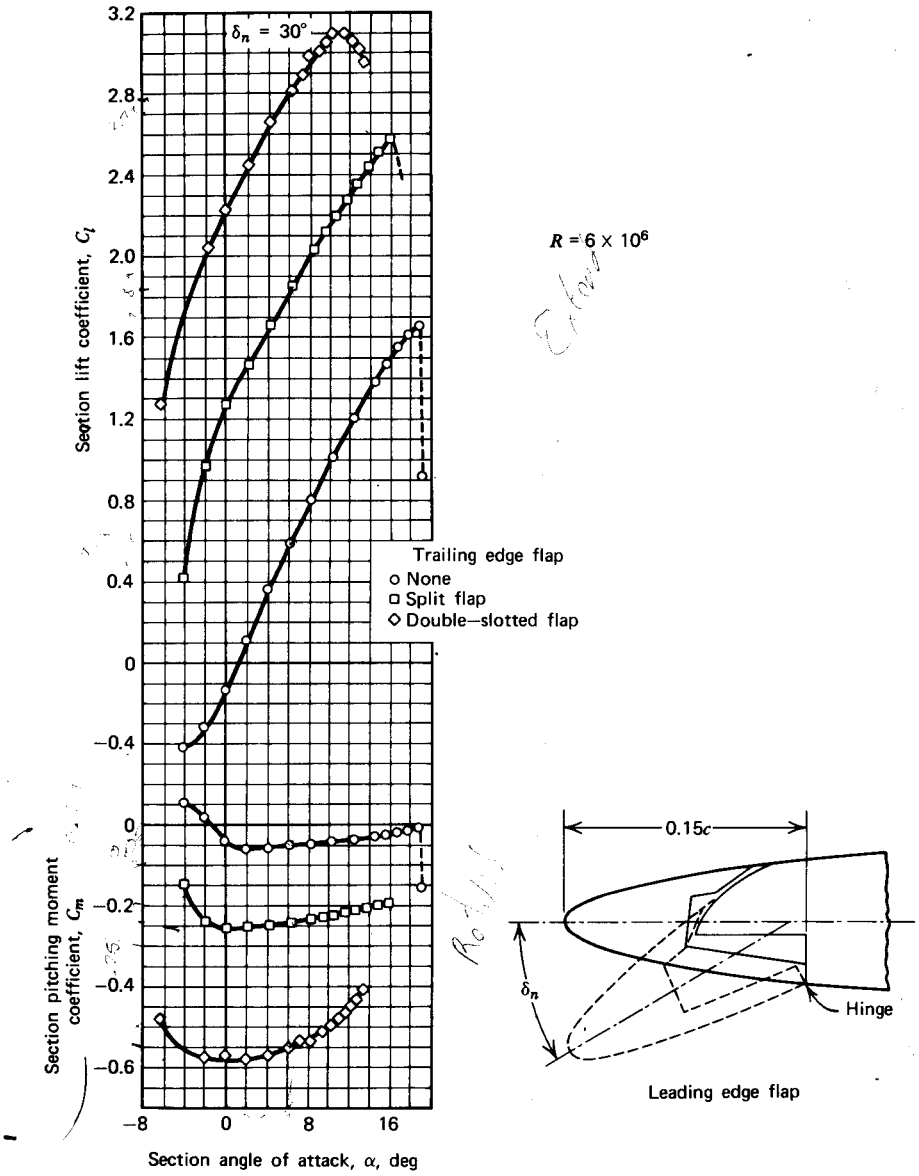

Figure 3.37 Effect of leading edge flap on NACA 64A010 airfoil with and without flaps.

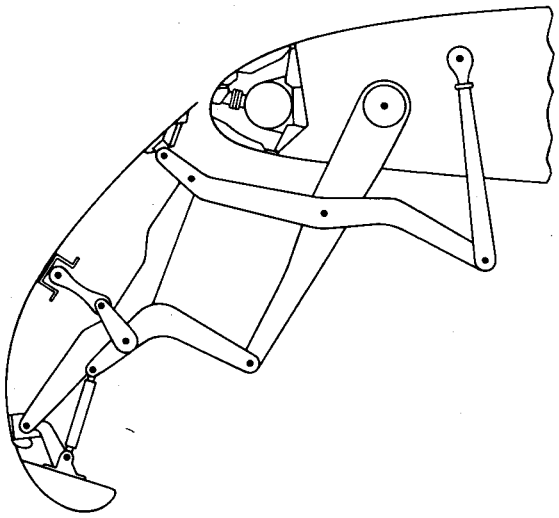

Figure 3.38 Flexible fiberglass leading edge flap used on the Boeing 747 and YC-14 airplanes.

the data presented in Figures 3.39 and 3.40. Figure 3.39 (taken from Ref. 3.18) shows that without a trailing edge flap the Kruger flap gives an increment in $C_{l_{max}}$ to the 64-012 airfoil of only 0.4. However, the plain airfoil has a higher $C_{l_{max}}$ to begin with than that of Figures 3.36 and 3.37. Hence, the total $C_{l_{max}}$ for the Kruger-flapped airfoil without a trailing edge flap is about the same as for the other two leading edge devices. However, with the split flap, the Kruger flap produces a combined $C_{l_{max}}$ equal to 3.0, which is 0.3 to 0.4 higher than the corresponding data of Figures 3.36 and 3.37.

The data of Figure 3.40 (taken from Ref. 3.21) are based on Kruger's original work.

The Optimum Airfoil for High Lift

Stratford, in References 3.23 and 3.24, examined both theoretically and experimentally the possibility of diffusing a turbulent boundary layer in such a way as to produce zero wall shear. Known as "imminent separation pressure recovery," Stratford found that it is indeed possible, with the proper pressure gradient, to maintain a velocity profile along a diffuser such that $\partial u(y)/\partial y$ is equal to zero at the wall. $u(y)$ is the velocity in the boundary layer parallel to the wall and is a function of the distance, y, from the wall. With the velocity gradient at the wall equal to zero, the boundary layer is just on the verge of separating, since a negative value of this gradient will result in reverse flow, as illustrated in Figure 3.41.

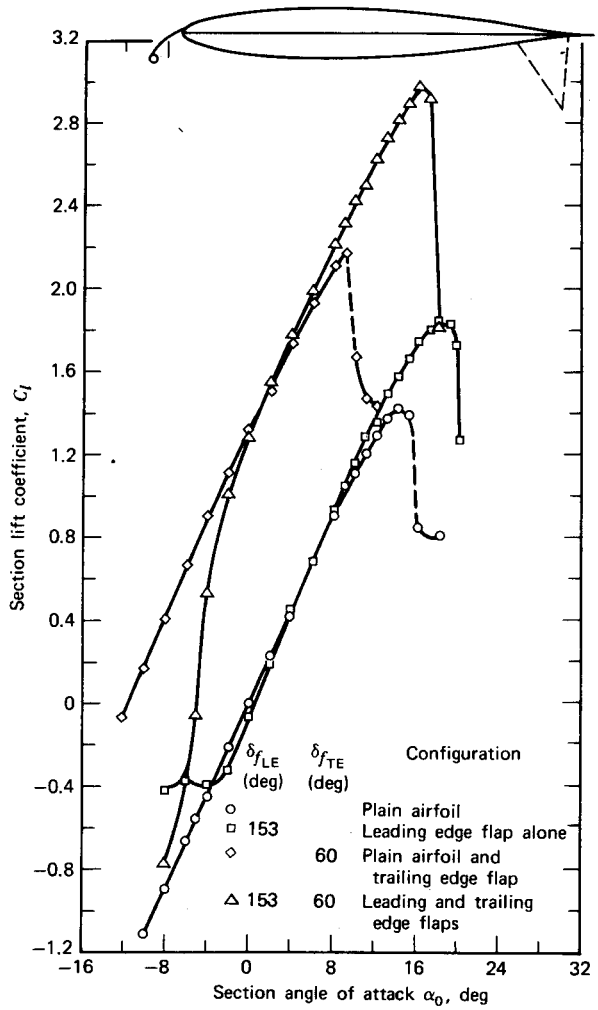

Figure 3.39 Section lift characteristics for the NACA 64_1–012 airfoil section equipped with a 0.10c upper-surface leading edge flap alone, and in combination with a 0.20c trailing edge split flap. $R = 6.0 \times 10^6$.

In the abstract to Reference 3.24, Stratford states:

"*No fundamental difficulty was encountered in establishing the flow and it had, moreover, a good margin of stability. The dynamic head in the zero skin friction boundary layer was found to be linear at the wall (i.e., $u \propto y^{1/2}$), as predicted theoretically in the previous paper. (Author's note, Stratford is referring to Ref.* 3.23.)

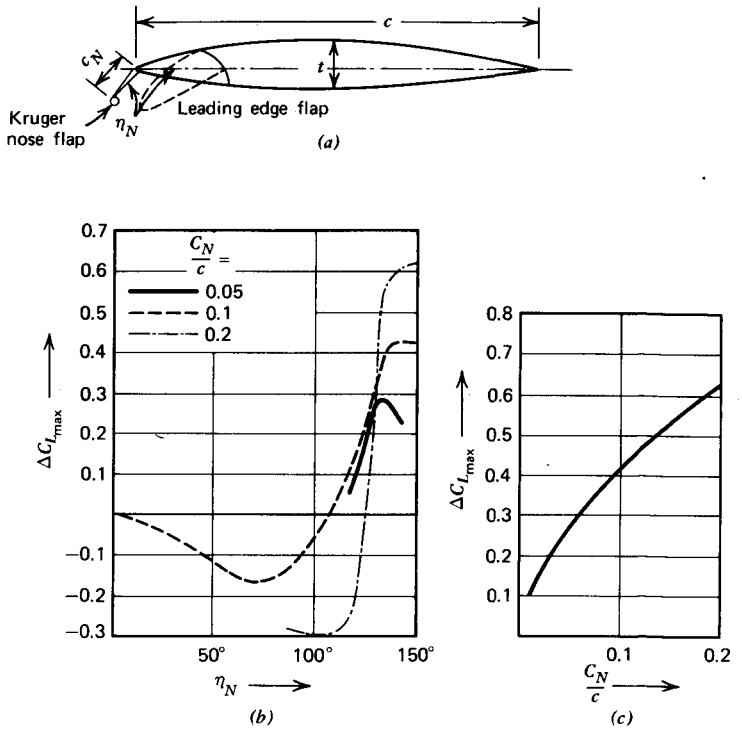

Figure 3.40 Characteristics of Kruger flaps. (*a*) Illustration of Kruger's type of nose flap and simple, hinged, leading edge flap. (*b*) Effect of flap angle on maximum lift coefficient. (*c*) Effect of flap chord on maximum lift coefficient.

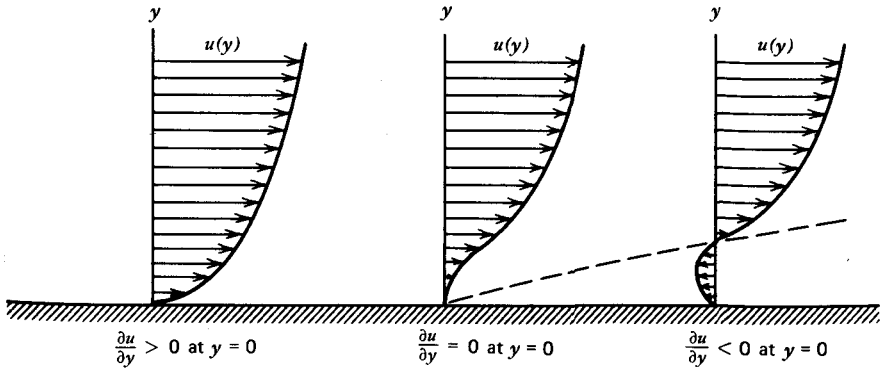

Figure 3.41 Relationship of velocity gradient at the wall to flow separation.

The flow appears to achieve any specified pressure rise in the shortest possible distance and with probably the least possible dissipation of energy for a given initial boundary layer. Thus, an airfoil which could utilize it immediately after transition from laminar flow would be expected to have a very low drag."

The Stratford imminent separation pressure recovery was adopted for airfoils by Liebeck and Ormsbee (Ref. 3.25) and was extended later by Liebeck (Ref. 3.22). Using variational calculus, optimum chordwise pressure distributions for the upper and lower surfaces are prescribed that are modified slightly by additional constraints not present in the optimization process. Specifically, the optimum C_p distributions are modified in order to (1) close the airfoil contour at the trailing edge, (2) round the leading edge to allow operation over an angle-of-attack range, and (3) satisfy the Kutta condition at the trailing edge.

The resulting modified form of the optimum pressure distribution is compared with the optimum distribution in Figure 3.42. Beginning at the stagnation point, the flow is accelerated up to a so-called rooftop region over which the velocity, and hence the pressure, is constant. Following the rooftop region, the Stratford pressure recovery distribution is employed to reduce the velocity over the upper surface to its value at the trailing edge.

One such airfoil design is presented in Figure 3.43 (taken from Ref. 3.22). Included on the figure is the pressure distribution to which the airfoil was designed. Test data on this airfoil obtained at a Reynolds number of 3×10^6 are presented in Figure 3.44*a* and 3.44*b*. Although this configuration is referred to by the reference as a "turbulent rooftop" case, transition does not occur until the start of the Stratford pressure recovery. In this case the performance of the airfoil is seen to be good from the standpoint of $C_{l_{max}}$ and C_d. The drag coefficient remains below the value of 0.01 over a wide range of C_l values from 0.6 to 1.6.

Artificially producing transition near the leading edge severely compromises $C_{l_{max}}$ and C_d, as shown in Figure 3.44*b*. Still, by comparison with the standard NACA airfoils, the Liebeck airfoil appears to offer superior performance at low speeds and, in the future, may find application to general aviation aircraft. One possible drawback in this regard is the sharp drop in its lift curve at stall.

Powered-Lift Systems

Figure 3.45 (taken from Ref. 3.26) presents the growth of $C_{L_{max}}$ over the years since the Wright Brothers' success. The two points labeled K and L are somewhat misleading, since these two aircraft were experimental in nature and used distributed suction over the wing to delay separation. From this figure and the preceding information on flapped and plain airfoils, $C_{L_{max}}$ of

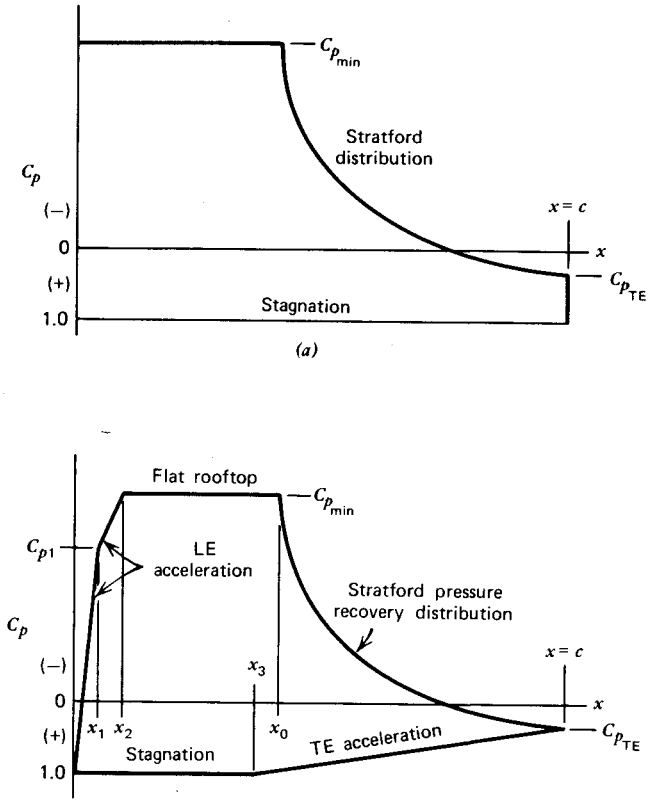

Figure 3.42 Pressure distributions for Liebeck airfoils. (*a*) Optimum airfoil pressure distribution according to variational analysis. (*b*) Modified form of optimum pressure distribution for airfoil upper and lower surfaces (not to scale). (R. H. Liebeck and A. I. Ormsbee, "Optimization of Airfoils for Maximum Lift", AIAA *Journal of Aircraft*, 1970. Reprinted from the *Journal of Aircraft* by permission of the American Institute of Aeronautics and Astronautics.)

slightly over 3 is probably the best that can be achieved without the addition of power. Although two-dimensional airfoils with double-slotted flaps can do better than this, as will be seen later, their full potential cannot be achieved when applied to an airplane. Generally, the flaps cannot be applied over the entire span of the wing. In addition to this loss in $C_{L_{max}}$, an added penalty results from the fuselage and tail download required for trim.

$C_{L_{max}}$ values considerably above those achievable with flap systems discussed so far are possible by the expenditure of power. Most of the powered-flap systems presently under consideration bear a resemblance, or can be

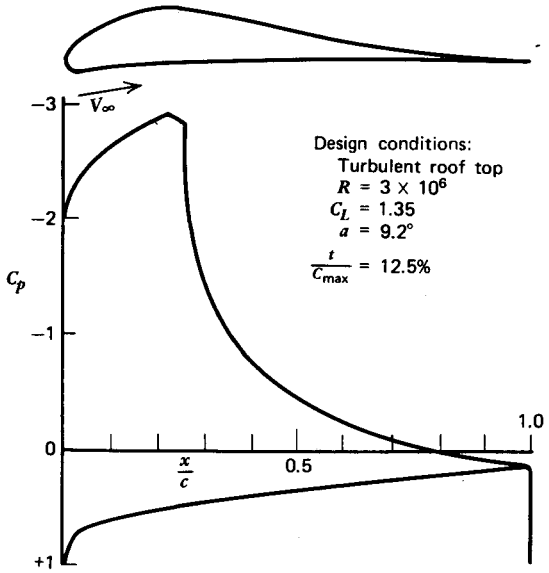

Figure 3.43 Liebeck airfoil with its pressure distribution. (R. H. Liebeck, "Class of Airfoils Designed for High Lift", AIAA *Journal of Aircraft*, 1973. Reprinted from the *Journal of Aircraft* by permission of the American Institute of Aeronautics and Astronautics.)

related in their performance, to the jet flap. Thus, in order to understand better the performance of systems such as upper surface blowing (USB), externally blown flaps (EBF), augmentor wing, and circulation control, we will begin with the jet flap shown in Figure 3.46. A thin sheet of air exits the trailing edge at a downward angle of δ relative to the airfoil zero lift line. This line is shown at an angle of attack α. If Γ_c is the total circulation around the airfoil then, assuming α and δ to be small, the total lift on the airfoil will be

$$L = \rho V \Gamma_c + m_j v_j(\alpha + \delta) \tag{3.52}$$

where m_j is the mass flux in the jet and v_j is the jet velocity.

As the jet leaves the airfoil, it gets turned in the direction of the free-stream velocity. In order to redirect the flux of jet momentum, it follows that a pressure difference must exist across the jet. This pressure difference, Δp, can be related to $m_j v_j$ and the radius of curvature R by the use of Figure 3.46*b*. Applying the momentum theorem in the direction of curvature,

$$\Delta p R\theta = m_j v_j \theta$$

or

$$\Delta p = \frac{m_j v_j}{R} \tag{3.53}$$

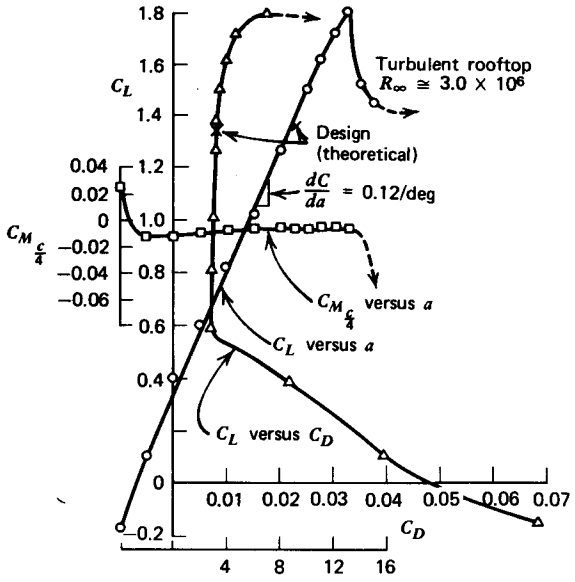

Figure 3.44a Experimental lift curve and drag polar for airfoil of Figure 3.43. (R. H. Liebeck, "Class of Airfoils Designed for High Lift", AIAA *Journal of Aircraft*, 1973. Reprinted from the *Journal of Aircraft* by permission of the American Institute of Aeronautics and Astronautics.)

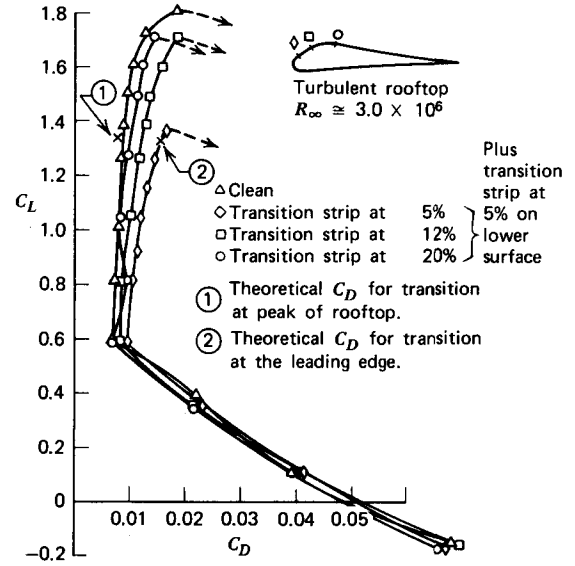

Figure 3.44b Effect of transition location on the lift and drag of a Liebeck airfoil. (R. H. Liebeck, "Class of Airfoils Designed for High Lift", AIAA *Journal of Aircraft*, 1973. Reprinted from the *Journal of Aircraft* by permission of the American Institute of Aeronautics and Astronautics.)

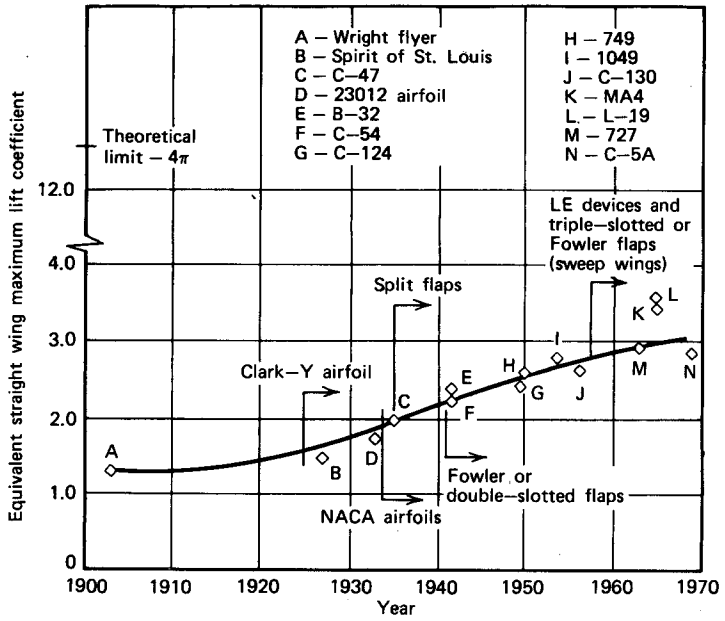

Figure 3.45 History of maximum lift coefficients for mechanical lift systems. (F. A. Cleveland, "Size Effects in Conventional Aircraft", AIAA *Journal of Aircraft*, 1970 Reprinted from the *Journal of Aircraft* by permission of the American Institute of Aeronautics and Astronautics.)

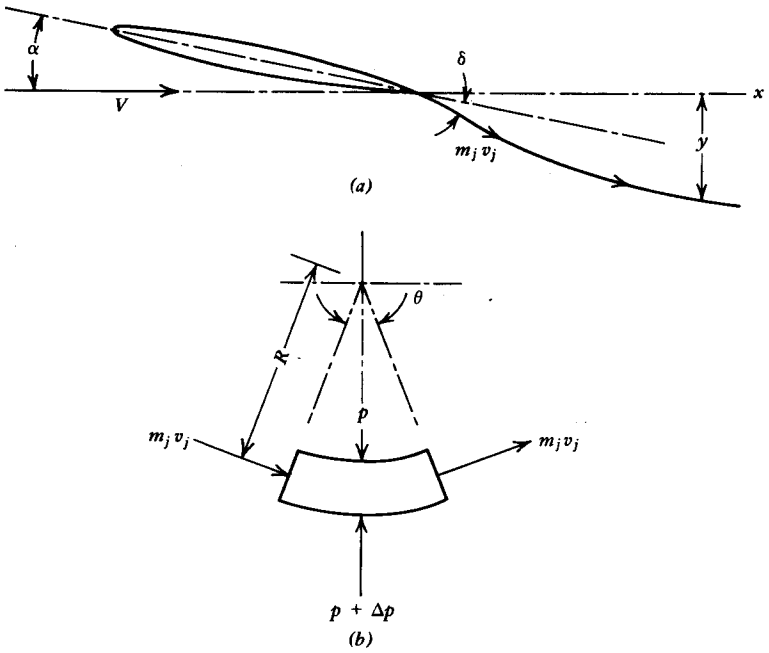

Figure 3.46 The jet flap.

Since the jet exerts a force on the fluid, it can be replaced by an equivalent continuous vortex sheet that exerts the same force. Letting γ_j be the strength per unit length of the sheet,

$$\Delta p R\theta = \rho V \gamma R\theta$$

or

$$\gamma_j = \frac{\Delta p}{\rho V} \tag{3.54}$$

Measuring the position of the jet, y, positively downward, the radius of curvature and y for a nearly horizontal jet are related by

$$\frac{1}{R} = -\frac{d^2y}{dx^2} \tag{3.55}$$

Combining Equations 3.53, 3.54, and 3.55 gives

$$\gamma_j = \frac{-m_j v_j}{\rho V}\frac{d^2y}{dx^2} \tag{3.56}$$

Equation 3.56 relates the jet vortex strength to the shape of the sheet and the jet momentum flux.

The total circulation of the jet vortex sheet can be obtained by integrating Equation 3.56 from $x = 0$ to ∞.

$$\begin{aligned}\Gamma_j &= \int_0^\infty \gamma_j \, d_x \\ &= -\frac{m_j v_j}{\rho V}\frac{dy}{dx}\Big|_0^\infty \\ &= \frac{m_j v_j}{\rho V}(\alpha + \delta)\end{aligned} \tag{3.57}$$

Combining Equations 3.52 and 3.57 shows that the Kutta–Joukowski relationship holds for the jet-flapped airfoil if the circulation is taken around both the airfoil and the jet.

$$L = \rho V(\Gamma_c + \Gamma_j) \tag{3.58}$$

The boundary value problem is then posed where the airfoil and jet sheet are each replaced by an unknown vortex distribution. Distributions must then be found that will induce a velocity at each point on the airfoil and combining with the free-stream velocity to give a resultant velocity tangent to the airfoil. Along the sheet the following must hold.

$$\frac{w(x)}{V} = \frac{dy}{dx}$$

The details of the solution are beyond the scope of this text and can be found in Reference 3.19.

Although the solution of Reference 3.19 is not in closed form, the results

can be expressed in a relatively simple way. As with a physical flap, the increment in C_l because of a change in angle of attack and flap angle can be expressed as a linear combination of the two angles.

$$C_l = C_{l_\alpha}\alpha + C_{l_\delta}\delta \tag{3.59}$$

where

$$C_{l_\alpha} = \frac{dC_l}{d\alpha}$$

$$C_{l_\delta} = \frac{dC_l}{d\delta}$$

The derivatives C_{l_α} and C_{l_δ} are a function of the ratio of the jet momentum flux to the product of the free-stream dynamic pressure and a reference area. This ratio, known as the momentum coefficient, C_μ, is defined for a two-dimensional airfoil by

$$C_\mu = \frac{m_j v_j}{qc} \tag{3.60}$$

If, in addition, the jet exits ahead of the trailing edge and blows over and is deflected by a physical flap having a chord of c_f (see the blown flap of Figure 3.24), then C_{l_δ} is also a function of c_f/c. For a pure jet flap ($C_f/C = 0$), C_{l_α} and C_{l_δ} are given by

$$C_{l_\delta} = [4\pi C_\mu(1 + 0.151C_\mu^{1/2} + 0.139C_\mu)]^{1/2} \tag{3.61}$$

$$C_{l_\alpha} = 2\pi(1 + 0.151C_\mu^{1/2} + 0.219C_\mu) \tag{3.62}$$

For c_f/c values other than zero, C_{l_δ} is given in Figure 3.47. The curve labeled $c_f/c = 1.0$ in this figure corresponds to Equation 3.62 since, for this case, $C_{l_\delta} = C_{l_\alpha}$.

Data concerning $C_{l_{max}}$ for jet-flapped airfoils is sparse. Generally, the jet flap follows the predictions of Figure 3.41 fairly closely, since the jet fixes the Kutta condition and provides some control over the boundary layer to prevent separation. As a preliminary estimate for $C_{l_{max}}$, Reference 3.3 recommends the use of the relationship presented in Figure 3.48. Here the difference in the angle of attack for stall, with and without blowing, is presented as a function of C_μ.

The negative pitching moment of the jet flaps is higher than the moment for conventional flaps for two reasons. First, the jet reaction acts at the trailing edge; second, the jet-flapped airfoil maintains lift all the way back to the trailing edge. As with the lift, C_M can be written as a linear combination of α and δ.

$$C_M = C_{M_\alpha}\alpha + C_{M_\delta}\delta$$

or

$$C_M = \left(\frac{\partial C_M}{\partial C_l}\right)_{\delta=\text{const}} C_{l_\alpha}\alpha + \left(\frac{\partial C_M}{\partial C_l}\right)_{\alpha=\text{const}} Cl_\delta\delta \tag{3.63}$$

In this equation $\partial C_M/\partial C_l$ can be obtained from Figure 3.49.

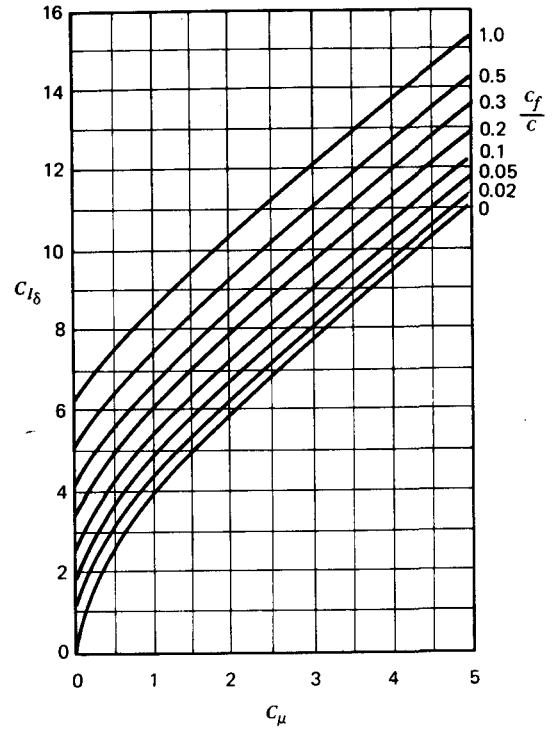

Figure 3.47 Blown flap effectiveness. (B. W. McCormick, *Aerodynamics of V/STOL Flight*, Academic Press, Inc. 1967. Reprinted by permission of Academic Press, Inc.

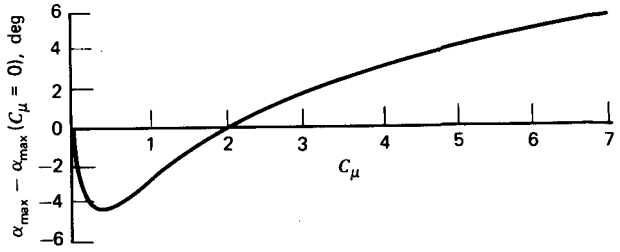

Figure 3.48 Effect of C_μ on α for $C_{l_{max}}$. (B. W. McCormick, *Aerodynamics of V/STOL Flight*, Academic Press, Inc. 1967. Reprinted by permission of Academic Press, Inc.)

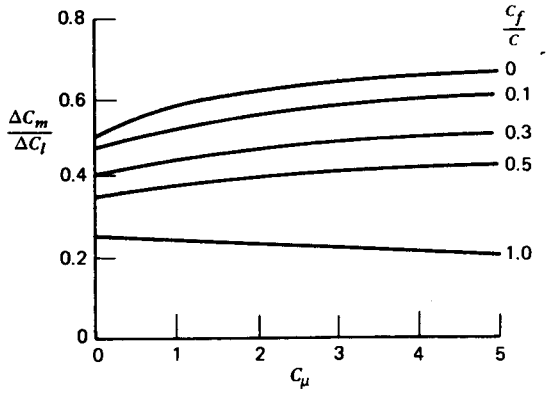

Figure 3.49 Effect of C_μ on pitching moments for blown flaps. (B. W. McCormick, *Aerodynamics of V/STOL Flight*, Academic Press, Inc. 1967. Reprinted by permission of Academic Press, Inc.)

To illustrate the use of the foregoing relationship for the jet-flapped airfoil, consider the prediction of $C_{l_{max}}$ for the NACA 63,4-421 airfoil (Figure 3.30) equipped with a 25% blown flap deflected 50°. The jet expands isentropically from a reservoir pressure of 25 psia and a temperature of 70 °F. The airfoil is operating at 50 mph at SSL conditions. It has a chord of 5 ft and the jet thickness is 0.2 in.

We begin by calculating the jet velocity from the compressible Bernoulli equation (Equation 2.31).

$$v_j^2 = \frac{2\gamma}{\gamma - 1}\left(\frac{p_0}{\rho_0} - \frac{p}{\rho}\right)$$

or, with the use of Equation 2.30,

$$v_j = \left\{\frac{2\gamma p_0}{(\gamma - 1)\rho_0}\left[1 - \left(\frac{p}{p_0}\right)^{(\gamma-1)/\gamma}\right]\right\}^{1/2}$$

From the equation of state (Equation 2.1),

$$p_0/\rho_0 = RT_0$$

Thus,

$$v_j = \left\{\frac{2(1.4)(1716)(529.7)}{0.4}\left[1 - \left(\frac{14.7}{25}\right)^{0.286}\right]\right\}^{1/2}$$

$$= 946.9 \text{ fps}$$

The mass density of the expanded jet will be

$$\rho_j = \rho_0\left(\frac{p}{p_0}\right)^{1/\gamma}$$

ρ_0 is calculated from the equation of state.

$$\rho_0 = \frac{25(144)}{1716(529.7)}$$
$$= 0.00396 \text{ slugs/ft}^3$$

Thus

$$\rho_j = 0.00271 \text{ slugs/ft}^3$$

The jet mass flux will be equal to

$$m_j = \rho_j A_j v_j$$
$$= 0.00271(0.2/12)(946.9)$$
$$= 0.0428 \text{ slugs/s}$$

The free-stream dynamic pressure is

$$q = \tfrac{1}{2}\rho V^2$$
$$= 0.002378(50 \times 1.467)^2/2$$
$$= 6.397 \text{ psf}$$

Thus,

$$C_\mu = \frac{(0.0428)(946.9)}{6.397(5)}$$
$$= 1.27$$

From Figures 3.47 and 3.48,

$$C_{l_\alpha} = 9.09/\text{rad}$$
$$C_{l_\delta} = 6.5/\text{rad}$$

$$\alpha_{\max} - \alpha_{\max}(C_\mu = 0) = -2°$$

From Figure 3.30, $C_{l_{\max}}$ for the unblown airfoil without a flap is equal approximately to 1.4. Using Figures 3.33 and 3.34, ΔC_l due to the plain flap ($C_\mu = 0$) is estimated as

$$\Delta C_l = 2\pi(0.6)(.41)\left(\frac{50}{57.3}\right) = 1.35$$

so that, using Figure 3.34

$$\Delta C_{l_{\max}} \simeq (0.72)(1.35) = 0.97$$

Thus, for $C_\mu = 0$ with the flap deflected, $C_{l_{\max}}$ is estimated to be 2.37. At $\alpha = 0$, C_l is estimated to be 1.5. Thus, with $C_{l_\alpha} = 0.109$ (from Figure 3.30),

$$\alpha_{\max} = \frac{2.23 - 1.5}{0.109}$$
$$= 6.7°$$

or, relative to the zero lift line, flaps up,

$$\alpha_{max} = 9.7°$$

For the operating C_μ, the angle of attack for the zero lift line at stall is estimated to equal 7.1°.
Thus,

$$C_{l_{max}} = C_{l_\alpha}\alpha_{max} + C_{l_\delta}\delta$$

or

$$C_{l_{max}} = 9.09\frac{7.1}{57.3} + 6.5\frac{50}{57.3}$$

$$= 6.8$$

The preceding answer must, of course, be further corrected, using Figure 3.43 and Equation 3.46, to account for trimming tail loads. Also, it should be emphasized that the preceding is, at best, an estimate for preliminary design purposes or relative parametric design studies. In the final analysis, model and prototype component testing of the blowing system must be performed.

Credit for the practical application of the jet flap must be given to John Attinello. Prior to 1951, all blown systems utilized pressure ratios less than critical in order to avoid supersonic flow in the jet. Such systems required large and heavy ducting. For his honors thesis at Lafayette College, Attinello demonstrated with "homemade" equipment that a supersonic jet would adhere to a deflected flap. This was contrary to the thinking of the day that not only would a supersonic jet separate from a blown flap, but the losses associated with the shock wave system downstream of the nozzle would be prohibitive. Later, more sophisticated testing performed by the David Taylor Model Basin confirmed Attinello's predictions (Ref. 3.38) of high lift coefficients for supersonic jet flaps. This led to the development of compact, lightweight systems using bleed air from the turbojet engine compressor section. The Attinello flap system was flight tested on an F9F-4 and produced a significant decrease in the stalling speed for an added weight of only 50 lb. Following this success, the Attinello flap went into production on the F-109, F-4, F8K, A5, and other aircraft, including several foreign models.

THE LIFTING CHARACTERISTICS OF A FINITE WING

A two-dimensional airfoil with its zero lift line at an angle of attack of 10° will deliver a lift coefficient, C_l, of approximately 1.0. When incorporated into a wing of finite aspect ratio, however, this same airfoil at the same angle of attack will produce a wing lift coefficient, C_L, significantly less than 1.0. The effect of aspect ratio is to decrease the slope of the lift curve C_{L_α} as the aspect ratio decreases. Figure 3.50 illustrates the principal differences in the

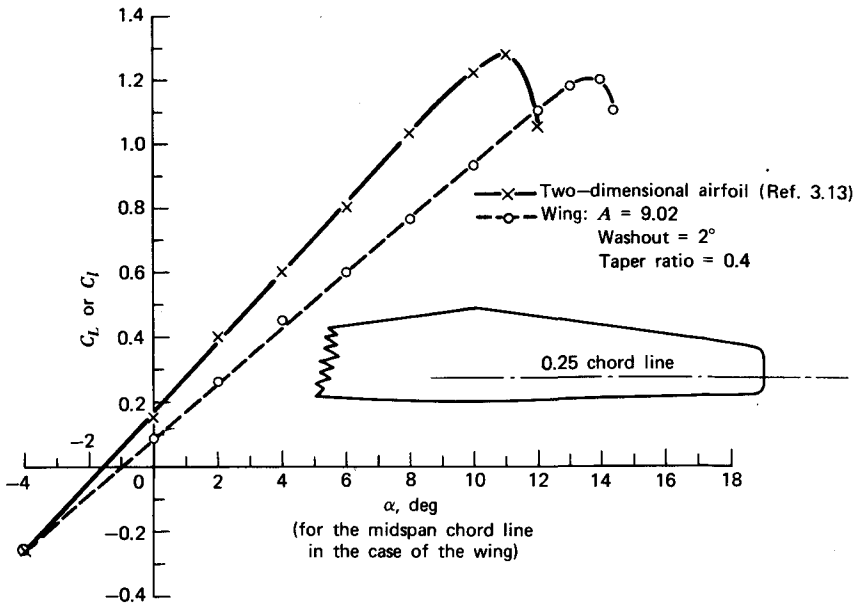

Figure 3.50 Comparison of NACA 65–210 airfoil lift curve with that of a wing using the same airfoil.

lift behavior of a wing and an airfoil. First, because the wing is twisted so that the tip is at a lower angle of attack than the root (washout), the angle for zero lift, measured at the root, is higher for the wing by approximately 0.6°. Next, the slope of the wing's lift curve, C_{L_α}, is approximately 0.79 of the slope for the airfoil. Finally, $C_{L_{max}}$ is only slightly less than $C_{l_{max}}$, in the ratio of approximately 0.94. These three differences are almost exactly what one would expect on the basis of wing theory, which will now be developed.

The Vortex System for a Wing

A wing's lift is the result of a generally higher pressure acting on its lower surface compared with the pressure on the upper surface. This pressure difference causes a spanwise flow of air outward toward the tips on the lower surface, around the tips, and inward toward the center of the wing. Combined with the free-stream velocity, this spanwise flow produces a swirling motion of the air trailing downstream of the wing, as illustrated in Figure 3.51. This motion, first perceived by Lanchester, is referred to as the wing's trailing vortex system.

Immediately behind the wing the vortex system is shed in the form of a vortex sheet, which rolls up rapidly within a few chord lengths to form a pair

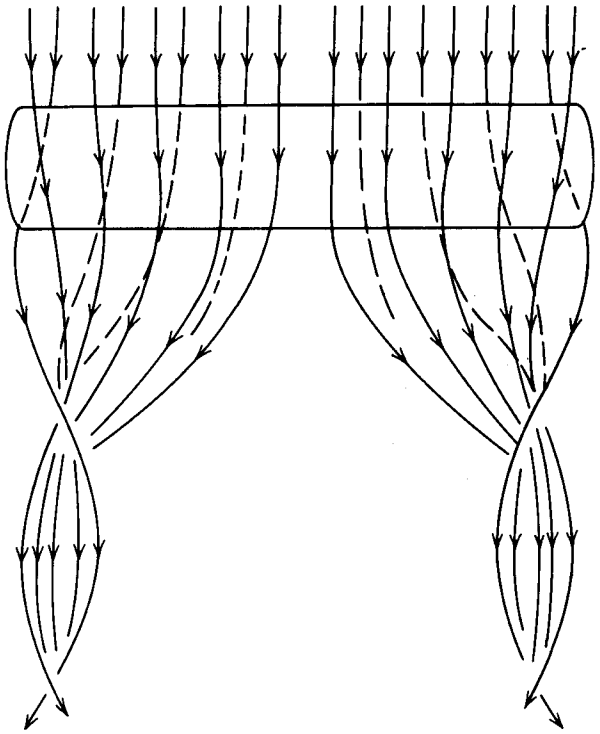

Figure 3.51 Generation of vortex system by finite aspect ratio wing.

of oppositely rotating line vortices. Looking in the direction of flight, the vortex from the left wing tip rotates in a clockwise direction; the right tip vortex rotates in the opposite direction.

The trailing vortex system, not present with a two-dimensional airfoil, induces an additional velocity field at the wing that must be considered in calculating the behavior of each section of the wing.

If the aspect ratio of the wing is large, approximately 5 or higher, the principal effect of the trailing vortex system is to reduce the angle of attack of each section by a small decrement known as the induced angle of attack, α_i. In this case Prandtl's classical lifting line theory (Ref. 3.28) applies fairly well. As shown in Figure 3.52, the wing is replaced by a single equivalent vortex line, known as the "bound vortex," since it is in a sense bound to the wing. The strength of this vortex, $\Gamma(y)$, is related to the lift distribution along the wing by the Kutta–Joukowski relationship.

$$\frac{dL(y)}{dy} = \rho V \Gamma(y) \tag{3.64}$$

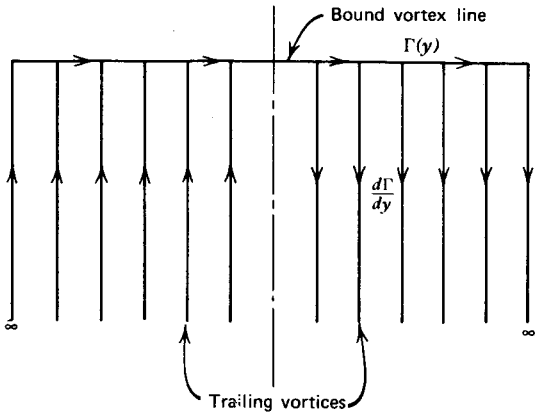

Figure 3.52 Lifting line model of a wing and trailing vortex system.

Expressing the lift per unit length of span in terms of the section chord length, $c(y)$, and section lift coefficient, $C_l(y)$, leads to

$$\Gamma(y) = \tfrac{1}{2}c(y)C_l(y)V \tag{3.65}$$

With no physical surface outboard of the wing tips to sustain a pressure difference, the lift, and hence Γ, must vanish at the tips.

According to the Helmholtz theorem regarding vortex continuity (Ref. 1.3, p. 120), a vortex line or filament can neither begin nor end in a fluid; hence it appears as a closed loop, ends on a boundary, or extends to infinity. Thus, it follows that if in going from y to $y + dy$ the bound circulation around the wing increases from Γ to $\Gamma + d\Gamma$, a free vortex filament of strength $d\Gamma$, lying in the direction of the free-stream velocity, must be feeding into Γ in order to satisfy vortex continuity. This statement may be clarified by reference to Figure 3.53.

The entire vortex system shown in Figure 3.52 can be visualized as being closed infinitely far downstream by a "starting" vortex. This vortex, opposite

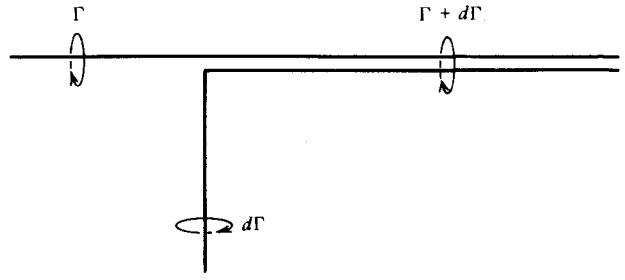

Figure 3.53 Illustration of vortex continuity.

in direction to the bound vortex, would be shed from the trailing edge of the wing as its angle of attack is increased from zero.

The trailing vortex system of strength $d\Gamma$ induces a downwash, $w(y)$, at the lifting line, as mentioned earlier. As pictured in Figure 3.54, this reduces the angle of attack by the small angle α_i. Thus the section lift coefficient will be given by

$$C_l = C_{l_\alpha}(\alpha - \alpha_i) \tag{3.66}$$

α being measured relative to the section zero lift line.

To a small angle approximation, the induced angle of attack, α_i, is given by w/V. The downwash, w, can be determined by integrating the contributions of the elemental trailing vortices of strength $d\Gamma$. If the vortex strength $d\Gamma$ trails from the wing at a location of y, its contribution to the downwash at another location y_0 can be found by Equation 2.64 to be

$$dw(y_0) = \frac{d\Gamma(y)}{4\pi(y_0 - y)} \tag{3.67}$$

Thus, α_i becomes

$$\alpha_i(y_0) = \frac{1}{4\pi V}\int_{-b/2}^{b/2} \frac{d\Gamma(y)}{y_0 - y} \tag{3.68}$$

Equations 3.65, 3.66, and 3.68 together relate $\Gamma(y)$ to $c(y)$ and $\alpha(y)$ so that, given the wing geometry and angle of attack, one should theoretically be able to solve for Γ and hence the wing lift. In order to accomplish the solution, it is expedient to make the coordinate transformation pictured in Figure 3.55.

$$y = \frac{b}{2}\cos\theta$$

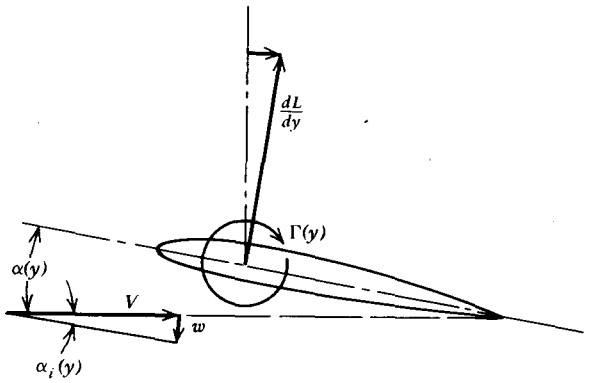

Figure 3.54 A wing section under the influence of the free-stream velocity and the downwash.

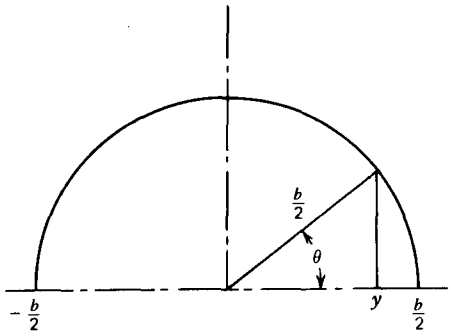

Figure 3.55 Coordinate transformation used in the reduction of the lifting line equations.

Hence, Equation 3.67 becomes

$$\alpha_i(\theta_0) = \frac{1}{2\pi b V}\int_0^{\pi} \frac{d\Gamma(\theta)}{\cos\theta - \cos\theta_0} \tag{3.69}$$

Since more elaborate and comprehensive treatments of wing theory can be found in texts devoted specifically to the subject (e.g., see Ref. 3.29), only the classical solution for the eliptic Γ distribution will be covered here. This particular case is easily handled and results in the essence of the general problem.

Assume that Γ is of the form

$$\Gamma = \Gamma_0\sqrt{1-\left(\frac{2y}{b}\right)^2} \tag{3.70}$$

This transforms to

$$\Gamma = \Gamma_0 \sin\theta$$

Here, Γ_0 is obviously the midspan value of the bound circulation. Thus Equation 3.69 becomes

$$\alpha_i(\theta_0) = \frac{\Gamma_0}{2\pi b V}\int_0^{\pi} \frac{\cos\theta\, d\theta}{\cos\theta - \cos\theta_0}$$

The preceding integral was encountered previously in thin airfoil theory and has a value of π. Thus, for an elliptic Γ distribution, α_i and hence the downwash is found to be a constant independent of y.

$$\alpha_i = \frac{\Gamma_0}{2bV} \tag{3.71}$$

If the wing is untwisted so that α is also not a function of y then, from

Equation 3.66, it follows that the section C_l is constant along the span. Thus,

$$L = \int_{-b/2}^{b/2} \frac{1}{2}\rho V^2 c C_l \, dy$$

$$= \frac{1}{2}\rho V^2 C_l \int_{-b/2}^{b/2} c \, dy$$

$$= \frac{1}{2}\rho V^2 C_l S$$

But

$$C_l = \frac{L}{qS}$$

Hence,

$$C_l = C_L$$

Equation 3.65 then gives

$$\Gamma(y) = \frac{1}{2} c(y) C_L V$$

or,

$$c(y) = \frac{2\Gamma_0}{C_L V}\sqrt{1 - \left(\frac{2y}{b}\right)^2}$$

$$= c_0\sqrt{1 - \left(\frac{2y}{b}\right)^2}$$

Thus it is found that, according to lifting line theory, an untwisted wing with an elliptical planform will produce an elliptic Γ distribution. Such a wing will have a constant downwash and section C_l.

Since C_l is constant and equal to C_L, Equations 3.65, 3.66, and 3.71 can be applied at the midspan position in order to determine the slope of the wing lift curve. First, from Equations 3.71 and 3.65,

$$\alpha_i = \frac{c_0 C_L}{4b}$$

But, for the planform given by Equation 3.66, c_0 and b are related to the aspect ratio by

$$A = \frac{4b}{\pi c_0}$$

Thus, α_i becomes

$$\alpha_i = \frac{C_L}{\pi A} \tag{3.72}$$

Inserted into Equation 3.66, the preceding results in

$$C_L = C_{l_\alpha}\left(\alpha - \frac{C_L}{\pi A}\right)$$

or,

$$C_L = C_{l_\alpha}\left[\frac{1}{(1 + C_{l_\alpha})/\pi A}\right]\alpha\left[\frac{1}{(1 + C_{l_\alpha})/\pi A}\right]$$

Using the theoretical value of 2π C_l/rad derived earlier, the preceding becomes

$$C_L = C_{l_\alpha}\left(\frac{A}{A+2}\right)\alpha \tag{3.73}$$

Equations 3.72 and 3.73 are important results. The induced angle of attack is seen to increase with decreasing aspect ratio which, in turn, reduces the slope of the lift curve, C_{L_α}. A wing having a low aspect ratio will require a higher angle of attack than a wing with a greater aspect ratio in order to produce the same C_L.

It was stated previously that the comparative performance between the wing and airfoil shown in Figure 3.50 could be explained theoretically. In this case, $A = 9.02$ so that, on the basis of Equation 3.73,

$$C_{L_\alpha} = 0.819\, C_{l_\alpha}$$

This result is within about 2% of the experimental results presented in Figure 3.50.

As the aspect ratio decreases, the lifting line becomes progressively less accurate. For example, for an aspect ratio of 4.0, Equation 3.73 is approximately 11% higher than that predicted by more exact methods.

As described in Reference 3.3, a more accurate estimate of C_{L_α} is obtained from

$$C_{L_\alpha} = C_{l_\alpha}\frac{A}{A + [2(A+4)/(A+2)]} \tag{3.74a}$$

An alternate to Equation 3.74*a* is offered by Reference 3.35 and is referred to as the Helmbold equation, after the original source noted in the reference. The Helmbold equation reads

$$C_{L_\alpha} = C_{l_\alpha}\frac{A}{(C_{l_\alpha}/\pi) + \sqrt{(C_{l_\alpha}/\pi)^2 + A^2}}$$

Replacing C_{l_α} by 2π in the denominator,

$$C_{L_\alpha} = C_{l_\alpha}\frac{A}{2 + \sqrt{4 + A^2}} \tag{3.74b}$$

Equation 3.74*a* and 3.74*b* agree within a couple of percent over the range of practical aspect ratios and approach each other in the limits of $A = 0$ or $A = \infty$. This holds for high or low aspect ratios and is based on an approximate lifting surface theory, which accounts for the chordwise distribution of bound circulation as well as the spanwise distribution.

Let us visualize an aerodynamically untwisted wing, that is, one for which the zero lift lines all lie in a plane. Imagine this wing to be at a zero angle of attack and hence operating at zero C_L. Holding the midspan section fixed, let us now twist the tip *up* through an angle ϵ_T. We will assume that the twist along the wing is linear, so that at any spanwise location y, the twist relative to the midspan section is given by

$$\epsilon = \frac{2\epsilon_T}{b}|y|$$

Obviously, the wing will now develop a positive C_L, since every section except the midspan is at a positive angle of attack. If we define the angle of attack of the wing to be that of the zero lift line at the root, the angle of attack of the wing for zero lift will be negative; that is, we must rotate the entire wing nose downward in order to return to the zero lift condition. For a C_L of zero, Equation 3.72 shows that on the average, α_i equals zero; thus, at any section,

$$C_l = C_{l_\alpha}\left(\epsilon_T \frac{|y|}{b/2} + \alpha_{w_0}\right)$$

where α_{w_0} is the angle of attack of the wing for zero lift. To find this angle, an expression is written for the total wing lift and is equated to zero.

$$L = \int_{-b/2}^{b/2} qcC_l\, dy$$

$$= \int_{-b/2}^{b/2} qcC_{l_\alpha}\left(\epsilon_T \frac{|y|}{b/2} + \alpha_{w_0}\right) dy$$

Equating this to zero and taking q and C_{l_α} to be constant (this is not quite true for C_{l_α}, but close) leads to,

$$\alpha_{w_0} = -\frac{2\epsilon_T}{bS}\int_{-b/2}^{b/2} c|y|dy \tag{3.75}$$

If ϵ is not linear,

$$\alpha_{w_0} = \frac{1}{S}\int_{-b/2}^{b/2} c\epsilon\, dy \tag{3.76}$$

Now consider a linearly tapered wing for which the chord distribution is given by

$$c = c_0 - (c_0 - c_T)\frac{2|y|}{b}$$

Defining the taper ratio λ as the ratio of the tip chord, c_T, to the midspan chord, C_0, the preceding equation can be written as

$$c = C_0\left[1 - (1-\lambda)\frac{2|y|}{b}\right]$$

Substituting this into Equation 3.75 and integrating results in the angle of attack of the wing for zero lift as a function of twist and taper ratio.

$$\alpha_{w_0} = -\frac{\epsilon_T}{3}\frac{(1+2\lambda)}{(1+\lambda)} \tag{3.77}$$

Most wings employ a negative twist referred to as "washout." Generally, ϵ_T is of the order of -3 or 4° to assure that the inboard sections of the wing stall before the tip sections. Thus, as the wing begins to stall, the turbulent separated flow from the inboard portion of the wing flows aft over the horizontal tail, providing a warning of impending stall as the pilot feels the resulting buffeting. In addition, with the wing tips still unstalled, the pilot has aileron control available to keep the wings level in order to prevent the airplane from dropping into a spin. At the present time, the stall-spin is one of the major causes of light airplane accidents.

The wing of the airplane in Figure 3.50 has a 2° washout and a taper ratio of 0.4. According to Equation 3.77, α_{w_0} for this wing will be $+0.8°$. This is close to the results presented in Figure 3.50, where the angle of attack of the wing for zero lift is seen to be approximately 0.6° greater than the corresponding angle for the airfoil. Thus, knowing an airfoil lift curve, one can estimate with reasonable accuracy the lift curve of a wing incorporating that airfoil by calculating the slope and angle for zero lift with the use of Equations 3.74 and 3.77 respectively.

As a further example, in the use of these equations, consider a wing having an NACA 63,4-421 airfoil (Figure 3.30) at its midspan that fairs linearly into an NACA 0012 airfoil at the tip. The wing has no geometric twist; that is, the section chord lines all lie in the same plane. The wing's aspect ratio is equal to 6.0, and it has a taper ratio of 0.5. The problem is to find the angle of attack of the wing measured relative to the midspan chord, which will result in a C_L value of 0.8.

To begin, we note from Figure 3.30 that the 63,4-421 airfoil has an angle of zero lift of $-3°$; thus, the zero lift line at the midspan is up 3° from the chord line. It follows that the aerodynamic twist ϵ_T is $-3°$, since the tip airfoil is symmetrical. Inserting this and the taper ratio into Equation 3.77 results in $\alpha_{w_0} = 1.3°$. From Equation 3.74, for an aspect ratio of 6.0,

$$C_{L_\alpha} = 0.706\ C_{l_\alpha}$$

From Figure 3.30 or Reference 3.1, C_{l_α} is nearly the same for the midspan and tip sections and is equal approximately to 0.107 C_l/deg. Hence, $C_{L_\alpha} = 0.076\ C_L$/deg. Therefore, over the linear portion of the lift curve, the equation for the wing C_L relative to the midspan zero lift line becomes

$$C_L = 0.076(\alpha - 1.3)$$

For C_L of 0.8, α is found to equal 11.8°. Thus, to answer the original problem, the angle of attack of the midspan chord, α_w, will equal $11.8 - 3$, or 8.8°.

The Maximum Lift of a Finite Wing

The maximum lift coefficient of a finite wing is influenced by several factors. Obviously, $C_{L_{max}}$ is strongly dependent on $C_{l_{max}}$; that is, the wing's performance depends on it's airfoil performance. Second, the spanwise extent to which the wing is flapped has a significant influence on $C_{L_{max}}$. Also in estimating $C_{L_{max}}$, one must account for the presence of the fuselage, the tail download required to trim the aerodynamic pitching moment, and the spanwise distribution of loading over the wing.

The effect of aspect ratio on $C_{L_{max}}$ is slight, as one might expect from the preceding considerations on the elliptic wing. The wing lift coefficient and section lift coefficients are nearly equal.

The detailed estimation of a wing's $C_{L_{max}}$ begins with a calculation of its spanwise load distribution. There are several methods to be found in the literature for doing this. Many of these fall into a class known as vortex lattice methods. One of the first of these can be found in Reference 3.30.

The vortex lattice method is similar to lifting line theory except that discrete vortex lines are also distributed in the chordwise direction. As illustrated in Figure 3.56, the wing is covered with a mesh of spanwise and

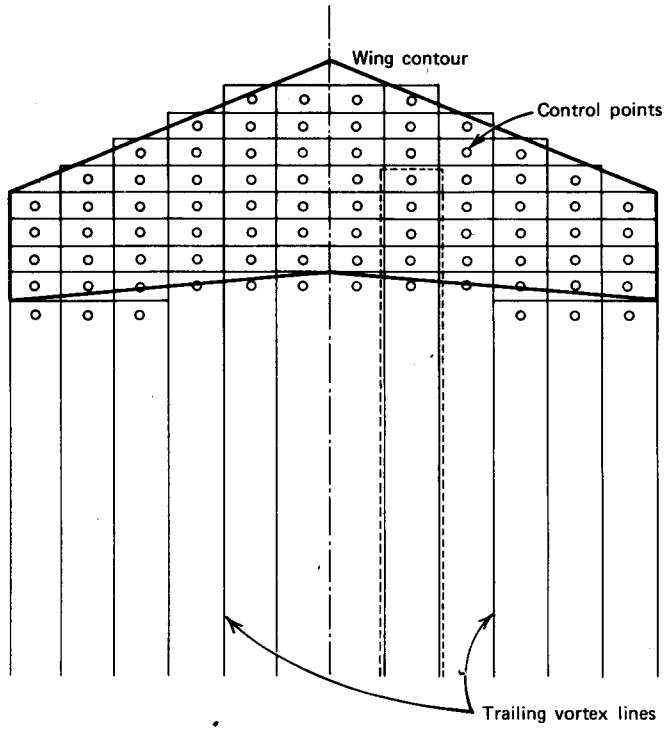

Figure 3.56 Vortex lattice model for a wing.

chordwise bound vortex lines with free vortex lines shed downstream from the trailing edge. At every juncture of the vortex lines, Helmholtz's law of vortex continuity must hold. In addition, control points are chosen over the wing equal in number to the number of unknown vortex line strengths. The unknown vortex strengths are then adjusted to assure that the resultant flow at each control point is tangent to the mean surface of the wing.

The lattice model shown in Figure 3.56, in the manner of Reference 3.30, is formed by the superposition of horseshoe-shaped line vortices. One such vortex is shown dashed for illustrative purposes. Note that the downstream control points are aft of the last bound vortex lines; some points are even slightly off of the wing's surface. Stipulating that the flow at these points parallels the camber surface at the trailing edge will satisfy approximately the Kutta condition.

Trends in the behavior of $C_{L_{max}}$ as related to wing geometry can be seen by the application of an approximate method for determining spanwise load distribution known as Schrenk's approximation (Ref. 3.31).

This method deals with two distributions: a basic lift distribution, and an additional lift distribution. The basic distribution is that which exists along the span when the total lift is equal to zero. Approximately, this lift distribution is taken as the average of a constant "zero" distribution and one obtained by neglecting any induced velocities. Thus,

$$\tfrac{1}{2}\rho V^2 c C_l = \tfrac{1}{2}[\tfrac{1}{2}\rho V^2 c C_{l_\alpha}(\alpha_{w_0} + \epsilon) + 0]$$

or the basic section lift coefficient, C_{l_b}, will be

$$C_{l_b} = \frac{C_{l_\alpha}}{2}(\alpha_{w_0} + \epsilon) \tag{3.78}$$

The additional lift distribution results from an angle of attack different from α_{w_0} and is assumed to be the average of an elliptic distribution and one proportional to the planform, both having the same total lift. For the latter,

$$cC_l \propto c$$
$$= kc$$

But

$$L = \int_{-b/2}^{b/2} qcC_l\, dy$$
$$= qk \int_{b/2}^{b/2} c\, dy$$
$$= qks$$

Thus, $k = C_L$.

For the elliptic distribution,

$$cC_L = K\sqrt{1 - \left(\frac{2y}{b}\right)^2}$$

so that

$$L = \int_{-b/2}^{b/2} qK\sqrt{1-\left(\frac{2y}{b}\right)^2}\,dy$$

The constant of proportionality, K, in this case becomes

$$K = \frac{4S}{\pi b} C_L$$

The additional section lift coefficient then becomes

$$C_{l_a} = \frac{C_L}{2}\left[1 + \frac{4S}{\pi bc}\sqrt{1-\left(\frac{2y}{b}\right)^2}\right] \tag{3.79}$$

Usually C_{l_a} is defined as the value of Equation 3.79 for a C_L of unity; thus,

$$C_l = C_{l_b} + C_{l_a} C_L \tag{3.80}$$

The manner in which this equation is used to estimate $C_{L_{max}}$ is best explained by an example. Consider the wing of Figure 3.50. This particular wing has a taper ratio of 0.4 and a washout of 2°. Using Equations 3.78 and 3.79, the basic and additional section lift coefficient distributions given in Figure 3.57 were calculated. Also graphed on this figure is $C_{l_{max}}$ as a function of spanwise location. In this instance, $C_{l_{max}}$ is taken from Figure 3.50 to be a constant. In many cases, $C_{l_{max}}$ decreases toward the tip as the airfoil becomes relatively thinner or as the chord lengths become smaller.

Combining C_{l_b} and C_{l_a} in the form of Equation 3.80, Figure 3.57 shows that a wing C_L of 1.22 results in a section C_l halfway out along the span, which is just equal to the section $C_{l_{max}}$ at that location. Any attempt to increase C_L above this value will therefore cause the wing to stall at this location. Since the C_l curve is rather flat in this location, the stalling would be expected to spread to either side of $2y/b$ equal to 0.5. Thus, to estimate the $C_{L_{max}}$ of a wing, one finds the wing C_L that results in a section C_l somewhere along the span, which is just equal to the section $C_{l_{max}}$. In this instance, the $C_{L_{max}}$ value of 1.22 compares favorably with the experimental results. Generally, however, the $C_{L_{max}}$ predicted by this method will be somewhat conservative, since the total wing C_L may still increase somewhat, even though a section of it begins to stall.

As a further and more extreme example of the method, consider the wing of Figure 3.50 equipped with 60% span, 20% chord split flaps deflected 60°. From Equation 3.43, ΔC_l is estimated to be

$$\begin{aligned}\Delta C_l &= C_{l_a} \tau \eta\, \delta \\ &= 0.108\ (0.545)(0.35)(60) \\ &= 1.236\end{aligned}$$

$\Delta C_{l_{max}}$, empirically, is approximately 0.83 of the preceding equation (Figure

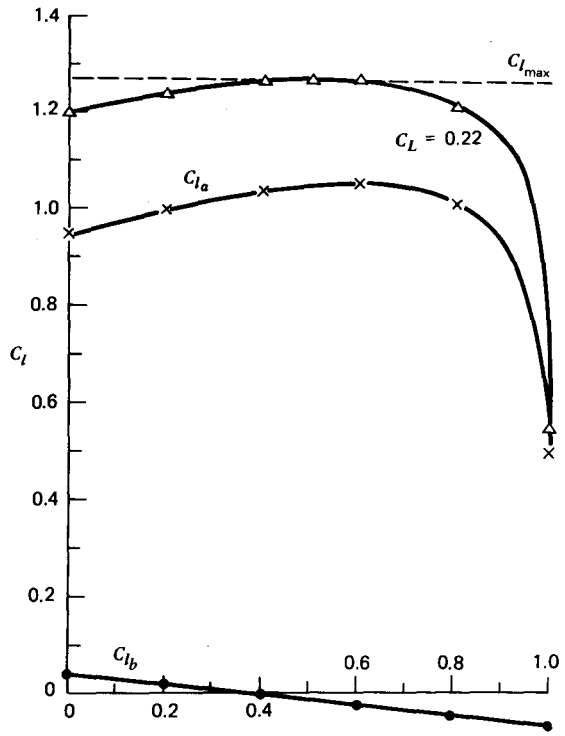

Figure 3.57 Predicted lift coefficient distributions for wing of Figure 3.50.

3.34) or 1.026. Thus, Figure 3.57 is revised as shown in Figure 3.58 to increase the section $C_{l_{max}}$ to 2.30 over the inner 60% of the span.

Aerodynamically the twist of the wing is changed by lowering the flaps. Relative to the midspan chord, the zero lift lines of the sections outboard of the flaps are reduced in angle of attack by $\Delta C_l/C_{l_\alpha}$, or 11.4°. Thus, for this flapped wing, ϵ, in degrees, becomes

$$\epsilon = -2\left|\frac{2y}{b}\right| \qquad 0 \le \left|\frac{2y}{b}\right| \le 0.6$$

$$\epsilon = -2\left|\frac{2y}{b}\right| - 11.4 \qquad \left|\frac{2y}{b}\right| > 0.6$$

For this twist distribution and a taper ratio of 0.4, the angle of attack of the midspan zero lift line, α_{w_0}, for zero lift becomes 4.24°. Thus

$$C_{l_b} = 0.054(4.24 + \epsilon)$$

The additional lift distribution remains the same, since the planform is

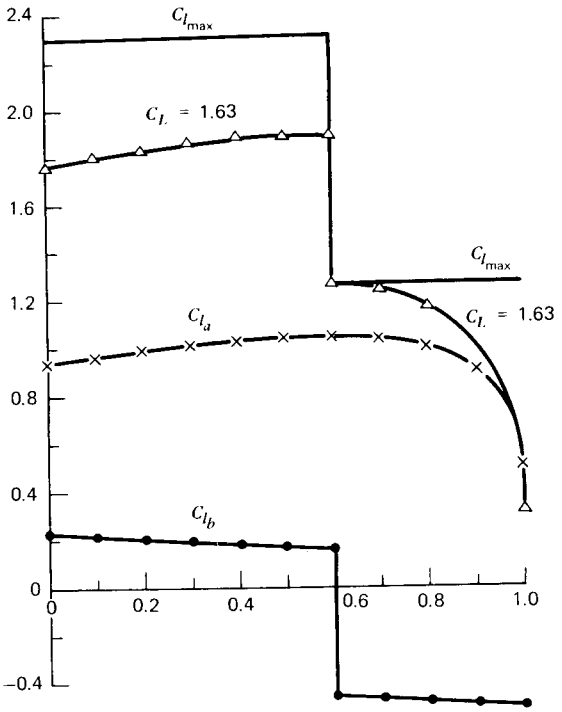

Figure 3.58 Predicted lift coefficient distributions for wing of Figure 3.50 with 60% span, 20% chord split flaps deflected 60°.

unchanged. The predicted C_l distributions with the partial span split flaps are presented in Figure 3.58.

Figure 3.58 predicts that the wing will begin to stall just outboard of the flaps at a wing C_L of 1.63. This result agrees exactly with Reference 3.27 with regard to both $C_{L_{max}}$ and the location of the initial stall. This agreement is somewhat fortuitous in view of Shrenk's approximation, which is obviously inexact, since it allows a finite loading at the tip and other discontinuities in the cC_l distribution. Nevertheless, for preliminary design studies, or in lieu of more exact lifting surface methods, Shrenk's approximation is a useful tool.

Effect of Fuselage on $C_{L_{max}}$

In working with a wing-fuselage combination, one normally defines the wing planform area to include the portion submerged within the fuselage. When a lift coefficient is quoted for the combination, it is based on this total wing planform area obtained by extrapolating the leading and trailing edges into the fuselage centerline. Generally, the fuselage will effect a decrease in

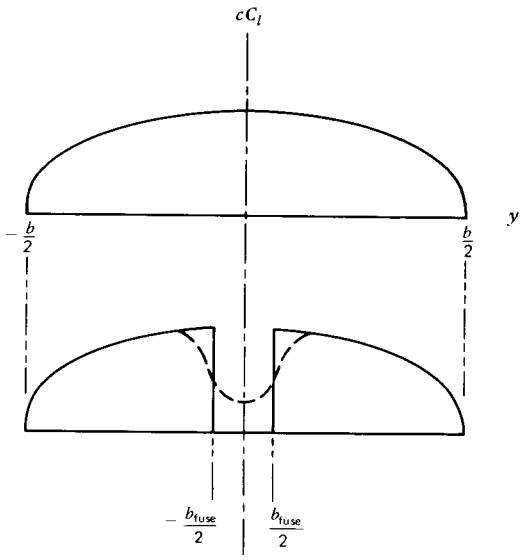

Figure 3.59 Effect of fuselage on spanwise lift distribution.

the lift per unit span over the portion of the wing covered by the fuselage. This is illustrated in Figure 3.59. The upper distribution is without the fuselage. The dashed line on the lower figure is the qualitative drop in cC_l due to the fuselage. As an approximation, let us assume that the fuselage effects a constant drop in cC_l over its width proportional to the midspan value of cC_l. Thus, the lift decrement resulting from the fuselage will be

$$\Delta L = -kqC_{l_0}S_{\text{fuse}}$$

S_{fuse} is the wing planform area submerged in the fuselage, and C_{l_0} is the nearly constant section C_l near the center of the wing. k is the constant of proportionality. Thus the total C_L with the fuselage, $C_{L_{\text{fuse}}}$, can be written in terms of C_L before the fuselage is added as

$$C_{L_{\text{fuse}}} = C_L\left(1 - k\frac{C_{l_0}}{C_L}\frac{S_{\text{fuse}}}{S}\right) \tag{3.81}$$

In Reference 3.27, two wings equipped with partial and full-span, split, single-slotted, and double-slotted flaps were tested with and without a fuselage. The fuselage was circular in cross-section and the wing was mounted slightly above the middle of the fuselage. The ratio S_{fuse}/S was equal to 0.083. The results of these tests are plotted in Figure 3.60 and compared with Equation 3.79 using $kC_{l_0}/C_L = 1.0$. Also plotted on Figure 3.60 are test results from References 3.32 and 3.33. The ratio S_{fuse}/S was nearly the same for these

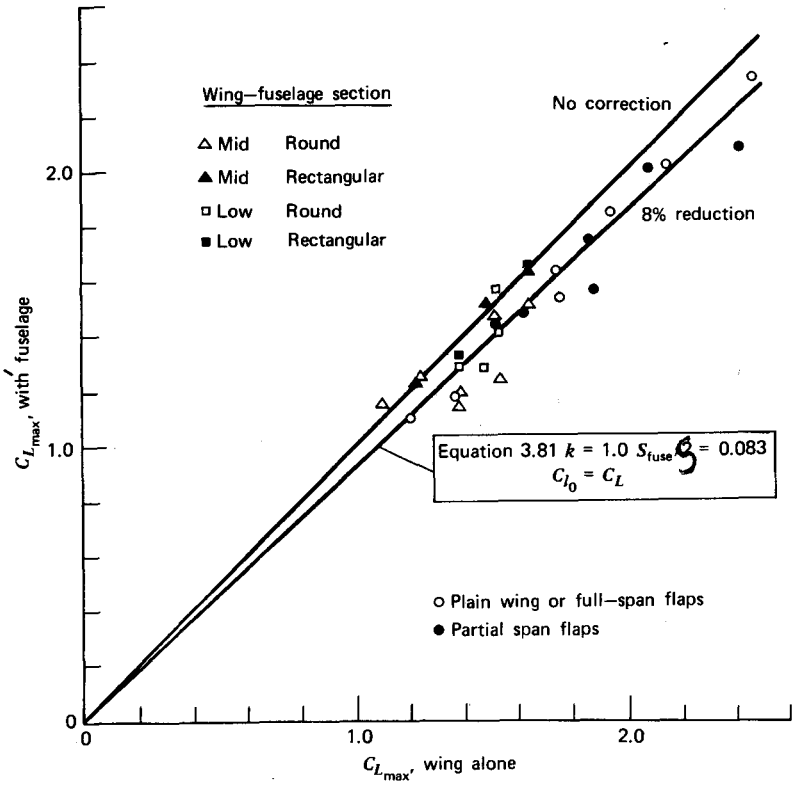

Figure 3.60 Effect of fuselage on $C_{L_{max}}$.

two references as for Reference 3.27. These data support the form of Equation 3.81, at least to the extent that the correction to $C_{L_{max}}$ for the fuselage appears to increase linearly with $C_{L_{max}}$ of the wing alone. The correction depends on the cross-sectional shape of the fuselage and seems to vanish or even be slightly favorable for a rectangularly shaped section. Reference 3.34 also shows the correction to be slight for elliptical shapes where the height is greater than the width.

The decrement in $C_{L_{max}}$ also depends on wing position and appears to be a maximum for the midwing configuration.

Effect of Trim on $C_{L_{max}}$

In order to calculate the stalling speed of an airplane in steady flight, one must consider that, in addition to the weight, the wing's lift must support any download on the horizontal tail required to trim the airplane around its pitching axis. In order to determine this additional trim load, refer to Figure

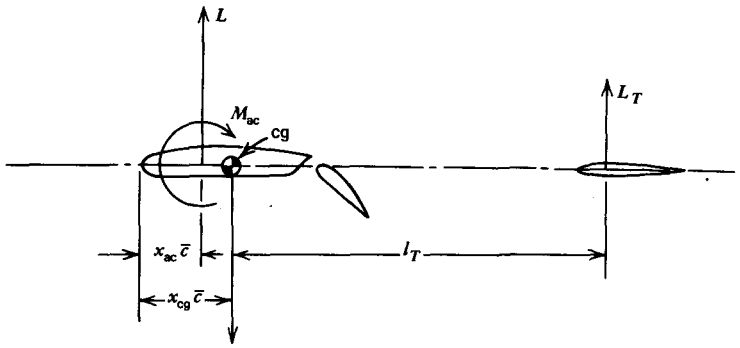

Figure 3.61 Longitudinal trim of an airplane.

3.61. Here, the wing lift L, the tail lift, L_T, the pitching moment about the wing's aerodynamic center, M_{ac}, and the weight are all shown in a positive sense. With the aerodynamic center of the tail located a distance of l_T behind the center of gravity and the wing's aerodynamic center a distance of $(x_{cg}-x_{ac})\bar{c}$ ahead, the tail lift to trim is given by

$$L_T = \frac{M_{ac}}{l_T} + L\frac{\bar{c}}{l_T}(x_{cg}-x_{ac})$$

In addition, static equilibrium in the vertical direction requires that

$$L + L_T = W$$

Therefore, it follows that

$$W = L\left[1+\frac{\bar{c}}{l_T}(x_{cg}-x_{ac})\right] + \frac{M_{ac}}{l_T}$$

In coefficient form this becomes

$$C_L = C_{L_W}\left[1+\frac{\bar{c}}{l_T}(x_{cg}-x_{ac})\right] + C_{M_{ac}}\frac{\bar{c}}{l_T} \tag{3.82}$$

Here, C_L is taken to mean the trim C_L.

$$C_L = \frac{W}{qS}$$

C_{L_W} refers to the untrimmed wing lift coefficient corrected for the fuselage.

It was mentioned earlier that the added drag caused by flaps must sometimes be considered in the trim of an airplane. If ΔC_D denotes this increment in the drag coefficient and if the flaps are located a distance of h above the center of gravity, Equation 3.82 modified to account for the flap

drag becomes

$$C_L = C_{L_W}\left[1 + \frac{\bar{c}}{l_T}(x_{cg} - x_{ac})\right] + C_{M_{ac}}\frac{\bar{c}}{l_T} + \Delta C_D \frac{h}{\bar{c}} \tag{3.83}$$

ΔC_D can be obtained experimentally or estimated on the basis of Equations 3.45 and 3.46.

$C_{M_{ac}}$ is normally negative and greater in magnitude than the moments resulting from C_{L_W} and ΔC_D. Thus C_L is normally less than C_{L_W}. Since Equation 3.83 holds for maximum lift conditions, it follows that the trim $C_{L_{max}}$ is normally less than the wing $C_{L_{max}}$.

In calculating $C_{M_{ac}}$ for use in Equation 3.83, the section aerodynamic moment determined from $C_{M_{ac}}$, including the increment because of the flaps, is integrated over the wing excluding the part submerged in the fuselage.

Estimation of $C_{L_{max}}$ for a Complete Airplane Configuration

A Piper Cherokee PA-28 is pictured in Figure 3.62. Pertinent dimensions, areas, weights, and other data are tabulated on the figure. Extrapolating the

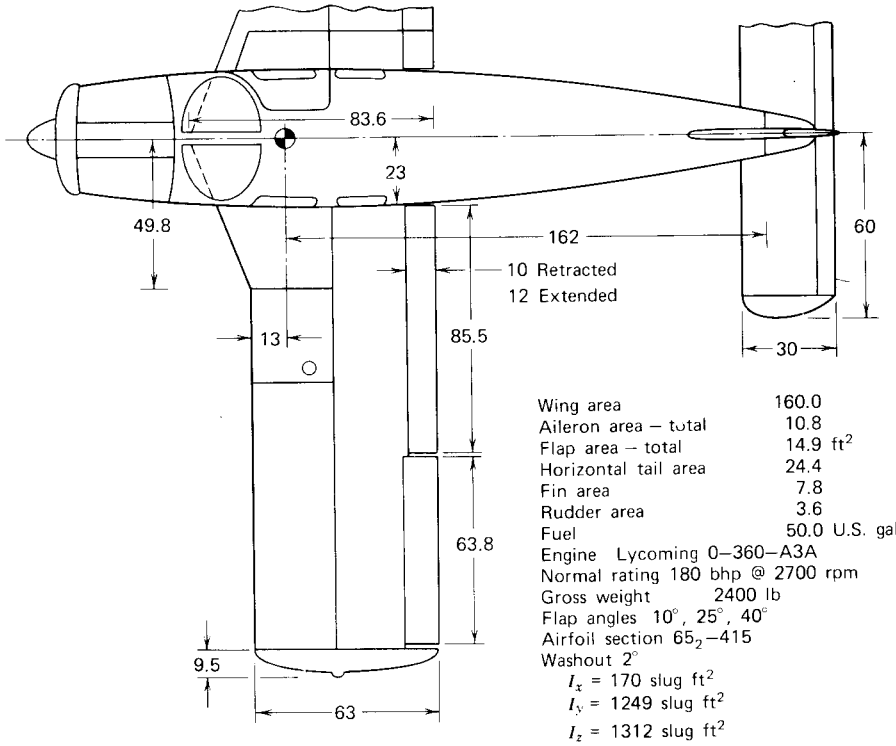

Figure 3.62 Piper Cherokee PA-28-180.

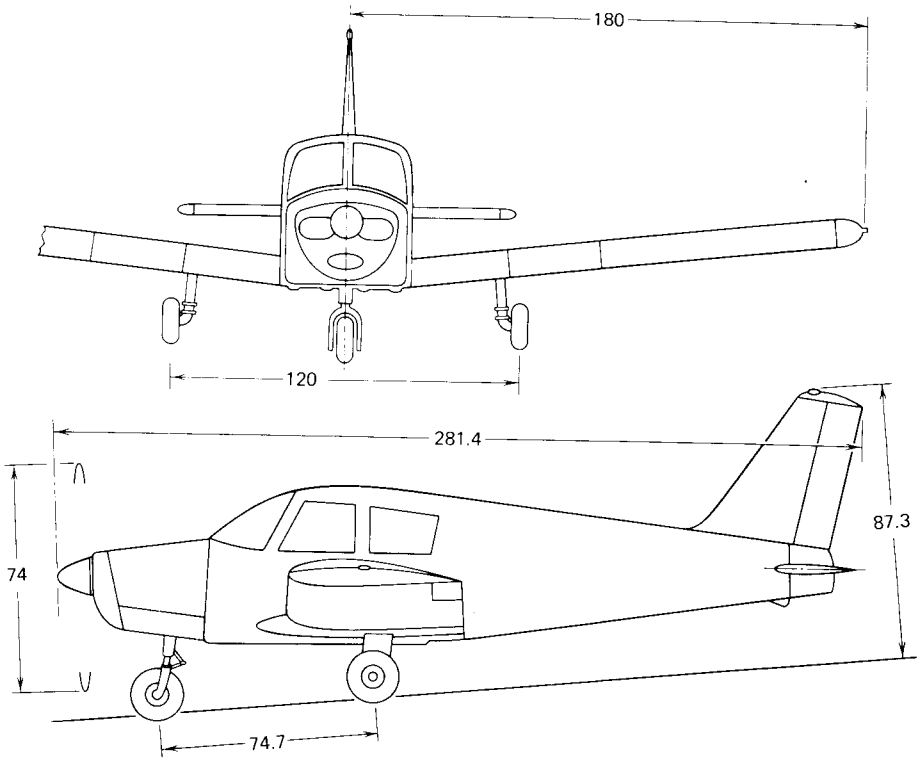

Figure 3.62 (Continued)

swept leading edge near the root into the fuselage centerline and accounting for the elliptically shaped tips gives a total wing area when the flaps are extended of 165.1 ft^2. The area of the wing within the fuselage is 25.3 ft^2. Assuming beforehand, or by iteration, a reasonable value for the "stalling speed" of 60 mph leads to a Reynold's number of approximately 3×10^6 for a wing section. For this Reynold's number, Reference 3.1 shows a value for $C_{l_{max}}$ of 1.45 for the plain 65_2-415 airfoil with a lift curve slope of 0.106 C_l/deg.

Using an 18.5% chord, single-slotted flap deflected 40°, Figures 3.32, 3.33, and 3.34 predict a ΔC_l of 1.37 corresponding to an increase of 12.9° in the angle of attack of the zero lift line. $\Delta C_{l_{max}}$ is estimated at 1.33 giving a $C_{l_{max}}$ of 2.78 for the flapped wing sections. The derivative dC_m/dC_l is estimated from Figure 3.31 to equal -0.20. Since $C_{M_{ac}} \simeq -0.07$ for the plain airfoil (Ref. 3.1), $C_{M_{ac}} \simeq -0.34$ for the flapped airfoil.

Accounting for the 2° of washout and the increment of α_{0l} caused by flaps leads to an α_{w_0} value of 6.0° from Equation 3.76. This is the angle of attack of the zero lift line at midspan for a zero wing C_L. C_{l_a} and C_{l_b} can then be calculated for the wing alone and are given in Table 3.3. The section $C_{l_{max}}$

Table 3.3 Calculated Additional and Basic Lift Coefficients for the PA-28 Wing with Flaps Down 40°

$\frac{2y}{b}$	$C_{l_a}(C_L = 1.0)$	C_{l_b}	$C_{l_{max}}$
0.1	1.04	0.62	2.78
0.2	1.09	0.59	2.78
0.3	1.12	0.57	2.78
0.4	1.09	0.55	2.78
0.5	1.06	0.53	2.78
0.6	1.02	0.51	2.78
0.7	0.98	−0.88	1.45
0.8	0.90	−0.90	1.45
0.9	0.79	−0.92	1.45
1.0	0.50	−0.94	1.45

values are also included in the table. A small amount of trial and error will show that the wing stalls initially at $2y/b$ of around 0.3 at a wing C_L of 1.97. This estimated wing $C_{L_{max}}$ must next be corrected for the effect of the fuselage.

However, since the cross section of the Cherokee's fuselage is essentially rectangular, and with the low-wing configuration, the correction to $C_{L_{max}}$ for the fuselage is taken to be zero.

The aerodynamic moment of the wing is determined by integrating the section pitching moments from the wing-fuselage juncture to the wing tip.

$$M = 2\int_{y\ \text{fuse}}^{b/2} qc^2 C_m\, dy$$

Expressed as a moment coefficient,

$$C_M = \frac{M}{qS\bar{c}}$$
$$= \frac{b\bar{c}}{S}\left[\int_{0.128}^{0.603}\left(\frac{c}{\bar{c}}\right)(-0.34)\,dx + \int_{0.603}^{1}\left(\frac{c}{\bar{c}}\right)(-0.07)\,dx\right]$$

In this case $b\bar{c} = S$ and $\bar{c} = 66$ in., and C_M becomes

$$C_M = -0.198$$

Assuming the increment in drag from the flaps to have a negligible effect on

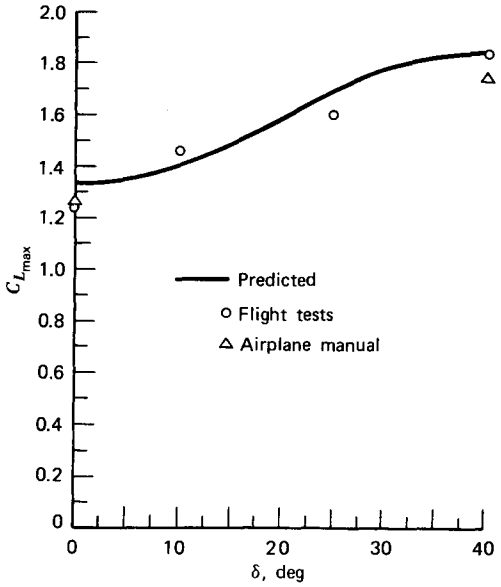

Figure 3.63 Maximum trim lift coefficient of a Piper Cherokee 180 versus flap angle.

the trim, Equation 3.82 becomes

$$C_{L_{max}} = 1.97\left[1 + \frac{5.5}{13.5}(0.214 - 0.25)\right] - 0.198\,\frac{5.5}{13.5}$$
$$= 1.86$$

In a similar manner, trim $C_{L_{max}}$ values were calculated for flap angles of 0, 10, and 25°. The resulting $C_{L_{max}}$ values were found to be 1.33, 1.42, and 1.70, respectively. These results are presented in Figure 3.63 together with experimental values. The points labeled "flight tests" were obtained by aerospace engineering students at The Pennsylvania State University as one of the experiments in a course on techniques of flight testing. The other two points were calculated from the stalling speeds quoted by the manufacturer in the airplane's flight manual.

AIRFOIL CHARACTERISTICS AT LOW REYNOLDS NUMBERS

Occasionally one has the need for airfoil characteristics at Reynolds number values much lower than those used by the NACA and others to obtain the majority of the readily available airfoil data. Most of these data

were obtained at R values of 3×10^6 and higher. For remote-piloted vehicles (RPV), model airplanes, and the like, Reynolds numbers as low as 5×10^4 can be encountered. A search of the literature will show little airfoil data available in this Reynolds number range. The most reliable low-Reynolds number airfoil data appear to be those given in Reference 3.35, where tests of five different airfoil shapes are reported for R values as low as 42,000. These tests were conducted in a low-turbulence tunnel.

The five airfoil shapes that were tested in Reference 3.37 are shown in Figure 3.64. These are seen to comprise a thin, flat plate, a thin, cambered plate, two 12% thick airfoils with 3 and 4% camber, and one 20% thick airfoil with 6% camber. The airfoil shapes are similar in appearance to the NACA four-digit series.

The lift curves for these airfoils are presented in Figure 3.65 for four different Reynolds numbers. As one might expect, the flat-plate results are nearly independent of R since the separation point at the leading edge is well defined. To a slightly lesser degree, the same can be said for the cambered plate. The form of the lift curves for the three airfoils is seen to change substantially, however, over the R range from 4.2×10^5 down to 0.42×10^5. Particularly at the very lowest Reynolds number, the C_l versus α curve is no longer linear. The flow apparently separates at all positive angles just downstream of the minimum pressure point, near the maximum thickness location.

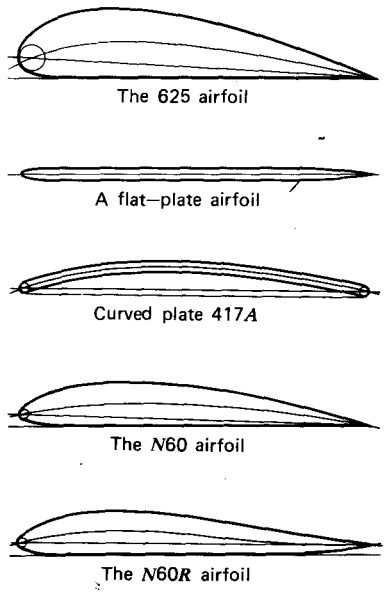

Figure 3.64 Airfoil shapes tested at low Reynolds numbers.

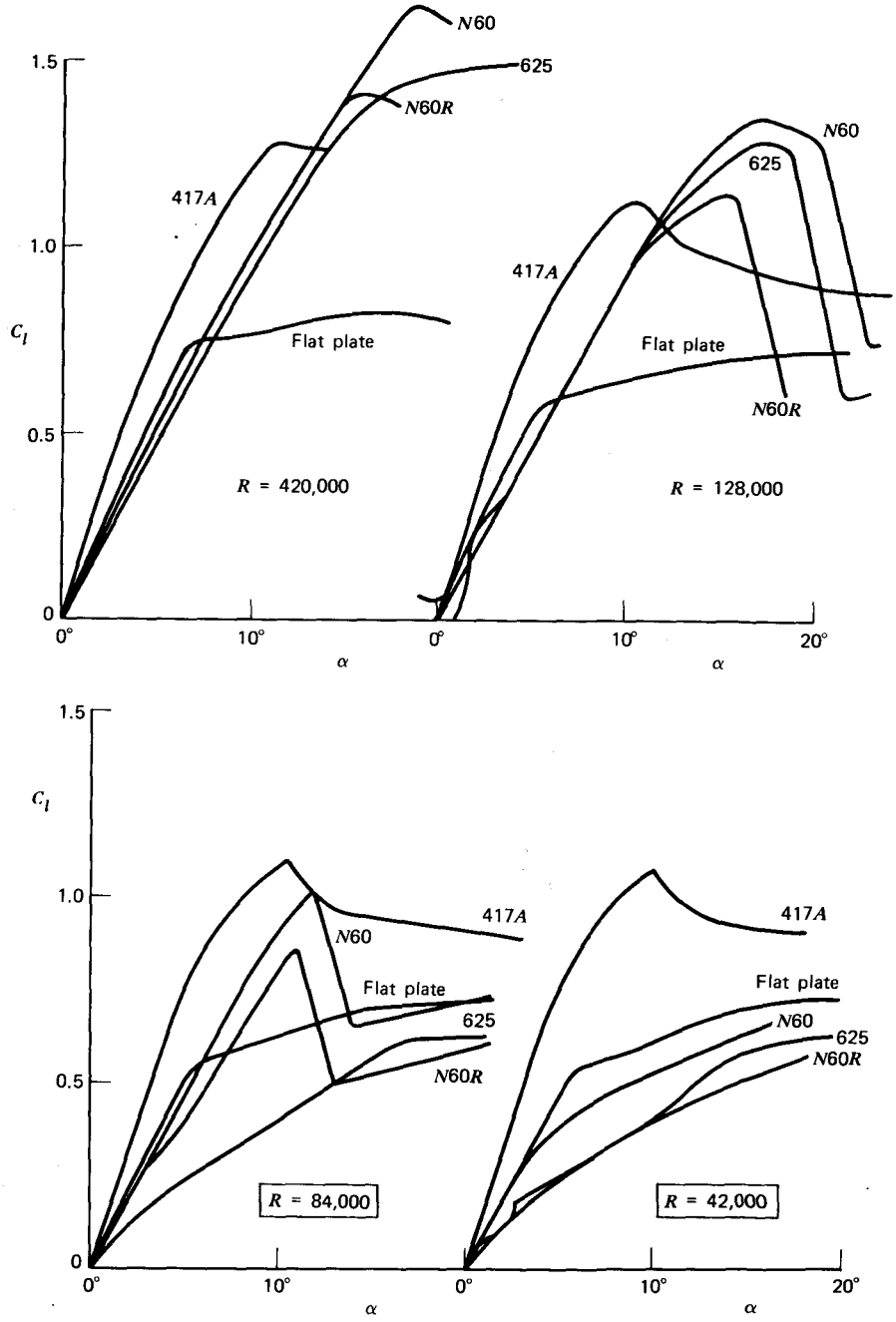

Figure 3.65 Effect of Reynolds number on airfoil lift coefficients.

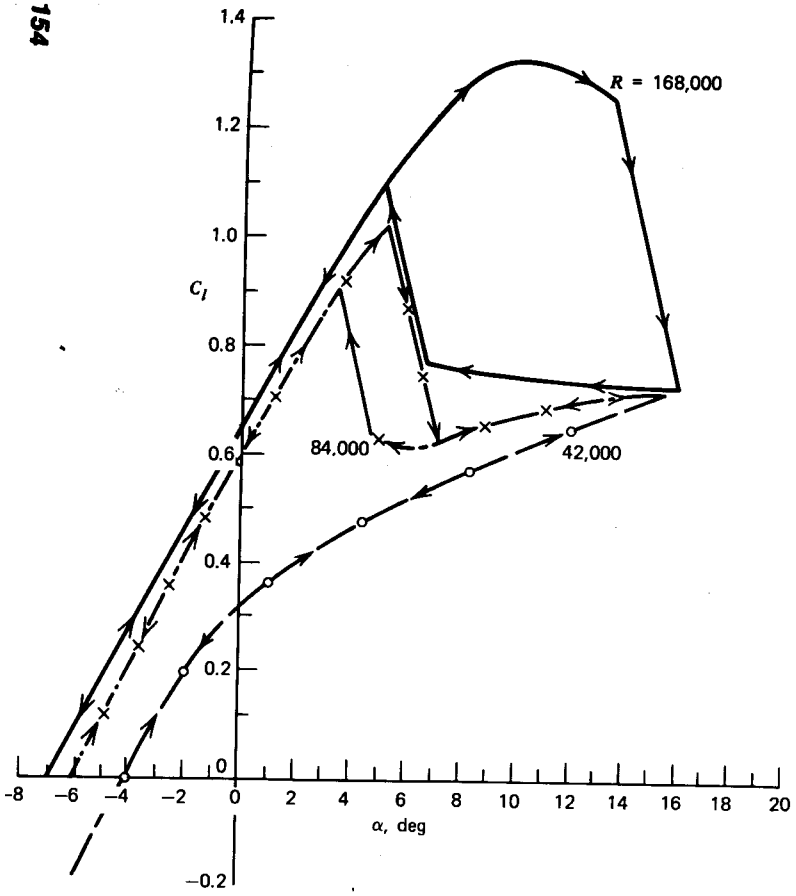

Figure 3.66 Lift curve for the N60 airfoil.

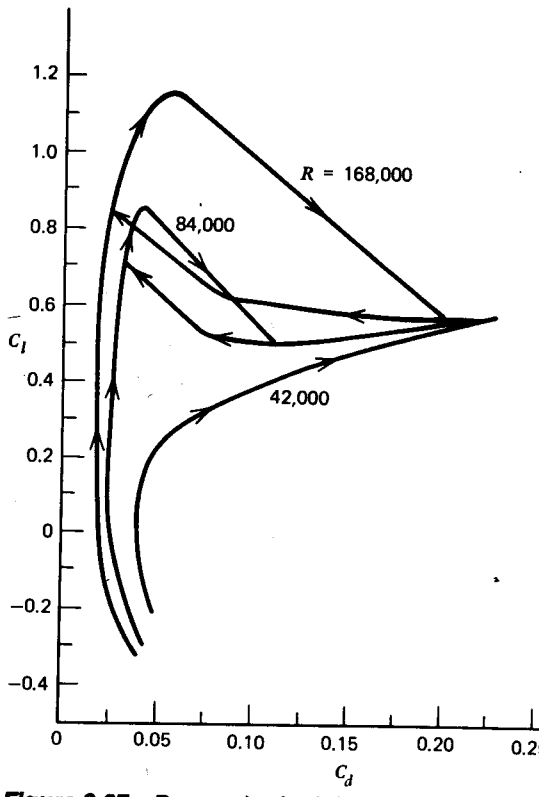

Figure 3.67 Drag polar for N60R airfoil at low R numbers.

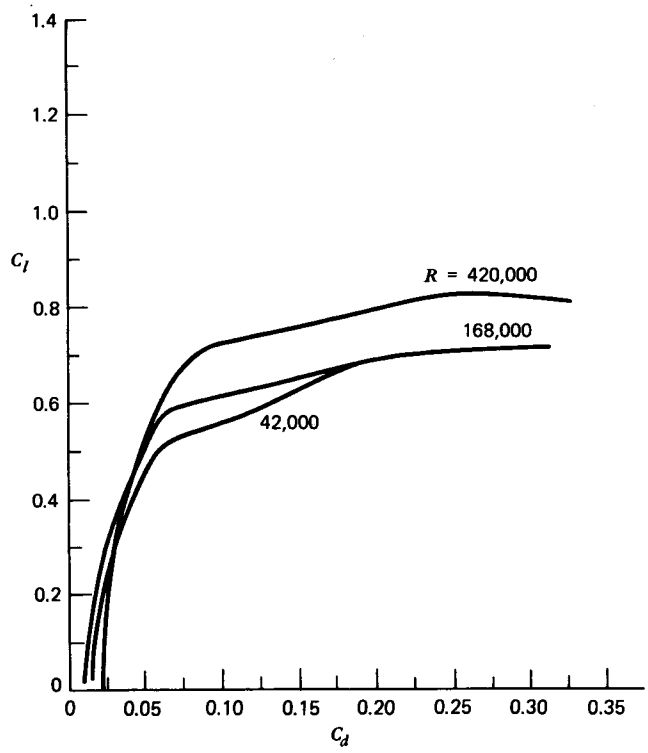

Figure 3.68 Drag polar for the flat-plate airfoil at low Reynolds numbers.

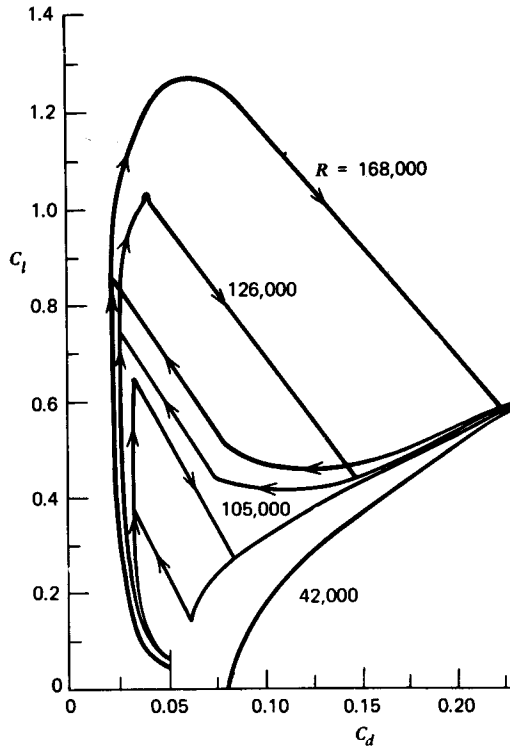

Figure 3.69 Drag polar for the 625 airfo Reynolds numbers.

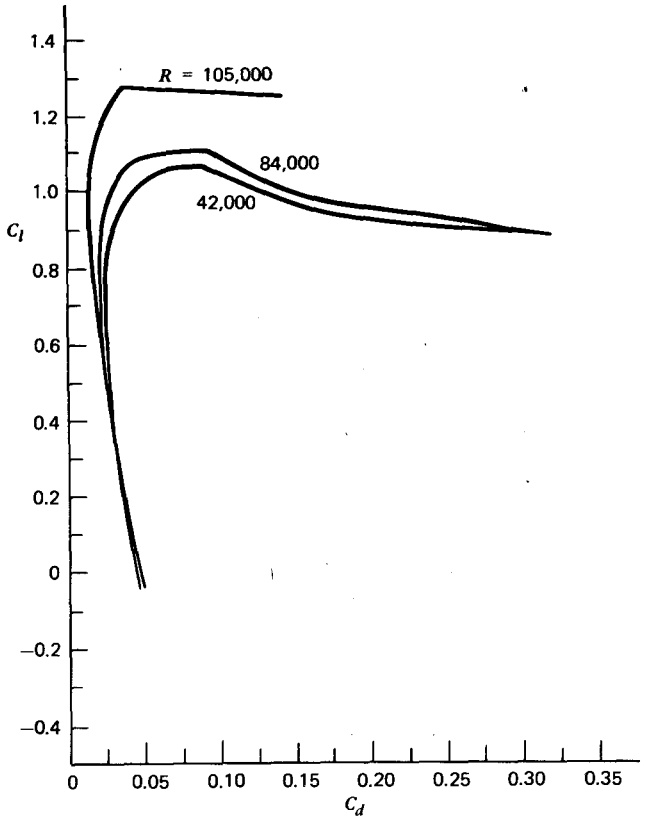

Figure 3.70 Drag polar for the 417a airfoil at low Reynolds numbers.

This explanation is substantiated by Figure 3.66. Here C_l versus α is given for the N60 airfoil. As α is first increased up to a value well beyond the stall and then decreased, a large hysteresis is seen to exist in the curves for the higher Reynolds numbers. Typically, as α is increased, complete separation on the upper surface occurs at around 12°. The angle of attack must then be decreased to around 5° before the flow will again reattach. At the lowest Reynolds number, the lift curve tends to follow the portion of the curves at the higher Reynolds numbers after stall has occurred and α is decreasing. Thus, above an α of approximately 0°, it would appear that the flow is entirely separated from the upper surface for the lower R values of 21,000 and 42,000.

Aerodynamic drag is considered in more detail in the following chapter. Nevertheless, the drag characteristics for these low-Reynolds number tests are presented now in Figures 3.67 to 3.71.

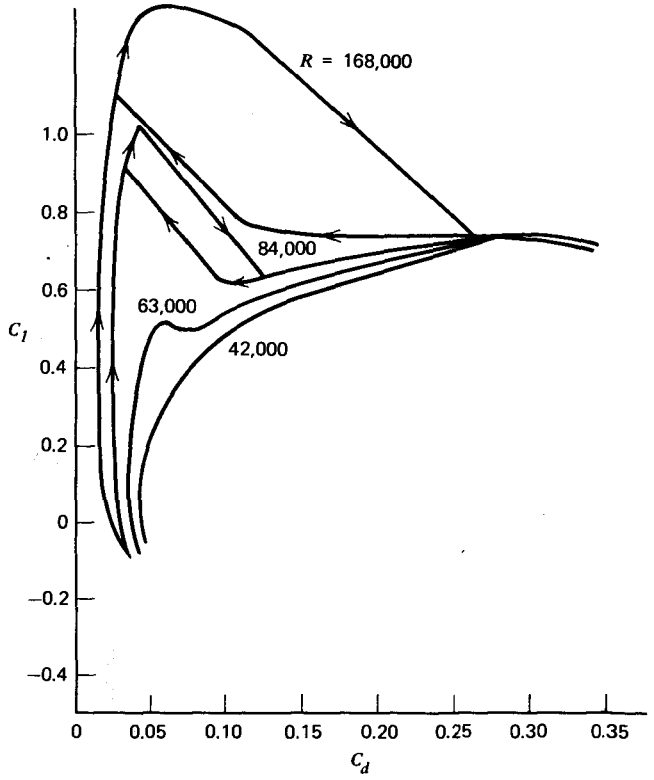

Figure 3.71 Drag polar for the N60 airfoil at low Reynolds numbers.

PROBLEMS

3.1 A wing has a taper ratio of 1/3, an area of 20 m^2, and a tip chord of 1.5 m. What is its aspect ratio?

3.2 A thin, cambered airfoil is approximated by two straight-line segments, as illustrated. Calculate C_l and $C_{m_{ac}}$ for this airfoil according to Equations 3.39 and 3.41.

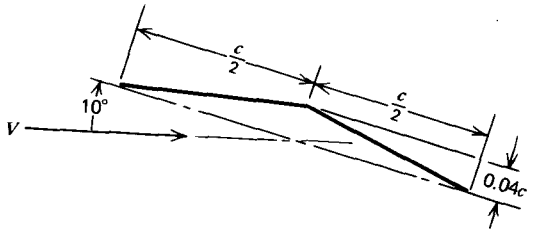

3.3 The airfoil of Problem 3.2 can be thought of as a flat-plate airfoil at an angle of attack with a 50% chord flap deflected through a given angle. What are these two equivalent angles? For this α and zero flap angle, what would C_l be? Comparing this C_l to the value from Problem 3.2, calculate the flap effectiveness factor τ and compare it with Figure 3.32.

3.4 Taking a cue from Problems 3.2 and 3.3, derive the equation for τ given in Figure 3.32.

3.5 A 23015 airfoil is equipped with a 25% fully extensible, double-slotted flap deflected at an optimum angle. It has a 6 ft chord and is operating at 100 mph at SSL conditions. Estimate $C_{l_{max}}$ from: (*a*) the summary observations listed at the beginning of the section on flaps, (*b*) the numerous tables and graphs of data, and (*c*) Figures 3.32, 3.33, and 3.34.

3.6 Estimate C_l for a thin flat-plate airfoil at a 5° angle of attack having a 33% c plain flap deflected 15°. Divide the chord into three equal segments and model the airfoil with three suitably placed point vortices.

3.7 The GA(W)-1 airfoil of Figure 3.10*a* is equipped with a pure jet flap. The jet expands isentropically from a reservoir pressure of 170 kPa absolute and a temperature of 290 °K. The airfoil is operating at SSL conditions at 15 m/s. The chord is 3 m long and the jet thickness equals 2.5 mm. Calculate C_l for an α of 2° and a jet flap angle of 30°.

3.8 A finite wing is simulated by an approximate lifting line model consisting of a bound vortex and two vortices trailing from each side, one from the tip and the other one halfway out along the span. Using the midspan and three-quarter-span stations as control points, calculate the section lift coefficients at these stations for a flat, untwisted rectangular wing with an aspect ratio of 6 at an angle of attack of 10°.

3.9 Use Schrenk's approximation instead of the approximate lifting line model to answer Problem 3.8.

3.10 The wing of Problem 3.1 has a washout of 4° and plain .3c flaps over the inboard 60% of the span. Assuming $R \simeq 9 \times 10^6$ and a smooth airfoil with the characteristics given by Figure 3.6, calculate $C_{L_{max}}$ for a flap angle of 40°. Do this by comparing section C_l and $C_{l_{max}}$ values along the span.

3.11 Write a computer program to solve the lifting line model illustrated in Figure 3.52. This is not as difficult and laborious as it may sound. Place symmetrically disposed trailing vortices of strength γ_i at a distance of $y_i(1,2,3,\ldots,n)$ from the centerline line. Choose control points of 0, $(y_1 + y_2)/2$, $(y_2 + y_3)/2, \ldots, (y_{n-1} + y_n)/2$. At each control point, the bound circulation equals the sum of the vortices shed outboard of the point. Also, it is easy to show that $C_l = 2\Gamma/cV$. But C_l is given by Equation 3.66, where $\alpha_i = w/V$. The downwash w can be expressed as a sum of contributions from each trailing vortex. Hence these relationships lead to a system of n simultaneous equations for the unknown vortex strengths $\gamma_1, \gamma_2, \ldots, \gamma_n$ Once these are found, Γ and C_l can be calculated.

Check your program by calculating the C_l distribution for an elliptic wing. You should find that C_l is nearly constant except near the tips, where the accuracy of the numerical model deteriorates. An n of 20 should suffice for this example.

3.12 A cambered airfoil has an angle of attack for zero lift of $-4°$. If this airfoil is incorporated into an untwisted wing having an elliptical planform, what will the wing lift coefficient be for an angle of attack of 8°? The wing aspect ratio is equal to 5.0.

REFERENCES

3.1 Abbot, Ira H., and Von Doenhoff, Albert E., *Theory of Wing Sections (including a summary of airfoil data)* Dover Publications, New York, 1958.

3.2 Kuethe, A. M., and Schetzer, J. D., *Foundations of Aerodynamics*, John Wiley, New York, 1959.

3.3 McCormick, B. W., *Aerodynamics of V/STOL Flight*, Academic Press, New York, London, 1967.

3.4 Rauscher, Manfred, *Introduction to Aeronautical Dynamics*, John Wiley, New York, 1953.

3.5 Stevens, W. A., Goradia, S. H., and Braden, J. A., *Mathematical Model for Two-Dimensional Multi-Component Airfoils in Viscous Flow*, NASA CR-1843, 1971.

3.6 Whitcomb, R. T., and Clark, L. R., *An Airfoil Shape for Efficient Flight at Supercritical Mach Numbers*, NASA TM X-1109, NASA Langley Research Center, July 1965.

3.7 Ayers, T. G., "Supercritical Aerodynamics Worthwhile over a Range of Speeds," *Astronautics and Aeronautics, 10* (8), August 1972.

3.8 McGhee, R. J., and Beasley, W. D., *Low-Speed Aerodynamic Characteristics of a 17-Percent Thick Airfoil Section Designed for General Aviation Applications,* NASA TN D-7428, December 1973.

3.9 Carlson, F. A., "Transonic Airfoil Analysis and Design Using Cartesian Coordinates," *AIAA J. of Aircraft, 13* (5), May 1976 (also NASA CR-2578, 1976).

3.10 Hurley, F. X., Spaid, F. W., Roos, F. W., Stivers, L. S., and Bandettini, A., "Supercritical Airfoil Flowfield Measurements," *AIAA J. of Aircraft, 12* (9), September 1975.

3.11 Lindsey, W. F., Stevenson, D. B., and Daley B. N., *Aerodynamic Characteristics of 24 NACA 16-Series Airfoils at Mach Numbers between 0.3 and 0.8,* NACA TN 1546, September 1948.

3.12 Anonymous, *Aerodynamic Characteristics of Airfoils-V (Continuation of Reports Nos. 93, 124, 182 and 244),*NACA R286, April 1928.

3.13 Abbott, I. H., von Doenhoff, A. E., and Stivers, Louis S., *Summary of Airfoil Data*, NACAR 824, 1945.

3.14 Anonymous, "Airfoil Information for Propeller Design," Ordnance Research Laboratory, The Pennsylvania State University, Report No. NOrd 7958–71, November 1947.

3.15 Cahill, J. F., *Summary of Section Data on Trailing-Edge High-Lift Devices*, NACAR 938, 1949.

3.16 Smith, A. M. O., "High-Lift Aerodynamics," *J. of Aircraft, 12,* (6), June 1975.

3.17 Kelly, J. A., and Hayter, N. F., *Lift and Pitching Moment at Low Speeds of the NACA 64A010 Airfoil Section Equipped with Various Combinations of a Leading-Edge Slat, Leading-Edge Flap, Split Flap, and Double-Slotted Flap*, NACA TN 3007, September 1953.

3.18 Fullmer, F. F., *Two-Dimensional Wind Tunnel Investigation of the NACA 64_1-012 Airfoil Equipped with Two Types of Leading-Edge Flap*, NACA TN 1277, May 1947.

3.19 Harris, T. A, and Recant, I. G., *Wind Tunnel Investigation of NACA 23012, 23021, and 23030 Airfoils Equipped with 40-Percent Chord Double Slotted Flaps*, NACAR 723, 1941.

3.20 Wenzinger, C. J., and Rogallo, F. M., *Résumé of Air-Load Data on Slats and Flaps*, NACA TN 690, March 1939.

3.21 Young, A. D., "The Aerodynamic Characteristics of Flaps," ARC R&M 2622, 1953.

3.22 Liebeck, R. H., "A Class of Airfoils Designed for High Lift in Incompressible Flow," *J. of Aircraft, 10* (10), October 1973.

3.23 Stratford, B. S., "The Prediction of the Separation of the Turbulent Boundary Layer," *J. of Fluid Mechanics, 5,* 1959.

3.24 Stratford, B. S., "An Experimental Flow with Zero Skin Friction Throughout its Region of Pressure Rise," *J. of Fluid Mechanics, 5,* 1959.

3.25 Liebeck, R. H., and Ormsbee, A. I., "Optimization of Airfoils for Maximum Lift," *J. of Aircraft, 7* (5), September–October 1970.

3.26 Cleveland, F. A., "Size Effects in Conventional Aircraft Design," *J. of Aircraft, 7* (6), November–December 1970.

3.27 Sivells, J. C., and Spooner, S. H., *Investigation in the Langley 19-Foot Pressure Tunnel of Two Wings of NACA 65-210 and 64-210 Airfoil Sections with Various Type Flaps*, NACA 941, 1949.

3.28 Prandtl, L., and Betz, A., "Vier Abhandlungen Zur Hydrodynamik und Aerodynamic," Göttingen, 1927 (reprint Edward Bros., 1943, Ann Arbor, Mich.).

3.29 Ashley, H., and Landahl, M., *Aerodynamics of Wings and Bodies*, Addison–Wesley, Reading, Mass., 1965.

3.30 Faulkner, V. M., "The Calculation of Aerodynamic Loading on Surfaces of Any Shape," ARC R&M 1910, 1943.

3.31 Schrenk, O., *A Simple Approximation Method for Obtaining the Spanwise Lift Distribution*, NACA TM 1910, 1940.

3.32 Jacobs, Eastman N., and Ward, Kenneth E., *Interference of Wing and Fuselage from Tests of 209 Combinations in the NACA Variable-Density Tunnel*, NACAR 540, 1936.

3.33 Sherman, Albert, *Interference of Wing and Fuselage from Tests of 28 Combinations in the NACA Variable-Density Tunnel*, NACA R 575, 1936.

3.34 Sherman, Albert, *Interference of Wing and Fuselage from Tests of 30 Combinations with Triangular and Elliptical Fuselages in the NACA Variable-Density Tunnel*, NACA TN 1272, 1947.

3.35 Lowry, J. G., and Polhamas, E. C., *A Method for Predicting Lift Increments Due to Flap Deflection at Low Angles of Attack in Incompressible Flow*, NACA TN 3911, January 1957.

3.36 Advanced Technology Airfoil Research Conference, NASA Langley Research Center, March 7–9, 1978.

3.37 Schmitz, F. W., *Aerodynamics of Model Aircraft Wing Measurements I*, R. T. P. Translation No. 2460, Issued by Ministry of Aircraft Production.

3.38 Attinello, J. S., An Interim Attack Airplane from a Navy Fighter, BuAir Report DR 1417, July 1952.

FOUR
DRAG

As a child, it was fun to stick your hand out of the car window and feel the force of the moving, invisible air. To the aeronautical engineer, however, there is nothing very funny about aerodynamic drag. A continuing struggle for the practicing aerodynamicist is that of minimizing drag, whether it is for an airplane, missile, or ground-based vehicle such as an automobile or train. It takes power to move a vehicle through the air. This power is required to overcome the aerodynamic force on the vehicle opposite to its velocity vector. Any reduction of this force, known as the drag, represents either a direct saving in fuel or an increase in performance.

The estimation of the drag of a complete airplane is a difficult and challenging task, even for the simplest configurations. A list of the definitions of various types of drag partly reveals why this is so.

Induced Drag The drag that results from the generation of a trailing vortex system downstream of a lifting surface of finite aspect ratio.

Parasite Drag The total drag of an airplane minus the induced drag. Thus, it is the drag not directly associated with the production of lift. The parasite drag is composed of many drag components, the definitions of which follow.

Skin Friction Drag The drag on a body resulting from viscous shearing stresses over its wetted surface (see Equation 2.15).

Form Drag (Sometimes Called Pressure Drag) The drag on a body resulting from the integrated effect of the static pressure acting normal to its surface resolved in the drag direction.

Interference Drag The increment in drag resulting from bringing two bodies in proximity to each other. For example, the total drag of a wing-fuselage combination will usually be greater than the sum of the wing drag and fuselage drag independent of each other.

Trim Drag The increment in drag resulting from the aerodynamic forces required to trim the airplane about its center of gravity. Usually this takes the form of added induced and form drag on the horizontal tail.

Profile Drag Usually taken to mean the total of the skin friction drag and form drag for a two-dimensional airfoil section.

Cooling Drag The drag resulting from the momentum lost by the air that passes through the power plant installation for purposes of cooling the engine, oil, and accessories.

Base Drag The specific contribution to the pressure drag attributed to the blunt after-end of a body.

Wave Drag Limited to supersonic flow, this drag is a pressure drag resulting from noncanceling static pressure components to either side of a shock wave acting on the surface of the body from which the wave is emanating.

With the exception of wave drag, the material to follow will consider these various types of drag in detail and will present methods of reasonably estimating their magnitudes. Wave drag will be discussed in Chapter 6.

SKIN FRICTION DRAG

Figure 4.1 depicts a thin, flat plate aligned with the free-stream velocity. Frequently the drag of a very streamlined shape such as this is expressed in terms of a skin friction drag coefficient, C_f, defined by,

$$C_f = \frac{D}{qS_w} \tag{4.1}$$

where S_w is the wetted surface area that is exposed to the flow. This coefficient is presented in Figure 4.1 as a function of Reynolds number for the two cases where the flow in the boundary layer is entirely laminar or entirely turbulent over the plate. Here the Reynolds number is based on the total length of the plate in the direction of the velocity. In a usual application, the boundary layer is normally laminar near the leading edge of the plate undergoing transition to a turbulent layer at some distance back along the surface, as described in Chapter Two. The situation is pictured in Figure 4.1, where the velocity profile through the layer is shown. In order to illustrate it, the thickness of the layer is shown much greater than it actually is.

As shown in this figure, a laminar boundary layer begins to develop at the leading edge and grows in thickness downstream. At some distance from the leading edge, the laminar boundary becomes unstable and is unable to suppress disturbances imposed on it by surface roughness or fluctuations in the free stream. In a short distance the boundary layer undergoes transition to a turbulent boundary layer. Here the layer suddenly increases in thickness and is characterized by a mean velocity profile on which a random fluctuating velocity component is superimposed. The distance, x, from the leading edge

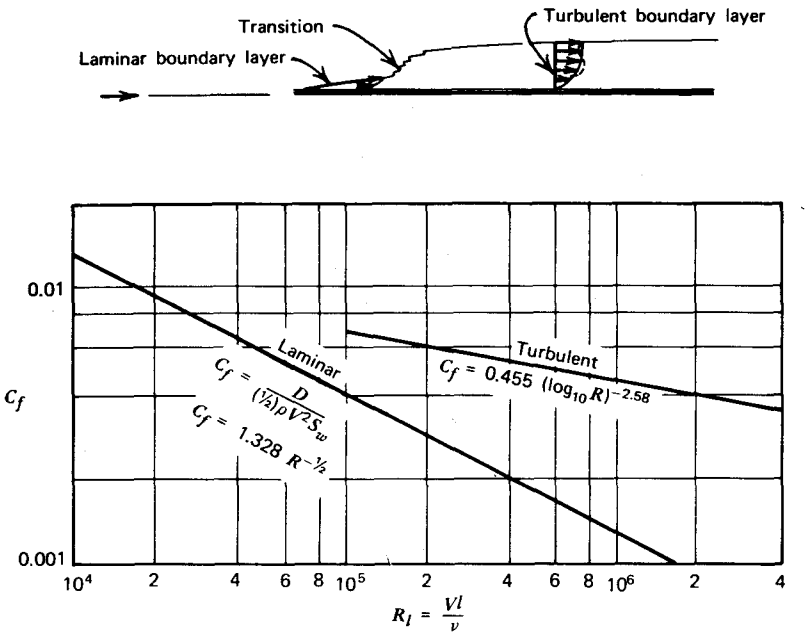

Figure 4.1 Drag of a thin flat plate.

of the plate to the transition point can be calculated from the transition Reynolds number, R_x. R_x is typically, for a flat plate, of the order of 3×10^5, R_x being defined by

$$R_x = \frac{\rho V x}{\mu} \tag{4.2}$$

For very smooth plates in a flow having a low level of ambient turbulence, R_x can exceed 1×10^6.

Since the velocity profile through the boundary layer approaches the velocity outside the layer asymptotically, the thickness of the layer is vague. To be more definitive, a displacement thickness, δ^*, is frequently used to measure the thickness of the layer. δ^* is illustrated in Figure 4.2 and is defined mathematically by

$$\delta^* = \int_0^\infty \left(1 - \frac{u}{V}\right) dy \tag{4.3}$$

where y is the normal distance from the plate at any location such that, without any boundary layer, the total flow past that location would equal the flow for the original plate with a boundary layer. To clarify this further, let δ be the boundary layer thickness where, for all intents and purposes, $u = V$.

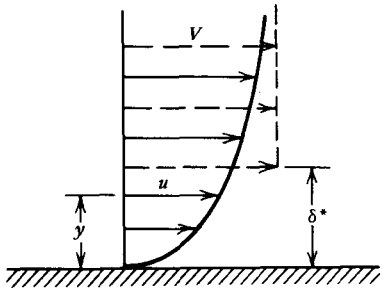

Figure 4.2 Displacement thickness.

Then

$$V(\delta - \delta^*) = \int_0^\infty u\,dy \tag{4.4}$$

Allowing δ to become infinite leads to Equation 4.3.

If we arbitrarily define δ as the value of y at which $u = 0.99V$ then, for a laminar layer,

$$\delta \simeq 5.2\left(\frac{\nu x}{V}\right)^{1/2} = 5.2x\left(\frac{Vx}{\nu}\right)^{-1/2} \tag{4.5}$$

$$\delta^* = \frac{\delta}{3} \tag{4.6}$$

For a turbulent layer,

$$\delta \simeq 0.37x\left(\frac{Vx}{\nu}\right)^{-1/5} \tag{4.7}$$

$$\delta^* = \frac{\delta}{8} \tag{4.8}$$

Observe that relatively speaking, the turbulent boundary layer is more uniform, with δ^* being only one-eighth of δ as compared to one-third for the laminar layer.

In order to clarify the use of Figure 4.1 and Equations 4.5 to 4.8, let us consider the horizontal tail of the Cherokee pictured in Figure 3.62 at a velocity of 60.4 m/s (135 mph) at a 1524 m (5000 ft) standard altitude. We will assume that the tail can be approximately treated as a flat plate at zero angle of attack.

From Figure 3.62, the length of the plate is 30 in or 0.762 m. The total wetted area, taking both sides and neglecting the fuselage, is 4.65 m^2 (50 ft^2). From Figure 2.3, at an altitude of 1.52 km, $\rho = 1.054$ kg/m^3 and $\nu = 1.639 \times 10^{-5}$ m^2/s. We will assume that the transition Reynolds number is equal to 3×10^5.

The distance from the leading edge to the transition point is found from Equation 4.2.

$$x = \frac{\nu R_x}{V}$$

$$= 1.639 \times 10^{-5} \times 3 \times \frac{10^5}{60.4}$$

$$= 0.0814 \text{ m } (3.2 \text{ in.})$$

The Reynolds number based on the total length will be equal to

$$R_l = \frac{Vl}{\nu}$$

$$= \frac{60.4\ (0.762)}{1.639 \times 10^{-5}}$$

$$= 2.81 \times 10^6$$

If the flow over the tail were entirely turbulent then, from Figure 4.1,

$$C_f = 0.455\ (\log_{10} R_l)^{-2.58} \tag{4.9}$$

$$= 0.00371$$

The dynamic pressure q for this case is

$$q = \rho V^2/2$$

$$= \frac{1.054\ (60.4)^2}{2}$$

$$= 1923 \text{ N/m}^2$$

Hence the total skin friction drag would be

$$D = qS_w C_f$$

$$= 1923\ (4.65)(0.00371)$$

$$= 33.17 \text{ N}$$

However, the leading portion of the plate is laminar. The wetted area of this portion is equal to 0.497 m^2. For laminar flow over this portion,

$$C_f = 1.328 R^{-1/2} \tag{4.10}$$

$$= 1.328\ (3 \times 10^5)^{-1/2}$$

$$= 0.00242$$

Hence the drag of this portion of the plate is equal to

$$D = qC_f S_w$$

$$= 1923(0.00242)(0.497)$$

$$= 2.31 \text{ N}$$

If the flow were turbulent over the leading portion of the plate, its C_f would be

$$\begin{aligned} C_f &= 0.455\ (\log_{10} R)^{-2.58} \\ &= 0.455\ (\log_{10} 3 \times 10^5)^{-2.58} \\ &= 0.00566 \end{aligned}$$

Thus its drag for a turbulent boundary layer would be

$$\begin{aligned} D &= qC_f S_w \\ &= (1923)(0.00566)(0.497) \\ &= 5.35\ \text{N} \end{aligned}$$

The above is $5.35 - 2.31$, or 3.04 N higher than the actual drag for laminar flow. Hence this difference must be subtracted from the total drag of 33.17 N previously calculated assuming the boundary layer to be turbulent over the entire plate. Hence the final drag of the total horizontal tail is estimated to be

$$\begin{aligned} D &= 33.17 - 3.04 \\ &= 30.13\ \text{N} \\ &= 6.77\ \text{lb.} \end{aligned}$$

The thickness, δ, of the laminar boundary layer at the beginning of transition can be calculated from Equation 4.5.

$$\begin{aligned} \delta &= 5.2\ (0.0814)(3 \times 10^5)^{-1/2} \\ &= 7.728 \times 10^{-4}\ \text{m} \\ &= 0.0304\ \text{in.} \end{aligned}$$

The thickness of the turbulent layer right after transition is found from Equation 4.7 assuming the layer to have started at the leading edge.

$$\begin{aligned} \delta &= 0.37(0.0814)(3 \times 10^5)^{-1/5} \\ &= 2.418 \times 10^{-3}\ \text{m} \\ &= 0.0952\ \text{in.} \end{aligned}$$

At the trailing edge, the thickness of the turbulent layer will be

$$\begin{aligned} \delta &= 0.37(0.762)(2.81 \times 10^6)^{-1/5} \\ &= 0.0145\ \text{m} \\ &= 0.5696\ \text{in.} \end{aligned}$$

The displacement thickness at the trailing edge is thus only 0.0018 m (0.071 in.).

Before leaving the topic of skin friction drag, the importance of surface roughness should be discussed. Surface roughness can have either a beneficial or adverse effect on drag. If it causes premature transition, it can result in a

reduced form drag by delaying separation. This is explained more fully in the next section. Adversely, surface roughness increases the skin friction coefficient. First, by causing premature transition, the resulting turbulent C_f is higher than C_f for laminar flow, in accordance with Figure 4.1. Second, for a given type of flow laminar or turbulent, C_f increases as the surface is roughened.

It is difficult to quantify the increment in C_f as a function of roughness, since roughness comes in many forms. For some information on this, refer to the outstanding collection of drag data noted previously (e.g., Ref. 4.4). Generally, if a roughness lies well within the boundary layer thickness, say of the order of the displacement thickness, then its effect on C_f will be minimal. Thus, for the preceding example of the horizontal tail for the Cherokee, the use of flush riveting near the trailing edge is probably not justified.

An approximate estimate of the effect of roughness, at least on streamlined bodies, can be obtained by examining the airfoil data of Reference 3.1. Results are presented for airfoils having both smooth and rough surfaces. The NACA "standard" roughness for 0.61-m (2-ft) chords consisted of 0.028-cm (0.011-in.) carborundum grains applied to the model surface starting at the leading edge and extending 8% of the chord back on both the upper and lower surfaces. The grains were spread thinly to cover 5 to 10% of the area.

An examination of the drag data with and without the standard roughness discloses a 50 to 60% increase in airfoil drag resulting from the roughness. It is difficult to say how applicable these results are to production aircraft. Probably the NACA standard roughness is too severe for high-speed aircraft employing extensive flush riveting with particular attention to the surface finish. In the case of a production light aircraft for general aviation usage, the standard roughness could be quite appropriate.

FORM DRAG

In addition to skin friction drag, a body generally experiences some form drag. Unlike the skin friction drag that results from viscous shearing forces tangential to a body's surface, form drag results from the distribution of pressure normal to the body's surface. The extreme case of a flat plate normal to the flow is pictured in Figure 4.3. Here the drag is totally the result of an unbalance in the normal pressure distribution. There is no skin friction drag present in this case.

Generally, form drag is difficult to predict. For that matter, so is skin friction drag except for the simplest cases. Thus, in general cases, such as that pictured in Figure 4.4, where the total drag results from both normal and tangential stresses (or pressures) one must usually resort to experimental data to estimate the drag.

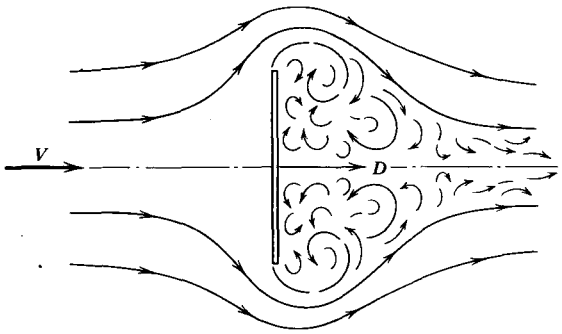

Figure 4.3 Flat plate normal to flow.

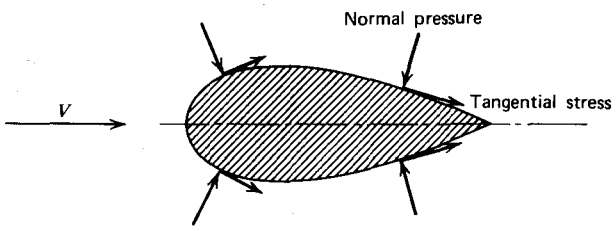

Figure 4.4 Body having both skin friction and form drag.

As with skin friction drag, form drag is generally dependent on Reynolds number. To see why, consider the flow around the circular cylinder pictured in Figure 4.5. In Figure 4.5*a* flow is pictured at a low Reynolds number. Here, beginning at the stagnation point, a laminar boundary layer develops. On the surface of the cylinder, the static pressure (normal) is highest at the stagnation point and decreases to a minimum at the top and bottom. Moving around toward the rear, beyond these points, the static pressure increases, tending toward the stagnation pressure at the very rear. In the absence of viscosity the normal pressure distribution would be symmetrical (Equation 2.78) and there would be no drag. This is a clear example of D'Alembert's paradox, which states that a body in a inviscid fluid will experience no drag. As the slower moving fluid in the laminar boundary layer moves beyond the minimum pressure point on the cylinder, its momentum is insufficient to move against the positive pressure gradient, referred to as an adverse gradient, and thus the flow separates just past the top and bottom locations on the cylinder. In the separated region over most of the rear portion of the cylinder the static pressure is constant and equal to the low pressure at the top and bottom. Thus the high pressure acting over the front and the low pressure over the rear result in a high form drag.

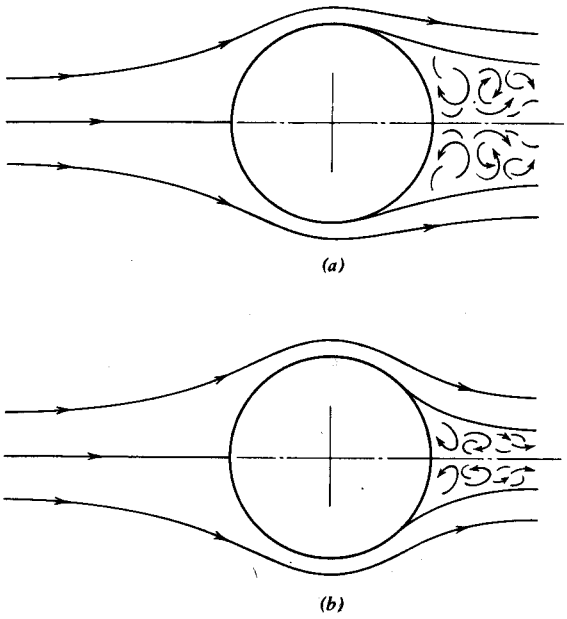

Figure 4.5 Flow over a circular cylinder. (*a*) Low Reynolds number. Separation occurs before transition. Large wake. (*b*) High Reynolds number. Transition occurs before separation. Small wake.

The high-Reynolds number case is shown in Figure 4.5*b*. Here the laminar boundary layer undergoes transition to a turbulent boundary layer before separating. The subsequent turbulent mixing increases the momentum and energy of the boundary layer so that it remains attached toward the rear of the cylinder, well beyond the separation point of the laminar layer. Thus, in this case, the separation region is much smaller and the static pressure is higher on the rear of the cylinder than for the laminar case. Therefore, because of reduced form drag, the drag coefficient of a cylinder is lower at higher Reynolds numbers.

C_d as a function of Reynolds number is presented in Figure 4.6 for both spheres and two-dimensional circular cylinders. Here, C_d is based on the projected frontal area. Note the rapid drop in C_d above an R value of approximately 2×10^5. This is the so-called critical Reynolds number, where the transition point is nearly coincident with the separation point. "Subcritical" refers to flow at Reynolds numbers that are less than critical; "supercritical" denotes R values that are higher than critical. A body shape having a well-defined separation point will not exhibit a critical Reynolds number; neither will streamlined shapes.

Although not concerned with drag per se, Figure 4.6*a* also includes the

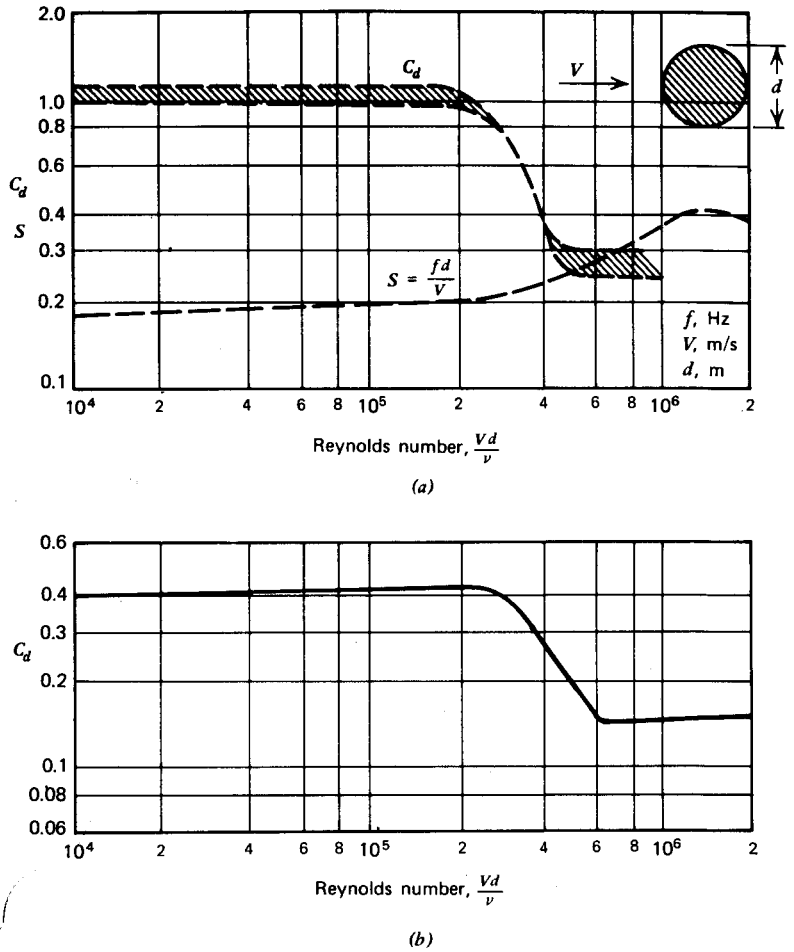

Figure 4.6 Drag coefficients of cylinders and spheres versus Reynolds number. (*a*) Two-dimensional circular cylinders. (*b*) Spheres.

quantity fD/V, known as the Strouhal number, S. S characterizes an interesting behavior of bluff bodies with rounded trailing edges. As such a body first begins to move through a fluid, the vorticity in the boundary layer is shed symmetrically from the upper and lower surfaces to form two vortices of opposite rotation. However, the symmetrical placement of the vortex pair is unstable, so that succeeding vortices are then shed alternately from the upper and lower surfaces. The resulting flow pattern of periodically spaced vortices downstream of the body is known as a Karman vortex street.

In the definition of Strouhal number, f is the frequency at which the

vortices are shed. As a vortex is shed from one surface of the cylinder, it produces a momentary circulation around the cylinder opposite in direction to the vortex. From the Kutta-Joukowski law, a force on the cylinder normal to V results. As the next vortex is shed, the force reverses its direction, resulting in an alternating force on the cylinder. This particular phenomenon is the cause for the "singing" of telephone wires in the wind.

As an example of the use of Figure 4.6*a*, consider a wire 2 cm in diameter in a wind blowing at a speed of 8 m/s. Assuming standard sea level conditions,

$$R = \frac{Vd}{\nu}$$
$$= \frac{8(0.02)}{1.456 \times 10^{-5}}$$
$$= 1.099 \times 10^4$$

From Figure 4.6*a*, for this Reynolds number,

$$C_d = 1.1$$
$$S \simeq 0.18$$

Thus the drag per unit length on the wire will be

$$D = qC_d d$$
$$= \frac{1}{2}(1.226)(8)^2(1.1)(0.02)$$
$$= 0.863 \text{ N/m}$$

The frequency of the alternating lift force on the wire will be,

$$f = \frac{VS}{d}$$
$$= \frac{8(0.18)}{0.02}$$
$$= 72 \text{ Hz}$$

Let us now consider the extreme case of form drag illustrated in Figure 4.3, where the point of flow separation is well defined and not dependent on Reynolds number. It is not too surprising to find that drag coefficients for such shapes are nearly constant over a wide range of Reynolds number values. A number of such shapes are pictured in Figure 4.7*a*.

This figure presents values for both two-dimensional and three-dimensional shapes. Three-dimensional shapes are all bodies of revolution. Observe that for the same profile shape,

$$\frac{C_d(\text{2-D})}{C_d(\text{3-}D)} \simeq 1.8$$

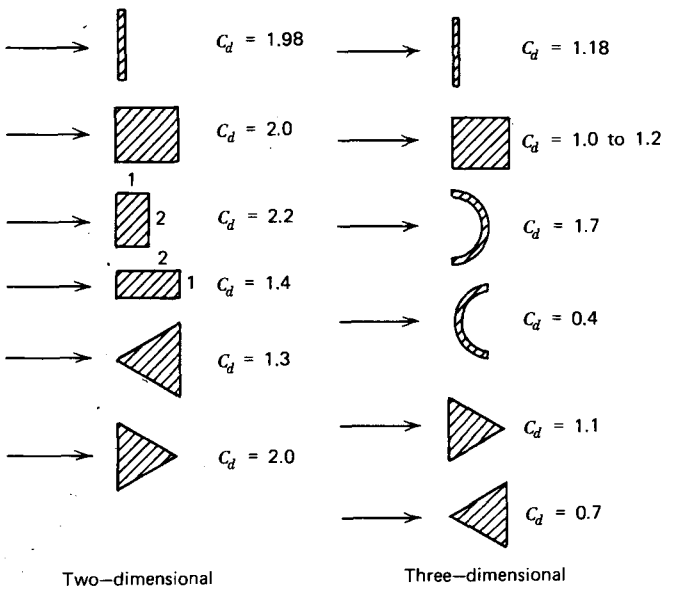

Figure 4.7a Examples of shapes having C_d values nearly independent of Reynolds number.

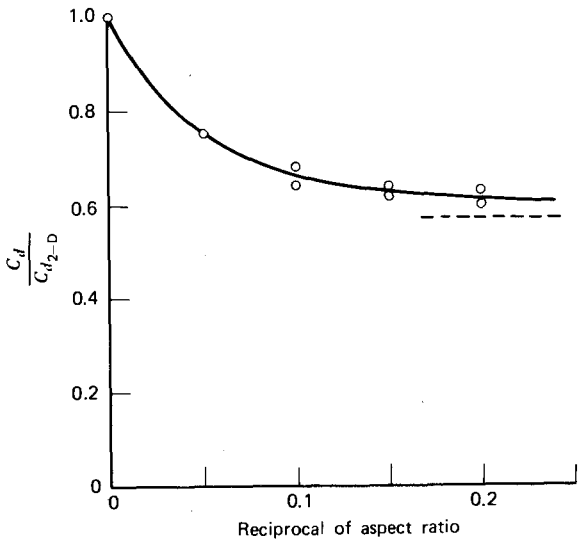

Figure 4.7b Transition from three-dimensional to two-dimensional drag for cylinders at supercritical Reynolds numbers.

If the ratio of the span to the height (or diameter) of a flat plate (or cylinder) normal to the flow is approximately 5 or less, C_d is nearly constant and equal to the 3-D value. For aspect ratios greater than 5, C_d varies approximately in the manner given by the normalized curve of Figure 4.7*b*. This curve is based on data from several sources, including Reference 4.4.

A qualitative evaluation of the drag coefficient for a given shape can be made using some "educated intuition." Referring to Figure 4.8, the drag

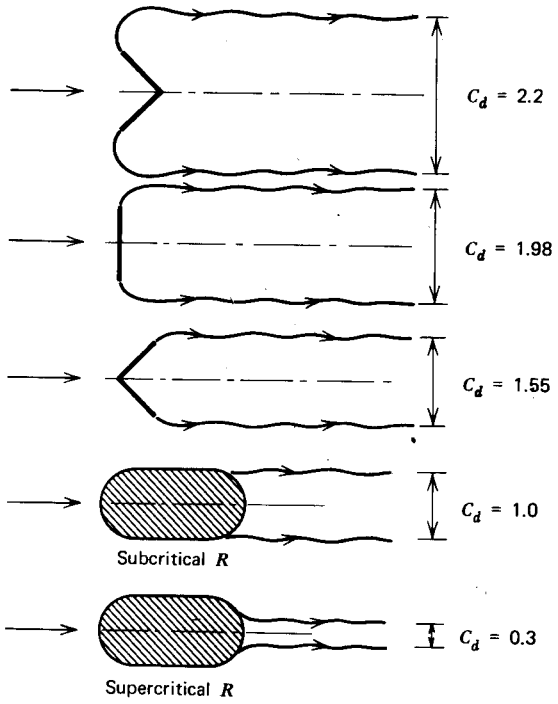

Figure 4.8 Qualitative estimate of drag for two-dimensional shapes.

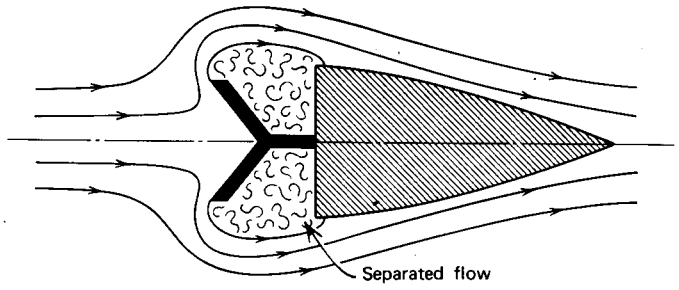

Figure 4.9 Drag reduction of a high drag shape.

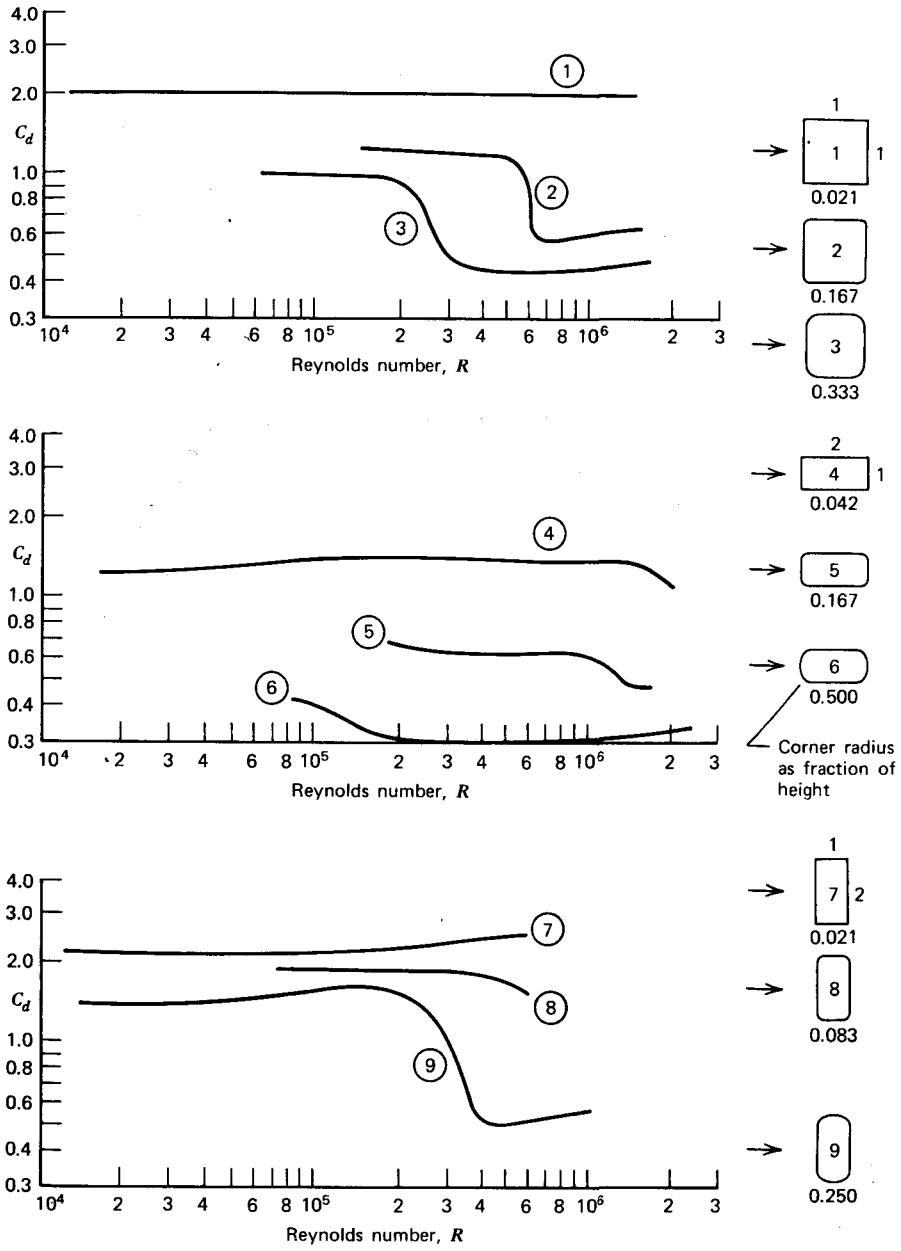

Figure 4.10 Drag coefficients for various cylindrical shapes as a function of Reynolds number.

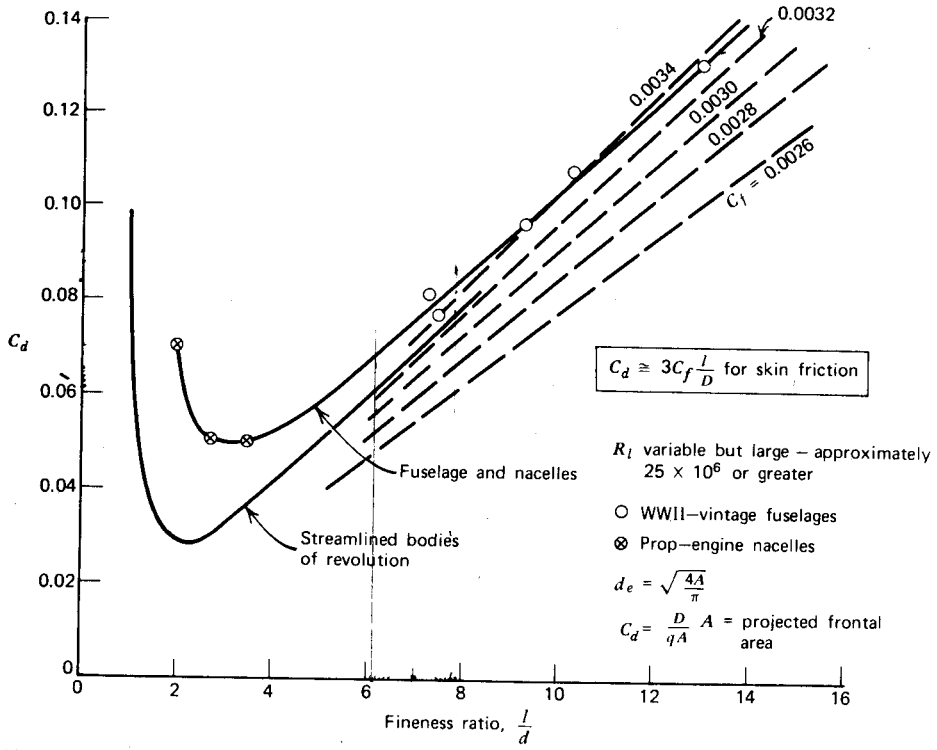

Figure 4.13 Drag of fuselages and similar shapes.

jected frontal areas becomes

$$\frac{C_d(\text{3-D})}{C_d(\text{2-D})} = \frac{S_w(\text{3-D})}{S_w(\text{2-D})} \frac{4}{\pi D}$$

where D is the maximum three-dimensional body diameter or the maximum thickness of the two-dimensional shape. For an elliptical two-dimensional shape compared to an ellipsoid, this becomes

$$\frac{C_d(\text{3-D})}{C_d(\text{2-D})} = \frac{\pi}{2} \tag{4.11}$$

This is close to the ratio from Figure 4.11 for a finess ratio of 8 and only slightly lower than the corresponding ratio given earlier for the form drag.

Minimum profile drag coefficients for NACA four- and five-digit airfoils are presented in Figure 4.12 as a function of thickness ratio at a Reynolds number of 6×10^6. Here, as is usual for airfoils, C_d is based on the chord length. The several data points at each thickness ratio result from airfoils of different camber ratios. Note that $C_{d_{\min}}$ does not vary significantly with

camber. $C_{d_{min}}$ appears to vary almost linearly with t/c and extrapolates to a value of 0.004 for a t/c of zero. This corresponds to a C_f value of 0.002. According to Figure 4.1, this would require laminar flow over these sections more extensive than one would expect. Probably, transition is delayed until approximately the 25% chord point, the location of maximum thickness. One would then expect a $C_{d_{min}}$ value of about 0.005.

Figure 4.13 presents three-dimensional drag data directly comparable to Figure 4.11, but with more detail. Data representing practical fuselage and nacelle construction are included in Figure 4.13 together with C_d results from torpedo-shaped bodies. Assuming a reasonable relationship between the frontal and wetted areas of such bodies, expected C_d values for various values of C_f are also included on the figure. For a given C_f value, the experimental results should approach one of these lines as the fineness ratio gets large.

For fully turbulent flow at an R of 25×10^6, C_f for a flat plate would be 0.0026, whereas the data appears to be approaching a C_f of 0.0032 to 0.0034. The higher skin friction drag on the bodies is probably the result of surface roughness.

It is interesting to examine the data of Figure 4.13 in terms of minimum drag for a given body volume. This is particularly important for airship and underwater applications. It is also of interest to the design of tip tanks, where minimum drag for a given volume of fuel is desirable. Denoting the volume by V_m, we will define another drag coefficient.

$$C_{d_V} = \frac{D}{qV_m^{2/3}} \tag{4.12}$$

C_{d_V} is related to C_d in Figure 4.13 by

$$C_{d_V} = \frac{A}{V_m^{2/3}} C_d$$

Obviously, the ratio of the frontal area, A, to the 2/3 power of the volume depends on the particular body shape. We will assume the body to be composed approximately of a hemispherical nose, a cylindrical midbody extending to the middle of the body, and a tail cone. For this particular shape,

$$\frac{A}{V_m^{2/3}} = \left[\frac{9\pi}{\left(4\frac{l}{d} - 1\right)^2}\right]^{1/3} \tag{4.13}$$

Using this relationship and Figure 4.13, the graphs presented in Figure 4.14 were obtained. From this figure it can be seen that to enclose a given volume with a minimum drag body, its fineness ratio should be higher than the optimum values from Figure 4.13. Indeed, for fuselages, the drag for a given volume is nearly constant for l/d values from 4 to 10.

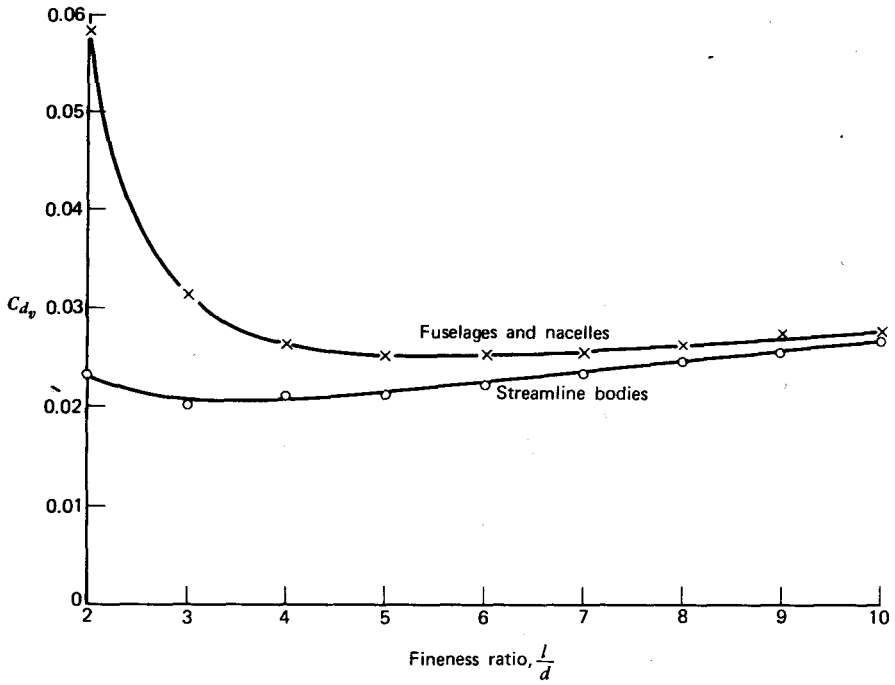

Figure 4.14 Drag coefficients based on volume for bodies as a function of fineness ratio.

For certain applications, it is desirable to keep the rear portion of a fuselage as wide and bluff as possible without paying too much of a drag penalty. If the afterbody is tapered too abruptly, flow separation will occur over the rear, resulting in an unduly high form drag. Some guidance in this regard is provided by Figure 4.15 (taken from Ref. 4.8). Here, the increment in C_d (based on frontal area) resulting from afterbody contraction is presented as a function of afterbody geometry. From this figure it appears that the ratio of the afterbody length to the equivalent diameter should be no less than approximately 2.0.

The importance of streamlining is graphically illustrated in Figure 4.16, which is drawn to scale. Conservatively (supercritical flow), the ratio of C_d for a circular cylinder to a two-dimensional streamlined shape having a fineness ratio of 4 is approximately 7.5. Thus, as shown in Figure 4.16, the height of the streamlined shape can be 7.5 times greater than the circular cylinder for the same drag. For subcritical flow the comparison becomes even more impressive, with the ratio increasing to approximately 25.

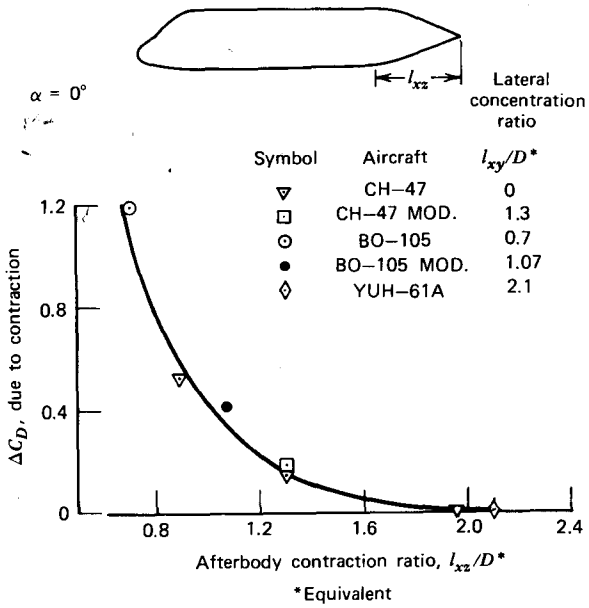

Figure 4.15 Effect of afterbody contraction ratio on drag. (C. Keys and R. Wiesner, "Guidelines for Reducing Helicopter Parasite Drag", 1975. Reprinted from the *Journal of the American Helicopter Society*, Vol. 20, No. 1 by permission of the American Helicopter Society.)

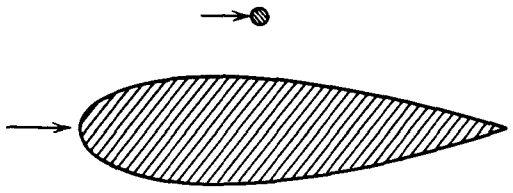

Figure 4.16 Two bodies having the same drag (supercritical flow).

INTERFERENCE DRAG

When two shapes intersect or are placed in proximity, their pressure distributions and boundary layers can interact with each other, resulting in a net drag of the combination that is higher than the sum of the separate drags. This increment in the drag is known as interference drag. Except for specific cases where data are available, interference drag is difficult to estimate accurately. Some examples of interference drag are presented in Figures 4.17, 4.18, and 4.19.

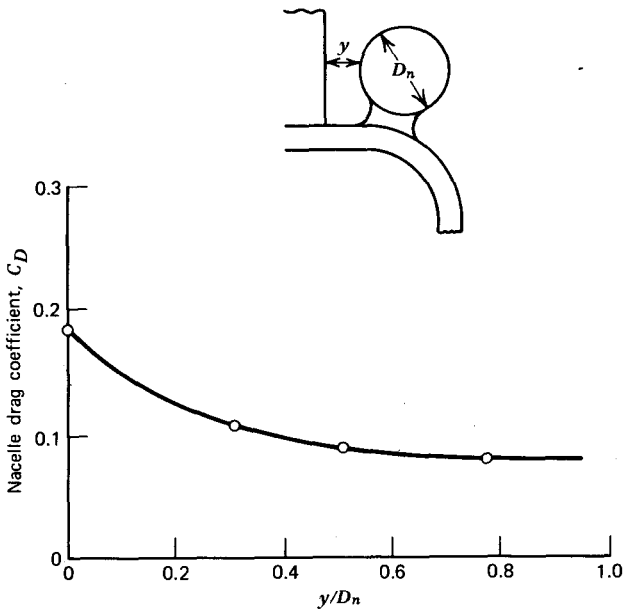

Figure 4.17 Effect of nacelle location on interference drag. (C. Keys and R. Wiesner, "Guidelines for Reducing Helicopter Parasite Drag", 1975. Reprinted from the *Journal of the American Helicopter Society*, Vol. 20, No. 1 by permission of the American Helicopter Society.)

Figure 4.17 illustrates the drag penalty that is paid for placing an engine nacelle in proximity to a rear pylon on a tandem helicopter (like a CH-47). In this particular instance, the interference drag is nearly equal to the drag of the nacelle alone, because the nacelle is mounted very close to the pylon. For spacings greater than approximately one-half of a nacelle diameter, the interference drag vanishes.

Figure 4.18 presents the interference drag between the rotor hub and pylon for a helicopter. The trends shown in this figure are similar to those in the previous figure. In both instances the added interference drag is not necessarily on the appended member; probably, it is on the pylon.

Figure 4.19 shows a wing abutting the side of a fuselage. At the fuselage-wing juncture a drag increment results as the boundary layers from the two airplane components interact and thicken locally at the junction. This type of drag penalty will become more severe if surfaces meet at an angle other than 90°. In particular, acute angles between intersecting surfaces should be avoided. Reference 4.4, for example, shows that the interference drag of a 45% thick strut abutting a plane wall doubles as the angle decreases from 90°

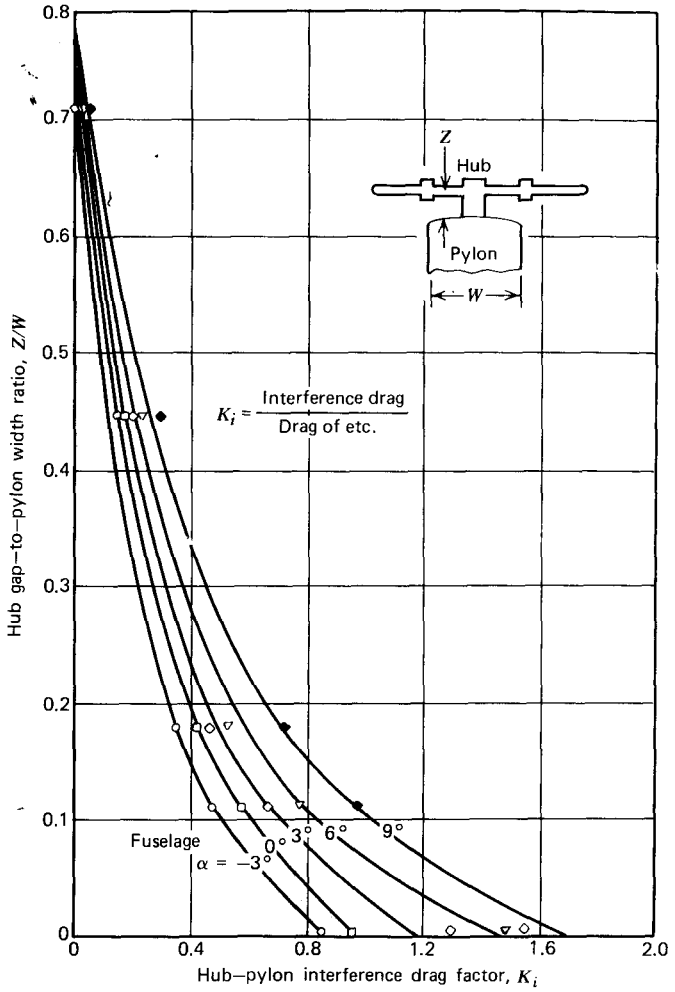

Figure 4.18 Effect of hub/pylon gap on interference drag. (C. Keys and R. Wiesner, "Guidelines for Reducing Helicopter Parasite Drag", 1975. Reprinted from the *Journal of the American Helicopter Society*, Vol. 20, No. 1 by permission of the American Helicopter Society.)

to approximately 60°. If acute angles cannot be avoided, filleting should be used at the juncture.

In the case of a high-wing configuration, interference drag results principally from the interaction of the fuselage boundary layer with that from the wing's lower surface. This latter layer is relatively thin at positive angles of attack. On the other hand, it is the boundary layer on the upper surface of a

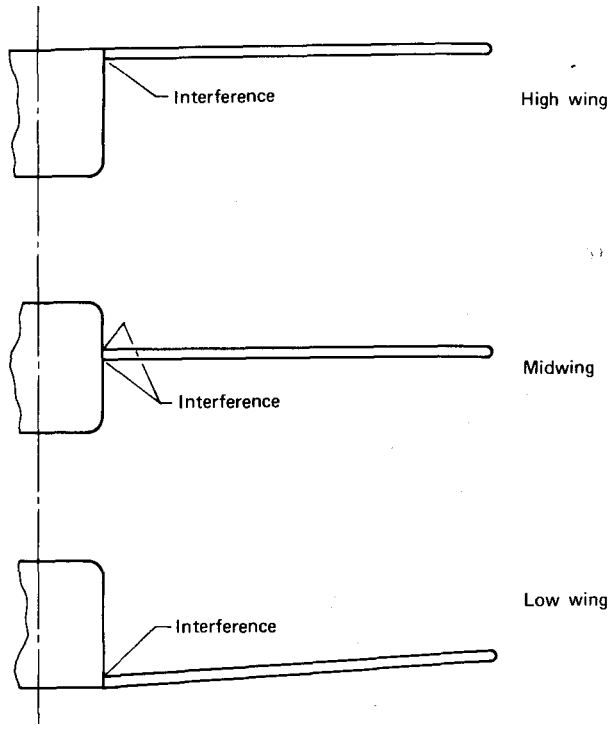

Figure 4.19 Wing-fuselage interference drag.

low wing that interferes with the fuselage boundary layer. This upper surface layer is appreciably thicker than the lower surface layer. Thus the wing-fuselage interference drag for a low-wing configuration is usually greater than for a high-wing configuration.

The available data on wing-fuselage interference drag are sparse. Reference 4.4 presents a limited amount but, even here, there is no correlation with wing position or lift coefficient. Based on this reference, an approximate drag increment caused by wing-fuselage interference is estimated to equal 4% of the wing's profile drag for a typical aspect ratio and wing thickness.

Although data such as those in Reference 4.4 may be helpful in estimating interference drag, an accurate estimate of this quantity is nearly impossible. For example, a wing protruding from a fuselage just forward of the station where the fuselage begins to taper may trigger separation over the rear portion of the fuselage.

Sometimes interference drag can be favorable as, for example, when one body operates in the wake of another. Race car drivers frequently use this to their advantage in the practice of "drafting." Some indication of this favor-

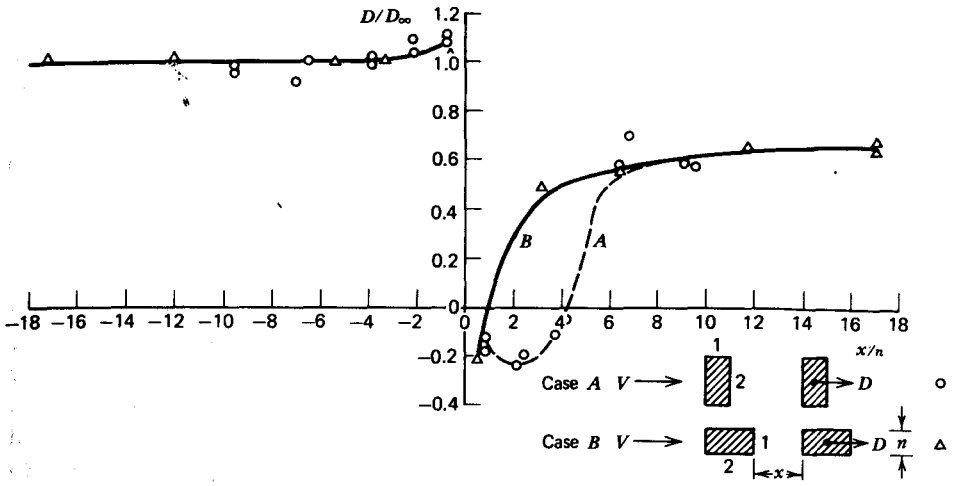

Figure 4.20 Interference drag for a two-dimensional rectangular cylinder in tandem with another.

able interference is provided by Figure 4.20, based on data obtained in Pennsylvania State University's subsonic wind tunnel. Here the drag on one rectangular cylinder in tandem with another is presented as a function of the distance between the cylinders. The cylinders have a 2:1 fineness ratio. Tests were performed with the long side oriented both with and normal to the free-stream velocity. The drag is referenced with respect to D_∞, the drag on the one cylinder alone. The spacing is made dimensionless with respect to the dimension of the cylinder normal to the flow. The spacing, x, is positive when the cylinder on which the drag is being measured is downstream of the other. Notice that the cylinder's drag is reduced significantly for positive x values and even becomes negative for small positive values of x. For small negative values of x, the drag is increased slightly. Similar data for circular cylinders presented in Reference 4.4 show somewhat similar results, except that interference on the forward cylinder is slightly favorable for spacings less than three diameters. For the downstream cylinder, the drag is reduced by a factor of 0.3 for spacings between three and nine diameters. For less than three diameters, the downstream drag is even less, and becomes negative for spacings less than approximately two diameters.

INDUCED DRAG

The two major components of the total drag of an airplane are the induced drag and the parasite drag. The parasite drag is the drag not directly associated with the production of lift. This drag, expressed as a coefficient, is

nearly constant and approximately equal to the drag for an airplane lift coefficient of zero. As the lift coefficient takes on a value different than zero, the drag coefficient will increase. This increment in C_d is defined as the induced drag coefficient, C_d. Thus, for an airplane,

$$C_D = C_{D_0} + C_{D_i} \tag{4.14}$$

Here C_{D_0} is the parasite drag coefficient and is not a function of C_L. On the other hand, the induced drag coefficient, C_{D_i}, varies approximately as the square of C_L. This dependence will be derived later.

Strictly speaking, this definition of C_{D_i} is not correct. Although it has become practice to charge to C_{D_i} any drag increase associated with C_L, some of this increase results from the dependency of the parasite drag on the angle of attack. What, then, is a more precise definition of C_{D_i}? Very simply, the induced drag at a given C_L can be defined as the drag that the wing would experience in an inviscid flow at the same C_L. D'Alembert's paradox assures us that a closed body can experience no drag in an inviscid flow. However, as we saw in the last chapter, a wing of finite aspect ratio generates a trailing vortex system that extends infinitely far downstream. Thus, the system in effect is not closed, because of the trailing vortex system that continuously transports energy across any control surface enclosing the wing, no matter how far downstream of the wing this surface is chosen.

Calculation of Induced Drag

Referring again to Figure 3.54, the lift vector for a wing section is seen to be tilted rearward through the induced angle of attack, α_i. As a result, a component of the lift is produced in the streamwise direction. This component, integrated over the wingspan, results in the induced drag. For a differential element,

$$\frac{dD_i}{dy} = \alpha_i \frac{dL}{dy} \tag{4.15}$$

Defining the induced drag coefficient as

$$C_{D_i} = \frac{D_i}{qS} \tag{4.16}$$

it follows that

$$C_{D_i} = \frac{\int_{b/2}^{b/2} \alpha_i C_L c \, dy}{S} \tag{4.17}$$

For the special case of an untwisted elliptic wing, α_i and C_l are constant over the span, so that Equation 4.17 becomes

$$C_{D_i} = \alpha_i C_L \tag{4.18}$$

The induced angle of attack for this case was given previously by Equation 3.72. Thus,

$$C_{D_i} = \frac{C_L^2}{\pi A} \tag{4.19}$$

This is a well-known and often-used relationship that applies fairly well to other than elliptic planforms. For a given aspect ratio and wing lift coefficient, it can be shown (Ref. 4.1) that Equation 4.19 represents the minimum achievable induced drag for a wing. In other words, the elliptic lift distribution is optimum from the viewpoint of induced drag.

In order to account for departures from the elliptic lift distribution and the dependence of the parasite drag on angle of attack, Equation 4.19 is modified in practice in several different ways. Theoretically one can calculate the downwash and section lift coefficients, either analytically or numerically, according to the methods of the previous chapter. These results can then be substituted into Equation 4.17 to solve for C_{D_i}. The final result for an arbitrary planform is usually compared to Equation 4.19 and expressed in the form

$$C_{D_i} = \frac{C_L^2}{\pi A}(1 + \delta) \tag{4.20}$$

δ, for a given planform shape, is a constant that is normally small by comparison to unity. It therefore represents, for a given wing, the fractional increase in the induced drag over the optimum elliptic case.

The numerical determination of δ will now be outlined for the simplified lifting line model and some typical results will be presented. As an exercise, develop your own program; it is not too lengthy if a subroutine is available for solving simultaneous linear algebraic equations.

A lifting line model composed of discrete vortex line elements is pictured in Figure 4.21. For clarity only five trailing vortices are shown on each side. Their strengths and positions are symmetrical about the centerline. These can be equally spaced but, with the loading dropping off faster at the tips, it is better to have a closer spacing in this region.

A particular trailing vortex is located a distance of y_V from the centerline. Control points are then chosen midway between the vortex lines. Generally,

$$y_{C_i} = \tfrac{1}{2}(y_{V_i} + y_{v_{i-1}}) \qquad 1 < i \leq n \tag{4.21}$$
$$y_{C_1} = 0$$

At a control point, the bound circulation, Γ, is equal to the sum of the strengths of the vortex lines shed outboard of the point. Thus, for n trailing vortices,

$$\Gamma_1 = \gamma_1 + \gamma_2 + \gamma_3 + \cdots + \gamma_n$$
$$\Gamma_2 = \gamma_2 + \gamma_3 + \gamma_4 + \cdots + \gamma_n$$

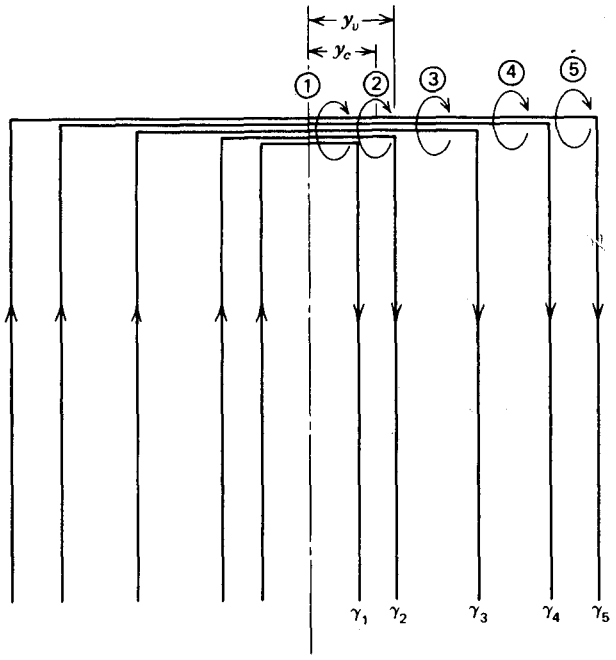

Figure 4.21 Lifting line model of a wing.

or, generally,

$$\Gamma_j = \sum_{i=j}^{n} \gamma_i$$

For computational efficiency, it should be recognized that

$$\Gamma_{i+1} = \Gamma_i - \gamma_i$$

Thus it is expedient to determine Γ_1 first and then apply this recursion relationship in order to determine $\Gamma_2, \Gamma_3, \ldots, \Gamma_n$.

The section lift is given by

$$\frac{dL}{dy} = \tfrac{1}{2}\rho V^2 c C_l$$

It can also be obtained from the Kutta-Joukowski law as

$$\frac{dL}{dy} = \rho V \Gamma$$

Comparing these two relationships for dL/dy, it follows that

$$\Gamma = \tfrac{1}{2} c C_l V \tag{4.22}$$

But C_l is given by

$$C_l = C_{l_\alpha}(\alpha - \alpha_i)$$
$$= C_{l_\alpha}\left(\alpha - \frac{w}{V}\right) \tag{4.23}$$

Thus Equations 4.21 to 4.23 are interrelated, since the downwash, w, depends on the Γ distribution.

By applying the Biot-Savart law to our discrete vortex line model, w can be determined along the lifting line (neglecting any contribution from the lifting line itself). The downwash at the jth control point produced by the ith trailing vortex is

$$\Delta w_j = \frac{\alpha_i}{4\pi}\left(\frac{1}{y_{c_j} + y_{v_i}} - \frac{1}{y_{c_j} - y_{v_i}}\right)$$

In the parentheses, the first term arises from the downwash at a point on the right side of the wing produced by a vortex trailing from the left. The second term is from the vortex of opposite rotation and symmetric position trailing from the right wing. This expression reduces to

$$\Delta w_j = \frac{1}{2\pi}\frac{y_{v_i}}{y_{v_i}^2 - y_{c_j}^2}\gamma_i \tag{4.24}$$

or

$$\Delta w_j = C_{i_j}\gamma_i \tag{4.25}$$

The total downwash at y_{c_j} is then found by summing Equation 4.13 over i from 1 to n.

$$w_j = \sum_{i-1}^{n} C_{i_j}\gamma_i \tag{4.26}$$

Without any loss of generality, it is convenient to set the free-stream velocity, V, the density, ρ, and the wing semispan, $b/2$, equal to unity. It then follows that

$$\Gamma_j = \tfrac{1}{2}c_j C_{l_\alpha}(\alpha_j - w_j) \tag{4.27}$$

or

$$\sum_{i=j}^{n}\gamma_i = \frac{c_j C_{l_\alpha}\alpha_j}{2} - \frac{c_j C_{l_\alpha}}{2}\sum_{i=1}^{n} C_{i_j}\gamma_i$$

This can be rewritten as

$$\sum_{i=1}^{n}\gamma_i\left(\frac{c_j C_{l_\alpha} C_{ij}}{2} + k\right) = \frac{c_j C_{l_\alpha}\alpha_j}{2}$$

where

$$k = 1 \qquad i \geq j$$
$$= 0 \qquad i < j$$

The preceding is of the form

$$\sum_{i=1}^{n} A_{ji}\gamma_i = B_j \qquad j = 1, 2, 3, \ldots, n \tag{4.28}$$

and represents n simultaneous linear algebraic equations that can be solved for the unknown vortex strengths $\gamma_1, \gamma_2, \ldots, \gamma_i, \ldots, \gamma_n$.

Since $b/2$ is set equal to unity, the chord lengths, c_j, must be expressed as a fraction of $b/2$. The values of c_j are defined at the control point locations. Having determined the γ_i values, the wing lift coefficient can be calculated from

$$L = 2[\Gamma_1 y_{v_1} + \Gamma_2(y_{v_2} - y_{v_1}) + \cdots + \Gamma_i(y_{v_i} - y_{v_{i-1}}) + \cdots + \Gamma_n(y_{v_n} - y_{v_{n-1}})]$$

or, in coefficient form,

$$C_L = A\left[\Gamma_1 y_{v_1} + \sum_{i=2}^{n} \Gamma_i(y_{v_i} - y_{v_{i-1}})\right] \tag{4.29}$$

The aspect ratio, A, appears, since the dimensionless reference wing area equals the actual area divided by $(b/2)^2$. w_i is calculated from Equation 4.26 so that the induced drag follows from Equation 4.15.

$$D_I = 2[\Gamma_1 y_{v_1} w_1 + \Gamma_2(y_{v_2} - y_{v_1})w_2 + \cdots + \Gamma_i(y_{v_i} - y_{v_{i-1}})w_i + \cdots + \Gamma_n(y_{v_n} - y_{v_{n-1}})w_n]$$

or, in coefficient form,

$$C_{D_I} = A\left[\Gamma_1 y_{v_1} w_1 + \sum_{i=2}^{n} \Gamma_i w_i(y_{v_i} - y_{v_{i-1}})\right] \tag{4.30}$$

The accuracy of the foregoing numerical formulation of the lifting line model can be tested by applying it to the elliptical planform. Using 25 vortices ($n = 25$) trailing from each side of the wing, Equations 4.26 to 4.30 are evaluated for flat, untwisted elliptical planform shapes having aspect ratios of 4, 6, 8, and 10 using a theoretical section lift curve slope of $2\pi C_l$/rad. The numerical results are presented in Table 4.1 for C_L and C_{D_i} where they are

Table 4.1 Comparison of C_L and C_{D_i} Values for Elliptic Wings as Predicted by Numerical and Analytical Methods

($\alpha = 10°$, $C_{l_\alpha} = 2\pi$)

A	C_L (Equation 4.29)	C_L (Equation 3.73)	C_{D_i} (Equation 4.30)	C_{D_i} (Equation 4.19)
4	0.74	0.73	0.0422	0.0425
6	0.83	0.92	0.0354	0.0359
8	0.89	0.88	0.0301	0.0306
10	0.92	0.91	0.0261	0.0266

compared with corresponding analytical values. The C_L values are seen to agree within 1% of each other, while the C_{D_i} values differ by only 2% at the most.

With confidence established in the numerical program, the calculations presented in Figures 4.22, 4.23, and 4.24 can be performed. Here unswept wings with linearly tapered planforms are investigated. For this family of wings, the spanwise chord distribution is defined by

$$c = c_0 - (c_0 - c_T)\frac{y}{b/2}$$

or

$$\frac{c}{c_0} = 1 - (1 - \lambda)X$$

where λ equals the taper ratio, c_T/c_0, c_T and c_0 being the tip and root chord, respectively. X is the distance along the span measured out from the centerline as a fraction of the semispan.

Figure 4.22 presents δ as a function of the taper ratio for aspect ratio values of 4, 6, 8, and 10. For all of the aspect ratios, δ is seen to be a minimum at a taper ratio of around 0.3, being less than 1% higher than the ideal elliptic case at this value of λ. The rectangular wing is represented by a λ value of 1.0. For this planform shape, used on many light, single-engine

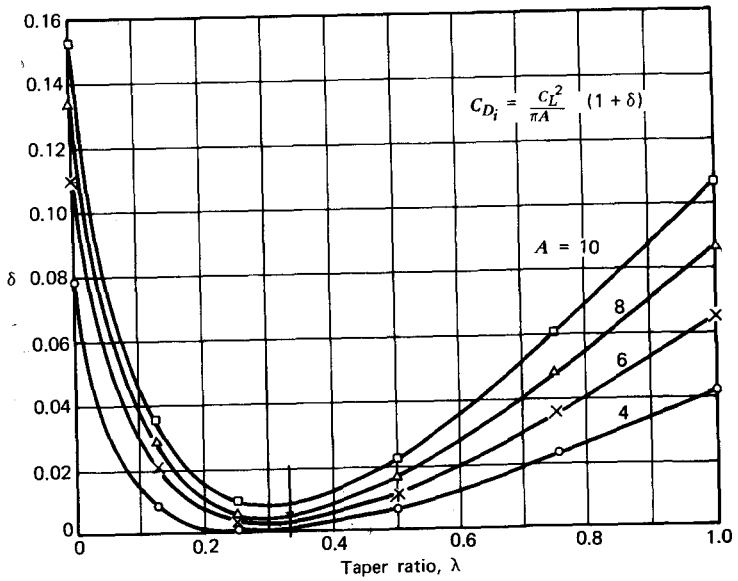

Figure 4.22 Induced drag factor for unswept linearly tapered wings.

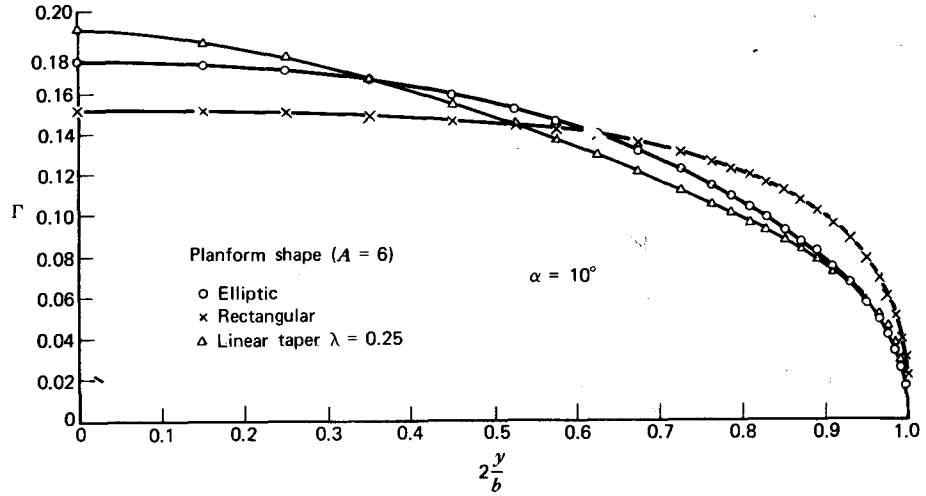

Figure 4.23 Spanwise distribution of bound circulation according to numerical solution of lifting line model ($n = 25$).

aircraft, the induced drag is seen to be 6% or higher than that for the elliptic wing for aspect ratios of 6 or higher.

The results of Figure 4.22 can be explained by reference to Figure 4.23, which presents spanwise distributions of Γ for the elliptic, rectangular, and 0.25 taper ratio wings. Observe that the distribution for $\lambda = 0.25$ is close to the elliptic distribution. Thus the kinetic energies of the trailing vortex systems shed from these two Γ distributions are about the same. On the other hand, the Γ distribution for the rectangular planform is nearly constant inboard out to about 70% of the semispan and then drops off more rapidly than the elliptic distribution toward the tip. Thus the kinetic energy per unit length of the trailing vortex system shed from the rectangular wing is approximately 6% higher than the energy left in the wake by the tapered or elliptic wing.

In view of the preceding one might ask why rectangular planforms are used in many general aviation airplanes instead of tapered planforms. Part of the answer lies with the relative cost of manufacture. Obviously, the rectangular planform with an untapered spar and constant rib sections is less costly to fabricate. Figure 4.24 discloses a second advantage to the rectangular planform. Here, the section lift coefficient is presented as a ratio to the wing lift coefficient for untwisted elliptic, rectangular, and linearly tapered planforms. For the elliptic wing, the section C_l is seen to be constant and equal to the wing C_L except in the very region of the tip, where numerical errors show an increase in C_l contrary to the analytical solution. The rectangular planform shows the section C_l to be higher than the wing C_L at the

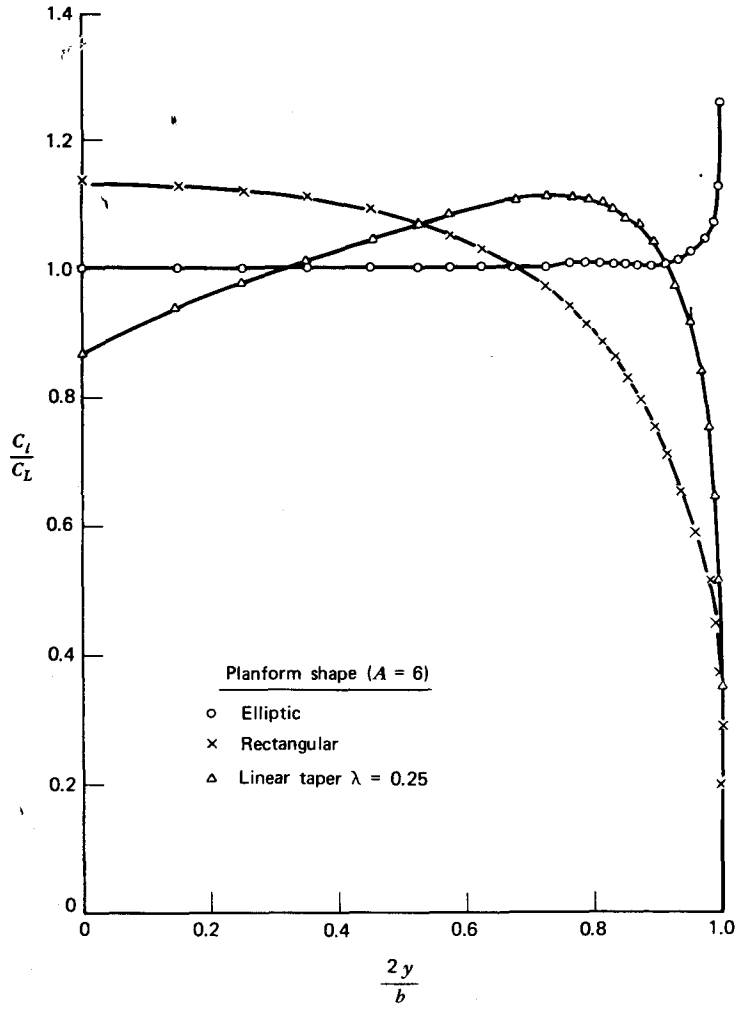

Figure 4.24 Spanwise section C_l distribution according to numerical solution of lifting line model ($n = 25$).

centerline and gradually decreasing to zero at the tip. The tapered planform, however, has a section C_l that is lower than the wing C_L at midspan. Its C_l then increases out to approximately the 75% station before decreasing rapidly to zero at the tip. Thus, again reiterating the discussions of the previous chapter, the tapered planform, unless twisted, will stall first outboard, resulting in a possible loss of lateral control.

Effective Aspect Ratio

It was stated earlier that the profile drag of an airfoil section increases approximately with the square of the section C_l. Combined with the induced drag, given by Equation 4.20, the total C_D for a wing can be written approximately as

$$C_D = C_{D_{\min}} + kC_L^2 + \frac{C_L^2}{\pi A}(1+\delta)$$

or

$$C_D = C_{D_{\min}} + \frac{C_L^2}{\pi A}(k\pi A + 1 + \delta) \tag{4.31}$$

where k is the constant of proportionality giving the rate of increase of C_d with C_l^2.

Equation 4.31 can be rewritten as

$$C_D = C_{D_{\min}} + \frac{C_L^2}{\pi A e} \tag{4.32}$$

where

$$e = \frac{1}{1+\delta+k\pi A}$$

The factor e is known as Oswald's efficiency factor (see Ref. 4.2). The product Ae is referred to as the "effective aspect ratio" and is sometimes written as A_e.

Consider data from References 3.1 and 3.27 in light of Equation 4.32. Figure 4.25 presents C_D as a function of C_L for the finite wing tested in Reference 3.27 and C_d versus C_l from Reference 3.1 for the 65-210 airfoil.

This particular airfoil section is conducive to laminar flow for C_l values between approximately 0.2 and 0.6, as reflected in the "drag bucket" in the lower curve of this figure. The "bucket" is not evident in the wing test results of Reference 3.27, either as the result of wing surface roughness or wind tunnel flow disturbances. Neglecting the bucket in the airfoil section C_d curve, the constant, k, is found to be 0.0038. From Figure 4.22, $\delta = 0.01$. Thus, from the airfoil C_d curve and lifting line theory, the wing C_D curve is predicted to be

$$C_D = 0.0055 + 0.0394C_L^2 \tag{4.33}$$

This equation is included on Figure 4.25, where it can be seen to agree closely with the test results. Thus one can conclude that the difference in the drag between an airfoil and a wing is satisfactorily explained by the induced drag. In this particular case, Oswald's efficiency factor is 0.89.

Generally, for a complete airplane configuration, e is not this high because of wing-fuselage interference and contributions from the tail and other components.

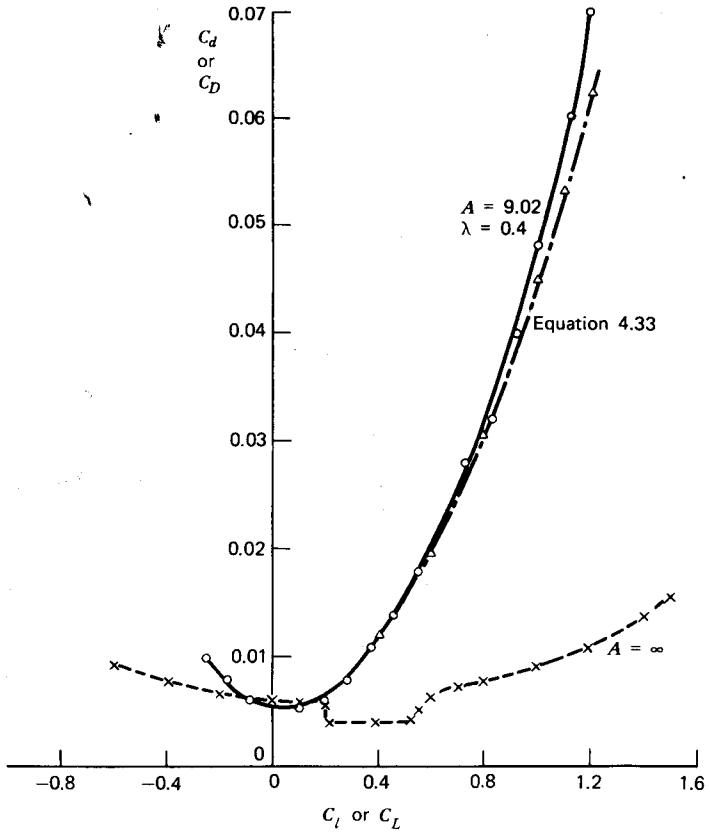

Figure 4.25 Comparison between predicted and measured drag polar for a wing having a finite aspect ratio.

High-wing and low-wing airplanes show a measurable difference in Oswald's efficiency factor. Most likely as the result of interference between the boundary layer on the wing's upper surface with that on the fuselage, e values for low-wing airplanes are lower than those for high-wing airplanes. The boundary layer on the upper surface of a wing is considerably thicker than the one on the lower surface. Combining with the boundary layer over the sides of the fuselage, the wing's upper surface boundary layer, for the low-wing airplane, can cause a rapid increase in the wing and fuselage parasite drag as the angle of attack increases. For a high-wing airplane, the relatively thin boundary layer on the lower surface of the wing interferes only slightly with the fuselage boundary layer. Typically, e is equal approximately to 0.6 for low-wing airplanes and 0.8 for high-wing airplanes. These values are

confirmed by the flight tests reported in Reference 4.3 and in other data from isolated sources.

DRAG BREAKDOWN AND EQUIVALENT FLAT-PLATE AREA

The parasite drag of an airplane can be estimated by estimating the drag of each component and then totaling the component drag while accounting for some interference drag. If C_{D_i} and S_i are the drag coefficient and reference area, respectively, for the ith component, then the total drag will be

$$\begin{aligned} D &= \tfrac{1}{2}\rho V^2 C_{D_1} S_1 + \tfrac{1}{2}\rho V^2 C_{D_2} S_2 + \cdots + \tfrac{1}{2}\rho V^2 C_{D_i} S_i + \cdots \\ &= \tfrac{1}{2}\rho V^2 (C_{D_1} S_1 + C_{D_2} S_2 + \cdots + C_{D_i} S_i + \cdots) \end{aligned} \tag{4.34}$$

Obviously, the drag coefficients of the components cannot be added since the reference areas are different. However, from Equation 4.34, the products $C_{D_i} S_i$ can be added. Such a product is referred to as the *equivalent flat-plate area*, f. One will also hear it referred to as the "parasite area" or simply, the "flat-plate area." The connotation "flat plate" is misleading, since it is not the area of a flat plate with the same drag. Instead, it is the reference area of a fictitious shape having a C_D of 1.0, which has the same drag as the shape in question. f is therefore simply D/q. It is a convenient way of handling the drag, since the f's of the drag components can be added to give the total f of an airplane.

$$\frac{D}{q} = C_{D_1} S_1 + C_{D_2} S_2 + \cdots$$

or

$$\begin{aligned} f &= \sum_{i=1}^{n} C_{D_i} S_i \\ &= \sum_{i=1}^{n} f_i \end{aligned} \tag{4.35}$$

This notation indicates that the flat-plate areas are to be summed for the ith component, from $i = 1$ to n where n is the total number of components.

DRAG COUNTS

As a measure of an airplane's drag, in practice one will frequently hear the term "drag count" used. Usually, it is used in an incremental or decremental sense, such as "fairing the landing gear reduced the drag by 20 counts." One drag count is defined simply as a change in the total airplane C_D, based on the wing planform area of 0.0001. Hence a reduction in drag of 20 counts could mean a reduction in the C_D from, say, 0.0065 down to 0.0045.

AVERAGE SKIN FRICTION COEFFICIENTS

In examples to follow, one will see that several uncertainties arise in attempting to estimate the absolute parasite drag coefficient (as opposed to incremental effects) of an airplane. These generally involve questions of interference drag and surface irregularities. In view of these difficulties, it is sometimes better to estimate the total drag of a new airplane on the basis of the known drag of existing airplanes having a similar appearance, that is, the same degree of streamlining and surface finish.

The most rational basis for such a comparison is the total wetted area and not the wing area, since C_f depends only on the degree of streamlining and surface finish, whereas C_D depends on the size of the wing in relation to the rest of the airplane. In terms of an average C_F, the parasite drag at zero C_L for the total airplane can be written as

$$D = qC_FS_w \tag{4.36}$$

where S_w is the total wetted area of the airplane. Since

$$f = \frac{D}{q}$$

it follows that the ratio of the equivalent flat-plate area to the wetted area is

$$\frac{f}{S_w} = C_F \tag{4.37}$$

In order to provide a basis for estimating C_F, Table 4.2 presents a tabulation of this quantity for 23 different airplanes having widely varying configurations. These range all the way from Piper's popular light plane, the Cherokee, to Lockheed's jumbo jet, the C-5A.

The data in this table were obtained from several sources and include results obtained by students taking a course in techniques of flight testing. Thus, the absolute value of C_F for a given airplane may be in error by a few percent. For purposes of preliminary design, the C_F ranges given in Table 4.3 are suggested for various types of airplanes. Where a particular airplane falls in the range of C_F values for its type will depend on the attention given to surface finish, sealing (around cabin doors, wheel wells, etc.), external protuberances, and other drag-producing items.

Additional drag data on a number of airplanes, including supersonic airplanes, are presented in Appendix A.3 as a function of Mach number and altitude.

Finally, with regard to average C_F values, Figure 4.26 (taken from Ref. 4.11) is presented. Although only a few individual points are identified on this figure, its results agree generally with Table 4.2. This figure graphically depicts the dramatic improvement in aerodynamic cleanliness of airplanes that has been accomplished since the first flight of the Wright Brothers.

Table 4.2 Typical Overall Skin Friction Coefficients for a Number of Airplanes Built from Approximately 1940 to 1976. Data Taken from Several Sources

C_F	Airplane Designation	Description
0.0100	Cessna 150	Single prop, high wing, fixed gear
0.0095	PA-28	Single prop, low wing, fixed gear
0.0070	B-17	Four props, World War II bomber
0.0067	PA-28R	Single prop, low wing, retractable gear
0.0066	C-47	Twin props, low wing, retractable gear
0.0060	P-40	Single prop, World War II fighter
0.0060	F-4C	Jet fighter, engines internal
0.0059	B-29	Four props, World War II bomber
0.0054	P-38	Twin props, twin-tail booms, World War II fighter
0.0050	Cessna 310	Twin props, low wing, retractable gear
0.0049	Beech V35	Single prop, low wing, retractable gear
0.0046	C-46	Twin props, low wing, retractable gear
0.0046	C-54	Four props, low wing, retractable gear
0.0042	Learjet 25	Twin jets, pod-mounted on fuselage, tip tanks
0.0044	CV 880	Four jets, pod-mounted under wing
0.0041	NT-33A	Training version of P-80 (see below)
0.0038	P-51F	Single prop, World War II fighter
0.0038	C-5A	Four jets, pod-mounted under wing, jumbo jet
0.0037	Jetstar	Four jets, pod-mounted on fuselage
0.0036	747	Four jets, pod-mounted under wing, jumbo jet
0.0033	P-80	Jet fighter, engines internal, tip tanks, low-wing
0.0032	F-104	Jet fighter, engines internal, midwing
0.0031	A-7A	Jet fighter, engines internal, high wing

Table 4.3 Typical Total Skin Friction Coefficient Values for Different Airplane Configurations

Airplane Configuration	C_F Range at Low Mach Numbers
Propeller driven, fixed gear	0.008–0.010
Propeller driven, retractable gear	0.0045–0.007
Jet propelled, engines pod-mounted	0.0035–0.0045
Jet propelled, engines internal	0.0030–0.0035

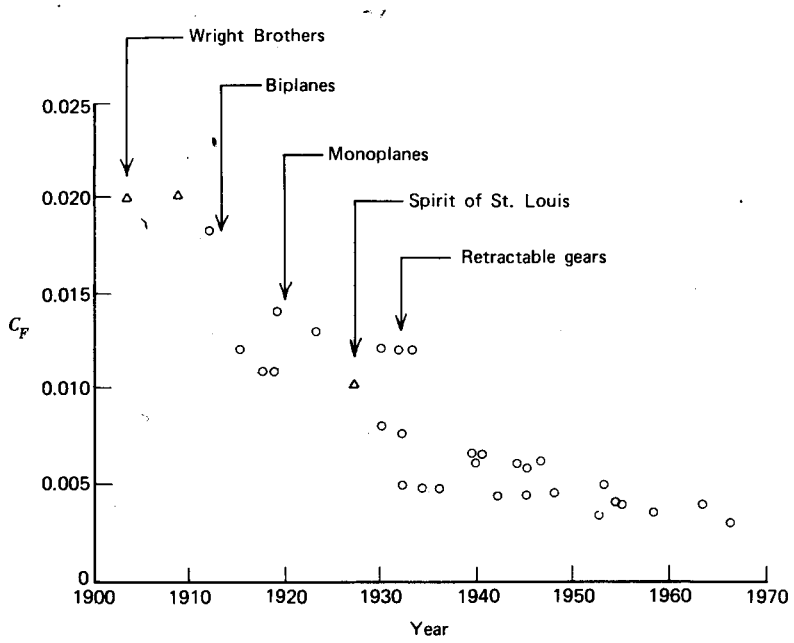

Figure 4.26 Historical survey of drag.

EXAMPLE ESTIMATES OF DRAG BREAKDOWN

The use of Equation 4.35 is illustrated in Table 4.4, where I have performed an estimate of the drag breakdown for the Cherokee (Figure 3.62). Armed with a tape measure, I made a visual inspection of the airplane, noting the dimensions of all drag-producing appendages. What you see here is a first estimate without any iteration. The total value for f of 0.36 m^2 (3.9 ft^2) is obviously too low and should be approximately 50% higher. This airplane has a total wetted area of approximately 58.06 m^2 (625 ft^2).

Undoubtedly, an aerodynamicist working continuously with this type of aircraft would be able to make a drag breakdown more accurate than the one shown in Table 4.4. Based on one's experience with his or her company's aircraft, the aerodynamicist can make more certain allowances for surface roughness, interferences and leakage. For example, in the case of the Cherokee's landing gear, the oleo struts have a bar linkage immediately behind them. The linkage, struts, wheel pants, and brake fittings produce a total drag for the entire landing gear that is probably significantly higher than the total f of 0.065 m^2 (0.7 ft^2) estimated for the wheels, wheel pants, and struts. The cylindrical oleo struts, in particular, being close to the wheel pants probably produce separation over the pants so that C_d for this item could be

Table 4.4 Drag Breakdown for Piper Cherokee 180

Item	Description	Reference Area	C_d	Basis for C_d	$F = C_dA$
Wing	See Figure 3.62	160 (plan)	0.0093	Figure 4.12 +50% for roughness	1.49
Fuselage	See Figure 3.62	15.2 (front)	0.058	Figure 4.13 $l/d_e = 5$	0.88
Horizontal tail	See Figure 3.62	25 (plan)	0.0084	Figure 4.12 +50% for roughness	0.21
Vertical tail	See Figure 3.62	11.5 (plan)	0.0084	Figure 4.12 +50% for roughness	0.10
Wheel struts	20 in. long 1.5 in. D half faired	0.63 (front)	0.3	Figure 4.6 supercritical	0.19
Wheel pants	12 in. high 7 in. wide streamlined	1.75 (front)	0.04	Figure 4.11	0.07
Wheels	6 in. below pants 5 in. wide	0.63 (front)	0.70	Figure 4.10 corrected to three-dimensional	0.44
Pitot-static tube	$\frac{1}{2}$ in. × 5 in. blunt/ rounded edge	0.02 (front)	1.0	Figure 4.7	0.02
Flap control horns	3 in. × $\frac{3}{4}$ in. blunt (6 total)	0.09 (front)	1.0	Figure 4.7*a*	0.09

Gas drain cocks	1 in. × $\frac{1}{2}$ in.blunt (2 total)	0.01 (front)	1.0	Figure 4.7	0.01
Rotating beacon	4 in. D × 5 in. semispherical	0.14 (front)	0.15	Figure 4.6	0.02
Tail tie-down	$3\frac{1}{2}$ in. × $\frac{3}{8}$ in. blunt	0.01 (front)	1.0	Figure 4.7	0.01
Wing tie-downs	1 in. × $\frac{3}{8}$ in. blunt (2)	0.01 (front)	1.0	Figure 4.7	0.01
Five whip antennas	$\frac{1}{4}$ in. D × 20 in. each	0.17 (front)	1.0	Figure 4.7 subcritical	0.17
Two pipes from engine step	3 in. D × 2 in. each	0.08 (front)	0.2	Figures 4.6 and 4.7*b*	0.02
	12 in. long, $\frac{3}{4}$ in. thick, 2 in. chord	0.06 (front)	0.06	Figure 4.11 +50% for roughness	0.04
OAT gage	3 in. × $\frac{3}{4}$ in. D blunt	0.02	1.0	Figure 4.7	0.02
Antenna fairing	3 in. deep × 6 in. width streamlined	0.13	0.06	Figure 4.11 +50% for roughness	0.01
Antenna supports	5 in. × $\frac{1}{2}$ in. D (two)	0.03	1.0	Figure 4.7	0.03
Interference					
Fuse vertical tail		0.11 (t^2)	0.05	Ref. 4.4	
Fuse horizontal tail		0.06 (t^2)	0.05		0.07
Fuse wing		0.6^2 (t^2)	0.1		
				Total	3.9 ft^2
Leakage?					
Cooling?					

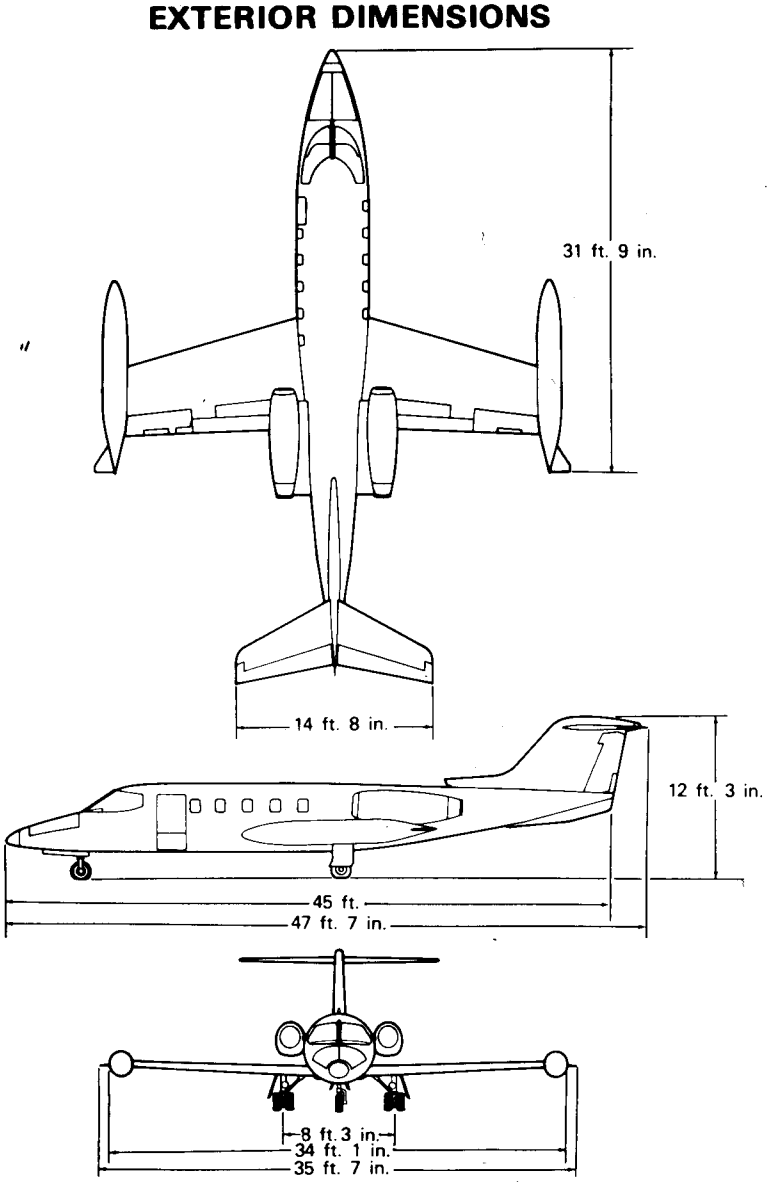

Figure 4.27 Gates Learjet Model 25. (Courtesy Gates Learjet Corp.)

Table 4.5 Parasite Drag Breakdown for Gates Learjet Model 25 (from Ref. 4.10)

Item	C_d (based on Wing Planform Area)	Percent of Total
Wing	0.0053	23.45
Fuselage	0.0063	27.88
Tip tanks	0.0021	9.29
Tip tank fins	0.0001	0.44
Nacelles	0.0012	5.31
Pylons	0.0003	1.33
Horizontal tail	0.0016	7.08
Vertical tail	0.0011	4.86
Interference	0.0031	13.72
Roughness and gap	0.0015	6.64
Total	0.0226	100.00

more like 0.4 or even higher instead of 0.04, as listed in Table 4.4. This would add another 0.06 m^2 (0.63 ft^2) to f.

Another example of a drag breakdown is provided by Reference 4.10. In this case, the airplane is the Gates Learjet Model 25 pictured in Figure 4.27. Table 4.5 was prepared on the basis of Reference 4.10. The authors of the reference chose to base C_d for each item on the wing area. This is therefore the case for Table 4.5, since dimensions and areas for each item were not available. Also, the reference did not include interference or roughness and gap drag in the parasite drag. Why this was done is not clear, and these two items are included in Table 4.5. These two somewhat elusive drag items are estimated to account for 20% of the parasite drag. Although not related to its parasite drag, according to Reference 4.10, this airplane has an Oswald's efficiency factor of 0.66.

TRIM DRAG

Basically, trim drag is not any different from the types of drag already discussed. It arises mainly as the result of having to produce a horizontal tail load in order to balance the airplane around its pitching axis. Thus, any drag increment that can be attributed to a finite lift on the horizontal tail contributes to the trim drag. Such increments mainly represent changes in the induced drag of the tail. To examine this further, we again write that the sum of the lifts developed by the wing and tail must equal the aircraft's weight.

$$L + L_T = W$$

Solving for the wing lift and dividing by qS leads to

$$C_{L_w} = C_L - C_{L_T}\frac{S_T}{S}$$

Here, C_{L_w} is the wing lift coefficient, C_L is the lift coefficient based on the weight and wing area, and C_{L_T} is the horizontal tail lift coefficient. The C_{D_i} of the wing, accounting for the tail lift, thus becomes

$$C_{D_{i_w}} = \frac{C_{L_w}^2}{\pi A e_w}$$

$$\simeq \frac{C_L^2}{\pi A e} - 2\frac{C_L^2}{\pi A e}\frac{C_{L_T}}{C_L}\frac{S_T}{S} \tag{4.38}$$

The term $[C_{L_T}(S_T/S)]^2$ has been dropped as being of higher order. Since $C_L^2/\pi Ae$ is the term normally defined as C_{D_i}, it follows from Equation 4.38 that the increment in the induced drag coefficient contributed by the wing because of trim is

$$\Delta C_{D_i} = -2C_{D_i}\frac{C_{L_T}}{C_L}\frac{S_T}{S} \tag{4.39}$$

The tail itself will have an induced drag given by

$$D_{i_T} = qS_T\frac{C_{L_T}^2}{\pi A_T e_T} \tag{4.40}$$

Expressed in terms of the wing area, this becomes

$$C_{D_{i_T}} = \frac{S_T}{S}\frac{C_L^2}{\pi Ae}\left(\frac{C_{L_T}}{C_L}\right)^2\frac{Ae}{A_T e_T} \tag{4.41}$$

Added to Equation 4.39 the total increment in the induced drag coefficient becomes

$$\Delta C_{D_{\text{trim}}} = \frac{S_T}{S}\frac{C_{L_T}}{C_L}\left(\frac{C_{L_T}Ae}{C_L A_T e_T} - 2\right)C_{D_i} \tag{4.42}$$

In order to gain further insight into the trim drag, consider the simplified configuration shown in Figure 4.28. For the airplane to be in equilibrium, it follows that

$$L_w + L_T = W$$

$$xL_w = (l - x)L_T$$

where l is the distance from the aerodynamic center of the wing to the aerodynamic center of the tail. x is the distance of the center of gravity aft of the wing's aerodynamic center. Solving for L_T gives

$$L_T = \frac{x}{l}W$$

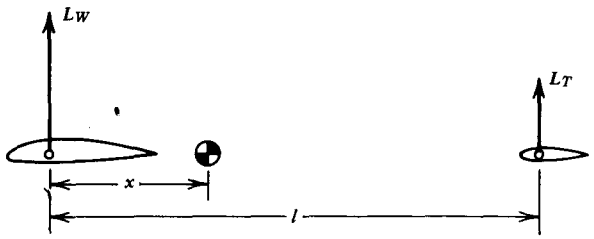

Figure 4.28 Equilibrium of wing and tail lifts.

Thus,

$$\frac{S_T C_{L_T}}{S C_L} = \frac{x}{l} \tag{4.43}$$

Substituting Equation 4.43 into Equation 4.42 leads to

$$\frac{\Delta C_{D_{\text{trim}}}}{C_{D_i}} = \frac{x}{l}\left[\frac{x}{l}\left(\frac{b}{b_T}\right)^2 \frac{e}{e_T} - 2\right] \tag{4.44}$$

The ratio of the wingspan to tailspan is of the order of 3, while e is equal approximately to e_T. With these magnitudes in mind, Figure 4.29 was prepared; it presents the trim drag as a fraction of the original induced drag as influenced by x/l.

Notice that the possibility of a negative trim drag exists for small, positive, center-of-gravity positions. This results from the slight reduction in wing lift, and hence its induced drag, for aft center-of-gravity positions. However, as the center of gravity moves further aft, the induced drag from the tail overrides the saving from the wing so that the net trim drag becomes more positive.

The aerodynamic moment about the airplane's aerodynamic center was neglected in this analysis. By comparison to the moment contributed by the tail, M_{ac} should be small. Qualitatively, the results of Figure 4.29 should be relatively unaffected by the inclusion of M_{ac}.

The trim drag is usually small, amounting to only 1 or 2% of the total drag of an airplane for the cruise condition. Reference 4.10, for example, lists the trim drag for the Learjet Model 25 as being only 1.5% of the total drag for the cruise condition. As another example, consider the Cherokee once again at an indicated airspeed of 135 mph. At its gross weight of 2400 lb, this corresponds to a C_L of 0.322. For this weight the most forward center of gravity allowed by the flight manual is 3% of the chord ahead of the quarter-chord point. With a chord of 63 in. and the distance between the wing and tail aerodynamic center of approximately 13 ft, x/l has a value of -0.012. Since $b \simeq 3b_T$, Figure 4.29 gives

$$\frac{\Delta C_{D_{\text{trim}}}}{C_{D_i}} = 0.028$$

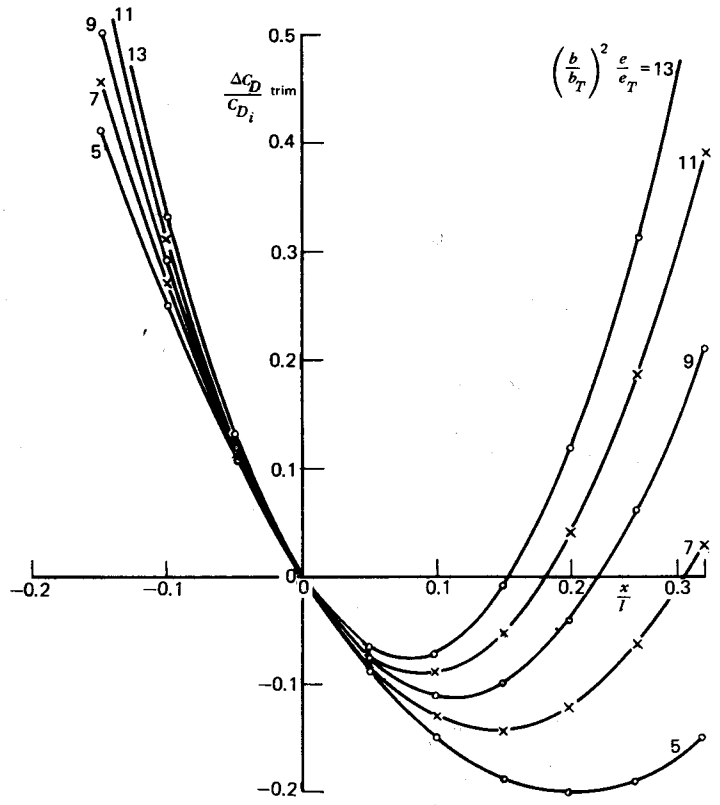

Figure 4.29 Effect of center-of-gravity position on trim drag.

With an effective aspect ratio of approximately 3.38, C_{D_i} will be equal to 0.0098, so that $C_{D_{trim}} = 0.0003$. The parasite drag coefficient is approximately 0.0037, so that the total C_D equals 0.0138. Thus, for the Cherokee in cruise, the trim drag amounts to only 2% of the total drag.

COOLING DRAG

Cylinder heads, oil coolers, and other heat exchangers require a flow of air through them for purposes of cooling. Usually, the source of this cooling air is the free stream, possibly augmented to some extent by a propeller slipstream or bleed air from the compressor section of a turbojet. As the air flows through the baffling, it experiences a loss in total pressure, Δp, thus extracting energy from the flow. At the same time, however, heat is added to

the flow. If the rate at which the heat is being added to the flow is less than the rate at which energy is being extracted from the flow, the energy and momentum flux in the exiting flow after it has expanded to the free-stream ambient pressure will be less than that of the entering flow. The result is a drag force known as cooling drag.

It is a matter of "bookkeeping" as to whether to penalize the airframe or the engine for this drag. Some manufacturers prefer to estimate the net power lost to the flow and subtract this from the engine power. Thus, no drag increment is added to the airplane. Typically, for a piston engine, the engine power is reduced by as much as approximately 6% in order to account for the cooling losses.

Because of the complexity of the internal flow through a typical engine installation, current methods for estimating cooling losses are semiempirical in nature, as exemplified by the Lycoming installation manual (Ref. 4.12). Before considering an example from that manual, let us examine the basic fundamentals of the problem. A cowling installation is schematically pictured in Figure 4.30. Far ahead of the cowling, free-stream conditions exist. Just ahead of the baffle, the flow is slowed so that the static pressure, P_B, and the temperature, T_B, are both higher than their free-stream values. As the flow passes through the baffle, P_B drops by an amount Δp because of the friction in the restricted passages. At the same time, heat is added at the rate Q, which increases T_B by the amount ΔT. The flow then exits with a velocity of V_E and a pressure of P_E, where P_E is determined by the flow external to the cowling. The exit area, A_E, and the pressure, p_E, can both be controlled by the use of cowl flaps, as pictured in Figure 4.31. As the cowl flaps are opened, the amount of cooling flow increases rapidly because of the decreased pressure and the increased area. Downstream of the exit, the flow continues to accelerate (or decelerate) until the free-stream static pressure is reached. Corresponding to this state, the cooling air attains an ultimate velocity denoted by V_∞.

If m represents the mass flow rate through the system, the cooling drag,

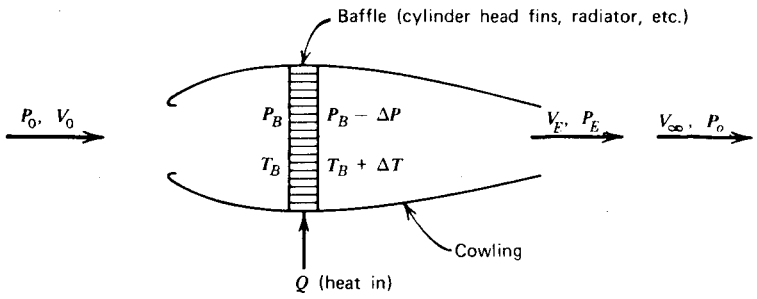

Figure 4.30 Schematic flow through a heat exchanger.

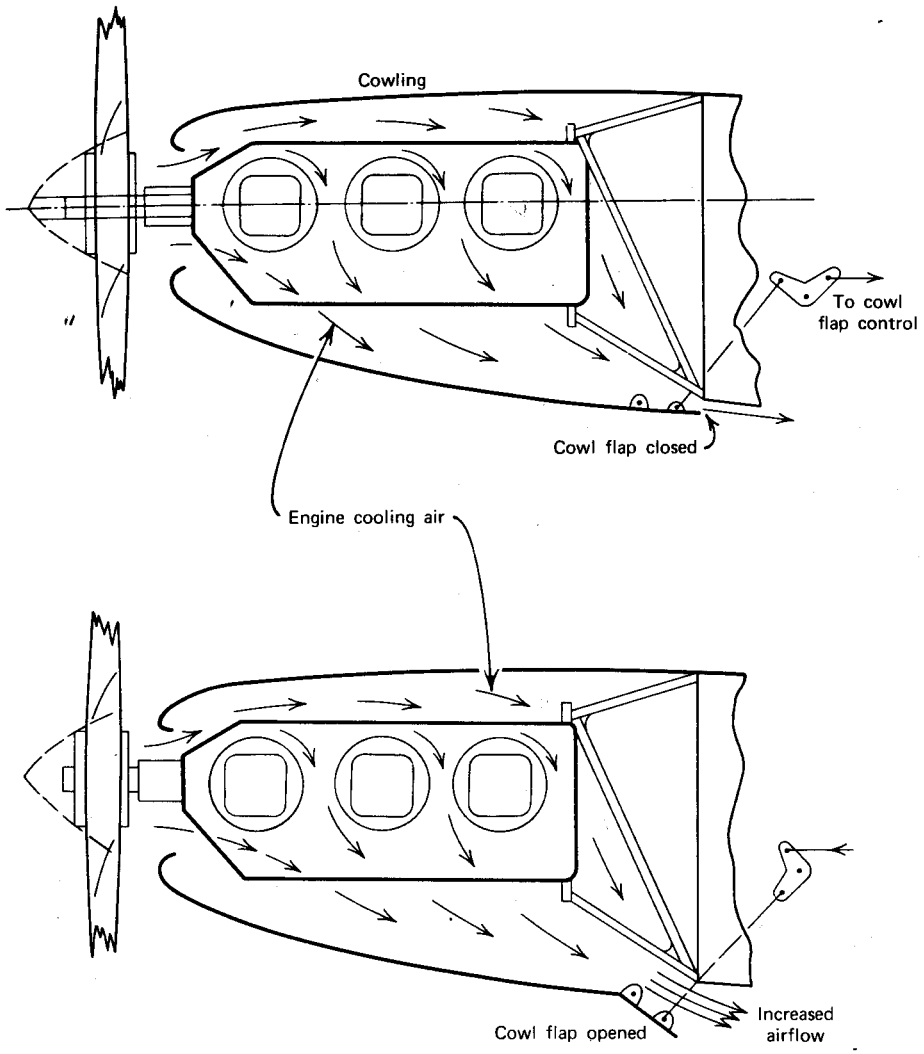

Figure 4.31 The use of cowl flaps to control engine cooling air. (a) Flow of cooling air around an air-cooled engine. (b) Typical cowl flaps on horizontally-opposed engine.

D_c, will be given by the momentum theorem as

$$D_c = \dot{m}(V_0 - V_\infty) \tag{4.45}$$

The rate, ΔW, at which work is extracted from the flow is

$$\Delta W = \tfrac{1}{2}\dot{m}(V_0^2 - V_\infty^2) \tag{4.46}$$

Observe that the cooling drag is obtained by dividing the increment in the

energy by a velocity that is the average between V_0 and V_∞; that is,

$$\Delta W = D_c \left(\frac{V_0 + V_\infty}{2}\right) \tag{4.47}$$

For a fixed-baffle geometry, the pressure drop through the baffle will be proportional to the dynamic pressure ahead of the baffle.

$$\Delta p \propto \tfrac{1}{2}\rho V_B^2 \tag{4.48}$$

V_B can be related to the mass flow, m, through the baffle and an average flow area through the baffle.

$$m = \rho A_B V_B \tag{4.49}$$

Substitution of Equation 4.49 into Equation 4.48 results in

$$\Delta p \propto \frac{m^2}{\rho} \tag{4.50}$$

In the preceding, for a fixed baffle, the fictitious area, A_B, has been absorbed into the constant of proportionality.

The rate at which heat is conducted away from the baffles by the cooling air must depend on the difference between the temperature of the baffles and that of the entering cooling air. For a piston engine, the baffle temperature is the cylinder head temperature (CHT). Denoting the cooling air temperature just ahead of the baffles by T_B, the rate of heat rejection by the engine can be written as

$$Q \propto \text{CHT} - T_B \tag{4.51}$$

In Equations 4.50 and 4.51, the constants of proportionality will depend on the particular engine geometry and power. These constants or appropriate graphs must be obtained from the manufacturer. One is tempted to scale Q in direct proportion to the engine power, P, and to scale A_B with the two-thirds power of the engine power, in which case Equations 4.50 and 4.51 become

$$\Delta p \propto \frac{m^2}{\rho p^{4/3}} \tag{4.52}$$

$$Q \propto (\text{CHT} - T_B)P \tag{4.53}$$

However, these are speculative relationships on my part; they are not substantiated by data and therefore should be used with caution.

If sufficient information is provided by the engine manufacturer to relate Δp, m, and ρ, and to estimate Q for a given temperature difference between CHT and the cooling air, then one is in a position to calculate the cooling drag. The details of this are best illustrated by means of an example given in Reference 4.12. In accordance with the reference, the English system of units will be used for this example.

This example will consider a horizontally opposed engine delivering 340 bhp operating at a 25,000 ft pressure altitude and a true airspeed of 275 mph. The outside air temperature is taken to be 20 °F higher than standard for this altitude, which means an OAT of −10 °F. Lycoming recommends 435 °F as a maximum continuous cylinder head temperature for maximum engine life. This example is to represent a cruise operation with cowl flaps closed. (This does not mean that the exit is closed; see Figure 4.31.) It is therefore assumed that the exit static pressure is equal to the ambient static pressure. Given the foregoing, the problem is to size the area of the exit and to calculate the cooling drag.

The mass density, ρ, can be calculated from the equation of state (Equation 2.1).

$$\rho = \rho_s \frac{T_s}{T}$$

where subscript s refers to standard values. From this, using Figure 2.3,

$$\rho = 0.00102 \text{ slugs/ft}^3$$

The free-stream dynamic pressure, q_0, is thus

$$q_0 = 83 \text{ psf}$$

Neglecting any contribution from the propeller slipstream for the cruise condition, the reference, on the basis of experience, calculates the temperature at the engine face by assuming a 75% recovery of the dynamic pressure with a resulting adiabatic temperature rise. From Equations 2.1 and 2.30,

$$\frac{T}{p^{[(\gamma-1)/\gamma]}} = \text{constant}$$

or

$$T_B = T_0 \left(\frac{p_B}{p_0}\right)^{(\gamma-1)/\gamma}$$

$$= 450 \left[\frac{786.3 + 0.75(83)}{786.3}\right]^{0.286}$$

$$= 460 \text{ °R}$$

Thus, the temperature at the engine face is 0 °F.

With the assumed 25% loss in dynamic pressure resulting from the diffusion by the cowling, the static pressure at the engine face, assuming the flow there to have a negligible velocity, will be

$$p_B = 848 \text{ psf}$$

This corresponds to a pressure altitude of 23,200 ft. Next, Figure 4.32 (provided by the manufacturer), is entered with the cooling air temperature at the

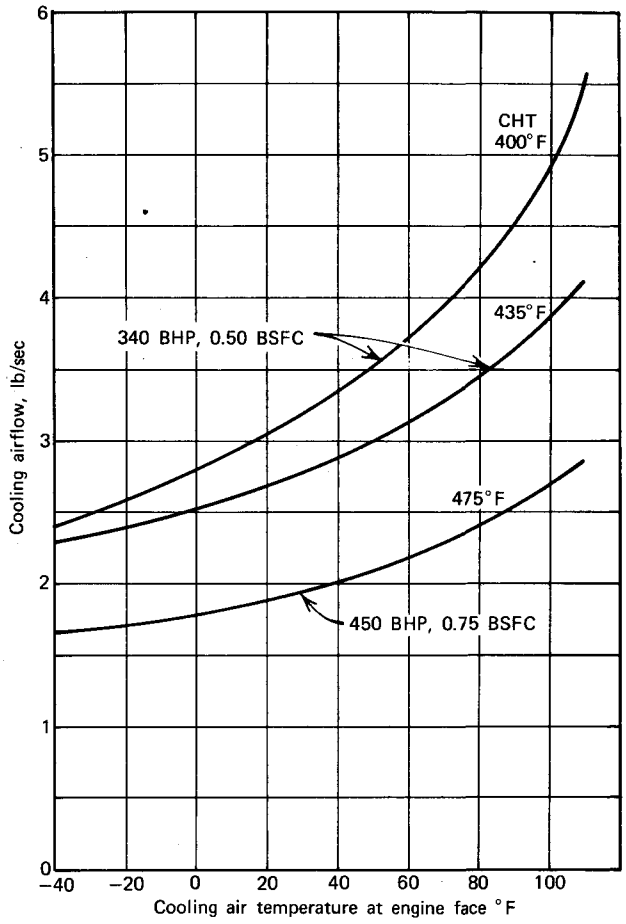

Figure 4.32 Required cooling airflow as a function of cooling air temperature at engine face.

engine face. For a CHT of 435 °F, this figure leads to a required cooling airflow of 2.55 lb/sec.

The baffle pressure drop is determined next from Figure 4.33 (also provided by the manufacturer). It would seem, in accordance with Equation 4.50, that this graph should be in terms of the density altitude instead of the pressure altitude. Nevertheless, it is presented here as taken from Reference 4.12. Entering this graph with an airflow of 2.55 lb/sec at a pressure altitude of 23,200 ft results in a pressure drop of 47 psf. Thus, downstream of the cylinders, the total pressure will be

$$p_B - \Delta p = 801 \text{ psf}$$

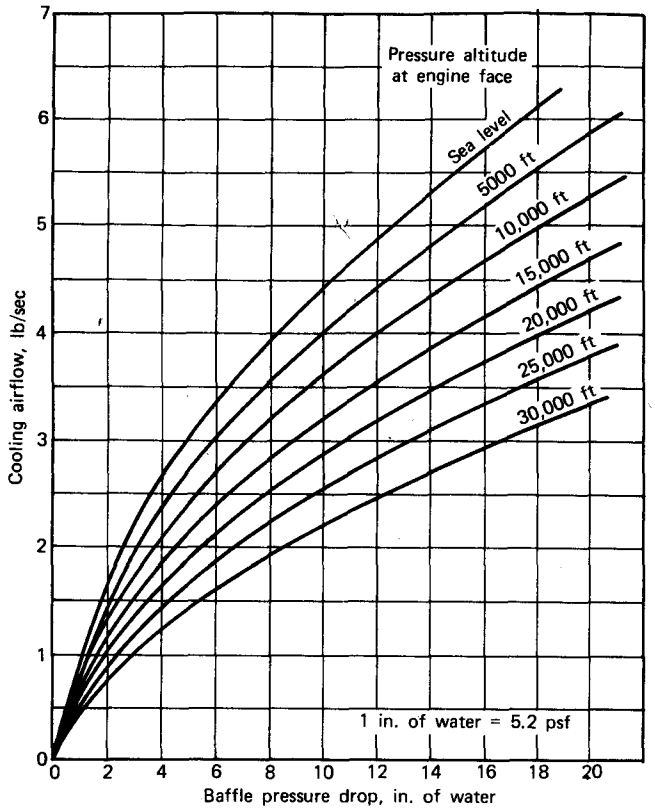

Figure 4.33 Baffle pressure drop as a function of cooling airflow.

Instead of using a heat flow, Q, per se, the reference assumes (presumably based on experience) that the cooling air will experience a temperature rise of approximately 150 °F across the cylinders. For this particular example, this temperature rise can be expressed in terms of Q by using the specific heat at constant pressure.

$$Q = C_p \Delta T m$$

For air $C_p \simeq 6000$ ft/lb/slug/°R. Thus, for the airflow of 2.55 lb/sec,

$$Q = 6000(150)\frac{2.55}{32.2}$$

$$= 71{,}273 \text{ ft-lb/sec}$$

$$= 129.6 \text{ hp}$$

Notice that the above rejected heat amounts to 38% of the engine power. This is close to the 40 to 50% quoted in other sources.

The cooling air density just downstream of the cylinder heads after the temperature rise can be calculated from the equation of state.

$$\rho_B' = \frac{p_B - \Delta p}{RT}$$
$$= \frac{801}{1711(460 + 150)}$$
$$= 0.000767 \text{ slugs/ft}^3$$

This flow is then assumed to expand adiabatically to the ambient static pressure of 786 psf. Thus the density at the exit, from Equation 2.30, is found to be

$$\rho_E = 0.00076 \text{ slugs/ft}^3$$

The corresponding velocity is determined by the use of Equation 2.31.

$$V_E = \left[\frac{2\gamma}{\gamma - 1}\left(\frac{p_B - \Delta p}{\rho_B'} - \frac{p_E}{\rho_E}\right)\right]^{1/2}$$
$$= \left[\frac{2(1.4)}{0.4}\left(\frac{801}{0.000767} - \frac{786}{0.000757}\right)\right]^{1/2}$$
$$= 205 \text{ fps}$$

This velocity, together with the density of the cooling flow at the exit and the required cooling flow, leads to a required exit area of 0.510 ft^2. This number, as well as V_E, differs slightly from Reference 4.12 as the result of calculating the flow state following the addition of heat in a manner somewhat different from the reference.

The resulting cooling drag for this example can be calculated from Equation 4.45.

$$D_c = \frac{2.55}{32.2}(403 - 205)$$
$$= 15.7 \text{ lb}$$

This corresponds to an increment in the flat-plate area of 0.19 ft^2. In terms of engine bhp, assuming a propeller efficiency of 85%, this represents a loss of 10.2 bhp, or 3% of the engine power.

For operating conditions other than cruise, it may be necessary to open the cowl flaps. Reference 4.12 states that a pressure coefficient at the cowl exit as low as -0.5 can be produced by opening the flaps to an angle of approximately 15°. By so doing, a relatively higher cooling flow can be generated at a lower speed, such as during a climb. Even though the engine power may be higher during climb, operating with open cowl flaps and with a richer fuel mixture can hold the CHT down to an acceptable value. Also, CHT values higher than the maximum continuous rating are allowed by the manufacturer for a limited period of time.

It will not be repeated here, but Reference 4.12 also performs a calculation similar to the foregoing but for climb conditions at 19,000 ft pressure altitude, 450 bhp, mixture rich, 130 mph true airspeed, and an OAT of 31 °F. A CHT of 475 °F is allowed with the cowl flaps open to give an exit C_p of -0.5.

For this case, the required airflow is determined to be 1.95 lb/sec with an exit velocity of 73.8 fps. Thus, for this case,

$$D_c = 7.1 \text{ lb}$$
$$f_c = 0.32 \text{ ft}^2$$

The equivalent power loss is only approximately 0.5% of the engine power for this case, even though the increment in equivalent flat-plate area is appreciably higher than that in cruise.

DRAG REDUCTION

Skin friction drag and induced drag are the major contributors to the total drag of an airplane, at least for a modern jet transport. For lower-speed, general aviation aircraft, form drag assumes more relative importance. A typical drag buildup (or breakdown, depending on your outlook) is presented in the bar graph of Figure 4.34 for a jet transport, as reproduced from

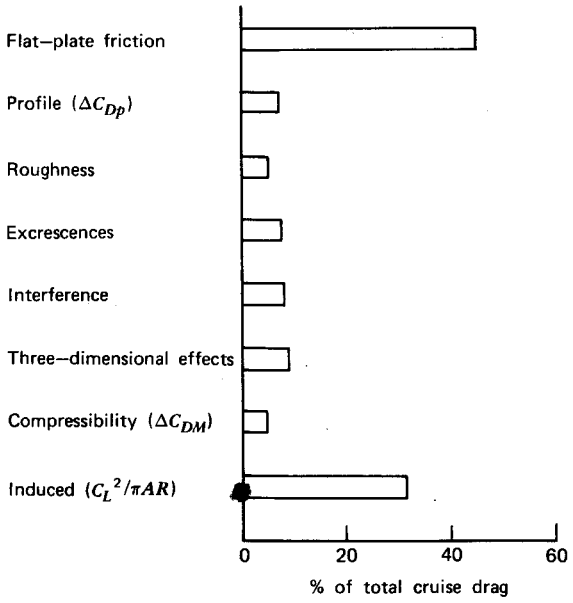

Figure 4.34 Typical drag buildup for jet transport.

Reference 4.11. It is seen that skin friction drag and induced drag account for approximately 75% of the total drag. Although the remaining 25% is not to be taken lightly, the potential for real savings in power or fuel rests with reducing the skin friction drag and induced drag.

Winglets

A recent development that holds some promise for reducing induced drag, short of increasing the aspect ratio, is the so-called winglet. The details of a winglet (studied in Ref. 4.15) are shown in Figure 4.35; Figure 4.36 pictures the winglet mounted on the wing tip of a first-generation jet transport (such as a Boeing 707).

The winglet is reminiscent of the tip plate, which has been tried over the years for the same purpose. These plates have never proven very successful for reasons that will become clear as the details of the winglet design are discussed.

Placing the winglet on an existing wing will alter the spanwise distribution of circulation along the wingspan and hence the structure of its trailing vortex system far downstream. One can calculate the reduction in the induced drag afforded by the winglet solely by reference to the ultimate wake, or so-called Treffetz plane. This is the method used by Reference 4.17 together with a numerical vortex-lattice, lifting-surface theory. Examining only the ultimate wake is not very satisfying, however, from a physical standpoint. Instead, consider the flow field into which the winglet is inserted.

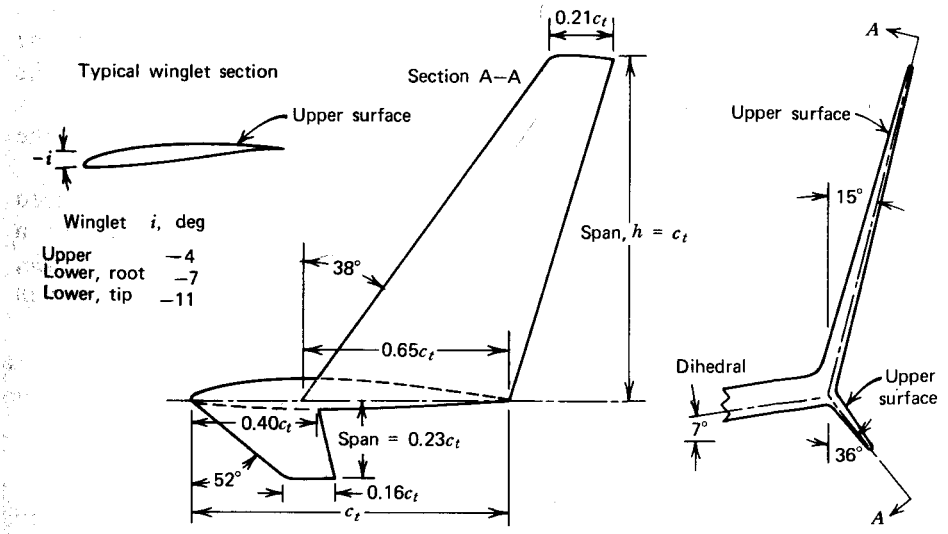

Figure 4.35 Winglet geometry.

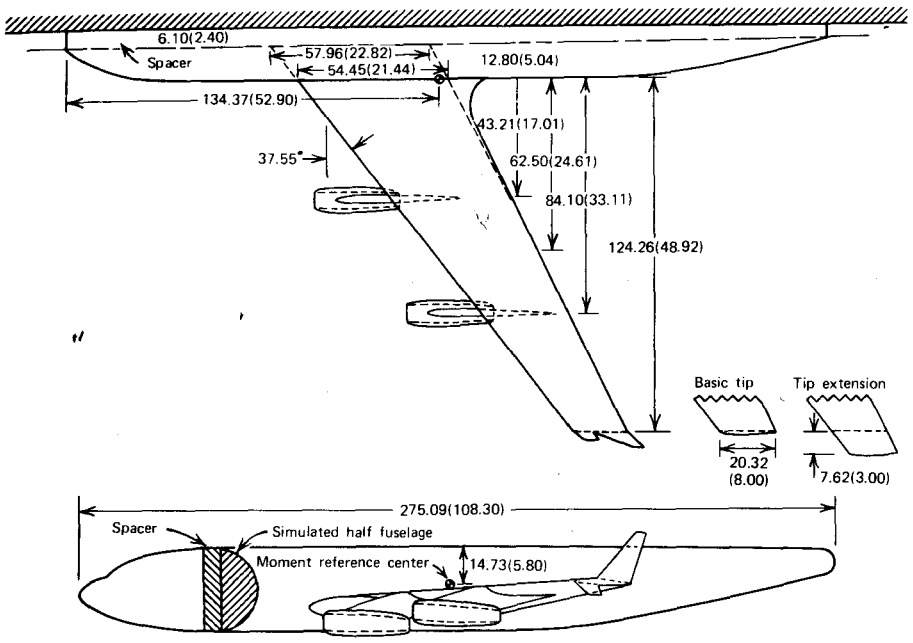

Figure 4.36 NACA model of first-generation jet transport with tip-mounted winglets.

Figure 4.37 qualitatively illustrates the situation. Outboard of the tip, the flow is nearly circular as air from beneath the wing flows outward along the span, around the tip, and inward on the upper surface. The velocities induced by the wing are shown. To these the free-stream velocity is vectorially added. The magnitudes of the induced velocities generally increase toward the tip. At a given spanwise location, the induced velocities are highest close to the surface of the wing, just outside of the boundary layer.

Consider a section of the winglet as shown in Figure 4.37*c*. The induced velocity U_i produced by the main wing combines with the free-stream velocity, V, to produce an angle of attack, α. Assuming α to be a small angle, a net forward component of force, $-dD$, results from the differential section lift and drag on the winglet. Denoting winglet quantities by a subscript w,

$$-dD = dL_w\alpha_w - dD_w$$

Observe that the same result is obtained if the winglet is mounted below the wing, where the induced velocity is outward.

Since we do not know the induced flow in sufficient detail to integrate along the span of the winglet, let us assume an average U_i acting over the

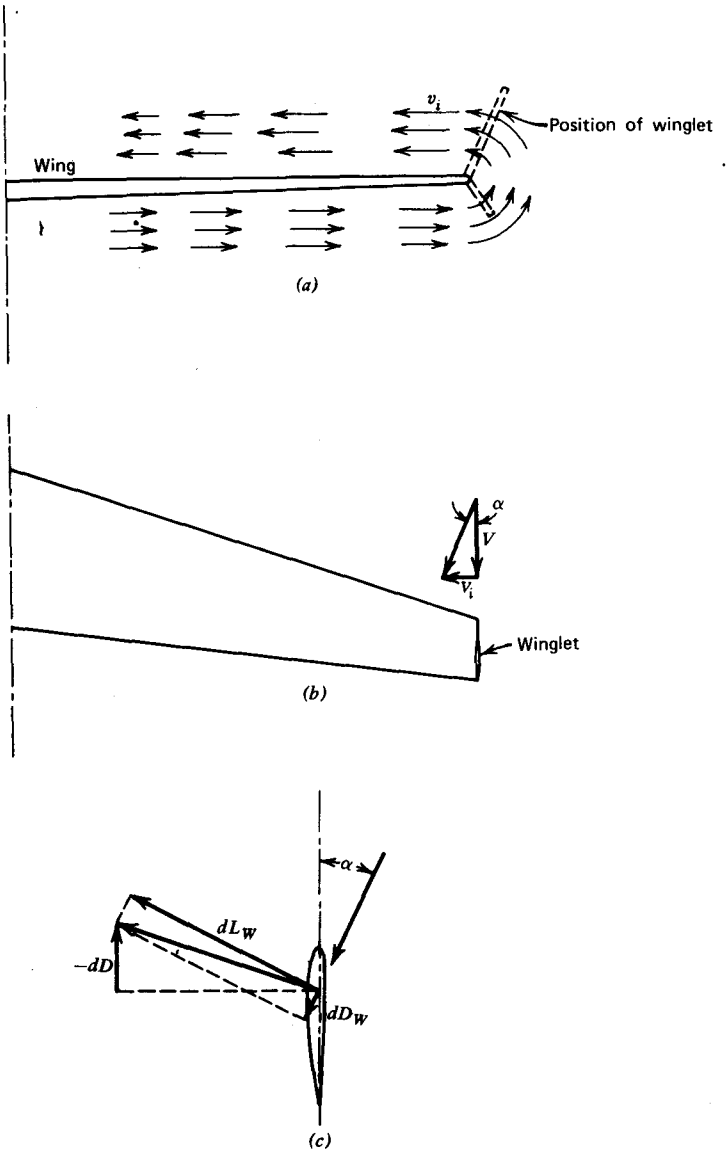

Figure 4.37 Generation of negative drag by winglet section. (a) Looking in direction of flight. (b) Planview. (c) Forces acting on winglet.

winglet for the purpose of disclosing trends. Thus,

$$\Delta D = -L_w\alpha_w + D_w$$

or

$$\Delta C_D = -\frac{S_w}{S}(C_{L_w}\alpha_w + C_{D_w})$$

Let

$$C_{D_w} = C_{D_{0_w}} + \frac{C_{L_w}^2}{\pi A_w}$$

Then

$$\Delta C_D = -\frac{S_w}{S}\left(+C_{L_w}\alpha_w - C_{D_{0_w}} - \frac{C_{L_2}^2}{\pi A_w}\right)$$

The induced angle, α_w, must be proportional to C_L. Therefore let

$$\alpha_w = KC_L$$

Also, approximately,

$$C_{L_w} = 2\pi\frac{A_w}{A_w + 2}\alpha_w$$

Therefore, Δc_d becomes

$$\Delta C_D = -\frac{S_w}{S}\left[2\pi\left(\frac{A_w}{A_w+2}\right)^2 K^2 C_L{}^2 - C_{D_{0_w}}\right] \tag{4.54}$$

This approximate analysis indicates that:

1. The reduction in C_D increases linearly with $C_L{}^2$.
2. At low C_L values, C_D will be increased by the addition of a winglet.
3. High winglet aspect ratios are desirable.

The severe limitations inherent in the assumptions leading to Equation 4.54 must be recognized. For a given value of S_w/S, it would appear that increasing A_w would always result in a greater reduction of C_D. This is not true, since increasing the winglet span will result in a smaller constant of proportionality, K. The same can be said for increasing S_w/S. Despite these limitations, the foregoing discloses the basic elements that are necessary for the design of an effective winglet. Its profile drag (including interference with the wing) must be low. Its aspect ratio should be fairly high to assure a high lift curve slope and low induced drag for the winglet. Not as apparent, the winglet should be mounted as near the trailing edge as possible in order to experience the highest induced velocities possible for a given wing C_L. Also, in this regard, a winglet would be expected to produce a larger decrement in C_D for a wing having a relatively higher loading near its tips.

Figure 4.38 presents experimental measurements of ΔC_D as reported in References 4.15 and 4.16. In the case of the second-generation jet transport

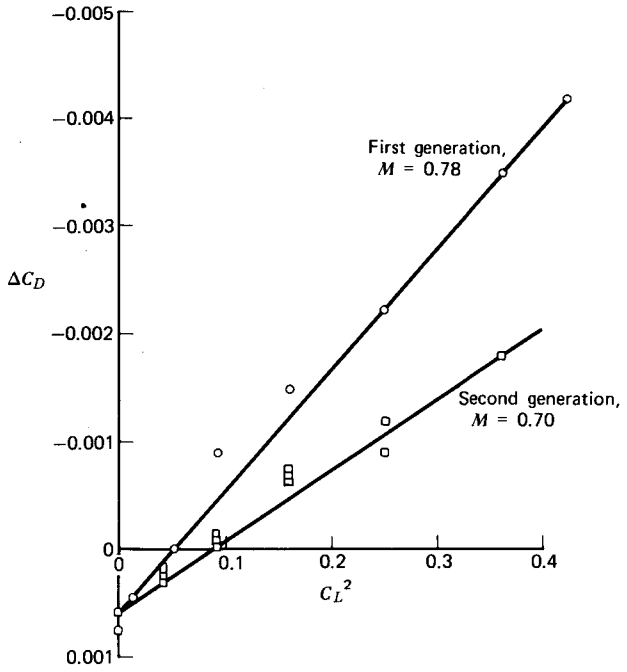

Figure 4.38 Effect of winglets on drag of first and second-generation jet transports.

(such as a DC-10), the loading is relatively lower near the wing tips, so the winglets are less effective. As predicted, ΔC_D is seen to vary nearly linearly with $C_L{}^2$. In the case of the first-generation jet transports, a decrement in C_D is achieved for C_L values greater than 0.22. This number increases to 0.30 for the second-generation jet transports.

The induced drag of a wing can also be reduced simply by extending its tip and thereby increasing its aspect ratio. Reference 4.17 considers this possibility and compares the savings in drag to be gained from extending the tips with those obtained by the use of winglets. Since either method will result in greater root bending moments and hence increased wing structure and weight, both the induced drag and wing root bending moments are treated by the reference. Typical results from this study are presented in Figure 4.39. It is emphasized that these results are from potential flow calculations and thus do not include the profile drag of the winglet or any interference drag. The trends determined by the reference are probably valid but somewhat optimistic with regard to the winglets. For identical increases in bending moment, the winglet can provide a greater reduction in induced drag than can be achieved with a tip extension. Referring to Figure 4.39, the ratio $e_{\text{with}}/e_{\text{without}}$ is simply

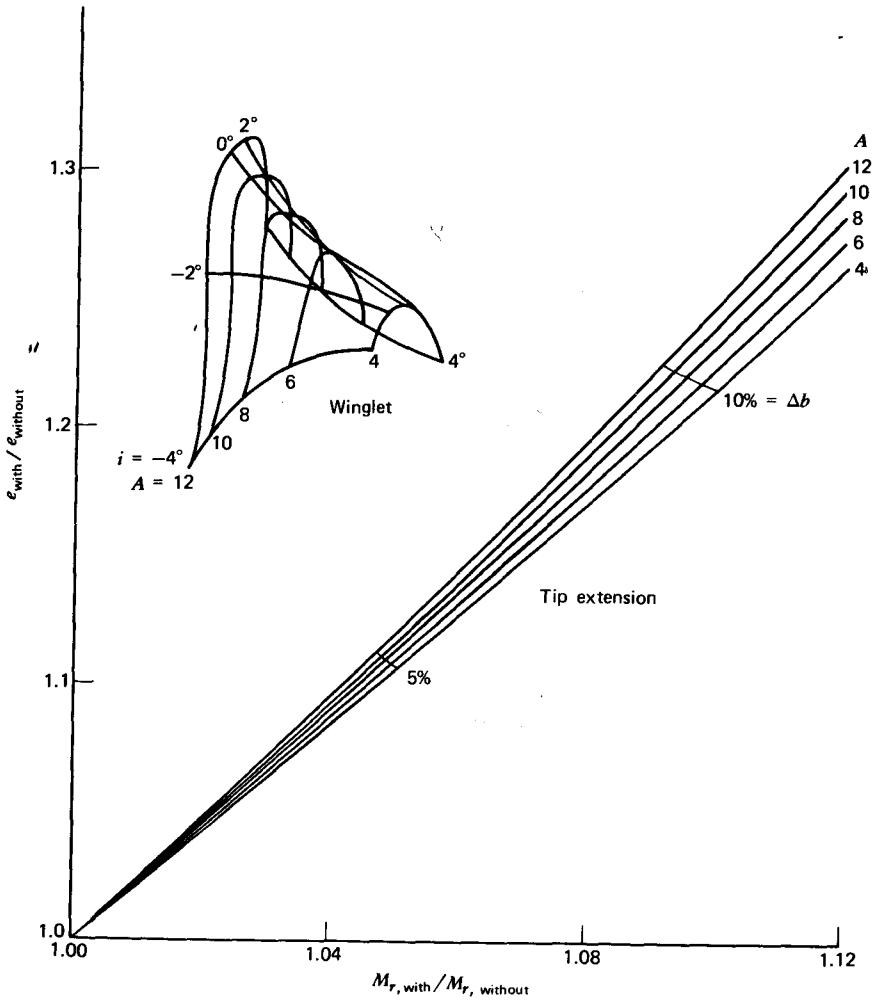

Figure 4.39 Comparison of tip extension and winglet when added to an untwisted wing.

the ratio of the induced drag coefficient of the original wing to the coefficient with a winglet or tip extension. Consider, for example, an untwisted wing with an aspect ratio of 8 and a taper ratio of 0.5. The leading edge, as with all the wing studies in Reference 4.17, is swept back 30°. With a winglet, the induced drag can be reduced by 24% with only a 2.6% increase in bending moment. For the same bending moment increase, extending the tip would save only 6% in the induced drag. To achieve the same reduction in the induced drag with a

tip extension as with the winglet would require a 13% increase in the bending moment.

Reduction of Skin Friction Drag

The contribution to the drag of a streamlined shape from skin friction can be reduced appreciably if transition from laminar to turbulent flow can be delayed. An estimate of the gains to be realized can be seen from Figure 4.40. This figure has been prepared based on Figure 4.1 and the methods outlined earlier for calculating the drag of a flat plate over which the boundary layer is partly laminar and partly turbulent. In this case, the total C_F is calculated from

$$C_F = C_{F_T}(R) - x_t[C_{F_T}(R_t) - C_{F_L}(R_t)] \tag{4.55}$$

In this equation, a subscript T refers to turbulent flow and a subscript L to a laminar flow. R_t is the transition Reynolds number based on the transition length, l_t, shown in Figure 4.40. x_t is the relative distance from the leading edge to the transition point expressed as a fraction of the total length. The notation $C_{F_T}(R_t)$, for example, does not indicate a product but, instead, shows that C_{F_T} is to be evaluated at the Reynolds number R_t.

From Figure 4.40, it is obvious that the skin friction can be reduced significantly if some means can be found to stabilize the laminar layer so as to prevent or delay transition to a turbulent layer. Such a procedure is known as boundary layer control (BLC) or laminar flow control (LFC). BLC is the more

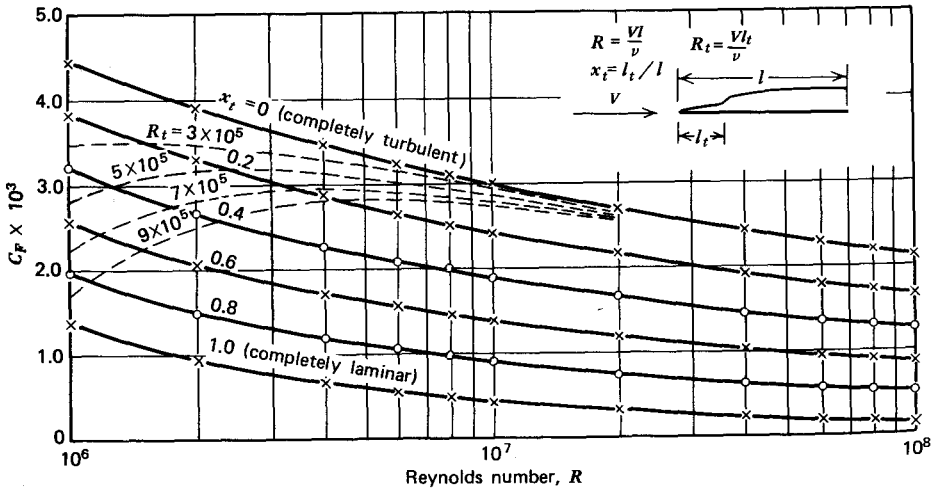

Figure 4.40 Skin friction coefficient for a flat plate as a function of Reynolds number for constant transition lengths.

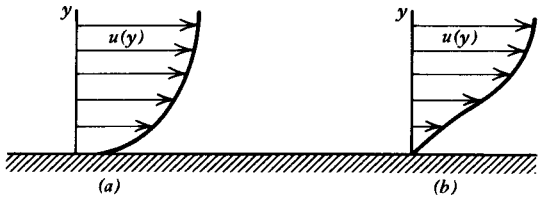

Figure 4.41 Boundary layer velocity profiles. (*a*) Stable velocity profile. (*b*) Less stable velocity profile.

general term and encompasses other purposes such as controlling the boundary layer, laminar or turbulent, in order to delay separation. LFC is therefore preferred when reference is made to stabilizing the laminar boundary layer.

It is not the purpose of this textbook to consider in detail the fluid mechanics involved with stabilizing the laminar layer. Generally, the problem is that of maintaining a boundary layer that is thin with a full velocity profile. This latter statement is clarified in Figure 4.41.

A passive method of maintaining laminar flow is by shape alone. A good example of this is the family of airfoils, the NACA 6-series airfoils discussed briefly in Chapter Three. One of these, the NACA 66_2-015 airfoil, is pictured in Figure 4.42 along with its chordwise pressure distribution. Note that because

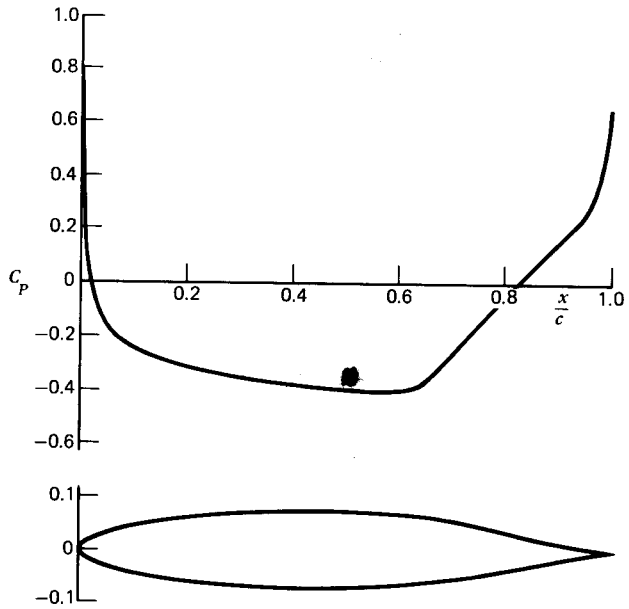

Figure 4.42 Chordwise pressure distribution for the NACA 66_2–015 airfoil.

of its shape, the pressure decreases with distance all the way back to the 65% chord position. This favorable pressure gradient is conducive to maintaining a thin boundary layer with a stable velocity profile. One might assume, as a first estimate, that its transition point is close to the 65% chord position.

For comparison, consider the NACA 0015 airfoil having the same thickness ratio but with its maximum thickness located further forward than the 66_2-015 airfoil. This airfoil, together with its pressure distribution, is shown in Figure 4.43. For this airfoil, one might expect transition to occur at around the 20% chord, where the flow first encounters an adverse pressure gradient.

Both the 66_2-015 and 0015 airfoils lie within the families of airfoils considered in Figure 4.44. For rough surfaces, C_d is approximately the same for both airfoil families. The roughness causes transition in both cases to occur near the leading edge. The picture is different in the case of smooth surfaces. Here C_d equals 0.0064 for the 0015 airfoil but only 0.0036 for the laminar flow airfoil. These correspond to C_f values of approximately 0.0032 and 0.0018 for the respective airfoils. Using Figure 4.40 and the transition points of $0.2C$ and $0.65C$, values of C_f of 0.0026 and 0.0014, respectively, are obtained corresponding to C_d values of 0.0052 and 0.0028. The difference between these values and the experimental results may be attributable to errors in the estimated transition locations. Most likely, however, the difference is attributable to form drag. For both airfoils, the differences are

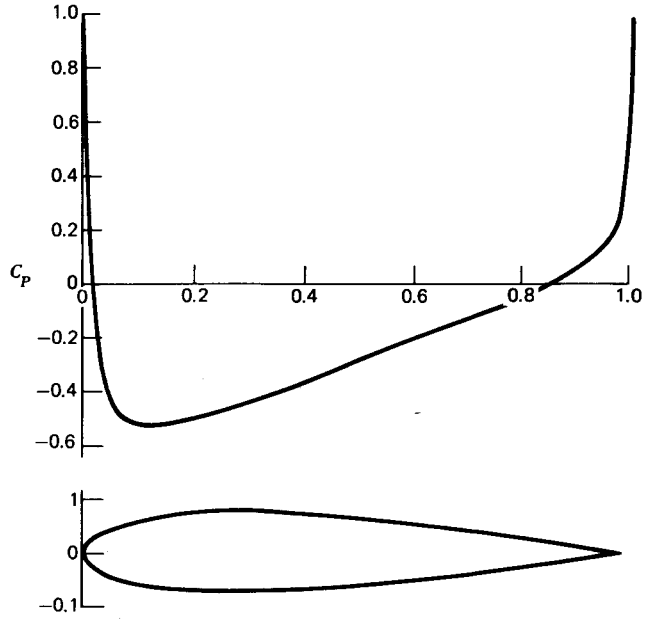

Figure 4.43 Chordwise pressure distribution for the NACA 0015 airfoil.

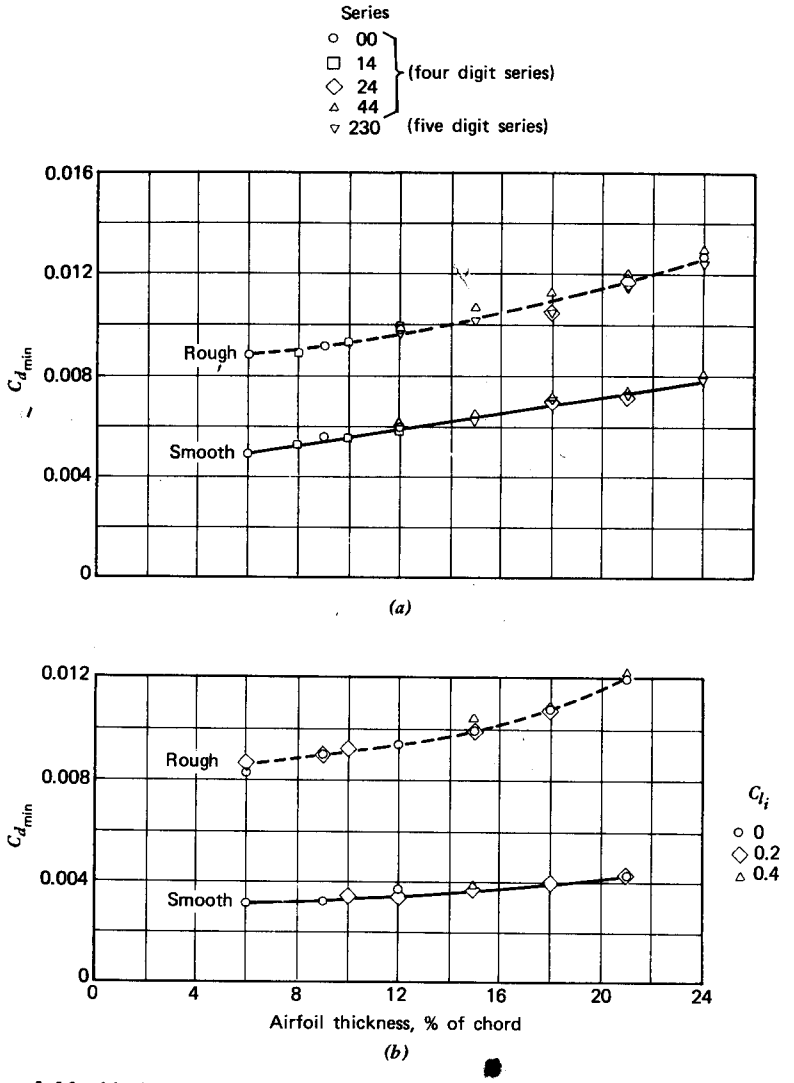

Figure 4.44 Variation of Section $C_{d_{min}}$ with thickness ratio for conventional and laminar flow NACA airfoils. (*a*) NACA four and five-digit series. (*b*) NACA 66-series.

close to the estimates of form drag that one obtains from examining the increase in total C_d with thickness ratio.

The favorable pressure distribution of the series-66 airfoils undoubtedly delays transition, thereby reducing the skin friction drag. For a particular airfoil, however, extensive laminar flow can only be maintained over a limited range of C_l values and for Reynolds numbers that are not too large. The C_d

versus C_l curve, known as the drag polar, for a laminar flow airfoil has the rather unusual shape typified by Figure 4.45 (or earlier by Figure 3.8). This drag bucket results from the fact that for C_l values between approximately + or −0.2, the chordwise pressure distribution is sufficiently favorable to maintain laminar flow over most of the airfoil. Without this "bucket," the drag curve extrapolates to a C_d value at a zero C_l close to that for a more conventional airfoil having this same thickness.

With careful attention to surface waviness and roughness, appreciable laminar flow can be achieved with airfoils up to Reynolds numbers in excess of 20 million, as shown by Figure 4.46 (Ref. 3.1). This same figure emphasizes the importance of surface finish. Unimproved paint is seen to be rough enough to cause premature transition at a Reynolds number of approximately 20×10^6. The result is a doubling in the drag coefficient for this particular airfoil.

One has to be somewhat careful in interpreting this figure. At first glance, it might appear that transition is being significantly delayed up to a Reynolds number of 60×10^6, since the drag coefficient is nearly constant up to this Reynolds number. A closer look shows the C_d to decrease up to an R of approximately 32×10^6. It then increases up until an R of approximately 54×10^6. Above this value of R, it appears that C_d is tending to decrease.

Obviously, from Figure 4.40, a constant C_d as R increases requires that the transition point move forward. This is assuming that the form drag is not dependent on R. This is a valid assumption; if anything, the form C_d tends to decrease with R.

It is difficult to divide the total drag into form and skin friction drag because of the dependence of the skin friction drag on the transition location. However, based on the potential flow pressure distribution, it is reasonable to assume that transition occurs at around the 50% chord point at the lower Reynolds numbers. With this assumption, the same form drag coefficient is obtained at R values of 12×10^6 and 30×10^6, that is, a form C_d, of 0.0013. For the same transition location and form C_d, Figure 4.40 leads to a predicted C_d of 0.0036. This is close to what one might expect if the data for Figure 4.46 *a* are extrapolated beyond an R of 32 million.

Using the form C_d of 0.0013 and Figure 4.40, the peak C_d of 0.0050 at an R of 54×10^6 leads to a transition location at this higher Reynolds number of 18% of the chord. Thus, it is concluded that the shape of the $65_{(421)}$-420 airfoil is able to stabilize the laminar boundary layer up to the midchord point for Reynolds numbers as high as 30 million. For higher Reynolds numbers, the transition point moves progressively forward.

The size of roughness that can be tolerated without causing transition can be estimated from Figure 4.47 (Ref. 3.1). It is somewhat surprising to find that the results do not depend significantly on the chordwise position of the roughness. In fact, it appears that the downstream positions are less tolerant to roughness height than positions near the leading edge.

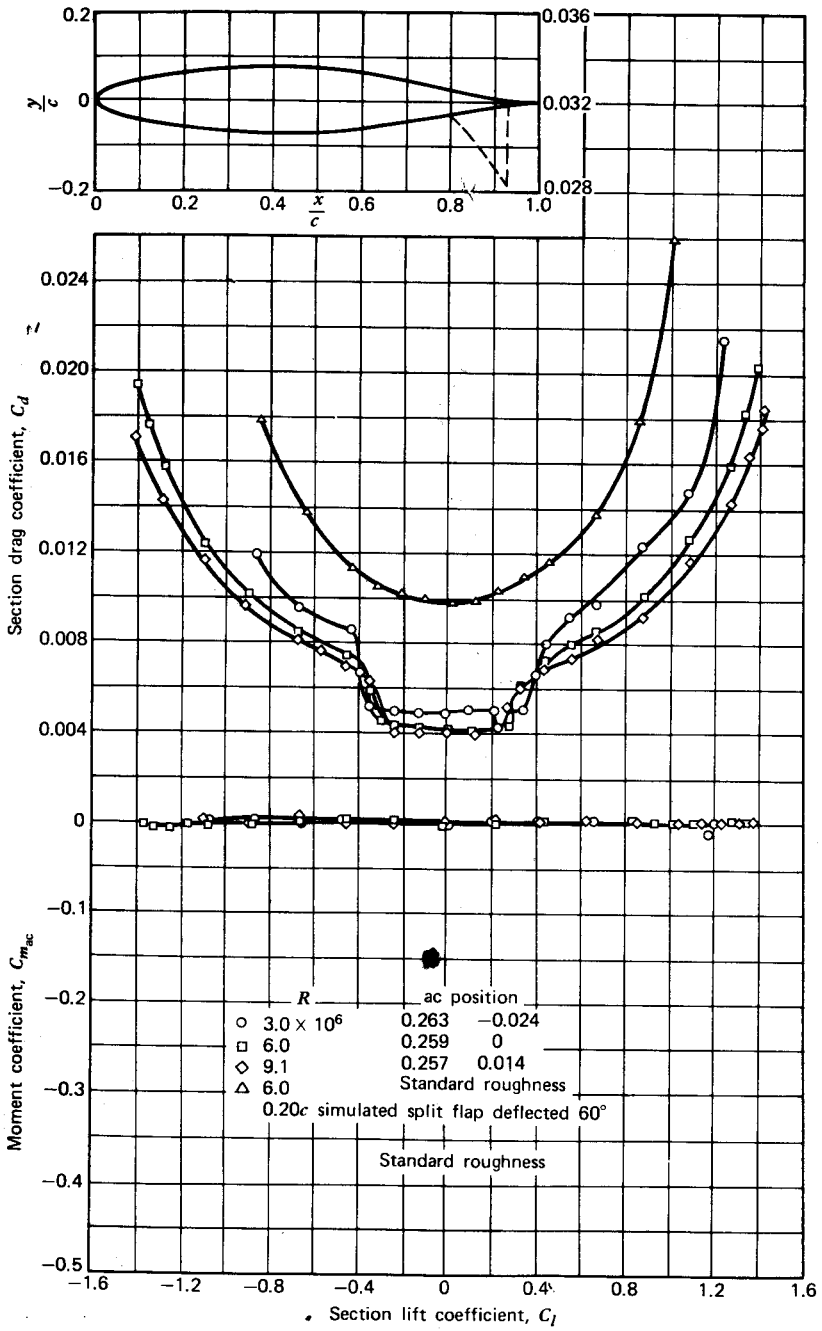

Figure 4.45 Characteristics of the NACA laminar flow 65_2–015 airfoil.

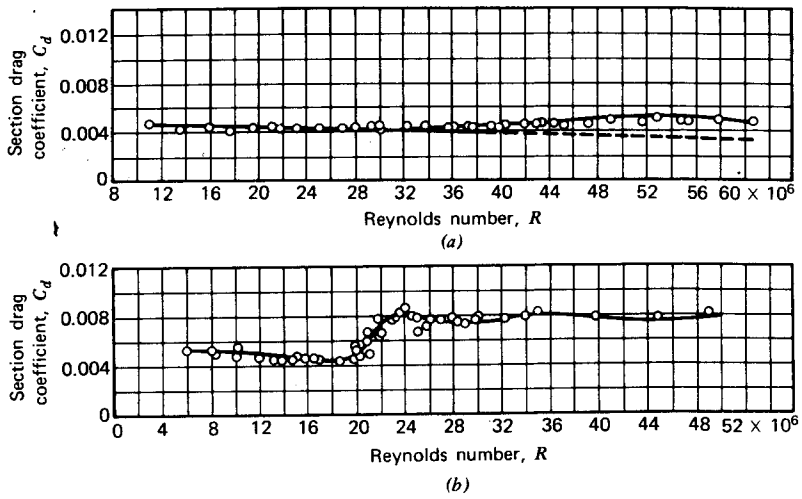

Figure 4.46 Variation of drag coefficient with Reynolds number for a 60 in.-chord model of the NACA $65_{(421)}$–420 airfoil for two surface conditions. (*a*) Smooth condition. (*b*) Lacquer camouflage unimproved after painting.

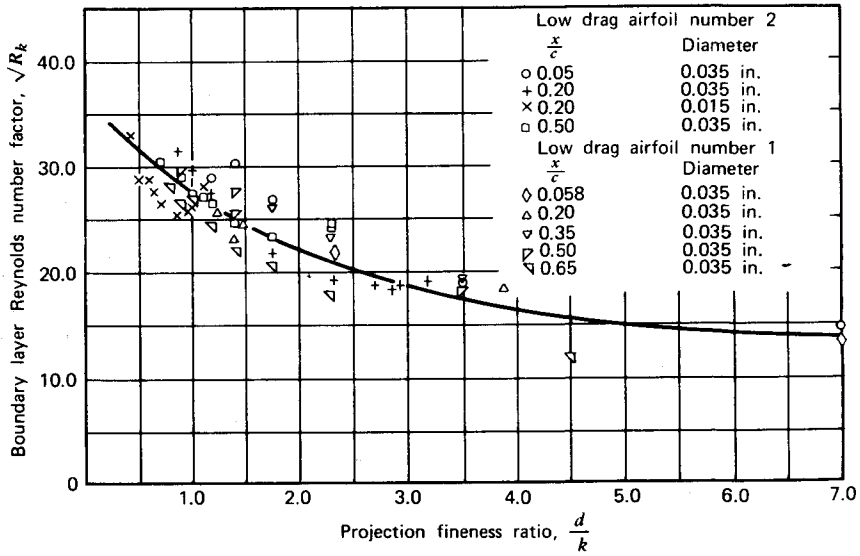

Figure 4.47 Variation of boundary layer Reynolds number with projection fineness ratio for two low drag airfoils. [R_{k_t} = transition Reynolds number based on height (which will cause transition) of protuberance, k, and local velocity outside transition of boundary layer.] (I. H. Abbott and A. E. VonDoenhoff, *Theory of Wing Sections*, Dover Publications, Inc., 1959. Reprinted by permission of Dover Publications, Inc.)

Since one can never be sure of the shape of a particle, based on Figure 4.47, a value of R_{kt} of 1400 is recommended as being reasonable. In the case of Figure 4.46, this criterion leads to a roughness as small as 0.004 in. in height as the cause of the drag rise at an R value of 20 million.

Figure 4.48 is a convenient graph for quickly determining Reynolds numbers at a given speed and altitude. For example, a typical light airplane operating at 10,000 ft at a speed of 150 mph has a unit Reynolds number of 1.1×10^6 or, for a chord of 5.5 ft, a Reynolds number of 6.05×10^6. A jet transport cruising at 35,000 ft at 500 mph has a unit R of 1.8×10^6. This results in an R of 27×10^6 for a chord length of 15 ft.

For the light plane, an R_{kt} of 1400 gives an allowable roughness height of 0.015 in. A height of 0.009 in. or less should not cause transition on the jet transport's wing. These may not be difficult criteria to meet for a wind tunnel model or an isolated panel. On an operational, full-scale aircraft with rivets, access panels, deicers, gas caps, wheel-well covers, and the like, the achievement of this degree of smoothness is a real challenge. Even if such smoothness is attained, a few bugs smashed on the leading edge can easily destroy the aerodynamic cleanliness.

An active method of providing LFC involves removing the boundary layer as it develops so as to keep it thin with a stable velocity profile. This requires that power be expended to apply suction to the boundary layer either through a porous surface or across closely spaced thin slots transverse to the flow, as shown in Figure 4.49. The latter method has received the most attention. One of the earliest investigations of LFC using discrete spanwise slots was reported in Reference 4.18. Here, laminar flow was achieved up to a Reynolds number of 7.0×10^6 on NACA 18-212, 27-215, and 0007-34 airfoils. This result is not very impressive in comparison to Figure 4.46, where transition is apparently delayed up to R values of 30×10^6 for a smooth surface and 20×10^6 for the painted surface. However, the airfoils tested by Reference 4.18 were prior to the series-6 airfoils and had pressure gradients less favorable than the laminar flow series developed later. It was found that, with only a small expenditure of power, the boundary layer could be stabilized over an extensive region having an adverse pressure gradient. Somewhat discouraging was the fact that the use of suction did not reduce the sensitivity of transition to roughness.

Flight testing performed in the mid-1960s provided more encouraging results, as reported in Reference 4.19. Two WB-66 airplanes were modified and redesignated X-21A. These airplanes had 30° swept wings with an aspect ratio of 7. The boundary layer was removed by approximately 120 slots on each surface. The slots varied in width from about 0.0035 to 0.01 in.

Difficulties were encountered with instabilities in the skewed boundary layer along the swept leading edge produced by the spanwise flow. However, the use of fences and chorwise suction slots spaced along the leading edge

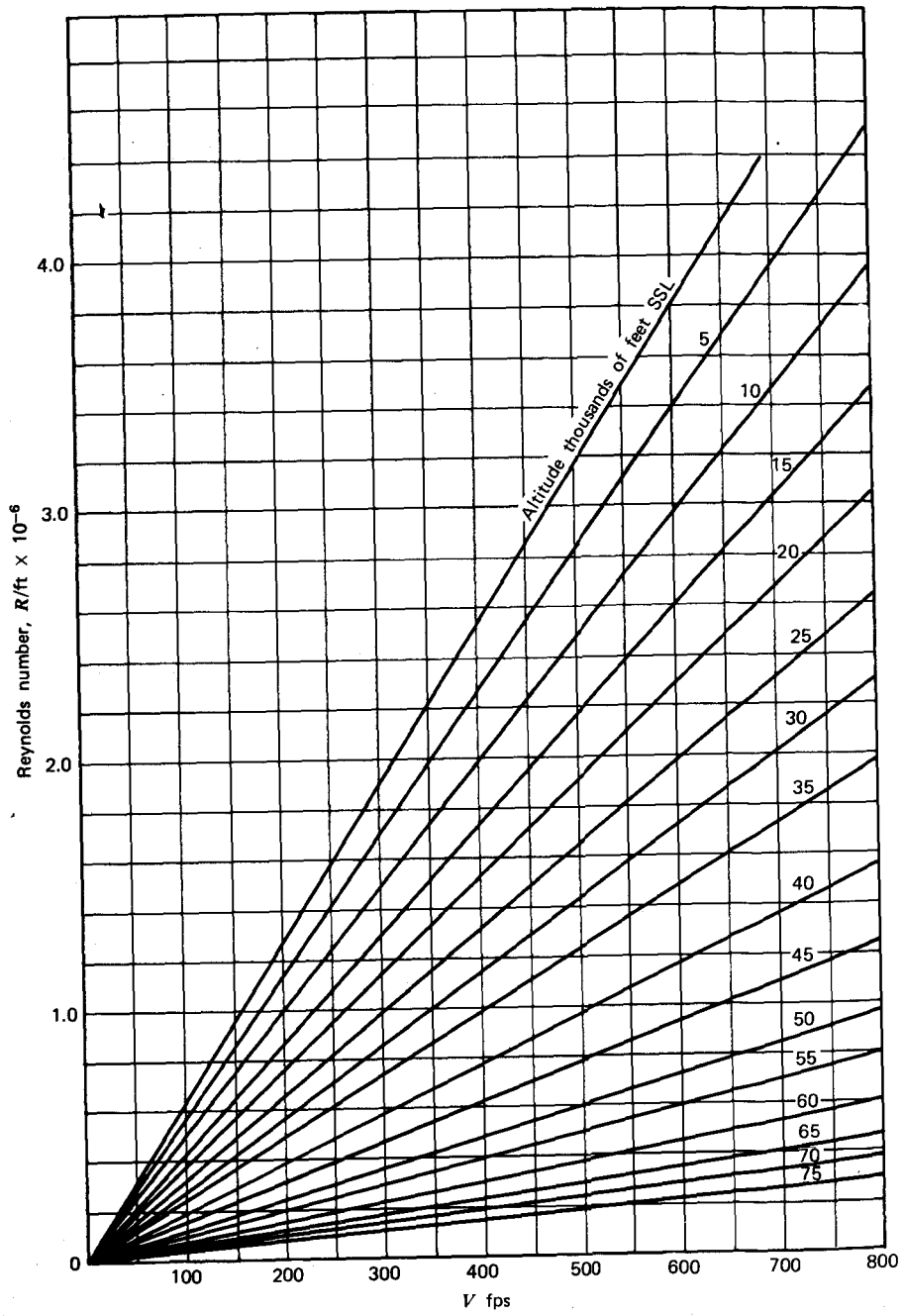

Figure 4.48 Reynolds number as a function of velocity and altitude.

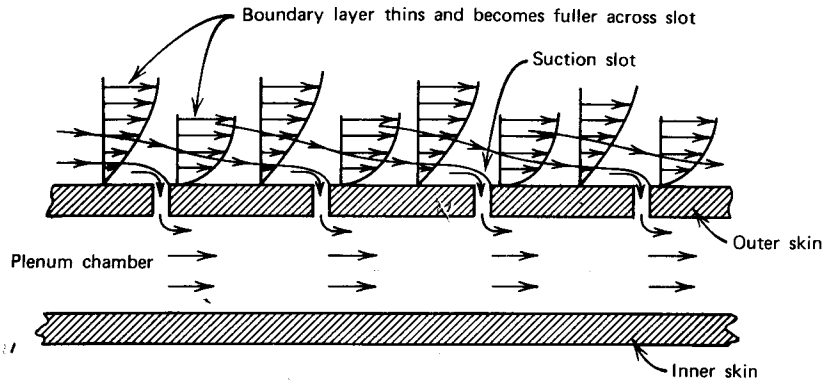

Figure 4.49 Laminar flow control by suction through thin slots transverse to the flow.

alleviated this problem. The final result was the attainment of full-chord laminar flow at a Reynolds number of 45.7×10^6.

The adoption of a powered LFC system represents a challenging exercise in systems analysis and design. The saving in drag must be measured against the weight and initial cost of the ducting, pumps, and double skin required to remove the boundary layer. According to Reference 4.19, performance analyses showed that the required engine size for a jet transport in the 300,000-lb class is smaller than that for the turbulent counterpart. This smaller engine results in a weight saving that offsets the weight penalty of the pumping equipment. With both the inner and outer skins contributing to the

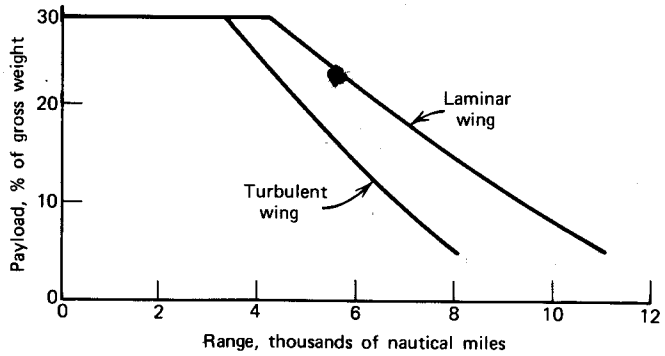

Figure 4.50 Performance gains from laminar flow control. (R. E. Kosin, "Laminar Flow Control by Suction as Applied to X-21A Airplane", AIAA *Journal of Aircraft*, 1965. Reprinted from the *Journal of Aircraft* by permission of the American Institute of Aeronautics and Astronautics.)

wing's structural integrity, the weight of all of the pumping equipment is estimated at between 1.3 and 1.4 psf. Considering the weight, drag, and specific fuel consumption, an optimized design incorporating LFC shows an increase of one-third in the range for a fixed payload or in the payload for a fixed range at a design range of 5000 nmi. These predicted performance gains are shown in Figure 4.50 (taken from Ref. 4.19).

DRAG CLEANUP

Laminar flow control has the potential for achieving significant drag reductions. However, it has yet to be proven on an operational aircraft. Even without LFC, the parasite drag of many of today's aircraft could be significantly reduced by cleaning up many small drag items that are negligible individually but are appreciable collectively.

Figure 4.51, based on full-scale wind tunnel tests, illustrates how the drag of an aircraft can deteriorate as items are added to the airframe. In Figure 4.51*a*, the airplane is shown in the faired and sealed condition. Then, as the

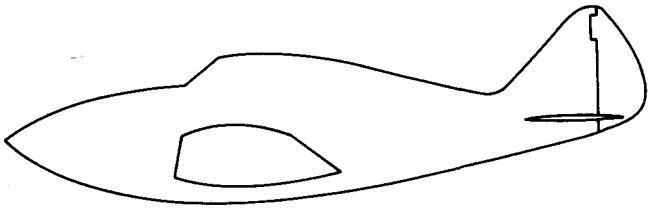

(*a*)

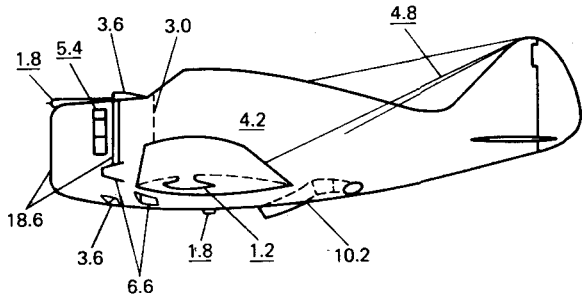

(*b*)

Figure 4.51 Drag penalties for an airplane. (*a*) Airplane in faired and sealed condition. (*b*) Airplane in service condition (numbers indicate drag increments in percent of total drag of clean airplane).

Table 4.6 Drag Items as Shown in Figure 4.51 (Ref. 4.14)

Power plant installation		
Open cowling inlet and exit		18.6%
Unfaired carburetor airscoop		3.6%
Accessory cooling airflow		3.0%
Exhaust stacks and holes		3.6%
Intercooler		6.6%
Oil cooler		10.2%
	Total	45.6%
Other items for service condition		
Remove seals from cowl flaps		5.4%
Opening case and link ejector		1.8%
Opening seals around landing gear doors		1.2%
Sanded walkway		4.2%
Radio aerials		4.8%
Guns and blast tubes		1.8%
	Total	19.2%

items tabulated in Table 4.6 were added, drag increments were measured. These are expressed as a percentage of the original clean airplane drag.

Table 4.6 shows that the drag of the original clean airplane is increased by nearly 65% by the total effect of these drag items. Some of this additional drag is, of course, necessary, but more than half of it is not. Additional tests and analysis of this particular airplane showed that the drag of the power plant items could be reduced to 26.6% of the initial drag.

The moral of the foregoing and other material contained in this chapter is that, with regard to drag, attention should be paid to detail. Surfaces should be smooth and protuberances streamlined or avoided if possible. Tight seals should be provided around wheel wells, door openings, and other cutouts. It is exactly this attention to detail (or lack of it) that explains the wide disparity in the C_F values tabulated in Table 4.2 for airplanes of the same class.

Possibly the ultimate in aerodynamic cleanliness is represented by the latest generation of sailplanes. Employing molded fiberglass or other types of plastics, ultrasmooth surfaces are achieved. Using very high aspect ratios, ranging from 10 to 36, and laminar flow airfoils, mainly of the Wortmann design (Ref. 4.20), lift-to-drag ratios as high as 40 have been accomplished.

TOTAL AIRPLANE DRAG

The foregoing material has considered the separate sources of drag that contribute to the total drag of an airplane. Adding these together, let us now

consider the behaviour of the integrated drag. The total drag can be written as

$$D = q(f + SC_{D_i}) \tag{4.56}$$

or, using Equation 4.32 and the definition of C_L, Equation 4.56 can be written as

$$D = qf + \frac{1}{\pi e}\left(\frac{W}{b}\right)^2 \frac{1}{q} \tag{4.57}$$

In terms of V,

$$D = \frac{\rho f}{2} V^2 + \frac{2}{\rho \pi e}\left(\frac{W}{b}\right)^2 \frac{1}{V^2} \tag{4.58}$$

Thus the drag is composed of two parts: the parasite drag, which varies directly with V^2, and the induced drag, which varies inversely with V^2. The drag has a minimum value when the parasite and induced drag are *equal*. This minimum value is easily determined from Equation 4.58 and is equal to

$$D_{\min} = 2\left(\frac{W}{b}\right)\sqrt{\frac{f}{\pi e}} \tag{4.59}$$

and occurs at a velocity equal to

$$V_{\min} = \left[\frac{4}{\pi e f}\left(\frac{W}{\rho b}\right)^2\right]^{1/4} \tag{4.60}$$

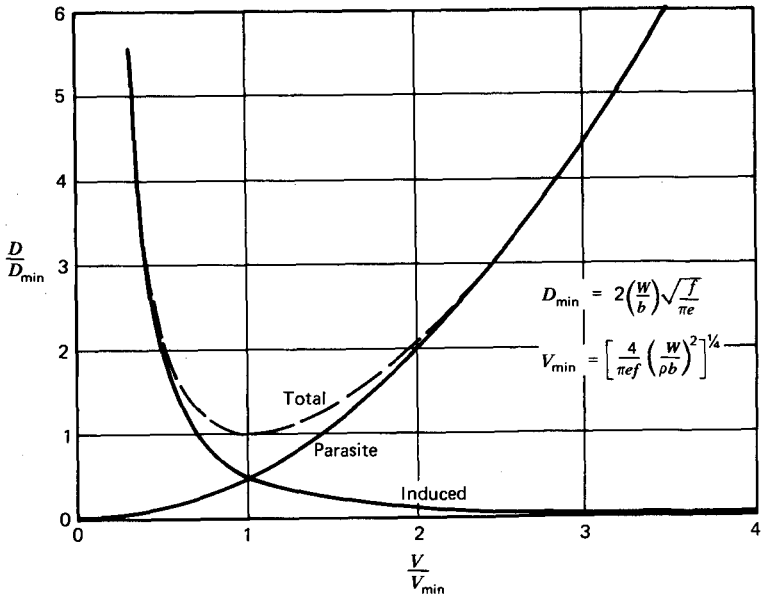

Figure 4.52 Generalized drag curves.

Observe that the minimum drag is independent of density and depends on the span loading instead of the wing loading.

D, D_{min}, and V_{min} can be combined and expressed in a general manner as

$$\left(\frac{D}{D_{min}}\right) = \frac{1}{2}\left(\frac{V}{V_{min}}\right)^2 + \frac{1}{2}\left(\frac{V}{V_{min}}\right)^{-2} \tag{4.61}$$

The first term on the right-hand side of Equation 4.61 represents the parasite drag; the second term is proportional to the induced drag. Both of these terms and the total drag ratio are presented in Figure 4.52.

PROBLEMS

4.1. A flat plate aligned with the flow has a length of 4 m and a width of 10 m. Calculate its skin friction drag at an airspeed of 40 m/s for SSL conditions. Assume a transition Reynolds number of 1×10^6.

4.2. For the plate in Problem 4.1, calculate the displacement thickness 1 m back from the leading edge.

4.3. Estimate the roughness height that would cause premature transition on the plate in Problem 4.1.

4.4. A "turbulence detector" uses a cylinder operating just below its critical Reynolds number. Stimulated by turbulence, its drag drops suddenly. What size cylinder should be used to detect turbulence in an airflow having a velocity of 120 mph, SSL conditions?

4.5. The preliminary design of a light, twin-engine, propeller-driven airplane is being undertaken. It will have a rectangular wing with an aspect ratio of 7, a wing loading of 960 Pa, and a gross weight of 17,800 N. Assuming a relatively clean airplane, estimate its drag at a speed of 90 m/s.

4.6. An airplane has four flap hinge brackets. Each bracket projects vertically below the wing a distance of 5 cm and is 0.6 cm thick, as shown.

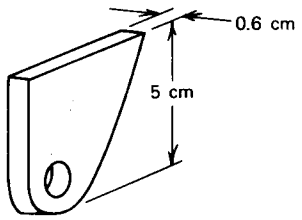

How many drag counts do these brackets add if the wing area is 18.6 m^2?

4.7. A low-wing airplane has an equivalent flat-plate area of 8 ft^2, a wing loading of 20 psf, an aspect ratio of 7.0, and a gross weight of 5000 lb.

Calculate its minimum drag and corresponding speed at SSL and 10,000 ft altitude.

4.8. A long, round cylinder has a diameter of 2.5 cm. Calculate the drag saved per meter of length at a velocity of 250 m/s, SSL, if a streamlined fairing is wrapped around this cylinder.

4.9. Choose an airplane whose geometry, weight, installed power, and performance you know. Estimate its drag, and hence the power required, as a function of V. Then compare your estimate of maximum rate of climb and V_{max} (level flight) with quoted performance.

4.10. Check the cooling drag example for the climb at 19,000-ft pressure altitude, 450 bph, mixture rich, 130 mph TAS, and an OAT of 31°F. Allowing a CHT of 475 °F with a cowl exit C_p of -0.5, show the cooling drag to be 7.1 lb.

REFERENCES

4.1. Keuthe, A. M., and Chow, C., *Foundations of Aerodynamics*, 3rd ed., John Wiley, New York, 1976.

4.2. Oswald, W. Bailey, *General Formulas and Charts for the Calculation of Airplane Performance*, NACA 408, 1933.

4.3. Raspet, August, "Application of Sailplane Performance Analysis to Airplanes," *Aeronautical Engineering Review, 13*(8), August 1954.

4.4. Hoerner, S. R., *Fluid-Dynamic Drag*, published by the author, Midland Park, N.J., 1965.

4.5. Delany, N. K., and Sorensen, N. E., *Low-Speed Drag of Cylinders of Various Shapes*, NACA TN 3038, November 1953.

4.6. Teper, G. L., *Aircraft Stability and Control Data*, NASA CR-96008, April 1969.

4.7. Heffley, R. K., and Jewell, W. F., *Aircraft Handling Qualities Data*, NASA CR-2144, December 1972.

4.8. Keys, C., and Wiesner, R., "Guidelines for Reducing Helicopter Parasite Drag," *J. of the American Helicopter Society, 20*(1), January 1975.

4.9. Roskam, Jan, *Methods for Estimating Drag Polars of Subsonic Airplanes*, published by the author, University of Kansas, 1971.

4.10. Ross, Richard, and Neal. R, D., "Learjet Model 25 Drag Analysis," a paper in *Proceedings of the NASA-Industry-University General Aviation Drag Reduction Workshop*, edited by Jan Roskam, Lawrence, Ka., July 14–16, 1975.

4.11. Anderson, A. A., "General Overview of Drag," a paper in *Proceedings of the NASA-Industry-University General Aviation Drag Reduction Workshop*, edited by Jan Roskam, Lawrence, Ka., July 14–16, 1975.

4.12. Anonymous, *Installation Design for Engine Cooling*, Avco Lycoming Division, Avco Corporation, an in-house manual available from Lycoming on request

4.13. Fraas, A. P., *Aircraft Power Plants*, McGraw-Hill, New York, 1943.

4.14. McKinney, M. O., "Summary of Drag Clean-Up Tests in NASA Langley Full-Scale Tunnel," a paper in *Proceedings of the NASA-Industry-University General Aviation Drag Reduction Workshop*, edited by Jan Roskam, Lawrence, Ka., July 14–16, 1975.

4.15. Whitcomb, R. T., *A Design Approach and Selected Wind-Tunnel Results at High Subsonic Speeds for Wing-Tip Mounted Winglets*, NASA TN D-D-8260, July 1976.

4.16. Flechner, S. G., Jacobs, P. F., and Whitcomb, R. T., *A High Subsonic Speed Wind-Tunnel Investigation of Winglets on a Representative Second-Generation Jet Transport Wing*, NASA TN D-8264, November 1976.

4.17. Heyson, H. H., Riebe, G. D., and Fulton, C. L., *Theoretical Parametric Study of the Relative Advantages of Winglets and Wing-Tip Extensions*, NASA Technical Paper 1020, September 1977.

4.18. Loftin, J. K., and Burrows, D. L., *Investigations Relating to the Extension of Laminar Flow by Means of Boundary-Layer Suction Through Slots*, NACA TN 1961, October 1949.

4.19. Kosin, R. E., "Laminar Flow Control by Suction as Applied to the X-21A Airplane," *J. Aircraft*, *2*(5), September–October 1965.

4.20. McMasters, John H., and Palmer, G. M., "Possible Applications of Soaring Technology to Drag Reduction in Powered General Aviation Aircraft", a paper in *Proceedings of the NASA-Industry-University General Aviation Drag Reduction Workshop*, edited by Jan Roskam, Lawrence, Ka., July 14–16, 1975.

FIVE
LIFT AND DRAG AT HIGH MACH NUMBERS

The preceding material on lift and drag was limited primarily to incompressible flows, that is, to Mach numbers less than approximately 0.4. Compressibility becomes more and more important as the Mach number increases. In the vicinity of a Mach number of unity, airfoils and wings undergo a radical change in their behavior. It is not too surprising, therefore, to find that the equations covering the flow of air undergo a similar change at around $M_\infty = 1.0$.

Many textbooks are devoted entirely to the subject of compressible flows. References 5.1 and 5.2 are two such examples. Here, the several equations and techniques for the study of gas dynamics are developed in considerable detail. An excellent, lucid, qualitative explanation of compressibility effects on wings and airfoils is found in Reference 5.3.

QUALITATIVE BEHAVIOR OF AIRFOILS AS A FUNCTION OF MACH NUMBER

We will consider three regimes of flow around an airfoil. In the first, the flow is everywhere subsonic with a relatively high Mach number. The second regime is referred to as transonic flow. Here the free-stream Mach number is less than unity, but sufficiently high so that the flow locally, as it accelerates over the airfoil, exceeds the local speed of sound; that is, locally the flow becomes supersonic. The lowest free-stream Mach number at which the local flow at some point on the airfoil becomes supersonic is known as the critical Mach number. The third regime is the supersonic flow regime, in which the free-stream Mach number exceeds unity. Even here, a small region of subsonic flow may exist near the leading edge of the airfoil immediately behind a shock wave depending on the bluntness of the leading edge. The sharper the leading edge, the smaller is the extent of the subsonic flow region.

FIVE
LIFT AND DRAG AT HIGH MACH NUMBERS

The preceding material on lift and drag was limited primarily to incompressible flows, that is, to Mach numbers less than approximately 0.4. Compressibility becomes more and more important as the Mach number increases. In the vicinity of a Mach number of unity, airfoils and wings undergo a radical change in their behavior. It is not too surprising, therefore, to find that the equations covering the flow of air undergo a similar change at around $M_\infty = 1.0$.

Many textbooks are devoted entirely to the subject of compressible flows. References 5.1 and 5.2 are two such examples. Here, the several equations and techniques for the study of gas dynamics are developed in considerable detail. An excellent, lucid, qualitative explanation of compressibility effects on wings and airfoils is found in Reference 5.3.

QUALITATIVE BEHAVIOR OF AIRFOILS AS A FUNCTION OF MACH NUMBER

We will consider three regimes of flow around an airfoil. In the first, the flow is everywhere subsonic with a relatively high Mach number. The second regime is referred to as transonic flow. Here the free-stream Mach number is less than unity, but sufficiently high so that the flow locally, as it accelerates over the airfoil, exceeds the local speed of sound; that is, locally the flow becomes supersonic. The lowest free-stream Mach number at which the local flow at some point on the airfoil becomes supersonic is known as the critical Mach number. The third regime is the supersonic flow regime, in which the free-stream Mach number exceeds unity. Even here, a small region of subsonic flow may exist near the leading edge of the airfoil immediately behind a shock wave depending on the bluntness of the leading edge. The sharper the leading edge, the smaller is the extent of the subsonic flow region.

Subsonic Flow at High Mach Numbers

Since weak pressure disturbances propagate at the speed of sound, the time that a fluid particle ahead of a moving body is influenced by the pressure field around the body is proportional to the difference between the acoustic velocity, a, and the speed of the body, V. As V increases to a (i.e., as M_∞ approaches unity), the fluid is displaced less and less ahead of the body. Thus the streamline pattern around an airfoil and hence its pressure distribution can be expected to change with M_∞, even though the flow is subsonic everywhere.

As long as the flow remains entirely subsonic, the effect of M_∞ on airfoil characteristics can be estimated by the use of a factor, β, where β is defined as

$$\beta = \sqrt{1 - M_\infty^2} \tag{5.1}$$

β is known as the Prandtl-Glauert compressibility correction factor.

In a later, more complete treatment of β, it will be noted that the local pressure coefficient at a given point on an airfoil in subsonic compressible flow, C_{p_c}, is related to the pressure coefficient in incompressible flow, C_{p_i}, by

$$C_{p_c} = \frac{C_{p_i}}{\beta} \tag{5.2}$$

It can easily be shown that

$$C_l = \int_0^1 (C_{p_l} - C_{p_u})\, dx \tag{5.3}$$

and

$$C_{m_{l_e}} = -\int_0^1 x(C_{p_l} - C_{p_u})\, dx \tag{5.4}$$

where x is the dimensionless distance along the airfoil chord and the subscripts l and u refer to lower and upper surfaces, respectively. Thus, it follows from Equations 5.2, 5.3, and 5.4 that the lift and moment coefficients for compressible flow are related to those for incompressible flow in a manner similar to Equation 5.2.

$$C_{l_c} = \frac{C_{l_i}}{\beta} \tag{5.5}$$

$$C_{M_c} = \frac{C_{M_i}}{\beta} \tag{5.6}$$

Notice from the use of Equations 3.11 and 3.12 that neither the center of pressure, X_{cp}, nor the location of the aerodynamic center, X_{ac}, varies with Mach number in the purely subsonic regime.

Obviously, the lift curve slope, C_{l_α}, also obeys Equation 5.5.

$$C_{l_{\alpha_c}} = \frac{C_{l_{\alpha_i}}}{\beta} \tag{5.7}$$

This relationship is presented graphically in Figure 5.1 together with the corresponding supersonic relationship, which will be discussed later. However, it must be used with caution. First, the theoretical basis on which it rests is valid only for Mach numbers less than critical. Second, by comparison with experiment, the ratio C_{l_c}/C_{l_i} is overestimated by Equation 5.5 in some cases and underestimated for others, depending on the airfoil geometry.

Reference 5.4 presents data on nine different airfoils at Mach numbers up to 1.0. These airfoils vary in thickness, design lift coefficient, and thickness distribution; they are illustrated in Figure 5.2. Pressure distribution measurements were made in order to determine lift and pitching moment, and wake surveys were taken for determination of drag. Unfortunately, it is difficult to generalize on the data, and they are too voluminous to present here. A sample of the data is presented in Figure 5.3 for the 64A009 airfoil (taken from Ref. 5.4). The normal force coefficient, C_n, is defined as the force normal to the chord line (obtained by integrating the normal pressure around the airfoil contour) divided by the product of the free-stream dynamic

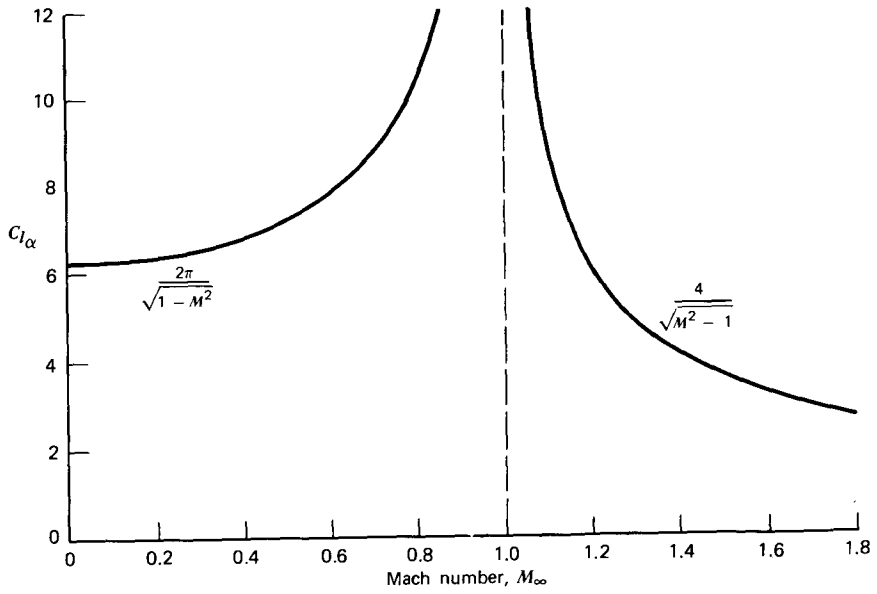

Figure 5.1 Theoretical lift curve slope as a function of free-stream Mach number.

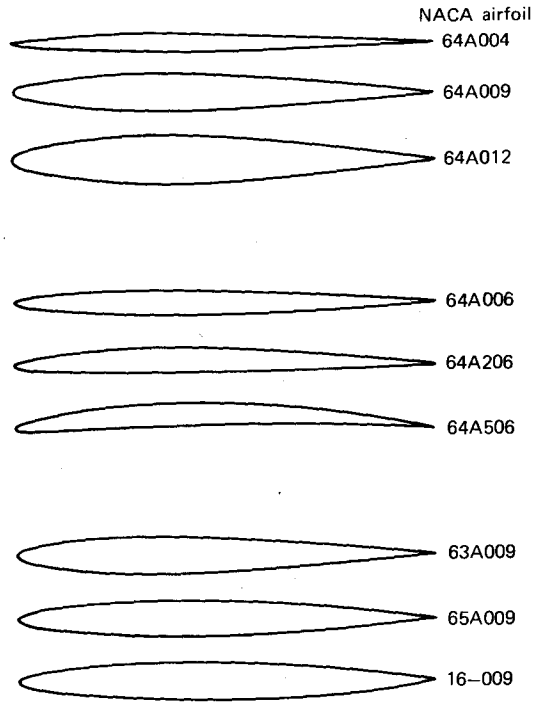

Figure 5.2 Airfoil profiles.

pressure and the airfoil chord. C_d is the usual drag coefficient and is composed of the skin friction drag and the component of C_n in the drag direction. The lift coefficient is slightly less than C_n and can be obtained from

$$C_l = C_n \cos \alpha \tag{5.8}$$

Estimated critical Mach numbers are indicated by arrows in Figure 5.3 and were obtained from calculated graphs found in Reference 3.13. An example of such a graph is presented in Figure 5.4*a* and 5.4*b*. The results of Figure 5.4*a* apply approximately to the airfoils of Figure 5.3 and were used to obtain the M_{cr} values shown there. The 64Axxx airfoils are similar to the 64-xxx airfoils except that the rear portion of the 64Axxx airfoils are less curved than the corresponding surfaces of the 64-xxx airfoils.

Observe that the thinner symmetrical airfoils, as one might guess, have the higher critical Mach numbers at a C_l of zero. However, the rate at which M_{cr} decreases with C_l is greater for the thinner airfoils. Thus, the thicker airfoils become relatively more favorable as C_l increases. As shown in Figure 5.4*b*, camber results in shifting the peak M_{cr} to the right. As a function of

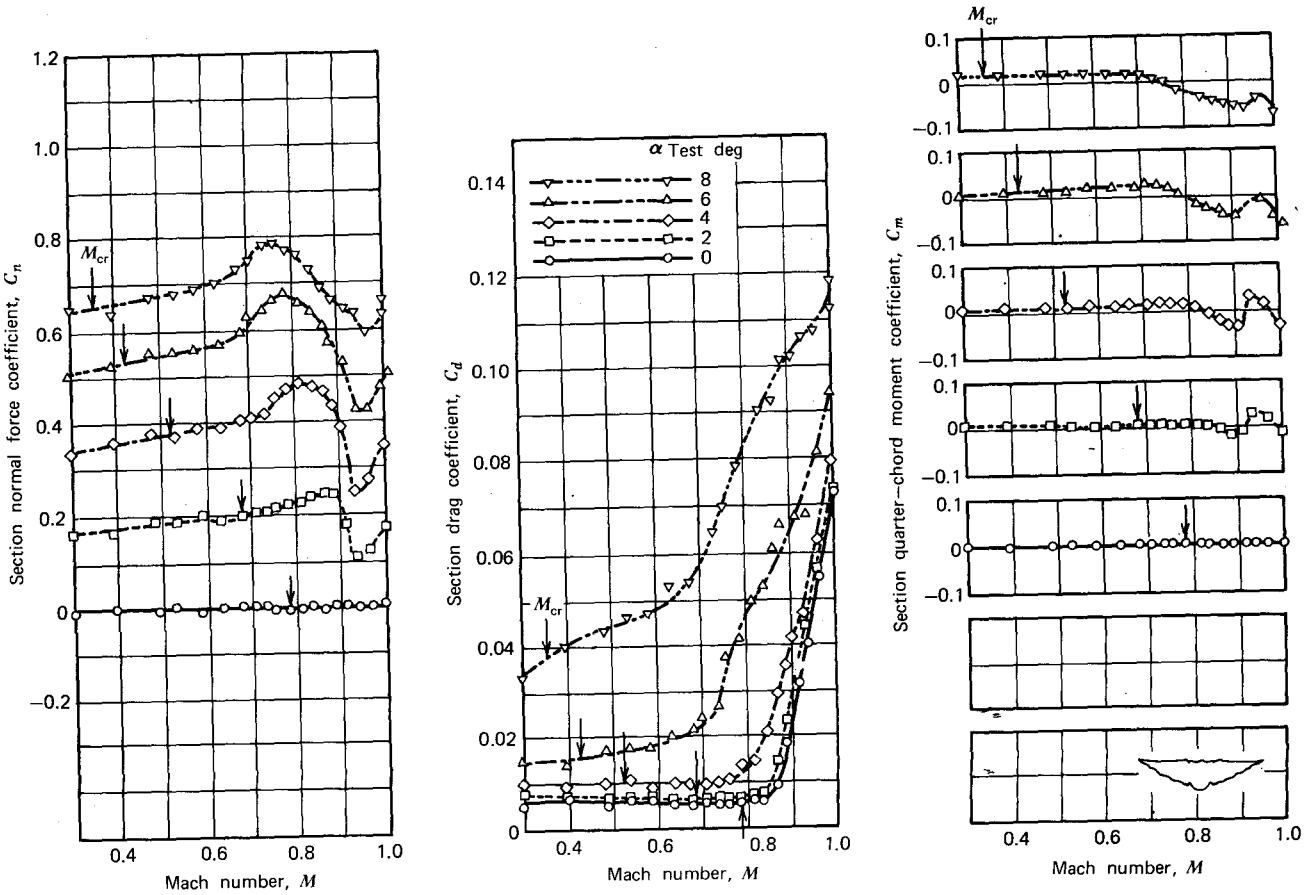

Figure 5.3 Aerodynamic characteristics of the NACA 64A009 airfoil at high subsonic Mach numbers.

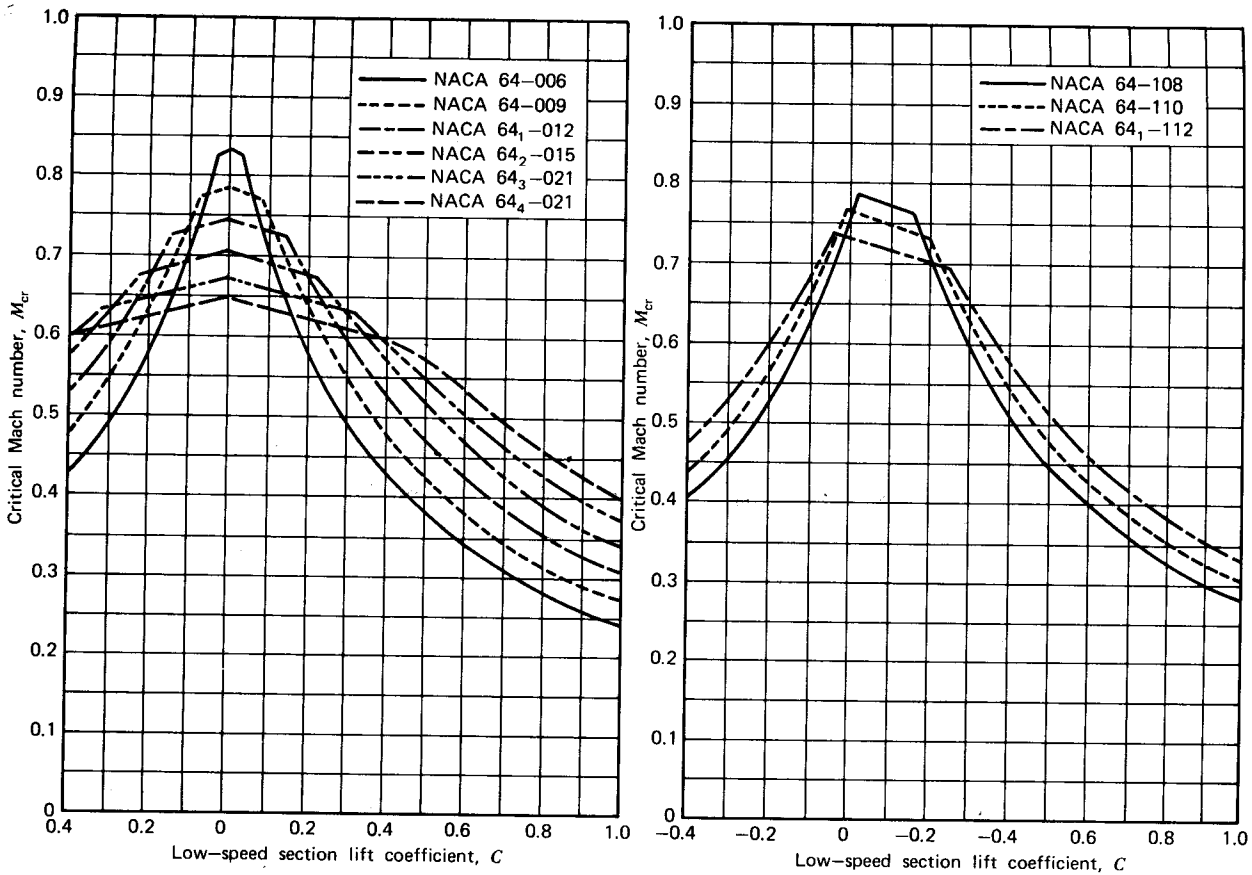

Figure 5.4a Variation of critical Mach number with low-speed section lift coefficient for several NACA 64-series symmetrical airfoil sections of various thicknesses.

Figure 5.4b Variation of critical Mach number with low-speed section lift coefficient for several NACA 64-series airfoil sections of various thicknesses, cambered for a design lift coefficient of 0.1.

thickness, the curves for the cambered airfoils are similar in appearance to those for the symmetrical airfoils.

It can be seen from Figure 5.3 that Equation 5.5 holds in a qualitative sense. At a given angle of attack, the lift coefficient increases with Mach number; however, the increase is not as great as Equation 5.5 predicts. For example, at an angle of attack of 6° and a Mach number of 0.3, C_l is equal to 0.51. Therefore, at this same angle of attack, one would predict a C_l of 0.61 at a Mach number of 0.6. Experimentally, however, C_l equals only 0.57 at the higher M value.

Figure 5.5, also based on the data of Reference 5.4, presents the variation with Mach number of the slope of the normal force coefficient curve for 4, 6, 9, and 12% thick airfoils. The theoretical variation of C_{n_α} with M, matched to the experiment at an M of 0.3, is also included. Again, the Glauert correction is seen to be too high by comparison to the experimental results. Contrary to these observations, Reference 5.2 states that Equation 5.2 underestimates the effect of Mach number and presents a comparison between theory and experiment for a 4412 airfoil to substantiate the statement.

Reference 5.6 presents a graph similar to Figure 5.5 for symmetrical airfoils varying in thickness from 6 to 18%. The results are somewhat similar except that, at the lower Mach numbers, below approximately 0.8, the trend of C_{l_α} with thickness is reversed. Both graphs show C_{l_α} continuing to increase with a Mach number above the critical Mach number. Unlike Figure 5.5, the

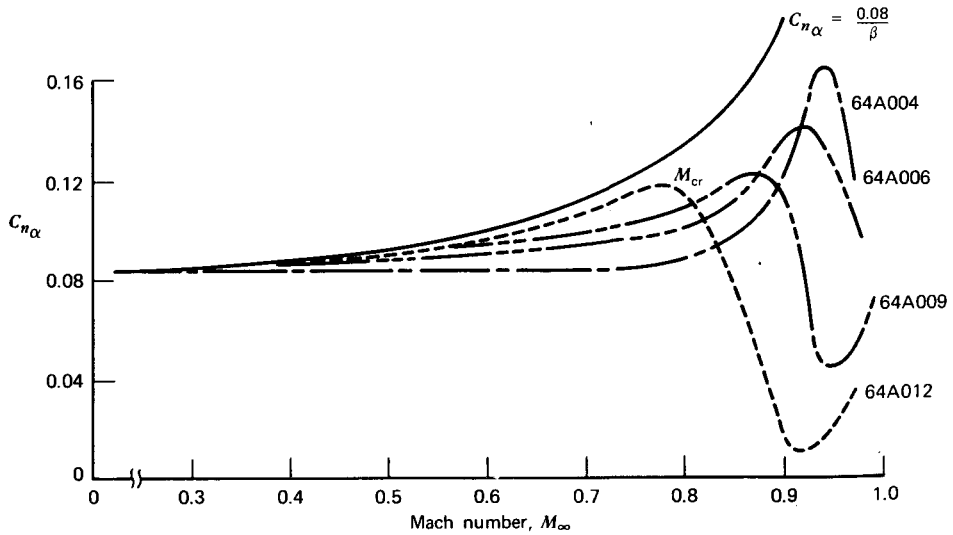

Figure 5.5 Effect of Mach number on the slope of the normal force coefficient angle-of-attack curve ($C_n = 0$).

results presented in Reference 5.6 show a closer agreement with the Prandtl-Glauert factor for the lower thickness ratios.

Reference 5.5 is a voluminous collection of data pertaining to aircraft and missiles. Subsonic and supersonic data are given for airfoil sections, wings, bodies, and wing-body combinations. Any practicing aeronautical engineer should be aware of its existence and have access to the wealth of material contained therein. In Section 4 of this reference, the Prandtl-Glauert factor is used up to the critical Mach number. Isolated examples given in this reference using β show reasonably good agreement with test results. Thus, in the absence of reliable data, it is recommended that the Prandtl-Glauert compressibility correction be used, but with caution, keeping in mind discrepancies such as those shown in Figure 5.5.

From Figures 5.3 and 5.5 it is interesting to note that nothing drastic happens to the lift or drag when the critical Mach number is attained. Indeed, the lift appears to increase at a faster rate with Mach number for M values higher than M_{cr}. Only when M_{cr} is exceeded by as much as 0.2 to 0.4 does the normal force coefficient drop suddenly with increasing M_∞. The same general behavior is observed for C_d, except that the increments in M_∞ above M_{cr} where the C_d curves suddenly bend upward are somewhat less than those for the breaks in the C_n curves.

The value of M_∞ above which C_d increases rapidly with Mach number is known as the drag-divergence Mach number. A reliable determination of this number is of obvious importance in estimating the performance of an airplane such as a jet transport, designed to operate at high subsonic Mach numbers.

FUNDAMENTALS OF GAS DYNAMICS

Before proceeding further into the question of airfoil characteristics at Mach numbers higher than M_{cr}, it is necessary to develop some basic relationships relating to compressible subsonic and supersonic flows.

One-Dimensional Isentropic Flow

We will begin by considering briefly a reversible, adiabatic flow where the state of the flow is a function only of the position along the flow direction as, for example, a uniform flow through a duct. This simple case illustrates some of the pronounced differences between subsonic and supersonic flows. Applying the momentum theorem to a differential fluid element, Euler's equation of motion along a streamline was derived in Chapter Two and is again stated here.

$$V\,dV + \frac{dp}{\rho} = 0 \tag{5.9}$$

Also, the continuity equation was derived earlier. For one-dimensional flow through a pipe having a variable cross-sectional area of A,

$$\rho A V = \text{constant} \tag{5.10}$$

For an inviscid fluid, the density and pressure are related through the isentropic process

$$\frac{p}{\rho^{\gamma}} = \text{constant} \tag{5.11}$$

Finally, the properties of the gas are related through the equation of state.

$$p = \rho R T \tag{5.12}$$

Differentiating by parts, Equation 5.10 can be written as

$$\frac{dp}{\rho} + \frac{dV}{V} + \frac{dA}{A} = 0 \tag{5.13}$$

From Chapter Two, the local acoustic velocity is given by

$$a^2 = \frac{dp}{d\rho} \tag{5.14}$$

Defining the local Mach number, M, as V/a and substituting Equations 5.14 and 5.13 into Equation 5.9 leads to a relationship between u and A.

$$\frac{dV}{ds} = \frac{-1}{1 - M^2} \frac{V}{A} \frac{dA}{ds} \tag{5.15}$$

Since V and A are both positive, we arrive at the surprising result (at least to those who have never seen it) that, for supersonic flow through a duct, an increase in cross-sectional area in the direction of flow will cause the flow to accelerate. Also, Equation 5.15 shows that a Mach number of unity can only occur if $dA/ds = 0$ since, for $M = 1$, dV/ds will be finite only if the cross-sectional area does not change with distance along the duct. This does not mean that M must equal unity when dA/ds equals zero but, instead, that dA/ds equal to zero is a necessary condition for $M = 1$.

Consider flow from a reservoir through a converging-diverging nozzle, as pictured in Figure 5.6. Such a nozzle is referred to as a Laval nozzle. If the

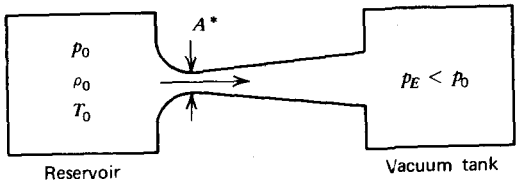

Figure 5.6 Flow from a reservoir through a converging-diverging nozzle.

reservoir pressure, p_0, is sufficiently high relative to the exit pressure, p_E, the flow will accelerate to Mach 1 at the throat. Beyond the throat, with dA/ds positive, the flow will continue to accelerate, thereby producing a supersonic flow. Downstream of the throat, pressure and density decrease as the velocity increases with the increasing area.

The compressible Bernoulli equation governing one-dimensional isentropic flow was derived earlier. In terms of the local acoustic velocity,

$$\frac{V^2}{2}+\frac{a^2}{\gamma-1}=\text{constant}$$

For this case of flow from a reservoir,

$$\frac{V^2}{2}+\frac{a^2}{\gamma-1}=\frac{a_0^2}{\gamma-1} \tag{5.16}$$

Dividing this equation through by a^2 and using the isentropic relationships among p, ρ, and T leads to these three quantities as a function of the local Mach number.

$$\frac{T}{T_0}=\left(1+\frac{\gamma-1}{2}M^2\right)^{-1} \tag{5.17a}$$

$$\frac{p}{p_0}=\left(1+\frac{\gamma-1}{2}M^2\right)^{-\gamma/(\gamma-1)} \tag{5.17b}$$

$$\frac{\rho}{\rho_0}=\left(1+\frac{\gamma-1}{2}M^2\right)^{-1/(\gamma-1)} \tag{5.17c}$$

These relationships, presented graphically in Figure 5.7, are valid for Mach numbers greater than unity if the flow is shockless. The subject of shock waves will be treated later.

At the throat the local velocity and the local acoustic velocity are equal. Designating this velocity by a^*, Equation 5.16 can be written as

$$\frac{a^{*2}}{2}+\frac{a^{*2}}{\gamma-1}=\frac{a_0^2}{\gamma-1}$$

or

$$\frac{a^*}{a_0}=\left[\frac{2}{(\gamma+1)}\right]^{1/2}$$
$$=0.913 \tag{5.18}$$

Using Equations 5.11 and 5.14, it follows that

$$\frac{p^*}{p_0}=\left[\frac{2}{(\gamma+1)}\right]^{\gamma/(\gamma-1)}$$
$$=0.528 \tag{5.19}$$

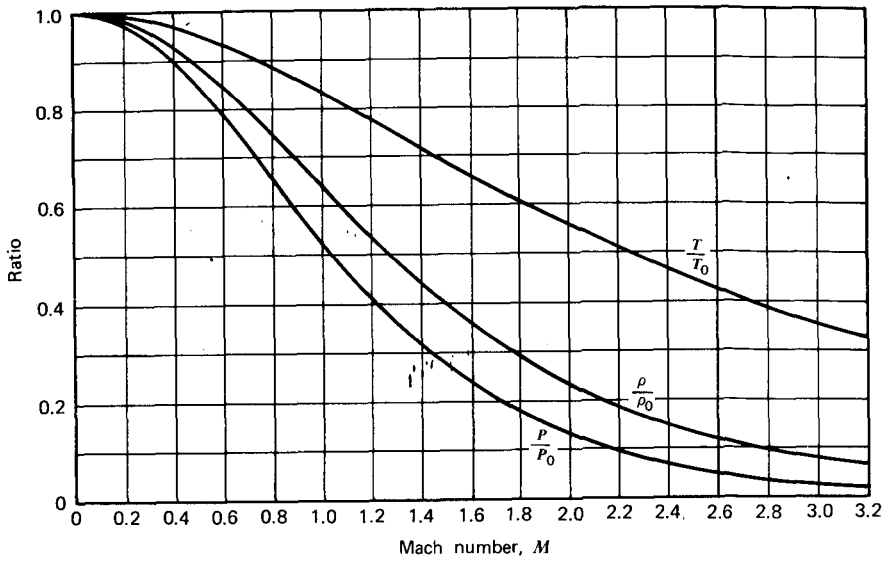

Figure 5.7 Isentropic flow. Pressure, density, and temperature as a function of Mach number.

$$\frac{\rho^*}{\rho_0} = \left[\frac{2}{(\gamma+1)}\right]^{1/(\gamma-1)}$$
$$= 0.634 \tag{5.20}$$

In these equations, the superscript * refers to the throat.

Equation 5.19 shows that the airflow from a reservoir will reach Mach 1 if the reservoir pressure exceeds the exit pressure by a factor of at least 1.894.

The mass flow rate, m, through the nozzle will be

$$m = \rho^* A^* a^* \tag{5.21}$$

where A^* is the throat area.

Using Equations 5.18 and 5.20, this becomes

$$m = 0.579 \rho_0 a_0 A^* \tag{5.22}$$

Observe that this is the maximum mass flow rate that can be obtained from a given reservoir independent of the exit pressure. For example, consider two tanks connected together through a nozzle having a throat area of 1 m^2, as pictured in Figure 5.6. Assume that the air in both tanks is at standard sea level conditions. We will now begin to lower the pressure in one tank, causing air to flow from the other tank into the one with the vacuum. As the pressure in the vacuum tank is gradually reduced, the mass flow through the pipe will increase continuously, assuming the volume in the other tank, or reservoir, is sufficiently large so that its pressure and density does not change

significantly. The pressure drop along the pipe resulting from skin friction will exactly equal the pressure difference between the two tanks. However, when the pressure in the vacuum tank is reduced to 53.5 kN/m^2 (from Equation 5.19), a value of $M = 1$ occurs at the throat. The nozzle, or flow, is then said to be "choked," since a further reduction in the pressure downstream of the throat will not result in any further increase in the mass flow. From Equation 5.22, this critical mass flow will equal 242.3 kg/s.

If we assume that the flow beyond the throat is still isentropic, Equations 5.17, 5.18, 5.20, and 5.21 can be combined to give

$$\left(\frac{A}{A^*}\right)^2 = \frac{\gamma - 1}{2} \frac{(2/\gamma + 1)^{(\gamma+1)/(\gamma-1)}}{[1 - (p/p_0)^{(\gamma-1)/\gamma}](p/p_0)^{2/\gamma}} \tag{5.23}$$

This is known as St. Venant's equation.

Substituting for the local pressure ratio in terms of Mach number, this can also be written as

$$\left(\frac{A}{A^*}\right)^2 = \frac{1}{M^2}\left[\frac{2}{\gamma+1}\left(1 + \frac{\gamma - 1}{2} M^2\right)\right]^{(\gamma+1)/(\gamma-1)} \tag{5.24}$$

Since p, ρ, and T are related through the adiabatic process and the equation of state, it follows from the foregoing that p, ρ, and T are all uniquely related to their corresponding reservoir values by the ratio of A to A^*. This obviously raises some problems since, in the example of Figure 5.6, the pressure at the exit into the vacuum tank does not necessarily have to match the pressure from Equation 5.23 corresponding to the area of the duct at its connection to the vacuum tank. Some nonisentropic mechanism must exist that will allow the pressure to adjust to exit conditions. This leads us to the concept of a shock wave.

Normal Shock Waves

Figure 5.8 pictures a shock wave normal to a one-dimensional flow through a duct having a unit cross-sectional area. The shock wave is a surface

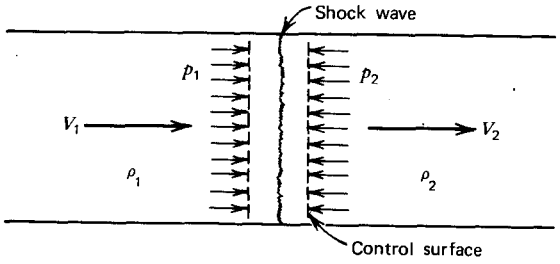

Figure 5.8 Flow through a normal shock wave.

across which the flow properties p, ρ, T, and V change discontinuously. We will now examine the equations governing the flow to see if such a standing wave is possible and to determine the relationships between the upstream and downstream fluid properties. To begin, the equations governing the conservation of mass and momentum must hold.

continuity

$$\rho_1 V_1 = \rho_2 V_2 = m \tag{5.25}$$

momentum

$$p_1 - p_2 = m(V_2 - V_1) \tag{5.26}$$

In addition, the equation of state, Equation 2.1, must also hold. It is repeated here for convenience.

equation of state

$$p = \rho RT \tag{5.27}$$

A fourth relationship, which has not been used as yet, is the energy equation.

energy

$$C_p T_1 + \frac{V_1^2}{2} = C_p T_2 + \frac{V_2^2}{2} = C_p T_0 \tag{5.28}$$

This equation, derived in Reference 5.6, applies to adiabatic flows where no heat is added to the flow. C_p is the specific heat at constant pressure. The product $C_p T$ is the enthalpy of the flow per unit mass. Thus Equation 5.28 states that the sum of the enthalpy and kinetic energy per unit mass of an adiabatic flow remains constant. C_p, R, γ, and the specific heat at constant volume, C_v, are all interrelated.

$$\begin{aligned} R &= C_p - C_v \\ \gamma &= \frac{C_p}{C_v} \\ C_p &= \frac{R\gamma}{(\gamma - 1)} \end{aligned} \tag{5.29}$$

If Equation 5.29 is substituted into the energy equation (Equation 5.28), it is interesting to note that one obtains the compressible Bernoulli equation (Equation 5.16). Thus Equation 5.16 and the energy equation are equivalent for isentropic flow. However, across the shock wave the flow is not a reversible, adiabatic process, so the changes in state are not related by Equation 5.11.

In order to see how p, ρ, T, and M change across a normal shock wave, we begin by substituting Equation 5.25 into Equation 5.26 so that,

$$p_1 + \rho_1 V_1^2 = p_2 + \rho V_2^2$$

Since $a^2 = \gamma p/\rho$, it follows that

$$p_1 + \gamma p_1 M_1^2 = p_2 + \gamma p_2 M_2^2$$

or

$$\frac{p_2}{p_2} = \frac{1 + \gamma M_1^2}{1 + \gamma M_2^2} \tag{5.30}$$

Manipulating Equation 5.28 in a similar manner, it follows that

$$\left(\frac{a_2}{a_1}\right)^2 = \frac{1 + [(\gamma - 1)/2]M_1^2}{1 + [(\gamma - 1)/2]M_2^2} = \frac{p_2\rho_1}{p_1\rho_2} = \frac{T_2}{T_1} \tag{5.31}$$

Thus,

$$\frac{p_2}{\rho_1} = \frac{\rho_2}{\rho_1}\frac{1 + [(\gamma - 1)/2]M_1^2}{1 + [(\gamma - 1)/2]M_2^2} \tag{5.32}$$

Next, Equation 5.25 is written as

$$\frac{\rho_1}{\rho_2}\frac{M_1}{M_2}\frac{a_1}{a_2} = 1.0$$

Substituting Equations 5.30, 5.31, and 5.32 into the preceding equations leads to an implicit relationship for M_2 as a function of M_1.

$$\frac{M_1\sqrt{1 + [(\gamma - 1)/2]M_1^2}}{1 + \gamma M_1^2} = \frac{M_2\sqrt{1 + [(\gamma - 1)/2]M_2^2}}{1 + \gamma M_2^2} = f(M) \tag{5.33}$$

Obviously, one solution of the above is $M_2 = M_1$, in which case $p_2 = p_1$, $\rho_2 = \rho_1$, and $T_2 = T$, so that there is no discontinuity in the flow and the solution is trivial. The other solution is apparent from Figure 5.9, where $f(M)$

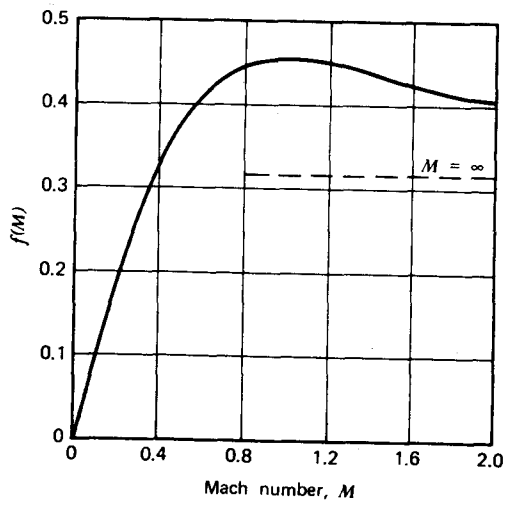

Figure 5.9 Function to determine conditions across a normal shock wave.

is presented as a function of M. It is seen that the same value for $f(M)$ is obtained from two different values of M, one greater and one less than unity. For example, if M_1 is equal to 2.0, Equation 5.33 would be satisfied by an M_2 value of approximately 0.57. One might, of course, say that a value of M_1 equal to 0.57 with M_2 equal to 2.0 would also satisfy Equation 5.33 which, indeed, would be the case. However, it can be argued on the basis of the second law of thermodynamics that the flow ahead of the shock wave must be supersonic (see Ref. 5.6, p. 234). An entropy loss, in violation of the second law, will occur if M_1 is less than unity. Therefore, in Figure 5.9, M_1 is greater than unity and M_2 is the value of M less than unity for which

$$f(M_2) = f(M_1)$$

Notice from Equation 5.33 that $f(M)$ approaches a value of $(\gamma - 1)^{1/2}/\gamma$, or approximately 0.319, as $M_1 \to \infty$. Thus, behind a normal shock wave, the Mach number has a lower limit of approximately 0.38.

Since there is an entropy gain across the normal shock wave, a loss occurs in the total, or reservoir, pressure as the flow passes through the wave. With some algebraic manipulation of the energy equation and application of the isentropic relationships before and after the wave (but not across it), the following equation can be obtained.

$$\frac{p_{0_2}}{p_{0_1}} = \frac{p_2}{p_1}\left[\frac{1 + [(\gamma - 1)/2]M_2^2}{1 + [(\gamma - 1)/2]M_1^2}\right]^{\gamma/(\gamma-1)} \tag{5.34}$$

p_{0_2} and p_{0_1} are the reservoir pressures behind and ahead of the wave, respectively.

Equations 5.30 to 5.34 are unwieldy to use because of their implicit nature. However, after some algebraic manipulation, they can all be reduced to explicit functions of M_1. These can be found in Reference 5.7 and are repeated here. Following the lead of Reference 5.7, the second form of each equation is for $\gamma = 7/5$.

$$\frac{p_2}{p_1} = \frac{2\gamma M_1^2 - (\gamma - 1)}{\gamma + 1} = \frac{7M_1^2 - 1}{6} \tag{5.35}$$

$$\frac{\rho_2}{\rho_1} = \frac{(\gamma + 1)M_1^2}{(\gamma - 1)M_1^2 + 2} = \frac{6M_1^2}{M_1^2 + 5} \tag{5.36}$$

$$M_2^2 = \frac{(\gamma - 1)M_1^2 + 2}{2\gamma M_1^2 - (\gamma - 1)} = \frac{M_1^2 + 5}{7M_1^2 - 1} \tag{5.37}$$

$$\frac{p_{0_2}}{p_{0_1}} = \left[\frac{(\gamma + 1)M_1^2}{(\gamma - 1)M_1^2 + 2}\right]^{\gamma/(\gamma-1)}\left[\frac{\gamma + 1}{2\gamma M_1^2 - (\gamma - 1)}\right]^{1/(\gamma-1)}$$
$$= \left(\frac{6M_1^2}{M_1^2 + 5}\right)^{7/2}\left(\frac{6}{7M_1^2 - 1}\right)^{5/2} \tag{5.38}$$

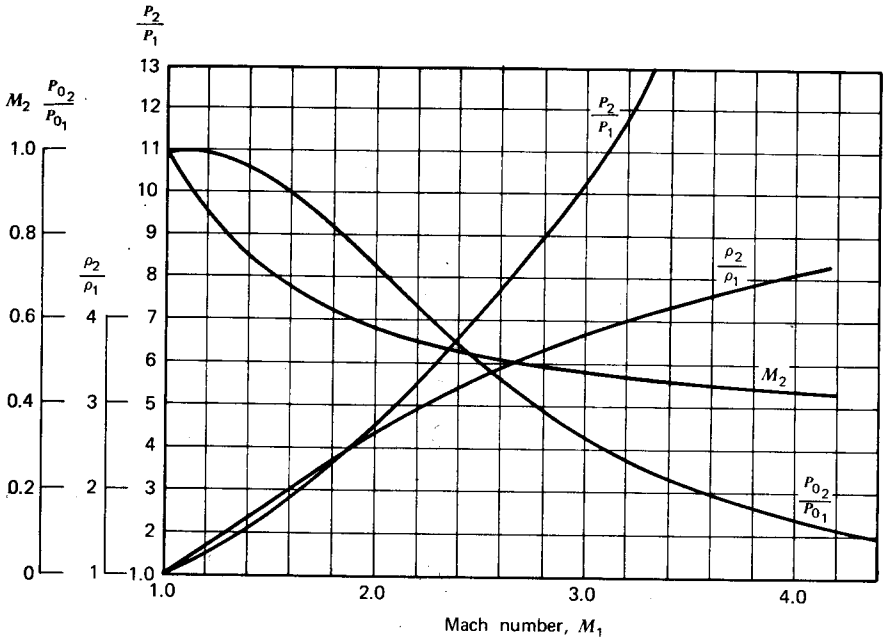

Figure 5.10 Pressure, density, and Mach number changes across a normal shock wave.

Figure 5.10 presents these relationships graphically and can be used for approximate calculations.

Let us now return to the problem of flow in the duct illustrated by Figure 5.8. Suppose the pressure in the vacuum tank is lowered to a value of 80 kN/m^2. Furthermore, let us assume that the area of the duct entering the second tank is large so that, as the air enters the tank, its velocity, and hence dynamic pressure, is low. Thus, 80 kN/m^2 would represent approximately the reservoir pressure downstream of a normal shock in the duct. The upstream reservoir pressure is equal to the standard sea level value of 101.3 kN/m^2. Thus,

$$\frac{p_{0_2}}{p_{0_1}} = 0.790$$

From Figure 5.10, the Mach number, M_1, just upstream of the normal shock wave equals 1.85. In addition,

$$\frac{p_2}{p_1} = 3.85$$

$$\frac{\rho_2}{\rho_1} = 2.43$$

$$M_2 = 0.605$$

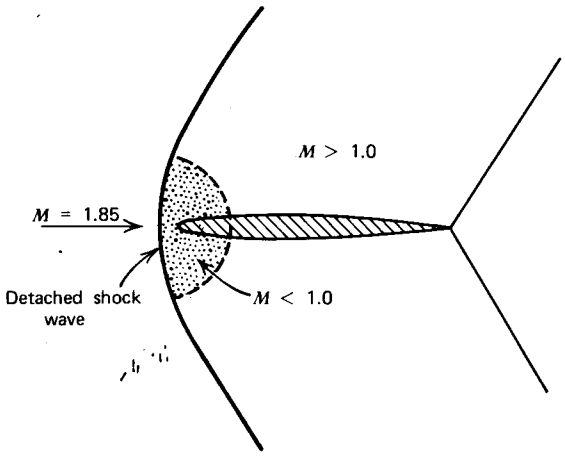

Figure 5.11 A detached shock wave ahead of a blunt-nosed shape traveling at supersonic speed.

Thus, from Equation 5.24

$$\frac{A}{A^*} = 1.50$$

Therefore, we predict for the pressure in the vacuum tank of 80 kN/m^2 that a normal shock wave must be positioned in the duct at a location where the duct area is one and a half times greater than the throat area.

This supersonic flow through a duct that must ultimately come to rest in the vacuum is directly comparable to a blunt-nosed body, or airfoil, traveling at supersonic speeds. Figure 5.11 depicts a supersonic airfoil with a rounded leading edge traveling at a Mach number of 1.85. Since the flow must come to rest at the stagnation point on the nose, it obviously must be subsonic for some extent ahead of the nose. The result is a shock wave that is normal to the flow in the vicinity of the nose. As in the case of the duct flow, immediately behind this wave, the flow is subsonic with a Mach number of 0.605. The shock wave, positioned away from the nose some small distance, is referred to as a "detached" shock wave, since it is detached from the surface.

Oblique Shock Waves

Generally, a shock wave is not normal to the flow. In Figure 5.11, for example, the wave becomes oblique to the flow as one moves away from the nose. Let us therefore examine this more general case in the same manner as we did the normal shock wave.

Figure 5.12 pictures a flow passing through an oblique shock wave that is

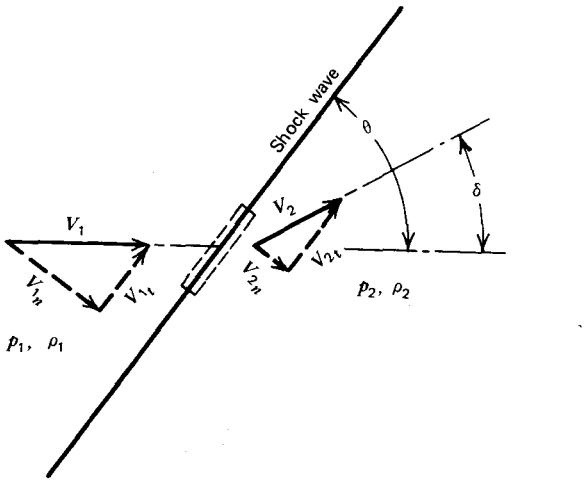

Figure 5.12 Flow through an oblique shock wave.

at an angle of θ relative to the incoming velocity vector. θ is equal to 90° for a normal shock. We will assume that the flow is deflected through the angle δ as it passes through the wave, with δ being in the direction shown in the figure.

Considering the flow through a control surface of unit area, as shown, we can write, in the direction normal to the wave, two equations directly comparable to Equations 5.25 and 5.26.

continuity

$$\rho_1 V_{1_n} = \rho_2 V_{2_n} = m \tag{5.39}$$

momentum

$$p_1 - p_2 = m(V_{2_n} - V_{1_n}) \tag{5.40}$$

In the direction tangential to the wave, the momentum theorem gives:

momentum

$$0 = M(V_{2_t} - V_{1_t})$$

or

$$V_{1_T} = V_{2_t} = V_t \tag{5.41}$$

Again, the energy equation holds.

energy

$$C_p T_1 + \frac{V_{1_n}^2 + V_{1_t}^2}{2} = C_p T_2 + \frac{V_{2_n}^2 + V_{2_t}^2}{2}$$

In view of Equation 5.41, the energy equation becomes

$$C_pT_1+\frac{V_{1_n}^2}{2}=C_pT_2+\frac{V_{2_n}^2}{2} \tag{5.42}$$

Equations 5.39, 5.40, and 5.42 are identical to Equations 5.25, 5.26, and 5.28 if V_{1_n} is replaced by V_1 and V_{2_n} by V_2. Thus, all of the relationships previously derived for a normal shock wave apply to an oblique shock wave if the Mach numbers normal to the wave are used. These relationships, together with the fact that the tangential velocity remains unchanged through the wave, allow us to determine the flow conditions downstream of the wave as well as the angles θ and δ.

As an example, consider the case where θ is equal to 50° and M_1 equals 2.0.

$$M_{1_n}=M_1\sin\theta$$
$$=1.532$$

From Equations 5.35 to 5.37,

$$\frac{p_2}{p_1}=2.57$$

$$\frac{\rho_2}{\rho_1}=1.92$$

$$M_{2_n}=0.69$$

Now we must be careful, because the tangential velocity is constant across the wave, *not* the tangential Mach number. To obtain M_{2_t}, we write

$$M_{2_t}=\frac{V_t}{a_2}$$

$$=M_{t_1}\frac{a_1}{a_2}$$

$$=M_1\cos\theta\sqrt{\frac{\rho_2/\rho_1}{p_2/p_1}}$$

or, in this case,

$$M_{2_t}=1.11$$

The turning angle, δ, can now be determined from the geometry of Figure 5.12.

$$\delta=\theta-\frac{\pi}{2}+\tan^{-1}\frac{M_{2_t}}{M_{2_n}} \tag{5.43}$$

or, in this example,

$$\delta=18.1°$$

Notice for this example that

$$M_2=\sqrt{M_{2_n}^2+M_{2_t}^2}$$
$$=1.31$$

Thus the flow is still supersonic after it has passed through the wave, unlike the flow through a normal shock wave.

As an exercise, repeat the foregoing example, but with a θ of 76.5°.

Surprisingly, the same turning angle is obtained for the same upstream Mach number but different wave angle, θ. For this steeper wave, which is more like a normal shock, the flow becomes subsonic behind the wave, M_2 being equal to 0.69.

The deflection angle, δ, as a function of θ, for a constant Mach will appear as shown qualitatively in Figure 5.13. For a given M_1, a maximum deflection angle exists with a corresponding shock wave angle. For deflections less than the maximum, two different θ values can accomplish the same deflection. The oblique shock waves corresponding to the higher θ values are referred to as strong waves, while the shock waves having the lower θ values are known as weak waves. There appears to be no analytical reason for rejecting either possible family of waves but, experimentally, one finds only the *weak* oblique shock waves. Thus, the flow tends to remain supersonic through the wave unless it has no other choice. If, for a given M_1, the boundary of the airfoil requires a turning greater than δ_{max}, the wave will become detached, as illustrated in Figure 5.11. The flow then becomes subsonic just behind the normal part of the wave and navigates around the blunt nose under the influence of pressure gradients propagated ahead of the

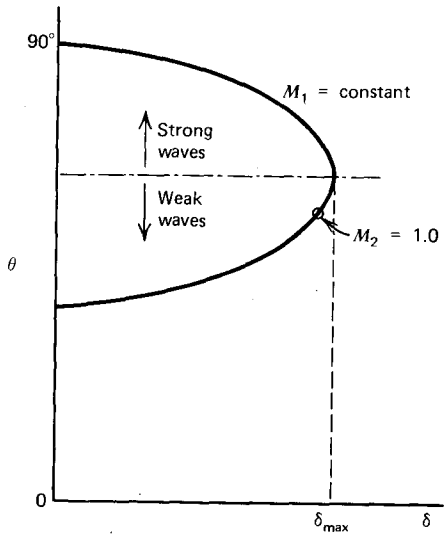

Figure 5.13 Relationship between the shock wave angle, θ, and the deflection angle, δ.

airfoil in the subsonic flow region. It then accelerates downstream, again attaining supersonic speeds.

An explicit relationship for δ as a function of M_1 and θ can be obtained by applying the equations for the normal shock wave to the Mach number normal components of the oblique shock wave, $M_1 \sin\theta$ and $M_2 \sin(\theta - \delta)$. After a considerable amount of algebraic reduction, one obtains the result

$$\tan\delta = \frac{M_1^2 \sin 2\theta - 2\cot\theta}{2 + M_1^2(\gamma + \cos 2\theta)}$$

$$= 5\frac{M_1^2 \sin 2\theta - 2\cot\theta}{10 + M_1^2(7 + 5\cos 2\theta)} \qquad (5.44)$$

(for $\gamma = 7/5$)

This equation is presented graphically in Figure 5.14 (taken from Ref. 5.7) for a range of Mach numbers and shock wave angles from 0 to 90°. θ values

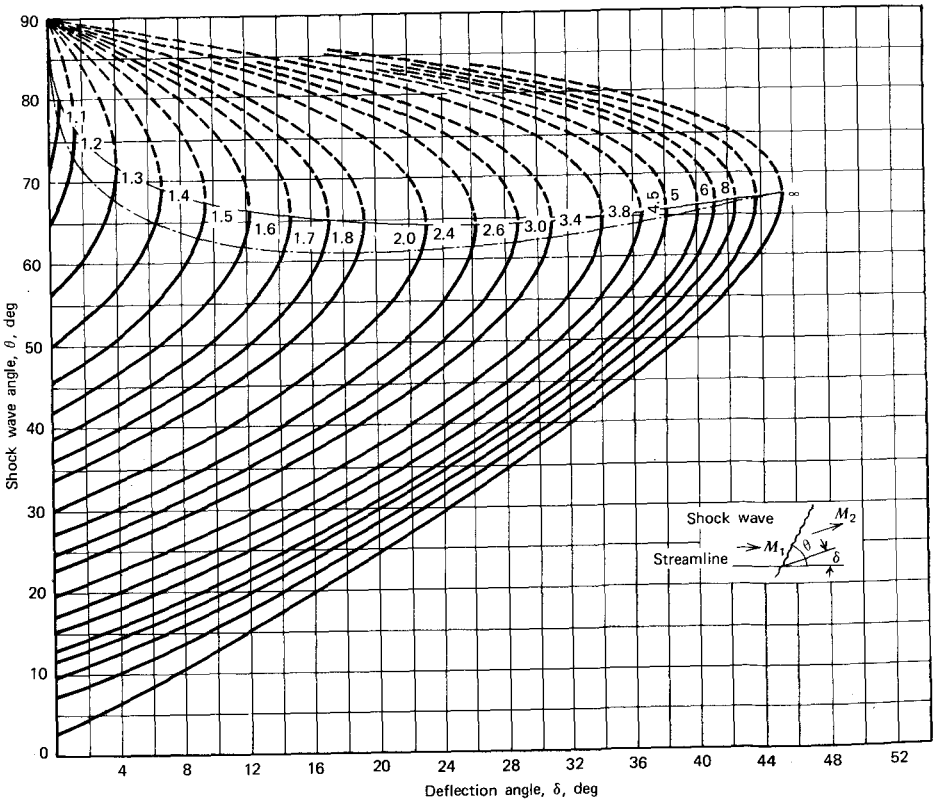

Figure 5.14 Variation of shock wave angle with flow deflection angle for various upstream Mach numbers.

lying below the broken line correspond to weak oblique shock waves. This dividing line is close to but slightly below the solid line through the maximum deflection angles.

Expansion Waves

Let us consider the two supersonic flows pictured in Figure 5.15*a* and 5.15*b*. When the flow is turned by a surface concave to the flow, as in Figure 5.15*a*, we have seen that an oblique shock originating from the bend in the surface will compress the flow and turn it though the angle, δ. The question then posed is, how is the flow turned around a bend convex to the flow, as shown in Figure 15*b*. As suggested by the figure, this is accomplished through a continuous ensemble of weak expansion waves, known as an expansion fan.

In order to examine the flow relationships in this case, we take an approach similar to that for oblique shock waves. Consider supersonic flow through a single, weak wave, known as a Mach wave, as illustrated in Figure 5.16. The wave represents a limiting case of zero entropy gain across the wave. Hence the turning and velocity changes are shown as differentials instead of as finite changes. Since the wave is a weak wave, it propagates

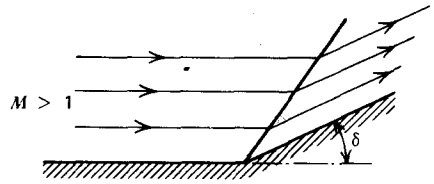

Figure 5.15a Deflection of a supersonic flow by an oblique shock wave (compression).

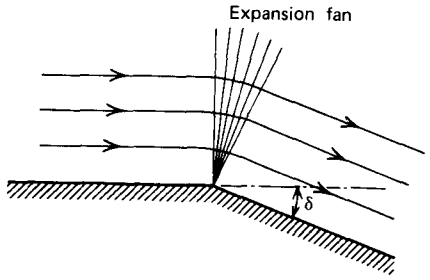

Figure 5.15b Deflection of a supersonic flow by a series of Mach waves (expansion).

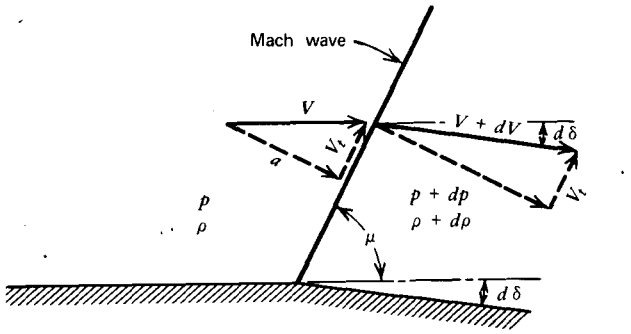

Figure 5.16 Deflection of flow through a Mach wave.

normal to itself at the acoustic velocity, a, which added vectorially to the free-stream velocity, V, defines the angle of the wave μ.

$$\mu = \sin^{-1}\frac{a}{V}$$

$$= \sin^{-1}\frac{1}{M} \tag{5.45}$$

Applying momentum principles across the wave, as done previously for the oblique shock wave, results in

$$dV_t = 0$$

and

$$-dp = \rho a[(V + dV)\sin(\mu + d\delta) - a]$$

This reduces to

$$-dp = \rho a^2\left[\frac{dV}{V} + \sqrt{M^2 - 1}\, d\delta\right]$$

Since the tangential velocity component is unchanged across the wave, it follows that

$$\frac{a}{\tan\mu} = (V + dV)\cos(\mu + d\delta)$$

Expanding this and substituting Equation 5.45 results in

$$\frac{dV}{d\delta} = \frac{V}{\sqrt{M^2 - 1}} \tag{5.46}$$

$$\frac{dp}{d\delta} = -\frac{\gamma p M^2}{\sqrt{M^2 - 1}} \tag{5.47}$$

Thus, this weak wave, deflecting the flow in the direction shown in Figure

5.16, results in an expansion of the flow, since $dp/d\delta$ is negative. It is also possible for small deflections in the opposite direction to produce a compression with a Mach wave. This represents a limiting case of an oblique shock wave.

The expansion fan shown in Figure 5.15*b* represents a continuous distribution of Mach waves. Each wave deflects the flow a small amount, so that the integrated effect produces the total deflection, δ. The changes in the flow can be related to the total deflection by integrating Equation 5.46. The energy equation is used to relate the local sonic velocity to V. It is convenient in so doing to let $\delta = 0$ at $M = 1.0$. This corresponds to $V = a^*$ for a given set of reservoir conditions. Therefore,

$$\delta = \int_{a^*}^{V} \frac{\sqrt{M^2 - 1}}{V}\, dV$$

The details of performing this integration will not be presented here. They can be found in several texts and in Reference 5.7. The final expression for δ becomes

$$\delta = \sqrt{\frac{\gamma+1}{\gamma-1}}\tan^{-1}\sqrt{\frac{\gamma-1}{\gamma+1}(M^2-1)} - \cos^{-1}\frac{1}{M} \tag{5.48}$$

This relationship is presented graphically in Figure 5.17 and is referred to as Prandtl-Meyer flow. To use this graph one relates a given flow state back to the $M = 1$ condition. For example, suppose the local Mach is equal to 3.0. This means that, relative to $M = 1$, the flow has already been deflected

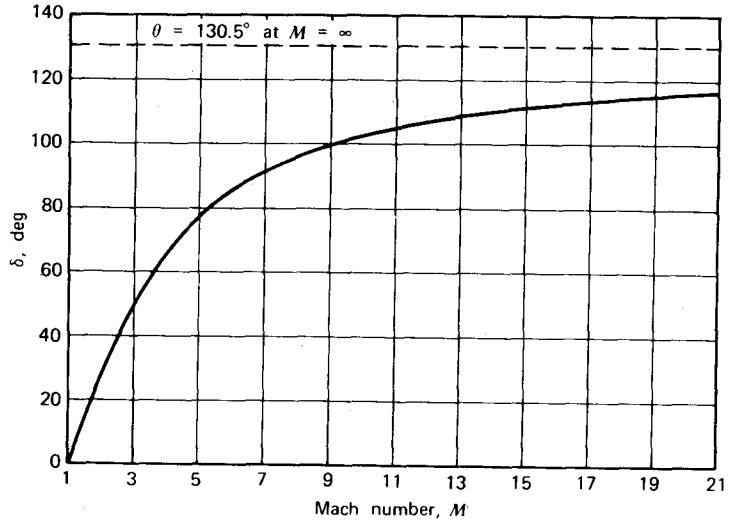

Figure 5.17 Deflection as a function of Mach number for expansion flows.

through an angle of approximately 50°. Suppose the flow is turned an additional 50°. Relative to $M = 1$, this gives a total deflection of 100°. Thus, one enters Figure 5.17 with this value of δ to determine a final Mach number slightly in excess of 9.0. Since the Prandtl-Meyer flow is isentropic, the flow state is determined completely by the reservoir conditions and the local Mach number (Equation 5.17).

TRANSONIC AIRFOILS

An airfoil operating at high, but subsonic, Mach numbers is pictured in Figure 5.18. If the free-stream Mach number is sufficiently high, the local flow as it progresses back along the upper surface will reach a point where the local Mach is equal to, or greater than, unity. As the flow continues along the concave surface, a region of supersonic flow develops. However, as the flow

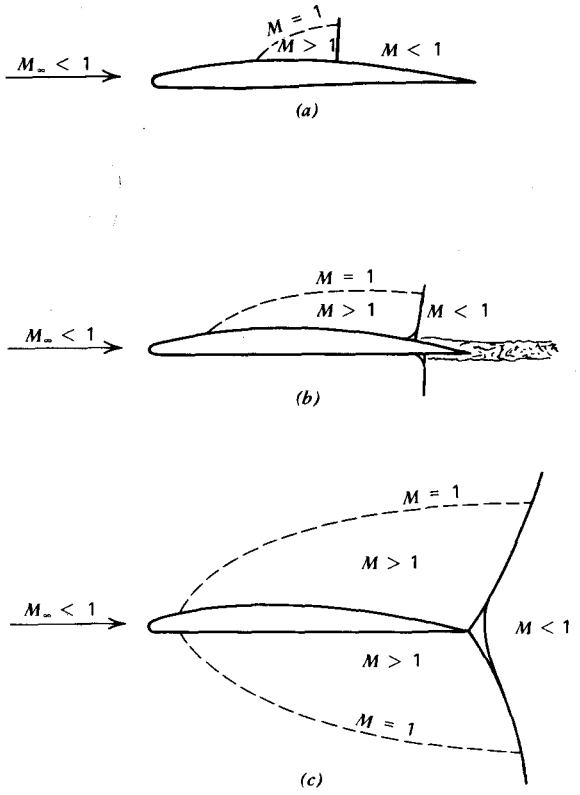

Figure 5.18 Airfoils in transonic flow.

approaches the trailing edge, it must eventually become subsonic again. As we saw in the preceding section, this can occur only through a shock wave.

If the compression to subsonic flow occurs before the trailing edge, as shown in Figure 5.18*a*, there is no deflection of the flow as it passes through the wave, so that the shock wave is normal to the flow. As the free-stream Mach number is increased, a similar transonic region will develop on the lower surface, as shown in Figure 5.18*b*. Immediately behind both normal shocks, the boundary layer will separate because of the strong positive pressure gradients. This results in a loss in lift and a sharp increase in the drag. Increasing M_∞ still further will result in the shock waves on both the upper and lower surfaces moving to the trailing edge. Here they become oblique shocks in order to turn the flow from both surfaces in the free-stream direction. Because of the developing boundary layer, as the shocks move toward the trailing edge, they assume a bifurcated or λ form, as shown. Here, within the boundary layer, compression begins initially through an oblique shock and continues through to a normal shock.

Increasing the Mach number also causes the sonic line, defining the forward extent of the supersonic flow, to move forward. This line, shown dashed in Figure 5.18, is a constant pressure surface along which $M = 1$.

A detailed treatment of analytical methods for predicting airfoil characteristics is beyond the scope of this text. However, an interesting aspect of transonic airfoil behavior, discussed in Reference 5.8, is the limiting Mach number concept, which also leads to a limit on pressure coefficients. This particular reference presents semiempirical methods for estimating two-dimensional and three-dimensional values of C_L and C_D through the transonic regime.

Combining Equations 5.35 and 5.17*b*, the pressure, p_2, immediately downstream of the normal shock can be written in terms of upstream reservoir pressure, p_0, and the local Mach number just ahead of the normal shock.

$$\frac{p_2}{p_{0_1}} = \left(1 + \frac{\gamma - 1}{2} M^2\right)^{-\gamma/(\gamma-1)} \left(\frac{2\gamma M^2 - \gamma + 1}{\gamma + 1}\right) \tag{5.49}$$

This ratio reaches a maximum value at a Mach number denoted as the limiting Mach number, M_{limit}, and given by,

$$M_{\text{limit}} = \sqrt{\frac{\gamma + 3}{2}}$$

$$= 1.483 \ (\gamma = 1.4) \tag{5.50}$$

Laitone argues in Reference 5.9 that the normal shock will be positioned on the surface of a transonic airfoil at the location where the local Mach number equals the limiting Mach number, thus assuring the maximum positive pressure downstream of the shock wave.

This limit on the local Mach number leads to a minimum pressure coefficient that can be attained on an airfoil surface ahead of the shock wave. C_p is defined as

$$C_p = \frac{p - p_\infty}{(1/2)\rho_\infty V_\infty^2}$$

which can be written as

$$C_p = \frac{2p_\infty}{\rho_\infty V_\infty^2}\left(\frac{p}{p_0}\frac{p_0}{p_\infty} - 1\right) \tag{5.51}$$

The ratio of the local pressure to the reservoir pressure, p_0, is a function of the local M, according to Equation 5.17*b*, and decreases monotonically with M. When the local M reaches M_{limit}, this ratio attains a minimum value of 0.279. Using Equation 5.17*b* also to relate the free-stream static pressure, p_∞, to p_0, a limiting value for C_p is obtained as a function of the free-stream Mach number.

$$C_{P_{\text{limit}}} = \frac{2}{\gamma M_\infty^2}\left[0.279\left(1 + \frac{\gamma - 1}{2}M^2\right)^{\gamma/(\gamma-1)} - 1\right] \tag{5.52}$$

This relationship is presented graphically in Figure 5.19. The limiting value of C_p is seen to decrease rapidly in magnitude as M_∞ increases. $C_{p_{cr}}$ is also presented on this same figure and is a value of C_p necessary to achieve local sonic flow. The value of M_∞ corresponding to $C_{p_{cr}}$ is equal to M_{cr}, the critical Mach number. $C_{p_{cr}}$ is obtained from Equation 5.51 by setting the local M equal to unity to obtain p/p_0. The result is identical to Equation 5.52 except for replacing the constant 0.279 by 0.528.

Before discussing the significance of these relationships, let us return to Equation 5.2, which allows us to predict C_p at subsonic Mach numbers based on predictions for incompressible flow. If C_{p_c} is the pressure coefficient at a given Mach number, the Prandtl-Glauert correction states that, for the same geometry, C_p at $M = 0$ will equal βC_{p_c}. Using this scaling relationship, the critical value for the incompressible C_p can be calculated from the compressible $C_{p_{cr}}$. This result is also presented in Figure 5.19.

As an example of the use of Figure 5.19, consider the Liebeck airfoil in Figure 3.43. The minimum C_p at $M_\infty = 0$ for this airfoil is approximately -2.8. Hence its critical Mach number is estimated from the lower curve of Figure 5.19 to be approximately 0.43. Its limiting Mach number, based on $C_p = -2.8$, would be 0.57. However, at this Mach number, the Prandtl-Glauert factor, β, equals 0.82, so that the minimum C_p at this Mach number is estimated to be -3.4. A second iteration on M_{limit} then gives a value of 0.52. Continuing this iterative procedure, a value of $M_{\text{limit}} = 0.53$ is finally obtained.

Next, consider the chordwise pressure distributions presented in Figure 5.20. Here, C_p as a function of chordwise position is presented for the NACA 64A010 airfoil for free-stream Mach numbers of 0.31, 0.71, and 0.85, all at a constant angle of attack of 6.2°. Only the pressure distributions over the upper

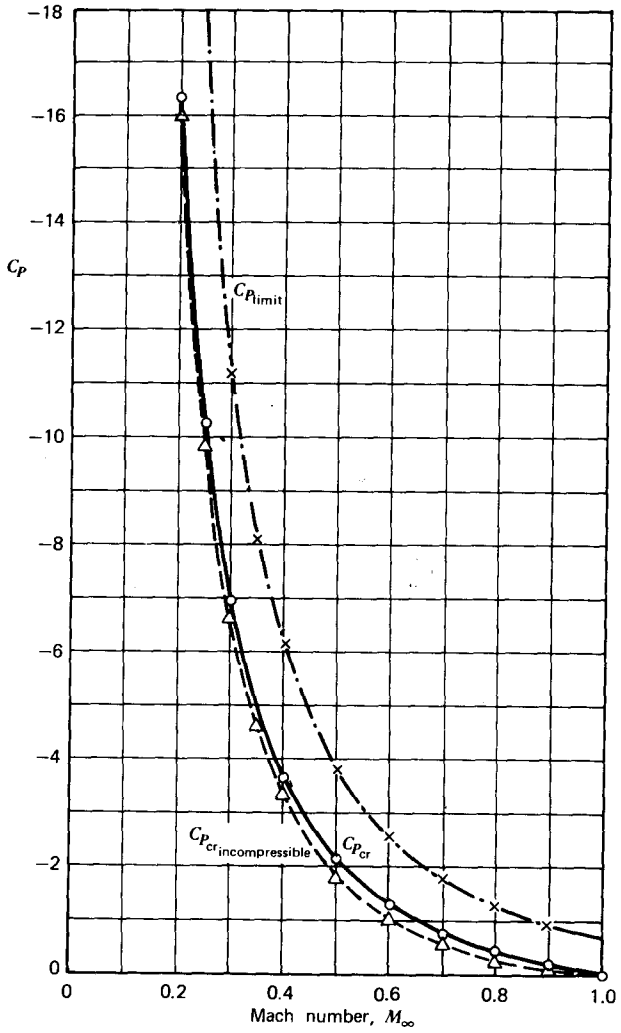

Figure 5.19 Limiting and critical pressure coefficients as a function of free-stream Mach number.

surface are shown. The critical Mach number for this airfoil, corresponding to the minimum C_p of approximately -3.0, is approximately $M_{cr} = 0.43$. Thus, at $M_\infty = 0.31$, this airfoil is operating in the subsonic regime. At $M_\infty = 0.71$, the flow is transonic and theoretically limited to a C_p of -1.7. Near the nose this value is exceeded slightly. However, the experimental values of C_p are indeed nearly constant and equal to $C_{p_{limit}}$ over the leading 30% of the chord. At between the 30 and 40% chord locations, a normal shock compresses the flow,

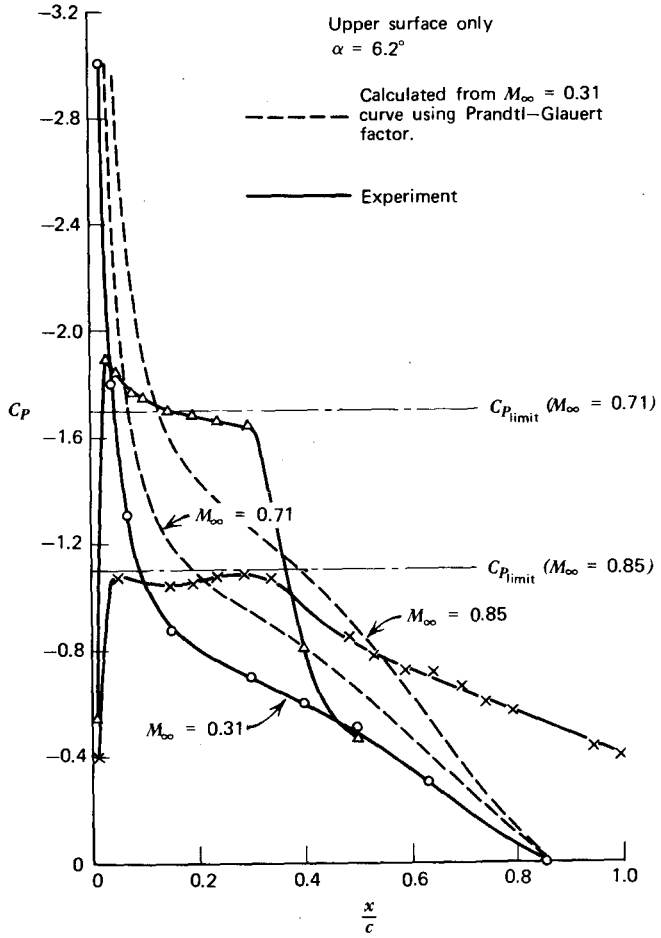

Figure 5.20 Pressure distributions for NACA 64A010 airfoil.

and the pressure rises over the after 60% to equal approximately the subsonic distribution of C_p over this region. Using the preceding relationships for isentropic flow, the pressure rise across a normal shock, and the limiting Mach number of 1.483, one would expect an increase in C_p of 1.56. The experiment shows a value of around 1.2. This smaller value may be the result of flow separation downstream of the shock.

The results at $M_\infty = 0.85$ are somewhat similar. Over the forward 35% of the chord, C_p is nearly constant and approximately equal to $C_{p_{limit}}$. Behind the normal shock, at around the 40% chord location, the increase in C_p is only approximately 0.25 as compared to an expected increment of approximately

1.24. Here the separation after the shock is probably more pronounced, as evidenced by the negative C_p values all the way to the trailing edge.

Notice the appreciable reduction in the area under the C_p curve for $M_\infty = 0.85$ as compared to $M_\infty = 0.71$ because of the difference in the $C_{p_{\text{limit}}}$ values of the two Mach numbers. This limiting effect on C_p is certainly a contribution to the decrease in C_l at the very high subsonic Mach numbers, the other major contributor being shock stall.

Considering the mixed flow in the transonic regime, results such as those shown in Figures 5.3, 5.5, and 5.20, and nonlinear effects such as shock stall and limiting Mach number, the prediction of wing and airfoil characteristics is a difficult task of questionable accuracy. Although the foregoing material may help to provide an understanding of transonic airfoil behavior, one will normally resort to experimental data to determine C_l, C_d, and C_m accurately in this operating regime.

SUPERSONIC AIRFOILS

When the free-stream Mach number exceeds unity, the flow around an airfoil will appear as shown in Figure 5.21*a* or 5.21*b*. If the nose of the airfoil is blunt, a detached bow shock will occur, causing a small region of subsonic flow over the nose of the airfoil. After the flow is deflected subsonically around the nose, it expands again through Mach waves fanning out from the convex surfaces to supersonic conditions. As it leaves the trailing edge, the flows along the upper and lower surfaces are deflected by oblique shock waves and become parallel to each other and to the free stream.

In the case of a sharp leading edge, which is the case for an airfoil designed to operate supersonically, the flow is deflected at the leading edge by oblique shock waves attached to the leading edge.

The diamond-shaped supersonic airfoil illustrated in Figure 5.21*b* is relatively easy to analyze, given the oblique shock and Prandtl-Meyer flow relationships. To begin, since pressure distributions cannot be propagated ahead, the flow will be uniform until it is deflected by the oblique shock waves above and below the leading edge. The streamlines, after passing through the oblique shocks, will remain parallel and straight until they are turned through the expansion fan, after which they are again straight and parallel until they are deflected to approximately the free-stream direction by the oblique shock waves from the trailing edge. This flow is illustrated in detail in Figure 5.22.

The flow from the trailing edge does not necessarily have to satisfy the Kutta conditions, as in the subsonic case. Instead, the final deflection, and hence the strength of the trailing oblique shock waves, is fixed by stipulating that the pressure and flow directions be the same for the flows from the upper and lower surfaces as they meet behind the trailing edge.

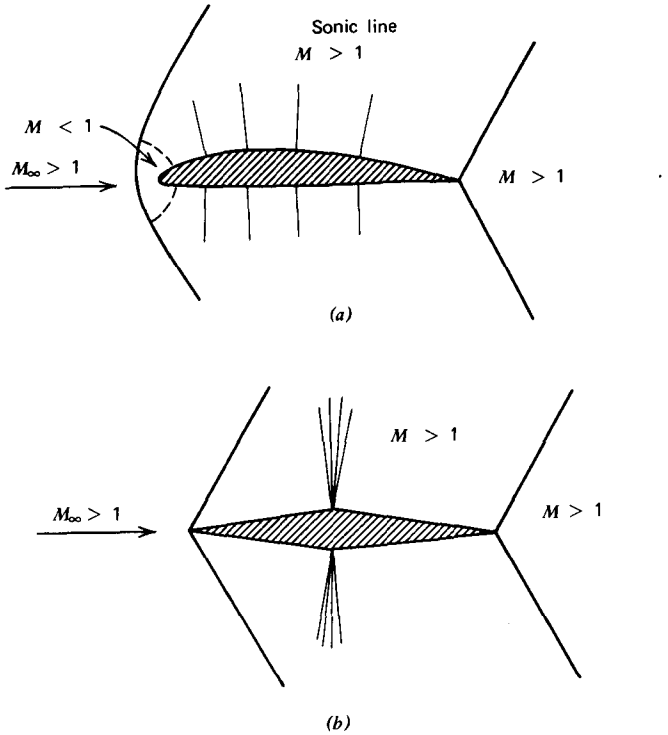

Figure 5.21 Supersonic airfoils. (a) Blunt-nosed airfoil. (*b*) Sharp-nosed airfoil.

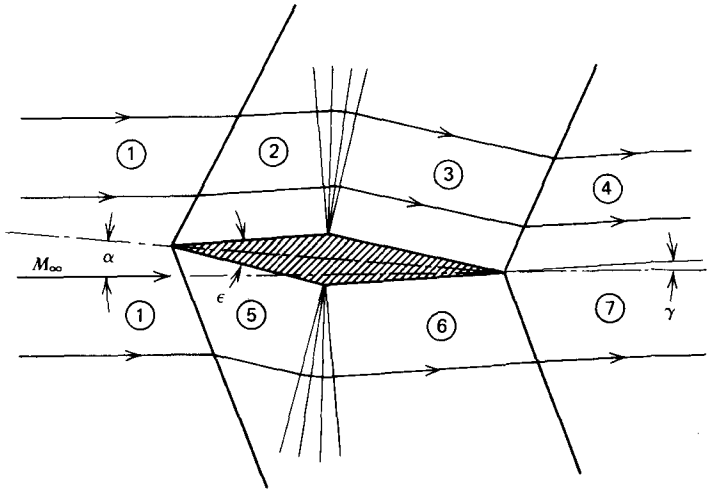

Figure 5.22 A symmetrical wedge airfoil in supersonic flow.

As an example, consider a supersonic airfoil having a symmetrical wedge configuration, as shown in Figure 5.22. We are given

$$\frac{t}{c} = 0.1$$

$$M_\infty = 2.0$$

$$\alpha = 2°$$

For this case, the angle ϵ in Figure 5.22 becomes 11.3°. Thus the required deflection angles are as follows.

region 1 to region 2	$\delta = 3.65°$
region 2 to region 3	$\delta = 11.3°$
region 3 to region 4	$\delta = 7.65° + \gamma$
region 1 to region 5	$\delta = 7.65°$
region 5 to region 6	$\delta = 11.3°$
region 6 to region 7	$\delta = 3.65° - \gamma$

γ is the unknown angle that must satisfy $\delta_{3\text{-}4} = \delta_{6\text{-}7}$. Figures 5.14 and 5.17 cannot be read with sufficient accuracy, so it is necessary to work with the oblique shock and Prandtl-Meyer relationships on which these figures are based. These relationships are easily programmed on a programmable calculator. In this way, the following numbers were readily obtained. For $M_1 = 2.000$ and $\delta_{1\text{-}2} = 3.65°$,

$$\theta = 33.08°$$

$$\frac{p_2}{p_1} = 1.224$$

$$\frac{\rho_2}{\rho_1} = 1.155$$

$$M_2 = 1.911$$

$$\frac{p_{02}}{p_{01}} = .999$$

For $M_2 = 1.911$ and $\delta_{2\text{-}3} = 11.3°$, the Prandtl-Meyer relationships are as follows.

$$\frac{p_2}{p_0} = 0.1467$$

$$\frac{\rho_2}{\rho_0} = 0.2539$$

$$M_3 = 2.337$$

$$\frac{p_3}{p_0} = 0.07548$$

$$\frac{\rho_3}{\rho_0} = 0.1579$$

$$\frac{p_3}{p_2} = 0.2973$$

$$\frac{\rho_3}{\rho_2} = 0.6219$$

For $M_1 = 2.000$ and $\delta_{1\text{-}5} = 7.65°$,

$$\theta = 36.86°$$

$$\frac{p_5}{p_1} = 1.513$$

$$\frac{\rho_5}{\rho_1} = 1.341$$

$$M_5 = 1.808$$

For the preceding with $\delta_{5\text{-}6} = 11.3°$, the Prandtl-Meyer relationships applied to the lower surface are as follows.

$$\frac{p_5}{p_0} = 0.1719$$

$$\frac{\rho_5}{\rho_0} = 0.2843$$

$$M_6 = 2.220$$

$$\frac{p_6}{p_0} = 0.09057$$

$$\frac{\rho_6}{\rho_0} = 0.1799$$

$$\frac{p_6}{p_5} = 0.3186$$

$$\frac{\rho_6}{\rho_5} = 0.6328$$

With this information, we can determine that

$$\frac{p_4}{p_1} = 0.3639 \frac{p_4}{p_3}$$

Also,

$$\frac{p_7}{p_1} = 0.4820 \frac{p_7}{p_6}$$

Thus, if p_4 and p_7 are to be equal, it must follow that

$$\frac{p_4}{p_3} = 1.325 \frac{p_7}{p_6}$$

The problem now is finding the value of γ that results in oblique shocks trailing from the upper and lower surfaces having compression ratios that satisfy the above.

Through the process of trial and error this was accomplished with the following results.

$$\gamma = 0.3°$$

$$\theta_{3\text{-}4} = 31.89 \qquad \theta_{6\text{-}7} = 29.69°$$

$$\frac{p_4}{p_3} = 1.612 \qquad \frac{p_7}{p_6} = 1.219$$

$$\frac{\rho_4}{\rho_3} = 1.402 \qquad \frac{\rho_7}{\rho_6} = 1.151$$

$$M_4 = 2.148 \qquad M_7 = 2.121$$

The ratio of the actual velocities can be found from

$$\frac{V_4}{V_7} = \frac{M_4}{M_7}\frac{a_4}{a_7} = \frac{M_5}{M_7}\frac{p_4}{p_7}\frac{\rho_7}{\rho_4}$$
$$= 0.982$$

Thus a shear layer, or vorticity, is generated downstream of the airfoil, since the loss in total temperature is slightly different between the upper and lower surfaces.

The lift coefficient can be expressed as

$$c_l = \frac{2}{\gamma M_\infty^2} \int_0^1 \left(\frac{p_l}{p_\infty} - \frac{p_u}{p_\infty} \right) dx \tag{5.53}$$

where x is the dimensionless distance along the chord and the subscripts l and u refer to lower and upper surfaces. In this example, the pressures are

constant, but with different values, over each half of the chord. Thus

$$C_l = \frac{2}{\gamma M_\infty^2}\left(\frac{1}{2}\right)\left[\frac{p_5}{p_1}\left(1+\frac{p_6}{p_5}\right)-\frac{p_2}{p_1}\left(1+\frac{p_3}{p_2}\right)\right]$$
$$= 0.0727$$

Unlike the two-dimensional, inviscid, subsonic flow, a drag known as wave drag exists for the supersonic case. This drag can be obtained by resolving the integral of the normal pressure forces over the body in the drag direction.

For the symmetrical wedge pictured in Figure 5.22, the wave drag is; therefore

$$D = [(p_2 - p_6)\sin 3.65° + (p_5 - p_3)\sin 7.65°]\frac{c}{2}$$

In dimensionless form, this becomes

$$C_d = \frac{2}{\gamma M_\infty^2}\left(\frac{1}{2}\right)\left[\left(\frac{p_2}{p_1}-\frac{p_6}{p_5}\frac{p_5}{p_1}\right)\sin 3.65° + \left(\frac{p_5}{p_1}-\frac{p_3}{p_2}\frac{p_2}{p_1}\right)\sin 7.65°\right]$$
$$= 0.0358$$

The moment coefficient about the leading edge will be given by

$$C_m = \frac{-2}{\gamma M_\infty^2}\int_0^1 \left(\frac{p_l}{p_\infty}-\frac{p_u}{p_\infty}\right)x\,dx$$
$$= \frac{-2}{\gamma M_\infty^2}\left(\frac{p_5}{p_1}\frac{1}{8}+\frac{p_6}{p_1}\frac{3}{8}-\frac{p_2}{p_1}\frac{1}{8}-\frac{p_3}{p_1}\frac{3}{8}\right)$$
$$= -0.0287$$

From C_m and C_l, the center of pressure for this symmetrical airfoil is seen to be 0.395 chord lengths behind the leading edge.

LINEARIZED COMPRESSIBLE POTENTIAL FLOW

The foregoing treatment based on Prandtl-Meyer and oblique shock relationships is somewhat tedious to apply. Also, the general behavior of supersonic airfoils is not disclosed by this approach. Therefore we will now consider a linearized solution that holds for slender profiles and for Mach numbers that are not too close to unity or not too high.

Assuming that the free-stream velocity is only perturbed by the presence of a slender body at a small angle of attack, the x and y components of the local velocity can be written as

$$V_x = V_\infty + u$$
$$V_y = v \qquad (5.54)$$

where

$$\frac{u}{V_\infty}, \frac{v}{V_\infty} \ll 1$$

We now define a perturbation velocity potential, ϕ, such that

$$u = \frac{\partial \phi}{\partial x} \tag{5.55}$$

$$v = \frac{\partial \phi}{\partial y}$$

If Equations 5.54 and 5.55 are substituted into the equations of fluid motion together with the isentropic relationships, the following linearized equation is obtained for the perturbation velocity potential.

$$(1 - M_\infty^2)\frac{\partial^2 \phi}{\partial x^2} + \frac{\partial^2 \phi}{\partial y^2} = 0 \tag{5.56}$$

In order to arrive at this equation, Reference 5.3 shows that the following must hold.

$$M_\infty^2(u/V_\infty) \ll 1 \tag{5.57a}$$

$$\frac{u}{V_\infty} \ll (1 - M_\infty^2) \tag{5.57b}$$

Thus, from Equation 5.57*a*, M_∞ cannot be too large (i.e., the application of Equation 5.56 to hypersonic flow is questionable). On the other hand, from Equation 5.57*b*, M_∞ is restrained from becoming close to unity, so that the application of Equation 5.56 to transonic flows is ruled out.

Subsonic Flow

For M_∞ values less than unity, Equation 5.56 is of the elliptic form. In this case, a disturbance at any point in the flow affects the flow at all other points. A solution to Equation 5.56 for the subsonic case can be obtained in terms of the solution for $M_\infty = 0$. This latter solution has been discussed in previous chapters.

Let $\phi_i(x, y)$ be a solution to Equation 5.56 for $M_\infty = 0$. Now consider a function, ϕ_c, given by

$$\phi_c = \frac{\phi_i(x, \beta y)}{\beta} \tag{5.58}$$

where, as before, β is defined as

$$\beta^2 = 1 - M_\infty^2$$

Thus,

$$\frac{\partial^2 \phi_c}{\partial x^2} = \frac{1}{\beta} \frac{\partial^2 \phi_i}{\partial x^2}$$

$$\frac{\partial^2 \phi_c}{\partial y^2} = \beta \frac{\partial^2 \phi_i}{\partial y^2}$$

Substituting this into the left side of Equation 5.56 gives

$$\beta\left(\frac{\partial^2 \phi_i}{\partial x^2} + \frac{\partial^2 \phi_i}{\partial y^2}\right)$$

Since the terms within the parentheses are equal to zero, it follows that Equation 5.58 is a solution of Equation 5.56.

Now consider a body contour $Y(x)$. At any point along the contour, the following boundary condition must hold.

$$\begin{aligned} \frac{dY}{dx} &= \frac{v}{V_\infty + u} \\ &\simeq \frac{v}{V_\infty} \end{aligned} \tag{5.59}$$

Equation 5.59 holds to the first order in the perturbation velocities.

Relating v to the incompressible perturbation velocity potential leads to

$$\frac{dY}{dx} = \frac{1}{V_\infty}\left[\frac{\partial \phi_i}{\partial y}(x, y)\right] \tag{5.60}$$

In the compressible case,

$$\frac{dY}{dx} = \frac{1}{V_\infty}\left[\frac{\partial \phi_i}{\partial y}(x, \beta y)\right] \tag{5.61}$$

$\partial \phi_i / \partial y$ can be expanded in a Maclaurin series to give

$$\frac{\partial \phi_i}{\partial y}(x, y) = \frac{\partial \phi_i}{\partial y}(x, 0) + y \frac{\partial^2 \phi_i}{\partial y^2}(x, 0) + \frac{y^2}{2} \frac{\partial^3 \phi_i}{\partial y^3}(x, 0) + \cdots$$

Since y and the derivatives of ϕ_i are assumed to be small, to a first order,

$$\frac{\partial \phi_i(x, y)}{\partial y} = \frac{\partial \phi_i(x, 0)}{\partial y} \tag{5.62}$$

Thus, by comparing Equations 5.60 and 5.61, it follows that the body contour for which ϕ_c holds is the same (to a first order) as that for ϕ_i.

We are now in a position to determine the pressure distribution for a given slender body shape as a function of Mach number. Along a streamline the resultant velocity, U, in terms of the perturbation velocities, can be written as

$$\begin{aligned} U &= [(V_\infty + u)^2 + v^2]^{1/2} \\ &= V_\infty + u \text{ (to a first order)} \end{aligned} \tag{5.63}$$

Euler's equation along a streamline was derived earlier in differential form. Expressed in finite difference form, it can be written as

$$U\,\Delta U + \frac{\Delta p}{\rho} = 0$$

Using Equation 5.63, this becomes

$$(V_\infty + u)u + \frac{\Delta p}{\rho} = 0$$

Finally,

$$\begin{aligned} C_p &= \frac{p - p_\infty}{(1/2)\rho V_\infty^2} \\ &= \frac{\Delta p}{(1/2)\rho V_\infty^2} \\ &= -2\frac{u}{V_\infty} \end{aligned} \tag{5.64}$$

Since $u = \partial\phi/\partial x$, it follows from Equations 5.64 and 5.58 that the pressure distribution over a slender body at a finite subsonic Mach number is related to the pressure distribution over the *same* body at $M = 0$ by

$$C_{p_c} = \frac{C_{p_i}}{\beta} \tag{5.65}$$

This was assumed earlier in this chapter as Equation 5.2.

Thus, to predict the lift and moment on a two-dimensional shape such as an airfoil, one simply calculates these quantities in coefficient form for the incompressible case and then multiplies the results by the factor $1/\beta$.

The three-dimensional case is somewhat more complicated, but not much. Here,

$$\phi_c = \frac{1}{\beta^2}\,\phi_i(x, \beta y, \beta z) \tag{5.66}$$

Hence, to find the compressible flow past a three-dimensional body with coordinates of x, y, and z, one solves for the incompressible flow around a body having the coordinates x, βy, and βz. The pressure coefficients are then related by

$$C_{p_c} = \frac{C_{p_i}}{\beta^2} \tag{5.67}$$

Supersonic Flow (Ackeret Theory)

If M is greater than unity, Equation 5.56 changes to a hyperbolic partial differential equation, specifically, to the following wave equation.

$$(M_\infty^2 - 1)\frac{\partial^2\phi}{\partial x^2} = \frac{\partial^2\phi}{\partial y^2} \tag{5.68}$$

Letting

$$B = \sqrt{M_\infty^2 - 1}$$

a general solution of Equation 5.68 can be written.

$$\phi = f(x - By) + g(x + By) \tag{5.69}$$

where f and g represent arbitrary functions of their arguments. As an exercise, verify that Equation 5.69 satisfies Equation 5.68. ϕ is seen to be constant along families of straight lines defined by

$$x - By = \text{constant} \tag{5.70a}$$

$$x + By = \text{constant} \tag{5.70b}$$

The slope of the lines represented by Equation 5.70*a* is

$$\frac{dy}{dx} = \frac{1}{B}$$
$$= (M^2 - 1)^{-1/2}$$

But this is the tangent of the Mach wave angle as defined by Equation 5.45. Thus ϕ is constant along a Mach wave. In the case of Equation 5.70*b*,

$$\frac{dy}{dx} = -\frac{1}{B}$$

On the upper surface of a body, this would correspond to a disturbance being propagated forward in the flow, which is physically impossible in a supersonic flow. Thus Equation 5.70*b* is ruled out for the upper surface. However, on the lower surface of a body, $g(x + By)$ is a physically valid flow and represents a disturbance being propagated rearward along a Mach wave. Similarly, $f(x - By)$ is not allowed as a solution on the lower surface of a body. The net result is pictured in Figure 5.23, where it is seen that $f(x - By)$ and $g(x + By)$ are solutions to ϕ on the upper and lower surfaces, respec-

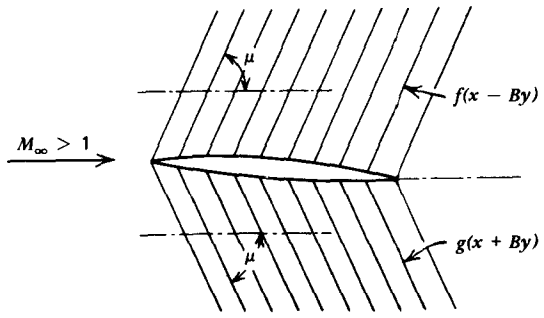

Figure 5.23 Mach waves emanating from upper and lower surfaces of a body.

tively. Since ϕ is constant along Mach waves emanating from disturbances from the upper and lower surfaces, it follows that the properties of the flow (velocity and state) are also constant along these waves.

Along the surface of the body the flow must be tangent to the body. Thus, if $Y(x)$ represents the body surface, it follows, to a first order in the perturbation velocities, that

$$\frac{1}{V_\infty}\left(\frac{\partial \phi}{\partial y}\right) = \left(\frac{dY}{dx}\right) \tag{5.71}$$

Consider the upper surface and let $x - By = z$. Then

$$\left(\frac{\partial \phi}{\partial y}\right)_u = \frac{df}{dz}\frac{\partial z}{\partial y}$$
$$= -Bf' \tag{5.72}$$

where f' denotes df/dz. In addition, from Equation 5.64,

$$C_{p_u} = -\frac{2}{V_\infty}\frac{\partial \phi}{\partial x}$$
$$= \frac{2}{V_\infty} f' \tag{5.73}$$

Thus, combining Equations 5.71 to 5.73,

$$C_{p_u} = \frac{2}{B}\left(\frac{dY}{dx}\right)_u \tag{5.74}$$

Similarly, on the lower surface,

$$C_{p_l} = -\frac{2}{B}\left(\frac{dY}{dx}\right)_l \tag{5.75}$$

Thus, according to Ackeret's linearized theory for supersonic flow around a slender body, the pressure locally on the body is determined by the slope of the surface at the particular location in question.

This simple result leads quickly to some interesting conclusions regarding the characteristics of thin, supersonic airfoils at low angles of attack. Since, for a unit chord,

$$C_l = \int_0^1 (C_{p_l} - C_{p_u})\, dx$$

you can quickly verify that

$$C_l = \frac{4\alpha}{B} \tag{5.76}$$

Thus, within the limitations of the linearized theory, the section lift coefficient of a supersonic airfoil depends only on its angle of attack. Camber is predicted to have no effect on C_l.

The wave drag coefficient is obtained by integrating the component of C_p in the drag direction around the airfoil.

$$C_{d_w} = \oint C_p \frac{dy}{dx}\, dx$$
$$= \frac{2}{B}\left[\int_0^1 \left(\frac{dy}{dx}\right)_u^2 dx + \int_0^1 \left(\frac{dy}{dx}\right)_l^2 dx\right] \tag{5.77}$$

If dy/dx is expressed in the form

$$\frac{dy}{dx} = -\alpha + \epsilon$$

where α is the angle of attack of the chord line and ϵ is the slope of the surface relative to the chord line, C_{d_w} becomes

$$C_{d_w} = \frac{4\alpha^2}{B} + \frac{2}{B}\int_0^1 (\epsilon_u^2 + \epsilon_l^2)\, dx \tag{5.78}$$

The wave drag coefficient can thus be viewed as the sum of two terms; the first results from lift and the second results from thickness and camber.

$$C_{d_w} = C_L\alpha + \frac{2}{B}\int_0^1 (\epsilon_u^2 + \epsilon_l^2)\, dx$$

The first term, $C_L\alpha$, is simply the streamwise component of the normal pressures integrated over the airfoil. In the case of a subsonic airfoil, this term is canceled by the leading edge suction force.

The pitching moment coefficient about the leading edge of a thin, supersonic airfoil can be written

$$C_{m_{LE}} = \int_0^1 C_{p_l} x\, dx - \int_0^1 C_{p_u} x\, dx$$
$$= \frac{2}{B}\int_0^1 \left[\left(\frac{dy}{dx}\right)_u + \left(\frac{dy}{dx}\right)_l\right] x\, dx$$
$$= -\frac{2}{B}\alpha + \frac{2}{B}\int_0^1 (\epsilon_u + \epsilon_l) x\, dx \tag{5.79}$$

Table 5.1 compares the results of the linearized theory with the more exact predictions made earlier for the symmetrical wedge airfoil pictured in Figure 5.22. In this particular case, the linearized theory is seen to be somewhat optimistic with regard to lift and drag and predicts the center of pressure to be further aft than the position obtained from the more exact calculations. Nevertheless, the Ackeret theory is valuable for predicting trends. For example, *for symmetrical airfoils*, the expressions of C_{d_w} and C_m reduce to

$$C_{d_w} = \frac{4}{\sqrt{M^2 - 1}}\left[\alpha^2 + \left(\frac{t}{c}\right)^2\right] \tag{5.80}$$

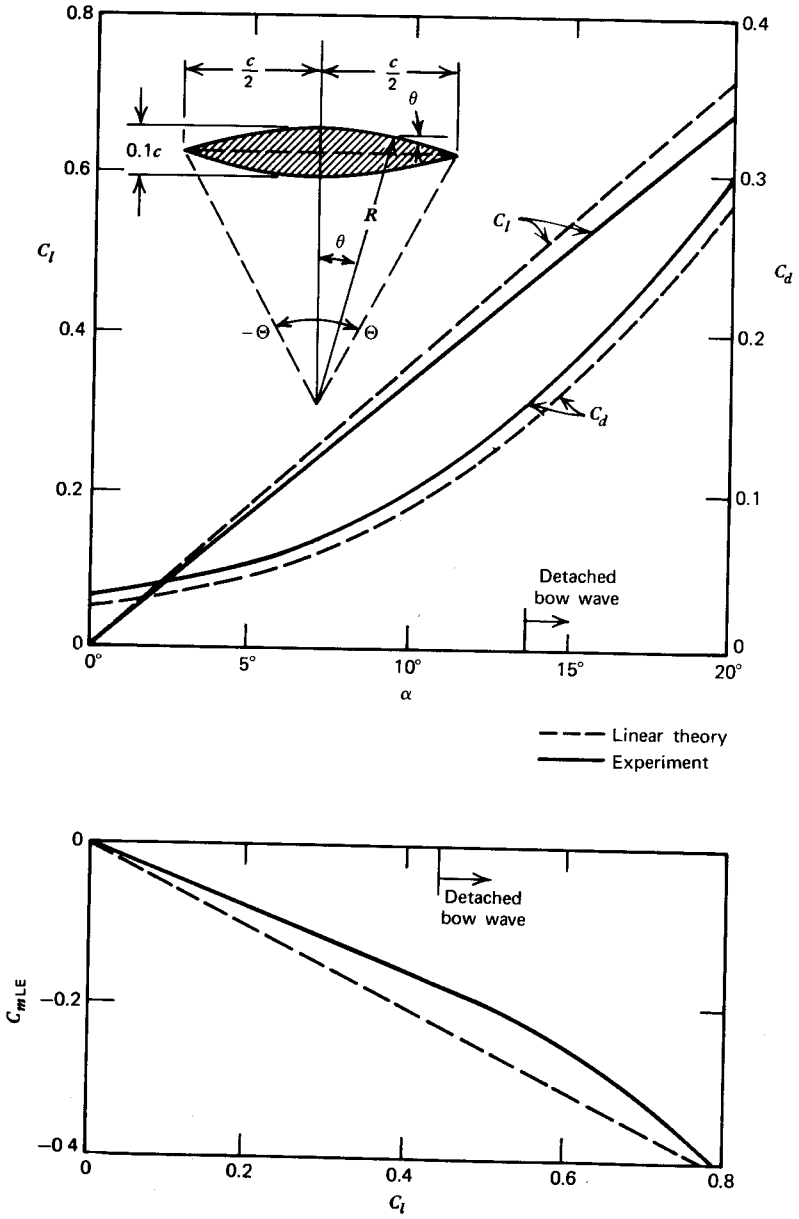

Figure 5.24 Comparison between measured aerodynamic characteristics (Ferri, 1939) and those predicted by linear theory at $M_\infty = 2.13$. Airfoil is biconvex, maximum thickness = 0.1c. (A. M. Kuethe and C. Y. Chow, *Foundations of Aerodynamics*, John Wiley & Sons, Inc., 1976. Reprinted by permission of John Wiley & Sons, Inc.)

Table 5.1 Predicted Characteristics of a Symmetrical, 10% thick, Double-Wedge Airfoil at a 2° Angle of Attack and a Mach Number of 2.0

	Using Oblique Shock Wave and Prandtl-Meyer Relationships	Linearized Ackeret Theory
C_l	0.0727	0.0806
C_{d_w}	0.0358	0.0259
C_m	−0.0287	−0.0403
Center of pressure	0.3950	0.5000

$$C_m = -\frac{2}{\sqrt{M^2-1}}\alpha \tag{5.81}$$

The center of pressure for a symmetrical airfoil in supersonic flow is thus predicted to be at the midchord point.

Figure 5.24 (taken from Ref. 5.6) provides a comparison between the linear theory and experiment for a 10% thick biconvex airfoil. This figure shows fairly good agreement of the theory with experiment with the differences being of the same signs as those in Table 5.1.

THREE-DIMENSIONAL WINGS

Wings designed to operate at high speeds are generally thin and employ sweepback in order to increase the critical Mach number. In some instances the sweep is variable to accommodate operation at both low and high speeds. Many airplanes for which the primary mission involves supersonic flight employ delta planforms. Generally, the trend is to increase the sweepback with increasing Mach number until a point is reached where the delta planform becomes more advantageous from a structural as well as aerodynamic viewpoint.

Typical operational aircraft with differing planform shapes are illustrated in Figure 5.25. The Boeing 727 has a midchord sweep angle of approximately 27° with a cruise Mach number of around 0.84 at 6705 m (22,000 ft). The aspect ratio of its wing equals 7.2. The Vought A-7D has about the same midchord sweep angle with a maximum Mach number in level flight at 1525 m (5000 ft) of around 0.88. Its aspect ratio of 4.0 is much lower than that of the 727. The Grumman F-14A and Aerospatiale/BAC Concorde have supersonic capability and employ planforms of a low aspect ratio that are approximately delta shaped. The F-14A employs variable sweep, sometimes

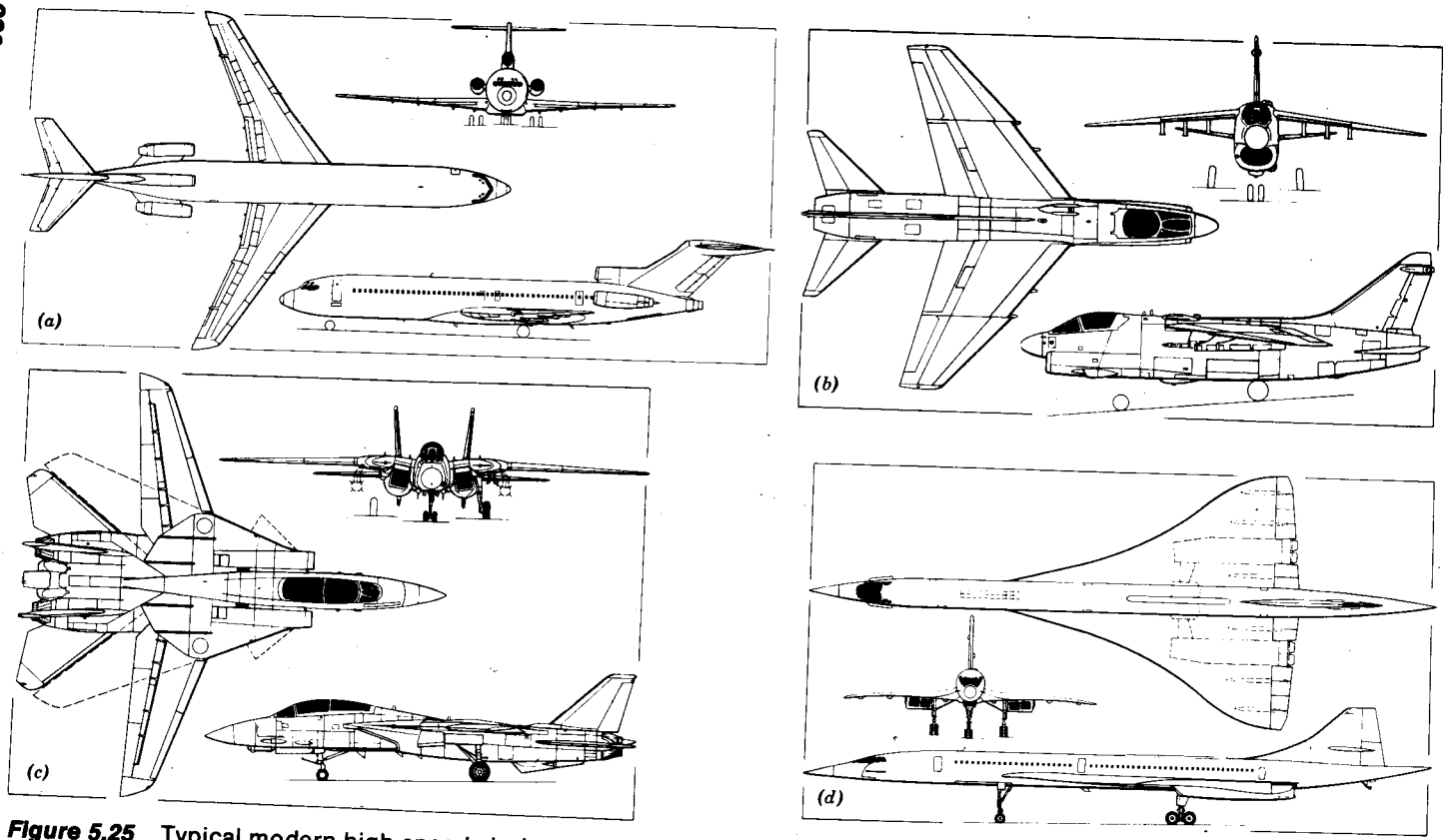

Figure 5.25 Typical modern high-speed airplanes. (*a*) Boeing 727–200 three-turbofan short/medium-range transport. (*b*) Vought A-7D tactical fighter version of the Corsair II for the USAF. (*c*) Grumman F-14A Tomcat carrier-based multimission fighter. (*d*) Aerospatial/BAC Concorde supersonic transport. (John W. R. Taylor, *Jane's All the World's Aircraft*, Pilot Press Ltd, 1977. Copyright © 1977 Pilot Press Ltd.)

referred to as a "swing wing." Fully forward its aspect ratio equals approximately 7.6. When swung to the rear, the wing and horizontal tail combine to produce a delta wing having an aspect ratio of approximately 1.0. The maximum design Mach number of the F-14A, according to Reference 5.11, is 2.4. The Concorde's planform shape is referred to as an ogee. It has an aspect ratio of 1.7 and is designed to cruise at a Mach number of 2.02 at 15,635 m (51,300 ft).

Characteristics of Sweptback Wings

Qualitatively, the effect of wing sweep can be seen by referring to Figure 5.26. In Figure 5.26*a*, a wing section is shown extending from one wall of a wind tunnel to the other. The test section velocity is denoted by V_n. Imagine that the wing in Figure 5.26*a* is only a section of an infinitely long wing that is being drawn through contoured slots in the tunnel walls at a velocity of v. Obviously, the pressure distribution around the section does not depend on v. V_n and v combine vectorially, as shown in Figure 5.26*b*, to give a velocity of V_∞ relative to the wing. As shown in Figure 5.26*c*, this is equivalent to a swept

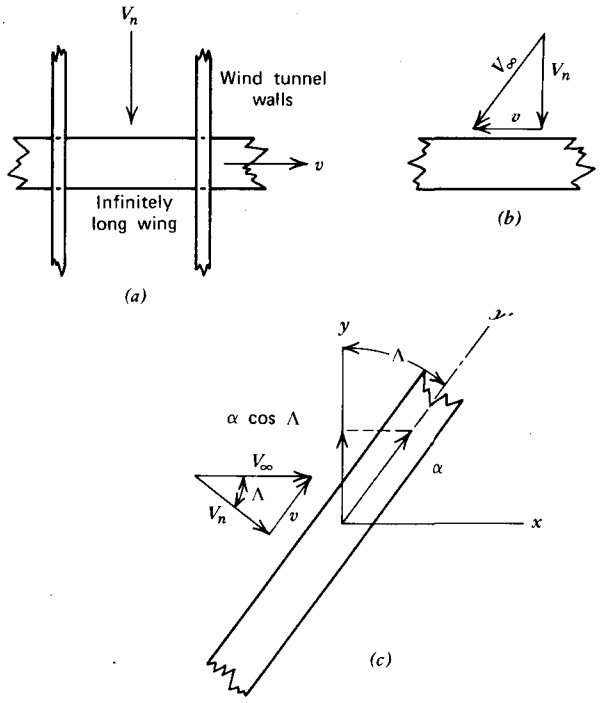

Figure 5.26 Effect of sweepback.

wing of an infinite aspect ratio with a sweep angle of Λ and a free-stream velocity of V_∞. Thus, the chordwise C_p distribution of such a wing depends only on the component of V_∞ normal to the span, which is given by

$$V_n = V_\infty \cos \Omega \tag{5.82}$$

Based on this velocity, a pressure coefficient can be defined as

$$C_{p_n} = \frac{p - p_\infty}{(1/2)\rho_\infty V_\infty^2 \cos^2 \Omega} = \frac{(p/p_\infty) - 1}{(1/2)\gamma M_{\infty_n}^2} \tag{5.83}$$

The Prandtl-Glauert transformation can then be applied to C_{p_n} using M_n in order to account for compressibility. In practice, a swept wing has a finite length. Near the apex of the wing and at the tips, a three-dimensional flow effect will be encountered. Indeed, one cannot test a two-dimensional swept wing in a wind tunnel (except in the manner shown in Figure 5.26*a*). For example, a wing placed wall to wall and yawed in a wind tunnel models a saw-toothed planform instead of an infinitely long swept wing. As illustrated in Figure 5.27, this results from the fact that the flow must be parallel to the wind tunnel walls at the walls. This can only be satisfied by assuming an image system of wings having alternating sweep, as shown.

The effect of sweepback on critical Mach number can be estimated using Equation 5.83. For example, suppose a straight wing has a certain chordwise and spanwise C_p distribution that produces a given lift. At some point on the wing, suppose that a minimum C_p is equal to -0.5. According to Figure 5.19, its M_{cr} value would equal 0.71. Now suppose the same wing were swept back 45° and its twist, camber, and angle of attack were adjusted to give the same chordwise C_p distribution (based on V_∞) at each spanwise station as for the unswept wing. The total lift for the two wings would then be the same. For the swept wing the minimum C_p based on V_n becomes $C_{p_n} = -1.0$. Thus, according to Figure 5.19, $M_{n_{cr}} = 0.605$. This corresponds to a free-stream

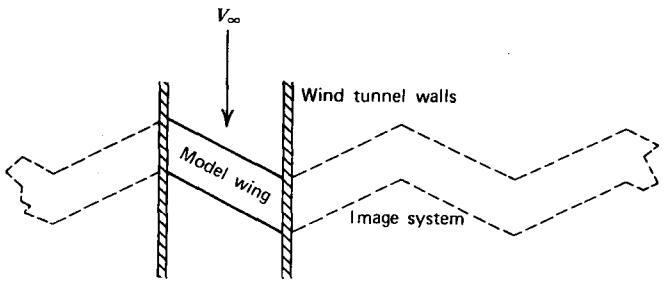

Figure 5.27 Swept wing in a wind tunnel.

critical Mach number, $M_{\infty_{cr}}$, of 0.86. Therefore, in this case, sweeping the wing back 45° for the same wing area and lift has increased the critical Mach number from 0.71 to 0.86.

Sweepback is also beneficial in supersonic flow. Mach waves propagate from the leading edge of the wing at the angle, μ (Equation 5.45). If the sweepback angle, Λ, is greater than the complement of μ, the flow component normal to the span is subsonic. Locally the resultant flow along a streamline is still supersonic, but the Mach waves generated at the leading edge deflect the flow, thereby lessening the strength of the oblique shocks.

Sweepback is not without its disadvantages, so it is normally used only when called for by compressibility considerations. Sweeping a wing will cause the loading to increase toward the tips unless it is compensated for by washout. At the same time, the spanwise component of V_∞ produces a thickening of the boundary layer in the tip region. Hence a swept wing is more likely to stall outboard by comparison to a straight wing; this characteristic is undesirable from the standpoint of lateral control. Also, tip stall (which might occur during a high-speed pull-up) can cause a nose-up pitching moment, further aggravating the stall.

Aeroelastic effects caused by sweep can also be undesirable. A sudden increase in angle of attack can cause the wing to bend upward. As it does, because of the sweep, the tips tend to twist more nose downward relative to the rest of the wing. Again, this can produce a nose-up pitching moment that increases the angle of attack even further. This behavior is an unstable one that can lead to excessive loads being imposed on the airframe.

Let us refer once again to Figure 5.26*c*. A rotation of α about a line along the wing is shown as a vector in the figure. Observe that the component of this vector normal to V_∞ is equal to $\alpha \cos \Lambda$. Thus an angle of attack of α relative to V_n results in a smaller angle of attack of $\alpha \cos \Omega$ relative to V.

The lift on a unit area of the wing will be given by

$$\begin{aligned} L &= \tfrac{1}{2}\rho V_n^2 C_{l_\alpha} \alpha \\ &= \tfrac{1}{2}\rho (V_\infty \cos \Lambda)^2 C_{l_\alpha} \alpha \end{aligned}$$

where C_{l_α} is the slope of the lift curve for an unswept two-dimensional airfoil section. The corresponding quantity for a swept section can be obtained by dividing the preceding equation by the free-stream dynamic pressure and the angle of attack relative to V_∞.

$$\begin{aligned} C_{l_\alpha}(\Lambda \neq 0) &= L/(\tfrac{1}{2}\rho V_\infty^2 \alpha \cos \Lambda) \\ &= C_{l_\alpha} \cos \Lambda \end{aligned} \tag{5.84}$$

Reference 3.35 presents an approximate equation for the lift curve slope of a wing with sweepback in a subsonic compressible flow. The equation is derived by assuming that Equation 3.74*b* holds for swept wings using the

section lift curve slope for swept wings. Compressibility is accounted for by applying the Prandtl-Glauert correction to Equation 5.84 using M_{x_n}.

Repeating Equation 3.74*b* for an unswept elliptic wing,

$$C_{L_\alpha} = \frac{aA}{(a/\pi) + \sqrt{(a/\pi)^2 + A^2}}$$

where a denotes C_{l_α}. Substituting

$$a = a_0 \cos \Lambda_{1/2} / \sqrt{1 - M_\infty^2 \cos^2 \Lambda_{1/2}}$$

the expression for C_{L_α} reduces to

$$C_{L_\alpha} = \frac{a_0 A}{(a_0/\pi) + \sqrt{(A/\cos \Lambda_{1/2})^2 + (a_0/\pi)^2 - (AM_\infty)^2}} \tag{5.85}$$

where $a_0 = C_{l_\alpha}$ for $\Lambda_{1/2} = M = 0$. Note that a subscript $\frac{1}{2}$ has been added to Λ to indicate that $\Lambda_{1/2}$ should be measured relative to a line through the midchord points. It is argued in Reference 3.35 that the use of $\Lambda_{1/2}$ makes Equation 5.85 independent of taper ratio, λ. This conclusion appears to be supported by Figure 5.28 (taken from Ref. 3.35). Here, Equation 5.85 (for $M = 0$) is seen to

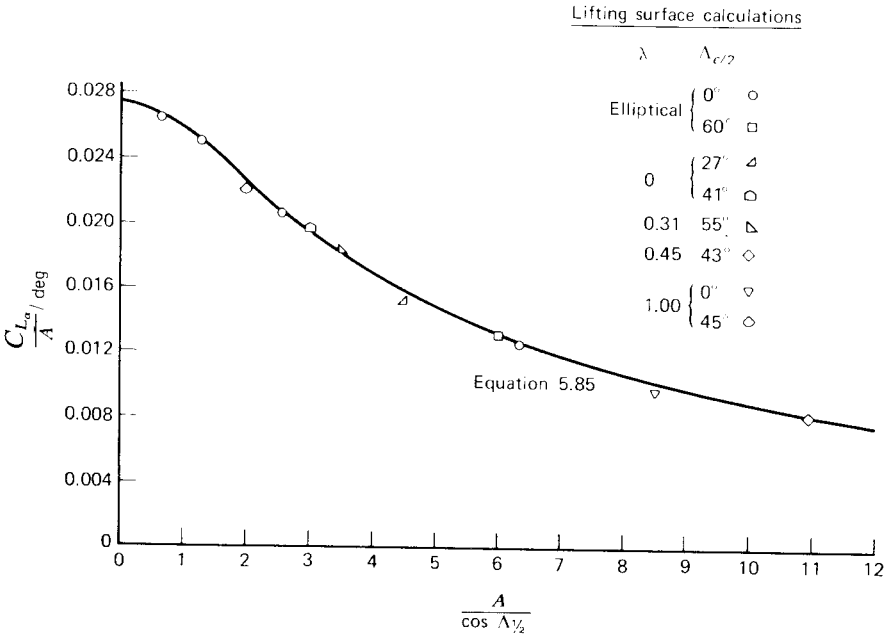

Figure 5.28 C_{L_α}/A with $A/\cos \Lambda_{1/2}$ as determined by several methods. $a_0 = 2\pi$, $M = 0$.

compare favorably with several lifting surface calculations for elliptical and tapered wings.

A tabulation of subsonic lift and moment characteristics for tapered, sweptback wings is presented in Table 5.2. Taken from Reference 5.12, these results are based on a numerical lifting surface theory. They should be more accurate than Equation 5.85, although not as convenient to use. As an example in the use of this table, let

$$\beta A = 5.0$$
$$\beta = 0.6$$
$$A \tan \Lambda_{1/2} = 4$$

It then follows that

$$A = 8.333$$
$$\Lambda_{1/2} = 25.6°$$
$$\beta C_{L_\alpha} = 3.43$$
$$C_{L_\alpha} = 5.717$$

For this example, Equation 5.85 gives a C_{l_α} value of 6.017, which is about 5% higher than the lifting surface theory result. Of course, both results can be expected to be somewhat high by comparison to experiment, since the theoretical value for a_0 of $2\pi C_l$/rad is a few percent higher than that found experimentally for most airfoils.

Figure 5.29 (from Ref. 5.14) presents some experimental results on C_{L_α} at low Mach numbers. Generally, the trends shown on this figure confirm the predictions of Figure 5.28. The two figures are not directly comparable, since the sweep angles of Figure 5.29 are relative to the leading edge instead of to midchord. To go from one reference angle to the other requires a knowledge of the taper ratio as well as the aspect ratio.

Figure 5.30 (taken from Ref. 5.13) presents a limited amount of information on $C_{L_{max}}$ for swept wings with various combinations of flaps. Remembering the "independence principle" for the velocity normal to the sweep line, one might expect that $C_{L_{max}}$ would decrease as $\cos^2 \Omega$. However, referring to the data points in Figure 5.30 without flaps, this variation with $\cos^2 \Lambda$ does not appear to be valid. For example, for $\Lambda = 45°$, $\cos^2 \Lambda = \frac{1}{2}$, yet the $C_{L_{max}}$ values for these swept wings are certainly greater than half of what one would expect for the unswept wings. Three-dimensional effects such as spanwise flow and leading edge vortices undoubtedly play an important role in determining the stalling characteristics of a swept wing. Figure 5.31 indicates that, if anything, there is a tendency for $C_{L_{max}}$ to increase with sweepback (or with sweep forward). Admittedly, this figure includes other factors affecting $C_{l_{max}}$, but the general impression that it portrays is probably valid; that is, sweep has little effect on $C_{L_{max}}$.

Table 5.2 Subsonic Theoretical Lift Slopes, Pitching Moments, and Aerodynamic Centers for Wings of Varying Sweep and Taper (M about leading edge at midspan, $\bar{c}$ = geometric mean chord)

λ	βA	$A \tan \Lambda_{1/2}$	$-\beta \frac{\partial C_M}{\partial \alpha}$	$\frac{1}{A} \frac{\partial C_L}{\partial \alpha}$	$\frac{x_{ac}}{\bar{c}}$
1.0	8.0	0	1.110	0.574	0.242
		2	3.156	0.563	0.701
		4	5.025	0.532	1.181
		6	6.579	0.490	1.677
	5.0	0	0.934	0.791	0.236
		2	2.628	0.761	0.691
		4	4.030	0.686	1.175
		6	5.032	0.599	1.680
	3.0	0	0.707	1.049	0.225
		2	1.998	0.982	0.678
		4	2.916	0.830	1.171
		6	3.446	0.682	1.684
	1.5	0	0.393	1.348	0.195
		2	1.230	1.232	0.665
		4	1.676	0.952	1.174
		6	1.869	0.738	1.689
0.5	8.0	0	1.888	0.592	0.399
		2	3.917	0.580	0.844
		4	5.728	0.548	1.306
		6	7.188	0.505	1.779
	5.0	0	1.600	0.814	0.393
		2	3.312	0.784	0.845
		4	4.663	0.708	1.317
		6	5.563	0.619	1.799
	3.0	0	1.224	1.072	0.381
		2	2.561	1.007	0.848
		4	3.419	0.856	1.331
		6	3.845	0.706	1.816
	1.5	0	0.714	1.360	0.350
		2	1.609	1.254	0.855
		4	1.989	0.982	1.350
		6	2.099	0.765	1.829

Table 5.2 (continued)

λ	βA	$A \tan \Lambda_{1/2}$	$-\beta \frac{\partial C_M}{\partial \alpha}$	$\frac{1}{A} \frac{\partial C_L}{\partial \alpha}$	$\frac{x_{ac}}{\bar{c}}$
0.25	8.0	0	2.465	0.594	0.418
		2	4.433	0.582	0.951
		4	6.155	0.551	1.397
		6	7.510	0.508	1.848
	5.0	0	2.100	0.816	0.515
		2	3.788	0.786	0.963
		4	5.062	0.711	1.423
		6	5.859	0.622	1.882
	3.0	0	1.623	1.071	0.505
		2	2.064	1.009	0.980
		4	3.750	0.861	1.452
		6	4.078	0.712	1.910
	1.5	0	0.978	1.351	0.483
		2	1.891	1.254	1.006
		4	2.203	0.990	1.484
		6	2.241	0.774	1.931
0	8.0	0	3.092	0.568	0.681
		2	4.818	0.557	1.081
		4	6.296	0.529	1.488
		6	7.433	0.491	1.894
	5.0	0	2.636	0.773	0.682
		2	4.143	0.746	1.111
		4	5.218	0.680	1.536
		6	5.841	0.600	1.948
	3.0	0	2.066	1.009	0.683
		2	3.286	0.953	1.149
		4	3.906	0.821	1.585
		6	4.092	0.685	1.991
	1.5	0	1.310	1.281	0.682
		2	2.150	1.190	1.205
		4	2.325	0.947	1.636
		6	2.263	0.746	2.022

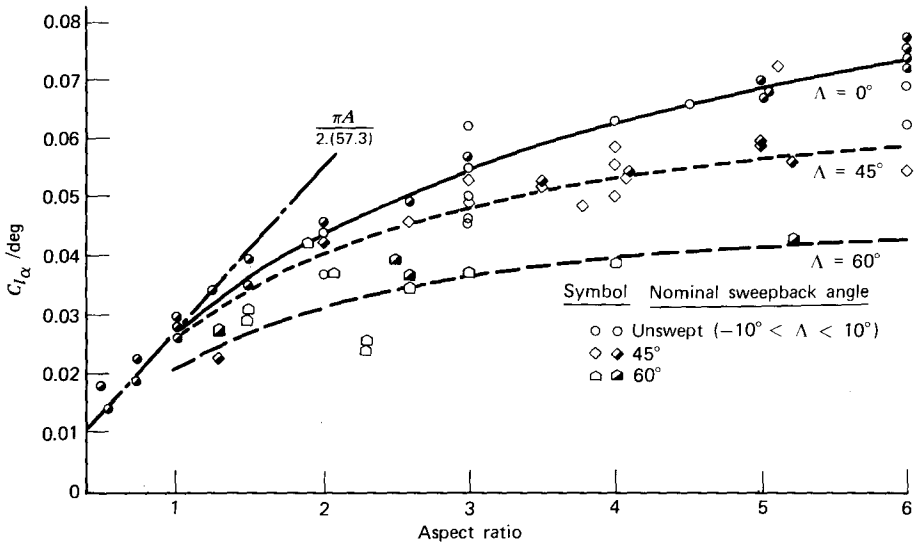

Figure 5.29 Lift curve slopes for swept, tapered wings.

The effect of sweepback on drag can be quickly summarized by Figures 5.32 and 5.33. Figure 5.32 allows one to estimate the induced drag as a function of sweepback, aspect ratio, and taper ratio. These graphs were prepared using Weissinger's first-order lifting surface theory. The bound vortex is placed at the quarter-chord points with control points at the three-quarter-chord points. (See the equivalent two-dimensional calculation leading to Equation 3.19.) These graphs apply only to $M_\infty = 0$, so they must be used in conjunction with the Prandtl-Glauert three-dimensional transformation. Qualitatively the graphs are reasonable. A rectangular wing ($\lambda = 1$) is already loaded more heavily toward the tip, so that sweep simply aggravates the situation, causing a continuous departure from the ideal elliptic loading. For the strongly tapered wing ($\lambda = 0$) the situation is reversed so that, in this case, sweep is beneficial. For the taper ratio of 0.25 there is practically no effect of sweep on the induced drag.

Figure 5.33 indicates that there is little, if any, effect of sweepback on the minimum drag coefficient. Thus one can estimate $C_{D_{min}}$ on the basis of two-dimensional airfoil measurements. Usually these drag measurements are taken at low Mach numbers so that it is necessary to correct the skin friction part of $C_{D_{min}}$ for compressibility effects. Such a correction is given by the graph of Figure 5.34 (Ref. 5.1) for Mach numbers as high as 10.0.

An empirical equation that closely fits the graph of Figure 5.34 is

$$\frac{C_f}{C_{f_i}} = (1 + 0.104\,M^2)^{-0.773} \tag{5.86}$$

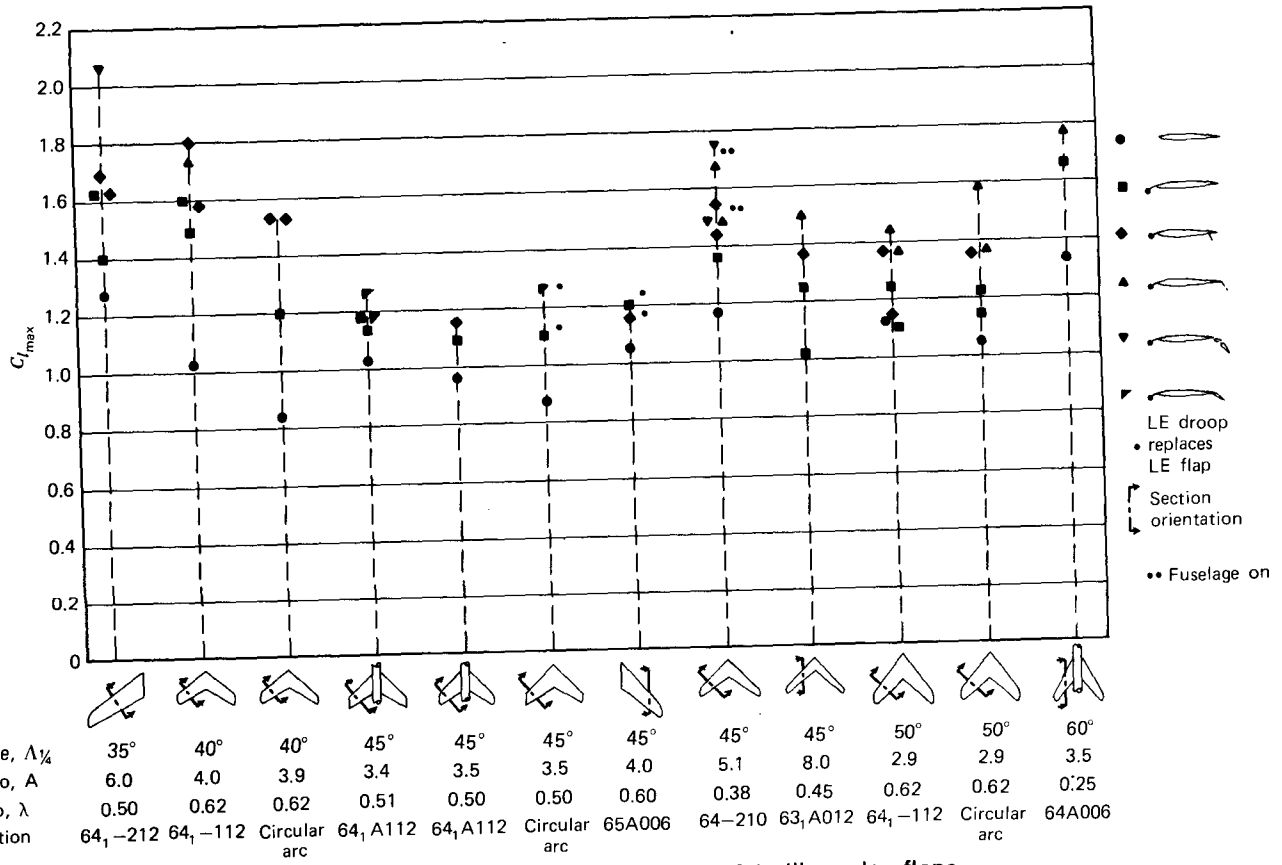

Sweep angle, $\Lambda_{1/4}$	35°	40°	40°	45°	45°	45°	45°	45°	45°	50°	50°	60°
Aspect ratio, A	6.0	4.0	3.9	3.4	3.5	3.5	4.0	5.1	8.0	2.9	2.9	3.5
Toper ratio, λ	0.50	0.62	0.62	0.51	0.50	0.50	0.60	0.38	0.45	0.62	0.62	0.25
Airfoil section	64_1–212	64_1–112	Circular arc	64_1A112	64_1A112	Circular arc	65A006	64–210	63_1A012	64_1–112	Circular arc	64A006

Figure 5.30 Maximum lift coefficients obtained with various types of trailing edge flaps.

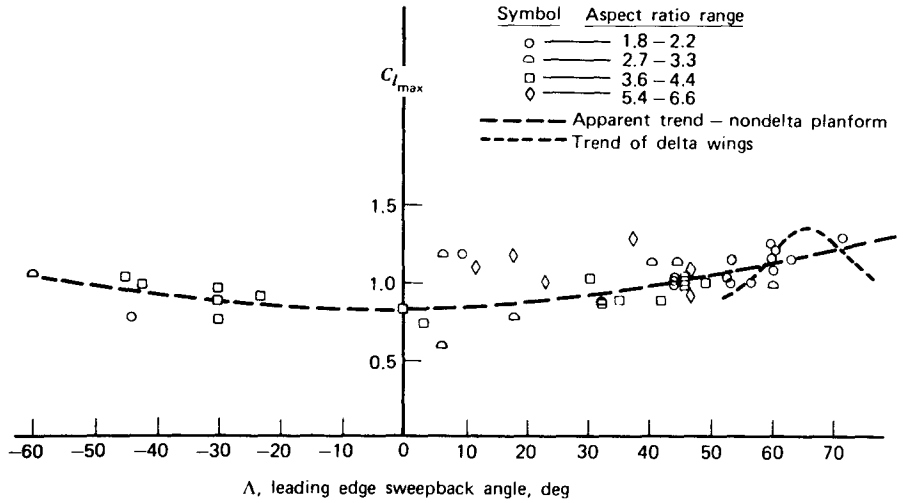

Figure 5.31 Variation of $C_{L_{max}}$ with sweepback for wings having planforms other than triangular.

Reference 5.16 offers two similar equations, one for a turbulent boundary layer and the other for a laminar layer.

$$\left(\frac{C_f}{C_{f_i}}\right)_{\text{turb}} = (1 + 0.2\,M^2)^{-0.467} \tag{5.87}$$

$$\left(\frac{C_f}{C_{f_i}}\right)_{\text{lam}} = (1 + 0.1305\,M^2)^{-0.12} \tag{5.88}$$

Equation 5.87 falls slightly above the graph of Figure 5.34, while Equation 5.88 gives values much closer to unity than the figure indicates.

As an example in the use of the foregoing relationships for swept wings, consider a swept wing having the following geometry and operating at a free-stream Mach number of 0.7 at 30,000 ft.

$A = 7.0$

$\lambda = 0.5$

$\Lambda_{LE} = 30°$ (leading edge)

64A009 airfoil (defined normal to midchord line)
(see Figure 5.3 for two-dimensional characteristics)
wing loading = 100 psf

In order to use Figure 5.28 or Equation 5.85 we need $\Lambda_{1/2}$. For a linearly

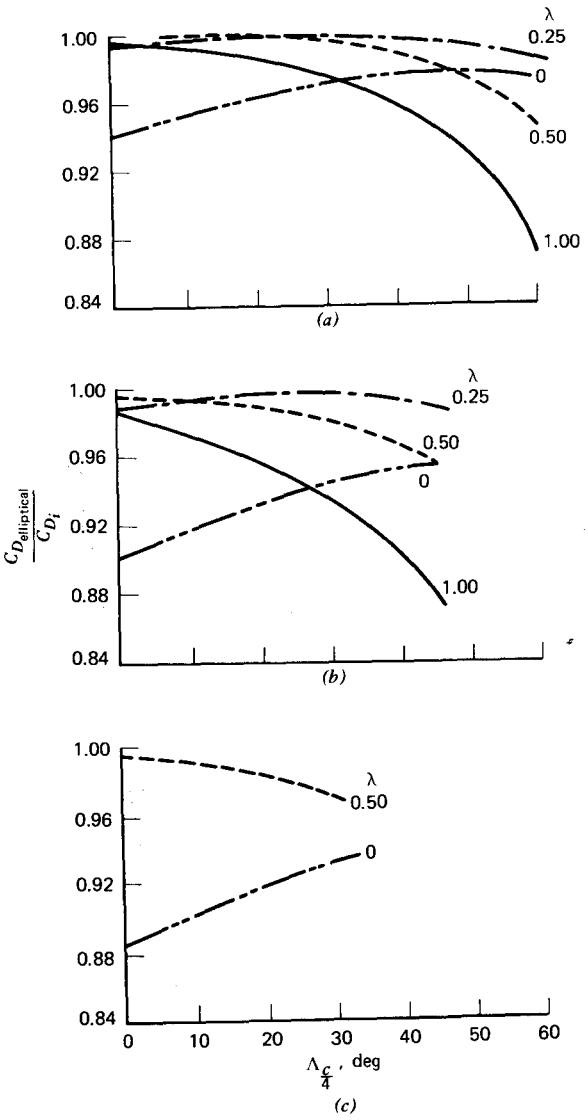

Figure 5.32 Variations with sweep angle of the ratios of induced drag coefficient for elliptical loading to the calculated induced drag coefficient for wings of various aspect ratios and taper ratios. Calculations made by the Weissinger method using 15 points in the solution. (*a*) $A = 3.5$. (*b*) $A = 6.0$. (*c*) $A = 8.0$.

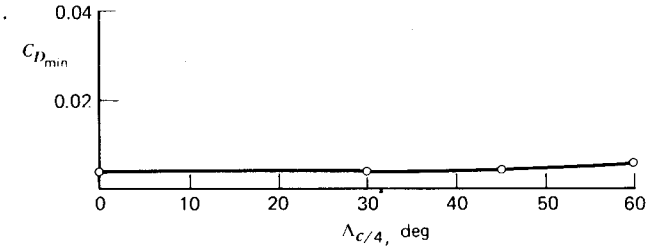

Figure 5.33 Variation of the minimum drag coefficient with sweep angle for a family of wings having aspect ratios of 4, taper ratios of 0.6, and NACA 65A006 airfoil sections parallel to the plane of symmetry.

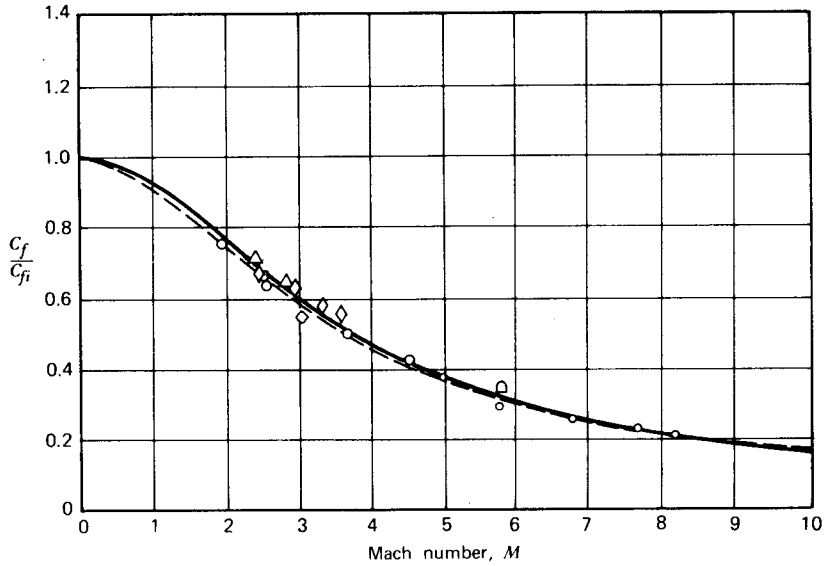

Figure 5.34 Variation of skin friction coefficient with Mach number for a turbulent boundary layer at zero heat transfer. C_{fi} is the value for incompressible flow. Solid and dashed lines represent two different theoretical solutions. (H. W. Liepmann and A. Roshko, *Elements of Gas Dynamics*, John Wiley & Sons, Inc., 1957. Courtesy of U.S. Naval Ordnance Laboratory.)

tapered swept wing, Λ_{LE} and $\Lambda_{1/2}$ can easily be shown to be related by

$$\tan \Lambda_{1/2} = \tan \Lambda_{LE} - \frac{(1-\lambda)}{(1+\lambda)} \frac{2}{A} \qquad \text{(a)} \qquad (5.89)$$

$$\tan \Lambda_{1/4} = \tan \Lambda_{LE} - \frac{(1-\lambda)}{(1+\lambda)} \frac{1}{A} \qquad \text{(b)}$$

Thus, for this case, $\Lambda_{1/2} = 25.7°$.

The incompressible slope of the lift curve, a_0, for this particular airfoil equals approximately 6.2 C_l/rad. Thus, for $M_\infty = 0.7$, using Equation 5.85, $C_{L_\alpha} = 5.21\ C_L$/rad.

According to Equation 5.66, the equivalent wing in incompressable flow will have its y dimensions decreased by the factor β. In this case, $\beta = 0.714$. Hence the equivalent wing's geometry becomes

$$A_i = 5.0$$
$$\Lambda_{i_{1/4}} = 36.6°$$

For this equivalent wing, from Figure 5.32,

$$\frac{C_{Di_{\text{elliptical}}}}{C_{D_i}} = 0.98$$

For the given wing loading and operating conditions,

$$C_L = \frac{W/S}{q}$$
$$= 0.462$$

Thus, for the given wing

$$C_{D_i} = \frac{1}{0.98}\frac{C_L^2}{\pi A}$$
$$= \frac{1}{0.98}\frac{(0.462)^2}{\pi(7)}$$
$$= 0.00990$$

We do not need to correct the profile drag for compressibility effects in this example, since Figure 5.3 provides us with the section C_d as a function of M and C_l. Assuming that the section C_l is equal approximately to the wing C_L of 0.462, C_d is read from Figure 5.3 to be 0.015 for an M_∞ of 0.7. According to Figure 5.33, this does not need to be corrected for sweep. The total wing C_D at the operating C_L and Mach number is thus estimated to equal 0.0249.

Before leaving this example, it is of interest to generalize on the calculation of C_{D_i}.

$$A_i = \beta A_c$$
$$C_{L_i} = \beta^2 C_{L_c}$$

Thus,

$$C_{D_{i_i}} = \frac{C_{L_i}^2}{\pi A_i}$$
$$= \beta^3 \frac{C_{L_c}^2}{\pi A_c}$$
$$= \beta^3 C_{D_{i_c}} \qquad (5.90)$$

This result can also be obtained by applying the three-dimensional Prandtl-Glauert transformation to the relationship

$$C_{D_i} = C_L \alpha_i$$

α_i, the induced angle of attack, is proportional to the vertical velocity associated with $\phi(x, \beta y, \beta z)$. Hence, α_i varies as $1/\beta$.

Delta Wings

The geometry of a delta wing is pictured in Figure 5.35*a*. Such a wing is also referred to as a triangular wing. The delta wing represents the limiting

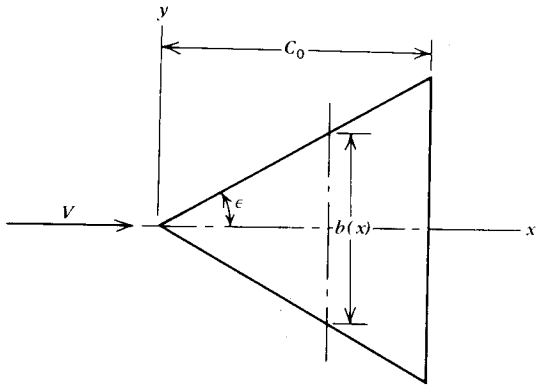

Figure 5.35a The planform of a delta wing.

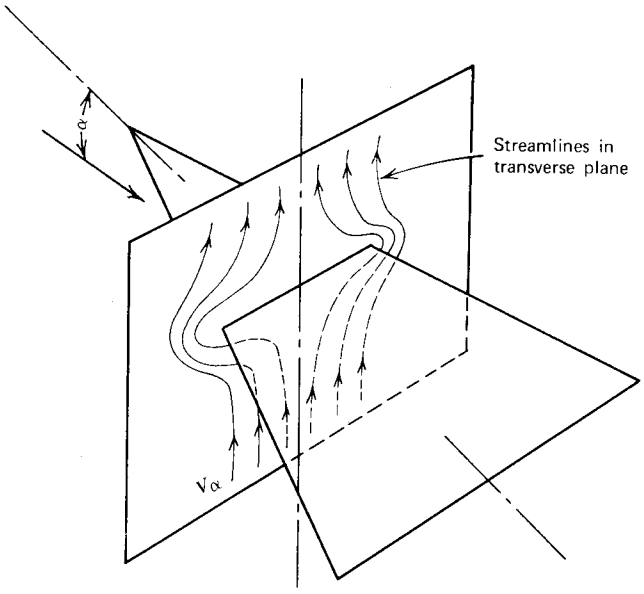

Figure 5.35b Two-dimensional flow approximation for a slender wing.

case of a swept wing with a taper ratio, λ, equal to zero. The midchord sweep angle is given by

$$\Lambda_{1/2} = \tan^{-1} \frac{b}{c_0} \tag{5.91}$$

The aspect ratio, apex angle, ϵ, and b/c_0 are related by

$$A = \frac{2b}{c_0} \tag{5.92a}$$

$$\epsilon = \tan^{-1} \frac{b}{2c_0} \tag{5.92b}$$

or

$$2 \tan (\epsilon) = \tan \Lambda_{1/2} \tag{5.92c}$$

and

$$\tan \epsilon = \frac{A}{4} \tag{5.92d}$$

The aerodynamic analysis of a delta wing in the general case is not an easy task because of nonlinear effects associated with the highly swept leading edge. At small angles of attack and low aspect ratios one can apply a linearized approach that is referred to as the slender wing (or wing-body) theory. The details of this theory will not be developed here; instead, refer to two of the original sources (Refs. 5.17 and 5.18) for the treatment of this theory. A brief treatment for the wing-alone case can be found in Reference 3.3. Basically, the theory assumes that the flow in any transverse plane is essentially two dimensional. This assumption eliminates the Mach number-dependent term in Equation 5.56 that governs the perturbation velocity potential, leaving only

$$\frac{\partial^2 \phi}{\partial y^2} + \frac{\partial^2 \phi}{\partial z^2} = 0 \tag{5.93}$$

Since $V_\infty \alpha$ is the velocity component normal to the plane of the wing, the problem is reduced to finding the two-dimensional flow in a transverse plane, as illustrated in Figure 5.35*b*.

For a flat wing, the pressure difference across the wing is predicted to

$$\Delta p = \frac{1}{2} \rho V^2 \frac{2\alpha}{\sqrt{1 - (2y/b_x)^2}} \left(\frac{db_x}{dx} \right) \tag{5.94}$$

where b_x is the local span a distance of x from the apex. y, b_x, and x are shown in Figure 5.35*b*.

Given db_x/dx as a function of x, Equation 5.94 can be integrated over the surface of the wing to obtain the wing lift coefficient. For a delta wing, db_x/dx

is constant, giving an elliptical spanwise loading. In this case,

$$C_{L_\alpha} = \frac{\pi A}{2} \tag{5.95a}$$

$$C_{D_i} = \frac{C_L^2}{\pi A} \tag{5.95b}$$

Notice that because of the assumption of slenderness, these results do not depend on Mach number.

Since the shape of the local spanwise pressure distribution is the same at all chordwise positions for a delta wing (db_x/dx is constant), it follows that the center of pressure is predicted to be at the centroid of the planform area, a distance of $2c_0/3$ back from the apex. Based on the wing area and geometric mean chord, the pitching moment coefficient about the apex is thus

$$C_{M_{LE}} = -\tfrac{2}{3}\pi A\alpha \tag{5.96}$$

Again, these results hold for any Mach number, providing the aspect ratio and angle of attack are sufficiently small. Depending on the desired accuracy, the limitations on A and α can be severe, possibly as low as 0.5 for A and 2 or 3° on α.

In order to predict the behavior of delta wings for higher α's and aspect ratios, it is necessary to rely on physical observations of the flow over such wings to form the basis for an analytical model. In subsonic flow a delta wing is observed to generate a vortex located just inboard and slightly above each leading edge.

A striking photograph showing the formation of these vortices is presented in Figure 5.36*a*. This photograph was taken in a water tunnel with dyed milk ejected from holes in the model wing in order to illustrate the streamlines. To clarify the flow further, the generation of these vortices is shown in Figure 5.37*a*. Figure 5.37*b* depicts the flow in a plane more or less normal to the leading edge. Observe that as the air flows from beneath the wing around the leading edge, it is unable to remain attached and separates from the upper surface. It spirals around and reattaches to the upper surface some small distance inboard of the leading edge.

According to Reference 5.19, this separated standing vortex is equivalent to the separated flow region at the leading edge of a thin airfoil, as shown in Figure 5.37*a*. The ideal potential flow case of a fully wetted, thin airfoil is shown in Figure 5.37*b*, where a singularity exists at the leading edge (see Equation 3.36). In view of D'Alembert's paradox, we know that a drag cannot exist in the case of Figure 5.37*b*. Therefore, the infinitely negative pressure acting over the vanishingly small leading edge, in the limit, must produce a force to cancel exactly the component in the drag direction of the normal pressure difference integrated over the chord. This force is known as the

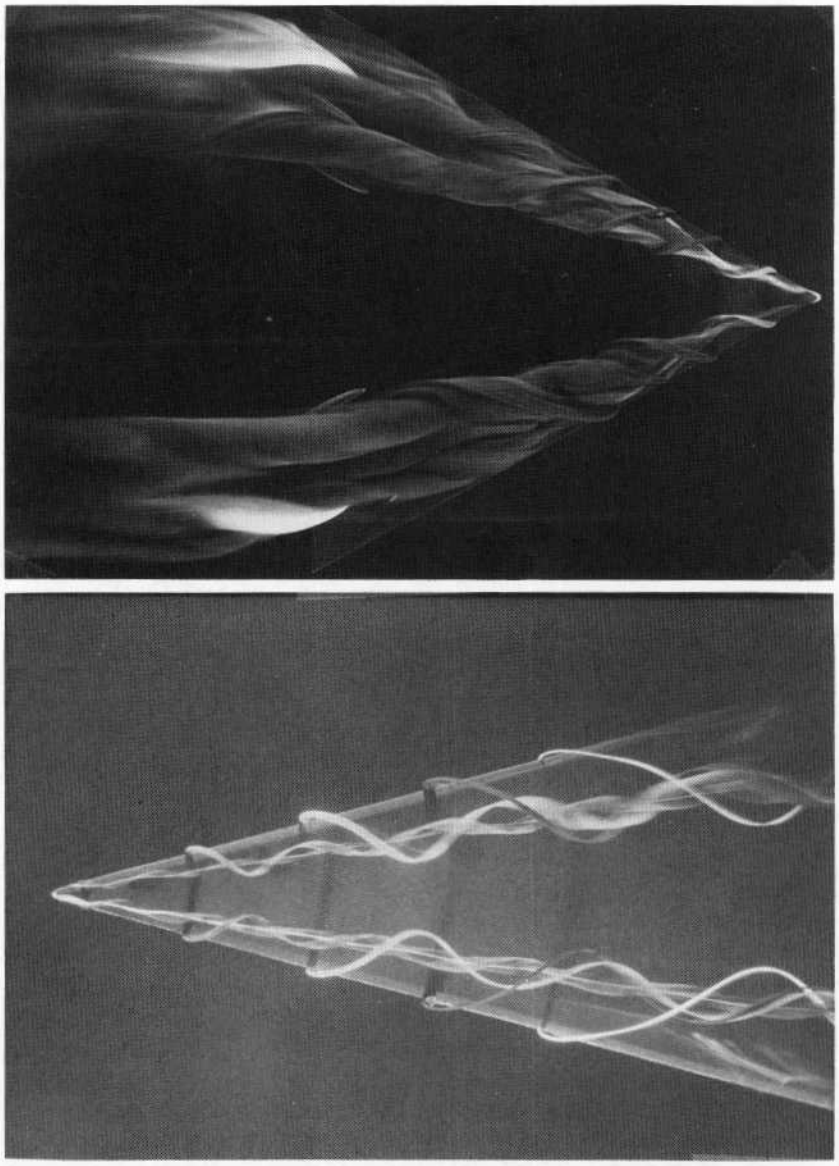

Figure 5.36a The vortex system of a delta wing. (Courtesy of the Office National D'Etudes Et De Recherches Aérospatiales.)

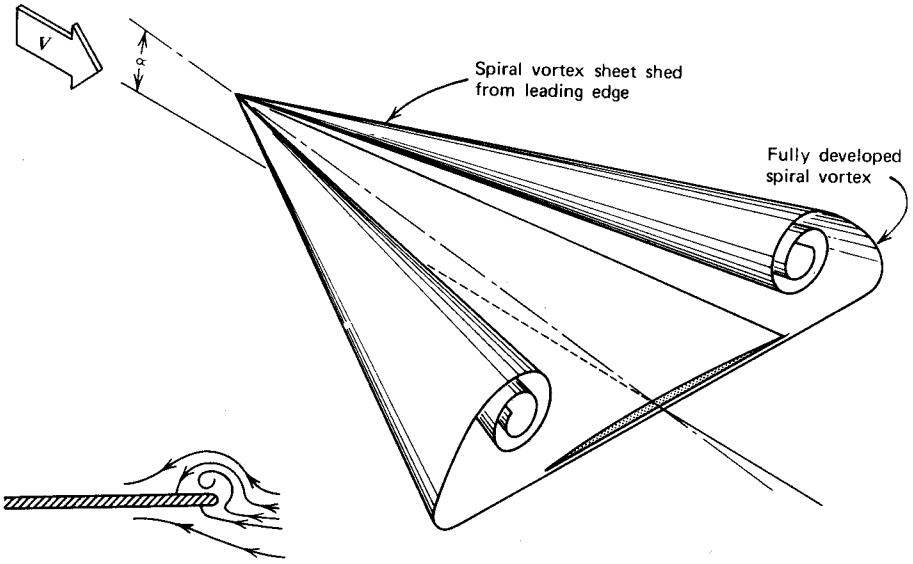

Figure 5.36b Leading edge vortices formed above a delta wing.
Figure 5.36c Leading edge flow.

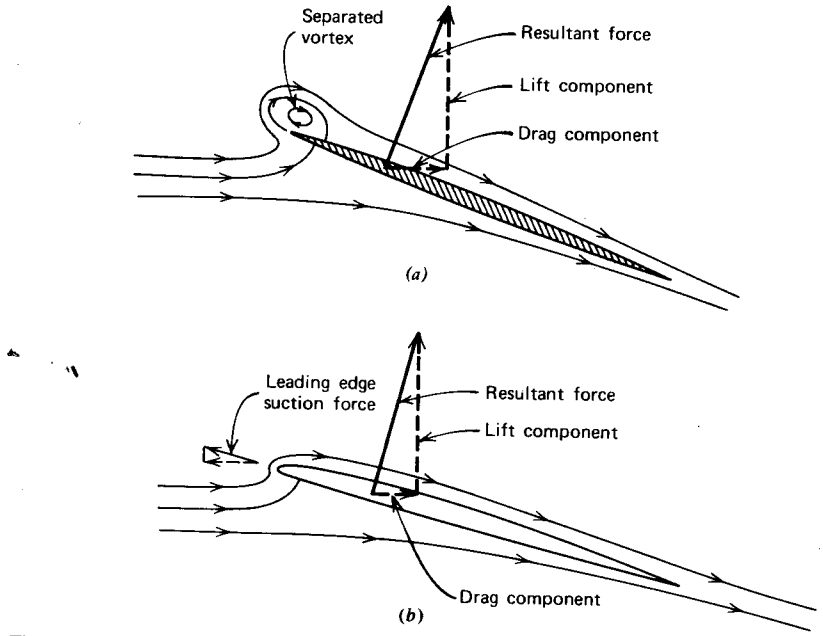

Figure 5.37 Reduction in the net drag by leading edge suction.

leading edge suction force. Its resultant lies in the plane of the chord and, hence, has components in the lift and drag directions.

The leading edge suction force is essentially independent of the leading edge radius. Thus, if the separated streamline in Figure 5.37*a* is replaced by a solid boundary, a leading edge suction force will be present. This suggests that without the boundary, the force on the separated flow region from the reduced pressure resulting from the curved flow must be approximately equal to the leading edge suction force. Assuming a circular flow (which is not quite true), this leads to a reaction in the upward direction normal to the chord and near the leading edge that is nearly equal in magnitude to the leading edge suction force for the fully wetted, potential flow case. This is the basis for the subsonic Polhamus delta wing theory presented in References 5.19 and 5.20.

Without delving further into the details of Polhamus's theory, the following results are obtained.

$$C_L = K_p \sin \alpha \cos^2 \alpha + K_v \cos \alpha \sin^2 \alpha \tag{5.97}$$

The term $K_p \sin \alpha \cos^2 \alpha$ represents the potential lift on the wing for the fully wetted case minus a small vertical component of the leading edge suction force, which is lost when the flow separates. The second term represents the added lift caused by the presence of the leading edge vortex. Not surprisingly, this is referred to as "vortex lift."

As α approaches zero, Equation 5.97 becomes

$$C_L = K_p \alpha \qquad (\alpha \to 0)$$

Thus it follows that the constant, K_p, is simply the slope of the wing lift curve for the fully wetted case according to the usual lifting surface theories. The constant, K_v, is obtained from

$$K_v = \frac{K_p - K_p^2 K_i}{\cos \Lambda_{LE}} \tag{5.98}$$

where $K_i = dC_{D_i}/dC_L^2$ and Λ_{LE} is the sweepback angle of the leading edge.

Again, K_i can be evaluated from the usual lifting surface methods. However, K_p and K_v have already been evaluated in the references and are presented here in Figure 5.38 as a function of aspect ratio.

Having C_L, the drag coefficient is easily obtained. Since there is no leading edge suction force parallel to the chord for the separated leading edge, it follows simply that

$$C_D = C_L \tan \alpha \tag{5.99}$$

Equations 5.97 to 5.99 hold only for $M = 0$. The effects of compressibility on these equations can be estimated by again using the Prandtl-Glauert transformation. Given an aspect of A, one calculates K_p (designated K_p') for a

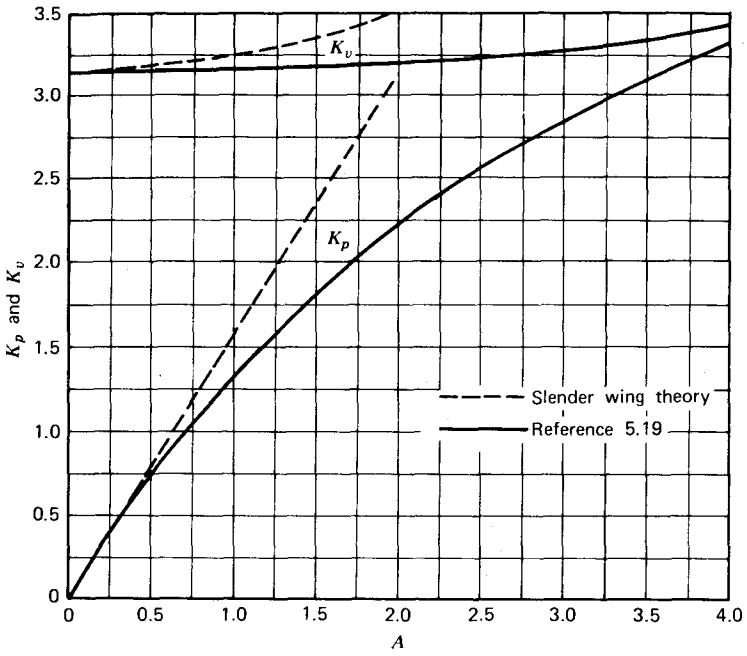

Figure 5.38 Variation of K_p and K_v for delta wings ($M \simeq 0$).

transformed aspect ratio A' given by,

$$A' = \beta A$$

K_p for the original wing is then found from

$$K_p = \frac{K'_p}{\beta} \tag{5.100}$$

The transformation for K_v is not as obvious. Reference 5.21 shows this to be

$$K_v = K'_v \sqrt{\frac{1 + \tan^2 \Lambda_{LE}}{\beta^2 + \tan^2 \Lambda_{LE}}}$$

or, if $\tan \Lambda'_{LE} = \tan \Lambda_{LE}/\beta$,

$$K_v = K'_v \sqrt{\frac{(1/\beta^2) + \tan^2 \Lambda'_{LE}}{1 + \tan^2 \Lambda'_{LE}}} \tag{5.101}$$

Figure 5.39*a* and 5.39*b* compares the foregoing theory with experiments for delta wings that have aspect ratios from 0.5 to 2.0. In addition, Figure 5.39*a* includes predictions based on neglecting the vortex lift but accounting

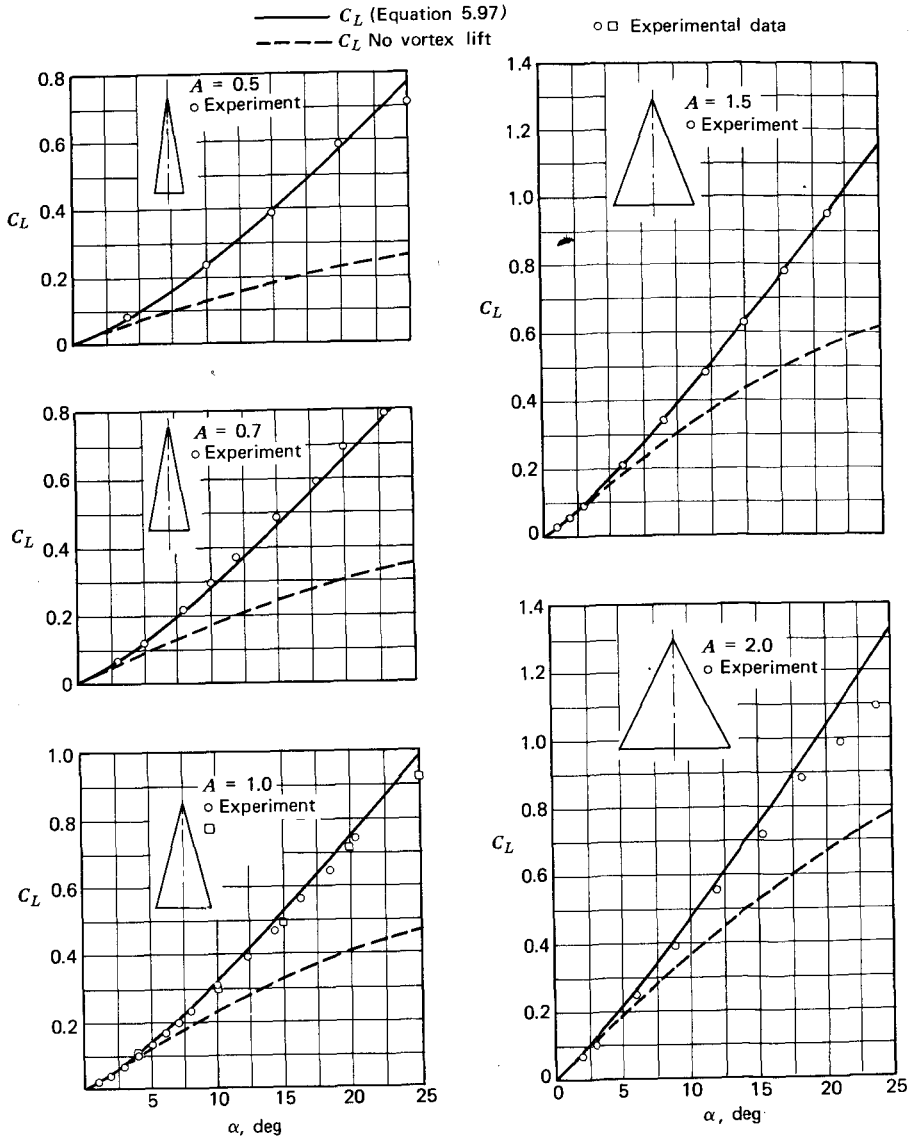

Figure 5.39a Comparison of theory with experimental data for sharp-edged delta wings.

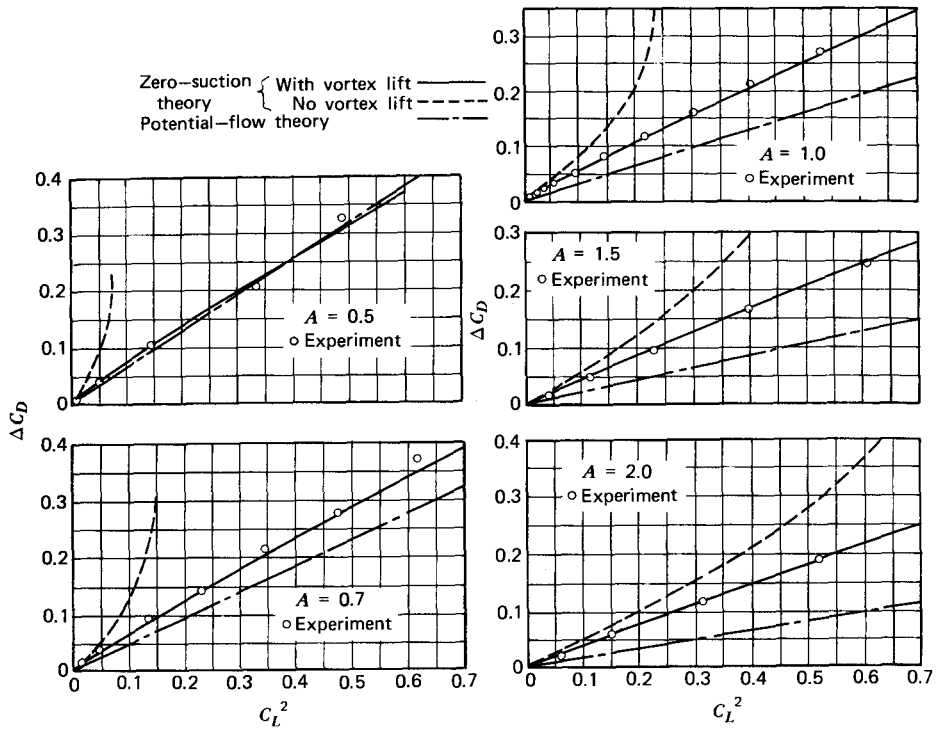

Figure 5.39b Comparison of experimental drag due to lift with the results of three theoretical methods ($M \simeq 0$).

for the loss of leading edge suction. Figure 5.39*b* also includes predictions based on fully wetted potential flow. Obviously, the potential flow results are questionable, whereas the predictions based on the leading edge suction force analogy agree closely with experiments up to angles of attack as high as 25°.

An estimate of $C_{L_{max}}$ for thin delta wings at low speeds can be gained from Figure 5.40. These points represent a miscellaneous collection of wings with different sweepback angles and thickness ratios. Unfortunately, systematic data could not be found to correlate $C_{L_{max}}$ with all of the pertinent parameters. Based on this limited presentation of data, it appears that aspect ratios between 1.5 and 2.5 can be expected to deliver $C_{L_{max}}$ values of at least 1.3. From Figure 5.39*a*, it can be seen that a C_L value of this magnitude corresponds to an extremely high angle of attack greater than 25°. In order to provide adequate forward vision during a landing, because of the high angle of attack, the Concorde supersonic transport pictured in Figure 5.25 droops the nose of the fuselage.

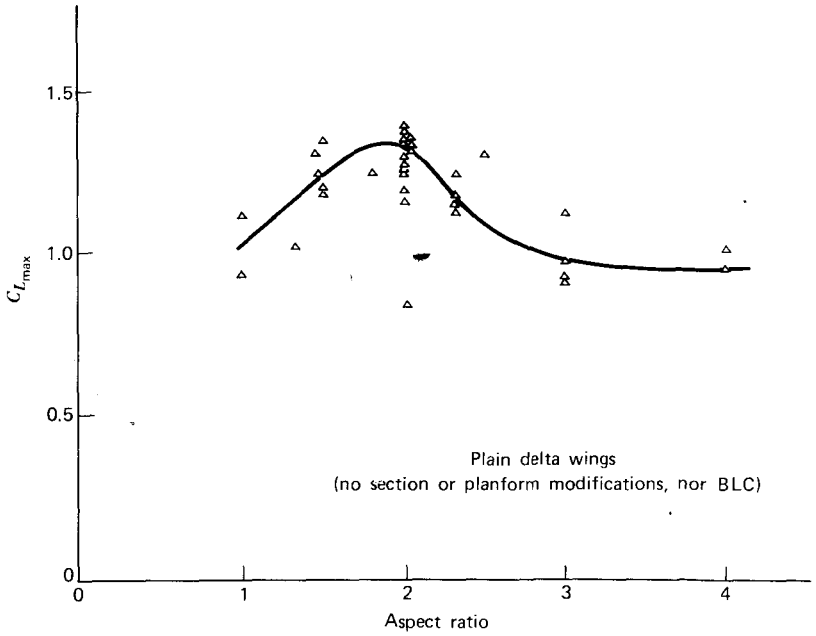

Figure 5.40 $C_{L_{max}}$ for thin delta wings.

SUPERSONIC WINGS

This section deals with wings operating at free-stream Mach numbers greater than unity. Since the governing flow equations change their form in going from subsonic to supersonic flow, the behavior of a wing changes its characteristics also. The induced drag, lift curve slope, and center of pressure are all affected significantly when M_∞ exceeds unity.

There are many variations possible in supersonic wing configurations, so that it is almost impossible (at least with the current state of the art) to present a universal approach that will satisfy the intended level of this text. Instead, we will examine two specific cases. The first case is that of swept wings (including delta wings) with subsonic leading edges and supersonic trailing edges; the second case is that of swept or unswept wings with supersonic leading and trailing edges. The term "subsonic leading edge" may be somewhat misleading. It refers to the case where the leading edge lies within the Mach cone generated at the apex. The Mach number normal to the edge is subsonic, so that even though such a wing is supersonic, because of the independence of the normal flow, it exhibits some of the characteristics of a subsonic wing (such as a leading edge suction force).

No attempt will be made to develop the theory of supersonic wings. Instead, a brief description will be offered of each theoretical approach together with the limitations. Results will then be presented that permit estimations of wing behavior in supersonic flow. We begin with the case of subsonic leading edges.

Subsonic Leading Edges

Reference 5.22 is a linearized treatment of delta wings with subsonic leading edges. The method is valid for large values of the apex angle up to and coincident with the Mach angle. Reference 5.23 extends the method of Reference 5.22 to include swept wings with pointed tips, but with trailing edges that are also swept. The trailing edges in Reference 5.22 are restricted only by the requirement that they be supersonic. Hence their sweep angle must be less than the "sweep" angle of the Mach wave. Thus, swept forward trailing edges are allowed. It is interesting to note that any triangular wing having subsonic leading edges and supersonic trailing edges will have the same pressure distribution along a ray from the apex as any other triangular wing having the same leading edge sweep angle and operating at the same Mach number. Thus, if one finds the pressure distribution over a "basic" delta wing, the effect of sweeping its trailing edges can be readily determined. The conclusion follows from the fact that disturbances cannot propagate ahead of the Mach cone in linearized supersonic flow. Figure 5.41 illustrates the foregoing principle.

For delta wings only, the following expression was obtained by Brown (Ref. 5.22) for the lift curve slope.

$$BC_{L_\alpha} = \frac{2\pi^2 \tan \epsilon}{\pi + \lambda} \tag{5.102}$$

λ is a function of the ratio of apex angle tangent to that of the Mach angle; it is presented in Figure 5.42. Note that when the leading edge of the wing and the Mach line are coincident, C_{L_α} reduces to equation 5.76; that is, the slope of the lift curves are the same for a supersonic two-dimensional airfoil and a delta wing, the leading edge of which is coincident with the Mach line. This also holds if the leading edge is supersonic. Thus, for values of $\tan \epsilon / \tan \mu$ greater than unity, the value of the λ function in Figure 5.42 is constant and equal to 1.793. Note also that Equation 5.102 reduces to the results from slender wing theory as the apex angle approaches zero.

For subsonic leading edges, Brown (Ref. 5.22) shows that a leading edge suction force will exist. As a result, an induced drag is obtained that is less than the streamwise component of the wing's normal force.

$$C_{D_i} = \frac{C_L^2}{\pi A}\left[2\left(1 + \frac{\lambda}{\pi}\right) - \sqrt{1 - B^2 \tan^2 \epsilon}\right] \tag{5.103}$$

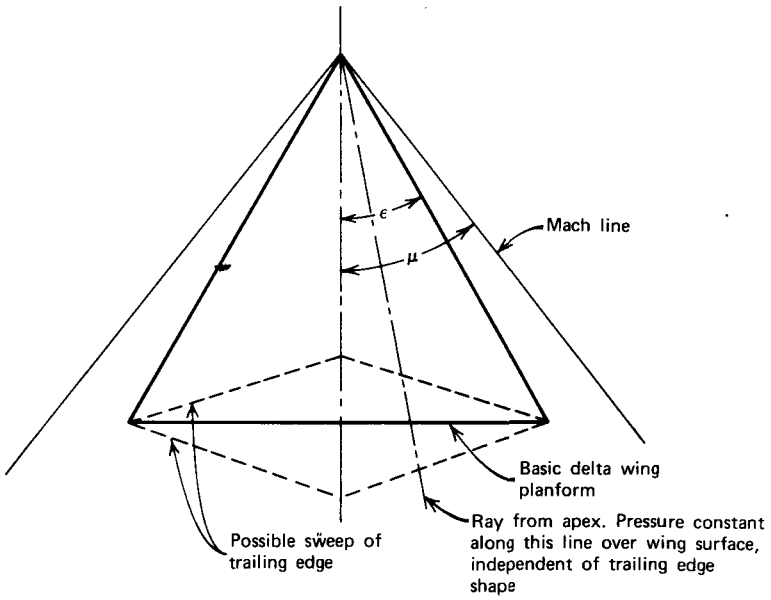

Figure 5.41 Supersonic delta wing.

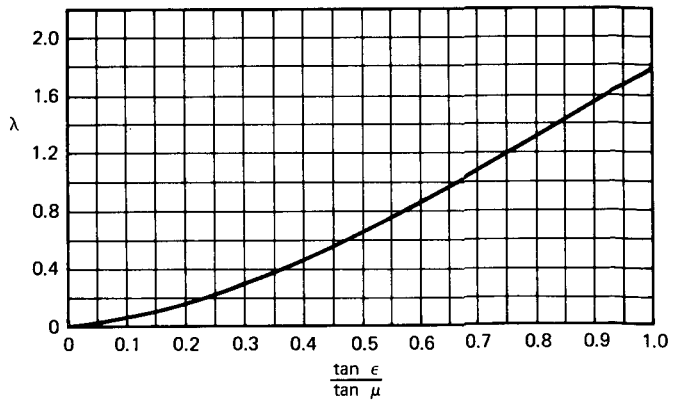

Figure 5.42 Variation of λ with $\tan \epsilon / \tan \mu$.

It is emphasized that Equations 5.102 and 5.103 hold only for delta wings with subsonic leading edges. λ in these particular equations refers to the function shown in Figure 5.42 and does *not* stand for the taper ratio. The taper ratio of a delta wing is zero. Since $\tan \mu = 1/B$ and λ is a function of $\tan \epsilon / \tan \mu$, we can write

$$\frac{C_{D_i}}{(C_L^2/\pi A)} = 2\left(1 + \frac{\lambda}{\pi}\right) - \sqrt{1 - \left(\frac{\tan \epsilon}{\tan \mu}\right)^2} \tag{5.104}$$
$$= f\left(\frac{\tan \epsilon}{\tan \mu}\right)$$

Referencing C_{L_α} to the two-dimensional value, we can also write

$$\frac{C_{L_\alpha}}{C_{L_{\alpha_{2\text{-D}}}}} = \frac{B}{4} C_{L_\alpha}$$
$$= \frac{\pi^2}{2(\pi + \lambda)} \left(\frac{\tan \epsilon}{\tan \mu}\right) \tag{5.105}$$
$$= g\left(\frac{\tan \epsilon}{\tan \mu}\right)$$

The functions, f and g, are presented in Figure 5.43. With regard to the drag, note that the leading edge suction force vanishes when the leading edge and Mach line are coincident. Thus, for μ values equal to or less than ϵ, the drag is simply equal to the streamwise component of the wing normal force. In coefficient form,

$$C_{D_i} = C_L \tan \alpha$$

But

$$C_L = \frac{4}{B} = 4 \tan \mu \qquad \text{and} \qquad A = 4 \tan \epsilon$$

Thus, for $\mu \leq \epsilon$,

$$\frac{C_D}{(C_L^2/\pi A)} = \pi$$

This is the value shown in Figure 5.43 for $\tan \epsilon / \tan \mu = 1$.

Figure 5.44 depicts the planform shapes treated in Reference 5.23. They might be described as truncated deltas with trailing edge sweep. Trends of C_{L_α} with M, A, Λ, and taper ratio are presented in Figure 5.45 (taken from Ref. 5.23). For this family of wings, A, λ, ϵ, and δ (see Figure 5.44) are related by

$$\tan \delta = \frac{(1 + \lambda) A \tan \epsilon}{(1 + \lambda) A - 4(1 - \lambda) \tan \epsilon} \tag{5.106}$$

Before leaving the subject of wings with subsonic leading edges, it should be emphasized once again that such wings can develop leading edge suction

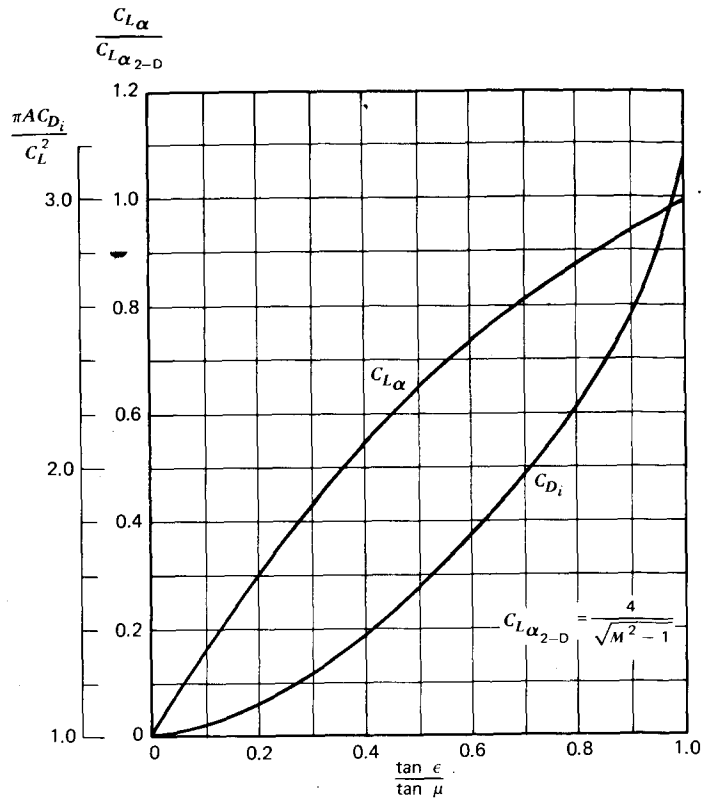

Figure 5.43 Lift curve slope and induced drag coefficient for delta wings with subsonic leading edges.

forces. Thus, to prevent leading edge separation in order to maintain this suction force, it is beneficial (from a drag standpoint) to round the leading edges of these wings, even though they are operating at a supersonic free-stream Mach number. Experimental proof of this (Ref. 5.26) is offered by Figure 5.46*a*. Here the lift-to-drag ratio as a function of C_L is presented for a delta wing with its leading edges lying within the Mach cone. Three different airfoil sections were tested, including one with a rounded leading edge. This latter section is seen to have a maximum L/D value approximately 8% higher than the other two.

Other data from the same reference are presented in Figure 5.46*b* to 5.46*f*, which shows the effects of aspect ratio and sweep on lift, moment, and drag for a family of tapered wings. These wings all have a taper ratio of 0.5 and employ the cambered wedge section having a maximum thickness ratio of 5%, pictured in Figure 5.46*b*.

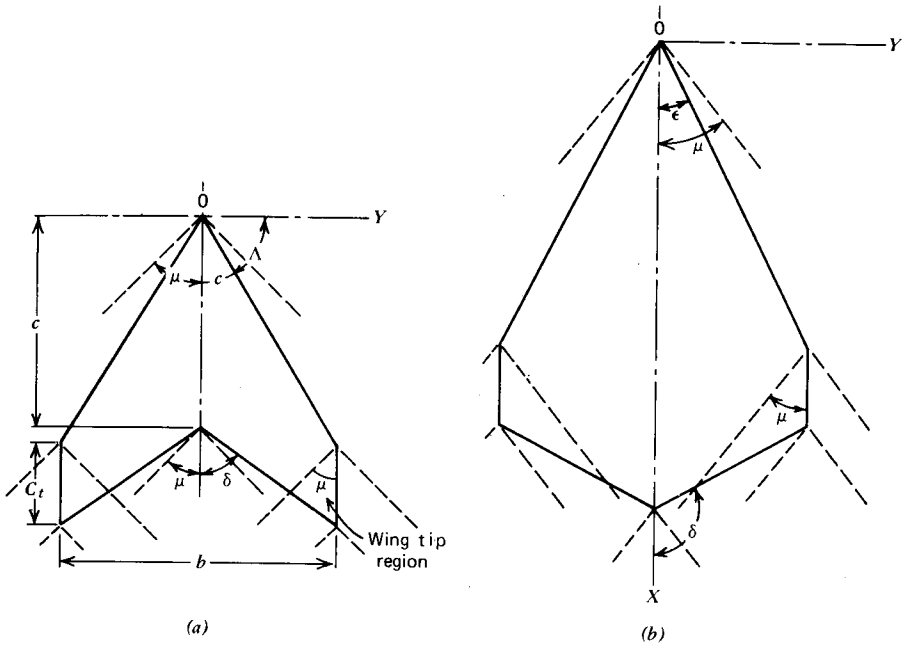

Figure 5.44 Supersonic wings and subsonic leading edges. (*a*) Sweptback trailing edge. (*b*) Sweptforward trailing edge.

The moment coefficients for this set of graphs are about the centroid of the planform area, with the mean aerodynamic chord as the reference length. If the aerodynamic center of a wing is a distance of x ahead of the centroid and M is the moment about the centroid, then

$$M_{ac} = M - xL$$

In coefficient form,

$$C_{M_{ac}} = C_M - C_L \frac{x}{\mathbf{c}}$$

Differentiating with respect to C_L and recalling that, by definition, $dC_{M_{ac}}/dC_L = 0$, gives

$$\frac{x}{\mathbf{c}} = \frac{dC_M}{dC_L}$$

Thus Figure 5.46*d* and 5.46*e* represents, in effect, the distance of the aerodynamic center ahead of the centroid.

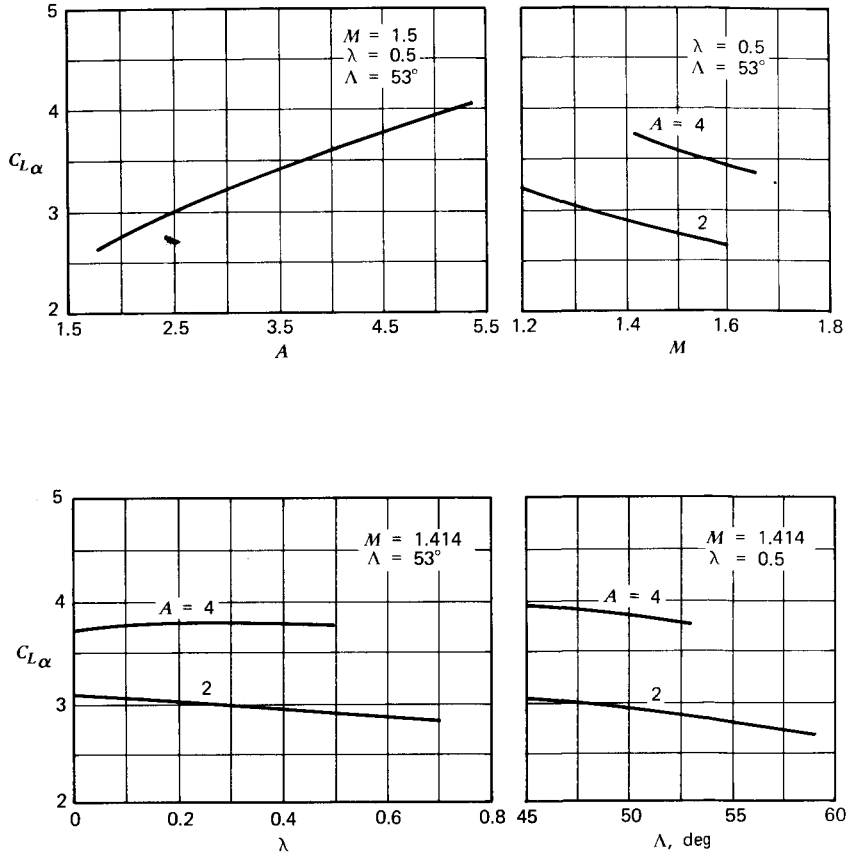

Figure 5.45 Some illustrative variations of lift curve slope C_{L_α} with Mach number, aspect ratio, sweepback, and taper ratio.

Supersonic Leading Edges

Reference 5.24 presents generalized expressions for the lift curve slope of thin, swept, tapered wings operating with supersonic leading and trailing edges. The results are restricted to the case where the Mach line from one tip does not intersect the other half of the wing. The analysis is based on a linearized theory for the surface velocity potential.

For the case (Figure 5.47*a*) where the Mach line from the apex intersects the tip chord between the leading and trailing edges, the following lengthy equation is obtained for C_{L_α}.

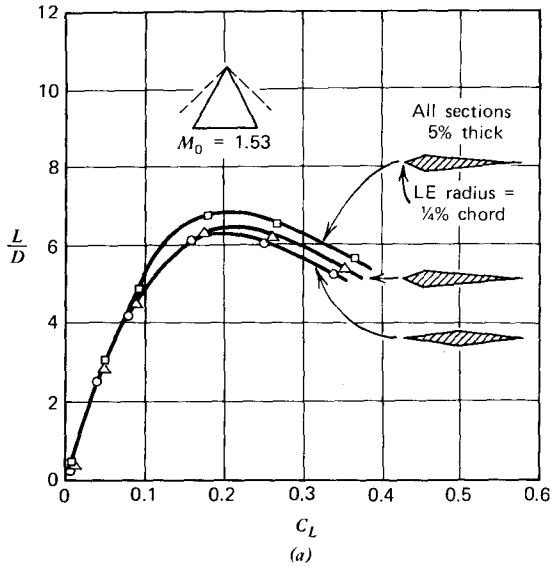

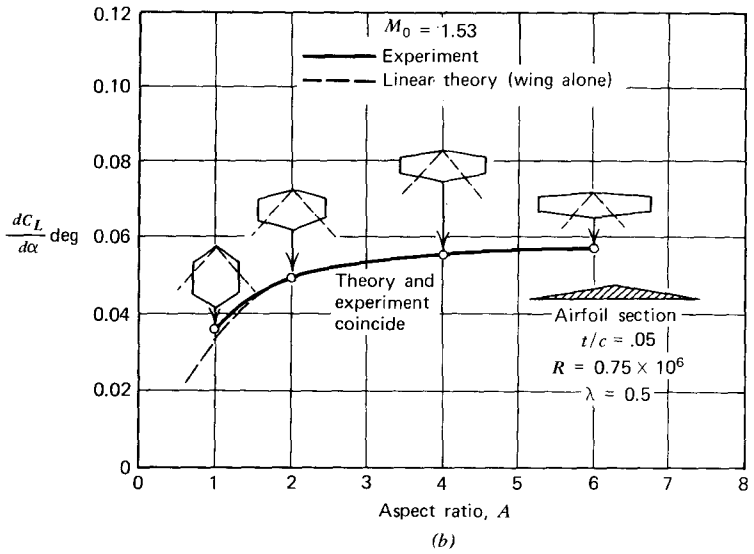

Figure 5.46 Supersonic wing characteristics. (*a*) Effect of wing section on lift drag ratio of triangular wings. (*b*) Effect of aspect ratio on lift curve slope. (*c*) Effect of sweep on lift curve slope. (*d*) Effect of aspect ratio on moment curve slope. (*e*) Effect of sweep on moment curve slope. (*f*) Effect of sweep on minimum drag.

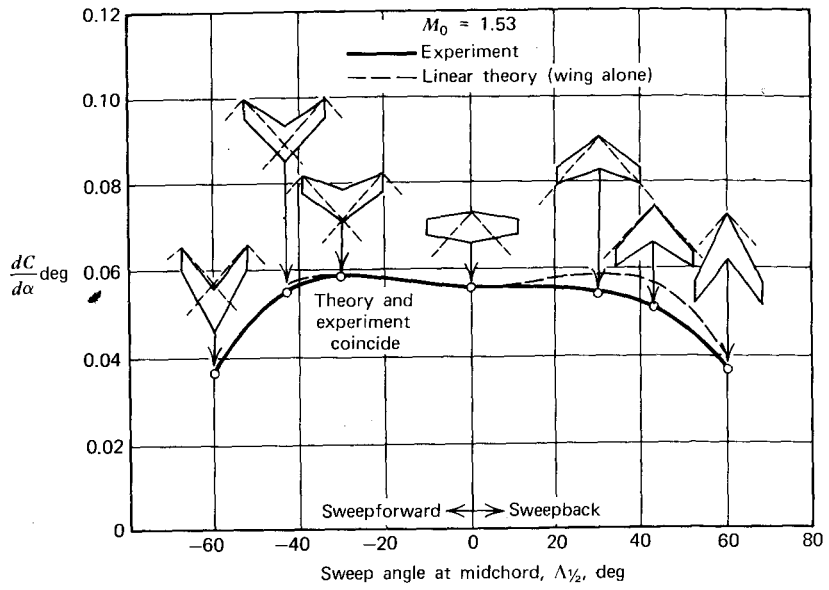

(c)

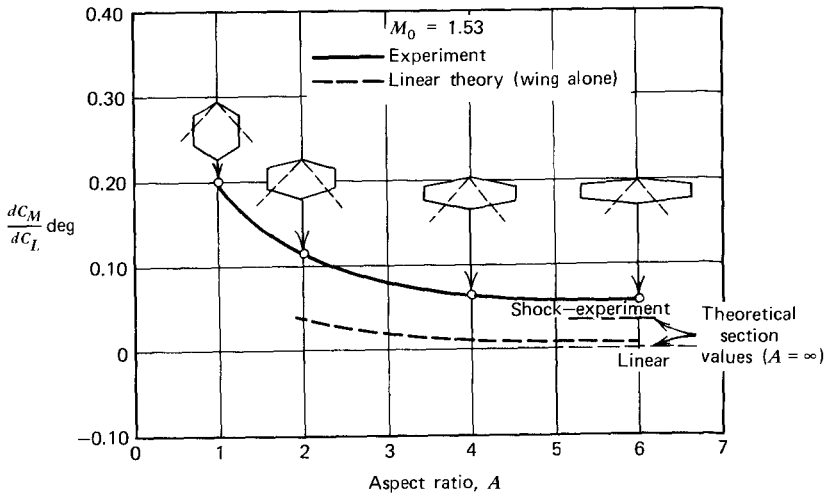

(d)

Figure 5.46 (continued)

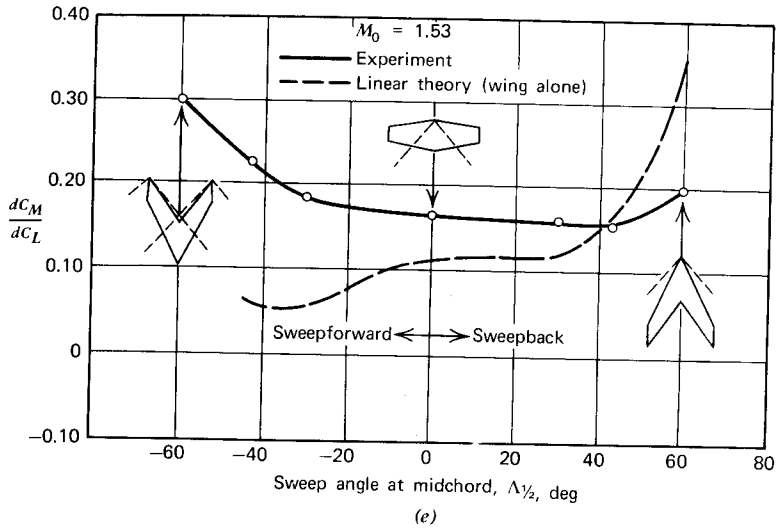

(e)

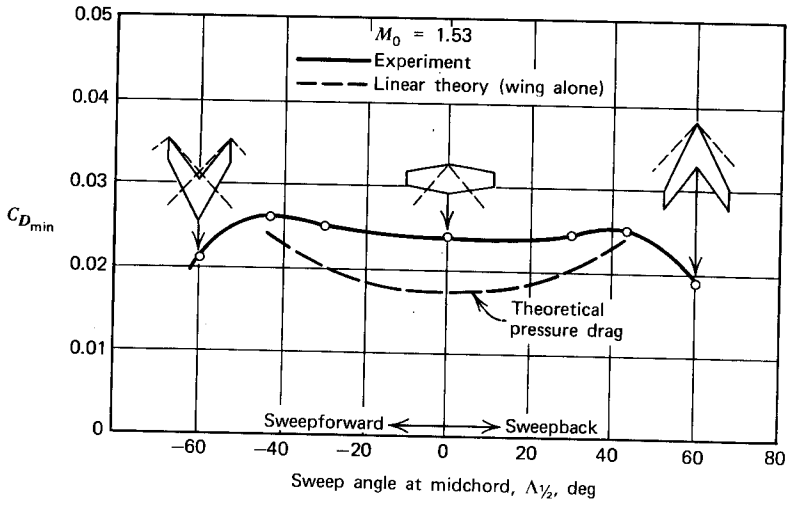

(f)

Figure 5.46 (continued)

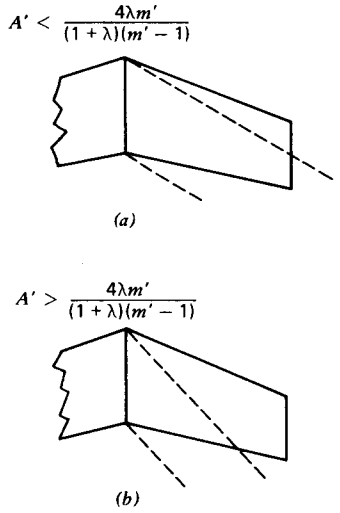

Figure 5.47 Wings with supersonic leading edges. (*a*) Mach line intersects tip chord. (*b*) Mach line intersects trailing edge.

$$C_{L_\alpha} = \frac{1}{\pi B\sqrt{m'^2-1}}\left\{\frac{[4m'k+A'(k-1)]^2}{2A'(k^2-1)}\left[\frac{1}{k}\cos^{-1}\frac{1}{m'}\right.\right.$$
$$\left.+\frac{k\sqrt{m'^2-1}}{\sqrt{(km'+1)(km'-1)}}\left(\cos^{-1}\frac{-1}{km'}-\cos^{-1}\frac{4km'(A'-1)-A'(k+3)}{4km'+A'(k-1)}\right)\right]$$
$$-\frac{[4m'k-A'(k-1)]^2}{4A'(k-1)}\sqrt{\frac{m'+1}{k(km'+1)}}\cos^{-1}\frac{4km'(1-A')+A'(3k+1)}{4km'-A'(k-1)}$$
$$\left.+\frac{[4m'k+A'(1+3k)]^2}{4A'(k+1)}\sqrt{\frac{m'-1}{k(km'+1)}}\cos^{-1}\frac{4km'(A'-1)+A'(k-1)}{4km'+A'(3k+1)}\right\} \tag{5.107}$$

If the Mach line from the apex intersects the trailing edge inboard of the tip, as shown in Figure 5.47*b*, C_{L_α} is given by

$$C_{L_\alpha} = \frac{1}{B\pi\sqrt{m'^2-1}}\left\{\frac{[4m'k+A'(k-1)]^2}{2A'(k^2-1)}\left[\frac{1}{k}\cos^{-1}\frac{1}{m'}\right.\right.$$
$$\left.\left.+\frac{k\sqrt{m'^2-1}}{\sqrt{(km'-1)(km'+1)}}\cos^{-1}\frac{-1}{km'}\right]-\frac{\pi[4km'-A'(k-1)]^2}{4A'(k-1)}\sqrt{\frac{m'+1}{k(km'+1)}}\right\} \tag{5.108}$$

In applying Equations 5.107 and 5.108, care must be taken to retain the signs of quantities under the radical. For example, if x and y are two arbitrary positive quantities,

$$\sqrt{(-x)(-y)} = \sqrt{(-1)^2xy} = -\sqrt{xy}$$

In order to use Equations 5.107 and 5.108, the following quantities are defined.

$$k = \frac{\cot \Lambda_{TE}}{\cot \Lambda}$$

$$= \frac{A(1+\lambda)}{A(1+\lambda) - 4m(1-\lambda)}$$

$$m = \cot \Lambda$$

λ = taper ratio (tip chord/root chord)

$$m' = Bm$$

$$A' = BA$$

Since there is no leading edge suction for a wing with a supersonic leading edge, its leading edges should be sharp to reduce the drag. The drag caused by lift in this case is given simply by

$$C_{D_i} = C_L \tan \alpha \tag{5.109}$$

To this must be added the wave drag and skin friction drag in order to obtain the total C_D.

A delta wing having the leading edge ahead of the Mach cone from the apex is a relatively simple case to treat. For this configuration, the expression for C_{L_α} is identical to that obtained for a two-dimensional airfoil (Equation 5.76).

For certain extreme cases, the lift of a supersonic wing can be quickly approximated using two-dimensional results. Such a case is pictured in Figure 5.48. Here, a moderately swept, fairly high aspect ratio wing is shown operating at a Mach number of around 2.0. Since pressure disturbances are not propagated outside the Mach cone, the flow over the wing is two dimensional in nature, except for the hatched regions shown within the Mach cones from the apex and tips. Thus, as a first approximation, the lift and wave drag for this wing can be calculated using the corresponding expressions derived for a two-dimensional supersonic airfoil section.

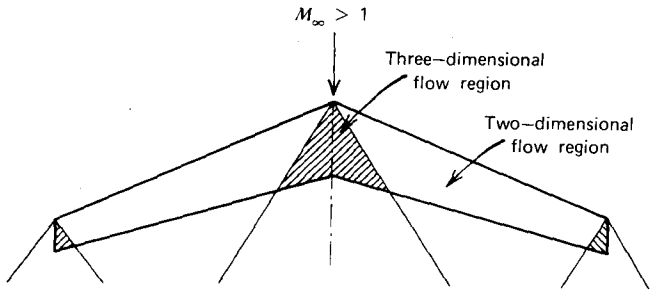

Figure 5.48 Supersonic wing over which the flow is mostly two-dimensional.

EFFECT OF MACH NUMBER ON THE ZERO LIFT DRAG OF TWO- AND THREE-DIMENSIONAL SHAPES

In subsonic flow, the drag of nonlifting shapes is relatively unaffected by Mach number until a critical value is reached. Below M_{cr}, the drag, excluding that due to lift, results from skin friction and the unbalance of normal pressures integrated around the body. The estimation of this drag has been covered in some detail in the preceding chapter. As the Mach number is increased, a value is reached where local shock waves of sufficient strength to produce separation are generated. At this point, the drag coefficient begins to rise. As the Mach number continues to increase, C_D will increase through the transonic flow region until supersonic flow is established. Depending on the particular shape, the rate of increase of C_D with M diminishes. C_D may continue to increase with M, but at a lower rate, it can remain fairly constant, or it can actually decrease with increasing Mach number. The behavior of C_D in the supersonic flow regime depends on the composition of the drag. Excluding the drag caused by lift, the remainder of the drag is composed of skin friction drag, wave drag, and base drag.

Base drag is a term not yet used. It refers to the drag produced by the pressure acting on the blunt rear end (base) of a body, such as that pictured in Figure 5.49. The base drag was not stressed in Chapter Four since, in subsonic flow, the shape of the base affects the flow over the rest of the body ahead of

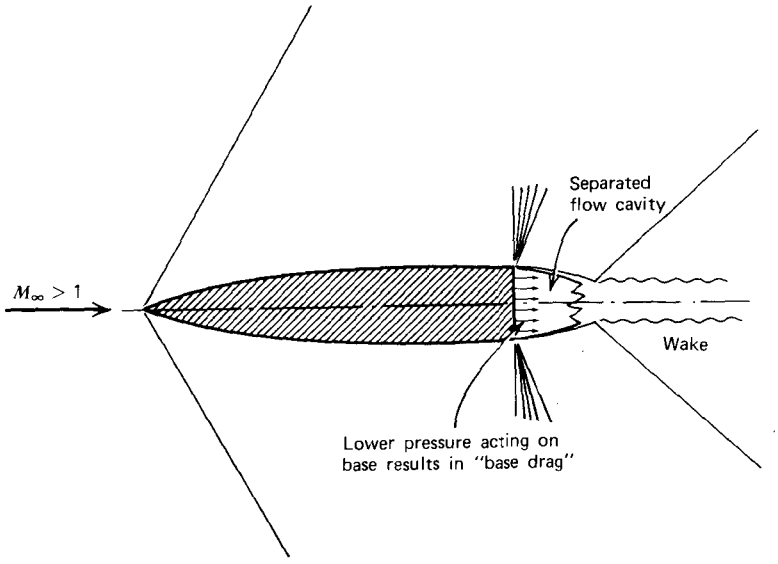

Figure 5.49 Origin of base drag.

it, so the base was viewed as simply an integral part of the overall pressure drag. In supersonic flow, however, the base does not affect the flow ahead of it, so it is convenient to treat it separately.

An upper limit on the base drag can be easily obtained by noting that the base pressure can never be less than zero. Hence the base pressure coefficient is bounded by

$$C_{p_B} = \frac{p_B - p_0}{(1/2)\rho_0 V^2}$$

$$> \frac{-p_0}{(1/2)\rho V^2}$$

$$> -\frac{2}{\gamma M^2}$$

Therefore, the base drag coefficient, *based on the base area*, must satisfy the inequality

$$C_{D_B} < \frac{2}{\gamma M^2} \tag{5.110}$$

There appears to be no accepted method available for calculating C_{D_B}. Generally, the base drag is affected by the thickness of the boundary layer just ahead of the base. Hence, C_{D_B} depends on the body shape, surface condition, and Reynolds number, as well as on the Mach number. In the supersonic regime, experimental data presented as a ratio to the upper limit (Equation 5.110) show the trends pictured in Figure 5.50.

The total drag coefficients of some basic shapes are presented in Figures 5.51 to 5.53. These curves are based on data from a number of sources. In Figure 5.51, C_D as a function of M is presented for circular disks and 2-dimensional flat plates, while Figure 5.52 presents the corresponding graphs for spheres and cylinders. In both cases, for the two-dimensional bluff shapes, C_d peaks at a Mach number of unity and then decreases, with increasing M reaching a value at approximately $M = 2$, which is equal to or slightly less than the low-speed value. Above $M = 2$, C_D remains nearly constant as M increases. The three-dimensional values, however, begin to rise at an M of approximately 0.7 and continue to rise until an M of approximately 2.0 is reached.

Figure 5.53 presents the drag of various conical heads having different apex angles as a function of Mach number. This is only the drag resulting from the pressure on the forward surface of the cone.

Drag data on a number of bodies of revolution are presented in Reference 5.25. Most of these data were derived by differentiating the velocity time history obtained by radar of free-flying, fin-stabilized models as

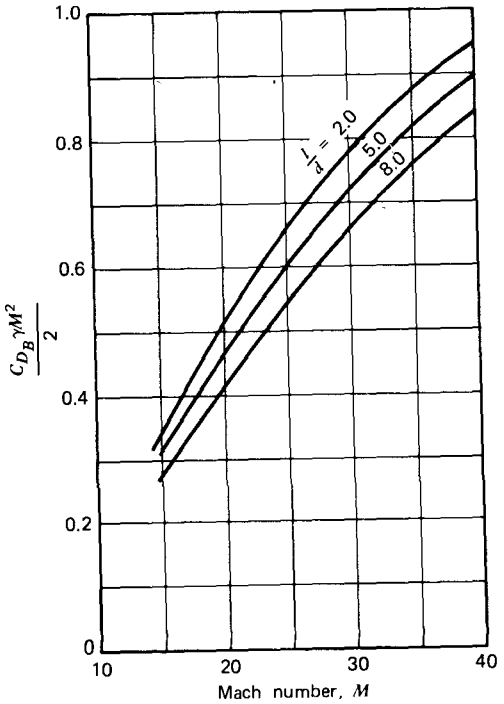

Figure 5.50 Ratio of base C_D to upper limit as a function of M and body-length-diameter ratio.

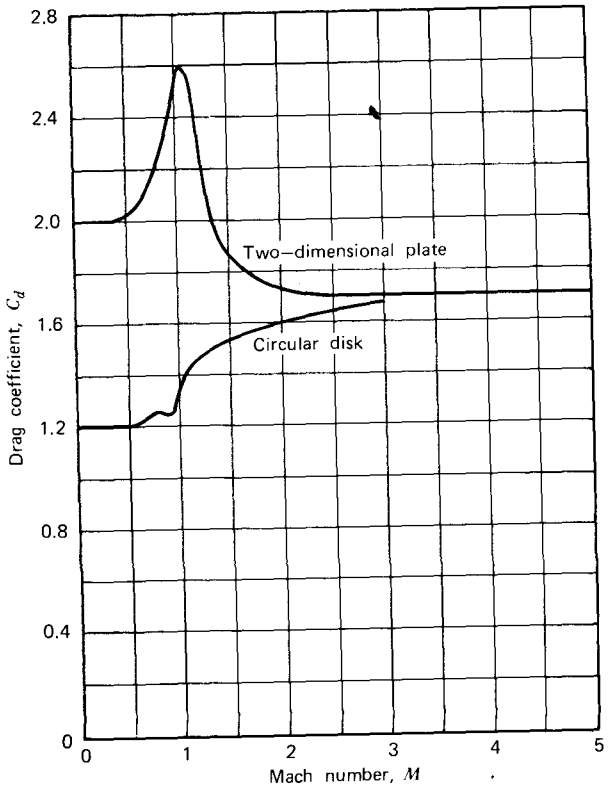

Figure 5.51 Drag of flat plates and discs normal to the flow as a function of Mach number.

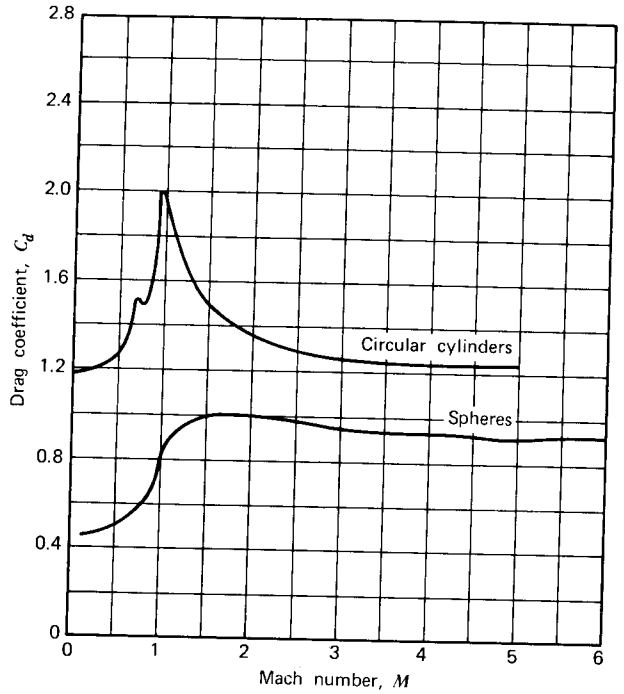

Figure 5.52 Drag of spheres and circular cylinders as a function of Mach number.

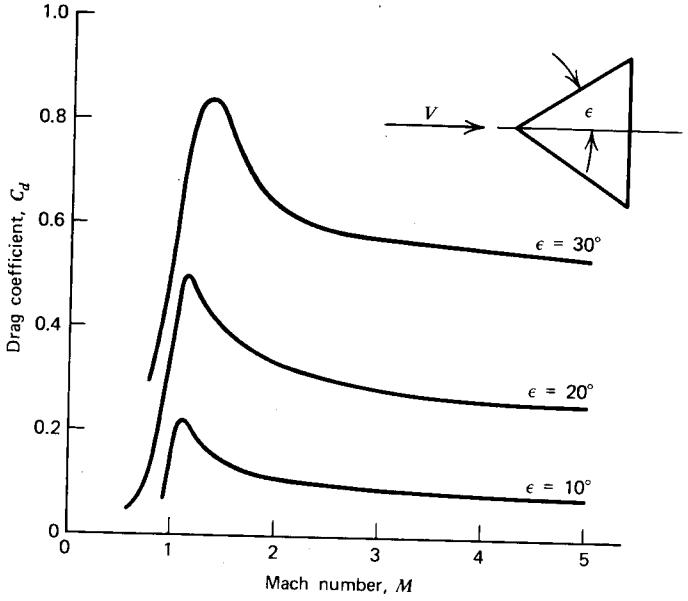

Figure 5.53 Drag as a function of Mach number for cones.

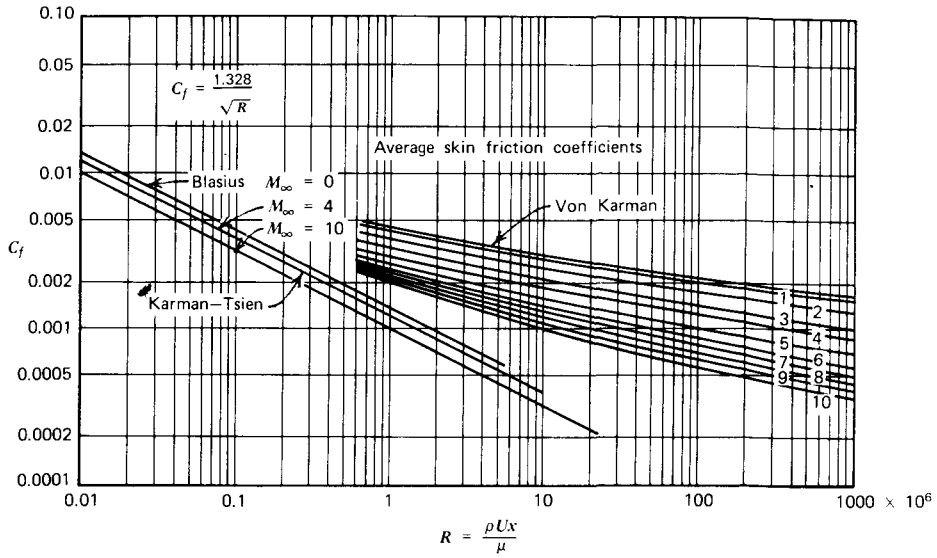

Figure 5.54 Average skin friction coefficients for flat plates based on wetted area.

they decelerated from supersonic to high subsonic Mach numbers. The data were then reduced, assuming that the effects of shape and fineness ratio could be considered separately. Skin friction drag was estimated on the basis of Figure 5.54, which presents C_f for flat plates as a function of Reynolds number for constant Mach numbers. This figure appears to be consistent with Figure 5.34 and Equations 5.87 and 5.88, and it is applicable to bodies of revolution, provided the length-to-diameter ratio, l/d, is sufficiently large.

Most of the shapes that were flown had afterbodies (i.e., a base diameter smaller than the maximum body diameter). For such bodies, the base drag is only a small fraction of the total drag and varies approximately as the third power of the ratio of the base diameter to the body diameter.

Figure 5.55 presents C_D as a function of Mach number for parabolic bodies having different fineness ratios and positions of maximum diameter. Similar data for degrees of nose roundness are given in Figure 5.56. The effect of afterbody shape on C_D can be estimated from Figure 5.57. Finally, for these data, the effect of shape on the pressure drag of noses is shown in Figure 5.58. Draw your own conclusions regarding an optimum shape from these data. The C_D values are all based on the maximum projected frontal area. Normally one is concerned with packaging a given payload; therefore, a C_D based on volume to the 2/3 power might be more informative.

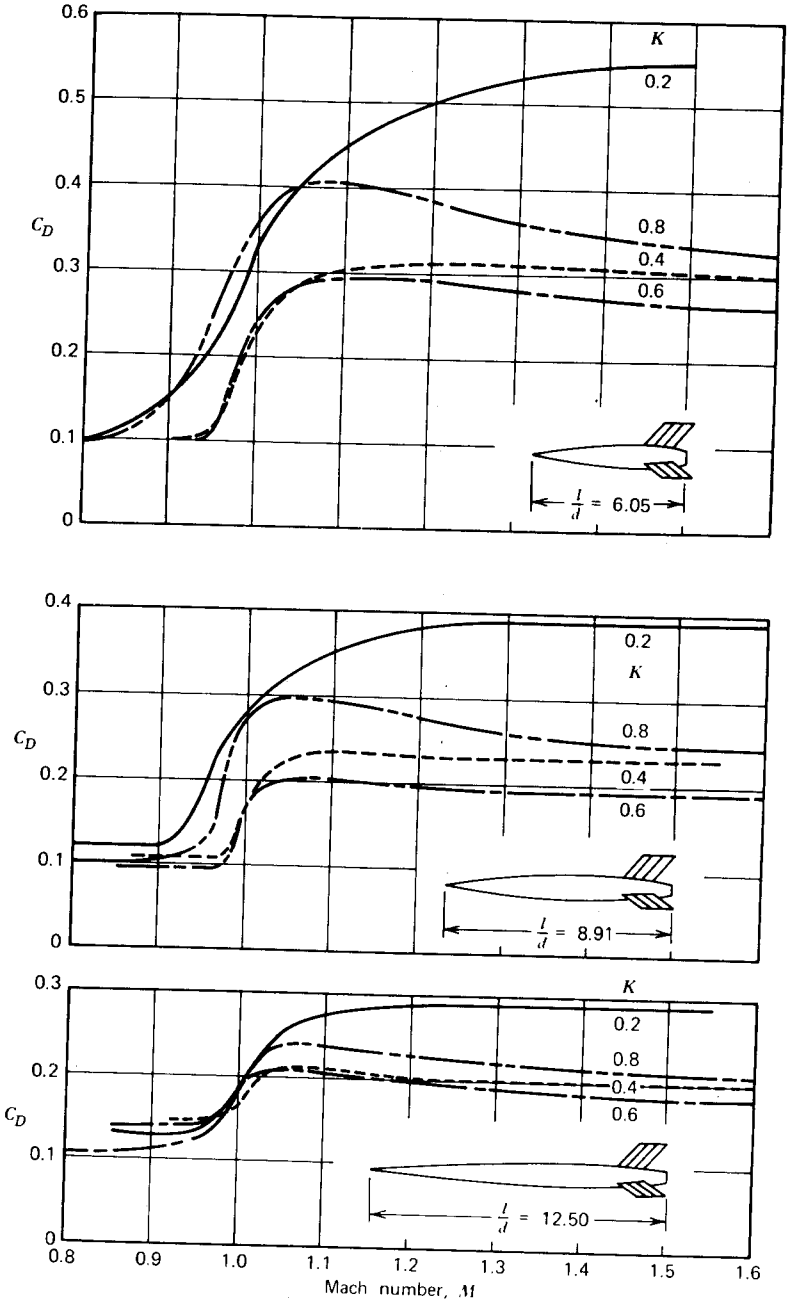

Figure 5.55 Drag coefficients of parabolic bodies showing effects of fineness ratio and position of maximum diameter. (k = position of max. diameter from nose as fraction of body length).

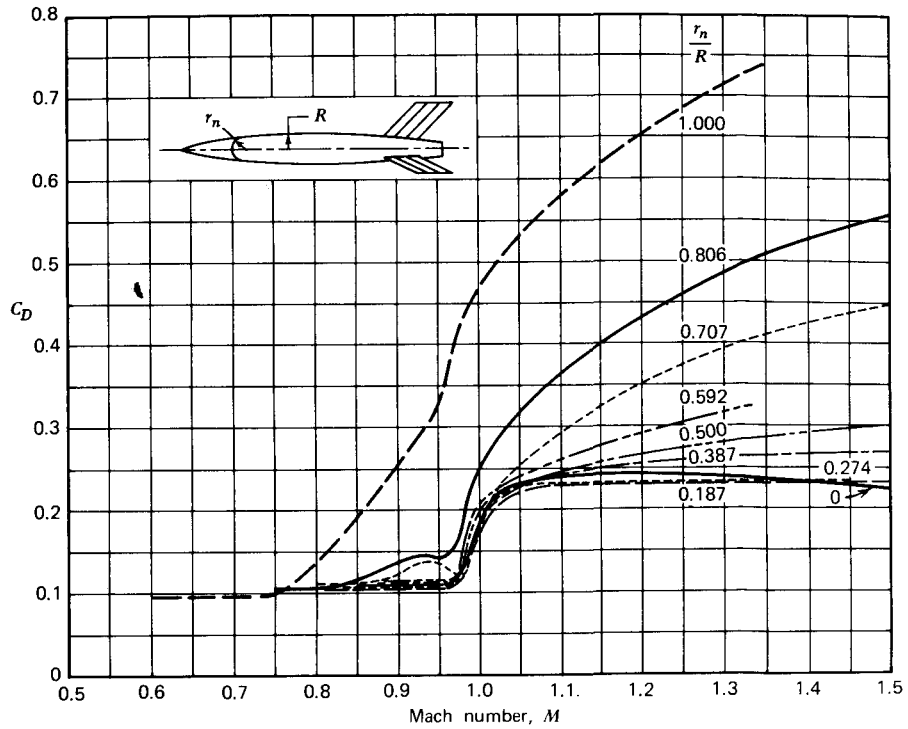

Figure 5.56 Drag coefficient plotted against Mach number for configurations obtained by rounding off nose of parabolic body of fineness ratio 8.91.

Area Rule for Transonic Flow

Reference 5.27 represents a significant contribution to the aerodynamics of high-speed aircraft. Whitcomb (Ref. 5.27) experimentally investigated the zero lift drag of wing-body combinations through the transonic flow regime. Based on analyses by Hayes (Ref. 5.28), Busemann (Ref. 5.29), and others, Whitcomb formulated some general guidelines for the design of wing-body combinations to have minimum wave drag that are reflected in most of today's aircraft designed to operate near or in excess of Mach 1. These guidelines are included in the general designation "area rule."

The essence of the area rule is contained in the data of Figures 5.59 to 5.62 (taken from Whitcomb's original NACA report). These figures present C_D at zero lift as a function of M for a cylindrical body alone and in combination with a triangular wing and a tapered swept wing. C_{D_0} is the total C_D measured for zero lift, while ΔC_{D_0} is obtained by simply subtracting C_{D_0} at $M = 0.85$

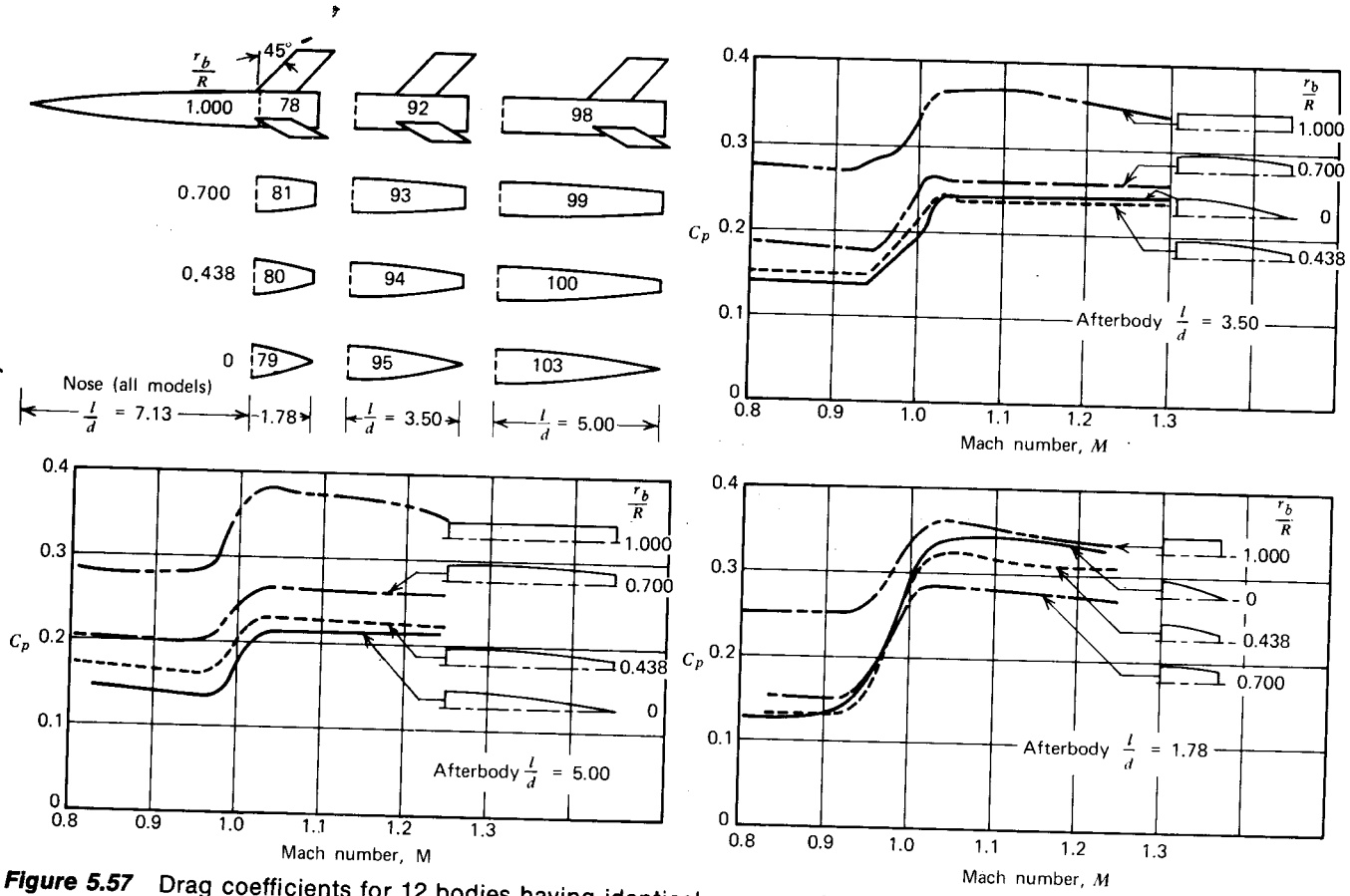

Figure 5.57 Drag coefficients for 12 bodies having identical noses and different afterbodies.

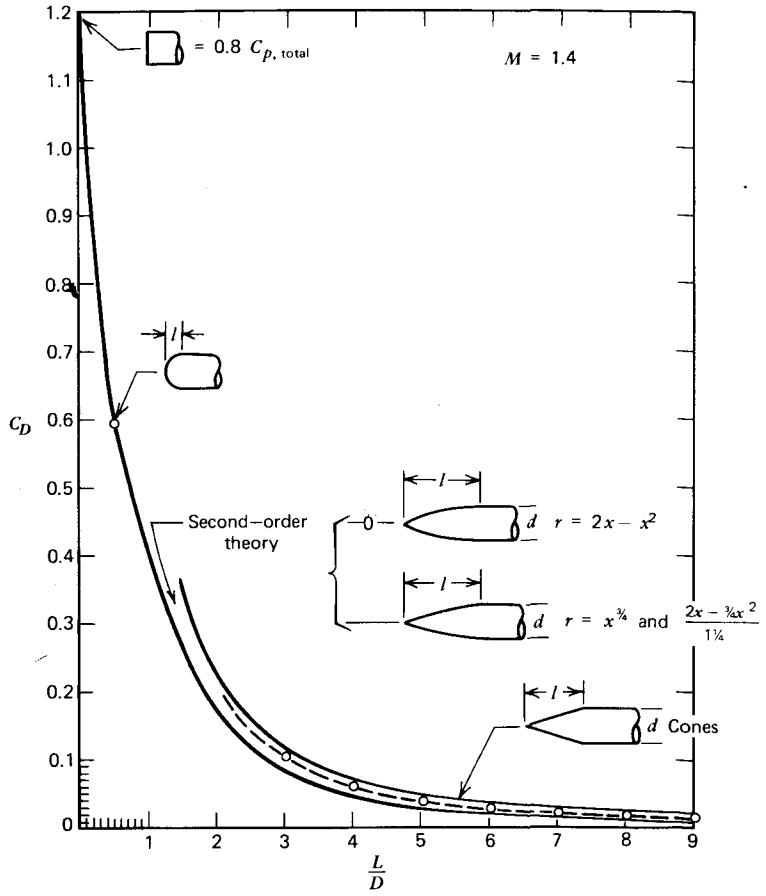

Figure 5.58 Drag coefficients due to pressure on noses at $M = 1.4$.

from the other C_{D_0} values. C_{D_0} at $M = 0.85$ is approximately equal to the skin friction C_D over the range of M values tested, so that ΔC_{D_0} represents the wave drag coefficient.

In these figures, there are essentially four different combinations.

1. Basic body alone.
2. Wing attached to the unaltered basic body.
3. A "flattened" body alone.
4. Wing attached to a "thinned" body.

For combinations 1 and 4, the longitudinal distribution of the total (wing

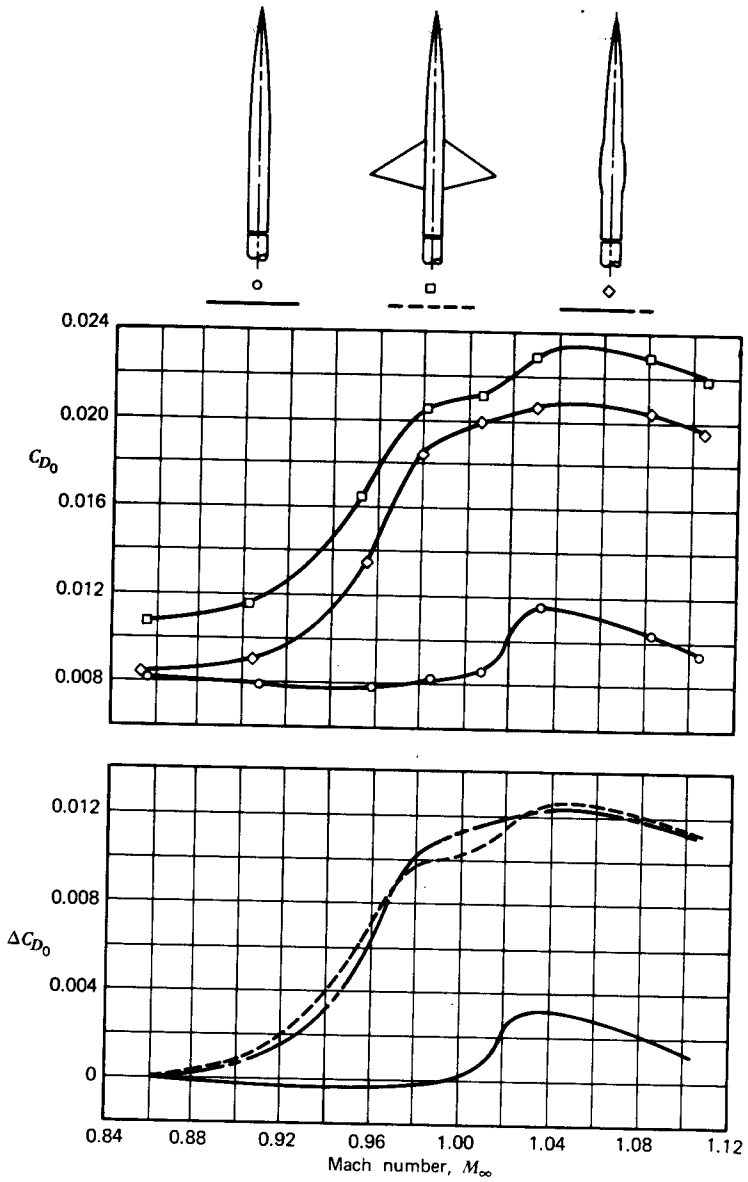

Figure 5.59 Comparisons of the drag rise for the delta wing-cylindrical body combination with that for the comparable body of revolution and the cylindrical body alone.

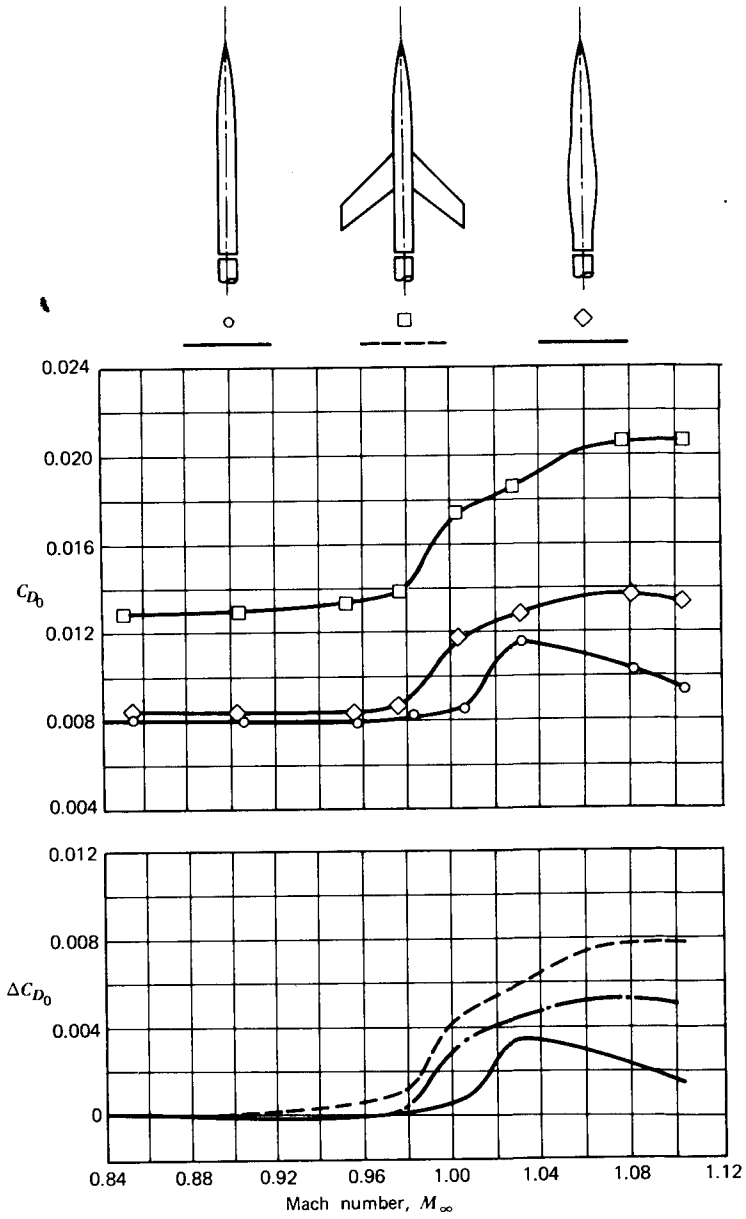

Figure 5.60 Comparisons of the drag rise for the swept wing-cylindrical body combination with that for the comparable body of revolution and the cylindrical body alone.

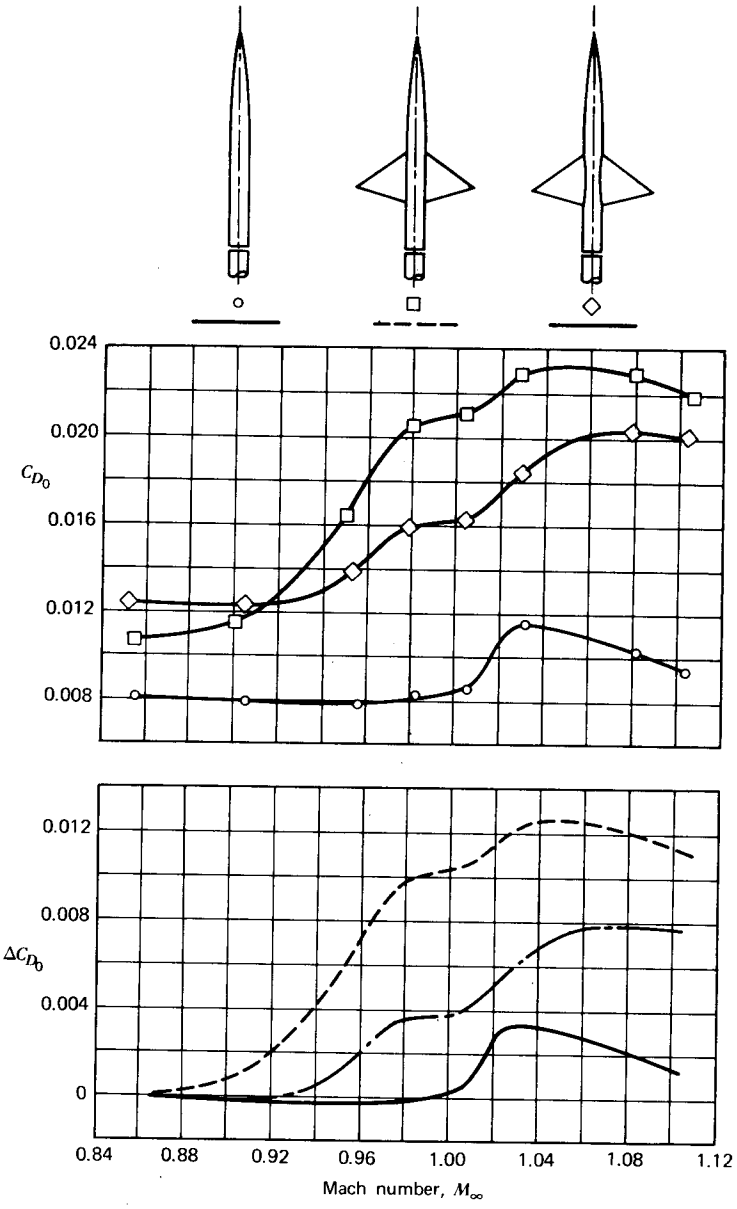

Figure 5.61 Drag rise for delta wing-body combinations.

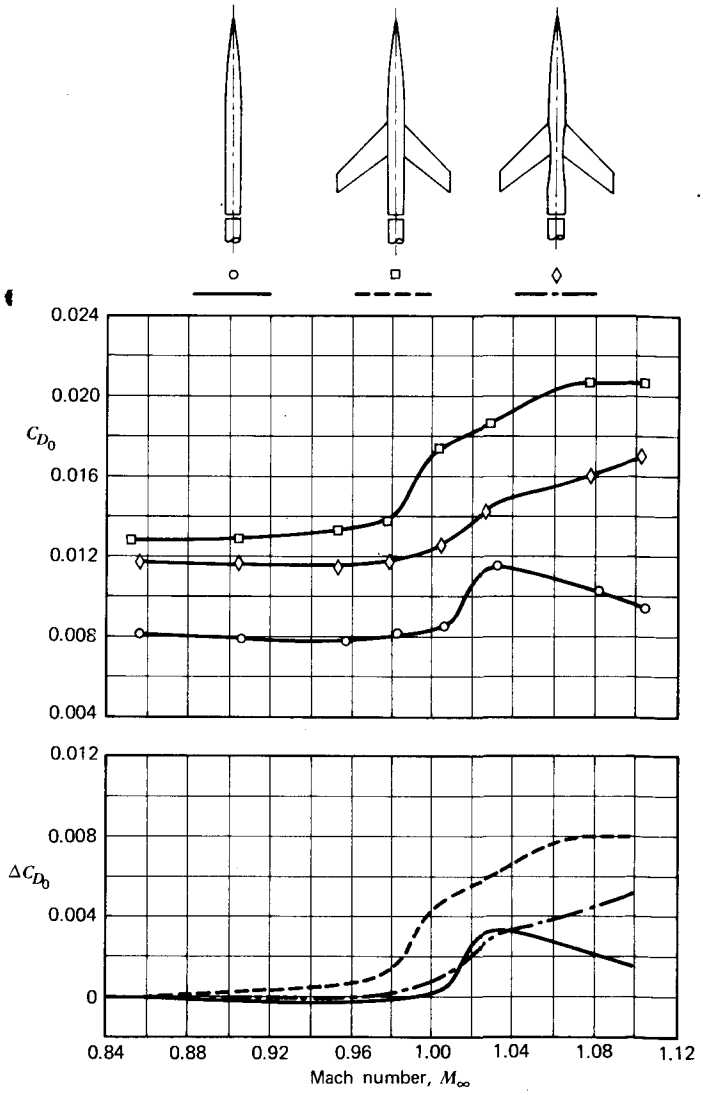

Figure 5.62 Drag rise for swept wing-body combinations.

plus body) cross-sectional area in any transverse plane is the same. This is also true in comparing combinations 2 and 3.

After considering these results and some others not presented here, Whitcomb states:

"Comparisons of the shock phenomena and drag-rise increments for representative wing and central-body combinations with those for bodies of

revolution having the same axial developments and cross-sectional areas normal to the airstream have indicated the following conclusions:

1. *The shock phenomena and drag-rise increments measured for these representative wing and central-body combinations at zero lift near the speed of sound are essentially the same as those for the comparable bodies of revolution.*
2. *Near the speed of sound, the zero-lift drag rise of a low-aspect-ratio thin-wing-body combination is primarily dependent on the axial development of the cross-sectional areas normal to the airstream. Therefore, it follows that the drag rise for any such configuration is approximately the same as that for any other with the same development of cross-sectional areas.*

Further results have indicated that indenting the bodies of three representative wing-body combinations, so that the axial developments of cross-sectional areas for the combinations were the same as for the original body alone, greatly reduced or eliminated the zero-lift drag-rise increments associated with wings near the speed of sound."

As a corollary to the conclusions stated by Whitcomb, the longitudinal distribution of the total cross-sectional area from the wing and fuselage should be a smooth one for minimum wave drag (i.e., significant increases or decreases of the total area over short distances in the streamwise direction should be avoided).

PROBLEMS

5.1 Consider an untwisted wing with a midchord sweep angle, $\Lambda_{1/2}$, of 40°, a taper ratio, λ, of 0.35, and an aspect ratio of 4.5. The wing characteristics at high subsonic Mach numbers are to be determined by testing equivalent wings in a low-speed tunnel having $M \simeq 0.2$. What is the shape of the wing to be tested to simulate the given wing at a Mach number of 0.7?

5.2 Given a thin circular arc airfoil having a 5% camber ratio and operating at zero angle of attack, what is its critical Mach number?

5.3 A 56.63 m^3 reservoir supplies the air for a blowdown supersonic wind tunnel that operates at $M = 2.0$ in a test section that measures 15.24 × 15.24 cm. If the reservoir is compressed initially to an absolute pressure of 2×10^6 Pa with a temperature of 20°C and the valve suddenly opened to the tunnel, how long will the tunnel operate at its design Mach number? Assume an adiabatic expansion in the reservoir. The test section exits to SSL conditions.

5.4 Redo the example given in the text for the airfoil pictured in Figure 5.22 at an angle of attack of 4° at $M = 2.0$. Use both Ackeret's theory and the oblique shock expansion wave method.

5.5 Using Ackeret's theory, predict C_l, C_d, and C_M for a convex airfoil that is flat on the bottom with a circular arc on the top. $t/c = 0.10$, $M = 1.5$, and $\alpha = 2°$.

5.6 Prove that Equations 5.66 and 5.67 satisfy equation 5.64 and the following: $\beta^2\phi_{xx} + \phi_{yy} + \phi_{zz} = 0$.

5.7 Check a point on Figure 5.24 using both Ackeret's theory and the oblique shock expansion wave method. As a class exercise, each student (or team) should take a different point in order to check the entire figure collectively.

5.8 Estimate the slope of the wing lift curve, position of the aerodynamic center, and dC_{D_i}/dC_L^2 for the Vought A7-D shown in Figure 5.25 at $M = 0.88$.

5.9 Given a thin, flat delta wing with $A = 2.0$, calculate C_L and C_D for $\alpha = 20°$ for $M = 0.9$. Include an estimate of skin friction drag. Assume SSL and a wing span of 30 ft.

5.10 Repeat Problem 5.9 for $\alpha = 5°$, $M = 2.0$.

5.11 Consider a thin, swept, tapered wing with $A = 4.0$, $\lambda = 0.5$, and $\Lambda_{LE} = 25°$. The wing loading equals 110 psf and the wing section is that described for Problem 5.5, with a slightly rounded leading edge. The mean geometric chord equals 10 ft. For the wing alone, estimate $C_{L_{max}}$ without flaps at SSL conditions. Then, beginning at the stalling speed, estimate C_D and, hence, L/D as a function of true airspeed up to a Mach number 20% higher than that which will make the Mach cone coincident with the leading edge. Use SSL conditions for M values below 0.5 and a standard altitude of 25,000 for higher Mach numbers.

5.12 Given a thin delta wing with $\Lambda_{LE} = 45°$ operating at $M = 2.0$, calculate C_{L_α} and dC_D/dC_L^2 at $\alpha = 0$. Repeat for a tapered wing with the same A, leading edge sweep, and $\lambda = 0.5$.

5.13 Estimate the total drag of the Concorde (Figure 5.25) at its design cruising speed and altitude. Assume that the fuselage is area-ruled so that the zero lift wave drag of the wing can be neglected if the fuselage were not indented. Use a wing planform area of 358 m^2 and a weight of 1434 kN. The wing span equals 25.56 m. Approximate the wing as a delta wing having the same A as the actual wing. Scale the drawing (Figure 5.25) as needed to get other dimensions and areas. Assume slightly rounded leading edges.

REFERENCES

5.1 Liepmann, H. W. and Roshko, A., *Elements of Gasdynamics*, John Wiley, New York, 1957.

5.2 Shapiro, Ascher H., *The Dynamics and Thermodynamics of Compressible Fluid Flow*, Vols. I and II, Ronald Press, New York, 1953.

5.3 Clancy, L. J., *Aerodynamics*, A Halsted Press Book, John Wiley, New York, 1975.

5.4 Daley, B. N., and Dick, R. S., *Effect of Thickness, Camber, and Thickness Distribution on Airfoil Characteristics at Mach Numbers Up to 1.0*, NACA TN 3607, March 1956.

5.5 *USAF Stability and Control Datcom*, Flight Control Division, Air Force Flight Dynamics Laboratory, Wright-Patterson Air Force Base, Ohio, October 1960 (revised January 1975).

5.6 Kuethe, A. M., and Chow, C., *Foundations of Aerodynamics, 3rd edition* (first two editions by A. M. Kuethe and J. D. Schetzer), Wiley, New York, 1976.

5.7 Ames Research Staff, *Equations, Tables and Charts for Compressible Flow*, NACA Report 1135, 1953.

5.8 Axelson, John A., "Estimation of Transonic Aerodynamics to High Angles of Attack," *J. of Aircraft, 14* (6), pp. 553–559, June 1977.

5.9 Laitone, E. V., *Limiting Velocity by Momentum Relations for Hydrofoils Near the Surface and Airfoils in Near Sonic Flow*, Proceedings of the Second U.S. National Congress of Applied Mechanics, pp. 751–753, June 14–18, 1954.

5.10 Stivers, L. S., Jr., *Effects of Subsonic Mach Number on the Forces and Pressure Distributions on Four NACA 64A-Series Airfoil Sections at Angles of Attack as High as* 28°, NACA TN 3162, March 1954.

5.11 *Jane's All the World's Aircraft*, published annually by Paulton House, London.

5.12 Garner, H. C., and Inch, S. M., *Subsonic Theoretical Lift-Curve Slope Aerodynamic Centre and Spanwise Loading for Arbitrary Aspect Ratio, Taper Ratio and Sweepback*, Aeronautical Research Council C.P. No. 1137, 1971.

5.13 Furlong, G. C., and McHugh, J. G., *A Summary and Analysis of the Low-Speed Longitudinal Characteristics of Swept Wings at High Reynolds Number*, NACA Report 1339, 1957.

5.14 Razak, Kenneth, and Snyder, M. H., *A Review of the Planform Effects of the Low-Speed Aerodynamic Characteristics of Triangular and Modified Triangular Wings*, NASA CR-421, April 1966.

5.15 Hopkins, E. J., Hicks, R. M., and Carmichael, R. L., *Aerodynamic Characteristics of Several Cranked Leading-Edge Wing-Body Combinations at Mach Numbers from 0.4 to 2.94*, NASA TN D-4211, October 1967.

5.16 Hicks, R. M., and Hopkins, E. J., *Effects of Spanwise Variation of Leading-Edge Sweep on the Lift, Drag, and Pitching Moment of a Wing-Body Combination at Mach Numbers from 0.7 to 2.94*, NASA TN D-2236, April 1964.

5.17 Jones, R. T., *Properties of Low-Aspect-Ratio Pointed Wings at Speeds Below and Above the Speed of Sound*, NACA Report 835, 1946.
5.18 Spreiter, J. R., *The Aerodynamic Forces on Slender Plane- and Cruciform Wing and Body Combinations*, NACA Report 962, 1950.
5.19 Polhamus, E. C., *A Concept of the Vortex Lift of Sharp-Edge Delta Wings Based on a Leading-Edge-Suction Analogy*, NASA TN D-3767, December 1966.
5.20 Polhamus, E. C., *Application of the Leading-Edge-Suction Analogy of Vortex Lift to the Drag due to Lift of Sharp-Edge Delta Wings*, NASA TN D-4739, August 1968.
5.21 Polhamus, E. C., *Charts for Predicting the Subsonic Vortex-Lift Characteristics of Arrow, Delta, and Diamond Wings*, NASA TN D-6243, April 1971.
5.22 Brown, C. E., *Theoretical Lift and Drag of Thin Triangular Wings at Supersonic Speeds*, NACA Report 839, 1946.
5.23 Malvestuto, F. S., Margolis, Kenneth, and Ribner, H. S., *Theoretical Lift and Damping in Roll At Supersonic Speeds of Thin Sweptback Tapered Wings with Streamwise Tips, Subsonic Leading Edges, and Supersonic Trailing Edges*, NACA Report 970, 1950.
5.24 Harmon, S. M., and Jeffreys, Isabella, *Theoretical Lift and Damping in Roll of Thin Wings with Arbitrary Sweep and Taper at Supersonic Speeds—Supersonic Leading and Trailing Edges*, NACA TN 2114, May 1950.
5.25 Stoney, W. E., *Collection of Zero-Lift Drag Data on Bodies of Revolution from Free-Flight Investigations*, NACA TN 4201, January 1958.
5.26 Vicenti, W. G., *Comparison Between Theory and Experiment for Wings at Supersonic Speeds*, NACA Report 1033, 1951.
5.27 Whitcomb, R. T., *A Study of the Zero-Lift Drag-Rise Characteristics of Wing-Body Combinations Near the Speed of Sound*, NACA Report 1273, 1956.
5.28 Hayes, W. D., *Linearized Supersonic Flow*, Report No. AL-222, North American Aviation, Inc. (now Rockwell International), June 18, 1947.
5.29 Busemann, Adolf, *Application of Transonic Similarity*, NACA TN 2687, 1952.

SIX
THE PRODUCTION OF THRUST

A BRIEF HISTORY OF THE PISTON ENGINE

The evolution of today's airplane has depended significantly on the development of power plant technology. As pointed out by Torell (Ref. 6.1),

"*Each successive generation of transport aircraft has been paced by the development of engines with greater power and improved efficiency, and more power for each pound of weight.*"

From 1903 until the early 1940s, the piston engine-propeller combination was the only type of power plant used to any extent for airplane propulsion. The earliest piston engine designs were water-cooled, in-line designs requiring bulky, high-drag radiators. The Wright Brothers' first engine was of this type. This engine had four upright cylinders, weighed 890 N, (200 lb), and developed approximately 8.95 kW (12 hp). The liquid-cooled airplane piston engine remained in extensive use through World War II and evolved into powerful, efficient configurations typified by the Rolls-Royce Merlin. This ethylene glycol-cooled V-12 design, weighing 6360 N (1430 lb), delivered 843 kW (1130 hp) at 3000 rpm.

Air-cooled airplane piston engines trace their lineage from the French Gnome rotary-radial design built in 1908. For this configuration, the propeller was attached to the cylinders which, displaced radially, rotated around the engine centerline. The first engines of this type delivered approximately 52 to 60 kW (70 to 80 hp) for a weight of approximately 1023 N (230 lb). The power-to-weight ratio of the rotary-radial engine was an improvement over the contemporary water-cooled designs; however, the fuel and oil consumption was high for the rotary-radial designs. Also, gyroscopic effects resulting from their high angular momentum were severe under maneuvering conditions.

The rotary-radial engine was superseded by the static, or stationary, radial configuration. In the 1920s, a competitive series of static-radial piston

engines were produced by the Wright Co. and the Pratt & Whitney Co. The first of these was the Wright Whirlwind. It was a Wright J-5C Whirlwind, nine-cylinder radial engine weighing approximately 2224 N (500 lb) and developing 164 kW (220 hp); that powered the Ryan monoplane "Spirit of St. Louis" in which Colonel Charles Lindbergh made his epic crossing of the Atlantic in May 1927. It was also the Wright Whirlwind, three of them each rated at 224 kW (300 hp), that took Admiral Richard Byrd to Antarctica in a Ford Tri-motor in 1929.

Pratt & Whitney's first radial engine, developed shortly after the Whirlwind, was designated the Wasp. This engine, weighing 2891 N (650 lb), developed 298 kW (400 hp) at 1900 rpm. The Wasp was followed by the more powerful Hornet and then by the Twin-Wasp, a radial engine with two rows of radially displaced cylinders. The Wright Cyclone was a similar design that first powered one of the most famous air transports of all time, the Douglas DC-3. Succeeding versions of the DC-3, were also powered with the Twin-Wasp designated the R-1830. The 1830 refers to the engine displacement in cubic inches. More than 10,000 of the Wasp-powered DC-3's were built, and many are still flying today.

Horizontally opposed, air-cooled piston engines for light aircraft appeared around 1932. These designs are still produced in large quantities today by Continental Motors and Avco Lycoming. Production of the larger radial engines ceased in the late 1950s with the development of the turboprop and turbojet engines.

PISTON ENGINE CHARACTERISTICS

An aircraft piston engine is similar to an automobile engine with a few differences. First, an aircraft engine is designed with weight as a primary consideration. Thus, the weight-to-power ratio is generally lower for an aircraft engine when compared with an automobile engine of comparable size. Weight-to-power ratios for various aircraft piston engine configurations are presented in Figure 6.1 as a function of engine power. The ratio is seen to improve as the engine gets larger. Turboprop engines are also included in this figure and are seen to have weight-to-power ratios that are less than half of those for the piston engines. The turboprop engine will be discussed in more detail later. Notice for the piston engines that the weight-to-power ratio trend is about the same for all of the engine configurations. The horizontally opposed, air-cooled configuration appears to be somewhat better than the rest, but this may be because most of these engines were designed and built at a later date than the radial or in-line engines.

Today's airplane piston engine is a very reliable piece of machinery. With recommended major overhaul periods of up to 2000 hr, one can get 400,000 to

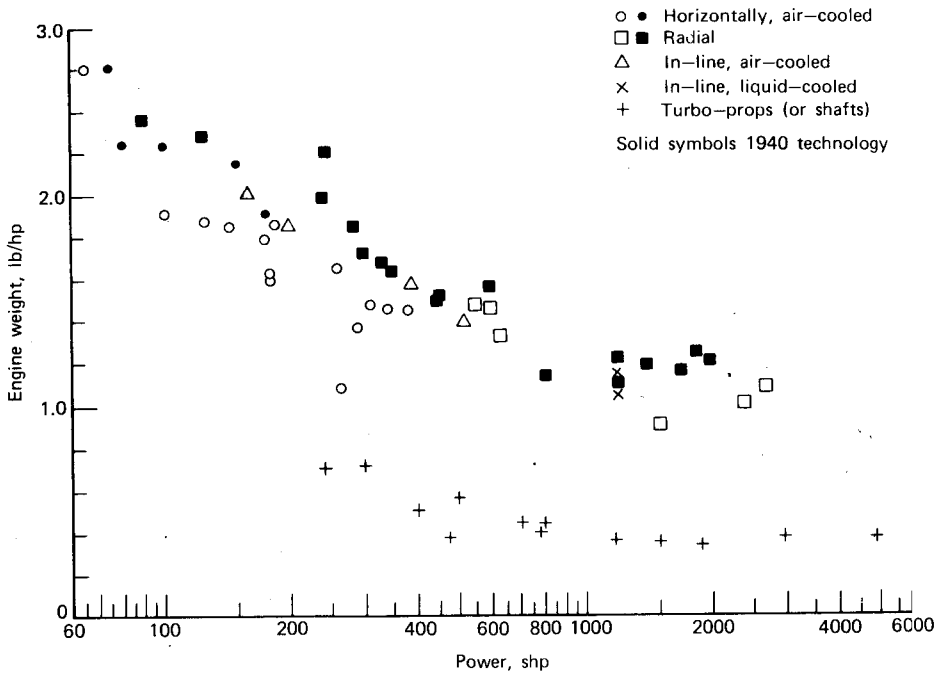

Figure 6.1 Piston engine weights.

800,000 km on an engine (depending on the cruising speed) before major components are replaced. An airplane engine has two spark plugs on each cylinder that are fired independently from engine-driven magnetos. Before taking off, a pilot checks to see that the engine will run smoothly on either "mag" alone. Many airplane engine systems also incorporate an additional fuel pump that is electrically driven, independent of the engine.

Since it must operate over a range of density altitudes, an airplane engine has a manual mixture control. At low altitudes, the mixture is set relatively rich and is leaned at the higher altitudes, where the air is less dense. During a continuous climb, where a large amount of power is required, the pilot will also set the mixture on the rich side in order to provide better cooling. The richer the mixture, the cooler the exhaust gases will be. Running too rich, however, can result in a loss of power and premature spark plug fouling. Therefore, many airplanes are equipped with an exhaust gas temperature (EGT) gage that allows the pilot to set the mixture control more accurately.

Carbureted airplane engines, as opposed to fuel-injected engines, have a carburetor heat control. In the "on" position, this control provides heated air to the carburetor in order to avoid the buildup of ice in the venturi. Since the air expands in the carburetor throat, the temperature in this region can be below freezing even when the outside air temperature is above freezing. If a

pilot is flying through rain or heavy clouds at temperatures close to freezing, he or she can experience carburetor icing with an attendant loss (possibly complete!) of power unless he or she pulls on the carburetor heat.

An airplane piston engine is operated with primary reference to two gages, the tachometer, which indicates the engine rpm and the manifold pressure gage, which measures the absolute pressure within the intake manifold. These two quantities, at a given density altitude, determine the engine power. To develop this point further, consider the characteristics of the Lycoming 0-360-A engine, which is installed in the Piper Cherokee 180 used previously as an example. A photograph of this engine is presented in Figure 6.2.

This horizontally opposed, four-cylinder, air-cooled engine is rated at 180 bhp at 2700 rpm. On a relative basis, its performance is typical of piston engines and will be discussed now in some detail. Operating curves for this engine are presented in Figure 6.3. Its performance at sea level is on the left and the altitude performance is on the right. These curves are given in English units, as prepared by the manufacturer. Generally, these curves must be used in conjunction with each other in order to determine the engine power. Their use is best illustrated by an example. Suppose we are operating at a part throttle condition at 2400 rpm and a pressure altitude (altitude read on altimeter set to standard sea level pressure) of 1800 ft. The manifold air pressure (MAP) reads 23.2 in. Hg and the outside air temperature (OAT) is 25 °F. First we locate point *B* on the sea level curve at the operating manifold pressure and rpm. This point, which reads 129 BHP, is then transferred to the altitude curve at sea level (point *C*). Next, point *A* is located on the full-throttle altitude curve for the operating manifold pressure and rpm. *A* and *C* are connected by a straight line and the power for standard temperature conditions read on this line at the operating pressure altitude. This point *D* gives a bhp of 133. Next we correct for the nonstandard OAT. At 1800 ft, the standard absolute temperature is 513 °R, whereas the actual OAT is 485 °R. The power varies inversely with the square root of the absolute temperature; thus,

$$\begin{aligned} \text{bhp} &= \text{bhp (standard)} \sqrt{\frac{T_{\text{standard}}}{T_{\text{actual}}}} \\ &= 133 \sqrt{\frac{513}{485}} \\ &= 137 \text{ hp} \end{aligned} \tag{6.1}$$

Thus the engine is developing 137 bhp under these conditions. To determine the fuel consumption, we enter the sea level curve with this power and the engine rpm (point *F*). We then read the fuel consumption at the same rpm and manifold pressure corresponding to point *F*. In this case, a consumption of 10.8 gph is determined.

These curves are typical of operating curves for nonsupercharged,

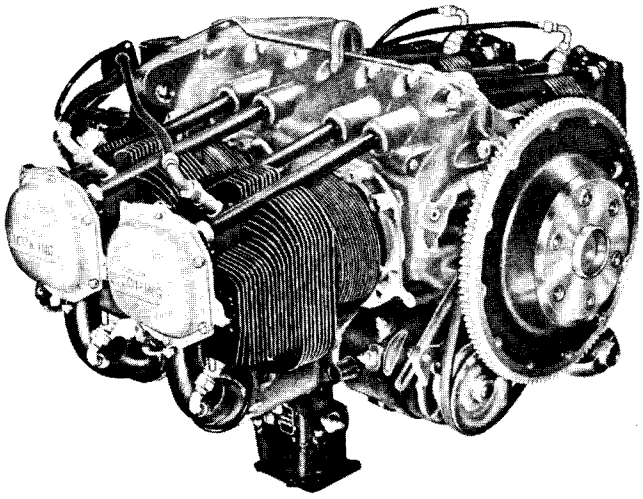

SPECIFICATIONS AND DESCRIPTION

TYPE—Four-cylinder, direct drive, horizontally opposed, wet sump, air-cooled engine

	0-360-A
FAA Type certificate	286
Takeoff rating, O-360-C2D only	
hp, rpm and manifold pressure	180 @ 2900 and 28 in. hg
Rated hp and rpm	180 @ 2700
Cruising rpm, 75% rated	135 @ 2450
65% rated	117 @ 2350
Bore, in.	5.125
Stroke, in.	4.375
Displacement, in.^{3}	361.0
Compression ratio	8.5:1
Cylinder head temperature, max	500°
Cylinder base temperature, max	325°
Fuel octane, aviation grade, min	91/96
Valve rocker clearance (hydraulic tappets collapsed)	0.028 to 0.080
Oil sump capacity, qt	8
Oil pressure, idling psi	25
normal psi	65 to 90
start and warmup psi	100
Spark occurs, deg BTC	25
Spark plug gap, fine wire	0.015 to 0.018
massive wire	0.018 to 0.022
Firing order	1-3-2-4
Standard engines (dry weight) (Includes 12-V–20-amp generator and 12-volt starter)	285 lb

Figure 6.2 Lycoming Aircraft engine. Three-quarter right front view. (Courtesy, Lycoming Division, Avco Corp.)

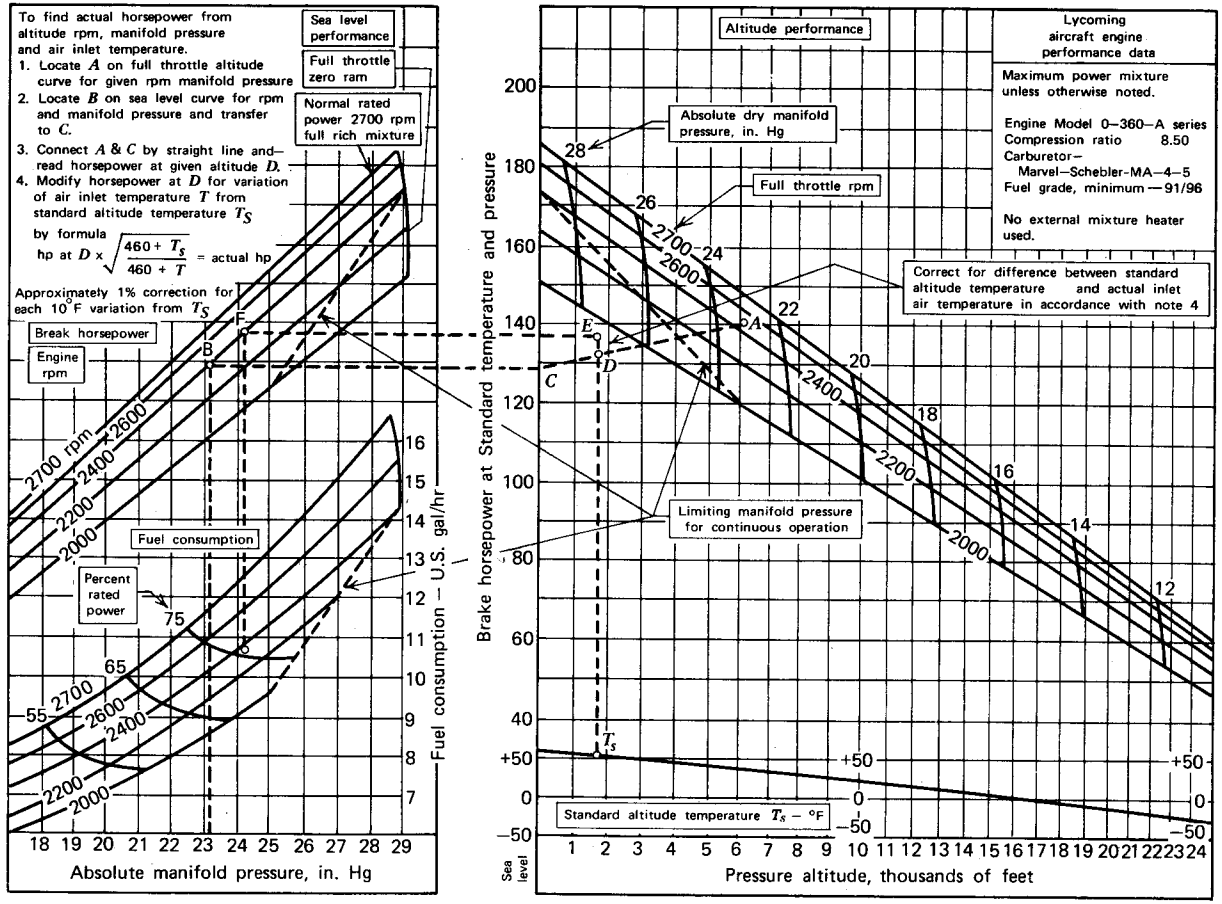

Figure 6.3 Lycoming Aircraft engine performance data. (Courtesy Lycoming Division, Avco Corp.)

reciprocating engines. It is interesting to note that all wide-open throttle (WOT) power curves at a constant rpm decrease linearly with density ratio approaching zero at a σ of approximately 0.1 corresponding to a standard altitude of approximately 18,000 m (59,000 ft).

Fuel consumption for a piston engine is frequently given as a brake specific fuel consumption (BSFC). This quantity is measured in pounds per brake horsepower hour. For the example just covered, since gasoline weighs 6 lb/gal,

$$\text{BSFC} = \frac{\text{gph (lb/gal)}}{\text{bhp}}$$

$$= \frac{(10.8)(6)}{137}$$

$$= 0.47 \text{ lb/bhp-hr}$$

Referring to Figure 6.4, the value 0.47 is seen to be reasonable. This figure presents BSFC as a function of engine size for both piston and turboshaft engines. Notice that BSFC tends to improve as engine power increases. Also observe that there is little difference in BSFC for the different piston engine types. Some gains (~6%) appear to be realized by the use of

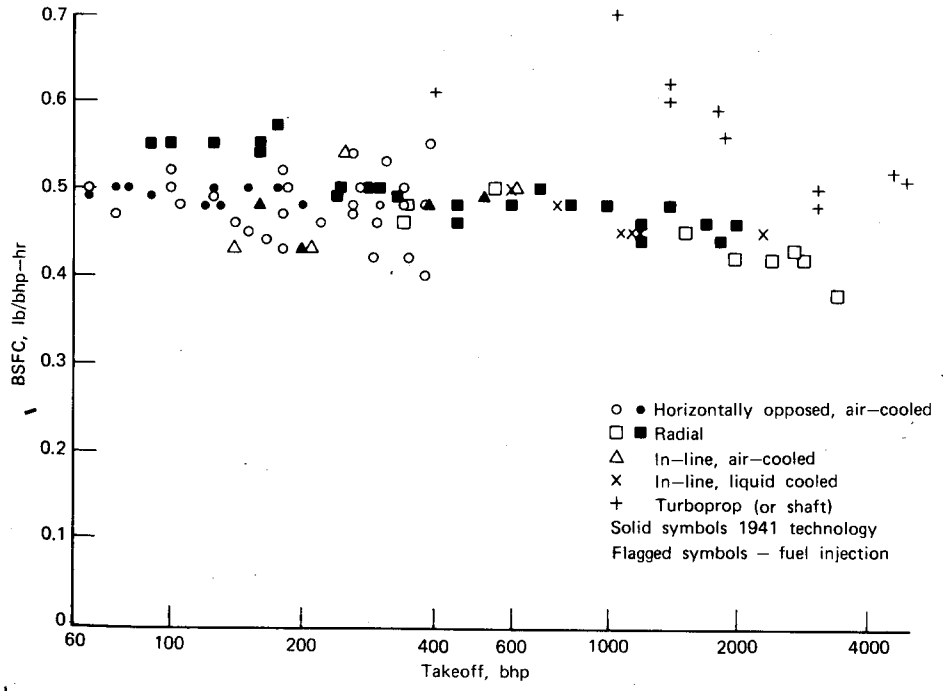

Figure 6.4 Brake specific fuel consumption for piston and turboshaft engines.

fuel injection. Turboshaft engines, to be discussed later, have specific fuel consumptions that are approximately 25% higher than those for a piston engine of the same power.

In the SI system of units, BSFC is expressed in Newtons per kilowatt-hour. In this system, the typical value of 0.5 lb/bhp-hr becomes 2.98 N/kWhr.

Supercharged Engines

The altitude performance of a piston engine can be improved by supercharging. This involves compressing the air entering the intake manifold by means of a compressor. In earlier supercharged engines, this compressor was driven by a gear train from the engine crankshaft; hence the term gear-driven supercharger. A typical performance curve for a gear-driven supercharged engine is presented in Figure 6.5. Such an engine is generally limited by the manifold absolute pressure (MAP), so the pilot cannot operate at full throttle at sea level. As the pilot climbs to altitude, the throttle is opened progressively, holding a constant MAP. The engine power will increase slightly until an altitude at which the throttle is wide open is reached. Above this altitude, known as the critical altitude, the power decreases linearly with density ratio in the same relative way as a nonsupercharged engine.

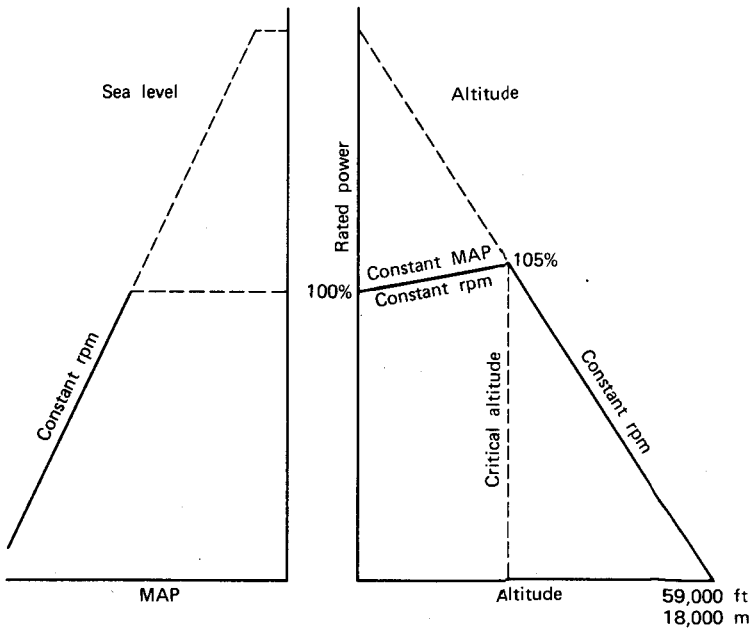

Figure 6.5 Performance curves for a gear-driven supercharged engine.

Today's supercharged engines employ a turbine-driven compressor powered by the engine's exhaust. This configuration is referred to as an exhaust turbosupercharger. The advantage of this type of supercharger as compared to the gear-driven type is twofold. First, the compressor does not extract power from the engine, but uses energy that would normally be wasted. Second, the turbosupercharger is able to maintain sea level-rated power up to much higher altitudes than the gear-driven supercharger.

Turbosupercharged engines are equipped with a regulating system that maintains an approximately constant manifold pressure independent of altitude. A density and pressure controller regulates the position of a waste gate, or bypass valve, which regulates the amount of exhaust gases through the turbine.

A modern, pressurized aircraft used by the general aviation industry is the Piper Navajo, pictured in Figure 6.6. This aircraft uses two Lycoming TIO-540 turbocharged engines, each driving a 2-m (6.6-ft) diameter, three-bladed propeller. Performance and fuel flow curves for this engine are presented in Figure 6.7. As shown, the engine is able to maintain its rated power up to an altitude of approximately 7300 m (24,000 ft). The use of these curves is straightforward, so they do not need any detailed explanation. Correction for nonstandard temperature is the same as that for a non-supercharged engine.

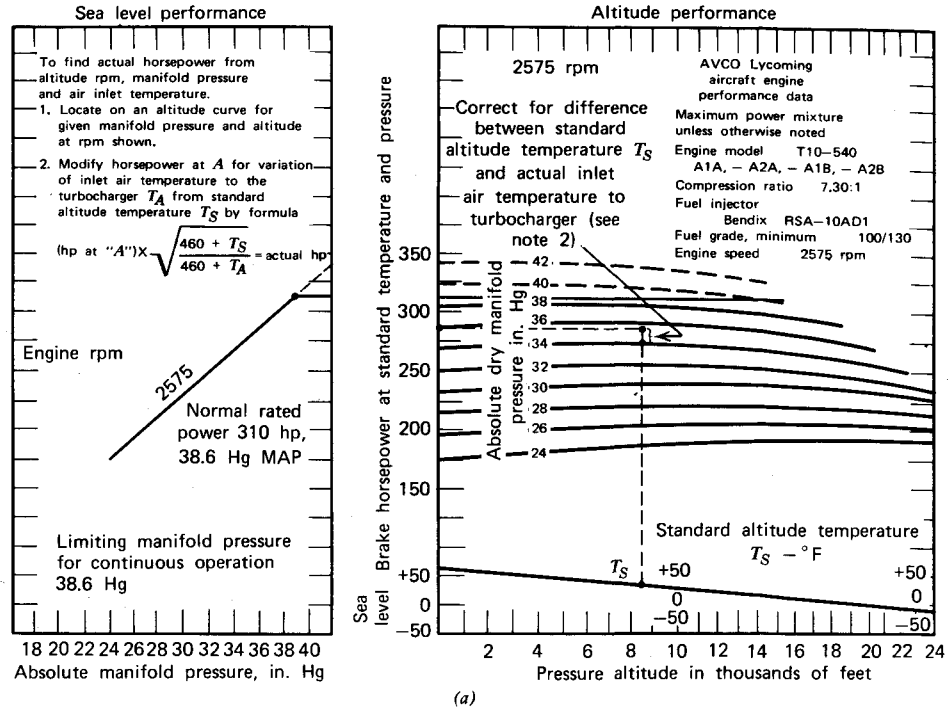
Sea level performance
To find actual horsepower from altitude rpm, manifold pressure and air inlet temperature.
1. Locate on an altitude curve for given manifold pressure and altitude at rpm shown.
2. Modify horsepower at A for variation of inlet air temperature to the turbocharger T_A from standard altitude temperature T_S by formula
(hp at "A")X$\sqrt{\frac{460 + T_S}{460 + T_A}}$ = actual hp
Engine rpm
2575
Normal rated power 310 hp, 38.6 Hg MAP
Limiting manifold pressure for continuous operation 38.6 Hg
18 20 22 24 26 28 30 32 34 36 38 40
Absolute manifold pressure, in. Hg
Altitude performance
2575 rpm
Correct for difference between standard altitude temperature T_S and actual inlet air temperature to turbocharger (see note 2)
AVCO Lycoming aircraft engine performance data
Maximum power mixture unless otherwise noted
Engine model T10–540 A1A, – A2A, – A1B, – A2B
Compression ratio 7.30:1
Fuel injector Bendix RSA–10AD1
Fuel grade, minimum 100/130
Engine speed 2575 rpm
Brake horsepower at standard temperature and pressure
Absolute dry manifold pressure in. Hg
42 40 38 36 34 32 30 28 26 24
350 300 250 200 150
Standard altitude temperature T_S – °F
Sea level
+50 0 –50
2 4 6 8 10 12 14 16 18 20 22 24
Pressure altitude in thousands of feet

(a)

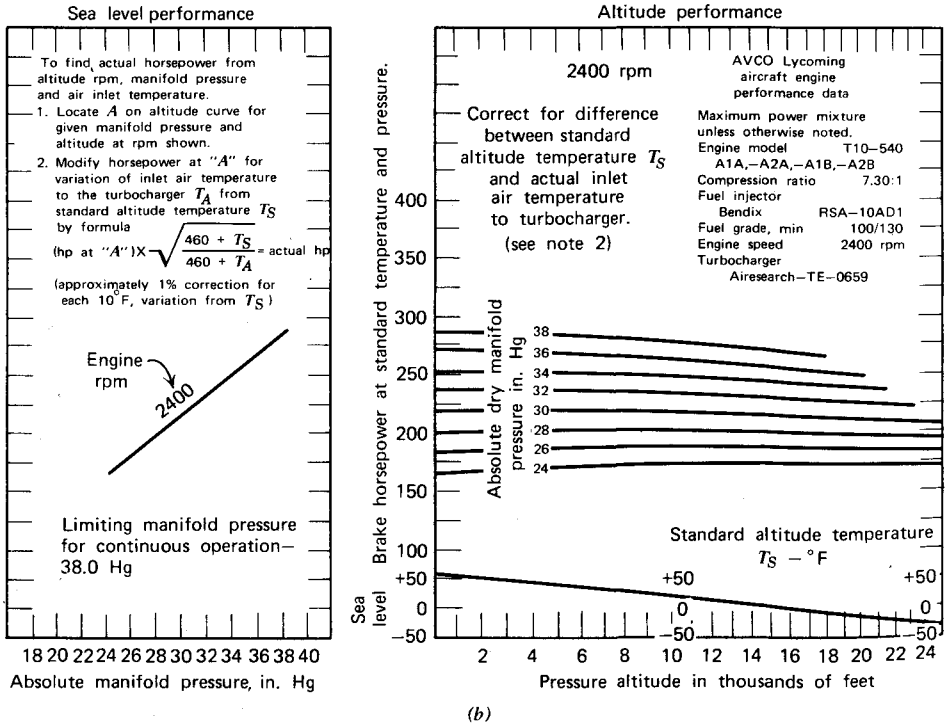
Sea level performance
To find actual horsepower from altitude rpm, manifold pressure and air inlet temperature.
1. Locate A on altitude curve for given manifold pressure and altitude at rpm shown.
2. Modify horsepower at "A" for variation of inlet air temperature to the turbocharger T_A from standard altitude temperature T_S by formula
(hp at "A")X$\sqrt{\frac{460 + T_S}{460 + T_A}}$ = actual hp
(approximately 1% correction for each 10°F, variation from T_S)
Engine rpm
2400
Limiting manifold pressure for continuous operation– 38.0 Hg
18 20 22 24 26 28 30 32 34 36 38 40
Absolute manifold pressure, in. Hg
Altitude performance
2400 rpm
Correct for difference between standard altitude temperature T_S and actual inlet air temperature to turbocharger. (see note 2)
AVCO Lycoming aircraft engine performance data
Maximum power mixture unless otherwise noted.
Engine model T10–540 A1A,–A2A,–A1B,–A2B
Compression ratio 7.30:1
Fuel injector Bendix RSA–10AD1
Fuel grade, min 100/130
Engine speed 2400 rpm
Turbocharger Airesearch–TE–0659
Brake horsepower at standard temperature and pressure.
Absolute dry manifold pressure in. Hg
38 36 34 32 30 28 26 24
400 350 300 250 200 150 100
Standard altitude temperature T_S – °F
Sea level
+50 0 –50
2 4 6 8 10 12 14 16 18 20 22 24
Pressure altitude in thousands of feet

(b)

Figure 6.6 Pressurized Navajo. (Courtesy of Piper Aircraft Corp.)

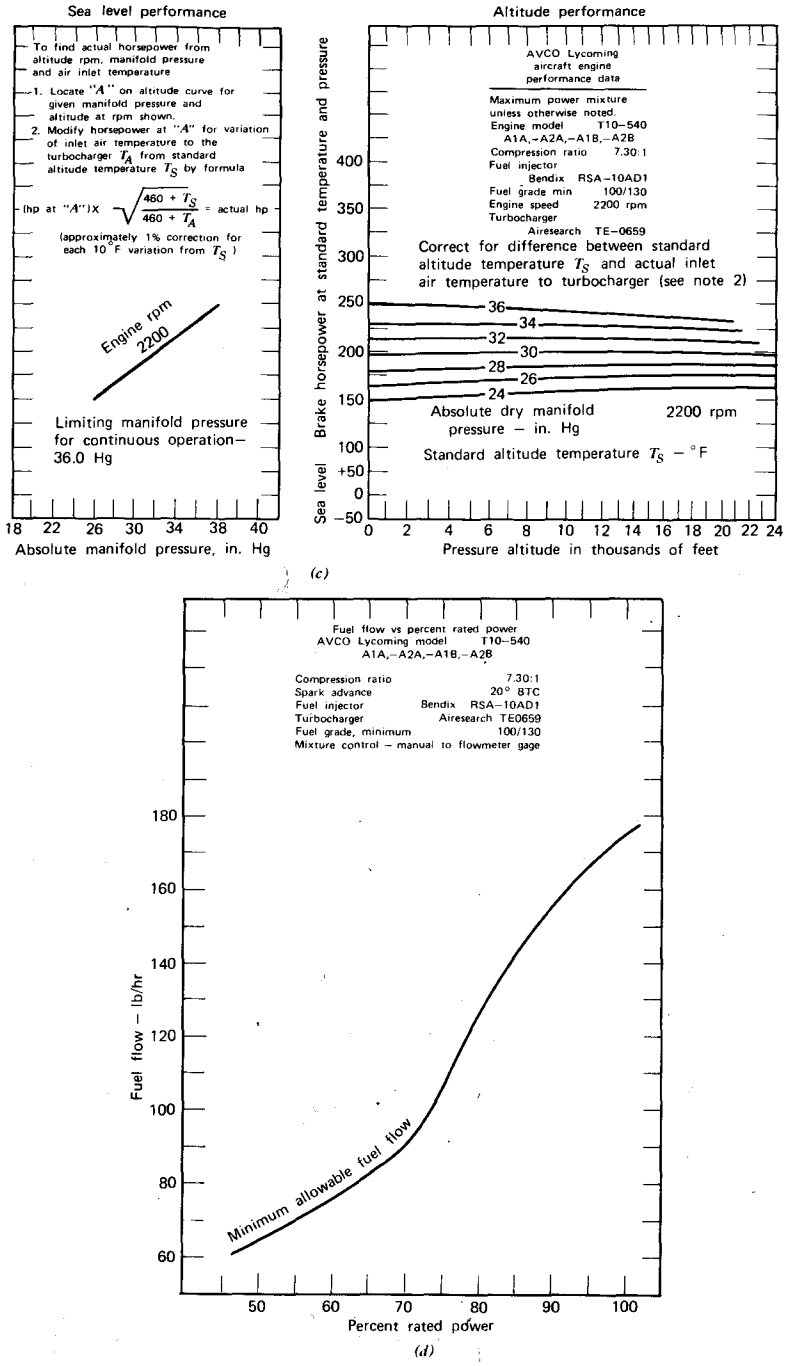

Figure 6.7 Performance of the Lycoming TIO-540 engine. (*a*) sea level and altitude performance cruise—TIO-540-A1A,-A2A,-A1B,-A2B, 2575 rpm. (*b*) sea level and altitude performance curve—TIO-540-A1A,-A2A,-A1B,-A2B, 2400 rpm. (*c*) sea level and altitude performance curve—TIO-540-A1A,-A2A,-A1B,-A2B, 2200 rpm. (*d*) fuel flow versus rated power curve—TIO-540-A1A,-A2A,-A1B,-A2B. (Courtesy, Lycoming Division, Avco Corp.)

PROPELLER ANALYSIS

The efficiency of a piston engine-propeller combination depends on a proper match of the propeller to the engine as well as a match of the two to the airframe. Understanding propeller behavior is important, even though we are currently in the "jet age." First, because of their cost, it is doubtful that gas turbine engines will be used in the smaller, general aviation airplanes in the foreseeable future. Second, there is currently a renewed interest in the turboprop engine because of its lower fuel consumption compared to turbojet or turbofan engines.

Momentum Theory

The classical momentum theory provides a basic understanding of several aspects of propeller performance. Referring to Figure 6.8, the propeller is approximated by an infinitely thin "actuator" disc across which the static pressure increases discontinuously. The assumptions inherent in this model are:

1. The velocity is constant over the disc.
2. The pressure is uniform over the disc.

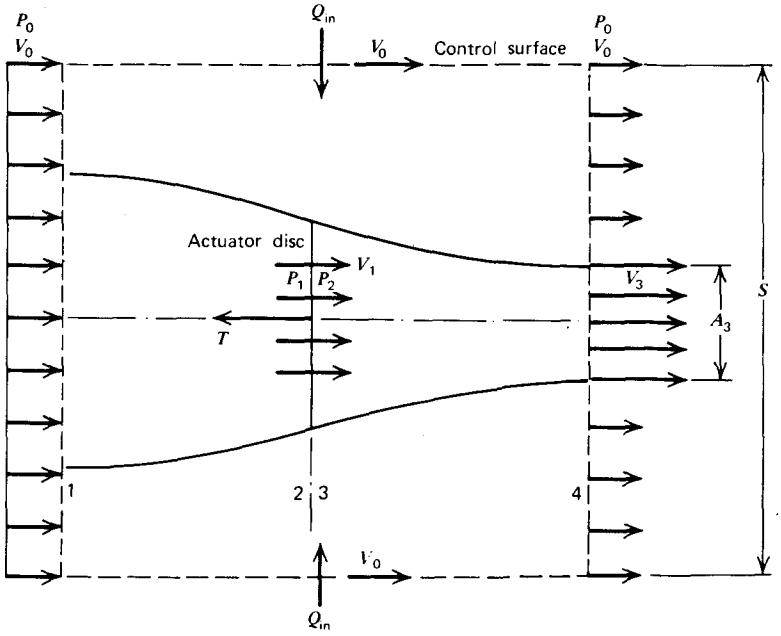

Figure 6.8 Idealized flow model for application of classical momentum theory.

3. Rotation imparted to the flow as it passes through the propeller is neglected.
4. The flow passing through the propeller can be separated from the rest of the flow by a well-defined streamtube.
5. The flow is incompressible.

The transverse plane 1 is far ahead of the propeller, while plane 4 is far downstream. Planes 2 and 3 are just upstream and downstream of the propeller, respectively. In planes 1 and 4 all streamlines are parallel, so that the static pressure is constant and equal to the free-stream static pressure p_0.

Let us first consider the continuity of flow in and out of the cylindrical control surface shown in the figure. This surface has a cross-sectional area of S. The flux passing out of the surface across plane 4 minus the flux entering across plane 1 will be

$$\Delta Q = A_3 V_3 + (S - A_3) V_0 - S V_0$$

or

$$\Delta Q = A_3 (V_3 - V_0) \tag{6.2}$$

Assume the nontrivial case where $V_3 \neq V_0$, it follows that the flux ΔQ must be entering the control surface along its sides. This flux has a velocity of V_0 in the direction opposite to the thrust.

Applying the momentum theorem to the cylindrical control surface and noting that the external pressures cancel out, we obtain

$$T = \rho[A_3 V_3^2 + (S - A_3) V^2] - \rho S V^2 - \rho \, \Delta Q V$$

Substituting Equation 6.2 into the preceding equation gives

$$T = \rho A_3 V_3 (V_3 - V) \tag{6.3}$$

A_3 is the cross-sectional area in the ultimate wake of the streamtube passing through the propeller. Thus, $\rho A_3 V_3$ is the mass flux passing through the propeller.

The thrust, T, is also equal to the pressure difference across the actuator disc multiplied by the disc area, A.

$$T = A(p_2 - p_1) \tag{6.4}$$

p_1 and p_2 can be related by applying Bernoulli's equation ahead of the propeller and downstream of the propeller. The equation cannot be applied through the propeller, since energy is added to the flow at the propeller.

$$p_0 + \tfrac{1}{2}\rho V^2 = p_1 + \tfrac{1}{2}\rho V_1^2 \tag{6.5}$$

$$p_0 + \tfrac{1}{2}\rho V_3^2 = p_2 + \tfrac{1}{2}\rho V_2^2 \tag{6.6}$$

Substracting Equation 6.5 from Equation 6.6 and noting that the velocity

is continuous through the propeller gives

$$p_2 - p_1 = \tfrac{1}{2}\rho(V_3^2 - V^2) \tag{6.7}$$

Using the fact from continuity that $A_3V_3 = AV_1$ and combining Equations 6.3, 6.4, and 6.7 results in the well-known relation

$$V_1 = \frac{(V_3 + V)}{2} \tag{6.8}$$

In words, the velocity through the propeller equals the average of the velocity far ahead of and far behind the propeller.

Let us now write

$$V_3 = V + 2w \tag{6.9}$$

where w is the propeller-induced velocity. It follows that

$$V_1 = V + w$$

so that

$$T = 2\rho A(V + w)w \tag{6.10}$$

This is easily remembered, since $\rho A(V + w)$ is the mass flux through the propeller and $2w$ is the total increase in the velocity of the flow.

Applying the energy theorem to this system gives, for the power, P, added to the flow,

$$P = \tfrac{1}{2}\rho A(V + w)[(V + 2w)^2 - V^2]$$

or

$$P = 2\rho Aw(V + w)^2 \tag{6.11}$$

Using Equation 6.10, this becomes

$$P = T(V + w) \tag{6.12}$$

This important result states that the power required by the propeller equals the product of its thrust and the velocity *through* the propeller. This can be divided into two parts. The first part is defined as the useful power.

$$P_{use} = TV \tag{6.13}$$

The second part is known as the induced power.

$$P_i = Tw \tag{6.14}$$

Equation 6.10 can be solved for the induced velocity to give

$$w = \frac{1}{2}\left[-V + \sqrt{V^2 + \left(\frac{2T}{\rho A}\right)}\right] \tag{6.15}$$

For the static case where V equals zero,

$$w_0 = \sqrt{\frac{T}{2\rho A}} \tag{6.16}$$

and

$$P_{i_0} = \frac{T^{3/2}}{\sqrt{2\rho A}} \tag{6.17}$$

As an example, consider a propeller 2 m (6.6 ft) in diameter driven by a 150 kW engine (201 hp). *The maximum* static thrust that one might expect from this propeller can be calculated by solving Equation 6.17 for T.

$$T = P_{i_0}^{2/3}(2\rho A)^{1/3} \tag{6.18}$$

Since 1 W = 1.00 m-N/s,

$$P_{i_0} = 151{,}050 \text{ m-N/s}$$
$$(110{,}550 \text{ ft-lb/sec})$$

For standard sea level conditions, $\rho = 1.226$ kg/m^2. Thus,

$$T = (151{,}050)^{2/3}(2 \times 1.226 \times 3.14)^{1/3}$$
$$= 5600 \text{ N } (1259 \text{ lb})$$

This value of T represents an upper limit that is not attainable in practice, since the momentum theory neglects profile drag of the propeller blades. Also, additional induced losses occur near the tips of the blades. Since the pressure difference across the blades must vanish at the tips, a trailing vortex system, helical in shape, is generated by the propeller in a manner similar to a finite wing.

In forward flight, an ideal efficiency, η_i, can be defined as the ratio of the useful power to the total power given by Equation 6.12.

$$\eta_i = \frac{TV}{T(V + w)}$$

or

$$\eta_i = \frac{1}{1 + (w/V)} \tag{6.19}$$

Using Equation 6.15, w/V can be written as

$$\frac{w}{V} = \frac{1}{2}(-1 + \sqrt{1 + T_c}) \tag{6.20}$$

where T_c is a thrust coefficient defined by

$$T_c = \frac{T}{qA} \tag{6.21}$$

Thus, η_i becomes

$$\eta_i = \frac{2}{1+\sqrt{1+T_c}} \tag{6.22}$$

The thrust of a propeller divided by its disc area is referred to as the disc loading. As this loading approaches zero, the ideal efficiency is seen to approach unity.

As an example, let us again consider the Cherokee 180 having a propeller diameter of 1.88 m (6.17 ft). At a cruising speed of 60.4 m/s (135 mph) at standard sea level, its drag will equal approximately 1390 N (312 lb). Thus $T_c = 0.224$, giving an η_i of 0.95. As we will see later, the actual propeller efficiency is more like 0.83. As with the static thrust, η_i given by the momentum theory is optimistic and represents an upper limit that is really not attainable.

Although the momentum theory is not too accurate with regard to predicting power, it is useful for estimating the induced velocity. An interesting and easily remembered relationship is the following. The dynamic pressure in the ultimate wake of a propeller is equal to the sum of the free-stream dynamic pressure and the disc loading. Proof of this statement is left to you.

Blade Element Theories

In order to design a propeller or to predict the performance of an existing propeller more accurately, it is necessary to examine the aerodynamics of the blade in detail. Figure 6.9*a* presents the front view of a three-bladed propeller that is rotating with an angular velocity of ω rad/s and advancing through the air with a velocity of V. Two cylindrical surfaces concentric with the axis of rotation and a differential distance of dr apart cut the propeller blade at a radius of r from the axis. The blade element thus defined is illustrated in Figure 6.9*b*. Here we are looking in along the blade. The section is moving to the right (due to rotation) and toward the top of the page as the propeller advances into the air. The velocities influencing the element are shown relative to the element.

For the following analysis, the pitch angle, β, of the section is defined relative to the zero lift line of the airfoil section. In this regard, however, one must be careful, since propeller pitch angles are frequently tabulated with respect to the chord line or to a flat lower surface.

The pitch of a propeller has reference to the corresponding quantity for the ordinary screw. In fact, the early literature refers to propellers as "airscrews." If the propeller "screws" itself through the air without slipping, the distance it would move forward in one revolution is the pitch, p. From Figure 6.9*b*,

$$p = 2\pi r \tan \beta \tag{6.23}$$

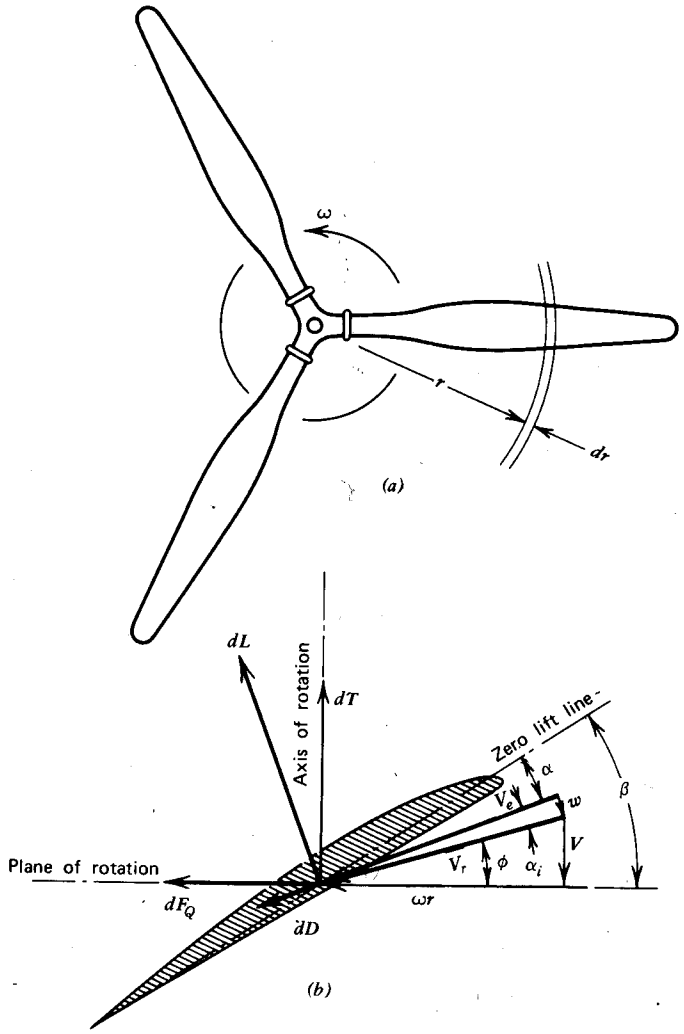

Figure 6.9 Velocities and forces acting on a propeller blade. (*a*) front view of a three-bladed propeller. (*b*) Blade element as seen looking in along blade.

Propellers are sometimes categorized by their pitch-diameter ratios. Thus,

$$\frac{P}{D} = \pi x \tan \beta$$

where $x = r/R$, the relative radius of the blade section.

A constant pitch propeller is one whose pitch does not vary with radius.

For such a propeller,

$$\beta = \tan^{-1}\frac{p/D}{\pi x} \tag{6.24}$$

At the tip, x equals unity so that,

$$\beta(x = 1) = \tan^{-1}\frac{p/D}{\pi}$$

The terms constant pitch, fixed pitch, and variable pitch are somewhat confusing. "Constant pitch" refers to the propeller geometry as just defined. "Fixed" or "variable" pitch refers to whether or not the whole blade can rotate about an axis along the blade (feathering axis) in order to vary the pitch angles of the blade sections all along the blade. Some propellers are equipped with governors to maintain a constant rpm as the engine throttle is varied. This is done by increasing the blade pitch angles as the propeller rpm tends to increase due to increased power or, vice versa, by decreasing the pitch for reduced power. Such a propeller is called a "constant speed" propeller.

Referring to Figure 6.9*b*, the contribution of one-blade element to the thrust, T, and torque, Q, will be,

$$dT = dL\cos(\phi + \alpha_i) - dD\sin(\phi + \alpha_i) \tag{6.25a}$$

$$dQ = r[dL\sin(\phi + \alpha_i) + dD\cos(\phi + \alpha_i)] \tag{6.25b}$$

dL and dD are the differential lift and drag forces, respectively. Similar to finite wing theory, α_i is an induced angle of attack resulting from the induced velocity, w. dL and dD can be calculated by

$$dL = \tfrac{1}{2}\rho V_e^2 c C_l\, dr \tag{6.26a}$$

$$dD = \tfrac{1}{2}\rho V_e^2 c C_d\, dr \tag{6.26b}$$

The chord, c, is usually a function of the local radius, r. The section C_d is primarily a function of the section C_l. It can also depend on the local Reynolds and Mach numbers. C_l can be found from

$$C_l = a(\beta - \phi - \alpha_i) \tag{6.27}$$

We are now at somewhat of a dilemma. We need α_i, which is a function of w, in order to get the blade loading. But w depends in turn on the blade loading.

Momentum-Blade Element Theory

The momentum-blade element theory is one means around this difficulty. If we assume α_i and the drag-to-lift ratio to be small, then $V_e \simeq V_r$, and

Equation 6.25 can be written approximately for B blades as

$$dT = \frac{B\rho}{2} V_r^2 ca(\beta - \phi - \alpha_i) \cos \phi \, dr$$

Applying momentum principles to the differential annulus and letting $w \simeq V_r \alpha_i$, we can also write, for dT,

$$dT = \rho(2\pi r \, dr)(V + V_r \alpha_i \cos \phi) 2 V_r \alpha_i \cos \phi$$

Equating these two expressions for dT/dr gives the following quadratic for α_i.

$$\alpha_i^2 + \alpha_i \left(\frac{\lambda}{x} + \frac{\sigma a V_r}{8x^2 V_T}\right) - \frac{\sigma a V_r}{8x^2 V_T}(\beta - \phi) = 0$$

where:

$$\lambda = \frac{V}{\omega R} \qquad V_r = V_T \sqrt{x^2 + \lambda^2}$$

$$\sigma = \frac{Bc}{\pi R} \qquad \phi = \tan^{-1} \frac{\lambda}{x}$$

$$V_T = \omega R \qquad x = \frac{r}{R}$$

The induced angle of attack then becomes

$$\alpha_i = \frac{1}{2}\left\{-\left(\frac{\lambda}{x} + \frac{\sigma a V_r}{8x^2 V_T}\right) + \left[\left(\frac{\lambda}{x} + \frac{\sigma a V_r}{8x^2 V_T}\right)^2 + \frac{\sigma a V_r}{2x^2 V_T}(\beta - \phi)\right]^{1/2}\right\} \qquad (6.28)$$

Given the geometry, forward speed, and rotational speed of a propeller, Equation 6.28 can be solved for α_i. Equation 6.25*a* and 6.25*b* can then be numerically integrated. Using equations 6.26 and 6.27 to give the thrust and torque.

The thrust and power of a propeller are normally expressed in coefficient form. These thrust and power coefficients are defined in various ways, depending on what particular reference areas and velocities are used. Test results on propellers almost always define the thrust coefficient, C_T, and power coefficient, C_p, as follows.

$$C_T = \frac{T}{\rho n^2 D^4} \qquad (6.29a)$$

$$C_p = \frac{P}{\rho n^3 D^5} \qquad (6.29b)$$

where n is the rotational speed in revolutions per second and D is the propeller diameter. The thrust, power, ρ, and D must be in consistent units. For this convention, one might say that nD is the reference velocity and D^2 is the reference area.

One would expect these dimensionless coefficients to be a function only of the flow geometry (excluding scale effects such as Mach number and Reynolds number). From Figure 6.9, the angle of the resultant flow, ϕ, is seen to be determined by the ratio of V to ωr.

$$\phi = \tan^{-1} \frac{V}{\omega r}$$

This can be written as

$$\phi = \tan^{-1} \frac{J}{\pi x} \tag{6.30}$$

The quantity, J, is called the advance ratio and is defined by

$$J = \frac{V}{nD} \tag{6.31}$$

Thus, C_T and C_p are functions of J.

In a dimensionless form, Equations 6.25 and 6.26 can be combined and expressed as

$$C_T = \frac{\pi}{8} \int_{x_h}^{1} (J^2 + \pi^2 x^2) \sigma [C_l \cos(\phi + \alpha_i) - C_d \sin(\phi + \alpha_i)] \, dx \tag{6.32a}$$

and, since $P = \omega Q$,

$$C_p = \frac{\pi}{8} \int_{x_h}^{1} \pi x (J^2 + \pi^2 x^2) \sigma [C_l \sin(\phi + \alpha_i) + C_d \cos(\phi + \alpha_i)] \, dx \tag{6.32b}$$

x_h is the hub station where the blade begins. x_h is rather arbitrary, but C_T and C_p are not too sensitive to its value.

To reiterate, one would be given D, V, ρ, and n. Also, c and β would be given as a function of x. At a given station, x, α_i is calculated from Equation 6.28. This is followed in order by C_l and C_d and, finally, dC_T/dx and dC_p/dx. These are then integrated from x_h to 1 to give C_T and C_p.

Given J and having calculated C_T and C_p, one can now calculate the propeller efficiency. The useful power is defined as TV and P is, of course, the input power. Thus,

$$\eta = \frac{TV}{P} \tag{6.33}$$

In terms of C_T, C_p, and J, this becomes

$$\eta = \frac{C_T J}{C_p} \tag{6.34}$$

Vortex Theory

Other blade element theories differ from the momentum-blade element theory principally in the way in which the induced velocities are calculated.

Numerically based methods use vortex lattice models, either with a prescribed geometry or using vortices that are free to align themselves with the resultant flow. These numerical approaches generally require computer run times that are extremely long.

Goldstein's classical vortex theory for predicting propeller performance is not much more difficult to apply than the momentum-blade element approach. The vortex theory is described in detail in Reference 3.3 and is briefly outlined here.

Figure 6.10 shows the induced velocity at the propeller plane in more detail. The resultant velocity w is normal to V_e and is composed of a tangential component, w_t, and an axial component, w_a. w_0 is a fictitious velocity to be discussed later. From the geometry, w_t and w_a are related by

$$\frac{V + w_a}{wr - w_t} = \frac{w_t}{w_a}$$

This can be solved for w_a as a function of w_t.

$$w_a = \tfrac{1}{2}[-V + \sqrt{V^2 + 4w_t(\omega r - w_t)}]$$

It is convenient to express all velocities in terms of V_T, so that the preceding equation becomes

$$\frac{w_a}{V_T} = \frac{1}{2}\left[-\lambda + \sqrt{\lambda^2 + 4\frac{w_t}{V_T}\left(x - \frac{w_t}{V_T}\right)}\right] \tag{6.35}$$

Goldstein's vortex theory relates w_t to the bound circulation, Γ, around any blade station by

$$B\Gamma = 4\pi r \kappa w_t \tag{6.36}$$

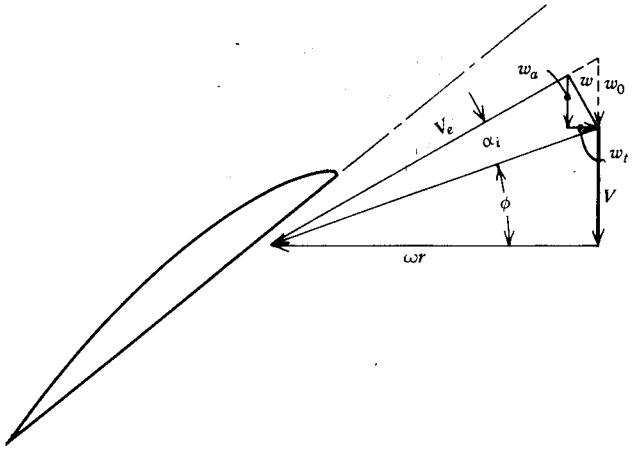

Figure 6.10 Velocity diagram for a blade element showing induced velocity components.

κ is known as Goldstein's kappa factor. This factor is not expressible in a closed form, but it is available in graphical form in the literature. An approximation of κ is Prandtl's tip loss factor, F, which becomes more exact as J becomes smaller or as the number of blades increases. Thus

$$B\Gamma \simeq 4\pi r F w_t \tag{6.37}$$

where

$$F = \frac{2}{\pi}\cos^{-1}\exp\left[-\frac{B(1-x)}{2\sin\phi_T}\right] \tag{6.38}$$

ϕ_T is the helix angle of the propeller's helical trailing vortex system at the tip. For a lightly loaded propeller,

$$\phi_T = \tan^{-1}\lambda \tag{6.39}$$

However, the lift must vanish at the tip of a propeller blade, which generally means that the local angle of attack at the tip must be zero. Thus, another expression for ϕ_T can be obtained by reference to Figure 6.6.

$$\phi_T = \beta_T \tag{6.40}$$

For most cases, Equation 6.40 is preferred to Equation 6.39.

From the Kutta-Joukowski theorem,

$$L = \rho V \Gamma$$

Thus,

$$\Gamma = \tfrac{1}{2}cC_l V_e \tag{6.41}$$

Substituting Equation 6.41 into Equation 6.37, the result can be expressed as

$$\sigma C_l \frac{V_e}{V_T} = 8xF\frac{w_t}{V_T} \tag{6.42}$$

C_l can be calculated from

$$C_l = a\left(\beta - \tan^{-1}\frac{w_t}{w_a}\right) \tag{6.43}$$

and V_e/V_T from

$$\frac{V_e}{V_t} = \left[\left(\lambda + \frac{w_a}{V_T}\right)^2 + \left(x - \frac{w_t}{V_T}\right)^2\right]^{1/2} \tag{6.44}$$

Equations 6.35 to 6.44 can be solved iteratively for w_t/V_T. C_l and the other quantities can be found to evaluate Equation 6.32*a* and 6.32*b*.

If α_i is assumed to be small, Reference 3.3 shows that α_i can be solved directly by assuming that

$$w_t = V_R\alpha_i \sin(\phi + \alpha_i) \tag{6.45}$$

The result is

$$\alpha_i = \tfrac{1}{2}(-X + \sqrt{X^2 + 4Y}) \tag{6.46}$$

where

$$X = \tan\phi + \frac{a\sigma}{8xF\cos\phi}$$

$$Y = \frac{\sigma a(\beta - \phi)}{8xF\cos\phi}$$

As the flow passes through a propeller, the axial component of velocity increases gradually. An estimate of this variation of w_a with axial distance, s, can be obtained from

$$w_a = w_{a_0}\left(1 + \frac{s}{\sqrt{s^2 + R^2}}\right) \tag{6.47}$$

w_{a_0} is the value of w_a at the plane of the propeller. Note that far ahead of the propeller ($s = -\infty$), w_a vanishes, while far behind the propeller ($s = +\infty$), w_a equals twice its value at the propeller plane.

The tangential component, w_t, increases from zero just ahead of the propeller to $2w_t$ just behind the propeller. This rapid change in w_t through the propeller results in a curved flow field that effectively reduces the camber of the blade sections. Expressed as a reduction in the section angle of attack, $\Delta\alpha$, Reference 3.3 derives the following expression for $\Delta\alpha$. Assuming $\Delta\alpha$ to be small,

$$\Delta\alpha = \frac{w_t(V + w_a)}{2[(\omega r - 2w_t) + (V + w_a)^2]} \tag{6.48}$$

As just given, $\Delta\alpha$ is in radians.

w_a and w_t can be obtained approximately from

$$w_t = V_r\alpha_i \sin(\phi + \alpha_i) \tag{6.49a}$$

$$w_a = V_r\alpha_i \cos(\phi + \alpha_i) \tag{6.49b}$$

As an example in the use of the vortex theory, consider the three-bladed propeller having the geometry shown in Figure 6.11. Wind tunnel testing of this particular propeller, designated 5868-R6, Clark-Y section, three blades, is reported in Reference 6.3. These measurements are presented in Figures 6.12, 6.13, and 6.14.

This particular propeller has nearly a constant pitch from the 35% radius station out to the tip corresponding to a 15° blade angle at the 75% station. From the definition of the pitch,

$$p = 2\pi r \tan\beta$$

Thus, $p/D = x\pi \tan\beta$. For an x of 0.75 and a β of 15°, $p/D = 0.631$. Thus, for

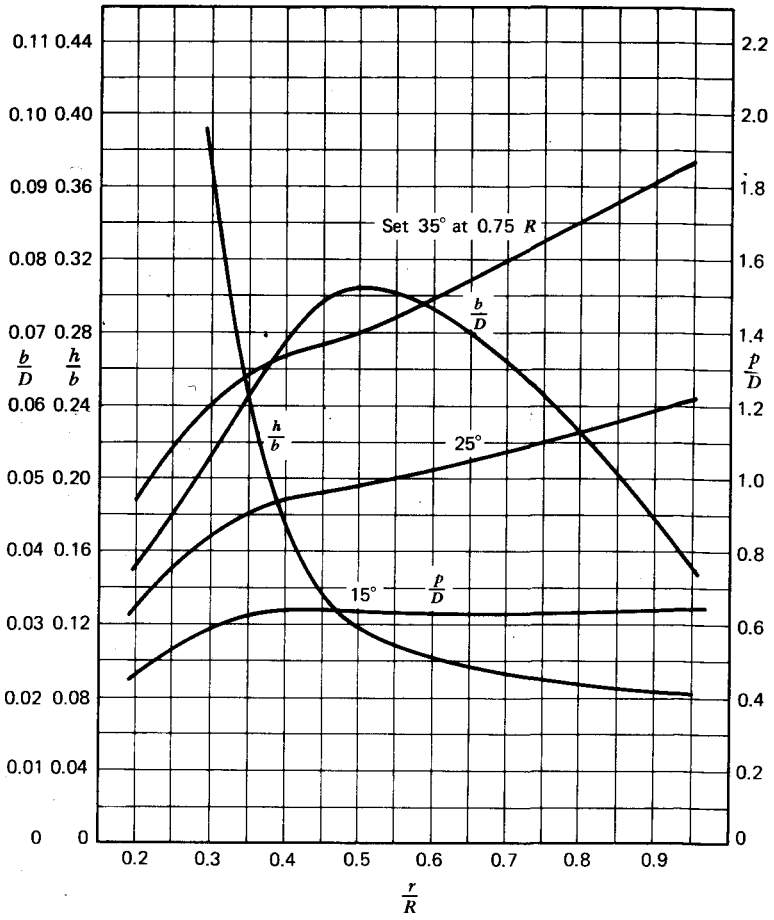

Figure 6.11 Geometry of example propeller. Blade-form curves for propellers 5868–9. *D*—diameter, *R*—radius to the tip, *r*—station radius, *b*—section chord, *h*—section thickness, *p*—geometric pitch.

a blade angle of 15° at $x = 0.75$, β at any other station will equal

$$\beta = \tan^{-1}\frac{0.631^\circ}{\pi x}$$

This propeller is a variable pitch propeller and the curves shown in Figures 6.12, 6.13, and 6.14 are for different values of β at the 75% station. If $\beta_{0.75}$ denotes this angle, then β will generally be given by

$$\beta = \beta_{0.75} - 15 + \tan^{-1}\frac{0.631^\circ}{\pi x}$$

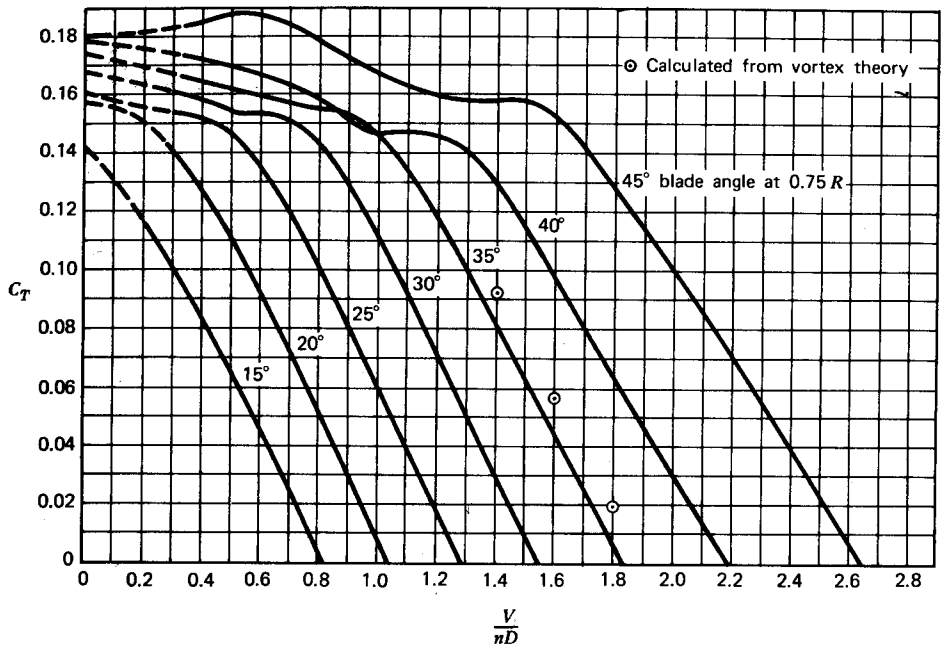

Figure 6.12 Thrust coefficient curves for propeller 5868–9, Clark-Y section, three blades.

The preceding β is measured relative to the chord line of the Clark-Y airfoil. The angle between the zero lift line and the chord line for this airfoil is equal approximately to

$$\alpha_{l_0} = 46\, t/c^\circ$$

where t/c is the section thickness-to-chord ratio. Thus, to obtain β of the zero lift line, α_{l_0} is added to the geometric pitch angle given by Equation 6.47.

Consider a value for $\beta_{0.75}$ and 35° and an x of 0.6. From Figure 6.7,

$$\frac{c}{D} = 0.073$$

$$\frac{t}{c} = 0.103$$

Using these values, α_{l_0}, β, and σ are calculated to be

$$\alpha_{l_0} = 4.7^\circ$$

$$\sigma = 0.139$$

$$\beta = 38.5^\circ$$

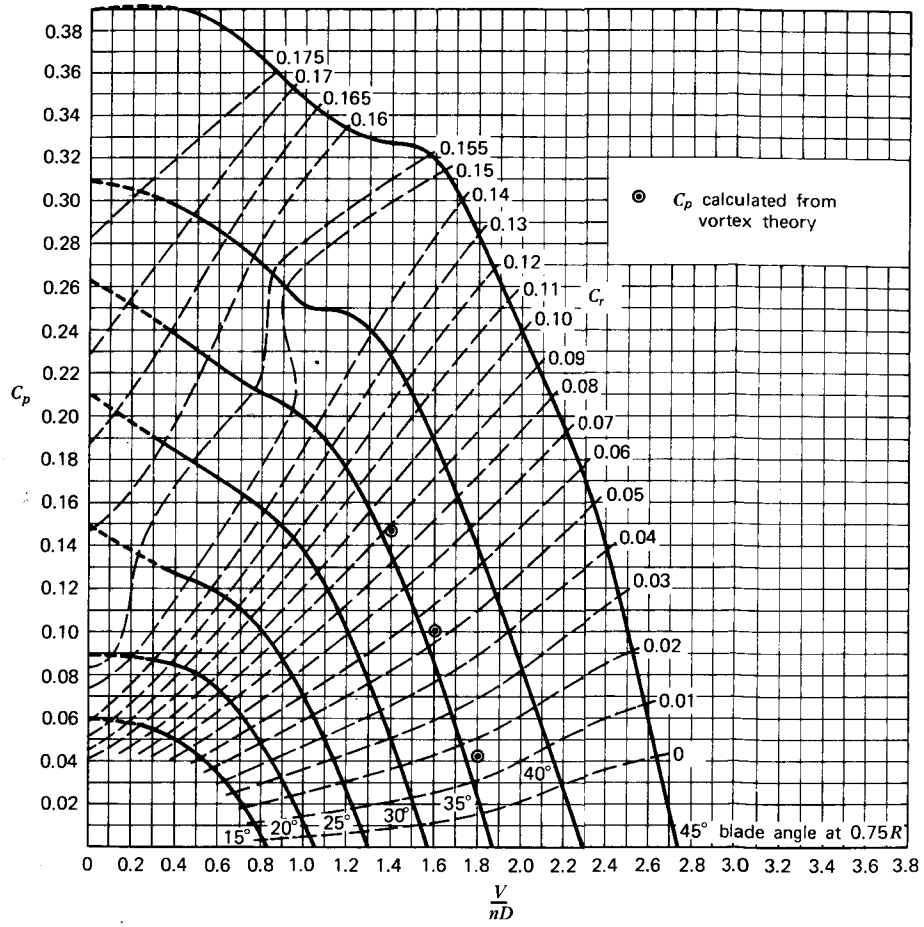

Figure 6.13 Power coefficient curves for propeller 5868–9, Clark-Y section, three blades.

For this example, assume the propeller to be operating at an advance ratio of 1.4. J and λ are related by

$$J = \pi\lambda$$

Thus, for this example,

$$\lambda = 0.446$$

For the Clark-Y airfoil,

$$a \simeq 6.0\ C_l/\text{rad}$$

$$C_d \simeq 0.006 + 0.010\,(C_l - 0.15)^2$$

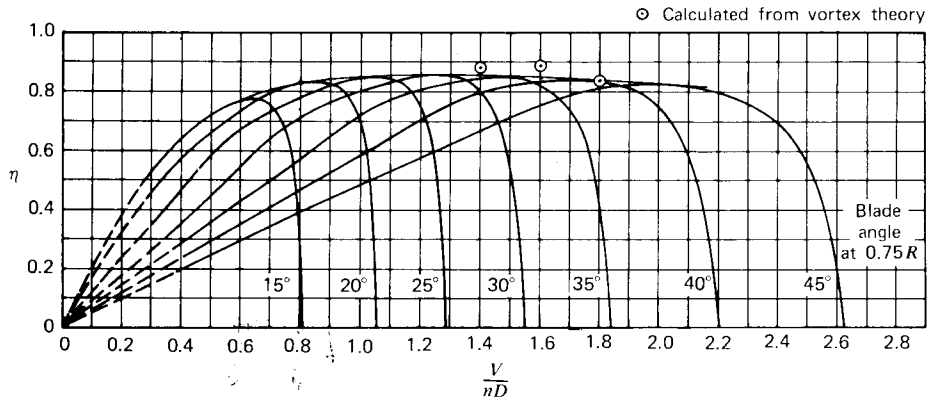

Figure 6.14 Efficiency curves for propeller 5868–9, Clark-Y section, three blades.

These are for an 8% thick airfoil. c_d, of course, will vary slightly with thickness. With these values for a and C_d, the following quantities can be calculated in the order listed.

$$\frac{V_r}{V_T} = 0.748 \qquad \Delta\alpha = 0.33°$$

$$\phi = 36.6° \qquad C_l = 0.477$$

$$\phi_T = 31.4° \qquad C_d = 0.0071$$

$$F = 0.795 \qquad dC_T/dx = 0.112$$

$$\sigma = 0.139 \qquad dC_p/dx = 0.172$$

$$\alpha_i = 1.73°$$

$$\frac{w_a}{V_T} = 0.0810$$

$$\frac{w_t}{V_T} = 0.0140$$

Since both induced and rotational losses are included in the vortex theory, it is more accurate than the momentum-blade element theory. The vortex theory also models the physical propeller more accurately, since the loading vanishes at the blade tip.

The vortex theory was programmed and numerically integrated using a programmable calculator. These calculated points are included in Figures 6.12, 6.13, and 6.14 for a blade angle of 35°. The theory is seen to predict the shapes of the thrust and power curves rather well and results in values of C_T and C_p that correspond to within 1° of the blade angle. In fact, if a blade angle

of 34° is used in the calculations, C_T and C_p values are obtained that lie almost exactly on the 35° experimental line over a range of J values from 1.1 to 1.8. Below an advance ratio of 1.1, the section angles of attack become large, so that the blades begin to stall. At this point the prediction of the propeller characteristics becomes very questionable.

Practical Use of Propeller Charts

The practicing aerodynamicist will normally have available both engine and propeller operating curves as supplied by the respective manufacturers. Using these curves together with a knowledge of the airplane's aerodynamic characteristics, one is able to estimate the airplane's performance. In order to illustrate the procedures that are followed in using a set of propeller charts, let us again use the Cherokee 180 as an example.

An estimated curve of efficiency as a function of advance ratio for the fixed pitch propeller used on the PA-28 is presented in Figure 6.15. This curve is applicable to the aircraft pictured in Figure 3.62 with the engine operating curves of Figure 6.3. This particular propeller has a diameter of 1.88 m (6.17 ft).

As an example in the use of the engine performance charts together with the graph of propeller efficiency, assume that in steady, level flight, the pilot of a PA-28 reads a manifold pressure of 24 in., an rpm of 2400, a pressure altitude of 3000 ft, an OAT of 65 °F, and an indicated airspeed of 127 mph. From this information, together with Figure 6.15, one can estimate the drag of the airplane at this indicated airspeed and density altitude.

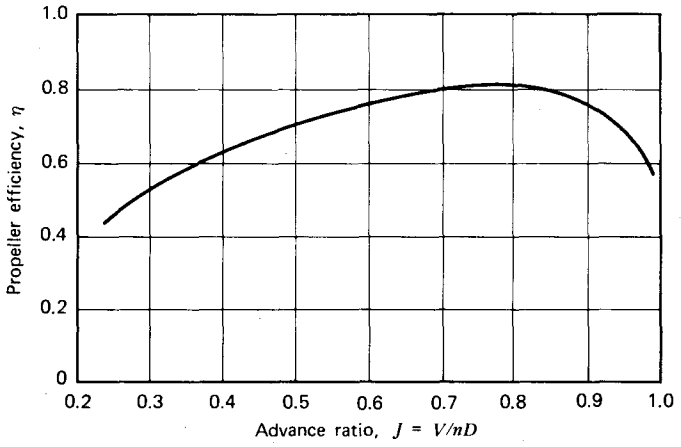

Figure 6.15 Estimated propeller efficiency for the Piper Cherokee PA-28.

From Figure 2.3 at 914 m (3000 ft),

$$\frac{p}{p_0} = 0.90$$

Thus, $p = 91{,}163$ Pa (1904 psf).

Furthermore, air obeys closely the equation of state for a perfect gas.

$$\frac{P}{\rho T} = \text{constant} = R \tag{6.50}$$

In Equation 6.50 T is the absolute temperature.

Using standard sea level values for p_0, ρ_0, and T_0, the preceding constant is seen to be

$$R = 287.1 \text{ (m/s)}^2/^\circ\text{R } [1717 \text{ (fps)}^2/^\circ\text{K}]$$

Thus, for this example, $T = 292\,^\circ$R (525 °K), so that

$$\rho = 1.087 \text{ kg/m}^3 \text{ (0.00211 slugs/ft}^3\text{)}$$

This corresponds to a σ of 0.888. Thus, from Figure 2.3, the density altitude is found to be 1006 m (3300 ft) and the true airspeed is calculated to be 60.4 m/s (135 mph or 198 fps).

The propeller advance ratio is defined by Equation 6.30.

$$J = 0.802$$

For this value of J, a propeller efficiency of 0.81 is read from Figure 6.15.

One can verify that the engine power for these operating conditions, from Figure 6.3, is equal to 138 bhp. Therefore, from Equation 6.33, knowing η, P, and V, the propeller thrust can be calculated as

$$T = \frac{\eta P}{V}$$

$$= 310 \text{ lb } (1380 \text{ N})$$

In steady, level flight, the propeller thrust and airplane drag must be equal. Thus, 310 lb is the drag of the airplane at this particular density altitude and airspeed.

For analyzing a variable pitch propeller a set of curves for different blade pitch angles is required. These are given in Figures 6.16 and 6.17 for the propeller installed on the Piper PA-28R, the Cherokee Arrow. Here we are given both η and C_p as a function of J. To illustrate the use of such graphs, let us assume that they apply to the preceding example for the PA-28. Here, $\rho = 0.00211$ slugs/ft^3, $D = 6.17$ ft, $V = 198$ fps, $n = 40$ rps, $J = 0.802$, and hp = 139. Thus,

$$c_p = \frac{P}{\rho n^3 D^5}$$

$$= 0.0633$$

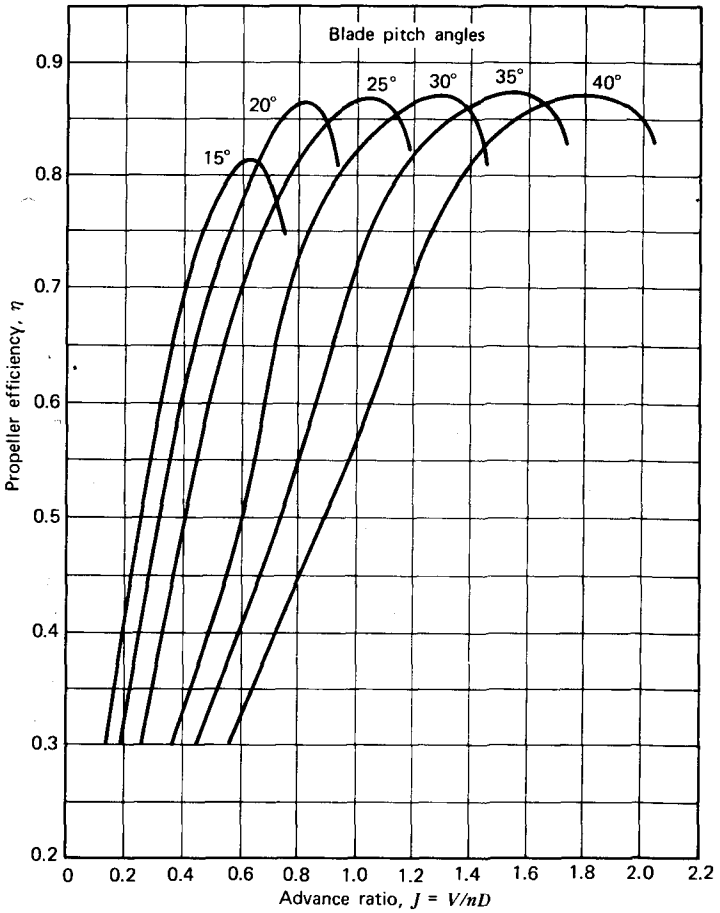

Figure 6.16 Estimated propeller efficiency for the Piper Cherokee Arrow PA-28R.

From Figure 6.17 for the preceding c_p and a J of 0.802, the blade pitch angle must be equal to 24°. Entering Figure 6.16 with this β and J results in an efficiency, η, of 0.83.

A well-designed propeller, or one carefully selected to match the engine and airplane on which it is to operate, can be expected to have a cruise efficiency of approximately 85%. At low speeds, however (e.g., during the takeoff roll), the efficiency is difficult to estimate. At zero forward speed, the efficiency of a propeller is zero by definition, even though its thrust is not zero. In fact, for the same shaft power, a variable pitch propeller will produce the most thrust at zero advance velocity (i.e., its static thrust is greater than the thrust produced in forward flight).

Figures 6.18 and 6.19 may be used to estimate the thrust attainable from a

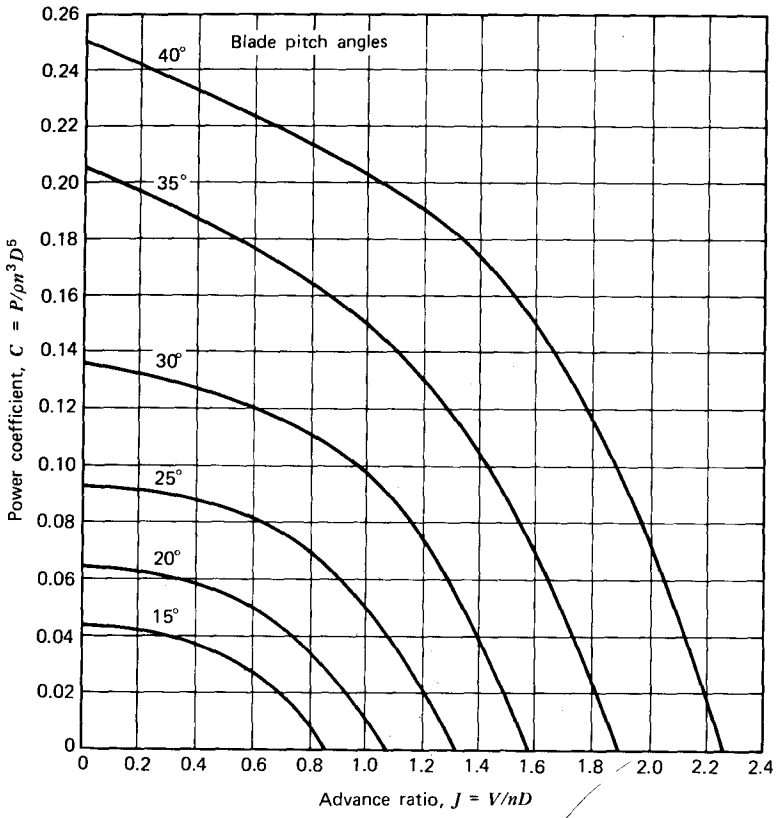

Figure 6.17 Estimated propeller power coefficients for the Piper Cherokee Arrow PA-28R.

variable pitch propeller at low forward speeds. The static thrust is first obtained from Figure 6.19 and then reduced by the factor from Figure 6.18 to give the thrust in forward flight. These curves apply only to a constant speed propeller, which will allow the engine to develop its rated power regardless of forward speed. As an example of the use of these figures, consider a propeller having a diameter of 6.2 ft, turning at 2700 rpm, and absorbing 200 hp. The power loading for this propeller is

$$\frac{\text{hp}}{A} = 6.62 \text{ hp/ft}^2$$

Hence, from Figure 6.19, the static thrust to power loading should be

$$\frac{T_0}{\text{hp}} = 4.9$$

resulting in a static thrust, T_0, for this propeller of 980 lb.

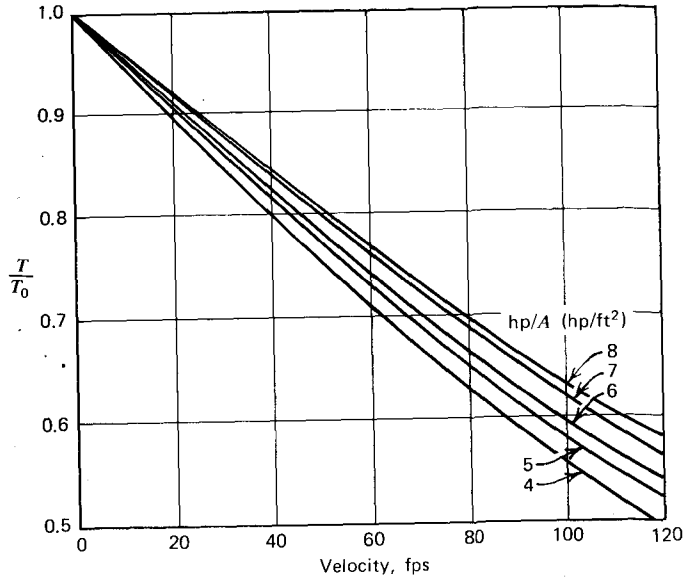

Figure 6.18 Decrease of thrust with velocity for different power loadings.

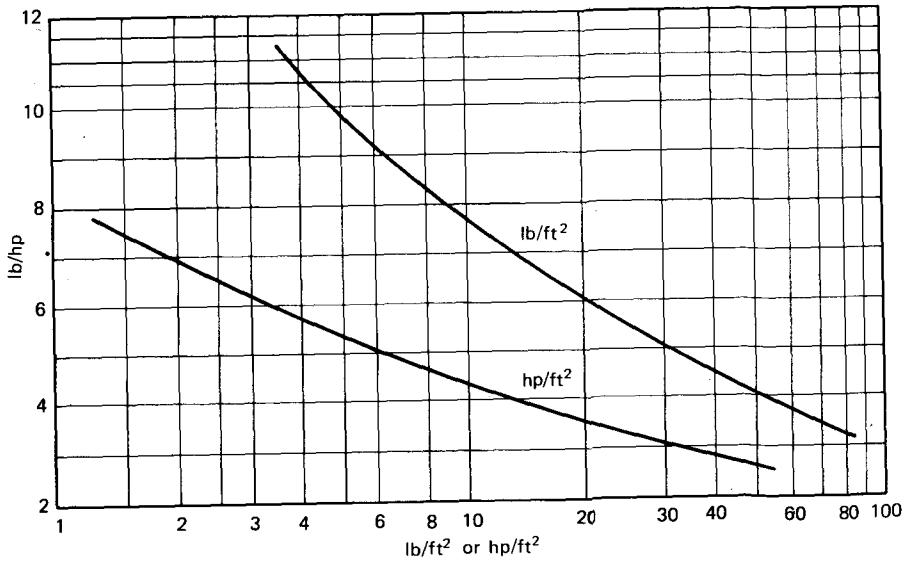

Figure 6.19 Static performance of propellers or rotors.

From Figure 6.18, the expected thrust at a speed of, say, 50 mph (22.4 m/s) can be calculated as

$$T = \left(\frac{T}{T_0}\right) T_0$$
$$= (0.715)(980)$$
$$= 700 \text{ lb}$$

Approximate Useful Relationships for Propellers

Figures 6.18 and 6.19 were prepared using some approximations that are fairly accurate and convenient to use. Referring to Equations 6.31 and 6.32, assume that σ, C_l, and C_d are constants, so that they can be removed from under the integral sign. In addition, it is assumed that α_i and $x_h \simeq 0$ and $C_d/C_l \ll 1$. With these assumptions, C_T and C_p can be written as

$$C_T = \frac{\pi^3 \sigma}{8} \overline{C_l} \int_0^1 x(\lambda^2 + x^2)^{1/2}\, dx \tag{6.51a}$$

$$C_P = JC_T + \frac{\pi^4 \sigma}{8} \overline{C_d} \int_0^1 x^2(\lambda^2 + x^2)^{1/2}\, dx. \tag{6.51b}$$

Performing the integrations, C_T and C_p become

$$C_T = \frac{\pi^3 \sigma}{24} \overline{C_l} f(\lambda) \tag{6.52a}$$

$$C_P = JC_T + \frac{\pi^4 \sigma}{32} \overline{C_d} g(\lambda) \tag{6.52b}$$

where

$$f(\lambda) = (1 + \lambda^2)^{3/2} - \lambda^3$$

$$g(\lambda) = \frac{1}{2}\left[(1 + \lambda^2)^{1/2}(2 + \lambda^2) - \lambda^4 \log \frac{1 + \sqrt{1 + \lambda^2}}{\lambda}\right]$$

$f(\lambda)$ and $g(\lambda)$ are given as a function of J in Figure 6.20. $\overline{C_l}$ and $\overline{C_d}$ indicate average values of these quantities as defined by Equation 6.51.

The term JC_T in the expression for C_p simply represents the useful power. The remaining term in C_p is the profile power, or the power required to overcome the profile drag of the blades. The induced power is missing, since α_i was assumed to be zero. Experience shows that the induced power is typically 12% higher than the ideal value given by Equations 6.14 and 6.15. Thus, in coefficient form,

$$C_{P_i} \simeq 1.12 C_T \frac{w}{nD} = 1.12 \frac{C_T}{2}\left[-J + \left(J^2 + \frac{8C_T}{\pi}\right)^{1/2}\right] \tag{6.53}$$

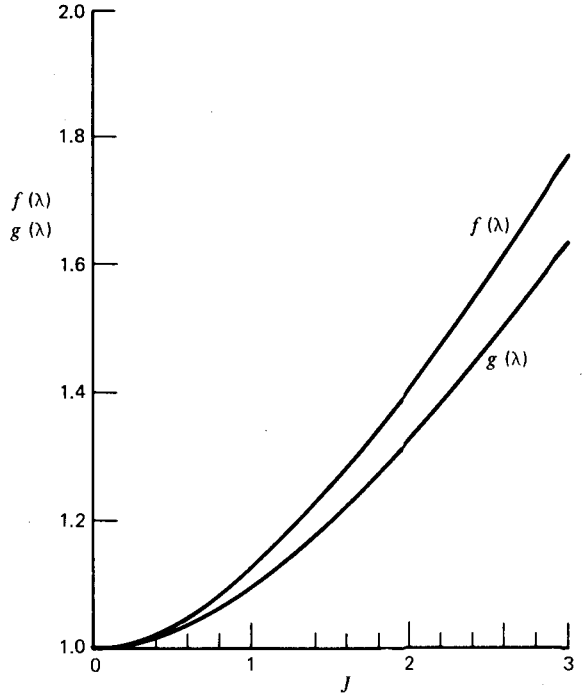

Figure 6.20 Functions for approximating C_T and C_P.

C_p then becomes approximately

$$C_p = C_T J + C_{p_i} + \frac{\pi^4 \sigma}{32} \overline{C_d} g(\lambda) \tag{6.54}$$

The average value of σ is referred to as propeller solidity and is equal to the ratio of blade area to disc area.

Propeller designs are sometimes identified by an "integrated design lift coefficient" and an activity factor. These are defined by

$$C_{L_d} = 3 \int_0^1 C_{l_d} x^2 \, dx \tag{6.55}$$

$$\text{AF} = \frac{100{,}000}{16} \int_0^1 \left(\frac{c}{D}\right) x^3 \, dx \tag{6.56}$$

The integrated design lift coefficient represents the average of the section design lift coefficients weighted by x^2. The activity factor is simply another measure of the solidity. The higher the activity factor, the higher are the values of C_T and C_p attainable by a propeller at a given integrated design C_L.

Equation 6.54 represents about the best one can hope to achieve with a well-designed propeller operating at its design point. For the propeller shown in Figure 6.11, this corresponds to blade angles of around 15 to 25°. Beyond this range, the twist distribution along the blade departs too much from the optimum for these relationships to hold.

PROPELLER SELECTION

Propeller manufacturers offer propellers covering a range of diameters, pitch values, and solidities. The choice of these parameters can depend on considerations other than aerodynamic efficiency. For example, to keep the noise level of a propeller low, one may have to employ wide blades with low tip speeds. As another example, the propeller diameter is sometimes limited by ground clearance considerations or by the distance from a nacelle to the fuselage. The dynamics of the propeller must also be matched to the engine. The natural frequency of the first bending mode of a blade should not coincide with an impulse frequency from the engine. For example, a horizontally opposed, six-cylinder engine has three torsional peaks per revolution. If a propeller being driven by this engine has a natural frequency close to 3/rev, it can lead to excessive vibration and fatigue stresses.

Aerodynamically, one strives to select a propeller that provides a high efficiency for cruise and a high static thrust for takeoff. These two requirements are easier to satisfy with a variable pitch propeller. A fixed pitch propeller is usually a compromise between these two operating regimes.

Given the results of a series of propeller tests, such as Figures 6.12 and 6.13, one can utilize these data to select the best propeller diameter and blade angle to match a given airplane-engine combination. One approach that is sometimes used is based on a coefficient C_s, the speed power coefficient, defined by

$$C_s = \left(\frac{\rho V^5}{Pn^2}\right)^{1/5} \tag{6.57}$$

Knowing C_p as a function of J, C_s can be calculated from

$$C_s = \left(\frac{C_p}{J^5}\right)^{1/5} \tag{6.58}$$

The advantage of C_s is that it does not contain the diameter in its definition.

Figure 6.21 presents J as a function of C_s for the same propeller for which Figures 6.12 and 6.13 hold. A maximum efficiency line is also shown in Figure 6.21. The use of this graph is best illustrated with an example. The problem will be to select the optimum diameter for this propeller if it is to be installed on a Cherokee 180. Consider the selection of a propeller to absorb

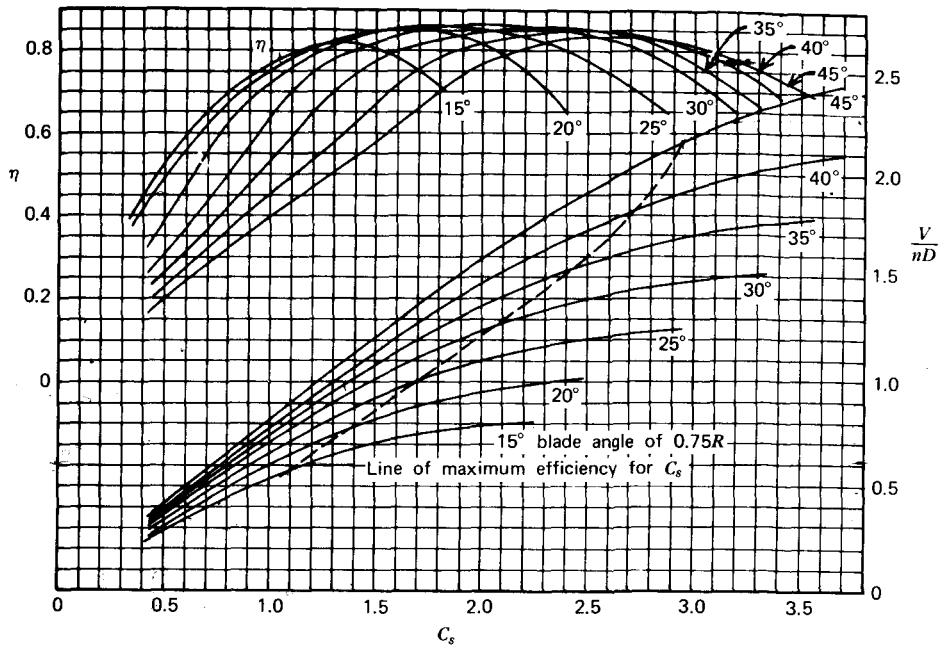

Figure 6.21 Design chart for propeller 5868–9, Clark-Y section, three blades.

75% of the maximum power of 180 bhp at 2500 rpm at standard sea level conditions. Using a value for f of 0.5 m^2 (5.38 ft^2) and an e of 0.6, C_D can be calculated as a function of V. C_T and C_D are then related by ($T = D$).

$$C_T = C_D \frac{SJ^2}{2D^2} \tag{6.59}$$

Assuming a value for V of 130 mph leads to a C_s of 1.360. From the maximum efficiency line in Figure 6.21, a J of 0.76 and a β of 20° are obtained. These values in turn lead to a C_T value of 0.0573, so obviously 130 mph will not be the trim speed for the optimum propeller at this power and rpm. By iteration, one obtains a trim speed of 132 mph and the following.

$$J = 0.76$$

$$\beta = 20°$$

$$C_T = 0.0592$$

$$\eta = 0.84$$

$$D = 6.1 \text{ ft}$$

DESIGN OF A NEW PROPELLER

This section deals mainly with the aerodynamic considerations of designing a new propeller. The optimum blade loading is prescribed by the Betz condition, which requires the trailing vortex system to lie along a helical surface in the ultimate wake. This condition will be met if

$$\omega r \tan(\phi + \alpha_i) = \text{constant} = V + w_0 \tag{6.60}$$

w_0 is a fictitious velocity called the impact velocity. Given the design advance ratio, one can arbitrarily choose a value of w_0/wR. From the geometry of Figure 6.10, it follows that

$$\frac{w_t}{V_T} = \frac{w_0}{V_T} \sin(\phi + \alpha_i) \cos(\phi + \alpha_i) \tag{6.61}$$

where

$$\phi + \alpha_i = \tan^{-1}\left(\frac{V + w_0}{xV_T}\right) \tag{6.62}$$

Substituting Equation 6.61 into Equation 6.42 leads to the product σC_l as a function of x. One must then decide how to choose between σ and C_l. The procedure for doing so is not well defined. First, one must choose the number of blades. This may be done on the basis of experience or arbitrarily as a first step in a design iteration. Similarly, a radial distribution of thickness is chosen. Ultimately, stress calculations must be made. Based on these results, the thickness may be changed.

A very practical and completely nonaerodynamic consideration in the choice of an airfoil section for a propeller blade is the question of stress concentrations resulting from leading and trailing edge nicks and scratches, particularly leading edge nicks. To elaborate on this point, consider the two airfoil sections pictured in Figure 6.22. From a stress-concentration viewpoint, the symmetrical airfoil on the left is preferred since, in bending, stresses are directly proportional to the distance from the neutral axis. From an aerodynamic viewpoint, the cambered section is preferred. Hence, the engineer is faced once again with another compromise, a practice that characterizes much of the engineering profession.

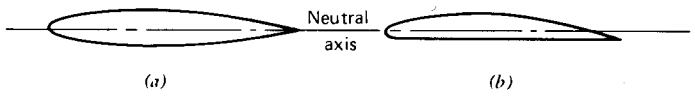

Figure 6.22 Susceptibility of airfoil shapes to leading and trailing edge stress concentrations. (*a*) Edges close to neutral axis. (*b*) Edges removed from neutral axis.

Having selected an airfoil family such as the NACA series-16 or the newer supercritical airfoil, one now chooses at each x a design C_l that will avoid compressibility effects. The steps for doing this are:

1. Choose C_l.
2. Calculate c from σC_l.
3. Determine M_{cr} from t/c and C_l.
4. Compare M_{cr} with the resultant local M.
5. If M_{cr} is less than M, decrease C_l and repeat.

If Mach number is not a consideration in the design, then one can choose C_{l_i} to give the lowest C_d to C_l ratio for the chosen airfoil family.

Having determined the radial distribution of c (and hence σ) and C_l, the corresponding C_d values are calculated. These, together with $(\phi + \alpha_i)$, are substituted into Equations 6.32*a* and 6.32*b* to determine thrust and power. The entire design process is performed with different w_0 values until the desired value of C_T or C_p is achieved. Generally, increasing w_0 will increase either of these coefficients.

Most propellers are designed to operate immediately in front of a fuselage or nacelle. The inflow velocity in this case is no longer a constant but is, indeed, a function of x, the dimensionless radial station. This three-dimensional flow field can be determined by the potential flow methods presented in Chapter Two. With V a function of x, the resultant flow angle, ϕ, becomes

$$\phi = \tan^{-1} \frac{V(x)}{wr} \tag{6.63}$$

or

$$\phi = \tan^{-1} \left(\frac{V(x)/V_0}{x} \frac{J}{\pi} \right) \tag{6.64}$$

For this case of a nonuniform, *potential* inflow, the Betz condition is *not*

$$V(x) + w_0 = \text{constant}$$

Instead, one should impose only

$$w_0 = \text{constant} \tag{6.65}$$

Equation 6.65 follows from superimposing the potential flow from the propeller on that produced by the body. In the ultimate wake $V(x)$ will approach V_0 and w_0 will approach $2w_0$, so that the Betz condition is again satisfied.

A BRIEF HISTORY OF THE TURBOJET

One might argue that the turbojet engine had its beginnings with the turbosupercharger, since the latter has an exhaust-driven turbine that drives a compressor to supply air to the engine. These are the essential ingredients of a turbojet engine. Dr. Sanford A. Moss is generally credited with developing the turbosupercharger, at least in this country. In 1918, Moss successfully tested his turbosupercharger atop Pikes Peak. Two years later, a La Pere biplane equipped with a turbosupercharger set a world altitude record of over 10,000 m.

In 1930, Frank Whittle (later to become Sir Frank Whittle) received a patent for a turbojet engine. Unfortunately, he was unable to gain support for the development of his design. It was not until 1935, when a young German aeronautical engineering student, Hans von Ohain, received a German patent on a jet engine, that development work began in earnest on the turbojet engine. On August 27, 1939 (some references say June 1939), the first turbojet engine was flown in a Heinkel He178. This engine designed by von Ohain delivered 4900 N (1100 lb) of thrust. It was not until May 1941 that Whittle's engine was flown in England.

German jet engine development progressed rapidly. By 1944, both BMW and Junkers turbojet engines were introduced into the Luftwaffe. One can imagine the astonishment of the allied aircrews upon first seeing propellerless airplanes zip by them at incredible speeds of over 500 mph.

On October 1, 1942, the first American jet-propelled airplane, the Bell Airacomet, was flown. This twin-engine airplane was powered by an American copy of Whittle's engine built by the General Electric Co. Designated the "I-A," the engine weighed approximately 4450 N (1000 lb) with a thrust-to-weight ratio of 1.25. The first production American jet aircraft, the Lockheed F-80, first flew in January 1944. In production form, it was powered by the J33 engine, which delivered a thrust of approximately 17,800 N (4000 lb) at a weight of 8900 N (2000 lb).

General Electric's J47 was the first turbojet power plant certified in the United States for commercial aviation in 1949. The world's first commercial jet transport to fly, however, on July 27, 1949, was the British built de Havilland Comet powered by four de Havilland Ghost 50 Mk1 turbojets. This engine, incorporating a centrifugal compressor, developed 19,800 N (4450 lb) of thrust. The Comet must be recognized as one of the most famous airplanes in history, because it truly ushered in the age of jet transportation. Unfortunately, its career was short-lived after three of the nine that had been built broke up in the air. An exhaustive investigation showed the cause to be fuselage structural fatigue because of repeated pressurizations. Despite its tragic demise, the Comet proved the feasibility of commercial jet transportation and paved the way for Boeing's successful 707. This airplane first

took to the air on July 15, 1954, powered by four Pratt & Whitney JT3 (military designation J57) turbojet engines. Each engine developed a static thrust of approximately 57,800 N (13,000 lb) with a dry weight of 18,200 N (4100 lb).

A historical note of interest is the following quotation taken from a report by the Gas Turbine Committee of the U.S. National Academy of Sciences in 1940.

"... Even considering the improvements possible... the gas turbine could hardly be considered a feasible application to airplanes mainly because of the difficulty with the stringent weight requirements...."

This conclusion, made by a panel of eminent persons, including Dr. Theodore von Karman, is a sobering reminder to any engineer not to be too absolute.

DESCRIPTION OF THE GAS TURBINE ENGINE

Basically, the gas turbine engine consists of a compressor, a combustion chamber, and a turbine. The combination of these basic components is referred to as the *gas generator* or *core engine.* Other components are then added to make the complete engine. It is beyond the scope of this text to delve into the details of gas turbine engine design. However, the various types of gas turbine engines will be described, and their operating characteristics will be discussed in some detail.

Beginning with the core engine, the turbojet engine pictured in Figure 6.23 is obtained by adding an engine air inlet and a jet nozzle. As the air

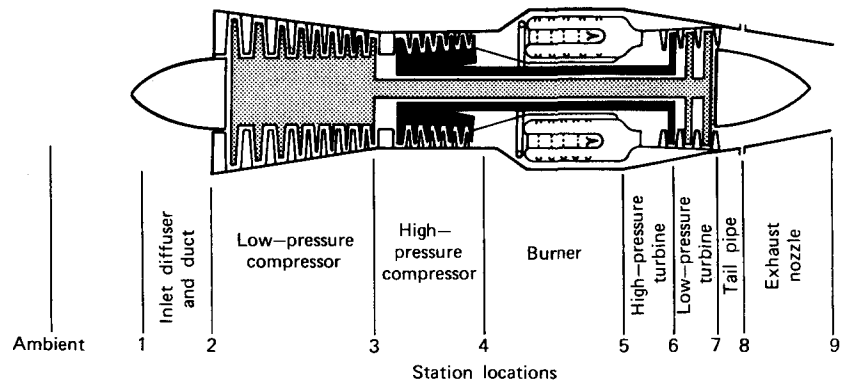

Figure 6.23 Typical dual rotor (two-spool) turbojet.

enters the inlet, it is diffused and compressed slightly. It then passes through a number of blade rows that are alternately rotating and stationary. The collection of rotating blades is referred to as the rotor; the assembly of stationary blades is called the stator. This particular compressor configuration is known as an axial-flow compressor and is the type used on all of today's larger gas turbine engines. Early gas turbine engines, such as Whittle's engine, employed a centrifugal compressor, as shown in Figure 6.24. Here, the air enters a rotating blade row near the center and is turned radially outward. As the air flows out through the rotating blade passage, it acquires a tangential velocity component and is compressed. A scroll or radial diffuser collects the compressed air and delivers it to the combustion chamber. Centrifugal compressors were used on the early turbojet engines simply because their design was better understood at the time. As jet engine development progressed, centrifugal compressors were abandoned in favor of the more efficient axial-flow compressors. The axial-flow compressor also presents a smaller frontal area than its centrifugal counterpart and is capable of achieving a higher pressure ratio.

Smaller sizes of gas turbine engines still favor the centrifugal compressor. Figure 6.25 is a cutaway drawing of the Garrett TPE 331/T76 turboprop engine. The compressor section of this engine consists of two stages of radial impellers made of forged titanium.

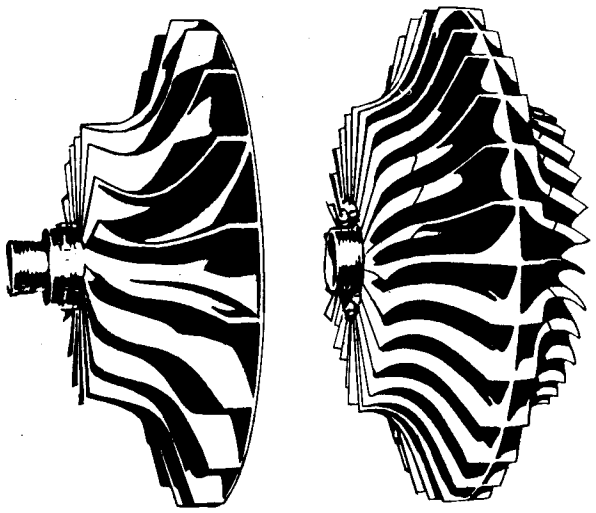

Figure 6.24 Typical centrifugal flow compressor impellers. (a) Single-entry impeller. (b) Double-entry impeller. (Courtesy General Electric Co.)

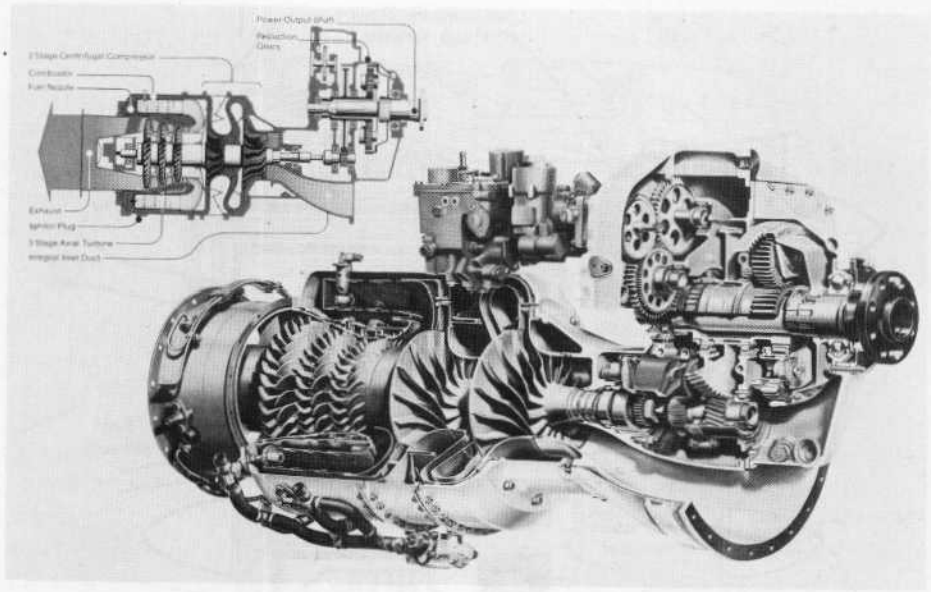

Figure 6.25 Cutaway of Garrett TPE 331/76. (Courtesy The Garrett Corp.)

After the compressed air leaves the compressor section, it enters the combustor, or burner, section. Atomized fuel is sprayed through fuel nozzles and the resulting air-fuel mixture is burned. Typically, the ratio of air to fuel by weight is about 60:1. However, only approximately 25% of the air is used to support combustion. The remainder bypasses the fuel nozzles and mixes downstream of the burner to cool the hot gases before they enter the turbine.

The mixed air, still very hot (about 1100 °C), expands through the turbine stages, which are composed of rotating and stationary blade rows. The turbines extract energy from the moving gases, thereby furnishing the power required to drive the compressor. Nearly 75% of the combustion energy is required to drive the compressor. The remaining 25% represents the kinetic energy of the exhaust, which provides the thrust. For example, in the General Electric CF6-6 turbofan engine [180,000 N (40,000 lb) thrust class], the turbine develops approximately 65,600 kW (88,000 shp) to drive the high- and low-pressure compressors.

Variations of the gas turbine engine are presented in Figure 6.26. In a turboprop or turboshaft engine, nearly all of the energy of the hot gases is extracted by the turbines, leaving only a small residual thrust. The extracted energy in excess of that required to drive the compressor is then used to provide shaft power to turn the propeller or a power-output shaft in general. Turboshaft engines power most of today's helicopters and are used extensively by the electric utilities to satisfy peak power load demands.

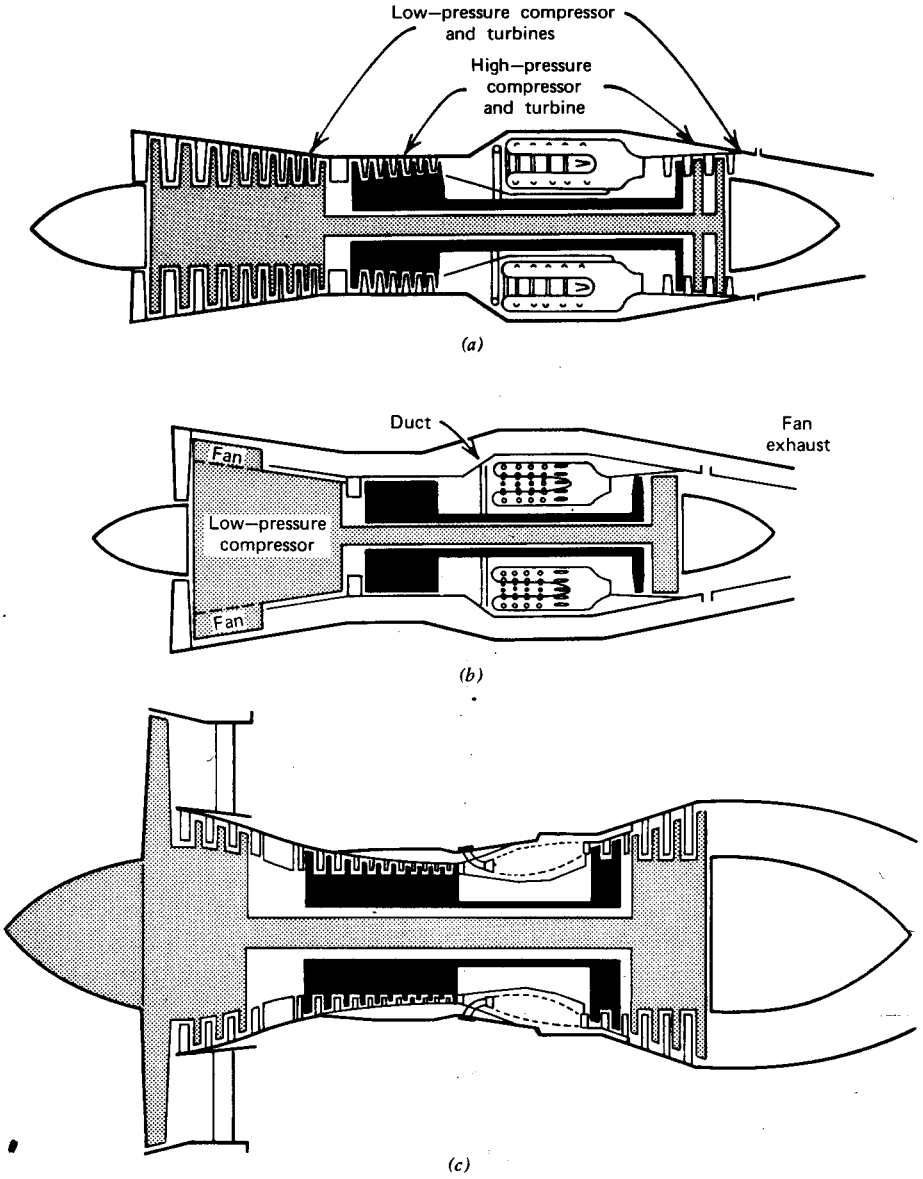

Figure 6.26 Variations on the gas turbine. (*a*) Dual axial-flow compressor turbojet. (*b*) Dual axial-flow compressor, forward fan engine with long ducts. (*c*) High bypass ratio turbofan with short ducts. (*d*) Single axial-flow compressor, direct propeller drive turboprop. (*e*) Single axial-flow compressor, free turbine propeller drive turboprop. (*f*) Dual axial-flow compressor, turbojet with afterburner. (*g*) Dual axial-flow compressor, industrial turboshaft engine.

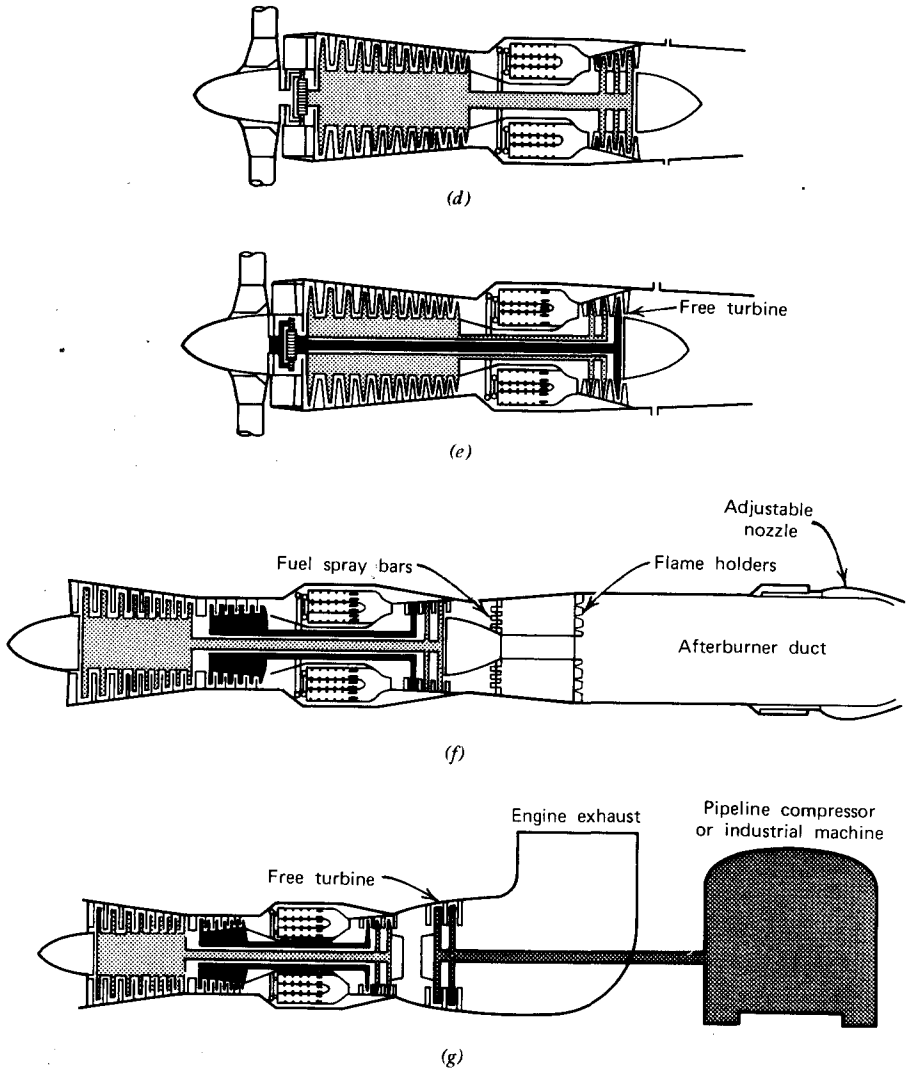

Figure 6.26 (continued)

A "spool" refers to one or more compressor and turbine stages connected to the same shaft and thus rotating at the same speed. Gas turbine engines generally use one or two spools and are referred to as single or dual compressor engines. A turboshaft engine may incorporate a free turbine that is independent of any compressor stage and is used solely to drive the shaft. Since the rotational speed of a turbine wheel is of the order of 10,000 rpm, a

reduction gear is required between the turbine shaft and the power output shaft.

A turboprop produces a small amount of jet thrust in addition to the shaft power that it develops; these engines are rated statically in terms of an equivalent shaft horsepower (eshp). This rating is obtained by assuming that 1 shp produces 2.5 lb of thrust. For example, the dash 11 model of the engine shown in Figure 6.25 has ratings of 1000 shp and 1045 eshp. From the definition of eshp, this engine therefore produces a static thrust from the turbine exhaust of approximately 113 lb.

A turbojet engine equipped with an afterburner is pictured in Figure 6.26*f*. Since only 25% or so of the air is used to support combustion in the burner section, there is sufficient oxygen in the turbine exhaust to support additional burning in the afterburner. Both turbofans and turbojets can be equipped with afterburners to provide additional thrust for a limited period of time. Afterburning can more than double the thrust of a gas turbine engine, but at a proportionately greater increase in fuel consumption. Essentially, an afterburner is simply a huge stovepipe attached to the rear of an engine in lieu of a tail pipe and jet nozzle. Fuel is injected through a fuel nozzle arrangement called spray bars into the forward section of the afterburner and is

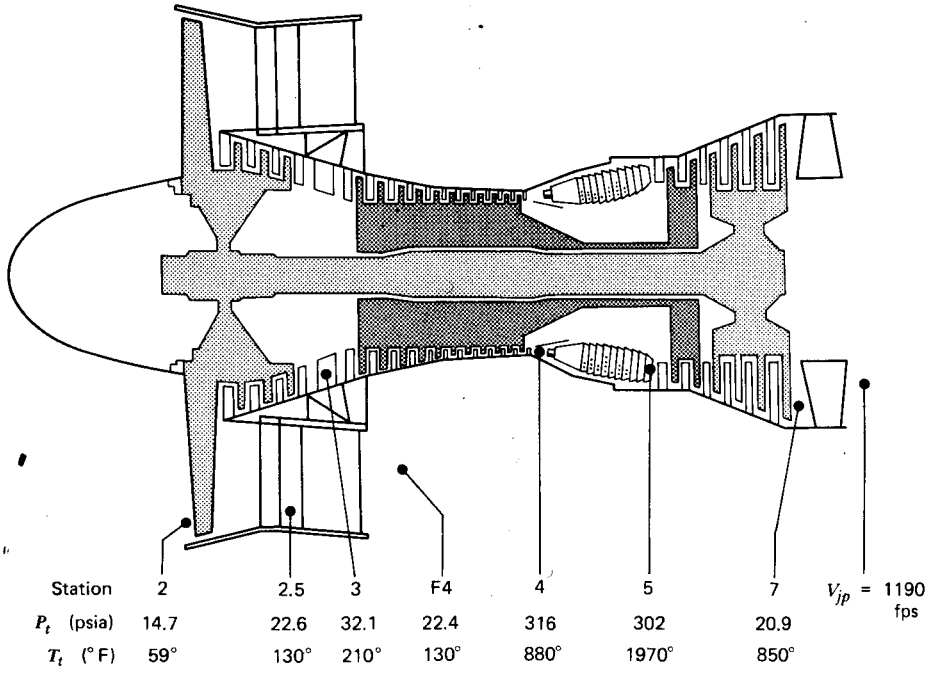

Figure 6.27 JT9D turbofan; internal pressures and temperatures.

ignited. This additional heat further expands the exhaust, providing an increased exhaust velocity and, thereby, an increased thrust. The afterburner is equipped with flame holders downstream of the spray bars to prevent the flames from being blown out of the tail pipe. A flame holder consists of a blunt shape that provides a wake having a velocity that is less than the velocity for flame propagation. An adjustable nozzle is provided at the exit of the afterburner in order to match the exit area to the engine operating condition.

Two different types of turbofan engines are shown in Figure 6.26*b* and 6.26*c*; the forward fan with a short duct and the forward fan with a long duct. These engines are referred to as bypass engines, since part of the air entering the engine bypasses the gas generator to go through the fan. The ratio by weight of the air that passes through the fan (secondary flow) to the air that passes through the gas generator (primary flow) is called the bypass ratio. Early turbofan engines had bypass ratios of around 1:1; the latest engines have ratios of about 5:1. One such engine, Pratt & Whitney's JT9D turbofan, is shown in Figure 6.27. Included on the figure are temperatures and absolute pressures throughout the engine for static operation at standard sea level conditions.

ENGINE RATINGS

An engine rating specifies the thrust that an engine can (or is allowed) to develop in a particular operating mode. For commercial certification, these ratings are defined as follows.

Takeoff (Wet) This is the maximum thrust available for takeoff for engines that use water injection. The rating is selected by actuating the water injection system and setting the aircraft throttle to obtain the computed "wet" takeoff thrust. The rating is restricted to takeoff, is time limited to 5 min, and has altitude and ambient air or water temperature limitations.

Takeoff (Dry) This is the maximum thrust available without the use of water injection. The rating is selected by setting the aircraft throttle to obtain the computed takeoff (dry) thrust for the prevailing conditions of ambient temperature and barometric pressure. The rating is time limited to 5 min and is to be used only for takeoff and, as required, for reverse thrust operations during landing.

Maximum Continuous This rating is the maximum thrust that may be used continuously, and is intended only for emergency use at the discretion of the pilot.

Maximum Climb Maximum climb thrust is the maximum thrust approved for normal climb. On some engines, maximum continuous and maximum

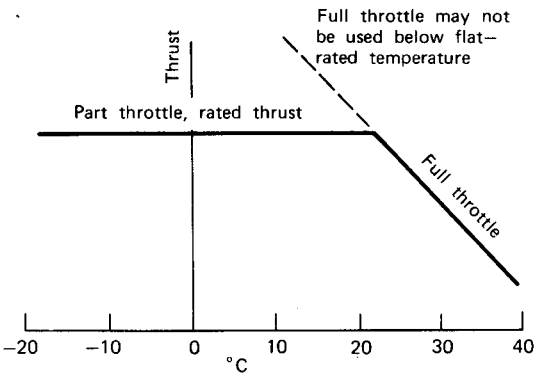

Figure 6.28 Thrust curve for a flat-rated engine.

climb thrusts are the same. For commercial engines, the term formerly used, normal rated thrust, has been replaced by the more appropriate term, maximum climb thrust.

Maximum Cruise This is the maximum thrust approved for cruising.

Flat Rating

Engines that must be operated at "part throttle" at standard ambient conditions to avoid exceeding a rated thrust are referred to as "flat-rated" engines. This refers to the shape of the thrust versus the ambient temperature curve. For example, the General Electric Company's CF6-6 high bypass turbofan engine is flat rated up to an ambient temperature of 31 °C at sea level, or 16 °C higher than a standard day. Thus, its thrust as a function of ambient temperature varies, as shown in Figure 6.28. At full throttle, the thrust is seen to decrease with increasing temperature. Therefore, by flat rating an engine out to a temperature higher than standard, one is able to maintain rated thrust on a hot day.

SOME CONSIDERATIONS RELATING TO GAS TURBINE PERFORMANCE

In order to understand, at least qualitatively, why a particular configuration of a gas turbine engine performs as it does, let us consider a few basic principles. The ideal thermodynamic cycle for the gas turbine engine is shown in Figure 6.29*a*, where it is compared to the cycle for the piston engine. The Otto cycle, which approximates the piston engine thermodynamics, consists of an isentropic compression of the gas followed by a rapid combustion at

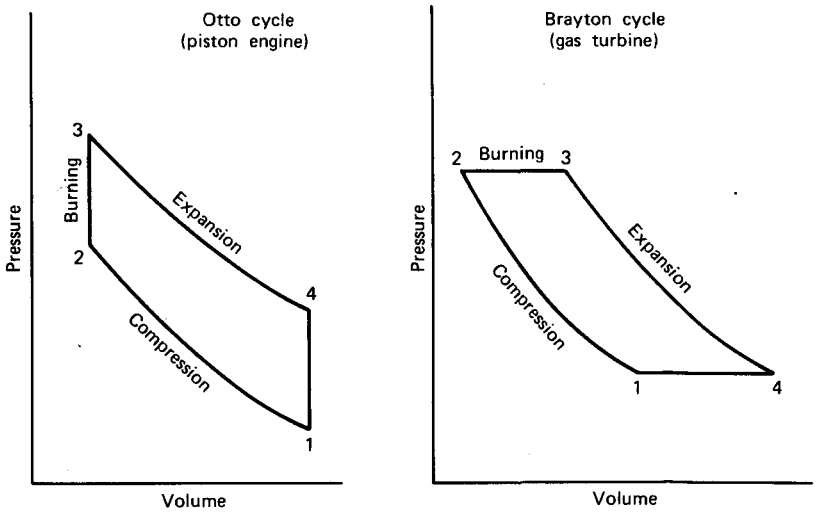

Figure 6.29a A comparison between the Otto and Brayton cycles.

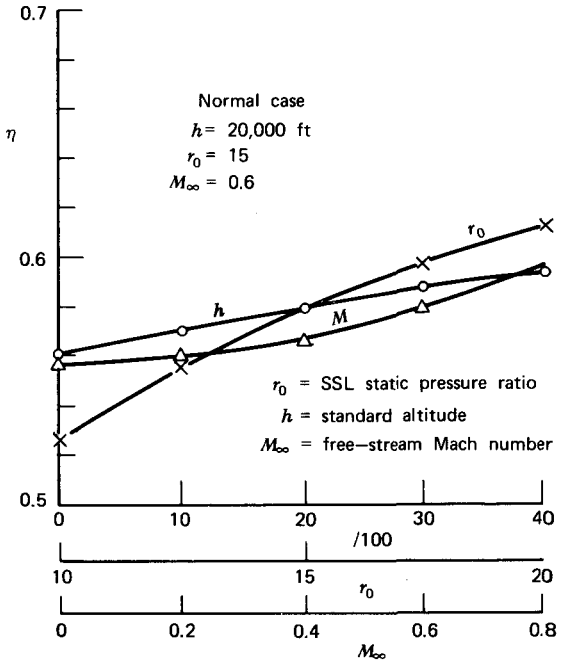

Figure 6.29b Effect of pressure ratio, altitude, and Mach number on the ideal thermal efficiency of a gas turbine engine.

nearly constant volume. The gas then expands isentropically, forcing the piston ahead of it. Unlike the piston engine, the gas turbine engine involves a continuous flow of the working gas. The Brayton or constant pressure cycle, which approximates the actual gas turbine cycle, begins with an isentropic compression of the air from ambient conditions. Part of this compression occurs prior to the compressor stages as the air enters the engine inlet. Following the compression, burning occurs at constant pressure, resulting in increased volume and total temperature. The air then expands isentropically through the turbines and jet nozzle to the ambient static pressure. In a turboprop or turboshaft engine, nearly all of the expansion occurs within the turbines in order to drive the compressor and produce shaft power. In a turbojet engine, an appreciable amount of expansion occurs after the turbines in order to produce the high-momentum jet.

The heat that is added to the flow per unit weight of gas is given by

$$Q_{\text{in}} = C_p(T_3 - T_2) \tag{6.66}$$

while the heat rejected is

$$Q_{\text{out}} = C_p(T_4 - T_1) \tag{6.67}$$

C_p is the specific heat at constant pressure, as used previously in Chapter Five. The work output per unit weight of gas equals the added heat minus that which is rejected. The thermal efficiency equals the work output divided by the added heat. Thus,

$$\eta = 1 - \frac{T_4 - T_1}{T_3 - T_2} \tag{6.68}$$

Let r denote the compression ratio, p_2/p_1 (or p_3/p_4). Since compression and expansion are both assumed to be isentropic,

$$\frac{T_2}{T_1} = \frac{T_3}{T_4} = r^{(\gamma-1)/\gamma} \tag{6.69}$$

Thus, Equation 6.68, in terms of the compression ratio, can be written as

$$\eta = 1 - \frac{1}{r^{(\gamma-1)/\gamma}} \tag{6.70}$$

As stated previously, the compression ratio r is achieved partly in the inlet (ram pressure), and the remainder is achieved through the compressor. The pressure increase across the compressor, at a constant rpm, as a first approximation, is proportional to the mass density, ρ_c, just ahead of the compressor.

$$\Delta p \propto \rho_c$$

If r_0 denotes the value of r for static sea level operation,

$$p = p_0(r_0 - 1)\frac{\rho_c}{\rho_0} \tag{6.71}$$

ρ_0 is, of course, the standard sea level value of mass density.

For isentropic compression in the inlet up to the compressor, the ambient mass density and ρ_c are related by

$$\frac{\rho_c}{\rho_\infty} = \left[\frac{1 + (\gamma - 1/2)M_\infty^2}{1 + (\gamma - 1/2)M^2}\right]^{1/(\gamma-1)} \tag{6.72}$$

where M_∞ is the free-stream Mach number and M is the local Mach number just ahead of the compressor. The pressure ratio, r, thus becomes

$$r = \frac{p_c + \Delta p}{p_\infty}$$

or

$$r = \frac{p_c}{p_\infty} + \frac{(r_0 - 1)}{\theta}\frac{\rho_c}{\rho_\infty} \tag{6.73}$$

p_c/p_∞ is given by

$$\frac{p_c}{p_\infty} = \left[\frac{1 + (\gamma - 1/2)M_\infty^2}{1 + (\gamma - 1/2)M^2}\right]^{\gamma/\gamma-1} \tag{6.74}$$

Thus r finally becomes

$$r = [f(M, M_\infty)]^{\gamma/(\gamma-1)} + \frac{r_0 - 1}{\theta}[f(M, M_\infty)]^{1/(\gamma-1)} \tag{6.75}$$

where

$$f(M, M_\infty) = \frac{1 + (\gamma - 1/2)M_\infty^2}{1 + (\gamma - 1/2)M^2}$$

Equation 6.75 is substituted into Equation 6.70 an expression for the thermal efficiency results that is a function of δ, r_0, M_∞, and M.

The effect of pressure ratio, altitude, and free-stream Mach number on the ideal thermal efficiency is shown in Figure 6.29*b*. This figure assumes the ratio of M to M_∞ just before the compressor to equal approximately zero. This is a fairly reasonable assumption, since values of this ratio up to at least 0.4 affect η by less than 1%. Figure 6.29*b* shows the effect of varying one parameter at a time while keeping the other two parameters at their normal values. Increasing M_∞ from zero to 0.8 is seen to result in a 7% improvement in η. The efficiency also improves with altitude, increasing by approximately 6% in going from sea level to 40,000 ft (12,200 m). Doubling the pressure ratio, r_0, from 10 to 20 results in a 16% improvement in η.

With regard to the production of thrust, η does not tell the whole story. η is simply a measure of how efficiently the air passing through the engine is

being used. The heat added to the flow, per unit weight, is given by

$$Q_{in} = \eta C_p (T_3 - T_2) \tag{6.76}$$

Thus, for the same efficiency, if T_3 is increased or the mass flow increased, the thrust will be increased.

QUALITATIVE COMPARISON OF THE PERFORMANCE OF TURBOJET, TURBOFAN, AND TURBOPROP ENGINES

Figure 6.30*a*, 6.30*b*, and 6.30*c* presents a qualitative comparison of the turbojet, turbofan, and turboprop engines, each having the same core engine.

The specific fuel consumption for a turbojet or turbofan engine is expressed as a thrust specific fuel consumption (TSFC). In the English system of units, one states TSFC as pounds of fuel per hour per pound of thrust, so that TSFC actually has the dimensions of 1/time. Thus its numerical value is the same in the SI system as in the English system. In the SI system, TSFC is given as N/hr/N. The characteristics of the three engines are seen to be quite different with the turbofan, not surprisingly, lying between the turboprop and turbojet. The relative differences in these curves are explained mainly by the momentum and energy considerations undertaken previously for the propeller. "Disc loadings" for turbojet engines are of the order of 81,400 Pa (1700 psf), while turbofans operate at approximately half of this loading and propellers at only approximately 4% of the disc loading for a turbojet. If we assume that the core engine is delivering the same power to each engine configuration then, from Equation 6.17, for static thrust one obtains,

$$F_0 \propto \left(\frac{F_0}{A}\right)^{-1/2}$$

Note that thrust for a turbojet engine is denoted by F instead of T, since T is understood to refer to temperature when working with a gas turbine. Thus, with its appreciably lower disc loading, one would expect the static thrust of a turboprop to be significantly higher than the corresponding turbojet, possibly even more so than that shown in Figure 6.29*a* (taken from Ref. 6.6).

The rapid decrease in thrust with airspeed for the turboprop and the more gradual changes for the turbofan and turbojet engines are also explained in part by the relative disc loadings. Combining Equations 6.13, 6.14, and 6.15 gives

$$P = \frac{F}{2}\left[V + \sqrt{V^2 + \left(\frac{2F}{\rho A}\right)}\right] \tag{6.77}$$

If the power to produce the thrust is assumed to be constant, then Equation

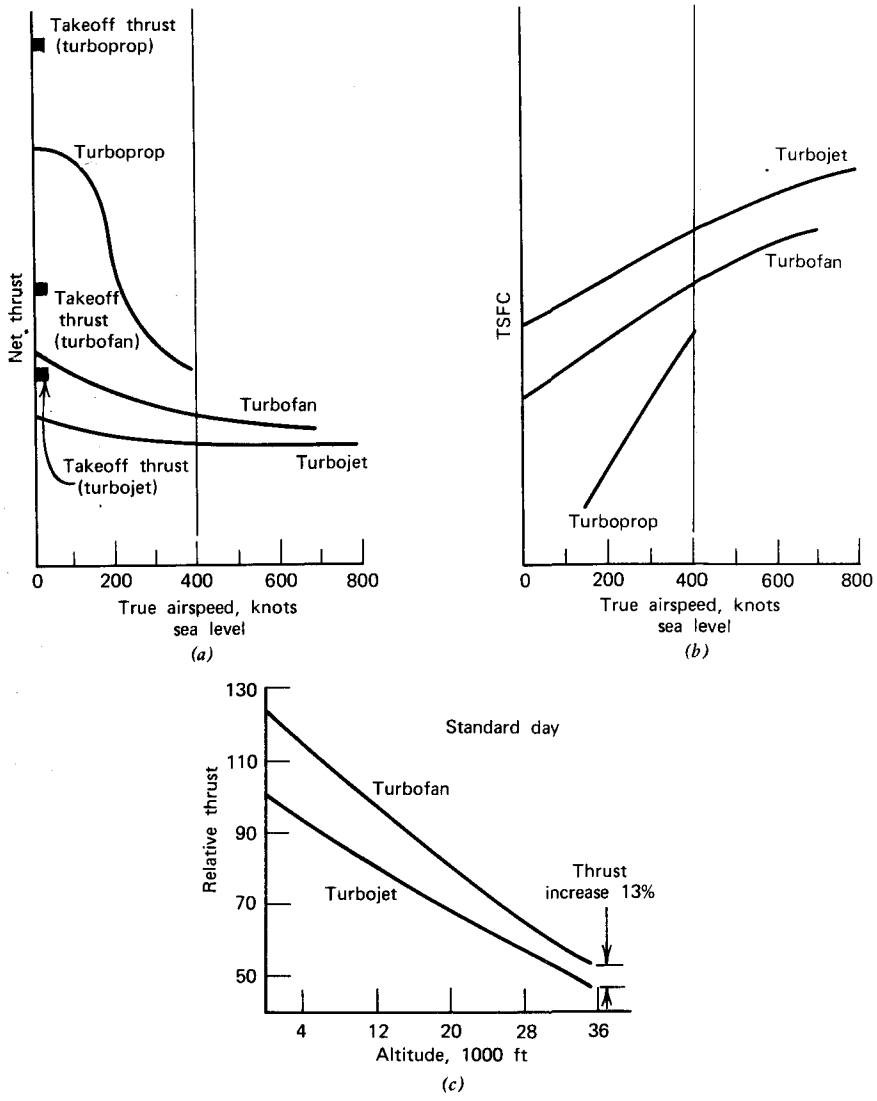

Figure 6.30a Comparative net thrust at sea level.
Figure 6.30b Comparative thrust specific fuel consumption.
Figure 6.30c Relative maximum continuous thrust comparison during climb.

6.77 can be written

$$\frac{F}{F_0} = 2\left[\frac{V}{w_0} + \sqrt{\left(\frac{V}{w_0}\right)^2 + 4\frac{F}{F_0}}\right]^{-1} \tag{6.78}$$

where F_0 is the static thrust and w_0 is the static-induced velocity given by Equation 6.16. This implicit relationship between F/F_0 and V/w_0 can be easily solved iteratively using a programmable calculator. The solution is presented graphically in Figure 6.31. Thus, it is not V per se that determines the ratio of F to F_0 but, instead, the ratio of V to w_0. For a high disc loading with a concomitant w_0, a given V will have a lesser effect on F than for the case of a low disc loading.

Disc loading is not the total explanation for the relative differences in T as a function of V shown in Figure 6.29*a*. Consider a typical turbojet with a static disc loading of around 81,400 Pa (1700 psf). For this engine at sea level, w_0 will equal approximately 180 m/s (600 fps). An airspeed of 400 kt in this case gives

$$\frac{V}{w_0} = 1.13$$

and

$$\frac{F}{F_0} = 0.64$$

However, Figure 6.30*a* shows only a 20% decrease in the thrust. This is because the gas generator power is not constant but also increases with V

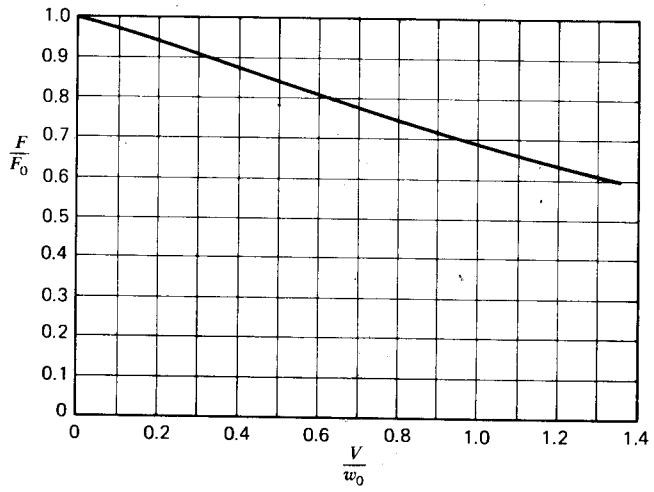

Figure 6.31 Predicted variation of thrust with forward velocity for a constant power.

because of the increased mass flow and ram pressure. If we tacitly assume the power proportional to the product of F and TSFC then, from Figure 6.30*b*, one would predict the core engine power to have increased by about 10%. This results in a decreased value of V/w_0 of 1.08, giving a new T/T_0 of 0.66. However, T_0 corresponds to the core engine power at 400 kt. Based on the original F_0 corresponding to the core engine power at $V = 0$, F/F_0 becomes 0.73. Figure 6.30*a*, 6.30*b*, and 6.30*c* is, of course, not too accurate and is really intended only to show relative differences. You may wish to apply Figure 6.31 to the performance curves of the JT9D-3 turbofan engine that follow. In this case, the predicted variation of F and V will be found to match closely the results given in the installation handbook.

SPECIFIC ENGINE CHARACTERISTICS AND PERFORMANCE

For illustrative purposes, this section will consider the characteristics and performance of specific engines.

Turbojet

The Pratt & Whitney JT4A-3 engine will be used as an example of a turbojet. This engine, installed on the Boeing 707-320 and McDonnell-Douglas DC-8-20, is a two-spool engine. The low-pressure compressor section has eight stages, with seven stages in the high-pressure section. The turbine has two low-pressure stages and one high-pressure stage. Other characteristics of this engine are presented in Table 6.1. This particular model of the JT4 engine has a takeoff thrust-to-dry weight ratio of 3.15. Later versions of this engine, such as the JT4A-12, develop T/W ratios of 3.58.

Table 6.1 Characteristics of the JT4A-3 Engine

Type—turbojet	
SSL static thrust	
Dry takeoff	70,300 N (15,800 lb)
Maximum continuous	55,600 N (12,500 lb)
TSFC	
Dry takeoff	0.780/hr
Maximum continuous	0.740/hr
Gas generator at dry takeoff	
Total airflow	1,108 N/s (249 lb/sec)
Overall pressure ratio	11.8
Engine dry weight	22,329 N (5020 lb)
Engine diameter	1.09 M (43 in.)
Engine length	3.66 M (144.1 in.)

The net thrust and fuel consumption curves for this engine are reproduced from the manufacturer's installation handbook in Figure 6.32*a*, 6.32*b*, 6.32*c*, and 6.32*d*. At this point, a definition of net thrust is needed. To do this we first define gross thrust, F_g, as the product of the mass flow rate in the jet exhaust and the velocity attained by the jet after expanding to ambient static pressure.

$$F_g = m_j V_j$$

The net thrust, F_n, is then defined by

$$F_n = F_g - m_i V_{am}$$

where m_i is the inlet mass flow and V_{am} is the velocity of the ambient air. For static operation, F_g and F_n are equal.

Net thrust for the takeoff rating of this engine is presented in Figure 6.33*a*, 6.33*b*, and 6.33*c* for speeds of 0, 100, and 200 kt and altitudes from sea level to 14,000 ft.

The curves of Figure 6.32 are for standard atmospheric conditions. One rarely finds a standard day, so it is usually necessary to correct engine performance for deviations from the standard. Without delving into the details of compressor design, one can argue that, for the same flow geometry (ratio of rotor speed to axial velocity and M_∞), the pressure increase across the compressor can be written as

$$\Delta p \propto \rho_\infty N^2$$

where N is the rotor angular velocity.

If Δp is expressed as a ratio to the ambient pressure, then

$$\frac{\Delta p}{p_\infty} \propto \frac{N^2}{p_\infty/\rho_\infty}$$

or

$$\frac{\Delta p}{p_\infty} \propto \frac{N^2}{T_\infty}$$

Thus, if N denotes the rpm of a compressor operating at an ambient temperature of T_∞, the rpm required to deliver the same pressure ratio at standard sea level conditions is known as the corrected rpm, N_c, given by

$$N_c = \frac{N}{\sqrt{\theta}} \tag{6.79}$$

θ being the ratio of the absolute temperature to the standard absolute temperature at sea level.

Similarly, one can say that the thrust, F, must be proportional to Δp, or

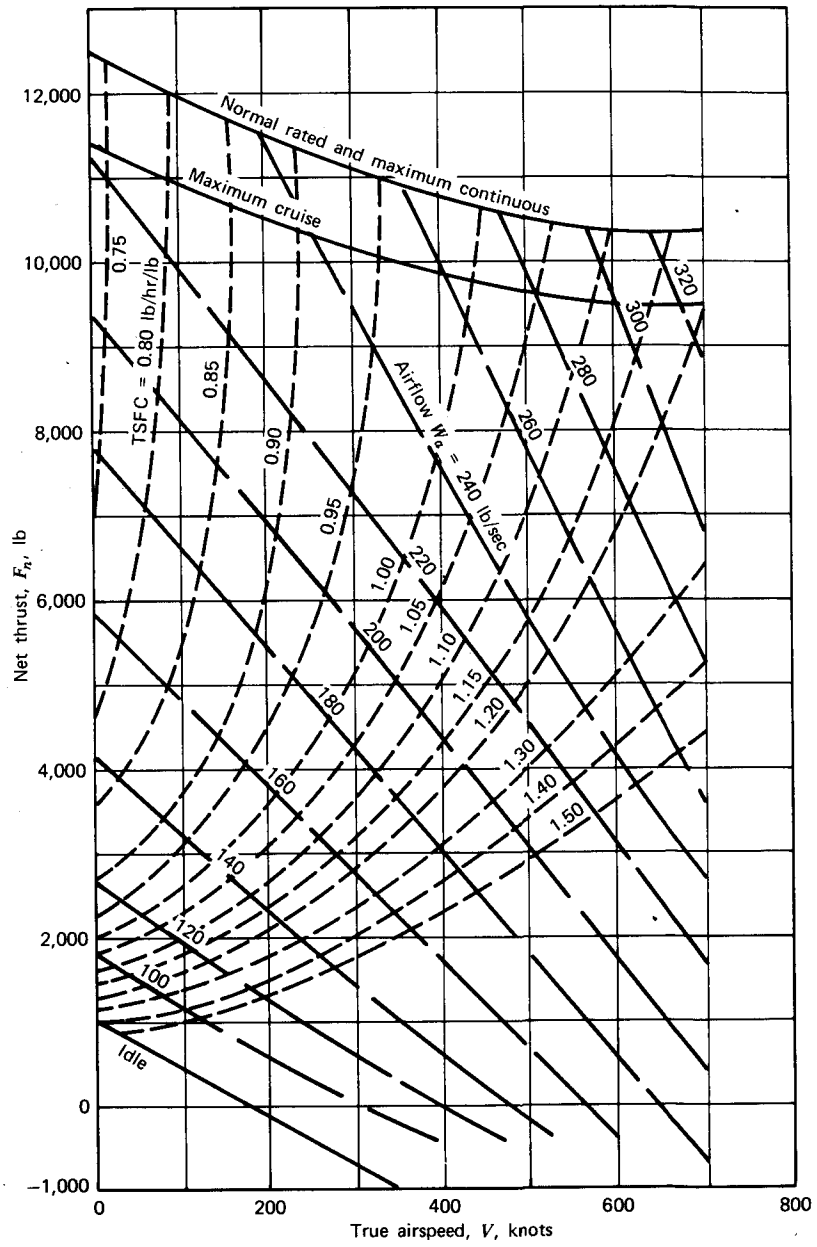

Figure 6.32a Pratt & Whitney Aircraft JT4A-3 turbojet engine. Estimated thrust, TSFC, and airflow at sea level. Standard atmospheric conditions, 100% ram recovery. (Courtesy, Pratt & Whitney.)

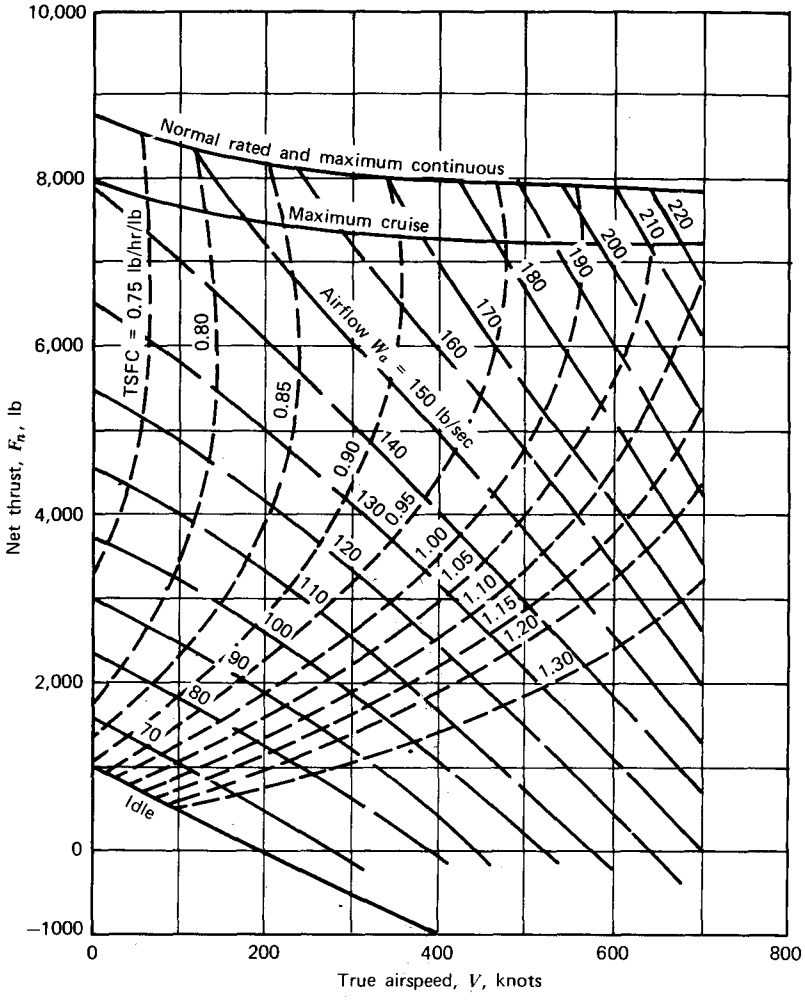

Figure 6.32b Pratt & Whitney Aircraft JT4A-3 turbojet engine. Estimated thrust, TSFC, and airflow at 15,000 ft. Standard atmospheric conditions, 100% ram recovery. (Courtesy, Pratt & Whitney.)

p_∞, for a constant pressure ratio. Thus, the corrected thrust, F_c, corresponding to the corrected rpm, is defined by

$$F_c = \frac{F}{\delta} \tag{6.80}$$

where δ is the ratio of the ambient pressure to standard sea level pressure.

Similarly, corrected values for fuel flow, airflow, and exhaust gas tem-

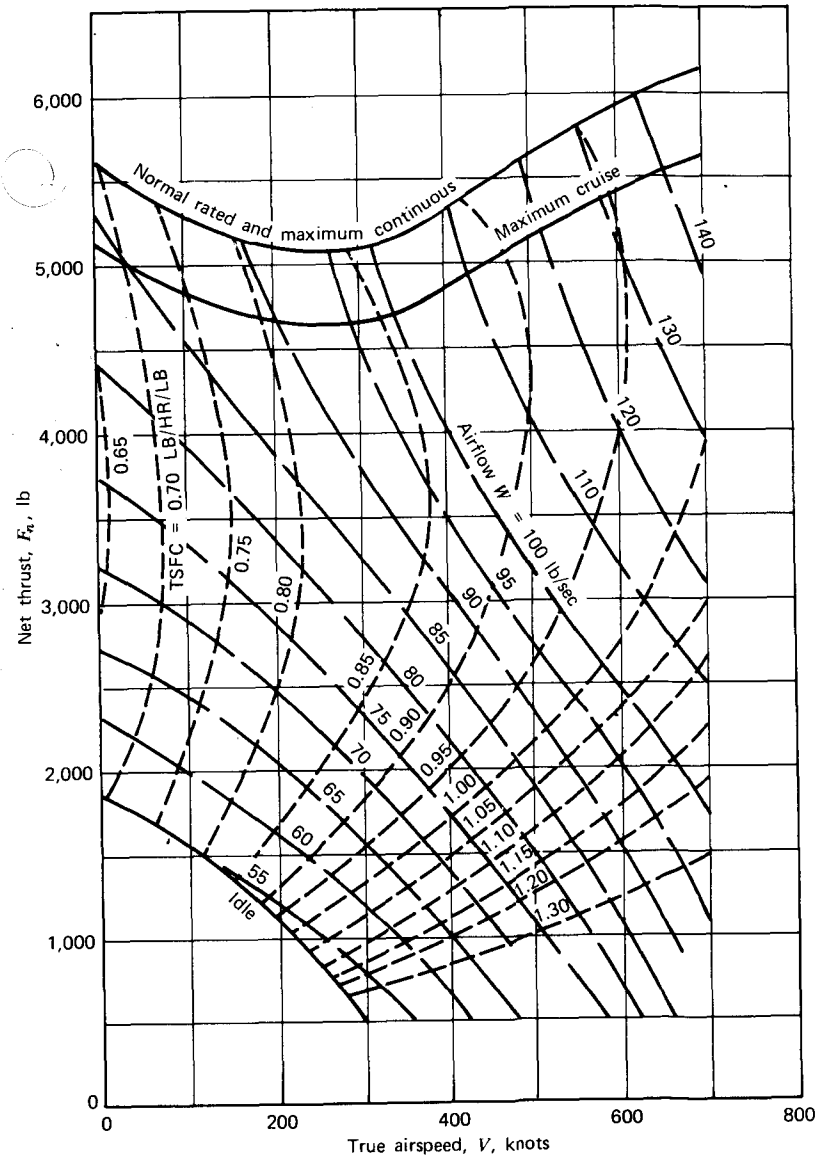

Figure 6.32c Pratt & Whitney Aircraft JT4A-3 turbojet engine. Estimated thrust, TSFC, and airflow at 30,000 ft. Standard atmospheric conditions, 100% ram recovery. (Courtesy, Pratt & Whitney.)

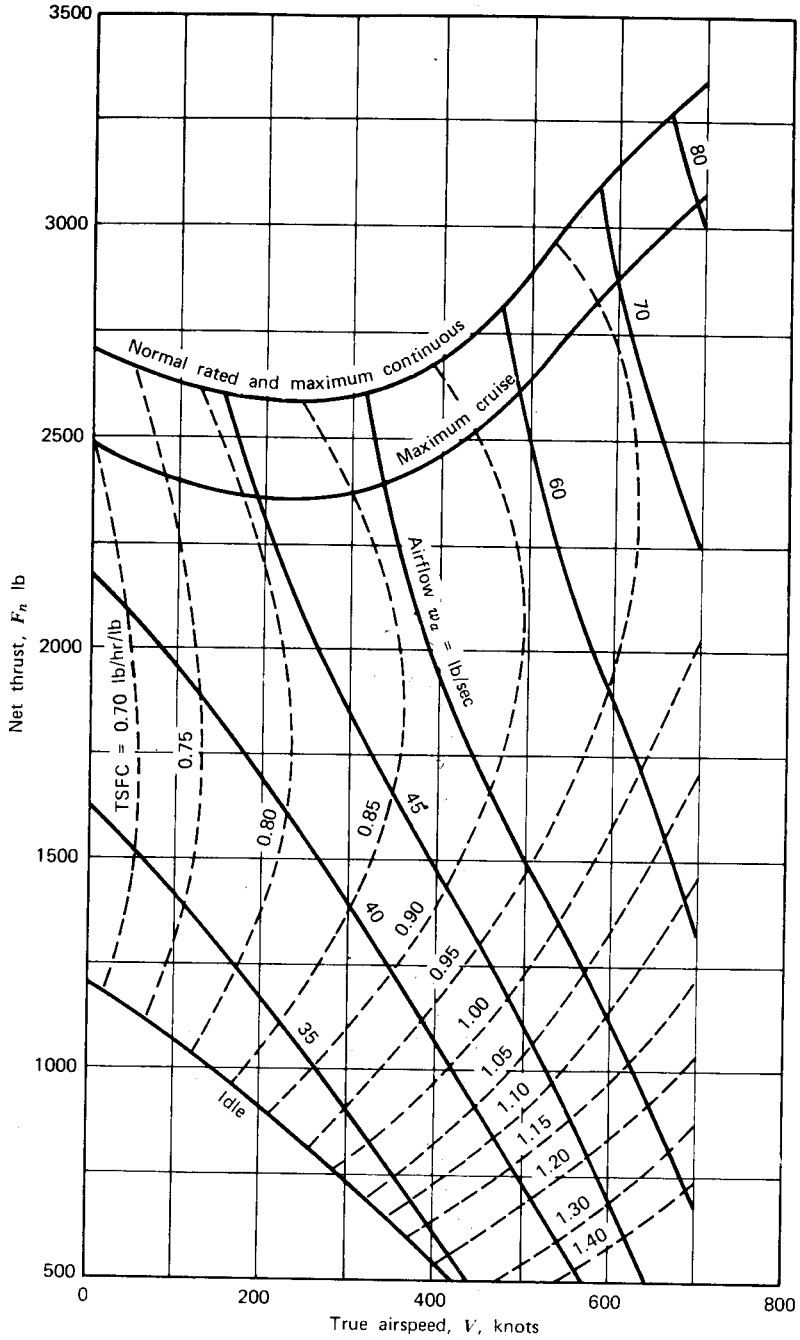

Figure 6.32d Pratt & Whitney Aircraft JT4A-3 turbojet engine. Estimated thrust, TSFC, and airflow at 45,000 ft. Standard atmospheric conditions, 100% ram recovery. (Courtesy, Pratt & Whitney.)

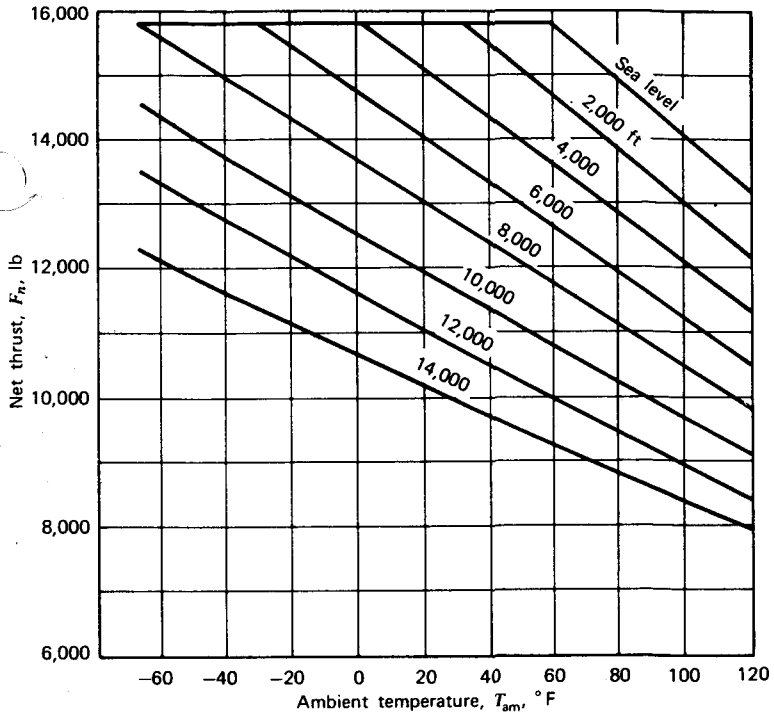

Figure 6.33a Pratt & Whitney Aircraft JT4A-3, -5 turbojet engines. Estimated net thrust on runway during takeoff. Zero knots. (Courtesy, Pratt & Whitney.)

perature (EGT) are defined by

$$W_{f_c} = \frac{W_f}{\delta\sqrt{\theta}} \tag{6.81}$$

$$W_{a_c} = \frac{W_a\sqrt{\theta}}{\delta} \tag{6.82}$$

$$\mathrm{EGT}_c = \frac{\mathrm{EGT}}{\theta} \tag{6.83}$$

A more elegant derivation of these corrected parameters, based on Buckingham's π theorem of dimensional analysis, can be found in Reference 6.9.

Excluding scale effects, the important point is made that the corrected thrust of a gas turbine engine is a unique function of the corrected values of N, W_a, and W_f. These, in turn, assure a constant value of the pressure ratio.

In practice, the pressure ratio used to monitor the corrected thrust is

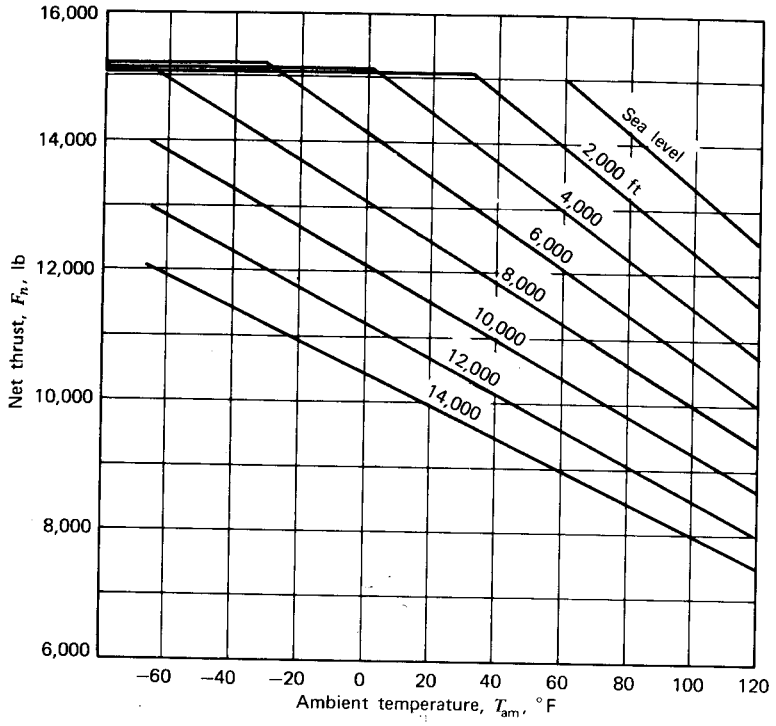

Figure 6.33b Pratt & Whitney Aircraft JT4A-3, -5 turbojet engines. Estimated net thrust on runway during takeoff. One hundred knots, 100% ram recovery. (Courtesy, Pratt & Whitney.)

referred to as the engine pressure ratio (EPR), defined by

$$\text{EPR} = \frac{p_{t7}}{p_{t2}} \tag{6.84}$$

The subscript t refers to the total stagnation pressure, the 7 and 2 refer to the engine stations shown in Figure 6.23. Thus EPR is the ratio of the total pressure at the turbine nozzle to the total pressure at the compressor inlet.

θ and δ, used to correct the operating parameters, are also based on the total temperature and pressure, respectively, at the compressor inlet.

$$\theta_{T2} = \frac{T_{t2}}{T_0} \tag{6.85}$$

$$\delta_{T2} = \frac{p_{t2}}{p_0} \tag{6.86}$$

where T_0 and p_0 are the standard sea level values of temperature and pressure. Assuming 100% ram pressure recovery, (i.e., that $M = 0$ at station

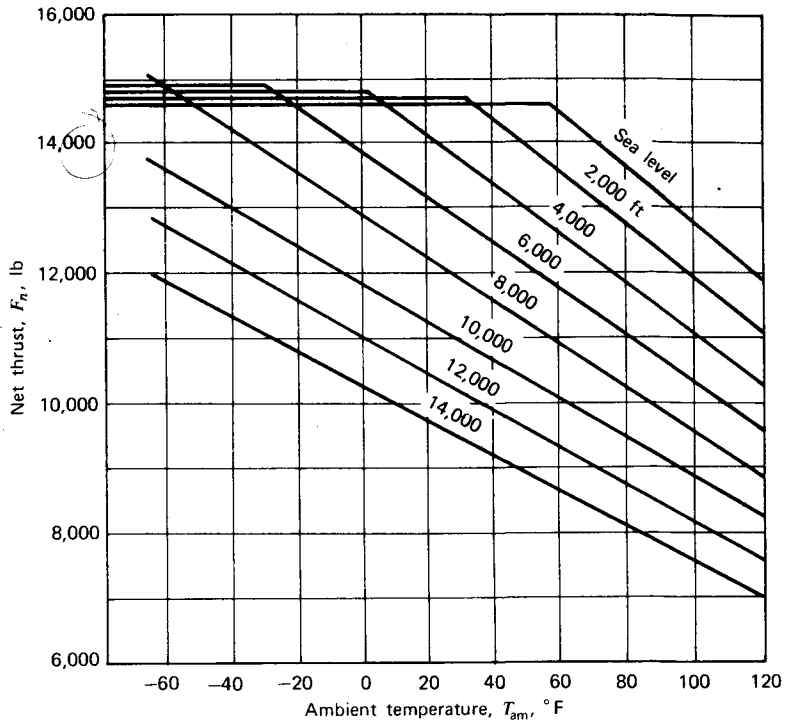

Figure 6.33c Pratt & Whitney Aircraft JT4A-3, -5 turbojet engines. Estimated net thrust on runway during takeoff. Two hundred knots, 100% ram recovery. (Courtesy, Pratt & Whitney.)

2), θ_{T2} and δ_{T2} can be calculated from

$$\theta_{T2} = \theta\,[1 + (\gamma - 1)\,M_\infty^2/2] \tag{6.87}$$

$$\delta_{T2} = \delta\,[1 + (\gamma - 1)\,M_\infty^2/2]^{\gamma/\gamma-1} \tag{6.88}$$

The operating curves for the JT4A-3 turbojet are presented in Figure 6.34*a* and 6.34*b*. Turbine discharge temperature, compressor speeds, and fuel flow are presented in Figure 6.34*a* as a function of EPR. Figure 6.34*b* shows the net thrust as a function of Mach number for constant values of EPR. All of the curves presented thus far for the JT4A-3 engine assume 100% ram recovery (no inlet duct loss) and a standard nozzle installation prescribed by the manufacturer. They also assume zero power extraction or compressor air bleed. In an actual airplane installation, corrections must be made for these factors. The details of these corrections are too lengthy to be presented here.

As an example of the use of the performance curves presented thus far for the JT4A-3 engine, consider its operation at an airspeed of 400 kt at an altitude of 30,000 ft. For the maximum continuous thrust rating, a net thrust of

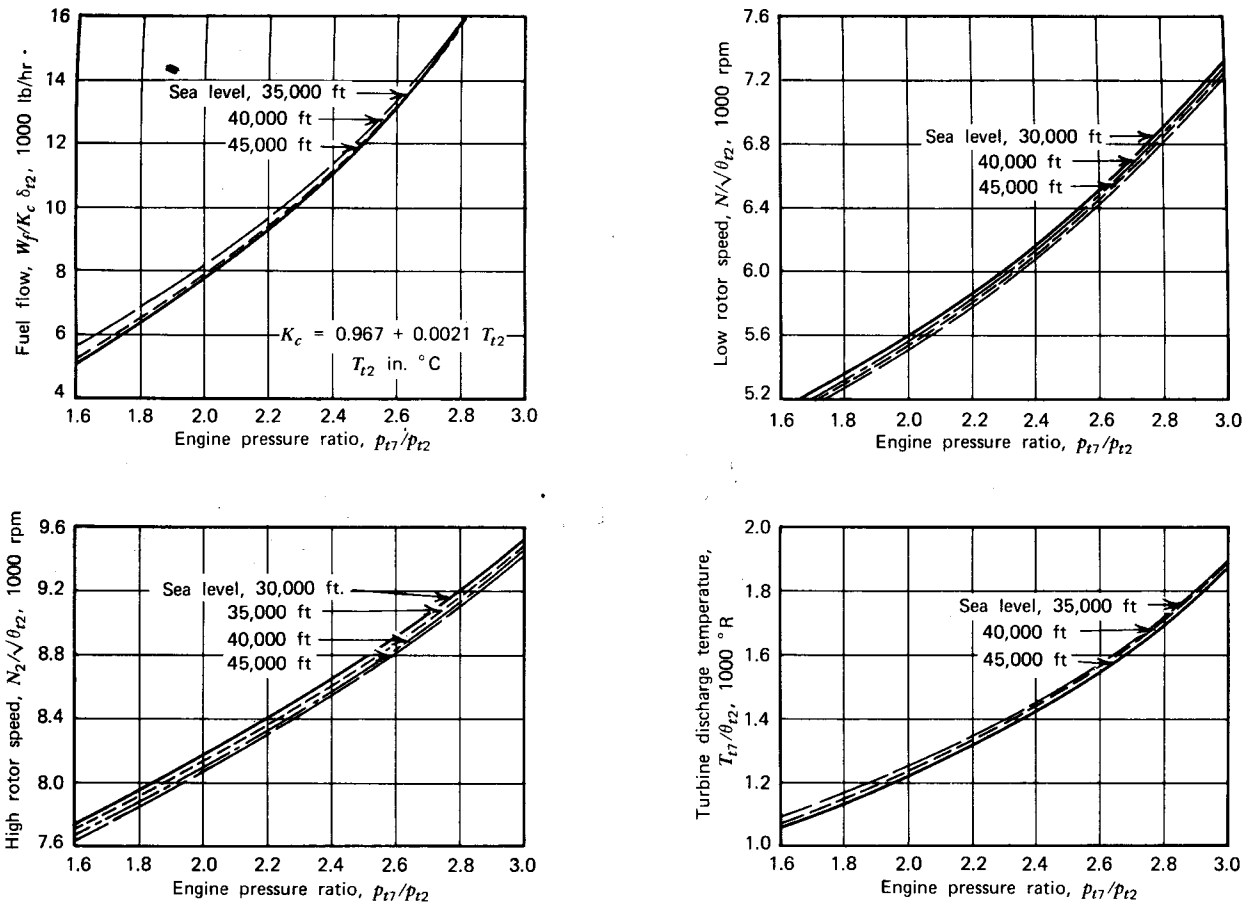

Figure 6.34a Operating curves for the JT4A-3 turbojet. (Courtesy, Pratt & Whitney.)

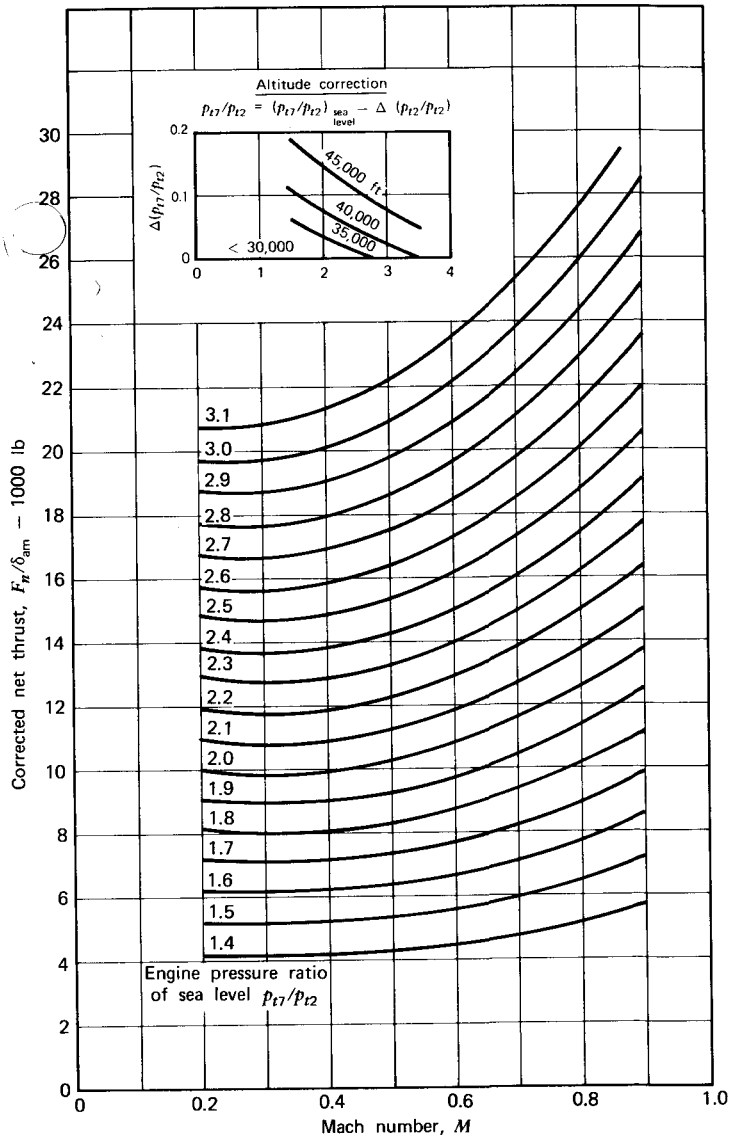

Figure 6.34b Net thrust for the JT4A-3 turbojet. One hundred percent ram recovery, standard exhaust nozzle, no airbleed, no power extraction. (Courtesy, Pratt & Whitney.)

5300 lb is read from Figure 6.32*c*. Thus, for this altitude and airspeed,

$$\frac{F_n}{\delta_{am}} = 17{,}785$$

$$M_\infty = 0.679$$

From Figure 6.34*b*,

$$\text{EPR} = 2.56$$

It follows from Figure 6.34*a* that

$$\frac{N_1}{\sqrt{\theta_{t2}}} = 6420 \text{ rpm}$$

$$\frac{N_2}{\sqrt{\theta_{t2}}} = 8850 \text{ rpm}$$

$$\frac{T_{t7}}{\theta_{t2}} = 1550 \text{ °R}$$

$$\frac{W_f}{K_c \delta_{t2}} = 12{,}700 \text{ lb/hr}$$

where N_1 = rpm of low-pressure compressor and turbine, N_2 = rpm of high-pressure compressor and turbine, and K_c = correction factor yet to be read from Figure 6.34*a*. At 30,000 ft, $\theta = 0.794$ and $\delta = 0.298$. Equations 6.87 and 6.88 give values of

$$\theta_{t2} = 0.867$$

$$\delta_{t2} = 0.406$$

From the preceding θ_{t2}, $T_{t2} = -23$ °C, so that $K_c = 0.915$. The actual values for the operating parameters can now be determined as

$$N_1 = 5978 \text{ rpm}$$

$$N_2 = 8240 \text{ rpm}$$

$$T_{t7} = 473 \text{ °C}$$

$$W_f = 4718 \text{ lb/hr}$$

Now consider operation at standard sea level conditions at this same Mach number and thrust rating. For this case, V equals 448 kt which gives a net thrust of 10,500 lb. From Figure 6.32*a*. Using the same procedure as that followed at 30,000 ft gives, in order,

$$\text{EPR} = 1.92$$

$$\frac{W_f}{K_c \delta_{t2}} = 7250$$

$$\frac{N_1}{\sqrt{\theta_{t2}}} = 5490$$

$$\frac{N_2}{\sqrt{\theta_{t2}}} = 8070$$

$$\frac{T_{7t}}{\theta_{t2}} = 1190$$

$$\delta_{t2} = 1.362$$

$$\theta_{t2} = 1.092$$

Hence,

$$N_1 = 5737 \text{ rpm}$$

$$N_2 = 8433 \text{ rpm}$$

$$T_{t7} = 449\,^{\circ}\text{C}$$

$$W_f = 10{,}418 \text{ lb/hr}$$

Note that the engine rotational speeds and exhaust gas temperature are approximately the same in both cases. Indeed, if other speeds and altitudes at the maximum thrust rating are examined, N_1, N_2, and T_{t7} values approximately equal to those just calculated are found. Thus the thrust available from a turbojet engine at a given speed and altitude depends on the maximum stress and temperature levels that can be tolerated by the engine materials. As

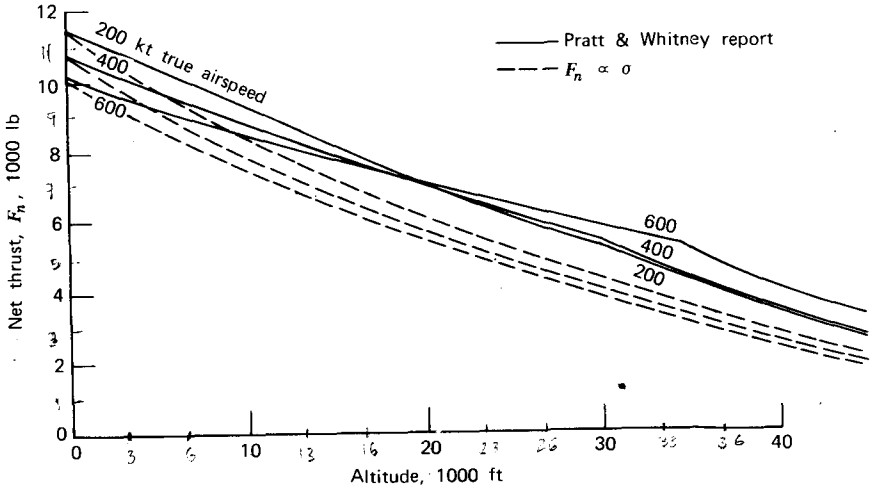

Figure 6.35 Estimated net thrust for the JT4A-3 turbojet engine at normal and maximum continuous ratings. (Courtesy, Pratt & Whitney.)

a result, the net thrust of a turbojet will not decrease with altitude in proportion to the density ratio, as with piston engines. As a rough approximation, one can assume F_n to be proportional to σ but, in practice, F_n will not decrease with altitude as rapidly as this approximation predicts. For the example just presented, one might predict a net thrust at 30,000 ft at 400 kt based on σ and the SSL value of F_n of 3941 lb. This value is 25.6% lower than the rated value previously noted. To illustrate further the accuracy of the approximation, Figure 6.35 presents the rated maximum continuous thrust at 200,400 and 600 kt as a function of altitude and compares this thrust with that obtained by multiplying the sea level values by σ. The approximation to F_n is seen to improve for the lower airspeeds and certainly predicts the proper trend. However, at the higher altitudes, the differences between the thrust curves are significant at all airspeeds.

Turbofan

The Pratt & Whitney JT9D-7A is representative of a modern high bypass turbofan engine. This engine has a dry weight of 8850 lb (39,365 N) and delivers a maximum continuous static thrust at SSL of 39,650 lb (176,363 N). The static dry takeoff rating of 45,500 lb (202,384 N) is flat rated up to 27 °C (80 °F). The diameter of the engine is 2.43 m (95.6 in.) with a length of 3.92 m (154.2 in.). The compressor incorporates one fan stage, three low-pressure stages, and eleven high-pressure stages. The turbine has two high-pressure stages and four low-pressure stages. The bypass ratio equals 5.1 at the dry takeoff rating, with a total airflow of 1545 lb/sec (6872 N/s). The dash 7A model of the JT9D is installed on several versions of the Boeing 747, including the 747-100, -200B, C, F, 747 SR, and 747 SP.

Figure 6.36 presents the rated takeoff thrust for this engine as a function of ambient temperature for altitudes up to 6000 ft. The net thrust is seen to drop approximately 14% in going from sea level to 6000 ft and to decrease rapidly with increasing Mach number.

Figures 6.37 and 6.38 give the rated maximum climb thrust and cruise thrust, respectively, as a function of Mach number for constant values of altitude up to 45,000 ft (13,700 m). Both figures also include lines of constant TSFC values. At the lower altitudes, the net thrust is seen to decrease rapidly as the Mach number increases. However, at the higher altitudes, T is nearly constant and even increases slightly with Mach number above 30,000 ft and M values greater than 0.7.

The range of operating Mach number decreases in the preceding figures at the higher altitudes. This is a reflection of the limitations of the operating envelope presented in Figure 6.39. Such an envelope can result from several limitations, including temperature restrictions, stress limits, surge, and compressor stall.

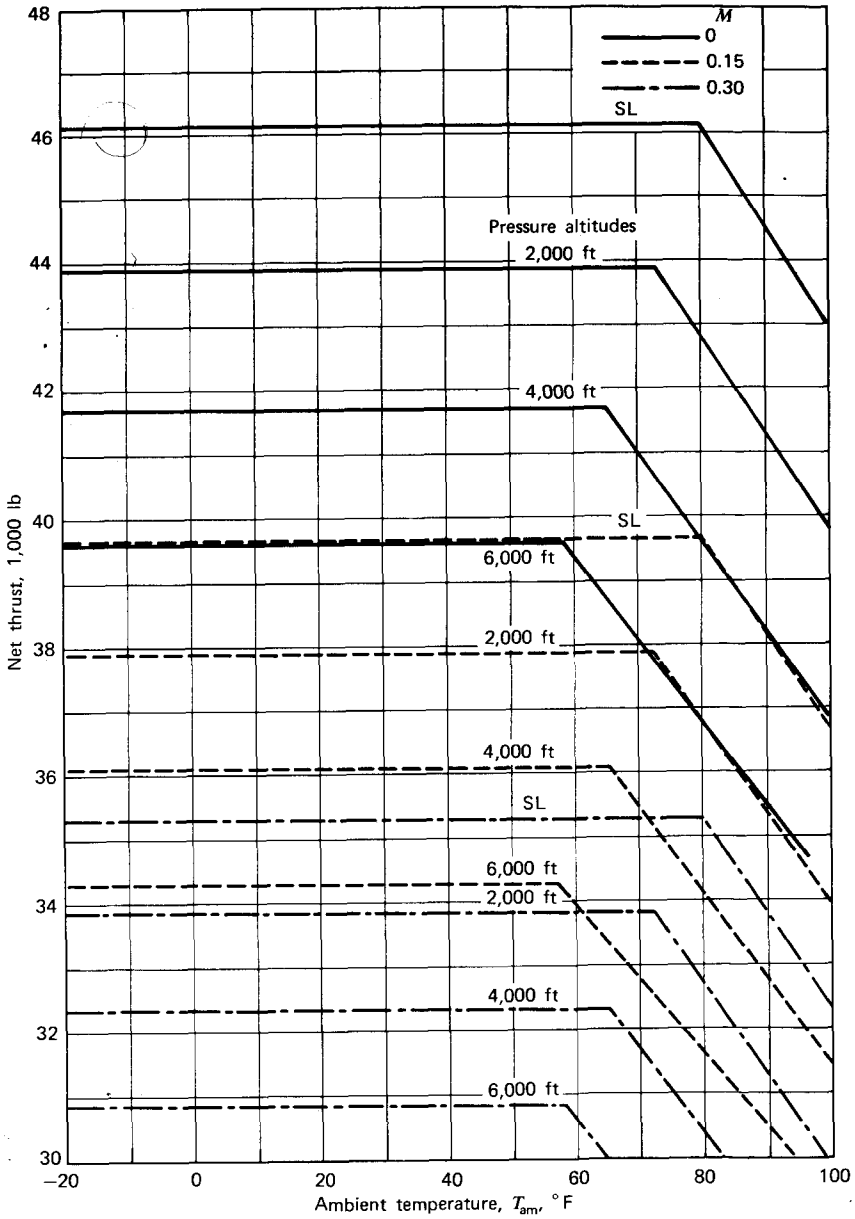

Figure 6.36 JT9D-7A net takeoff thrust. Dry, 100% ram recovery, no airbleed, no power extraction, Pratt & Whitney Aircraft standard exhaust. (Courtesy, Pratt & Whitney.)

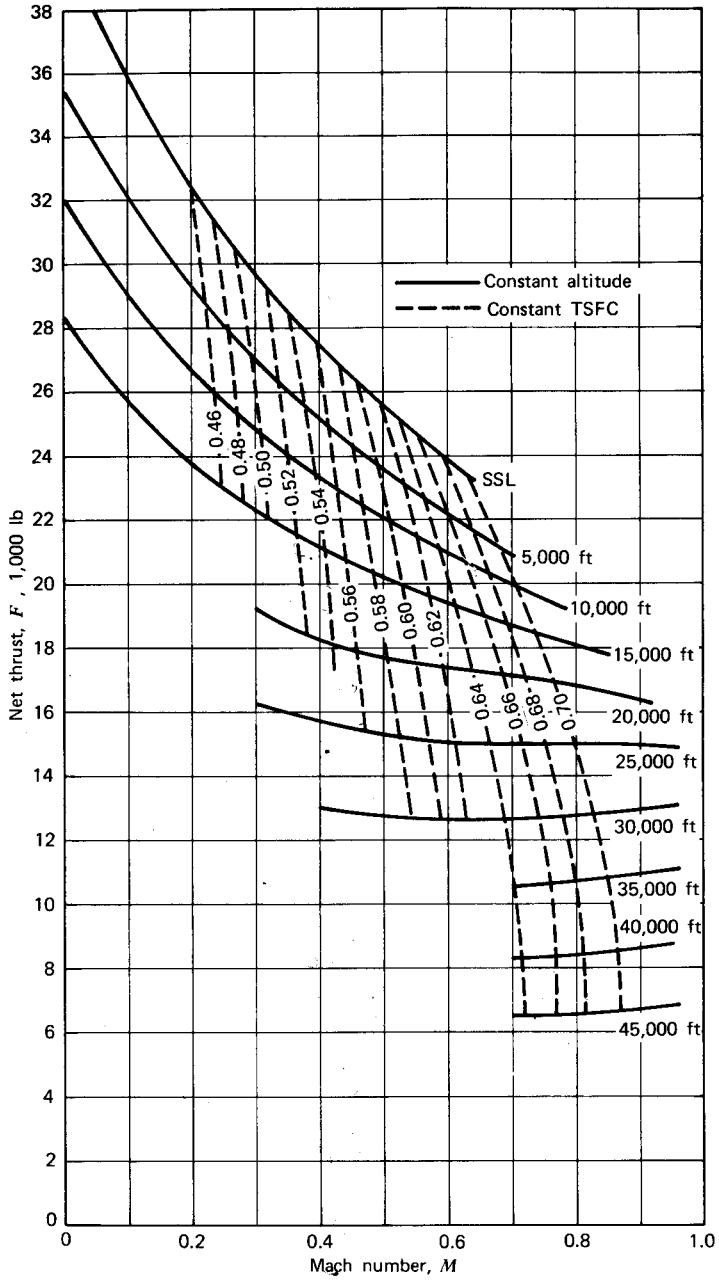

Figure 6.37 JT9D-7A maximum climb thrust. One hundred percent ram recovery, no airbleed, no power extraction, Pratt & Whitney Aircraft reference exhaust system, all curves for ICAO standard day +10°C and below. (Courtesy, Pratt & Whitney.)

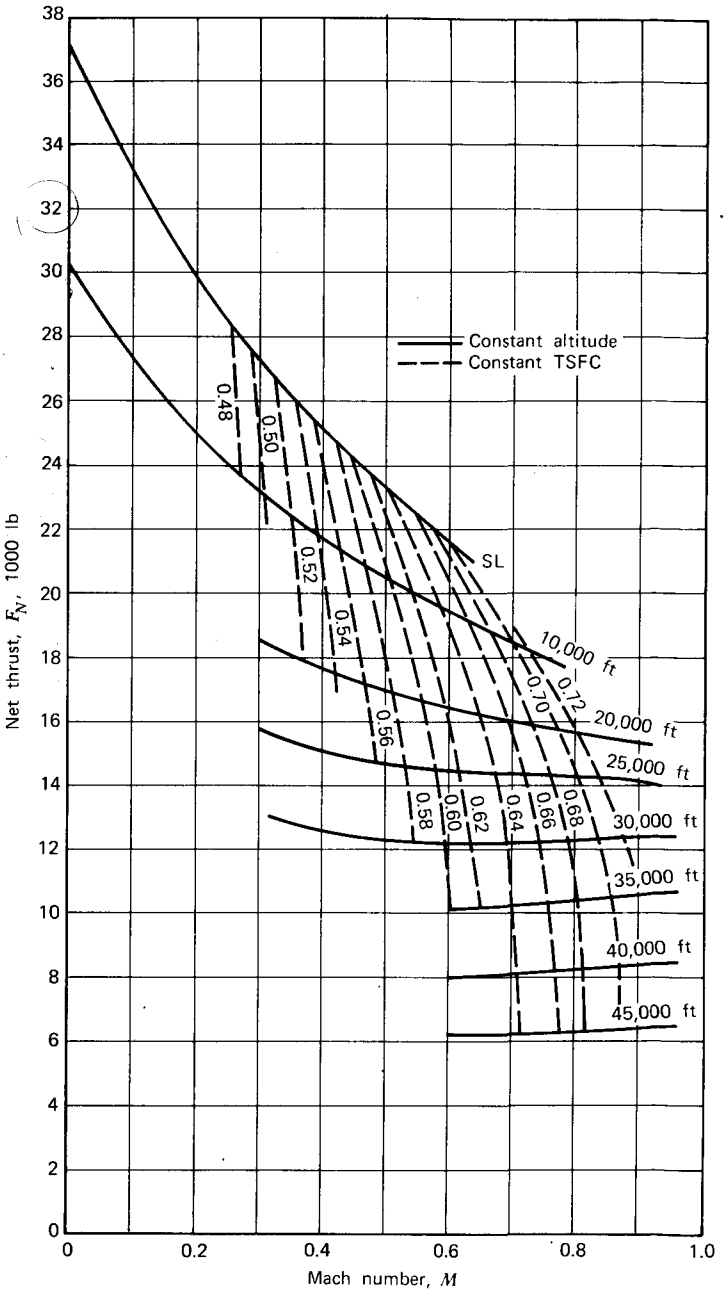

Figure 6.38 JT9D-7A maximum cruise thrust. One hundred percent ram recovery, no airbleed, no power extraction, Pratt & Whitney Aircraft reference exhaust system, all curves for ICAO standard day +10°C and below. (Courtesy, Pratt & Whitney.)

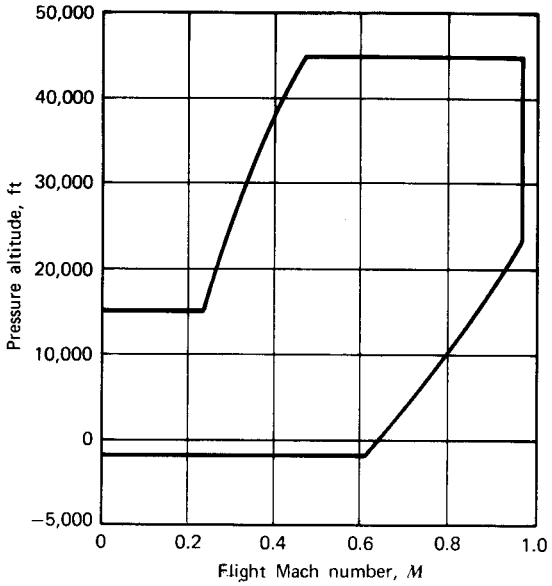

Figure 6.39 JT9D turbofan engine. Estimated engine operating envelope. One hundred percent ram recovery. (Courtesy, Pratt & Whitney.)

Temperature restrictions are normally associated with the turbine inlet temperature (TIT). High-pressure turbines in the latest high bypass turbofan engines operate with gas temperatures in the 2000 to 2300 °F (1094 to 1260 °C) range. Various techniques have been developed that keep blade metal temperatures equal to those of uncooled blades used in earlier turbine designs. Normally, blade cooling is only required in the first or first and second turbine stages. After these stages, sufficient energy has been extracted from the burner exhaust to cool the hot gases to a tolerable level.

Three forms of air cooling are described in Reference 6.7; these are used singly or in combination, depending on the local temperatures. The air for this cooling is bleed air taken from the compressor section. Even though this air is warmer than ambient air, it is still considerably cooler than the burner exhaust.

Convection Cooling Cooling air flows inside the turbine vane or blade through serpentine paths and exits through the blade tip or through holes in the trailing edge. This form of cooling is limited to blades and vanes in the area of the lower gas temperatures.

Impingement Cooling Impingement cooling is a form of convection cooling, accomplished by directing cooling air against the inside surface of the airfoil through small, internal, high-velocity air jets. Impingement cooling

is concentrated mostly at critical sections, such as the leading edges of the vanes and blades.

Film Cooling Film cooling is a process whereby a layer of cooling air is maintained between the high-temperature gases and the external surfaces of the turbine blades and vanes.

Of the three forms of air cooling, film cooling is the most effective and the least demanding as far as airflow is concerned.

These types of cooling are illustrated in Figure 6.40, which shows their application to both stationary and rotating turbine stages.

Surge and compressor stall are related but are not the same thing. Surge refers to oscillations in the rotational speed of the entire engine. This surge is usually related to compressor stall, where the local angles of attack of the rotor blades, for various reasons, achieve sufficiently high values to cause local stalling. Some of these reasons include inlet airflow distortion from gusts, inlet design or uncoordinated maneuvering, rapid power changes, water ingestion, and Reynolds number effects.

A typical compressor map is given in Figure 6.41. This map shows qualitatively the relationship among the corrected rpm, corrected airflow, and total pressure ratio across the compressor. A small insert in the figure illustrates an airfoil on the compressor rotor under the influence of two velocities, one proportional to the airflow and the other proportional to the rotational speed. At a fixed blade angle, the angle of attack of this section obviously increases as N increases or W_a decreases. This is reflected in the map, which shows one approaching the surge zone as N increases for a constant W_a or as W_a decreases for a constant N.

As the altitude increases, the surge zone drops down, mainly because of Reynolds number effects. At the same time, the steady-state operating line moves up. Thus compressor stall and surge are more likely to be encountered at the higher altitudes.

Accelerating the engine can also lead to compressor stall. Suppose, in attempting to get from the steady operating point A to point B, the rpm is suddenly increased. The airplane may be unable to accelerate rapidly enough to follow the rpm, so the airflow is less than the steady-state value. Surge can be alleviated by unloading the compressor during certain operating conditions. This is accomplished by bleeding air near the middle or end of the compressor. Stators having variable blade angles are also used to delay compressor rotor blade stall. The JT9D, for example, has variable stators automatically positioned by hydraulic actuators on the first four stages of the high-pressure compressor. Their function is to provide an adequate surge margin during engine starting, acceleration, and partial thrust operation.

A small, modern turbofan engine typical of others of this size is shown in Figure 6.42*a* and 6.42*b*. Only the rotating assemblies of the JT15D-1 engine

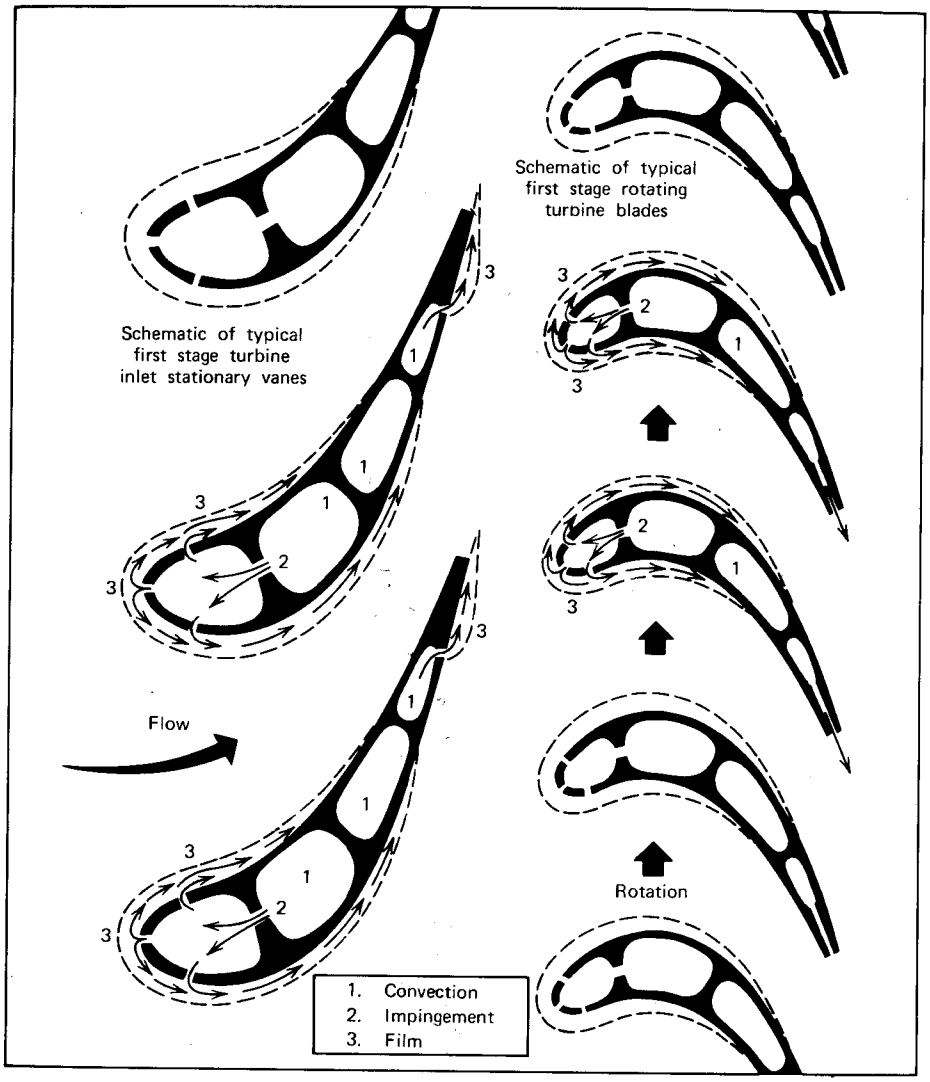

Figure 6.40 Types of air cooling of turbine vanes and blades. (Courtesy General Electric Co.)

are shown in order to emphasize its relative simplicity and general configuration. The JT15D-9 is a growth version of the -1 model and was achieved by adding one additional axial stage to the low compressor. Although this decreases the bypass ratio, the pressure ratio across the compressor is increased so that the rated thrust of the -4 engine is approximately 14%

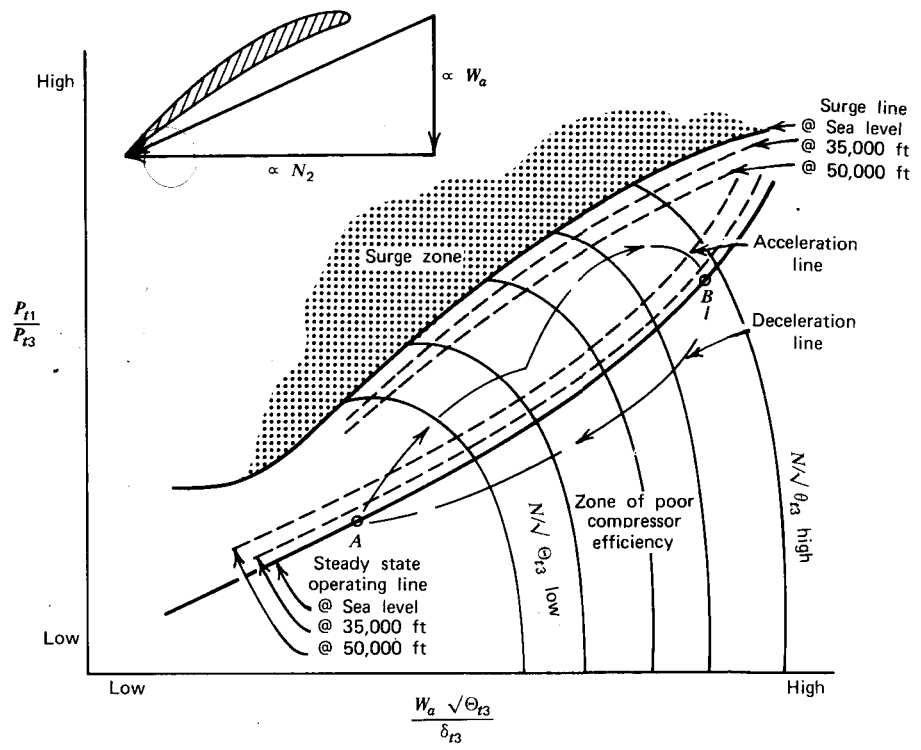

Figure 6.41 Typical compressor map.

greater than that of the -1 engine. Notice that the high-pressure section of the compressor for the JT15D employs a centrifugal compressor similar to that of the Garrett TPE 331/T76 engine. Specifics on the JT15D-1 and -4 turbofan engines are given in Table 6.2.

Turboprop

The PT6A-27 turboprop engine manufactured by Pratt & Whitney Aircraft of Canada, Ltd. is representative of the latest technology for turboprop engines of this size. Airplanes in which this engine is installed include the Beech 99A, the de Havilland Twin Otter, and the Pilatus Turbo Porter. The arrangement of this engine is shown in Figure 6.43. Compared to a turbojet, the core engine is reversed with the air being taken toward the rear of the engine and flowing forward through the compressor, burner, turbines, and then exhausted through stacks at the front of the engine.

A typical nacelle installation for this engine is illustrated in Figure 6.44.

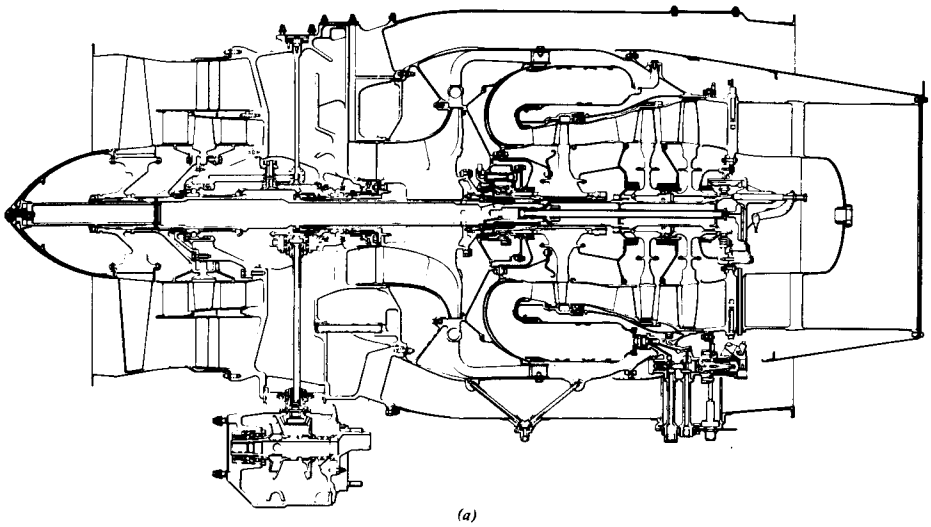

(a)

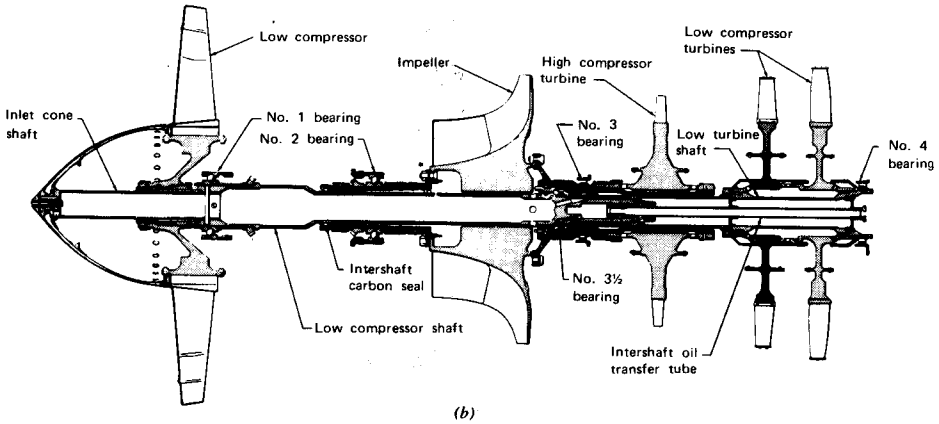

(b)

Figure 6.42 JT15D-4 Engine. Rotating components for the JT15D-4 engine.

An inlet duct channels the air to the rear of the engine, where it must turn in order to enter the engine. In good weather, the vane is raised from the position shown to lie flush with the surface above it, and the bypass door is closed. When ice or other types of particles are encountered, the bypass door is opened and the vane is lowered, as pictured. The air-particle mixture is then deflected downward. Because of their inertia, the heavier particles continue

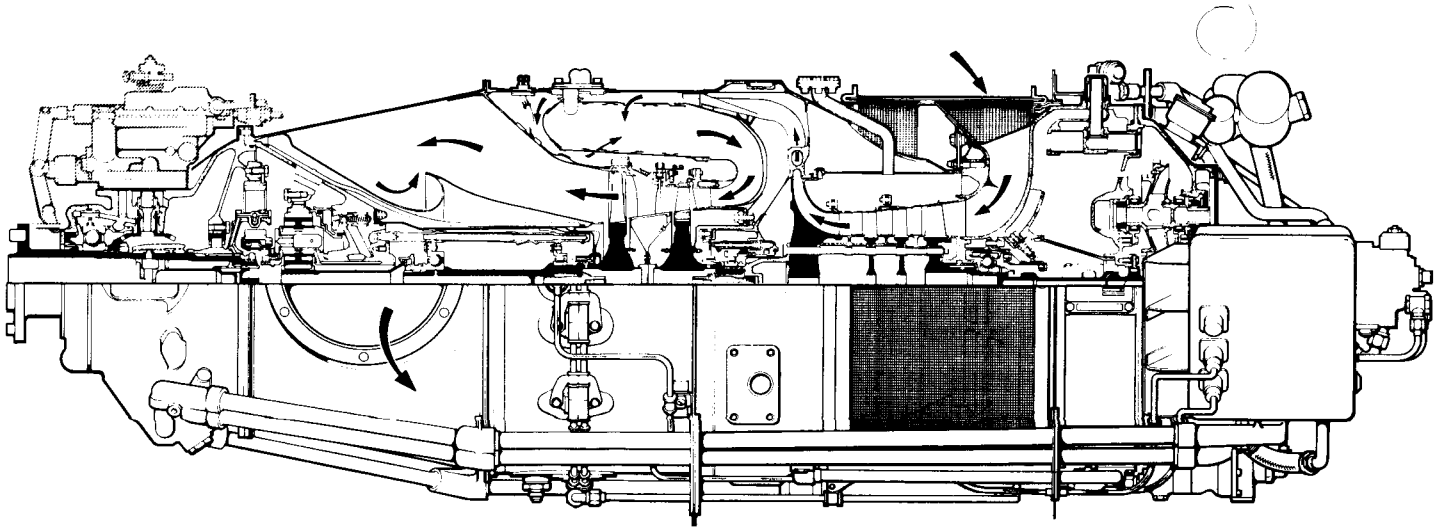

Figure 6.43 The PT6A-27 turboprop engine. (Courtesy Pratt & Whitney of Canada.)

Table 6.2 Characteristics of the JT15D Turbofan Engine Manufactured by Pratt & Whitney Aircraft of Canada, Ltd.

Installation	JT15D-1 Cessna Citation	JT15D-4 Cessna Citation II Aerospatiale Corvette
Thrust—takeoff, lb	2,200	2,500
Maximum continuous	2,090	2,375
Maximum cruise	2,065	2,345
TSFC—takeoff	0.540	0.562
Maximum continuous	0.538	0.556
Maximum cruise	0.537	0.555
Mass flow, lb/sec	75	77
Bypass ratio	3.3	2.7
Pressure ratio	8.5	10.1
Engine dry weight, lb	514	557
Engine diameter, in.	27	27
Engine length, in.	59	63
Compressor stages	1 fan, 1 centrifugal	1 fan, 1 axial, 1 centrifugal
Turbine stages	2 power, 1 compressor	2 power, 1 compressor

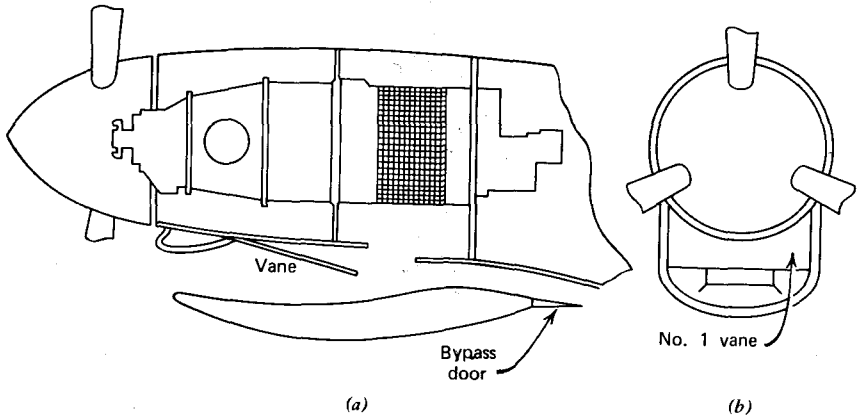

Figure 6.44 Basic inertial separator design. (a) Side view. (b) Front view.

on out through the bypass door, while the air is turned and drawn into the engine.

The specifications for this engine are presented in Table 6.3, and its performance is given in Figures 6.45 and 6.46*a* and 6.46*b*. These curves, taken from the installation handbook, assume no losses. Figures 6.45 and 6.46*a* are

Table 6.3 PT6A-27 Turboprop Engine Specifications

Static Sea Level Ratings	shp	eshp	SFC (lb/eshp/hr)
takeoff	680	715	0.602
Maximum continuous	680	715	0.602
Maximum climb	620	652	0.612
Maximum cruise	620	652	0.612
Mass flow	6.1 lb/sec		
Pressure ratio	6.3		
Dry weight	300 lb		
Diameter	19 in.		
Length	62 in.		
Compressor—3 axial and 1 centrifugal stage			
Turbine—1 power stage and 1 compressor stage			

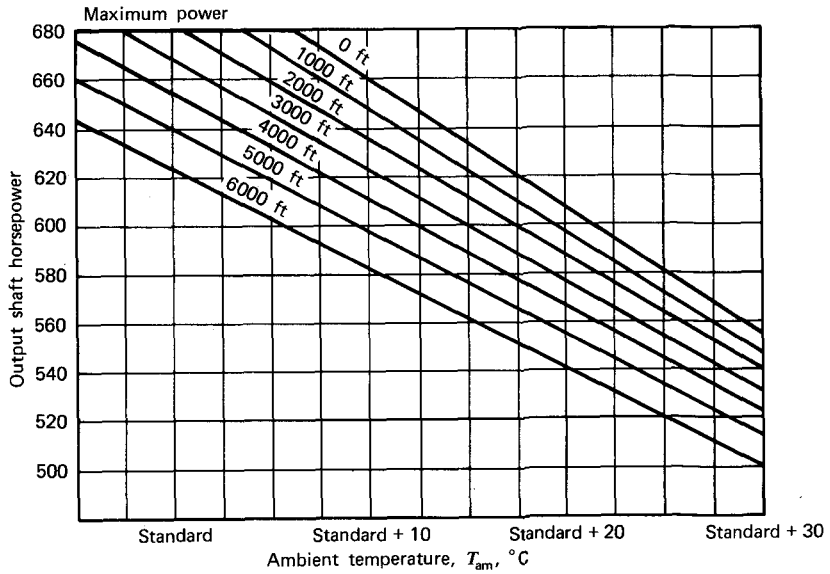

Figure 6.45 PT6A-27 takeoff performance. Prop speed—2200 rpm. (Courtesy, Pratt & Whitney of Canada.)

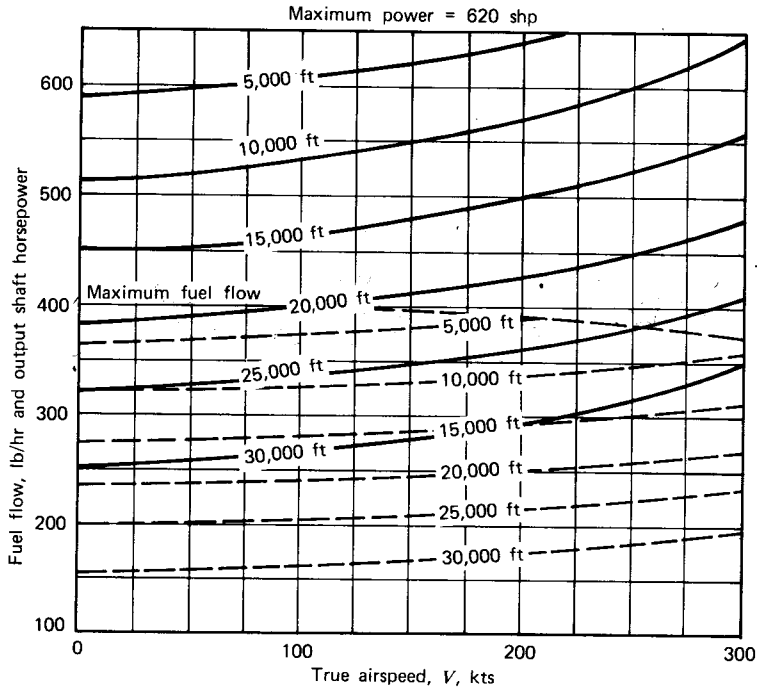

Figure 6.46a PT6A-27 maximum cruise performance. Prop speed—2200 rpm. (Courtesy, Pratt & Whitney of Canada.)

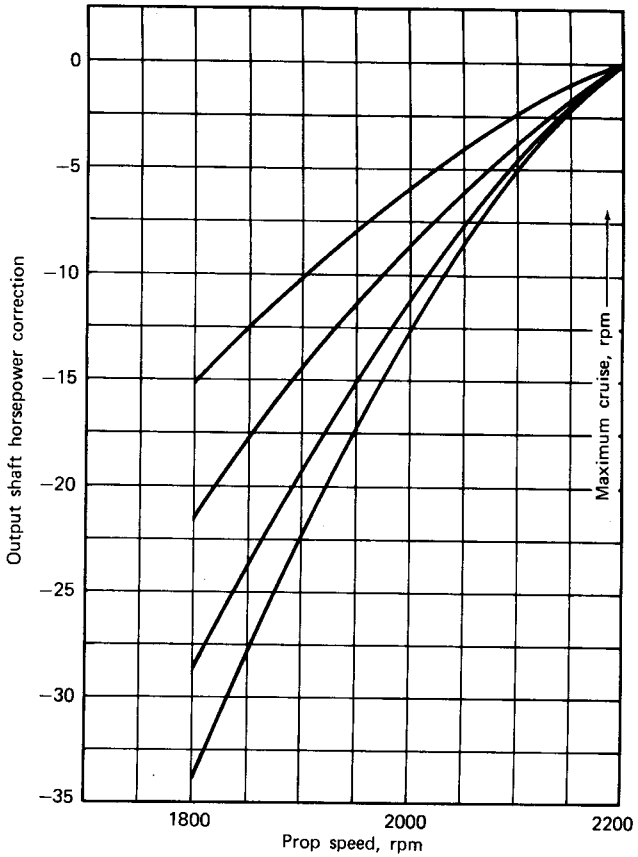

Figure 6.46b PT6A-27/28 maximum cruise data. Approximate Δ SHP versus prop speed, 100 to 300 kts. (Courtesy, Pratt & Whitney of Canada.)

for the rated propeller rpm of 2200, while Figure 6.46*b* presents a correction to the power for operation at lower rpm values. Only the maximum cruise and maximum takeoff ratings are given, since these are the same as the maximum climb and maximum continuous ratings, respectively. The power curves are for actual shaft power and do not include an effective power increment for the residual thrust. Statically, from Table 6.3, this thrust appears to equal approximately 80 lb. This represents about a 5% correction to the shaft power.

INSTALLATION LOSSES

The performance curves that have been presented for the JT4A-3 turbojet, the JT9D-7A turbofan, and the PT6A-27 turboprop are all optimistic, since they do not include installation losses. These losses result from:

- Total pressure loss in the inlet ducting.
- Total pressure loss in the exhaust nozzle.
- Bleed air requirements.
- Power extraction for accessories.
- Deicing requirements.

Methods for calculating these losses are not included here because of the extensive information that is required. In practice, an engine manufacturer supplies a computer deck to the airframe manufacturer in order to estimate corrections to the engine performance resulting from installation losses. Typically, these losses equal approximately 0.4% for inlet, 5% for antiicing, and 8 to 22 hp/engine for accessories.

TRENDS IN AIRCRAFT PROPULSION

The title of this section was borrowed directly from an interesting paper (Ref. 6.11) by Rosen. From the preceding material and examples of specific engines, it is hoped that you now have a pretty good feeling of engine performance capabilities in the 1978 time frame. Let us now consider what developments we might expect in the near future. Our considerations will be limited to subsonic airspeeds. To do otherwise is beyond the limitations of this text. It may also be beyond the price that society is willing to pay for speed with the emphasis on fuel economy and noise.

Regarding fuel consumption, Figure 6.47 presents the static TSFC as a function of net thrust for turbojets with afterburners, turbojets, and turbofans. The points represent engines that are currently operational. Generally,

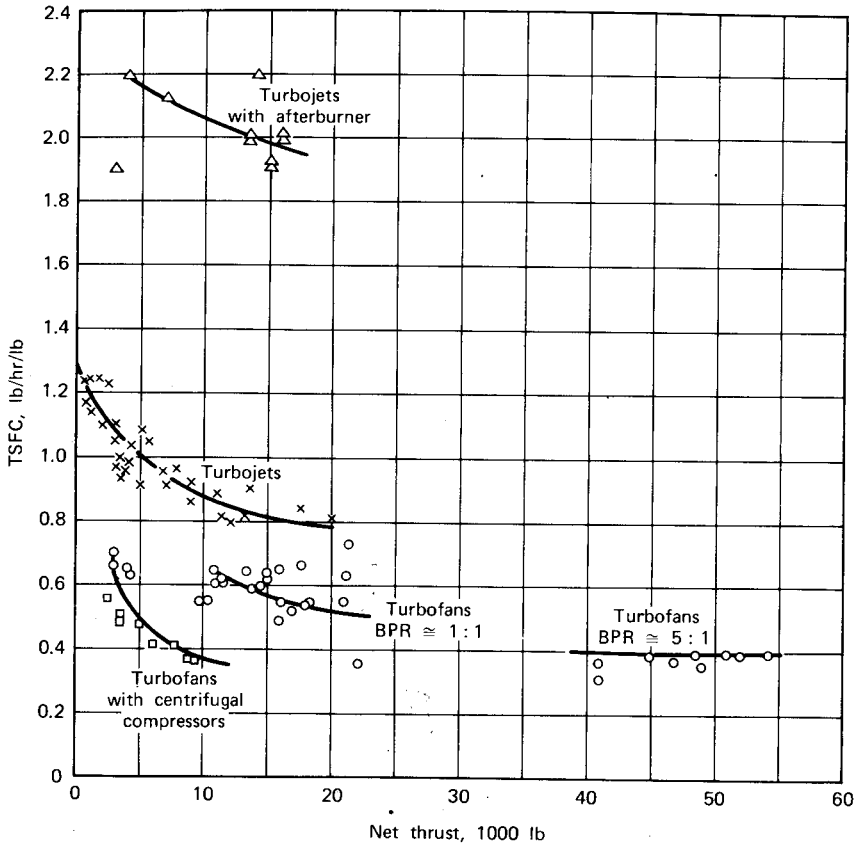

Figure 6.47 Static specific fuel consumption for turbojet and turbofan engines.

there is a tendency, as with piston engines, for the TSFC to improve with size for any given engine type, particularly at the lowest thrust values. However, the important point is the obvious gain to be realized by going to higher bypass ratios. This point is emphasized by Rosen in a slightly different manner, as shown in Figure 6.48 (taken from Ref. 6.11).

• It is interesting that, in a sense, the application of gas turbines to commercial aircraft propulsion has nearly completed a cycle. The sudden transition to the turbojet for commercial transportation in the 1950s introduced the air traveler to above-the-weather flying at significantly higher speeds with a power plant that was almost vibrationless. In doing so, the bypass ratio went from a high value, where most of the air goes through the propulsor as compared to the air that goes through the power plant, to a value of zero, where all of the air goes through the power plant. Over the years, the

BPR has gradually increased, *but at no sacrifice in comfort or convenience to the passenger.* Indeed, today's high bypass ratio turbofan is quieter, consumes less fuel, and is relatively much lighter (Figure 6.49) than the turbojet.

As Rosen notes in Figures 6.48 and 6.49, for a given BPR, there is a gradual improvement in engine performance with time. This improvement is the result of better materials and cooling techniques, which allow operation at higher pressure ratios and turbine inlet temperatures. It would therefore appear that improved propulsion efficiency in the future will depend on further increases in the pressure ratio, turbine inlet temperatures, and bypass ratios.

In 1971, Rosen was a fairly accurate soothsayer when he targeted turbine inlet temperatures of 2700 °F (1480 °C) and pressure ratios of 30:1 in the 1980s. We are not there yet, but the numbers are getting close. He also recommended a further increase in the bypass ratio by advocating a so-called prop-fan configuration. This configuration is a controllable pitch, ducted fan (or one might call it a propeller) with 8 to 12 blades, a 1.1 to 1.2 pressure ratio across the fan, and a tip speed of around 750 fps (230 m/s).

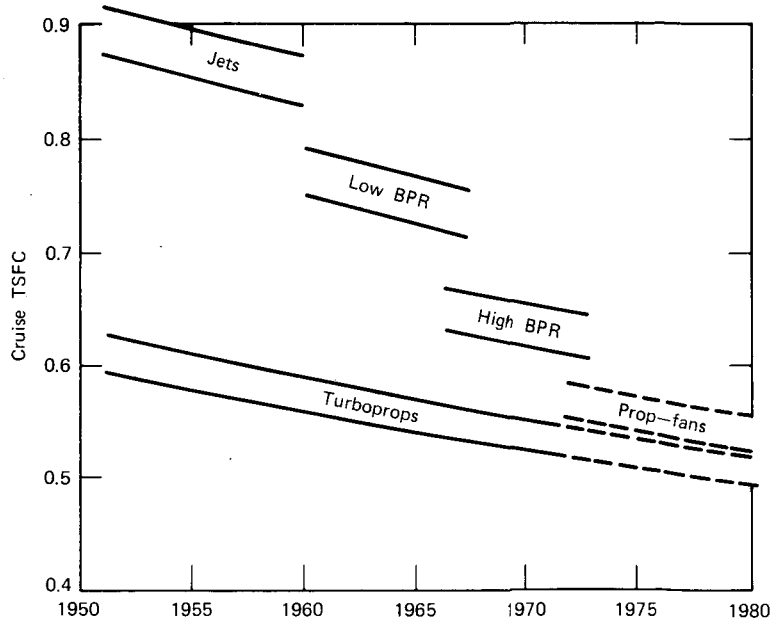

Figure 6.48 Specific fuel consumption trend. (George Rosen, "Trends in Aircraft Propulsion," CASI Paper No. 72/10, 12th Anglo-American Aeronautical Conference, Canadian Aeronautics and Space Institute, 1971. Reprinted by permission of Canadian Aeronautics and Space Institute.)

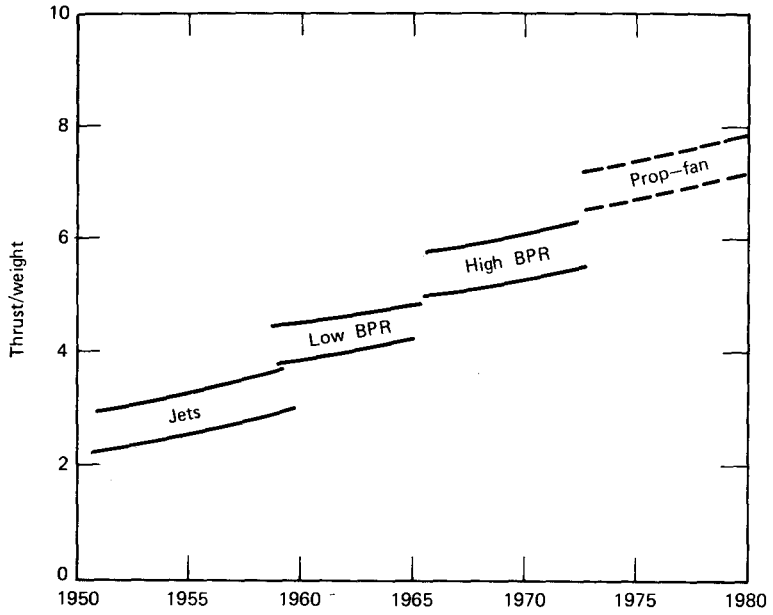

Figure 6.49 Specific thrust trend. (George Rosen, "Trends in Aircraft Propulsion," CASI Paper No. 72/10, 12th Anglo-American Aeronautical Conference, Canadian Aeronautics and Space Institute, 1971. Reprinted by permission of Canadian Aeronautics and Space Institute.)

More recently, NASA has been taking another look at propellers for application to high subsonic speeds. Reference 6.12 discusses the design philosophy of these propellers and reports on some early test results. These propellers are multibladed and incorporate thin, transonic airfoil sections. One such propeller that has been tested by NASA's Lewis Research Center is shown in Figure 6.50. Preliminary test data obtained in their supersonic wind tunnel and presented here as Figure 6.51 appear promising.

The design characteristics for this propeller are:

0.8 cruise Mach number.
10.7 km (35,000 ft) cruise altitude.
8 blades.
203 activity factor per blade.
301 kW/m^2 (37.5 hp/ft^2) power loading.
243.8 m/s (800 fps) tip speed.
0.08 integrated design lift coefficient.

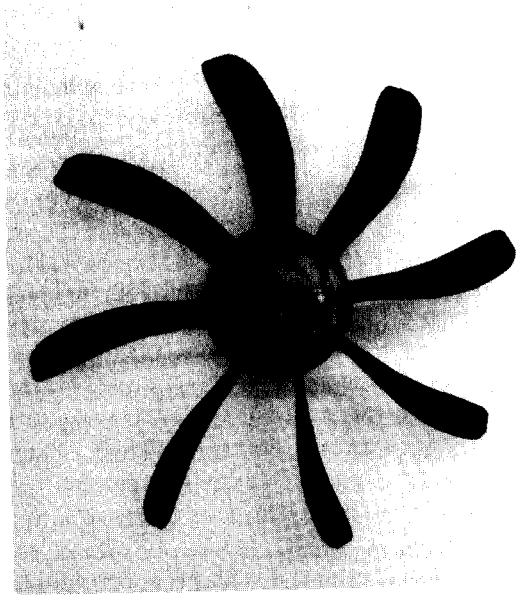

Figure 6.50 Advanced turboprop design for operation at 0.8 Mach number. (Courtesy of the NASA Lewis Research Center.)

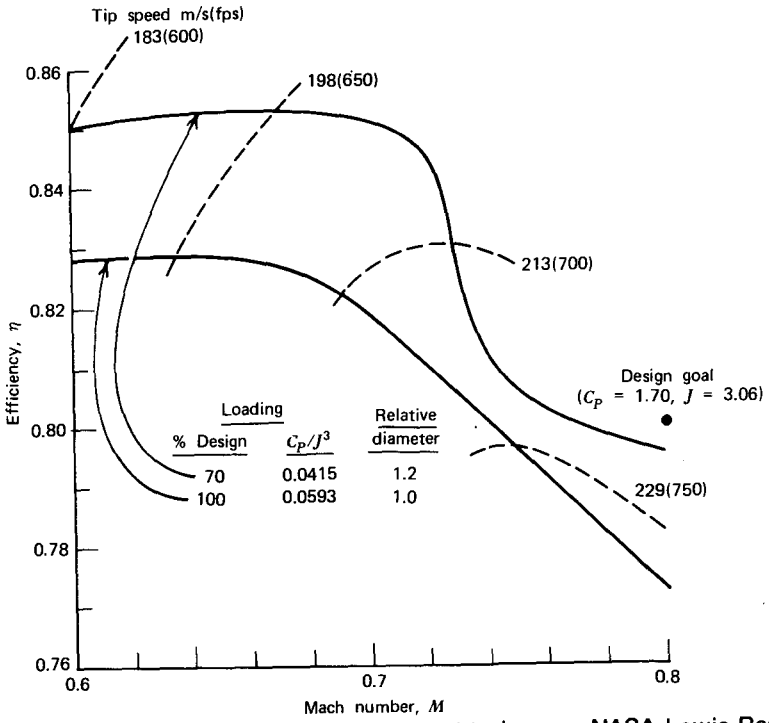

Figure 6.51 Preliminary test data on advanced turboprop NASA Lewis Research Center 8- by 6-ft wind tunnel.

If this propeller meets its design goal of 80% efficiency at 0.8 Mach number, this would represent a reduction of approximately 30% in fuel consumption compared to existing turbofan engines.

PROBLEMS

6.1 A light airplane powered by the Lycoming 0-360 engine (Figure 6.3) and the propeller of Figure 6.15 is cruising at a pressure altitude of 1500 m. The OAT is 20 °C. In addition, rpm = 2400, MAP = 61 cm hg, and IAS = 60 m/s. Calculate the fuel flow and propeller thrust.

6.2 An airplane powered by a single JT4A-3 turbo jet engine has a maximum cruising speed of 500 kt at a standard altitude of 6000 m. What is the airplane's drag in Newtons and at what rate is fuel being expended?

6.3 A JT4A-3 turbojet engine is operating at a pressure altitude of 12,000 m. The ambient temperature is −70 °C. At its maximum continuous thrust rating, calculate fuel flow, turbine discharge temperature, and high rotor rpm at a true airspeed of 450 kts.

6.4 Four JT9D-7A turbofan engines power a transport airplane. At maximum climb power, at what rate is fuel being consumed as the airplane climbs through an altitude of 3500 m at a true airspeed of 300 kt? Assume a standard atmosphere and neglect installation losses.

6.5 Determine the maximum cruise thrust and fuel flow for the JT9-7A turbofan engine at a standard altitude of 9 km and an indicated airspeed of 130 m/s.

6.6 From the family of propellers represented by Figures 6.11, 6.12, 6.13, 6.14, and 6.21, select the propeller diameter to operate on the PT6A-27 turboprop engine at a standard altitude of 25,000 ft, 2200 rpm, and a true airspeed of 200 kt.

6.7 For the propeller selected in Problem 6.6, calculate the takeoff thrust at standard sea level conditions.

REFERENCES

6.1 Torell, Bruce N., *The Significance of Propulsion in Commercial Aircraft Productivity*, The Seventeenth Sir Charles Kingsford-Smith Memorial Lecture, September 15, 1975, Royal Aeronautical Society, Sydney, Australia.

6.2 Wilkinson, Paul A., *Aircraft Engines of the World*, Published annually by Paul H. Wilkinson, Washington, D.C.

6.3 Hartman, E. P., and Biermann, David, *The Aerodynamic Characteristics of Full-Scale Propellers Having 2, 3, and 4 Blades of Clark Y and R.A.F. 6 Airfoil Sections*, NACA Report 640, November 1937.

6.4 Neumann, G., *Powerplants—Past, Present and Future*, The Fifth William Littlewoval Memorial Lecture, SAE SP-398, 1975.
6.5 Taylor, John W. R., and Munson, Kenneth, *History of Aviation*, Crown, New York, 1972.
6.6 Anonymous, *The Aircraft Gas Turbine Engine and its Operation*, PWA Operating Instruction 200, Pratt & Whitney Aircraft, East Hartford, Conn., June 1952 (rewritten August 1970).
6.7 Anonymous, *Aircraft Gas Turbine Guide*, The General Electric Aircraft Engine Group, Cincinnati, Ohio/Lynn, Mass., AEG-607, April 1972.
6.8 Anonymous, *JT9D Commercial Turbofan Engine Installation Handbook*, Pratt & Whitney Aircraft, East Hartford, Conn., March 1967.
6.9 Hesse, W. J., and Mumford, N. V. S., *Jet Propulsion for Aerospace Applications*, 2nd edition, Pitman, New York, 1964.
6.10 Anonymous, *PT6 Gas Turbine Installation Handbook*, Pratt & Whitney Aircraft of Canada, Longueuil, Quebec, Canada, revised July 1977.
6.11 Rosen, George, *Trends in Aircraft Propulsion*, CASI Paper No. 72/10, 12th Anglo-American Aeronautical Conference, July 1971.
6.12 Mikkelson, D. C., Blaha, B. J., Mitchell, G. A., and Wikete, J. E., *Design and Performance of Energy Efficient Propellers for Mach 0.8 Cruise*, NASA TM X-73612, presented at 1977 National Business Aircraft Meeting, Wichita, Kansas, March 29, 1977 (SAE Paper No. 770458).

SEVEN
AIRPLANE PERFORMANCE

When a customer buys an airplane, whether it be a private individual, a corporation, an airline, or the military, the buyer wants to know what the airplane will do. How fast will it fly, how high, and how far? How long a runway is required from which the airplane will operate? How expensive will it be to operate, and what are the operating limitations? How fast will it climb? Will it take a half hour to get up to cruising altitude or only 5 min? This chapter provides methods for answering these questions and others related to the general subject of airplane performance. The groundwork for doing so has been presented in the preceding chapters. With the use of this material, one can calculate lift, drag, and thrust. Aside from weight, these are the principle forces acting on an airplane that determine its performance. We will begin, as every flight begins, by first considering the problem of calculating the distance required to take off safely over a prescribed obstacle height.

TAKEOFF

The takeoff of an airplane certified in the transport category is illustrated in Figure 7.1. Starting from a resting position at the far left, the airplane accelerates under takeoff power. At some point the velocity exceeds the stalling speed, V_s. Beyond this point, the airplane is capable of flying. However, the airplane continues to accelerate on the ground until the *minimum control speed*, V_{mc} is reached. At this speed, if a critical engine fails, the manufacturer has demonstrated that the airplane is able to maintain straight flight at that speed with zero yaw or with a bank angle of less than 5°. Under these conditions at this speed, the required rudder force may not exceed 180 lb. Continuing to accelerate on the ground, the airplane reaches a calibrated airspeed of V_1, the *critical engine failure speed.* This speed may not be less than V_{mc} and represents the speed at which the *average* pilot could safely continue with the takeoff in the event of a critical engine failure. At a speed that can equal V_1 but that must be 5% higher than V_{mc}, the pilot rotates the airplane. This speed, V_R, is called *takeoff rotation speed.*

Because of tail interference with the ground, the angle of attack at V_R may not be sufficient to lift the airplane. The pilot therefore continues to

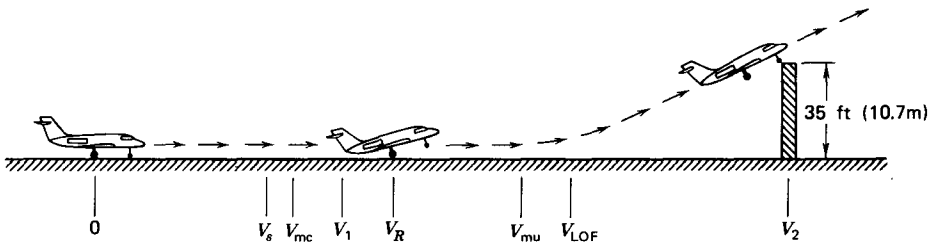

Figure 7.1 FAR Part 25 takeoff.

accelerate up to a speed of V_{mu}, the *minimum unstick speed.* At this speed, the pilot could lift the airplane off of the runway and continue the takeoff, even with one engine inoperative, without any hazardous characteristics. However, to provide an additional margin of safety, the airplane continues to accelerate to the *lift-off speed,* V_{LOF}, at which point the airplane becomes airborne. V_{LOF} must be at least 10% higher than V_{mu}, with all engines operating or 5% higher than V_{mu} with one engine inoperative. After lift-off, the airplane continues to accelerate up to the *takeoff climb speed,* V_2. V_2 is the speed attained at a height of 35 ft (10.7 m) above the ground. V_2 must be greater than 1.2 V_s in the takeoff configuration *and* 1.1 V_{mc}.

This description, applicable to the takeoff of a turbojet or turbofan transport, is in accordance with the definition of these various speeds as presented in the Federal Air Regulations (FAR) Part 25. These regulations govern the airworthiness standards for airplanes in the transport category. Similar regulations for other categories of nonmilitary airplanes can be found in FAR Part 23. The Cherokee 180, which has been used as an example in the preceding chapters, is certified under FAR Part 23. The total horizontal distance, ground roll and airborne, which is required to reach the altitude of 35 ft, starting from rest, is referred to as the FAR takeoff distance.

FAR Part 23 is simpler in specifying the takeoff procedure. For airplanes over 6000 lb (26,700 N), maximum weight in the normal, utility, and acrobatic categories, it is stated simply that the airplane must attain a speed at least 30% greater than the stalling speed with one engine out, V_{S_1}. For an airplane weighing less than 6000 lb, the regulations state simply that the takeoff should not require any exceptional piloting skill. In addition, the elevator power must be sufficient to lift the tail (for a "tail dragger") at 0.8 V_{S_1} or to raise the nose for a nose-wheel configuration at 0.85 V_{S_1}.

Ground Roll

The forces acting on an airplane during the ground roll portion of the takeoff are shown in Figure 7.2. From Newton's second law of motion,

$$T - D - \mu(W - L) = M\dot{V} \tag{7.1}$$

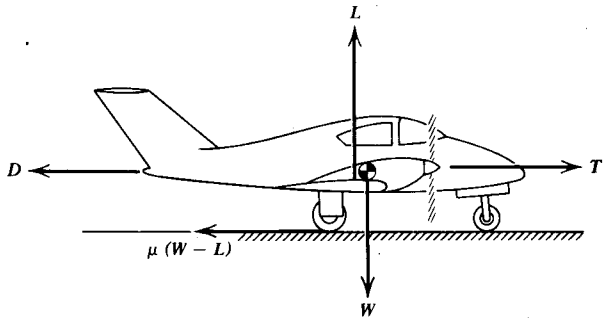

Figure 7.2 Forces on an airplane during the ground roll.

μ is the coefficient of rolling friction, and a dot above the V denotes differentiation with respect to time. μ values can range from approximately 0.02 to 0.1, depending on the surface. The lower value corresponds to a hard, dry surface; the higher value might correspond to moderately tall grass.

Before rotation, the attitude of the airplane on the ground is constant and hence C_L and C_D are constant. After rotation, C_L and C_D increase, but still remain constant until lift off. The most direct means of solving Equation 7.1 is numerically, using a digital computer. This will require a table lookup or a curve fit for T as a function of D. After V is obtained as a function of time, it can then be numerically integrated to obtain s so that V will be known as a function of s.

A word of caution regarding C_D is in order. Ground effect may reduce the induced drag significantly. Hence C_D as a function of C_L is less during the ground roll than it is in the air. In view of this, a fairly good approximation is to neglect the induced drag for calculating the total airplane drag during the ground roll, particularly for tricycle landing gears where the wing is nearly level during the ground roll.

A simple model that can be used to predict the relative effect of the ground on C_{D_i} can be obtained by replacing the wing by a simple horseshoe vortex. The span of the vortex is taken to equal $\pi/4$ times the span of the wing, b, since the vortex sheet shed from an elliptic wing can be shown to roll up into a pair of vortices spaced this distance apart. This horseshoe vortex system, together with the image system required to cancel vertical velocities at the ground, is shown in Figure 7.3. The ratio of the downwash induced at the midspan of the bound vortex, including the image system to the downwash without the image, equals approximately the ratio of the induced drag in ground effect (IGE) to the induced drag, out-of-ground effect (OGE). Using the Biot–Savart law, this ratio becomes

$$\frac{C_{D_i}(\text{IGE})}{C_{D_i}(\text{OGE})} = \frac{(16h/b)^2}{1+(16h/b)^2} \tag{7.2}$$

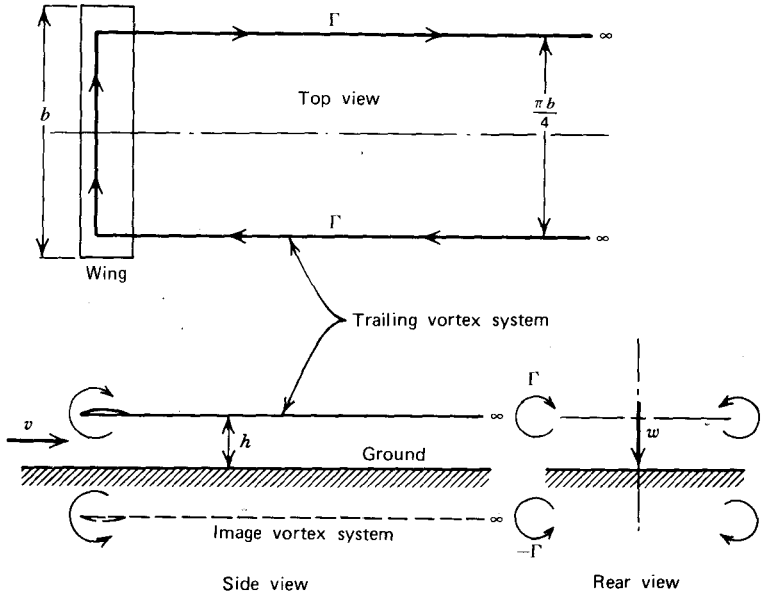

Figure 7.3 Simplified vortex model for calculating the effect of the ground on induced drag.

Equation 7.2 is plotted in Figure 7.4 where, for a typical value of h/b of 0.1, the induced drag IGE is seen to equal only 20% of the induced drag OGE for the same C_L.

During the ground roll an increment to the parasite drag is required for airplanes with retractable landing gear. This increment can be estimated using the material presented in Chapter Four or on the basis of Figure 7.5. (Ref. 7.4). This figure presents the equivalent flat-plate area, f, as a function of gross weight for three different types of landing gear.

Returning to Equation 7.1, let us apply a simple Euler method to the numerical integration of this equation. For illustrative purposes, a Boeing 747-100 will be used. This airplane is powered by four JT9D-7A turbofans having the rated takeoff thrust shown in Figure 6.36. This thrust at sea level for one engine is approximated closely by

$$T = 46{,}100 - 46.7\ V + 0.0467\ V^2$$

where T is in pounds and V is in feet per second.

Standard sea level conditions are chosen together with a gross weight of 733,000 lb (3260 kN). h/b for this airplane is approximately 0.08, giving an 86% reduction in the induced drag due to ground effect. Since takeoff is made with partially deflected flaps, a C_L of 1.0 will be assumed. Clean, the equivalent flat-plate area for this airplane is estimated to be 100 ft^2 (9.3 m^2). With gear

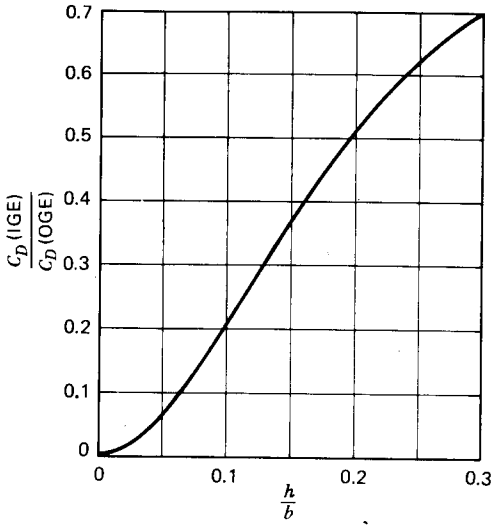

Figure 7.4 Reduction in C_{D_i} resulting from ground effect.

and flaps down, f is assumed to double, having a value of 200 ft^2 (18.6 m^2). (See Equation 3.46 and Figure 7.5.) These numbers are strictly estimates and may not agree with those used by the manufacturer. These numbers, together with other constants to be used for this example, are listed below.

$$W = 733{,}000 \text{ lb}$$
$$S = 5500 \text{ ft}^2$$
$$A = 6.69$$
$$e = 0.7$$
$$b = 196 \text{ ft}$$
$$\mu = 0.02$$
$$C_{D_i}(\text{IGE})/C_{D_i}(\text{OGE}) = 0.14$$
$$f = 100 \text{ ft}^2 \text{ clean}$$
$$= 200 \text{ ft}^2 \text{ gear and flaps down}$$

The numerical integration uses the following approximations.

$$V(t + \Delta t) = V(t) + \dot{V}(t)\,\Delta t$$
$$s(t + \Delta t) = s(t) + [V(t) + V(t + \Delta t)]\frac{\Delta t}{2}$$

Initially the airplane is at rest, so that $\dot{V}$ is calculated from

$$\dot{V} = g\left(\frac{T}{W} - \mu\right)$$
$$= 7.46 \text{ ft/s}^2$$

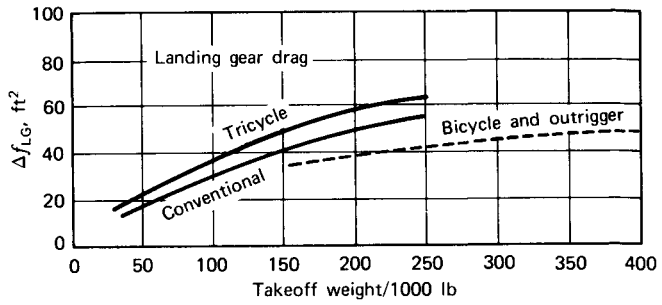

Figure 7.5 Landing gear flat-plate area. (L. M. Nicolai, *Fundamentals of Aircraft Design*, L. M. Nicolai, 1975. Reprinted by permission of L. M. Nicolai.)

Choosing a time increment, Δt, of 0.1 sec for the numerical integration, at the next time step,

$$t = 0.1 \text{ sec}$$
$$V = 0 + (7.46)(0.1)$$
$$= 0.746 \text{ fps}$$
$$s = 0 + (0 + 0.746)(0.1)/2$$
$$= 0.0378 \text{ ft}$$

With V now finite, the drag must be calculated. For this time step, D is negligible, being equal to only 0.17 lb. However, if this numerical integration is continued to, say, 32 sec, a distance of 3509 ft and a velocity of 210.3 fps are calculated. At this instant of time and for this velocity, the total thrust equals 153,377 lb and the lift and drag are calculated to be 289,200 lb and 13,146 lb respectively. At this speed the drag is indeed significant. The instantaneous acceleration is found from Equation 7.1.

$$V = g\left[\frac{T}{W} - \frac{D}{W} - \mu\left(1 - \frac{L}{W}\right)\right]$$
$$= 5.77 \text{ ft/sec}^2 \tag{7.3}$$

Figure 7.6 presents the numerical solution of Equation 7.1 up to a velocity of 274.5 fps for the 747-100. This particular velocity is 10% above the stalling speed, assuming a $C_{L_{max}}$ of 1.8. In the next section, this particular value of V is chosen as the lift-off speed for calculating the flare distance over an obstacle.

Since C_L and f are uncertain, Figure 7.7 was prepared to show the sensitivity of the ground roll distance to these parameters for a constant lift-off speed for the 747-100. s is seen to increase almost linearly with f while being rather insensitive to C_L.

For preliminary design studies, an approximate method is frequently used to calculate the ground roll distance. The method is based on assuming that

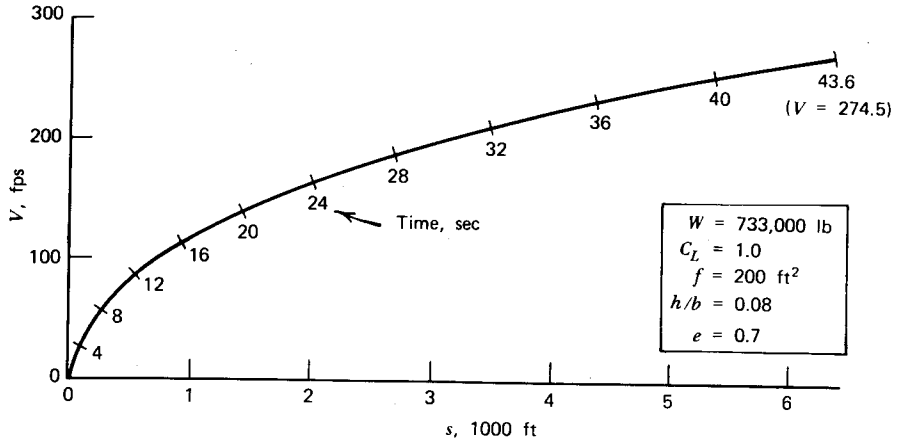

Figure 7.6 Calculated velocity as a function of distance along the runway for a Boeing 747-100.

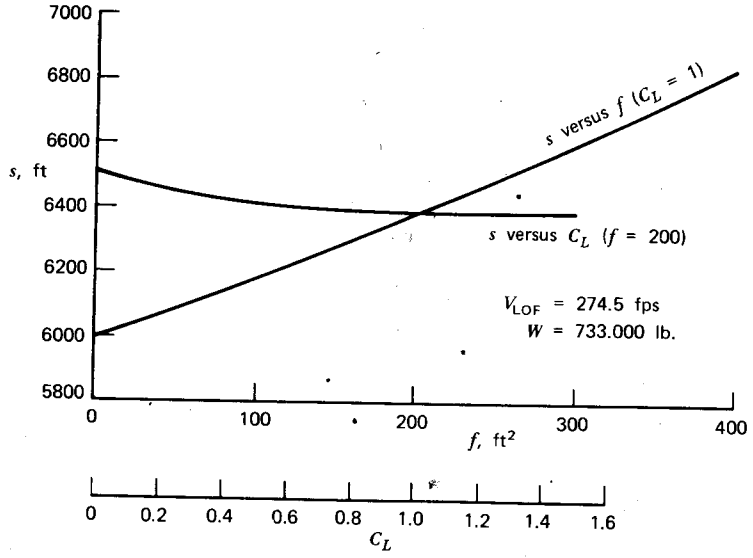

Figure 7.7 Sensitivity of predicted ground roll distance to flat-plate area and C_L for Boeing 747-100.

the inverse of the acceleration is a linear function of the square of the velocity. There appears to be no real rational basis for this assumption other than the fact that the results to which it leads are reasonable. To begin, let

$$\frac{dV}{dt} = \frac{dV}{ds}\frac{ds}{dt} = V\frac{dV}{ds} = \frac{1}{2}\frac{dV^2}{ds}$$

Assuming

$$\frac{dV}{dt} = (a + BV^2)^{-1} \tag{7.4}$$

After integrating, the following results

$$s = \frac{(V^2/2)(A + BV^2)}{2} \tag{7.5}$$

The term in parentheses can be identified as the reciprocal of the acceleration evaluated at V divided by $\sqrt{2}$. Thus, Equation 7.5 becomes

$$s = \frac{V^2}{2\bar{a}} \tag{7.6}$$

where $\bar{a}$ is an average acceleration evaluated at $V/\sqrt{2}$. For example, consider the foregoing 747 example for a C_L of 1.0, an f of 2000 ft^2, and a V of 274.5 fps.

$$\frac{V}{\sqrt{2}} = 194.1 \text{ fps}$$

At this speed,

$$T = 155{,}180 \text{ lb}$$
$$D = 11{,}200 \text{ lb}$$
$$L = 247{,}100 \text{ lb}$$

so that, from Equation 7.3,

$$\bar{a} = 5.90 \text{ ft/sec}^2$$

The ground roll distance is then calculated from Equation 7.6 to be

$$s = \frac{247.5^2}{2(5.9)}$$
$$= 6386 \text{ ft}$$

This result, by comparison to Figure 7.6, is seen to be within 1% of the more exact value obtained by the numerical methods.

Effect of Wind

A headwind will always reduce the ground roll distance required for an airplane to attain a desired airspeed. Although the headwind increases the drag and decreases the thrust for a given ground speed, it increases the lift and adds directly to the ground speed to increase the airspeed so that the net effect on takeoff distance is favorable.

The effect of the wind is most easily determined by using the approximation of Equation 7.4, keeping in mind that T, D, and L depend on the airspeed and not the ground speed.

If V_G denotes the ground speed and V_w the headwind then, for this case, Equation 7.4 becomes

$$\frac{dV_G}{dt} = [A + B(V_G + V_w)^2]^{-1} \tag{7.7}$$

Integrating gives

$$s = \frac{V_G^2}{2}\left[A + \frac{BV_G^2}{2} + \frac{4BV_wV_G}{3} + BV_w^2 2\right]$$

Again, if the terms in the brackets are interpreted as equal to the reciprocal of an average acceleration evaluated at some fraction, k, of the *airspeed*, $(V_G + V_w)$, then equating these terms to Equation 7.7 gives

$$k^2(V_G + V_w)^2 = \frac{V_G^2}{2} + \frac{4V_wV_G}{3} + V_w^2$$

This reduces to

$$k = \left[\frac{1}{2}\left(1 + \frac{2x + x^2}{3}\right)\right]^{1/2} \tag{7.8}$$

where

$$x = \frac{V_w}{V_G + V_w}$$

The factor k is presented graphically in Figure 7.8.

Suppose, in the previous example, that the 747 was taking off into a 30-kt (50.7-fps) headwind. Using the same lift-off velocity of 274.5 fps gives a ratio of headwind to airspeed of 0.185. From Figure 7.8, k equals 0.0753. Thus the average acceleration should be evaluated at an airspeed of 207 fps. At this speed,

$$T = 153{,}700 \text{ lb}$$
$$D = 12{,}736 \text{ lb}$$
$$L = 280{,}200 \text{ lb}$$

Therefore, $\bar{a} = 5.79 \text{ ft/sec}^2$.

The ground roll distance is thus determined to be

$$s = \frac{V_G^2}{2\bar{a}}$$
$$= \frac{(274.5 - 50.7)^2}{2(5.79)}$$
$$= 4325 \text{ ft} \tag{7.9}$$

Compared to the no-headwind case, the 30-kt headwind decreases the ground roll distance by more than 30%.

It should be noted that FAR Part 25 requires a conservative estimate of

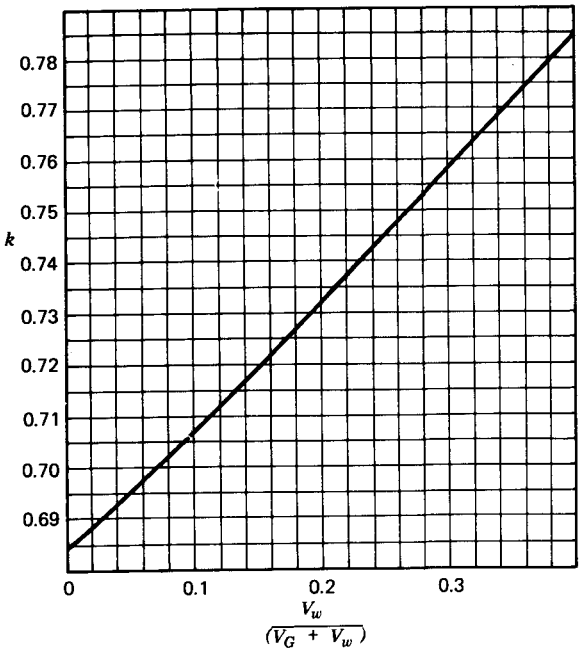

Figure 7.8 Fraction of lift-off airspeed at which to calculate average acceleration as a function of headwind-to-lift-off airspeed ratio.

headwind effects. Takeoff and landing distances must be calculated on the basis of 50% of reported headwinds and 150% of reported tailwinds. Since the wind can vary from one instant to another, the intent of FAR Part 25 is to use only half of any wind that improves performance but 150% of the opposite.

Airborne Distance

Becoming airborne at the speed V_{LOF}, an airplane continues to accelerate to the speed V_2 over the obstacle height. An airplane that is accelerating both normal to and along its flight path is pictured in Figure 7.9. As shown, $V(d\theta/dt)$ is the acceleration normal to the flight path and dV/dt is the acceleration along the flight path. The equations of motion normal to and along the flight path can be written as

$$T - D - W \sin\theta = \frac{W}{g}\frac{dV}{dt} \tag{7.10}$$

$$L - W \cos\theta = \frac{W}{g}\frac{d\theta}{dt}V \tag{7.11}$$

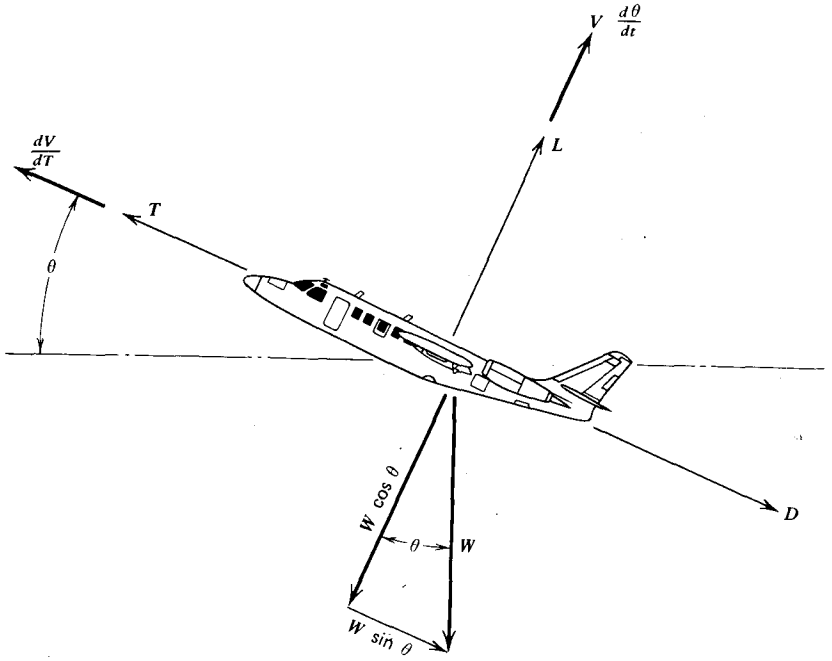

Figure 7.9 The forces on an airplane in an accelerating climb.

The rate of climb, dh/dt, and denoted by V_c in Chapter One, is found from

$$dh/dt = V \sin \theta \tag{7.12}$$

Rate of climb is also denoted in the literature by R/C. Solving for sin θ from Equation 7.10, Equation 7.12 can be written as

$$\frac{dh}{dt} = V\left[\frac{(T-D)}{W} - \frac{dV/dt}{g}\right] \tag{7.13}$$

This can also be expressed as

$$(T-D)V = W\frac{dh}{dt} + \frac{d}{dt}\left(\frac{1}{2}\frac{W}{g}V^2\right) \tag{7.14}$$

TV *is the available power* and DV is the *required power.* Thus $(T-D)V$ is the *excess power* that, as Equation 7.14 shows, can be used either to climb or to accelerate. Actually, Equation 7.14 is an energy relationship that states that the excess power equals the sum of the time rates of change of the potential energy and the kinetic energy.

Let us now apply these relationships to the calculation of the horizontal

distance required during the takeoff flare to attain a specified height. The actual flight path that is followed during the flare, or transition, segment of the takeoff depends on pilot technique. Referring to Equations 7.10 and 7.11, V and θ are the independent variables, while g, W and T are known, the latter as a function of V. L and D are functions of V and the airplane's angle of attack α. By controlling α, and hence C_L, the pilot can fly a desired trajectory (i.e., the pilot can accelerate or climb or do some of each). During the takeoff, however, in attempting to clear an obstacle, FAR Part 25 limits the operating C_L to approximately $C_{L_{max}}/1.21$ at V_{LOF} and to $C_{L_{max}}/1.44$ at V_2. Therefore, in calculating the flare distance, it will be assumed that C_L varies linearly with V between these limits and is constant for speeds above V_2. Thus, if V_2 is attained before the specified obstacle height is reached, the stall margin on C_L is maintained.

Returning to the example of the 747 at 733,000-lb takeoff weight, let us assume a $C_{L_{max}}$ with partially deflected flaps of 1.8. In addition, let V_{LOF} be 10% above the stall speed. Thus, at sea level,

$$V_{LOF} = 83.7 \text{ m/s}$$
$$C_{L_{LOF}} = 1.49$$
$$V_2 = 91.2 \text{ m/s}$$
$$C_{L_2} = 1.25$$

Assuming an f of 18.6 m^2 (200 ft^2) and calculating the induced drag obtained using C_L, the effective aspect ratio, and Figure 7.4, the drag can be determined at V_{LOF} to be

$$D = qS\left(\frac{f}{S} + C_{D_i}\right)$$

where $q = 4289$ Pa and $C_{D_i} = 0.0203$. Thus,

$$D = 225.8 \text{ kN}$$

The rated takeoff thrust at this speed for the four JT9D-7A engines equals 654.7 kN. From Equation 7.10 for an initial θ of zero,

$$\frac{dV}{dt} = 0.132g$$

Initially at V_{LOF}, L and W are exactly equal, so that $d\theta/dt$ is zero from Equation 7.11. For illustrative purposes, however, let us take a time increment of 1 sec and assume the preceding acceleration to be constant over that time. At the end of 1 sec, V then becomes 85.0 m/s and C_L is reduced slightly to 1.45. Thus, at this time,

$$L = 3280 \text{ kN } (737{,}400 \text{ lb})$$

$d\theta/dt$ from Equation 7.11 then becomes 0.000693 rad/sec. Averaged over the

1 sec, this value of $d\theta/dt$ gives a climb angle of approximately 0.02° 1 sec after lift-off.

The rate of climb, dh/dt is obtained from Equation 7.12. Over the 1 sec, the average rate of climb will equal

$$dh/dt \text{ (average)} = \tfrac{1}{2}(85) \sin (0.02)$$
$$= 0.0148 \text{ m/s}$$

Using this average rate of climb results in an altitude gain of 0.0148 m over the 1 sec.

The complete numerical solution of this example is shown in Figure 7.10. A time increment of 0.1 sec was used in the numerical integration. It can be see that a distance of 3140 ft (957 m) and 10.3 sec are required to attain an altitude of 35 ft (10.7 m). For the first half of the flare following lift-off, the airplane is primarily accelerating with little of the excess power going into climb. After approximately 7 sec, the acceleration decreases and the rate of climb increases rapidly.

The flare distance to clear 35 ft together with the ground roll distance of 6350 ft shown in Figure 7.6 to reach V_{LOF} gives a total calculated takeoff distance of 9490 ft. Reference 5.11 quotes a value of 9450 ft at the same gross weight. This agreement may be fortuituous in view of the uncertainty on f with the gear and flaps down.

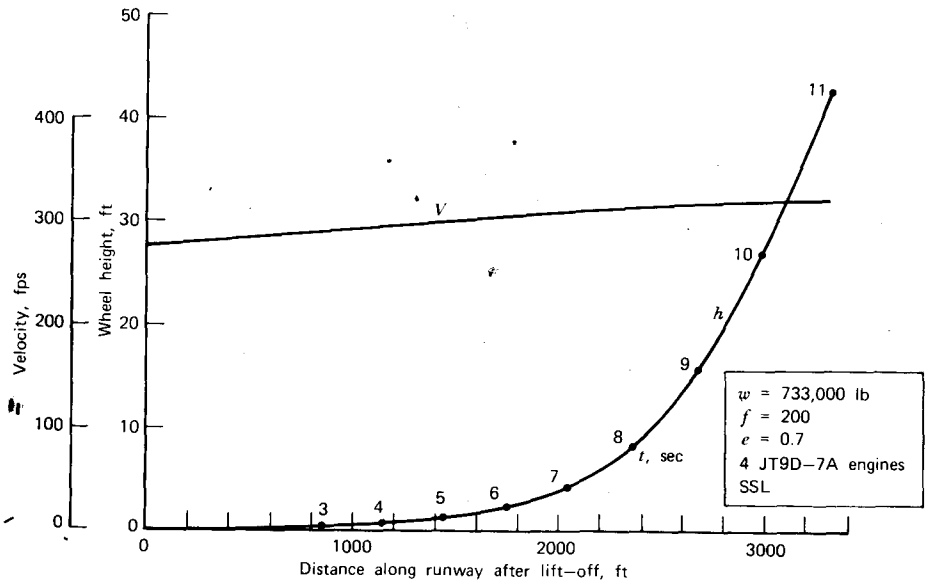

Figure 7.10 Calculated takeoff flare performance for a Boeing 747-100.

Balanced Field Length

During the takeoff run the pilot of a jet transport has the option of aborting the takeoff up to the speed V_1. Above this speed, in the event of an engine failure, the takeoff should be continued. Figure 7.11 (from Ref. 7.1) clearly illustrates these options. A balanced field length is defined as one where the distance to continue the takeoff following the recognition of an engine failure at V_1 is equal to the distance required to stop if the takeoff should be aborted. On Figure 7.11, the field length is balanced if the sum of segments B and C equals the sum of D and E. FAR Part 25 stipulates the field length to be the greatest of the accelerate-and-go distance, the accelerate-and-stop distance, or 115% of the all-engine-operating distance to a 35-ft height. The stop-and-go portions need not be balanced.

The distance to stop can be found by numerically integrating Equation 7.1. In this case, T will be negative and equal to the reverse thrust. μ is the braking coefficient and, with antiskid systems, can be as high as 0.6 on a dry, hard surface. Detailed considerations relating to the deceleration of an airplane will be deferred until the later section on landing distance.

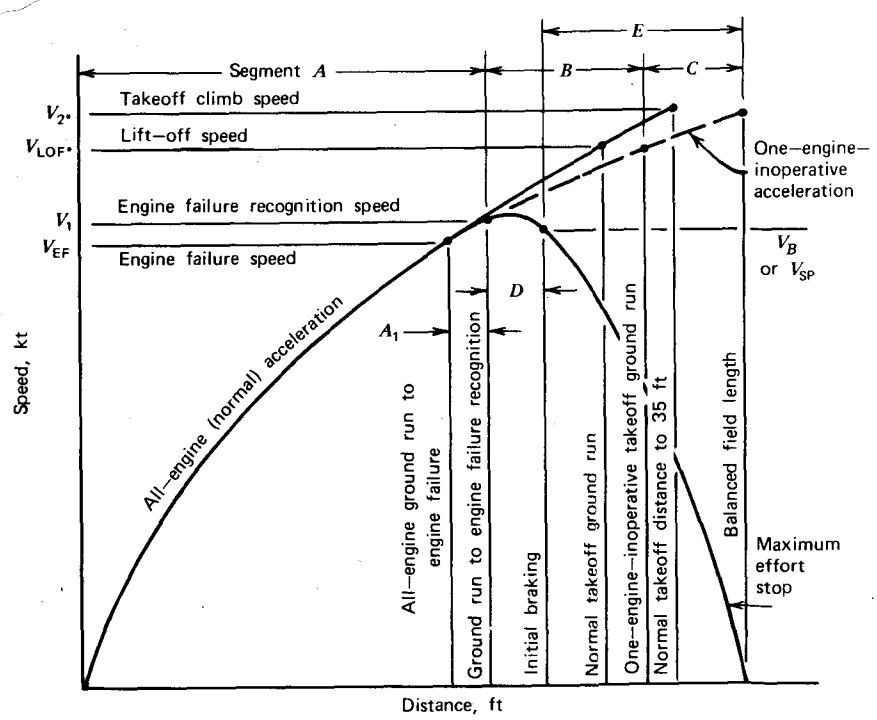

Figure 7.11 Definition of balanced field length.

RATE OF CLIMB, TIME TO CLIMB, AND CEILINGS

The rate of climb was given previously by Equation 7.13. For a steady climb this equation becomes

$$\frac{dh}{dt} = \frac{V(T - D)}{W} \tag{7.15}$$

It can be expanded and expressed, as noted previously, as

$$\frac{dh}{dt} = \frac{P_a - P_r}{W} \tag{7.16}$$

where P_a and P_r are the available power and required power, respectively.

$$P_a = TV$$
$$P_r = DV$$

For a gas turbine engine, T is known as a function of altitude and velocity, so that Equation 7.15 is the obvious form to use in this case to determine the rate of climb, R/C. In the case of a propeller-driven airplane,

$$P_a = \eta P_{\text{shaft}}$$

where P_{shaft} is the shaft power delivered to the propeller and η is the propeller efficiency.

As a function of V, the required power is determined by

$$P_r = DV$$

Let us apply Equation 7.15 to the 747-100 example using the rated climb thrust given in Figure 6.37. Flaps and gear during the climb are assumed to be retracted, so that f reduces to 100 ft^2 (9.29 m^2). As an example, take a speed of 200 m/s at an altitude of 6000 m. The acoustic velocity of this altitude equals 318 m/s. Hence the operating Mach number equals 0.629. From Figure 6.37.

$$T = 311 \text{ kN (4 engines)}$$

The mass density at 6096 m equals 0.662 kg/m^3. V and ρ result in a dynamic pressure of

$$q = 13{,}240 \text{ Pa}$$

With a weight of 3260 kN and a wing area of 511 m^2, the lift coefficient equals 0.482. Hence $C_{D_i} = 0.0152$. Therefore,

$$D = q(f + C_{D_i}S)$$
$$= 226 \text{ kN}$$

Equation 7.15 gives, for the rate of climb,

$$\text{R/C} = \frac{200(311 - 226)}{3260}$$
$$= 5.2 \text{ m/s}$$

In this way, the curves presented in Figure 7.12 were obtained. Here the rate of climb is plotted as a function of true airspeed at four different altitudes. At the highest altitude and air speeds, the curve is probably optimistic, since the drag rise beyond the drag-divergence Mach number is not considered.

At a given altitude, there exists an optimum airspeed for maximum rate of climb. In this case, the airspeed for the best rate of climb is seen to correspond to a nearly constant indicated air-speed of 296 kt.

The speed for the best climb angle is less than the speed for the best R/C. The angle of climb, θ_c, in radians, is given by

$$\theta_c = \frac{\text{R/C}}{V}$$

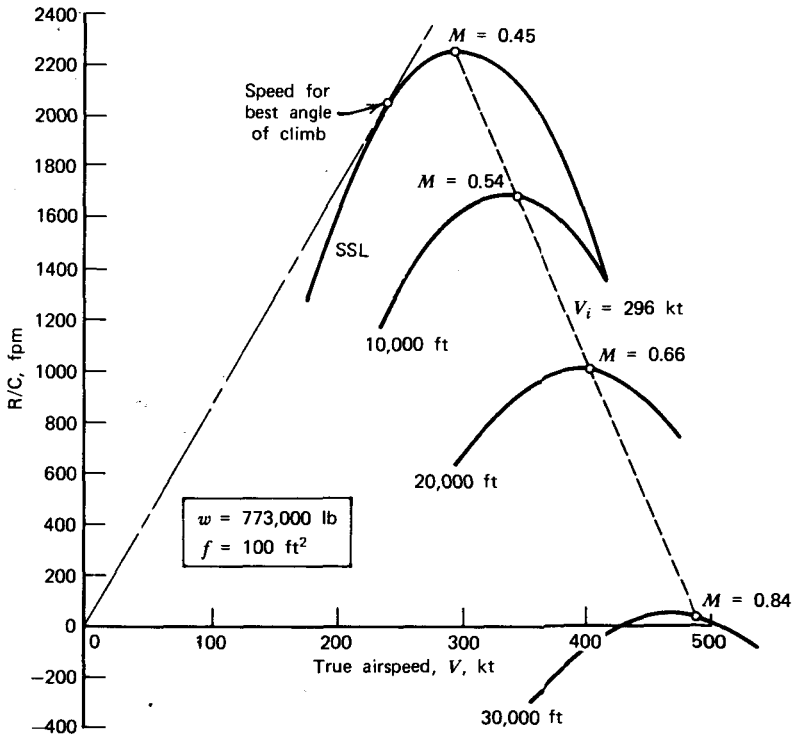

Figure 7.12 Calculated rate of climb for Boeing 747-100 as a function of true airspeed for several altitudes.

For any velocity, this angle is represented by the angle between the abscissa and a straight line from the origin to the R/C curve on Figure 7.12. As shown for the sea level curve, this angle is a maximum for the straight line that is tangent to the curve. Thus, to clear an obstacle ahead, a pilot should fly slightly slower than the speed that gives the maximum rate of climb.

The optimum airspeed for maximum rate of climb can be obtained approximately from Equation 7.15 for a turbojet or turbofan.

$$T - D + V\left(\frac{\partial T}{\partial V} - \frac{\partial D}{\partial V}\right) = 0 \tag{7.17}$$

D is of the form

$$D = C_1 V^2 + \frac{C_2}{V^2} \tag{7.18}$$

where $C_1 = \rho f/2$.

$$C_2 = \frac{2(W/B)^2}{\pi \rho e}$$

It is convenient and approximately correct to express T in the form

$$T = T_0 + k_T V^2 \tag{7.19}$$

where k_T is a constant for a given altitude. Equations 7.18 and 7.19 substituted into Equation 7.17 leads to an optimum velocity for best climb given by

$$V^2 = \frac{T_0 + [T_0^2 + 12(C_1 - k_t)C_2]^{1/2}}{6(C_1 - k_t)} \tag{7.20}$$

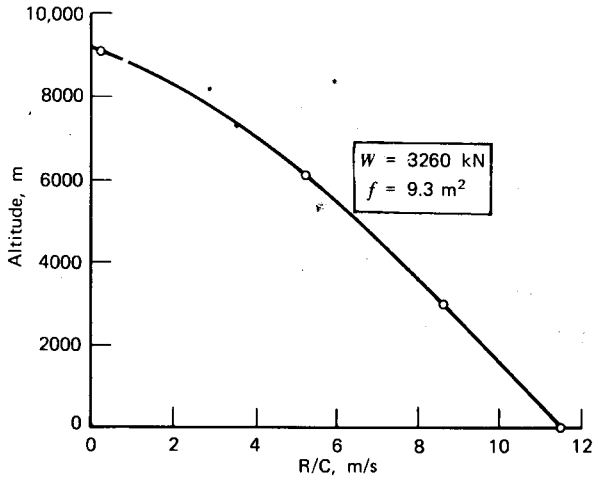

Figure 7.13 Calculated maximum rate of climb for Boeing 747-100 as a function of altitude.

The maximum rates of climb obtained from Figure 7.12 are plotted as a function of altitude in Figure 7.13. The *absolute ceiling* is defined as the altitude for which the R/C equals zero. In this case, this corresponds to an altitude of 9.20 km.

Consider now the rate-of-climb calculation for a propeller-driven airplane. We will use as an example the Piper Cherokee Arrow that is similar to the Cherokee 180 except that the former has a retractable landing gear, a 200-bhp (149-kW) piston engine, and a constant speed propeller. The engine is rated at 2700 rpm but, for a continuous climb in accordance with recommended practice, an rpm of only 2500 will be used. At standard sea level, the engine develops 185 bhp (138 kW) at this rpm. For higher altitudes, the engine power is estimated on the basis of Figure 6.2. The following values are known or have been estimated for this airplane.

Flat-plate area,	$f = 4.5\ \text{ft}^2\ (0.418\ \text{m}^2)$
Span efficiency,	$e = 0.70$
Propeller diameter,	$D = 6.17\ \text{ft}\ (1.88\ \text{m})$
Span,	$b = 32.2\ \text{ft}\ (9.81\ \text{m})$
Wing area,	$S = 169\ \text{ft}^2\ (15.7\ \text{m}^2)$
Aspect ratio,	$A = 6.14$
Weight,	$W = 2650\ \text{lb}\ (11.1\ \text{kN})$

The propeller performance curves for this airplane were presented in Figures 6.16 and 6.17. These curves, together with the engine power, are used to estimate the available power. As an example, consider an altitude of 10,000 ft (305 m). The engine power at this altitude equals 130 bhp. At a speed of, say, 140 fps, the advance ratio will be

$$\begin{aligned} J &= V/nD \\ &= 140(0.1467)/(2500/60)/6.17 \\ &= 0.389 \end{aligned}$$

The power coefficient equals

$$\begin{aligned} C_P &= \frac{P}{\rho n^3 D^5} \\ &= 130(550)/(0.00176)(41.7)^3(6.17)^5 \\ &= 0.063 \end{aligned}$$

This power coefficient and advance ratio lead to a blade angle of 21° from Figure 6.16. Using this blade angle, together with J, results in a propeller efficiency, η, of 0.70 from Figure 6.17. Thus the available power at this speed

and altitude equals 91 thp where thp stands for "thrust horsepower." The equivalent term in the SI system would be tkW, for "thrust kilowatts."

The power required for the Arrow is calculated from

$$P_r = DV$$

which can be expressed in the form

$$P_r = \frac{\rho f}{2} V^3 + \frac{2(W/b)^2}{\pi \rho e} \frac{1}{V} \tag{7.21}$$

The first term on the right side is the parasite power and the second term the induced power. The shape of this relationship will be discussed in more detail later. For now let us simply evaluate Equation 7.21 at the altitude of 10,000 ft and a speed of 140 fps. The obvious substitutions result in a required power of 65.3 hp. The rate of climb can now be calculated from Equation 7.16. However, in so doing, the excess power must be expressed in foot-pounds per second.

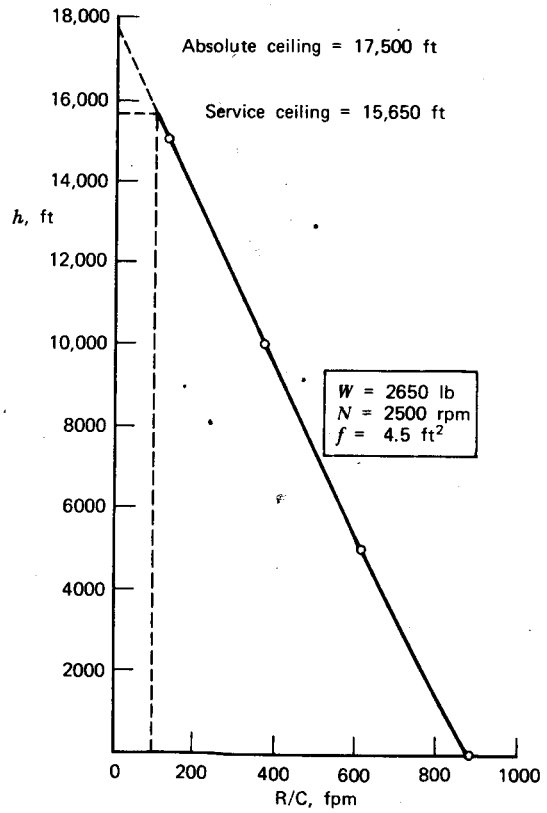

Figure 7.14 Rate of climb for the Cherokee Arrow versus altitude.

$$\text{R/C} = \frac{P_a - P_r}{W}$$

$$= \frac{(91 - 65.3)550}{2650}$$

$$= 5.34 \text{ fps}$$

It is current practice in the American aviation industry to express the R/C in feet per minute, so that the above becomes 320 fpm (1.63 m/s).

In this manner, the rate of climb can be calculated over a range of speeds for several altitudes for the Arrow. The maximum rates of climb thus determined are presented in Figure 7.14, where the R/C is seen to decrease almost linearly with altitude. The altitude for which the R/C equals 100 fpm (0.5 m/s) is shown on Figure 7.14 and is called the *service ceiling.* In this example, the calculated service ceiling and sea level rate of climb are close to the corresponding values quoted by the manufacturer.

The power-required and power-available curves calculated for this example at sea level are presented in Figure 7.15. Similar to the drag curve in Figure 4.52, the power-required curve has a minimum value at some speed. Below this speed, it actually requires more power to fly slower. This part of the curve is referred to as the backside of the power curve.

The speed for minimum required power can be found by setting to zero

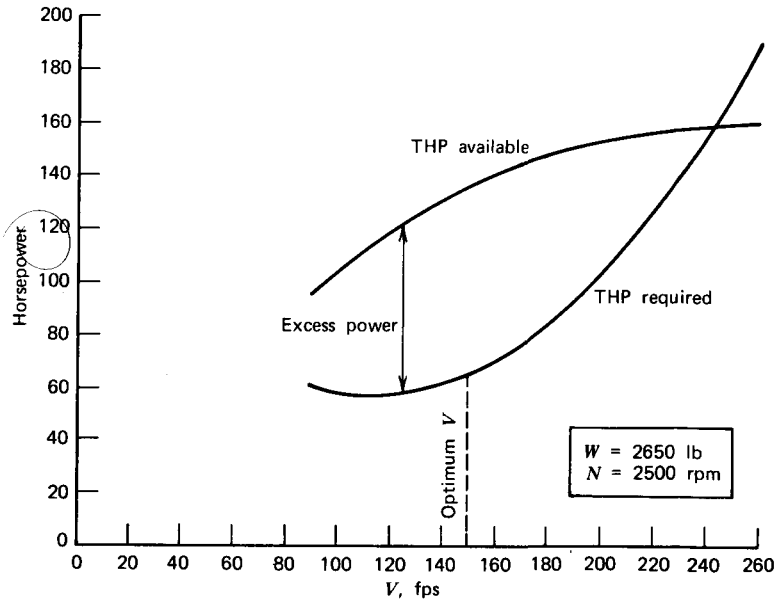

Figure 7.15 Sea level power-required and power-available curves for the Cherokee Arrow.

the derivative of equation 7.21 with respect to V. This leads to

$$V\sqrt{\sigma} = \left[\frac{4(W/b)^2}{3\pi\rho_0^2 ef}\right]^{1/4} \tag{7.22}$$

The preceding speed is, of course, not necessarily the speed for maximum rate of climb, since the available power varies with airspeed. In the case of the Arrow, Figure 7.15 shows the optimum speed to be greater than the value given by Equation 7.22. Nevertheless, one might expect the two speeds to be related. Equation 7.22 shows the minimum required power to occur at a constant indicated airspeed. This suggests that the maximum rate of climb will also occur at a constant indicated airspeed. This was found to be true for the 747-100 and also holds for piston engine airplanes.

Generalized Power-Required Curve

In flying (or flight testing) an airplane, one rarely finds a standard atmosphere. In addition, the gross weight of the airplane is generally different from that used by the manufacturer to quote performance. The following method is useful for interpreting power measurements taken at any gross weight and density altitude.

V_{ew} and P_{ew} are defined as the velocity and required power at sea level, where "ew" signifies equivalent weight. These quantities are related to a standard weight, W_s, by,

$$V_{ew} = \left(\frac{2W_s}{\rho_0 C_L S}\right)^{1/2} \tag{7.23}$$

$$P_{ew} = \left(\frac{2W_s^2 C_D^2}{\rho_0 S C_L^3}\right)^{1/2} \tag{7.24}$$

For any other density or gross weight, the velocity and power are given by

$$V = \left(\frac{2W}{\rho C_L S}\right)^{1/2}$$

$$P_r = \left(\frac{2W^3 C_D}{\rho_0 S C_L^3}\right)^{1/2}$$

Thus, at the same lift coefficient, V and V_{ew} are related by

$$V_{ew} = V\sqrt{\sigma}\left(\frac{W_s}{W}\right)^{1/2} \tag{7.25}$$

Similarly,

$$P_{ew} = P_r\sqrt{\sigma}\left(\frac{W_s}{W}\right)^{3/2} \tag{7.26}$$

A graph of P_{ew} versus V_{ew} will simply be the sea level power required curve at the standard gross weight. As an example, take the Cherokee Arrow at a gross weight of 2400 lb, a density altitude of 5000 ft and an airspeed of 100 kt. Using Figure 7.15 as the standard,

$$\frac{W_s}{W} = 1.104$$

At 5000 ft, σ equals 0.861. Therefore,

$$V_{ew} = 97.5 \text{ kt}$$
$$= 164.8 \text{ fps}$$

From Figure 7.15,

$$P_{ew} = 73 \text{ hp}$$

Therefore, from Equation 6.26,

$$P_r = 67.8 \text{ hp}$$

In this manner, given a sea level power required curve at a standard gross weight, one can easily determine the power required at any altitude, airspeed, and gross weight.

These relationships are particularly useful in flight testing. Power-required data taken at any altitude and gross weight are reduced to a plot of $P_{ew}V_{ew}$ versus V_{ew}^4. Such a plot will be a straight line having a slope proportional to f and an intercept proportional to $1/e$. Thus all of the data collapses to a single, easily fitted line enabling one to determine accurately e and f. The equation of this straight line follows directly from Equation 7.21.

$$P_{ew}V_{ew} = \frac{2(W_s/b)^2}{\pi\rho_0} + \frac{\rho_0 f}{2}V_{ew}^4 \tag{7.27}$$

Time to Climb

The time required to climb from one altitude, h, to another, h_2, can be determined by evaluating the integral

$$t = \int_{h_1}^{h_2} \frac{dh}{\text{R/C}} \tag{7.28}$$

Knowing the R/C as a function of h, this integral can easily be evaluated numerically. A solution in closed form can be obtained if one assumes that the rate of climb decreases linearly with altitude. A feeling of how valid this assumption is can be gained from Figures 7.13 and 7.14.

Let

$$\text{R/C} = (\text{R/C})_0(1 - h/h_{abs}) \tag{7.29}$$

where h_{abs} = absolute ceiling.

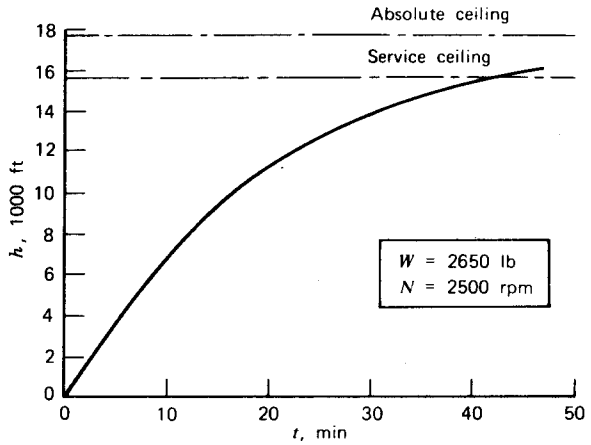

Figure 7.16 Time to climb for Cherokee Arrow.

Equation 7.28, for $h_1 = 0$, then reduces to

$$t = \frac{h_{abs}}{(R/C)_0} \ln \frac{1}{1 - h/h_{abs}} \tag{7.30}$$

This represents the time required to climb from sea level to the altitude, h. The time required to climb from one altitude to another is obtained directly from Equation 7.30 by subtracting, one from the other, the times required to climb from sea level to each altitude.

Time to climb is presented for the Cherokee Arrow in Figure 7.16. This curve was calculated on the basis of Equation 7.30. For this particular example, it requires approximately 42.5 min to climb to the service ceiling.

RANGE

The range of an aircraft is the distance that the aircraft can fly. Range is generally defined subject to other requirements. In the case of military aircraft, one usually works to a mission profile that may specify a climb segment, a cruise segment, a loiture, an enemy engagement, a descent to unload cargo, a climb, a return cruise, a hold, and a descent. In the case of civil aircraft, the range is usually taken to mean the maximum distance that the airplane can fly on a given amount of fuel with allowance to fly to an alternate airport in case of bad weather.

Let us put aside the range profile for the present and consider only the actual distance that an airplane can fly at cruising altitude and airspeed on a given amount of fuel. For a propeller-driven airplane, the rate at which fuel is

consumed is

$$W_f = (\text{BSFC})(\text{bhp}) \text{ lb/hr}$$

In the SI system,

$$W_f = (\text{SFC})(\text{kW}) \text{ N/s}$$

where SFC is in units of newtons per kilowatt per second.

Using the SI notation, the total fuel weight consumed over a given time will be

$$W_f = \int_0^t (\text{SFC})(\text{kW})\, dt$$

This can be written as

$$W_f = \int_0^s \frac{(\text{SFC})(\text{kW})}{V} ds$$

Since the shaft power equals the thrust power divided by the propeller efficiency,

$$W_f = \frac{1}{1000} \int_0^s \frac{(\text{SFC})D}{\eta}\, ds \tag{7.31}$$

where D is the drag. The constant represents the fact that 1kW equals 1000 mN/s.

Given the velocity and weight, Equation 7.31 can be integrated numerically. One of the difficulties in evaluating Equation 7.31 rests with the weight, which is continually decreasing as fuel is burnt off.

A closed-form solution can be obtained for Equation 7.31 by assuming that the SFC and η are constant and that the airplane is flown at a constant C_L. With these assumptions, the fuel flow rate, with respect to distance, becomes

$$\frac{dW_f}{ds} = \frac{(\text{SFC})\epsilon}{1000\,\eta} W$$

where ϵ is the drag-to-lift ratio, which is a function of C_L, and W is the airplane weight. dW_f/ds is the negative of dW/ds. Thus,

$$\frac{dW}{w} = -\frac{(\text{SFC})\epsilon}{1000\,\eta} ds$$

Integrating gives

$$\ln \frac{W_I}{W} = \frac{(\text{SFC})\epsilon}{1000\,\eta} s$$

where W_I is the initial weight of the airplane. If W_F is the total fuel weight, the distance, or range, R, that the airplane can fly on this fuel is finally, in meters,

$$R = \frac{1000\,\eta}{(\text{SFC})\epsilon} \ln\left(1 + \frac{W_F}{W_E}\right) \tag{7.32}$$

W_E denotes "weight empty," meaning "empty of fuel." Normally, weight empty refers to the airplane weight without any fuel or payload. This equation, which holds only for propeller-driven aircraft, is a classical one known as the Breguet range equation.

In the case of a turbojet-propelled airplane, the fuel flow becomes

$$W_f = (\text{TSFC})D$$

so that

$$\frac{dW}{W} = -\frac{(\text{TSFC})\epsilon\, ds}{V}$$

In order to integrate this relationship, we must assume that the airplane operates at a constant ϵ/V and that TSFC is constant. When this is done, the modified Breguet range equation for jet-propelled aircraft is obtained.

$$R = \frac{V}{(\text{TSFC})\epsilon} \ln\left(1 + \frac{W_F}{W_E}\right) \tag{7.33}$$

Thus, for maximum range, ϵ should be minimized for propeller-driven airplanes and ϵ/V should be minimized for turbojets. In the case of turbojets, this can lead to the airplane cruising slightly into the drag rise region that results from transonic flow.

Referring to Equation 7.18, ϵ will be a minimum when

$$V_{\text{opt}} = \left(\frac{C_2}{C_1}\right)^{1/4} \text{(propeller-driven airplane)} \tag{7.34}$$

ϵ/V will have a minimum at

$$V_{\text{opt}} = \left(\frac{3C_2}{C_1}\right)^{1/4} \text{(turbojet)} \tag{7.35}$$

For propeller-driven airplanes this leads to a minimum ϵ value of

$$\epsilon_{\text{min}} = 2\left(\frac{f/S}{\pi eA}\right)^{1/2} \tag{7.36}$$

$$V_{\text{opt}} = \left[\frac{4}{\pi eA\rho_0^2}\frac{(W/S)^2}{\sigma^2(f/S)}\right]^{1/4} \tag{7.37}$$

For turbojet-propelled airplanes, ϵ/V has a minimum value of

$$\left(\frac{\epsilon}{V}\right)_{\text{min}} = (3^{1/4} + 3^{-1/4})\left[\frac{\rho_0^2(f/S)^3}{4\pi eA(W/S)^2}\right]^{1/4}\sigma^{1/2} \tag{7.38}$$

The optimum V for the above is equal to that given by Equation 7.37 multiplied by $3^{1/4}$.

Some interesting observations can be made based on Equations 7.36, 7.37, and 7.38. For either propeller or turbojet airplanes, the indicated air-

speed for maximum range is a constant independent of altitude. However, for the same wing loading, effective aspect ratio, and parasite drag coefficient, the optimum cruising speed for the turbojet airplane is higher than that for the propeller-driven case by a factor of 1.316. The optimum range for a propeller-driven airplane is independent of density ratio and hence altitude. However, with the indicated airspeed being constant, the trip time will be shorter at a higher altitude.

The optimum range for a turbojet is seen to increase with altitude being inversely proportional to the square root of the density ratio. This fact, together with the increase in true airspeed with altitude, results in appreciably higher cruising speeds for jet transports when compared with a propeller-driven airplane. As an example in the use of Equations 7.38 and 7.37 (multiplied by 1.316), consider once again the 747-100 at a gross weight of 2700 kN. In this case,

$$\frac{W}{S} = 5284 \text{ N/m}^2$$

$$f/s = 0.0182$$

$$Ae = 4.9$$

Thus,

$$V_{opt} = 167/\sqrt{\sigma} \text{ m/s}$$

Dividing this velocity by the speed of sound, the optimum Mach number as a function of altitude shown in Figure 7.17 can be obtained. Above a Mach number of approximately 0.8, this curve cannot be expected to hold, since drag divergence will occur.

The second curve shown in Figure 7.17 presents the optimum range divided by the sea level value of this quantity. This curve is calculated on the basis of Equation 7.38 and the TSFC values for the JT9D-7A engine presented in Figure 6.38 as a function of altitude and Mach number. This curve is reasonably valid up to an altitude of 7500 m. Above this, because of Mach number limitations, the range ratio will level off. However, despite the Mach number limitations, the gains to be realized in the range by flying at the higher altitudes are appreciable, of the order of 30% or more.

In the case of propeller-driven airplanes, the optimum cruising velocity given by Equation 7.37 does not reflect practice. To see why, consider the Cherokee Arrow. In this case, at a gross weight of 2650 lb, the optimum velocity is calculated to equal 87.8 kt. This velocity is appreciably slower than the speeds at which the airplane is capable of flying. It is generally true of a piston engine airplane that the installed power needed to provide adequate climb performance is capable of providing an airspeed appreciably higher than the speed for optimum range. Therefore, ranges of such aircraft are quoted at some percentage of rated power, usually 65 or 75%.

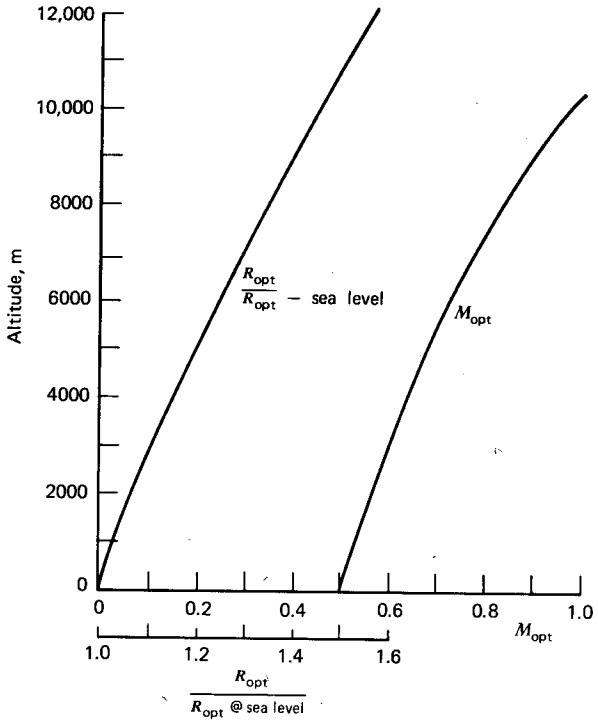

Figure 7.17 Effect of altitude on optimum range and cruising Mach number for 747-100.

The cruising speed at some specified percentage of the rated power can be found from the power curves, such as those presented in Figure 7.15 for the Cherokee Arrow. For example, 75% of the rated power corresponds to approximately 81% of the available power shown in Figure 7.15. This increase results from the rating of 200 bhp at 2700 rpm as compared to only 185 bhp output at 2500 rpm for which the figure was prepared. A line that is 81% of the available power crosses the power-required curve at a speed of 223 fps or 132 kt. This speed is therefore estimated to be the cruising speed at 75% of rated power at this particular rpm.

The penalty in the range incurred by cruising at other than the optimum speed can be found approximately from Equations 7.18 and 7.34. The ratio of the drag at any speed to the minimum drag can be expressed as a function of the ratio of the speed to the optimum speed. The result is

$$\frac{D}{D_{min}} = \frac{1}{2}\left[\left(\frac{V}{V_{opt}}\right)^2 + \left(\frac{V_{opt}}{V}\right)^2\right] \tag{7.39}$$

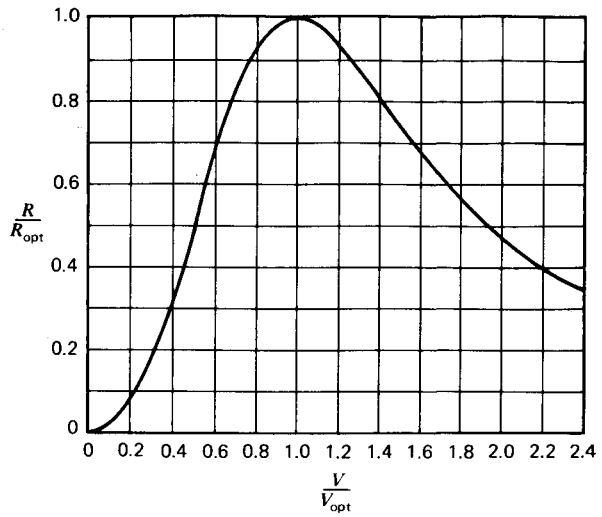

Figure 7.18 Effect of departing from optimum velocity on range for propeller-driven aircraft.

This relationship is presented graphically in Figure 7.18. In the preceding example of the Cherokee, this figure shows a loss of approximately 25% in the range by cruising at 75% power instead of the optimum. Of course, the time required to get to your destination is 33% less by cruising at 75% power.

The effect of wind on range is pronounced. To take an extreme, suppose you were cruising at the optimum airspeed for no wind into a headwind of equal magnitude. Your ground speed would be zero. Obviously, your airspeed is no longer optimum, and it would behoove you to increase your airspeed. Thus, without going through any derivations, we conclude that the optimum airspeed increases with headwind.

Correcting Equation 7.32 for headwind is left to you. If V_w denotes the headwind, this equation becomes (now expressed in the English system),

$$R = \frac{550\,\eta}{(\text{BSFC})\epsilon}\left(1 - \frac{V_w}{V}\right)\ln\left(1 + \frac{W_f}{W_E}\right) \tag{7.40}$$

The effect of headwind on the optimum cruising airspeed can be obtained by minimizing $\epsilon/(1 - V_w/V)$. Without going into the details, this leads to the following polynomial

$$2\left(\frac{V}{V_{opt}}\right) - 3\left(\frac{V_w}{V_{opt}}\right)\left(\frac{V}{V_{opt}}\right)^4 - 2\left(\frac{V}{V_{opt}}\right) + \frac{V_w}{V_{opt}} = 0$$

Here V is the optimum cruising velocity for a given headwind and V_{opt} is the value of V for a V_w of zero.

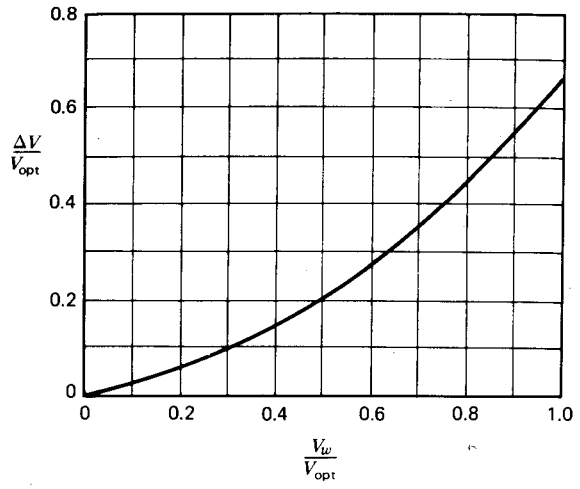

Figure 7.19 Effect of headwind on optimum cruising velocity.

$$\frac{V}{V_{opt}} = 1 + \Delta V / V_{opt}$$

$\Delta V / V_{opt}$ is presented as a function of V_w / V_{opt} in Figure 7.19. This figure shows, for example, that if one has a headwind equal to 50% of the optimum velocity for no wind, he or she should cruise at an airspeed 20% higher than the optimum, no-wind velocity.

MAXIMUM ENDURANCE

Endurance refers to the time that elapses in remaining aloft. Here one is concerned with the time spent in the air, not the distance covered. A pilot in a holding pattern awaiting clearance for an instrument landing is concerned with endurance. The maximum endurance will be obtained at the airspeed that requires the minimum fuel flow rate. In the case of a turbojet or turbofan engine, the product of TSFC and the drag is minimized.

Assuming a constant TSFC for the jet airplane leads to Equations 7.36 and 7.37, which relate to the maximum range for a propeller-driven airplane. Thus, for a given weight of fuel, W_f, the maximum endurance, t_e, of a turbojet will be

$$t_e = \frac{1}{2(\text{TSFC})} \left(\frac{W_f}{W}\right) \left[\frac{\pi e A}{(f/S)}\right]^{1/2} \tag{7.41}$$

Notice that the endurance is independent of altitude. This follows from

the fact that the minimum drag does not vary with altitude. To obtain this endurance, the airplane is flown at the airspeed given by Equation 7.37.

Assuming a constant SFC, a propeller-driven aircraft will have its maximum endurance when flown at the airspeed for minimum required power. This speed has been given previously as Equation 7.22. At the minimum power, the induced power is three times the parasite power. Hence,

$$P_{\min} = 2\rho f V^3$$
$$= \frac{2}{\sqrt{\sigma}}\left[\frac{4(W/b)^2}{3\pi_e}\right]^{3/4}\frac{f^{1/4}}{\rho_0^{1/2}} \tag{7.42}$$

The endurance time for a propeller-driven airplane then becomes

$$t_e = \frac{\sqrt{\sigma}}{2(\mathrm{SFC})}\left[\frac{3\pi e}{4(w/b)^2}\right]^{3/4}\frac{\rho_0}{f^{1/4}} \tag{7.43}$$

(SFC) in this equation has units consistent with the other terms; that is, weight per power second where the weight is in newtons or pounds with the power in newton meters per second or foot-pounds per second. For example, if

$$\mathrm{BSFC} = 0.5 \text{ lb/bhp-hr}$$

then

$$\mathrm{SFC} = 2.53 \times 10^{-7} \text{ lb/(ft-lb/sec)/sec}$$

Actually SFC used in this basic manner has the units of l/length. In the English system this becomes ft^{-1} and in the SI system it is m^{-1}.

Notice that the endurance of a propeller-driven airplane decreases with altitude. This follows from the fact that the minimum power increases with altitude.

Some of the foregoing equations for range and endurance contain the weight which, of course, varies with time as fuel is burned. Usually, for determining the optimum airspeed or the endurance time, it is sufficiently accurate to assume an average weight equal to the initial weight minus half of the fuel weight. Otherwise, numerical and graphical procedures must be used to determine range and endurance.

DESCENT

The relationships previously developed for a steady climb apply as well to descent. If the available thrust is less than the drag, Equation 7.15 results in a negative R/C. In magnitude this equals the rate of descent, R/D. The angle of descent, in radians, θ_D, is given by,

$$\theta_D = \frac{D - T}{W} \tag{7.44}$$

Civil aircraft rarely descend at angles greater than 10°. The glide slope for an ILS (instrument landing system) approach is only 3°. Steeper slopes for noise abatement purposes are being considered, but only up to 6°.

The minimum θ_D value in the event of an engine failure is of interest. From Equation 7.44 we see that this angle is given by

$$\theta_{D_{min}} = \epsilon_{min} \text{ rad} \tag{7.45}$$

Thus, the best glide angle is obtained at the C_L giving the lowest drag-to-lift ratio. This angle is independent of gross weight. However, the greater the weight, the higher the optimum airspeed will be. The minimum ϵ and corresponding airspeed have been given previously as Equations 7.36 and 7.37. Of course, in the event of an engine failure, one must account for the increase in f caused by the stopped or windmilling propeller, or by the stopped turbojet.

LANDING

The landing phase of an airplane's operation consists of three segments; the approach, the flare, and the ground roll. FAR Part 25 specifies the total landing distance to include that required to clear a 50-ft (15.2-m) obstacle. A sketch of the landing flight path for this type of approach is shown in Figure 7.20. The ground roll is not shown, since it is simply a continuous deceleration along the runway. FAR Part 25 specifies the following, taken verbatim.

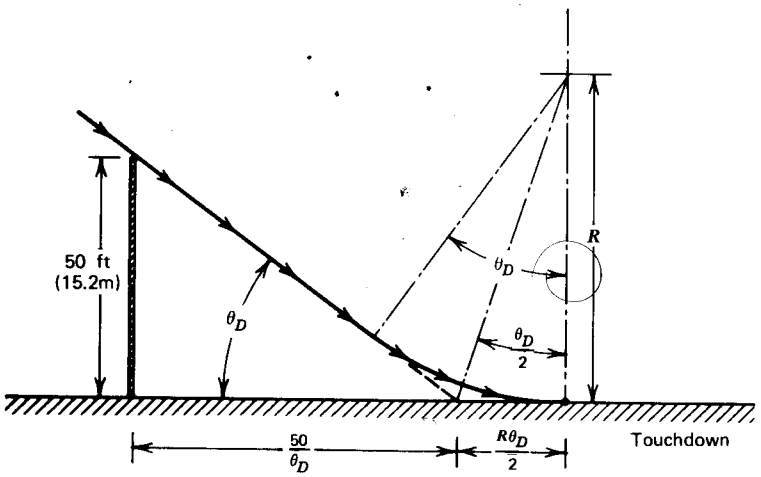

Figure 7.20 Landing approach and flare.

§ 25.125 Landing.

(a) The horizontal distance necessary to land and to come to a complete stop (or to a speed of approximately 3 knots for water landings) from a point 50 feet above the landing surface must be determined (for standard temperatures, at each weight, altitude, and wind within the operational limits established by the applicant for the airplane) as follows:
  (1) The airplane must be in the landing configuration.
  (2) A steady gliding approach, with a calibrated airspeed of not less than 1.3 V_s, must be maintained down to the 50 foot height.
  (3) Changes in configuration, power or thrust, and speed, must be made in accordance with the established procedures for service operation.
  (4) The landing must be made without excessive vertical acceleration, tendency to bounce nose over, ground loop, porpoise, or water loop.
  (5) The landings may not require exceptional piloting skill or alertness.

(b) For landplanes and amphibians, the landing distance on land must be determined on a level, smooth, dry, hard-surfaced runway. In addition—
  (1) The pressures on the wheel braking systems may not exceed those specified by the brake manufacturer;
  (2) The brakes may not be used so as to cause excessive wear of brakes or tires; and
  (3) Means other than wheel brakes may be used if that means—
    (i) Is safe and reliable;
    (ii) Is used so that consistent results can be expected in service; and
    (iii) Is such that exceptional skill is not required to control the airplane.

(c) For seaplanes and amphibians, the landing distance on water must be determined on smooth water.

(d) For skiplanes, the landing distance on snow must be determined on smooth, dry, snow.

(e) The landing distance data must include correction factors for not more than 50 percent of the nominal wind components along the landing path opposite to the direction of landing, and not less than 150 percent of the nominal wind components along the landing path in the direction of landing.

(f) If any device is used that depends on the operation of any engine, and if the landing distance would be noticeably increased when a landing is made with that engine inoperative, the landing distance must be determined with that engine inoperative unless the use of compensating means will result in a landing distance not more than that with each engine operating.
The total distance thus calculated must be increased by a factor of 1.667.

FAR Part 23 is somewhat simpler in defining the landing for airplanes certified in the normal, utility, or acrobatic categories. It states the following,

§ 23.75 Landing.

(a) For airplanes of more than 6,000 pounds maximum weight (except skiplanes for which landplane landing data have been determined under this paragraph and furnished in the Airplane Flight Manual), the horizontal distance required to land and come to a complete stop (or to a speed of approximately three miles per hour for seaplanes and amphibians) from a point 50 feet above the landing surface must be determined as follows:
  (1) A steady gliding approach with a calibrated airspeed of at least 1.5 V_{s_1} must be maintained down to the 50 foot height.
  (2) The landing may not require exceptional piloting skill or exceptionally favorable conditions.
  (3) The landing must be made without excessive vertical acceleration or tendency to bounce, nose over, ground loop, porpoise, or water loop.

(b) Airplanes of 6,000 pounds or less maximum weight must be able to be landed safely and come to a stop without exceptional piloting skill and without excessive vertical acceleration or tendency to bounce, nose over, ground loop, porpoise, or water loop.

Airborne Distance

From Figure 7.20, since θ_D is a small angle, the total airborne distance, s_A, is given by

$$s_A = \frac{15.2}{\theta_D} + \frac{R\theta_D}{2} \text{ m} \tag{7.46}$$

This assumes the flare to be a circular arc having a radius of R. If V_A is the approach velocity, this velocity is assumed to remain constant throughout the flare. The acceleration toward the center of curvature, a_n, will therefore be

$$a_n = \frac{V_A^2}{R}$$

However,

$$L - W = \frac{W}{g} a_n$$

Thus,

$$R = \frac{V_A^2}{g(L/W - 1)}$$

If C_{L_A} denotes the lift coefficient during the steady approach then, during the flare,

$$\frac{L}{W} = \frac{C_L}{C_{L_A}}$$

The flare radius can therefore be expressed as

$$R = \frac{V_A^2}{g[(C_L/C_{L_A}) - 1]} \tag{7.47}$$

FAR Part 25 requires that V_A exceed the stalling speed in the landing configuration by 30%. Thus,

$$C_{L_A} \leq \frac{C_{L_{max}}}{1.69} \tag{7.48}$$

Thus the ratio C_L/C_{L_A} can vary anywhere, from just above 1 to 1.69 or higher. A typical value of this ratio for jet transports is 1.2. Using this value, but keeping in mind that it can be higher, the total airborne distance, in meters, becomes

$$s_A = \frac{15.2}{\theta_D} + \frac{V_A^2 \theta_D}{0.4g} \tag{7.49}$$

A jet transport approaches typically at a speed of 125 kt at an angle of 3°. Thus,

$$\begin{aligned} s_A &\simeq 290 + 55 \\ &= 350 \text{ m } (1155 \text{ ft.}) \end{aligned}$$

After touchdown, an approximately 2-sec delay is allowed while the pilot changes from the landing to the braking configuration. During this period the airplane continues to roll at the speed V_A. Actually, practice has shown that the speed decreases during the flare by approximately 5 kt typically. Denoting this portion by a subscript "tran" for transition,

$$\begin{aligned} s_{\text{tran}} &\simeq 2(V_A) \\ &\simeq 130 \text{ m } (427 \text{ ft}) \end{aligned}$$

Ground Roll

The calculation of the ground roll in landing follows along the same lines used for a takeoff ground roll, but with different parameters and initial conditions. The braking coefficient of friction varies from approximately 0.4 to 0.6 on a hard, dry surface to 0.2 on wet grass or 0.1 on snow. With spoilers the lift is essentially zero. Also, with flaps and spoilers the parasite drag coefficient may be higher.

Beginning with an initial value of V_A, the equations of motion can be numerically integrated, accounting for the variation with V of any reverse thrust, drag, and possibly lift. One can also use the approximate relationship

derived previously, equation 7.6. In the case of landing, this becomes

$$s = \frac{V_A^2}{2\bar{a}} \qquad (7.5$$

where $\bar{a}$ is the magnitude of the deceleration evaluated at $V_A/\sqrt{2}$.

As an example, consider the 747-100 at its maximum landing weight 2500 kN (564,000 lb). Assuming a μ of 0.4, an f of 80 m^2 (260 ft^2) and V_A equ to 65 m/s (126 kt) gives

$$\bar{a} = 4.05 \text{ m/s}^2$$

Therefore, the ground roll distance is estimated to be,

$$s = 522 \text{ m } (1710 \text{ ft})$$

This gives a total estimated FAR landing distance, including the factor of 1.667, (

$$s(\text{total}) = 1670 \text{ m } (5480 \text{ ft})$$

This compares favorably with the distance of 1880 m (6170 ft) quoted Reference 5.11. The difference is easily attributable to uncertainties in tl approach speed and the braking friction coefficient.

Lighter aircraft, except on an instrument approach, tend to descend at a angle steeper than 3°. With their lower wing loadings, light aircraft also touc down at much lower speeds. Hence, their landing distances are significant less than those for a jet transport. A Cherokee Arrow, for example, touchir down at approximately 65 kt can be stopped with moderate braking with 300 m (1000 ft).

RANGE PAYLOAD

Specifications of military aircraft and many larger civil aircraft incluc range-payload curves. This is a graph that for a particular mission profil presents the effect of trading off payload for fuel on the range of an airplan In determining such a curve, one must consider the operational phases th have been treated thus far in this chapter.

As an example in calculating a range-payload curve, consider the Cessn Citation I. Figure 7.21 presents a side-view sketch of this airplane. Table 7. presents a general description and some of its specifications. The rang calculation will include:

- Taxi and takeoff allowance.
- Climb from sea level to 41,000 ft.
- Cruise at maximum cruise thrust.
- Descent to sea level.
- Land with 45-min reserve fuel.

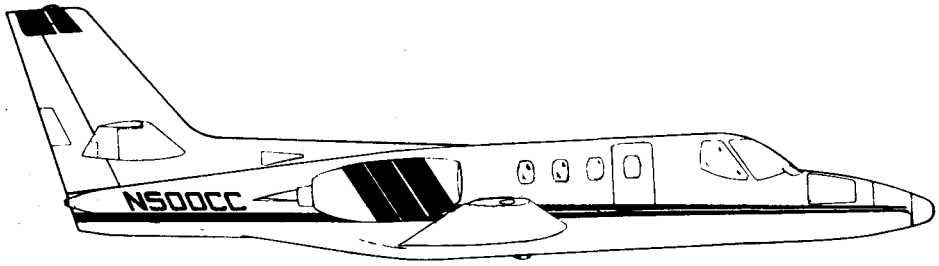

Figure 7.21 The Cessna Citation I.

The reserve fuel is calculated on the basis of holding at 25,000 ft (7620 m).

Using methods similar to those just presented and given engine performance curves (including installation losses), one can calculate, for a number of fixed airplane weights, information similar to that presented in Tables 7.2 to 7.5.

The maximum ramp weight for Citation I is 12,000 lb (53.4 kN). During taxi, 150 lb of fuel is assumed to be burned, so that the maximum allowable takeoff weight is 11,850 lb (52.7 kN). The maximum fuel capacity at this takeoff weight allowing for the 150 lb expended during taxi is 3630 lb (16.3 kN). This is the fuel available to fly the cruise profile. This maximum fuel together with the empty weight of 6470 lb (28.7 kN) and an oil weight of 34 lb leaves 1716 lb for payload. Thus, if 10 persons are on board (including the crew) at 200 lb per person, 284 lb of fuel must be removed resulting in a direct reduction in the range.

The total fuel for the range profile can be expressed as

$$W_f = W_{f_{CLB}} + W_{f_{CR}} + W_{f_{HLD}} + W_{f_{DES}} \tag{7.51}$$

where CLB, CR, HLD, and DES refer to climb, cruise, hold, and descent.

Figures 7.22 and 7.23 present in graphical form data from Tables 7.2, 7.3, and 7.5 necessary to determine the range-payload curve. In determining the range, in a manner of speaking, we begin at the ends and work toward the middle. During the hold, the average airplane weight will equal

$$\bar{W} = W_{TO} - W_f + W_{f_{DES}} + \frac{W_{f_{HLD}}}{2} \tag{7.52}$$

In Equation 7.52 $W_{f_{DES}}$ is the fuel required to descend from the holding altitude of 25,000 ft. Consider first takeoff at maximum allowable takeoff weight with full fuel. Thus,

$$W_{TO} = 11{,}850 \text{ lb}$$
$$W_f = 3630 \text{ lb}$$
$$W_{f_{DES}} = 83 \text{ (Table 7.4) lb}$$

Table 7.1 *Cessna Citation I*

MANUFACTURER	Cessna Aircraft Company
MODEL	500

1. GENERAL DESCRIPTION

The Cessna CITATION I aircraft is an all-metal, pressurized, low-wing monoplane with provisions for seven to ten persons and suitable allowance for luggage and optional equipment.

Two Pratt & Whitney Aircraft of Canada Limited JT15D-1A turbofan engines, rear fuselage mounted. Tricycle landing gear with single wheels.

U.S. FAA certified to requirements of FAR 25 – Transport Category, Day, Night, VFR and IFR (including Category II) Flight into known icing conditions – optional. Limited sod or dirt runway operations are authorized. Gravel runway operations – optional.

Approximate Dimensions	**Wing**	**Tail**	
		Horizontal	Vertical
Span	47′1″ (14.35 m)	18′10″ (5.74 m)	8′8″ (2.64 m)
Area	278.5 ft² (25.87 m²)	70.6 ft² (6.56 m²)	50.9 ft² (4.73 m²)
Sweep	0° @ 35% chord	0° @ 60% chord	33° @ 25% chord
Aspect ratio	7.83	5.00	1.50
Overall height			14′4″ (4.37 m)
Overall length			43′6″ (13.26 m)
Cabin			
Height (maximum over aisle)			4′4″ (1.32 m)
Length (Forward pressure bulkhead in flight compartment to aft pressure bulkhead in main baggage compartment)			17′6″ (5.33 m)
Width (maximum)			4′11″ (1.50 m)

Landing gear		Turning clearance	Wall to Wall	Curb to Curb
Tread	12′7″ (3.84 m)	Towing	47′1″ (14.35 m)	22′2″ (6.75 m)
Wheel base	15′8″ (4.78 m)	Taxiing	59′11″ (18.25 m)	30′0″ (9.14 m)

2. DESIGN WEIGHT AND CAPACITIES

Maximum ramp weight	12,000 lb
Maximum takeoff weight	11,850 lb
Maximum landing weight	11,350 lb
Maximum zero fuel weight	8,400 lb[a]
Approximate licensed empty weight[b]	6,470 lb
Useful load	5,530 lb
Fuel capacity (usable) 6.75 lb/gal	3,780 lb

[a] 9500 lb available on optional basis.

[b] *Note* Approximate licensed empty weight is based on the 323-lb avionics package, a complete standard interior, plus the standard exterior paint scheme.

Table 7.2 Climb Performance. Maximum Rate Climb; 175 KIAS at Sea Level; Time, Distance and Fuel;[a] Standard Day

TO Wt. 1000 Lb	11.85	11.50	10.50	9.50	11.85	11.50	10.50	9.50
Pressure Altitude		5,000 ft				10,000 ft		
Min	2	2	2	2	4	4	4	3
Nmi	6	5	5	4	12	12	10	8
Lb	65	63	56	50	129	124	111	99
Pressure Altitude		15,000 ft				21,000 ft		
Min	6	6	6	5	10	9	8	7
Nmi	20	19	16	13	13	29	25	21
Lb	194	186	165	147	272	261	231	204
Pressure Altitude		25,000 ft				29,000 ft		
Min	12	12	10	9	15	15	13	11
Nmi	40	38	32	26	52	48	40	33
Lb	327	313	276	243	387	369	323	284
Pressure Altitude		31,000 ft				33,000 ft		
Min	17	16	14	12	19	18	16	14
Nmi	59	55	45	38	68	63	52	42
Lb	419	399	349	305	455	433	376	328
Pressure Altitude		35,000 ft				37,000 ft		
Min	22	21	18	15	26	24	20	17
Nmi	79	73	59	48	94	86	69	55
Lb	497	470	406	351	549	517	440	378
Pressure Altitude		39,000 ft				41,000 ft		
Min	32	29	24	20	53	42	29	23
Nmi	121	108	83	65	214	165	107	79
Lb	631	585	485	411	886	741	555	454

[a]Time in "min" (minutes), distance in "nmi" (nautical miles), fuel in "lb" (pounds used).

Table 7.3 Cruise performance. Maximum Cruise Thrust; Standard Day

Cruise Altitude 1000 ft	Total Fuel Consumption lb/hr	Cruise Speed Knots True Airspeed — Aircraft Weight 11,500 lb	10,500 lb	9,500 lb	8,500 lb
5	1515	281	281	281	281
10	1461	302	302	302	302
15	1505	328	333	334	335
20	1345	337	340	342	343
25	1195	344	346	348	350
30	1045	345	350	353	355
33	950	345	351	355	357
35	905	343	350	355	358
37	834	335	344	350	354
39	757	321	335	343	348
41	688	280	317	332	340

The average weight for holding thus becomes

$$\bar{W} = 8303 + \frac{W_{f_{HLD}}}{2} \tag{7.53}$$

Referring to Figure 7.23, guess at a $\bar{W}$ of 8500 lb. This leads to a fuel flow rate of 540 lb/hr or, for 45 min, a holding fuel of 405 lb. From Equation 7.53, $\bar{W}$ is then calculated to be 8708, which is higher than the guessed value. Iterating in this manner, the holding fuel is found to equal 415 lb.

The fuel to climb to 41,000 ft from Figure 7.22 equals 886 lb. To descend from 41,000 ft to sea level requires 134 lb. Thus, the fuel left for cruising equals:

$$W_{f_{CR}} = W_f - W_{f_{HLD}} - W_{f_{DES}} - W_{f_{CLB}}$$
$$= 2195 \text{ lb}$$

The average weight during the cruise will be

$$\bar{W} = W_{TO} - W_{f_{CLB}} - \frac{W_{f_{CR}}}{2}$$
$$= 9867 \text{ lb}$$

From Figure 7.23, the cruising speed at this weight equals 328 kt. The fuel

Table 7.4 Descent Performance. Low-Power Descent, 3000 ft/min; Fuel Flow at 3000 lb/hr/Engine; Gear and Flaps Up; Speed Brakes Retracted; Zero Wind

Pressure Altitude (1000 ft)	Time (min)[a]	Fuel Used (lb)[a]	Distance (nmi)[a]
41[b]	13.7	134	69
39[b]	13.0	129	65
37[b]	12.3	124	61
35	11.7	117	57
33	11.0	110	53
31	10.3	103	48
29	9.7	97	44
27	9.0	90	41
25	8.3	83	37
23	7.7	77	33
21	7.0	70	30
19	6.3	63	26
17	5.7	57	23
15	5.0	50	20
10	3.3	33	13
5	1.7	17	6

[a]Time, fuel used, and distance are for a descent from indicated altitude to sea level, standard day.
[b]Use high-speed descent between 41,000 and 35,000 ft.

Table 7.5 Holding Fuel; Two-Engine Fuel Consumption, lb/hr

Aircraft Weight (lb)	Speed (KIAS)	Pressure Altitude (1000 ft)						
		S.L.	5	10	15	20	25	30
10,500	165	955	870	792	728	691	673	661
9,500	155	886	810	738	673	625	607	590
8,500	145	807	745	682	622	569	536	522
7,500	135	705	678	625	570	520	479	460

Source.

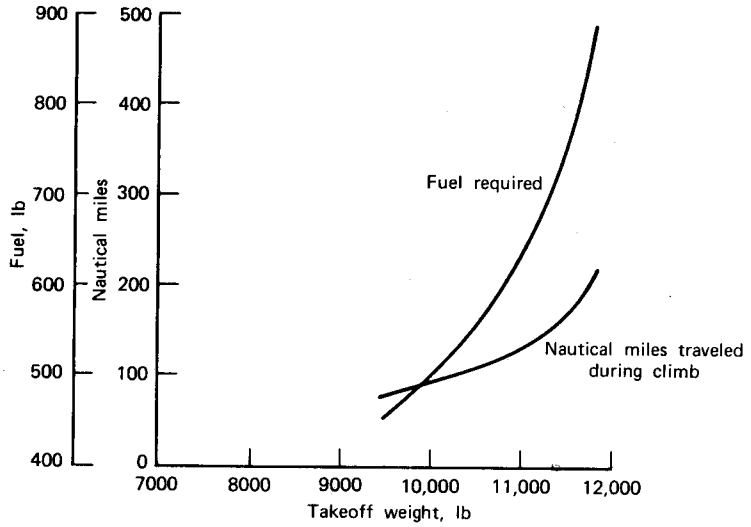

Figure 7.22 Fuel required and distance traveled by Citation I in climbing to 41,000 ft.

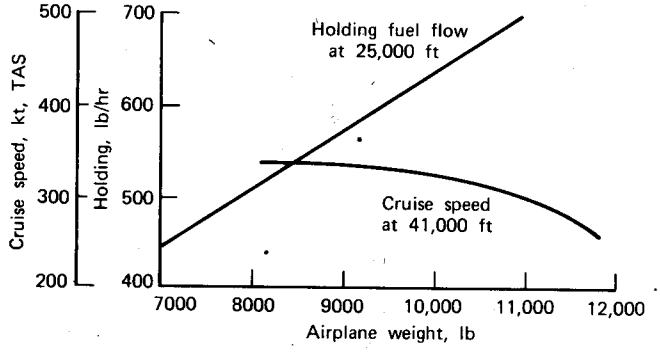

Figure 7.23 Holding fuel flow and cruising airspeed for Citation I.

flow rate for maximum cruising thrust is found from Table 7.3 to equal 688 lb/hr. The total cruising fuel, fuel flow, and speed give a distance covered during the cruise of 1046 nmi. To get the range, we add to this the distance covered during the climb and descent. These are obtained from Figure 7.22 and Table 7.4, respectively. These two distances total 283 nmi. giving a total range of 1329 nmi.

This range and payload represent one point on the range-payload curve. A break in the slope of the range-payload curve will occur at this point because

of the following. For lighter payloads, the gross weight will decrease, resulting in increased ranges for the same total fuel. For heavier payloads, less fuel must be put aboard, resulting in a direct loss of range. At a cruising airspeed of around 328 kt and a fuel flow of 688 lb/hr, one can see immediately that the range will decrease by approximately 48 nmi/100 lb of additional payload over 1716 lb.

Consider two additional points on the range-payload curve: a payload of 2000 lb corresponding to a crew of two and eight passengers at 200 lb per person, and a minimum payload of 400 lb corresponding to the crew alone.

For the 2000-lb payload, the takeoff weight will remain the same, but the fuel weight is reduced by 284 lb to 3346 lb after taxi. The average holding weight now becomes

$$\bar{W} = 8587 + \frac{W_{f_{\text{HLD}}}}{2}$$

By iteration, $W_{f_{\text{HLD}}} = 421$ lb

The fuel to climb remains unchanged, so that

$$W_{f_{\text{CR}}} = 1905 \text{ lb}$$

The average weight during cruise equals 10,012 lb. From Figure 7.23, the cruising speed at this average weight will be 325 kt. This speed and a fuel rate of 688 lb/hr result in a distance of 900 nmi. The distances gained during climb and descent remain unchanged, so the total range for the 2000 lb payload becomes 1183 nmi.

For a minimum payload of 400 lb, the takeoff gross will be reduced to 10,534 lb.

The equation for the average holding weight now reads

$$\bar{W} = 6987 + \frac{W_{f_{\text{HLD}}}}{2}$$

so $W_{f_{\text{HLD}}} = 344$ lb. The fuel weight to climb to 41,000 ft at this reduced gross weight equals 557 lb and the distance travelled during the climb is 110 nmi. The descent fuel and distance are assumed to remain the same. Thus the fuel for cruising equals 2595 lb. The average cruising weight becomes 8680 lb. At this weight, the cruising speed equals 339 kt with the fuel consumption rate unchanged. Therefore the cruising distance equals 1279 nmi. Added to the distances covered during climb and descent, this figure results in a total range of 1458 nmi.

The preceding three points define the range-payload curve for the Citation I as presented in Figure 7.24. The calculated points are shown on the curve. Again, the break in this curve corresponds to maximum allowable takeoff weight with a full fuel load.

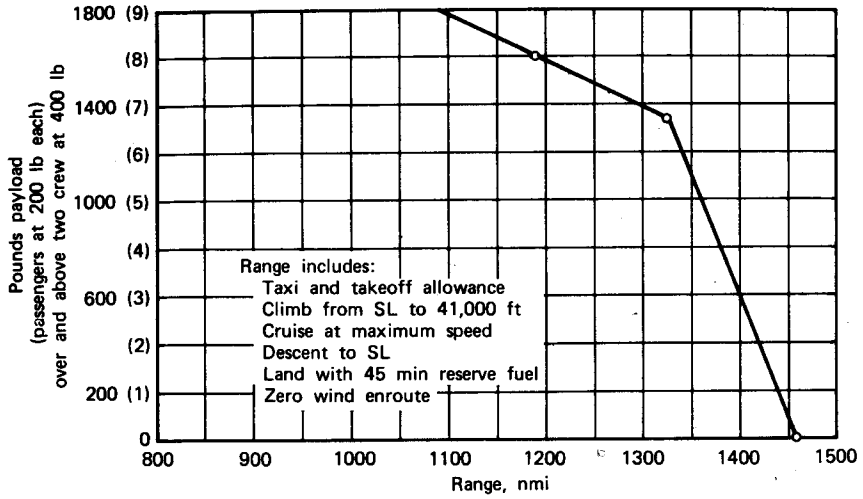

Figure 7.24 Range-payload curve for the Cessna Citation I.

OPERATING LIMITATIONS

Flight Envelope

An airplane's flight envelope is the region on an airspeed-altitude plot in which the airplane is capable of operating. Within this region, an airplane is limited at low speeds by stall and at high speeds by the available thrust. The stall boundary as a function of altitude is easily determined from

$$V^2 = \left(\frac{2W/S}{\rho_0 C_{L_{max}}}\right)\frac{1}{\sigma} \tag{7.54}$$

The high-speed boundary is determined from power-available, power-required curves such as those presented in Figure 7.15. As an example, let us again consider the Cherokee Arrow. Figure 7.25 was prepared using a gross weight of 11.8 kN, a $C_{L_{max}}$ of 1.6, a constant propeller efficiency of 0.85, and a sea level engine power of 149 kW. The Cherokee is capable of level flight within the region bounded by the two curves labeled "stall" and "maximum" power.

A typical flight envelope for a supersonic aircraft is given in Figure 7.26. At high subsonic Mach numbers, a phenomenon known as buffet can limit flight to speeds higher than the stalling speeds. This type of buffeting is caused by an instability in the position of the shock waves near the trailing edge of the upper and lower wing surfaces. As the stall is approached, these

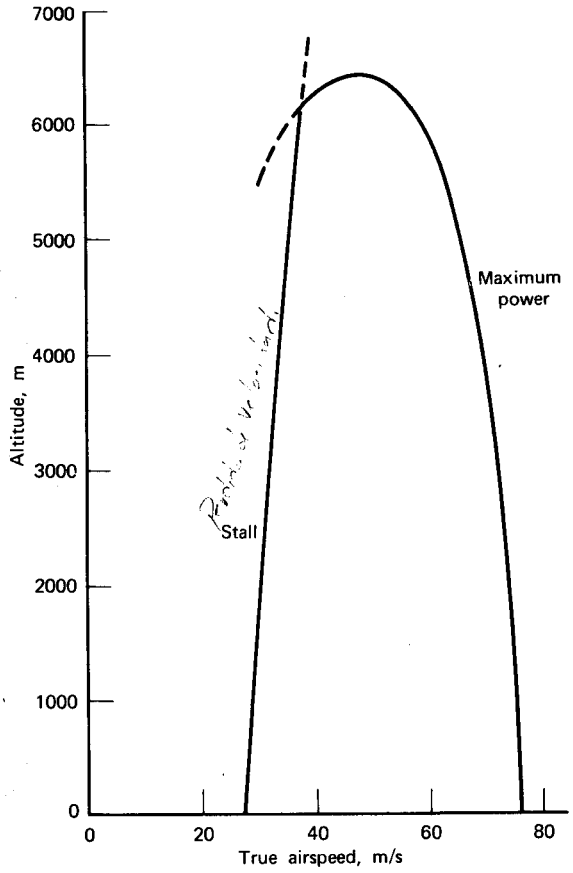

Figure 7.25 Flight envelope for the Cherokee Arrow.

waves begin to move fore and aft out of phase with each other, producing a periodic flow behind the wing that resembles a Karman vortex street. The tail, in proximity to this unsteady flow, can produce a severe shaking of the airplane.

Also shown on Figure 7.26 is a limit on the maximum dynamic pressure that can be tolerated. This boundary arises from structural considerations and involves items such as flutter, torsional divergence, and static pressure within an engine inlet diffuser.

An aerodynamic heating limit as shown in Figure 7.26 also exists for airplanes designed to operate at high Mach numbers. It is beyond the scope of this text to consider in depth the subject of aerodynamic heating. However, one can gain some appreciation for the problem by calculating the stagnation

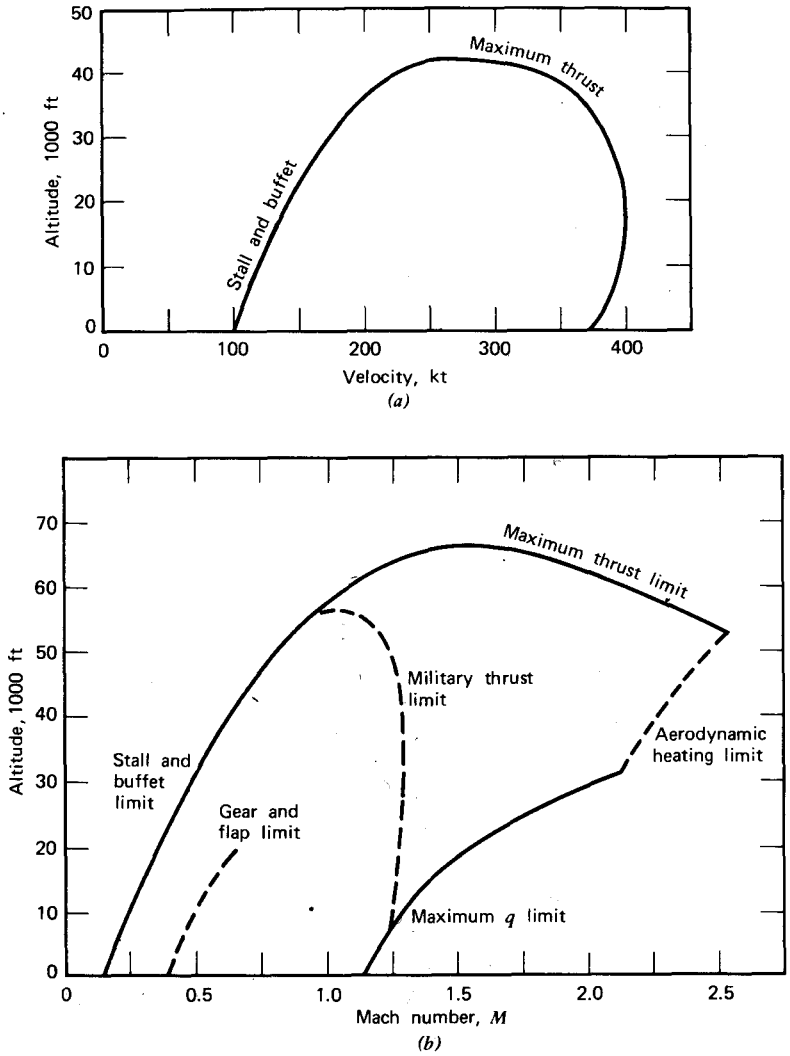

Figure 7.26 Typical aircraft flight envelopes. (*a*) Subsonic aircraft. (*b*) Supersonic aircraft. (L. M. Nicolai, *Fundamentals of Aircraft Design*, L. M. Nicolai, 1975. Reprinted by permission of L. M. Nicolai.)

temperature as a function of Mach Number. This can be accomplished using the relationships covered in Chapter Five with the results shown in Figure 7.27. Along the leading edge of a wing, these temperatures will be alleviated somewhat by sweep. Nevertheless, temperatures of the order of 250 °C or higher can be expected for Mach numbers exceeding 2.0.

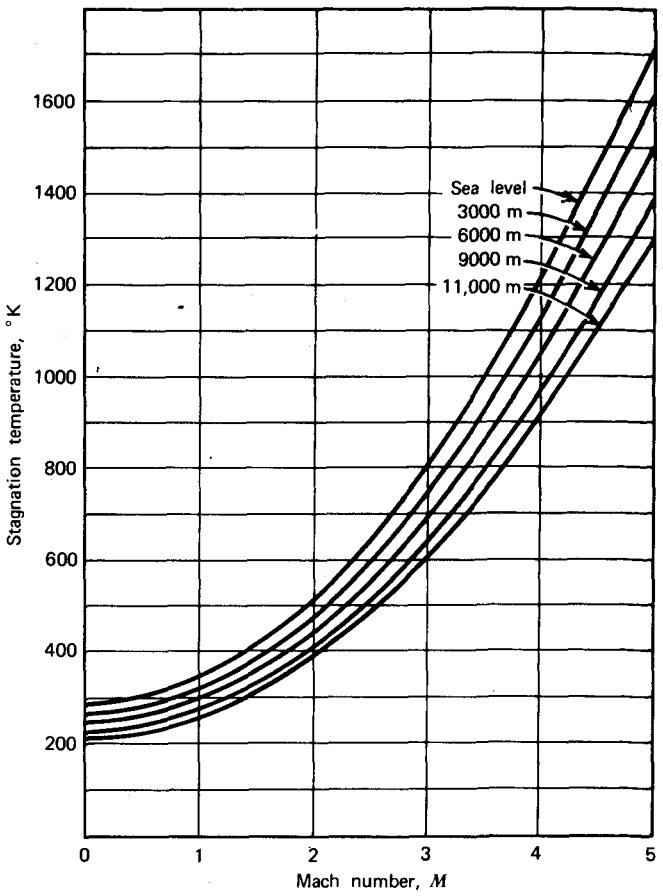

Figure 7.27 Stagnation temperature as a function of altitude and Mach number.

Maneuvering Envelope (V-n Diagram)

The lift distribution on a wing is illustrated in Figure 7.28. If y represents the spanwise distance to the center of lift of one side, the bending moment at the wing root will be given approximately by

$$M \simeq \mathrm{y}\frac{L}{2}$$

where L is the total lift on the wing. Generally, L will be greater than the airplane's weight, in which case the airplane is accelerating upward at a value

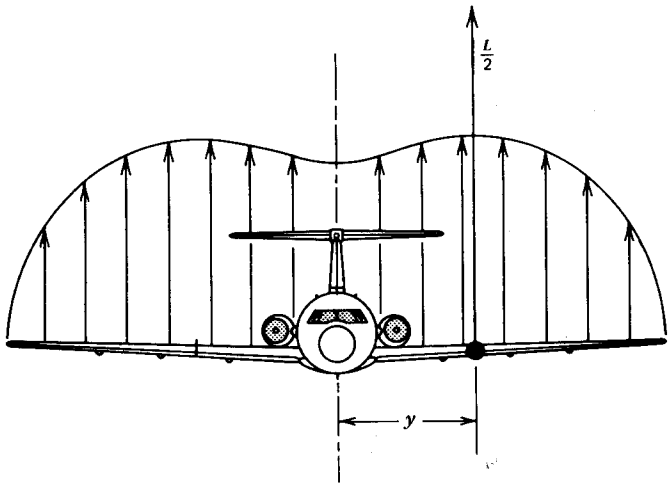

Figure 7.28 Wing bending moment due to spanwise lift distribution.

equal to

$$a = g\left(\frac{L}{W} - 1\right)$$

In terms of acceleration,

$$L = W\left(1 + \frac{a}{g}\right) \tag{7.55}$$

so that the bending moment becomes

$$M = y\frac{W}{2}\left(1 + \frac{a}{g}\right)$$

The term $(1 + a/g)$ is known as the load factor, n.

$$n = 1 + \frac{a}{g} \tag{7.56}$$

In this example, the wing bending moment in steady flight is seen to increase by the factor n. Similarly, n is a measure generally of the increase in the loads on any member of the airplane resulting from accelerations. In steady, level flight, n is equal to 1. As a result of maneuvering or gusts, n can increase in magnitude to high values and can be positive or negative.

The value of n that can be achieved by maneuvering can be obtained from

$$n = \frac{L}{W}$$

$$= \frac{\frac{1}{2}\rho V^2 S C_{L_{max}}}{W}$$

But $2W/\rho SC_{L_{max}}$ equals the stalling speed, V_s. Therefore

$$n = C_{L_{max}}\left(\frac{V}{V_s}\right)^2 \tag{7.57}$$

Since V can be appreciably greater than the stalling speed, V_s, it is not practical to design an airplane's structure to withstand the highest possible load factors that it could produce. Instead, based on experience, airplanes are certified to withstand different limit load factors, depending on the airplane's intended use. A limit load is one that can be supported by a structure without yielding. In addition to designing to the limit loads, FAR Parts 23 and 25 require factors of safety of 1.5 to be applied to the sizing of the structure. Since the ultimate allowable stress of aluminum alloys is approximately 50% greater than the yield stress, a factor of safety of 1.5 applied to the limit loads is approximately equivalent to designing to ultimate load factors with no factor of safety.

Civil airplanes are designed in the normal, utility, acrobatic, and transport categories. For the first three categories, FAR Part 23 states:

§ 23.337 Limit maneuvering load factors.

(a) The positive limit maneuvering load factor n may not be less than

[(1) $2.1 + \frac{24{,}000}{W + 10{,}000}$ for normal category airplanes, except that n need not be more than 3.8;]

(2) 4.4 for utility category airplanes; or

(3) 6.0 for acrobatic category airplanes.

(b) The negative limit maneuvering load factor may not be less than—

(1) 0.4 times the positive load factor for the normal and utility categories; or

(2) 0.5 times the positive load factor for the acrobatic category.

(c) Maneuvering load factors lower than those specified in this section may be used if the airplane has design features that make it impossible to exceed these values in flight.

For the transport category, FAR Part 25 states:

§ 25.337 Limit maneuvering load factors.

(a) Except where limited by maximum (static) lift coefficients, the airplane is assumed to be subjected to symmetrical maneuvers resulting in the limit maneuvering load factors prescribed in this section. Pitching velocities appropriate to the corresponding pull-up and steady turn maneuvers must be taken into account.

(b) The positive limit maneuvering load factor n for any speed up to V_D may not be less than 2.5.

(c) The negative limit maneuvering load factor—
  (1) May not be less than -1.0 at speeds up to V_C; and
  (2) Must vary linearly with speed from the value at V_C to zero at V_D.
(d) Maneuvering load factors lower than those specified in this section may be used if the airplane has design features that make it impossible to exceed these values in flight.

In these regulations, V_C is referred to as the design cruising speed. It need not exceed V_H, the maximum speed in level flight at maximum continuous power. Otherwise, it must not be less than V_B plus 43 knots where V_B is the lowest speed that can produce a load factor of 2.5. V_D is the design dive speed, and for the transport category it need not be greater than V_H.

Gust Load Factors

A wing suddenly penetrating a "sharp-edged" gust is pictured in Figure 7.29. The gust velocity is denoted by U_{de} in accordance with FAR notation. After penetrating the gust and before the wing begins to move upward, the angle-of-attack increment resulting from the gust, $\Delta\alpha$, equals

$$\Delta\alpha = \frac{U_{de}}{V} \tag{7.58}$$

The increase in the wing's lift then becomes

$$\Delta L = \frac{1}{2}\rho V^2 Sa\frac{U_{de}}{V}$$

Before encountering the gust, in level flight,

$$W = \frac{1}{2}\rho V^2 Sa\alpha$$

The load factor, n, resulting from the gust encounter therefore becomes

$$n = \frac{L}{W}$$
$$= \frac{W + \Delta L}{W}$$
$$= 1 + \frac{U_{de}}{V\alpha}$$

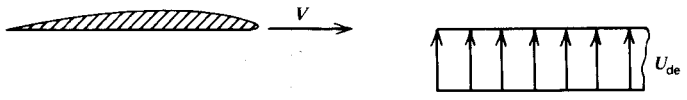

Figure 7.29 A wing penetrating a sharp-edged gust.

or

$$n = 1 + \frac{\rho V U_{de} a}{2(W/S)} \tag{7.59}$$

In practice, one never encounters a truly sharp-edged gust. Therefore U_{de} is multiplied by an alleviation factor less than unity, again based on experience, which lessens the acceleration due to the gust. The final result, given in FAR Part 23, for the load factor resulting from a gust is expressed as follows.

$$n = 1 + \frac{K_g U_{de} V a}{498\,(W/S)} \tag{7.60}$$

where

$$K_g = \frac{0.88\,\mu}{5.3 + \mu} = \text{gust alleviation factor}$$

$$\mu = \frac{2(W/S)}{\rho \bar{c} a g} = \text{airplane mass ratio}$$

U_{de} = "derived" gust velocity, fps

$\bar{c}$ = mean geometric chord $= S/b$

V = equivalent airspeed in knots

a = slope of the airplane normal force coefficient C_N/rad

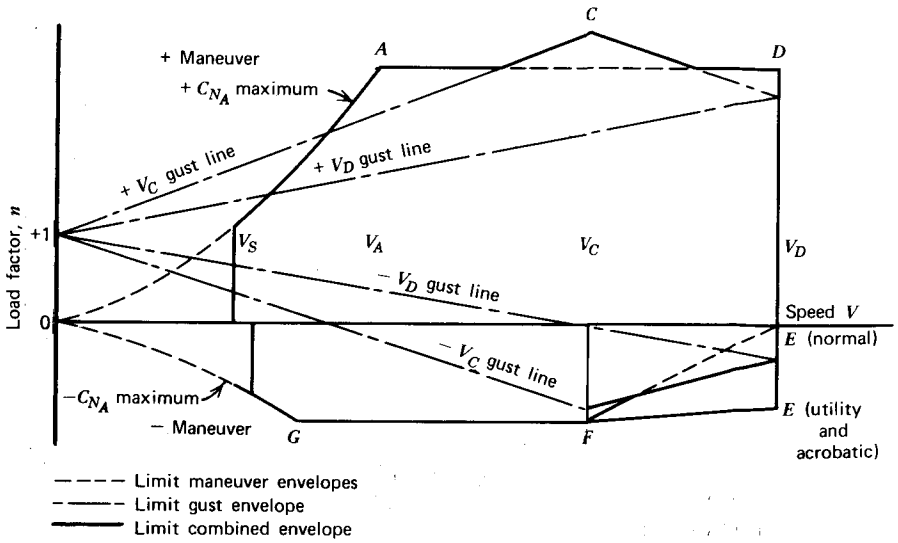

Figure 7.30 *V-n* diagram for airplanes in the normal, utility, and acrobatic categories.

Positive and negative values of U_{de} up to 50 fps must be considered at V_c at altitudes between sea level and 20,000 ft. The gust velocity may be reduced linearly from 50 fps at 20,000 ft to 25 fps at 50,000 ft. Positive and negative gusts of 25 fps at V_D must be considered at altitudes between sea level and 20,000 ft. This velocity can be reduced linearly to 12.5 fps at 50,000 ft.

For FAR Part 23, the foregoing criteria for the maneuvering and gust loads results in the type of V-n diagram pictured in Figure 7.30 In certifying an airplane, one must demonstrate the structural integrity of the airplane subjected to the aerodynamic loadings that can exist throughout the V-n diagram.

ENERGY METHODS FOR OPTIMAL TRAJECTORIES

The problem to be considered briefly in this section concerns the altitude-velocity (or Mach number) schedule, which should be flown to minimize the time or fuel required to go from one speed and altitude to another speed and altitude. As pointed out in Reference 7.4, this problem can be solved by the application of variational calculus. However, the result is a formidable computer program. As an alternate method, which is approximate but close to the more exact solution, one can obtain a graphical solution by considering the energy state of the airplane.

As noted previously, Equation 7.14 is an energy relationship for the rate of climb. If we let h_e denote the total energy, kinetic and potential, per unit weight of the airplane, Equation 7.14 can be written in terms of this specific energy as

$$\frac{dh_e}{dt} = \frac{V(T - D)}{W} \tag{7.61}$$

where

$$h_e = h + \frac{V^2}{2g} \tag{7.62}$$

dh_e/dt will be denoted by P_s and is called the excess specific power.

The rate of change of h_e with respect to fuel weight, W_f, will be denoted by f_s and can be written as

$$\begin{aligned} f_s &= \frac{dh_e}{dW_f} \\ &= \frac{dh_e/dt}{dW_f/dt} \\ &= \frac{dh_e/dt}{T(\text{SFC})} \text{ (ft/lb or m/N)} \end{aligned} \tag{7.63}$$

The time required to go from one energy level to another will be given by

$$\Delta t = \int_{h_{e_1}}^{h_{e_2}} \frac{1}{P_s} dh_e \tag{7.64}$$

The path to minimize Δt at any altitude and airspeed will be the one that gives the maximum rate of change of h_e for a given P_s value. Therefore, if contours of constant h_e and constant P_s values are plotted as a function of altitude and Mach number, the path for minimum time will be the locus of points for which the contours are parallel. Similarily, contour plots of constant f_s and h_e values provide an altitude-Mach number schedule for minimum fuel consumption.

As an example, consider a hypothetical subsonic turbojet airplane with the thrust and drag given by

$$T = T_0\sigma$$

$$D = \frac{\rho V^2 f}{2} + \frac{2(W/b)^2}{\pi\rho e}\frac{1}{V^2}$$

In this case, one can write, for the density ratio σ

$$\sigma = \frac{B + \sqrt{B^2 + 4AC}}{2}$$

where

$$A = T_0 - \frac{\rho_0 f V^2}{2}$$

$$B = \frac{P_s W}{V}$$

$$C = \frac{2(W/b)^2}{\pi e \rho_0 V^2}$$

The curves of altitude versus airspeed presented in Figure 7.31 were prepared by evaluating σ over a range of airspeeds for constant values of P_s. For the standard atmosphere, σ and h are related by $h = 44.3\ (1 - \sigma^{0.235})$ km. Curves of constant h_e are also shown in Figure 7.31. The altitude-airspeed schedule for climbing from sea level to V_{max} at 11.8 km is indicated by the dashed line in this figure. This line passes through points on the P_s curves where these curves would be tangent to lines of constant h_e. In this example, where the thrust and drag are well behaved, the result is about as one would expect.

The results are substantially different, however, for an airplane designed to operate through Mach 1, particularly if the thrust is marginal in the transonic region. Such a case is presented in Figure 7.32 (taken from Ref. 7.4). As indicated by the dashed line, in this case the optimum trajectory consists

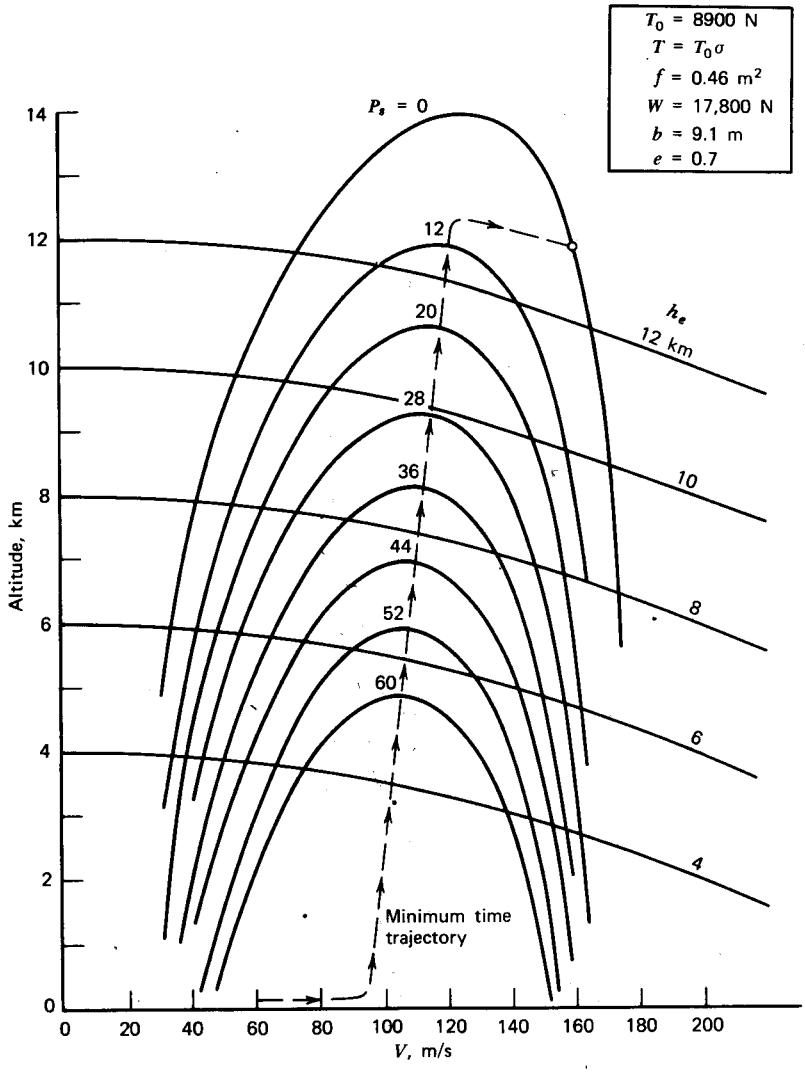

Figure 7.31 Excess specific power and specific energy for a hypothetical subsonic airplane.

of a subsonic climb at a nearly constant Mach number to 33,000 ft followed by a descent through the transonic drag rise region to 20,000 ft and a Mach number of 1.25. A climb to 39,000 ft at increasing Mach numbers then ensues up to 39,000 ft and Mach 2.1. The remainder of the climb up to 50,000 ft is accomplished at a nearly constant Mach number, as shown.

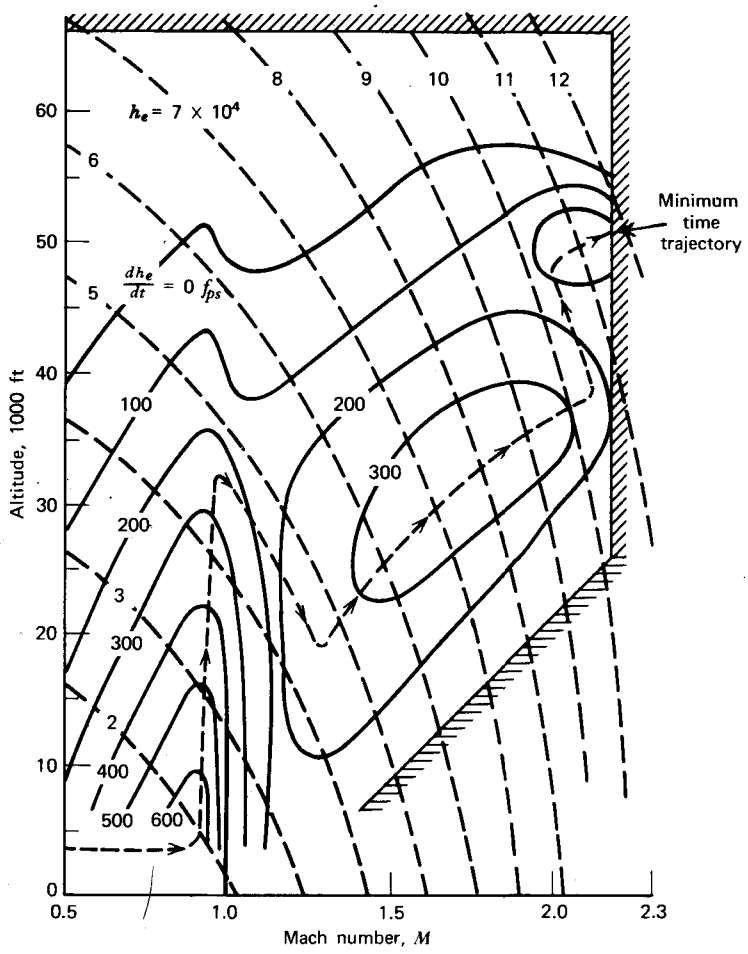

Figure 7.32 Excess specific power and specific energy for the F-104 at maximum power and a weight of 18,000 lb(80,064 N). (L. M. Nicolai, *Fundamentals of Aircraft Design*, L. M. Nicolai, 1975. Reprinted by permission of L. M. Nicolai.)

THE ART OF ESTIMATING AND SCALING

Sometimes one must give a reasonable estimate of an airplane's characteristics or performance without having all the facts at hand. It is therefore a good idea to commit to memory a few principles and numbers. The "square-cube" scaling law is a good one to remember. For two geometrically similar airplanes designed to the same stress levels and using the same materials, one would expect their areas to be proportional to the characteristic

length squared and their volumes, and hence weight, proportional to the length cubed.

$$S \propto l^2$$
$$W \propto l^3$$

It follows that $l \propto W^{1/3}$. One would therefore expect the wing loading of aircraft to vary as

$$\frac{W}{S} \propto W^{1/3} \tag{7.65}$$

Figure 7.33 was prepared with Equation 7.65 in mind. This figure indicates that while the square-cube law can be helpful in estimating the gross weight of an airplane, other factors must also be considered. For performance reasons, wing loadings are sometimes made purposefully higher or lower than the average. Generally, the aircraft with higher cruising speeds lie on the high side of the shaded portion in Figure 7.33. This upper boundary is given by

$$\frac{W}{S} = 2.94\,(W^{1/3} - 6)\ \text{psf}$$
$$= 85.5\,(W^{1/3} - 9.9)\ \text{N/m}^2 \tag{7.66}$$

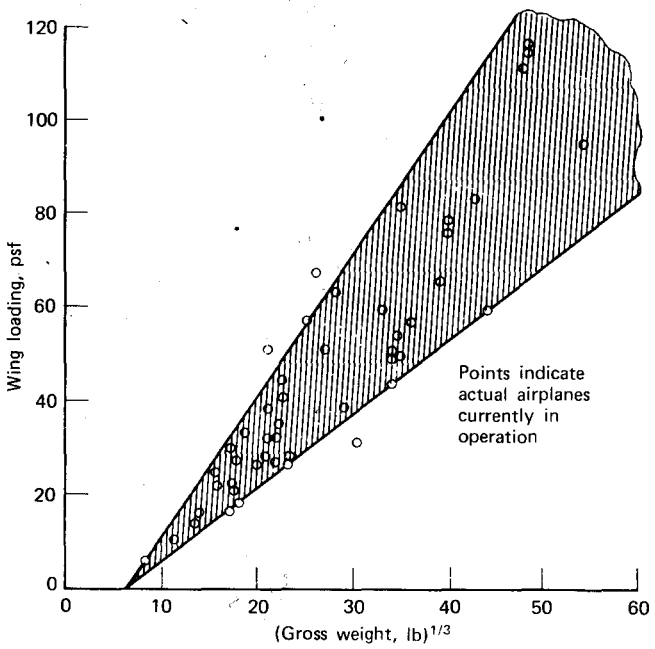

Figure 7.33 Square-cube law.

The lower boundary is approximated by,

$$\frac{W}{S} = 1.54\,(W^{1/3} - 6)\ \text{psf}$$
$$= 44.8\,(W^{1/3} - 9.9)\ \text{N/m}^2 \qquad (7.67)$$

The foregoing must be qualified somewhat. Scaling, such as this, is valid only if pertinent factors other than size remain constant, for example, the structural efficiency of materials. Also, for purposes of their mission, aircraft are designed for different load factors.

In sizing an aircraft, it is also of value to note that the empty weights of aircraft average close to 50 or 60% of the design gross weights as shown in Figure 7.34. Thus, knowing the payload and fuel and having some idea of the aerodynamic "cleanliness" of the aircraft, one can undertake a preliminary estimate of its weight and performance.

For example, suppose we are designing a four-place, light aircraft with fixed gear. Let us arbitrarily decide on 300 lb of fuel. The gross weight will be

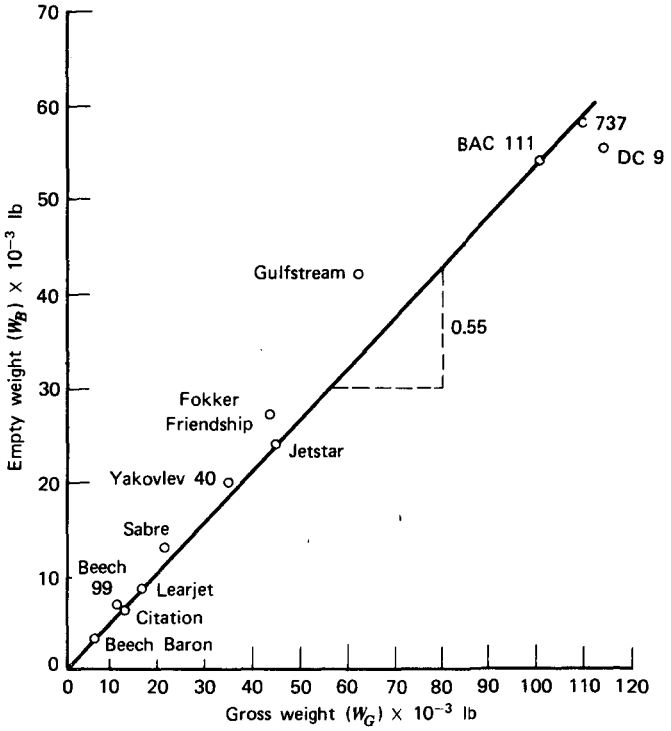

Figure 7.34 Relationship between gross and empty weight.

approximately

$$\text{Gross weight} = \text{Weight empty} + \text{Payload} + \text{Fuel weight}$$

$$W = W_E + W_{PL} + W_F \tag{7.68}$$

Assuming each passenger and baggage to weigh 200 lb gives

$$W = W_E + 800 + 300$$

But $W_E \simeq 0.55\ W$, so that

$$W \simeq 2400 \text{ lb}$$

From Figure 7.34 for this weight, the wing loading should be approximately

$$W/S = 14.7 \text{ psf}$$

This results in a wing area of $S = 163 \text{ ft}^2$. If we decide on a low-wing airplane,

Table 7.6 Summary of Approximate Relationships

$\frac{\text{Weight empty}}{\text{Gross weight}} \simeq 0.55$	
$W/S = 2.94\ (W^{1/3} - 6)$ psf	High performance (W in lb)
$W/S = 85.5\ (W^{1/3} - 9.9)$ N/m^2	High performance (W in N)
$W/S = 1.54\ (W^{1/3} - 6)$ psf	Low performance (W in lb)
$W/S = 44.8\ [W^{1/3} - 9.9]$ N/m^2	Low performance (W in N)
$C_f \simeq 0.0065$	Light aircraft, fixed gear
$\simeq 0.0045$	World War II prop-driven fighters
$\simeq 0.0035$	Turbojet aircraft
$C_{D_0} \simeq 0.037$	Light aircraft, fixed gear
$\simeq 0.025$	Light aircraft, retractable gear
$e \simeq 0.6$	Low-wing aircraft
$\simeq 0.8$	High-wing aircraft
$C_{L_{max}} \simeq 1.3$	No flaps
$\simeq 1.8$	Plain flaps
$\simeq 2.5$	Double-slotted flaps
BSFC $\simeq 0.5$ lb/bhp-hr	Piston engines
$\simeq 3.0$ N/kW-hr	
TSC $\simeq 0.35$ 1/hr	High-bypass turbofan
$\simeq 0.6$ 1/hr	Moderate-bypass turbofan
$\simeq 0.8$ 1/hr	Turbojet
$\eta \simeq 0.85$	Propeller in cruise
$\simeq 0.70$	Propeller in climb

Note. Output from turbojet engines, approximately proportional to density ratio, σ. For piston engines, $P \simeq P_0\ (\sigma - 0.1)/0.9$.

then an e of 0.6 is reasonable. Also, for a fixed-gear aircraft, a parasite C_D of 0.037 was recommended in Chapter Four. We are now in a position to construct power-required curves for various altitudes. The next step would be to select a power plant so that performance estimates can be made. In so doing, we would make use of a typical BSFC of 0.5 lb/bhp-hr for piston engines (unless performance curves on the particular engine selected were available). The value of developing a "feeling" for reasonable values for airplane parameters should be obvious. Table 7.6 summarizes some of these.

PROBLEMS

7.1 All questions refer to the same airplane. In answering a given question, use any assumptions given in preceding questions.

(*a*) An "ultralight" aircraft (such as a BD-5) is powered with a sea level-rated 60-hp piston engine driving a 3.7-ft diameter propeller. It carries 200 lb of payload and 10 gal of gasoline. What would be a reasonable estimate of its empty weight?

(*b*) Assuming the gross weight of the airplane to be 600 lb, what would be a reasonable estimate of its wing loading?

(*c*) Assuming a wing area of 65 ft^2 and an aspect ratio of 6 with no flaps, at 20% above its stalling speed, what would you estimate for its landing speed?

(*d*) Assuming a takeoff speed of 55 mph, what would the ground roll distance be for the airplane?

(*e*) Assuming retractable gear and a low wing configuration, construct power required curves for sea level and 8000 ft. What is the minimum power required at these altitudes?

(*f*) Assuming a propeller efficiency during climb of only 70%, calculate the rate of climb at sea level and 8000 ft at the speed for minimum power required.

(*g*) Cruising at 75% of sea level-rated power, calculate the cruising velocities and ranges (no reserve and neglect climb) at sea level and 8000 ft. Assume an η of 85%.

7.2 For a propeller-driven airplane, show that the minimum required power varies inversely with the square root of the density ratio. If the available power is assumed proportional to $(\sigma - 0.1)/0.9$, show that the density ratio for the absolute ceiling is governed by the relationship

$$\sigma^{3/2} - 0.1\sigma^{1/2} = 0.9\left[1 - \frac{W(R/C)_0}{P_0}\right]$$

where P_0 and $(R/C)_0$ are the sea level values for the available power and rate of climb.

7.3 An airplane has a constant thrust to weight ratio of 0.25 and a braking friction coefficient, μ, of 0.5. While taking off on an 850-m strip and not yet airborne, the engine fails. At that instant, the plane had attained a speed of 69 kt. The pilot immediately applies the brakes. Will the plane stop before the end of the runway (neglect aerodynamic drag)? Justify your answer.

7.4 A fairing is to be added to a Cherokee Arrow. This fairing will reduce f by 0.25 ft^2, but weighs 12 lb. At its maximum gross weight this will require decreasing the fuel by 2 gal. From a range standpoint, will the fairing be beneficial?

7.5 An advanced medium STOL transport has an approach speed of 85 kt with a descent angle of 6.6°. It weighs 670 kN and has a wing loading of 4300 N/m^2. On touching down it has a constant deceleration of 0.25g.What is its total landing distance over a 15-m obstacle?

7.6 An airplane has a R/C of 1000 fpm at sea level and 500 fpm at 7000 ft. How much time will it require to climb from an altitude of 2000 ft up to 10,000 ft?

7.7 The Beech 99 is a turboprop airplane popular with commuter airlines. It is powered by two P&W PT6A-27 engines. The performance of this engine can be found from Figures 6.45 and 6.46 and Table 6.3. Estimate the various performance items for this airplane and compare with the numbers given in Reference 5.11.

7.8 Calculate the available thrust for the Cherokee Arrow as a function of airspeed up to 45 m/s at SSL conditions. Assume 2700 rpm and 149 kW. How do your results compare with Figures 6.18 and 6.19? For the standard gross weight of 11.8 kN, calculate the ground roll distance to attain a velocity of 36 m/s.

7.9 For a normally aspirated piston engine airplane, show that the absolute ceiling is a function of the sea level rate of climb. Derive an equation relating the two performance items.

REFERENCES

7.1 Anonymous, *Jet Transport Performance Methods*, The Boeing Co., Commercial Airplane Group, Seattle, Wash., Boeing Document No. D6-1420, 6th Edition, May 1969.

7.2 Anonymous, *Cessna/Citation I Specification and Description*, Cessna Aircraft Co., Commercial Jet Marketing Division, Wichita, Kans., January 1977.

7.3 Anonymous, *Cessna/Citation I Flight Planning Guide*, Cessna Aircraft Co., Commercial Jet Marketing Division, Wichita, Kans., February 1977.

7.4 Nicolai, L. M., *Fundamentals of Aircraft Design*, distributed by School of Engineering, University of Dayton, Dayton, Ohio, 1975.

EIGHT
STATIC STABILITY AND CONTROL

INTRODUCTION

FAR Part 23 (Ref. 8.1) states that "the airplane must be safely controllable and maneuverable during—(1) take off; (2) climb; (3) level flight; (4) dive; and (5) landing (power on and off) (with the wing flaps extended and retracted)." Part 23 also says that "The airplane must be longitudinally, directionally, and laterally stable." This particular FAR, which defines the airworthiness standards for normal, utility, and acrobatic airplanes, then goes into detail to state what requirements an airplane must meet in order to satisfy the foregoing general statements on controllability and stability.

Stability of an airplane refers to its movement in returning, or the tendency to return, to a given state of equilibrium, frequently referred to as trim. More specifically, static stability refers to the tendency of an airplane under steady conditions to return to a trimmed condition when disturbed rather than any actual motion it may undergo following the disturbance. The forces and moments are examined to determine if they are in the direction to force the airplane back to its equilibrium flight conditions. If so, the airplane is statically stable.

Dynamic stability encompasses the unsteady behavior of an airplane responding to time-dependent aerodynamic forces and moments produced by the airplane's motion. Following a disturbance of the airplane from a trimmed condition, its movement under the influence of the unsteady forces and moments is examined to determine whether or not the airplane ultimately returns to its trimmed condition. To the uninitiated, it comes as a surprise to learn that many airplanes exhibit a dynamic instability known as spiral divergence. Unless counteracted by control input, many airplanes will gradually drop one wing and go into an ever tightening spiral dive. Fortunately, this spiral divergence initially is so gradual that the pilot will compensate for it without even realizing it. However, if a noninstrument-rated pilot is suddenly without a reference to the horizon, the spiral divergence instability can prove disastrous.

An airplane that is statically stable will not necessarily be dynamically stable. However, one that is statically unstable will be dynamically unstable; that is, static stability is necessary but not sufficient for dynamic stability. In this chapter we will consider static stability and control; in other words, we will consider the forces and moments acting on an airplane undergoing steady motion.

COORDINATE SYSTEM—FORCES, MOMENTS, AND VELOCITIES

Figure 8.1 illustrates the right-handed set of body axes that will be used in the material to follow. These axes are fixed at the center of gravity relative to the body and, hence, move with the body. The system is easily remembered. x is directed forward, y to the right, and z downward. X, Y, and Z are the aerodynamic force components along their respective axes; u, v, and w the velocity components of the center of gravity along these axes; L, M, and N are the moments about these axes; and P, Q, and R are the angular velocities about the x-, y-, and z-axes, respectively. L, M, and N are defined as the rolling, pitching, and yawing moments, respectively. Similarly, P, Q, and R are called the roll, pitch, and yaw rates.

We will see later that for many problems concerning stability and control of an airplane, its motion in the plane of symmetry (x-z plane) can be uncoupled from the motion of the plane of symmetry. The former is referred

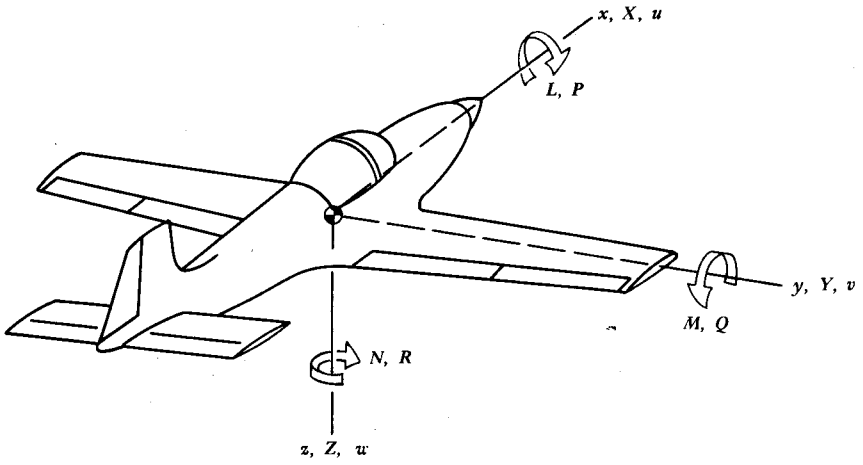

Figure 8.1 Right-handed coordinate system. x,y,z = coordinates; X,Y,Z = aerodynamic forces along axes; u,v,w = velocity components along axes; L,M,N = aerodynamic moments about axes; P,Q,R = angular velocities about axes.

to as longitudinal motion and treats linear motion along the x- and z-axes, and rotation about the y-axis. Motion of the plane of symmetry, known as lateral or lateral-directional motion, deals with linear motion along the y-axis and angular rotations about the x- and z-axes.

LONGITUDINAL STATIC STABILITY

Because this material is an introduction to the subject of airplane stability and control, a certain amount of elegance will be foresaken for the sake of simplicity and clarity. Most of the derivations to follow will relate to a "basic airplane" consisting simply of a wing and a tail. Analysis of this simple configuration will disclose the basic principles involved in determining the motion of the complete airplane. Following these fundamental developments, the effects of the fuselage and propulsion system will then be considered.

Stick-Fixed Stability

The forces and moments on a wing-tail combination in the longitudinal plane are shown in Figure 8.2. The x-axis in this case is chosen to coincide with the zero lift line of the wing. Relative to this line, the tail is shown nose down at an incidence angle of i_t. The positive direction of i_t is an exception to the right-hand rule followed for other angles, angular velocities, and moments. Pointing one's right thumb along the y-axis, the fingers curl in the direction of a positive rotation (but not for i_t).

The angle of attack of the wing's zero lift line is shown as α. At the tail,

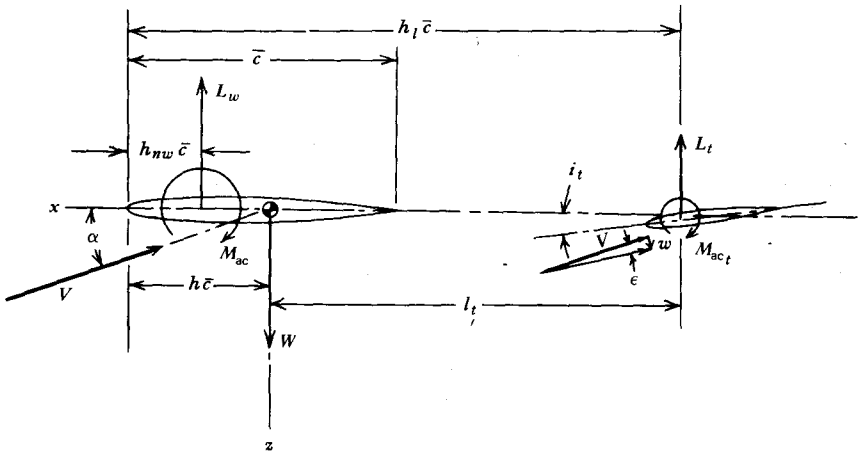

Figure 8.2 Forces and moments acting on a wing-tail combination.

however, the angle of attack is reduced by an angle ϵ due to the downwash from the wing. The aerodynamic center of the wing is located a distance of $(h - h_{nw})\ \bar{c}$ ahead of the center of gravity. Thus h and h_{nw} are dimensionless fractions of the mean aerodynamic chord $\bar{c}$ and are measured from the leading edge back to the center of gravity and aerodynamic center, respectively.

If the "airplane" is in trim, the vector sum of the forces and the moments about the center of gravity will be zero.

$$\sum Z = 0$$

$$\sum M = 0$$

or

$$W - L_w - L_t = 0 \tag{8.1a}$$

$$L_w(h - h_{nw})\bar{c} - L_t l_t + M_{ac} + M_{ac_t} = 0 \tag{8.1b}$$

Now consider the graph in Figure 8.3, which presents the pitching moment about the center of gravity as a function of α. In trim α must be positive in order to produce lift. Thus M must be zero for a positive α. Now the question is, "Should the slope of M versus α be positive or negative for static pitch stability?" To answer this, suppose the airplane is trimmed at point A when it is disturbed, possibly by a gust, so that its angle of attack is increased to a value of A'. If the slope of M versus α is positive, a positive moment, corresponding to point B, will be generated. This positive moment, being a nose-up moment, will increase α even more, thus tending to move the airplane even further from its trimmed angle of attack. This is an unstable

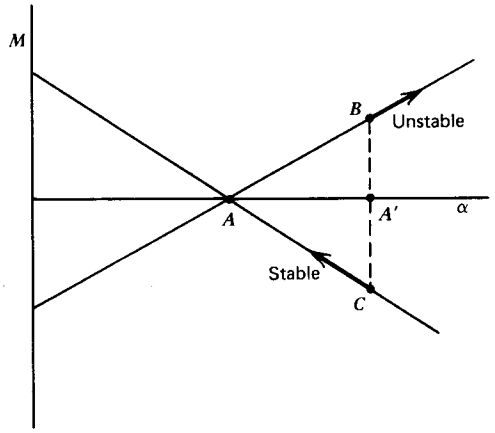

Figure 8.3 Pitching moment versus angle of attack.

situation, as noted on the figure. On the other hand, if the slope is negative, so that point C is reached, a negative moment is produced that will reduce α to its trimmed value.

Expressing the moment in terms of a moment coefficient, it follows that the requirement for longitudinal static stability is

$$\frac{dC_M}{d\alpha} < 0 \tag{8.2}$$

where $M = qS\bar{c}C_M$.

Stick-Fixed Neutral Point and Static Margin

Denoting $dC_M/d\alpha$ by C_{M_α}, we note that C_{M_α} will vary with center of gravity position. There is one particular location for the center of gravity, known as the *neutral point*, for which $C_{M_\alpha} = 0$. The neutral point can be thought of as an aerodynamic center for the entire airplane.

$$L_w = qSa\alpha \tag{8.3a}$$

$$L_t = \eta_t q S_t a_t \left(\alpha - i_t - \frac{d\epsilon}{d\alpha}\alpha\right) \tag{8.3b}$$

$$M_{ac} = qS\bar{c}C_{M_{ac}} \tag{8.3c}$$

where

$$a = \frac{dC_L}{d\alpha}$$

$$a_t = \frac{dC_{L_t}}{d\alpha_t}$$

$$\eta_t = \frac{q_t}{q}$$

M_{ac_t} will be neglected as being small by comparison to the other terms in the equation. Usually M_{ac_t} will be zero anyway, since most tail surfaces employ symmetrical airfoil sections.

The term $d\epsilon/d\alpha$ is the rate of change of downwash angle at the tail with α and, for a given wing-tail configuration, is assumed to be a constant (although it can vary with the trim condition). From here on it will be denoted by ϵ_α. The determination of ϵ_α will be discussed in more detail later.

Substituting Equation 8.3 into Equation 8.1*b* gives

$$C_M = (h - h_{nw})a\alpha - \eta_t \frac{S_t}{S}\frac{l_t}{\bar{c}} a_t[\alpha(1 - \epsilon_\alpha) - i_t] + C_{M_{ac}} \tag{8.4}$$

Note that for $\alpha = 0$,

$$C_{M_0} = \eta_t V_H a_t i_t + C_{M_{ac}} \tag{8.5}$$

where V_H is called the horizontal tail volume and is defined by

$$V_H = \frac{S_t}{S}\frac{l_t}{\bar{c}} \tag{8.6}$$

C_M can therefore be written as

$$C_M = C_{M_0} + C_{M_\alpha}\alpha \tag{8.7}$$

where

$$C_{M_\alpha} = (h - h_{nw})a - \eta_t a_t V_H(1 - \epsilon_\alpha) \tag{8.8}$$

In order to find the neutral point, we set C_{M_α} equal to zero and h equal to h_n. However, the term V_H includes l_t, which is a function of the center-of-gravity position. From Figure 8.2,

$$\frac{l_t}{\bar{c}} = h_t - h \tag{8.9}$$

Also, we can write, for the total lift of the wing and tail,

$$L = qSa\alpha + \eta_t q S_t a_t[\alpha(1 - \epsilon_\alpha) - i_t]$$

or

$$C_L = [a + \eta_t \frac{S_t}{S} a_t(1 - \epsilon_\alpha)]\alpha - i_t\eta_t \frac{S_t}{S} a_t \tag{8.10}$$

Thus, the combined lift curve slope is given by

$$C_{L_\alpha} = a + \eta_t \frac{S_t}{S} a_t(1 - \epsilon_\alpha) \tag{8.11}$$

Substituting Equations 8.9 and 8.11 into Equation 8.8 and equating the result to zero gives

$$h_n = \frac{h_{nw} + [(C_{L_\alpha}/a) - 1]h_t}{C_{L_\alpha}/a} \tag{8.12}$$

If this result and Equations 8.9 and 8.11 are substituted into Equation 8.8, a surprisingly simple result is obtained for C_{M_α}.

$$C_{M_\alpha} = -C_{L_\alpha}(h_n - h) \tag{8.13}$$

Considering Equations 8.5 and 8.13 in light of Figure 8.3, it is obvious that a trimmed, statically stable airplane must have a *positive tail incidence angle and its center of gravity must be ahead of the neutral point.*

The quantity $(h_n - h)$ is known as the static margin. It represents the distance that the center of gravity is ahead of the neutral point expressed as a fraction of the mean aerodynamic chord. To assure adequate static longitudinal stability, a static margin of at least 5% is recommended. Let us briefly examine the foregoing for the light airplane pictured in Figure 3.62.

For this wing-tail combination the following quantities are calculated from the drawing.

$$h_t = 2.78$$

$$S_t/S = 0.153$$

For the 65_2–415 airfoil,

$$C_{M_{ac}} = -0.07$$

$$h_{nw} = 0.27$$

Using Equation 3.74 and a C_{l_α} of 0.106/deg,

$$a = 0.0731/\text{deg}$$

$$a_t = 0.0642/\text{deg}$$

η_t, the ratio of q at the tail to the free-stream q, is assumed to be 1.0. η_t can be greater or less than unity, depending on the fuselage boundary layer and any effects from the propulsion system (such as a propeller slipstream).

Using a procedure to be described shortly, ϵ_α is estimated to be 0.447. Thus,

$$C_{L_\alpha} = 0.0785\ C_L/\text{deg}$$

$$h_n = 0.443$$

so that

$$C_{M_\alpha} = -0.0785\ (0.443 - h)$$

There are configurations other than the conventional wing-tail combination that are trimmable and are longitudinally statically stable. Since the preceding relationships regarding longitudinal static stability place no restriction on the relative sizes of the wing and tail, it is easily seen that the smaller surface can be placed ahead of the larger. This is referred to as a Canard configuration. In this case, the rear lifting surface is called the wing, and the forward "tail" is referred to as the Canard surface. For purposes of supplemental control, Canard surfaces are occasionally employed with conventional wing-tail arrangements or with delta wings such as the XB-70A, pictured in Appendix A.3. In the case of a true Canard configuration, the center of gravity will be toward the rear, just ahead of the wing.

An unswept cambered wing without a tail can be made stable simply by flying it upside down. In this case, $C_{M_{ac}}$ becomes positive so that, with the center of gravity ahead of the aerodynamic center, the resulting aerodynamic moment curve about the center of gravity will appear like the stable curve of Figure 8.3. A swept wing with positive camber can be made stable by washing out the tips. The result will again be a positive value of the $C_{M_{ac}}$ for the wing, even though $C_{M_{ac}}$ is negative for the wing section. Similarly, the $C_{M_{ac}}$ for a delta wing is made positive by reflexing the trailing edges; that is, by turning them up slightly.

$C_{M_{ac}}$ and Aerodynamic Center Location for a Finite Wing

The location of the aerodynamic center and the $C_{M_{ac}}$ for a finite wing can be determined precisely by applying the lifting surface methods described in Chapter Three. These quantities will now be determined approximately for a linearly tapered wing. The method should indicate how one would apply a more rigorous approach to the calculations and, at the same time, provide results that are readily usable for approximate calculations.

With reference to Figure 8.4, the line through point A swept back through the angle Λ is the locus of the section aerodynamic centers. Therefore the pitching moment about a line through A normal to the chord line will be

$$M_A = q\int_{-b/2}^{b/2} c^2 C_{m_{ac}}\, dy - q\int_{-b/2}^{b/2} cC_l y \tan\Lambda\, dy \tag{8.14}$$

If X_A is the distance of the aerodynamic center behind the point A, then

$$M_{ac} = M_A + LX_A$$

Dividing by $qS\bar{c}$, this becomes

$$C_{M_{ac}} = C_{M_A} + C_L \frac{X_A}{\bar{c}}$$

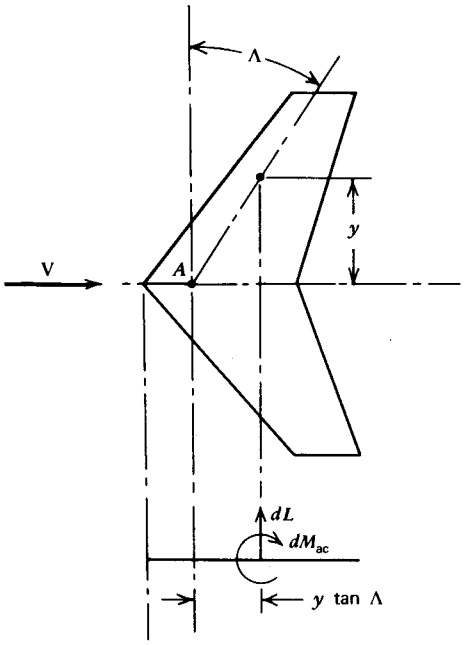

Figure 8.4 Calculation of wing aerodynamic center.

Differentiating $C_{M_{ac}}$ with respect to α gives

$$0 = \frac{dC_{M_A}}{d\alpha} + \frac{X_A}{\bar{c}} C_{L_\alpha}$$

Substituting Equation 8.14 and recalling that

$$\frac{dC_{m_{ac}}}{d\alpha} = 0$$

results in

$$X_A = \frac{1}{C_{L_\alpha} S} \int_{-b/2}^{b/2} cC_{l_\alpha} y \tan \Lambda \, dy$$

If it is assumed that C_{l_α} is constant the preceding equation can be written in the form

$$X_A = \tan \Lambda \left[\frac{\int_0^{b/2} cy \, dy}{S/2} \right]$$

or

$$X_A = \bar{y} \tan \Lambda \tag{8.15}$$

where $\bar{y}$ is the spanwise distance from the centerline out to the centroid of the half-wing area. Equation 8.15 is applicable to any wing where the section aerodynamic centers lie on a straight line.

For a linearly tapered wing, Equation 8.15 becomes

$$X_A = \left(\frac{1 + 2\lambda}{1 + \lambda} \right) \frac{1}{3} \left(\frac{b}{2} \tan \Lambda \right) \tag{8.16}$$

The mean aerodynamic chord, $\bar{c}$, is defined as the chord length that, when multiplied by the wing area, the dynamic pressure, and an average $C_{M_{ac}}$, gives the total moment about the wing's aerodynamic center. If the $C_{M_{ac}}$ is not constant along the span, one has a problem in defining an "average" $C_{M_{ac}}$. We will therefore calculate $\bar{c}$ according to

$$\bar{c} = \frac{1}{S} \int_{-b/2}^{b/2} c^2 \, dy \tag{8.17}$$

This definition of $\bar{c}$ follows directly from the preceding relationships if the section C_l and $C_{M_{ac}}$ values are assumed to be constant. For a linear tapered wing, $\mathbf{c}$ becomes

$$\bar{c} = \frac{2c_0}{3} \frac{1 + \lambda + \lambda^2}{1 + \lambda}$$

where c_0 is the midspan chord.

Downwash Angle

The estimation of a representative angle at the tail that allows for the downwash from the wing is a difficult task. The vortex system shed from the wing is unstable and rolls up into two trailing vortices, so the model for the trailing vortex system is not well defined. Even if one could circumvent this problem, the downwash in the region of the horizontal tail will not be uniform over the tail. Thus, to use a simple correction to the tail angle of attack leaves something to be desired.

With these reservations in mind, the simple model illustrated in Figure 8.5 is proposed to calculate ϵ_α. The wing is replaced by a single bound vortex with a vortex trailing from each tip. As the vortex sheet rolls up, the edge moves in toward the centerline, so that the span between the two trailing vortices, b', is less than the wingspan. For an elliptic wing, it can be shown that

$$\frac{b'}{b} = \frac{\pi}{4} \tag{8.18}$$

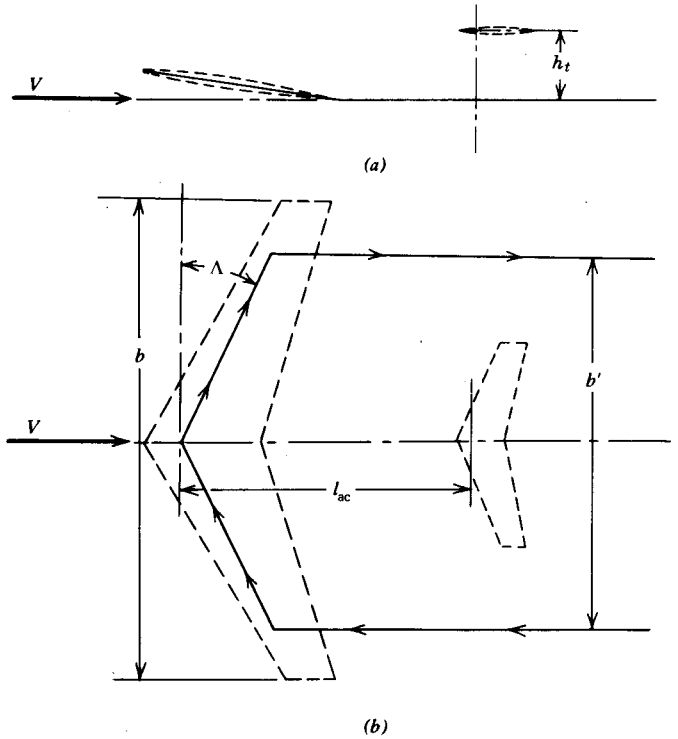

Figure 8.5 Equivalent vortex system for calculating downwash at tail. (*a*) Side view. (*b*) Planform view.

Using the model shown in Figure 8.5 and the Biot-Savart law (Equation 2.64), the graphs of Figure 8.6*a* and 8.6*b* were prepared. To obtain ϵ_α from these graphs, one first determines the distance, l_{ac}, from the quarter-chord of the tail to the quarter-chord of the wing. b' is calculated from Equation 8.18 to give l_{ac}/b'. Figure 8.6*a* is then entered interpolating for h_t/b'. Note that h_t is the height of the tail above the plane containing the wing and parallel to V. The value of ϵ_α obtained from Figure 8.6*a* is then multiplied by the factor presented in Figure 8.6*b* to correct for sweepback.

With the use of these graphs, an estimate of ϵ_α can now be made for the light plane of Figure 3.62. In this case,

$$l_{ac} = 159 \text{ in.}$$

$$b = 360 \text{ in.}$$

$$S = 160 \text{ ft}^2$$

Because of the dihedral and at an angle of attack, h_t is approximately zero. Using Equation 3.74 and a value for a_0 of 6.07/rad leads to a value for a of 4.19/rad. From Figure 8.6*a*,

$$\frac{A\epsilon_\alpha}{a} = 0.6$$

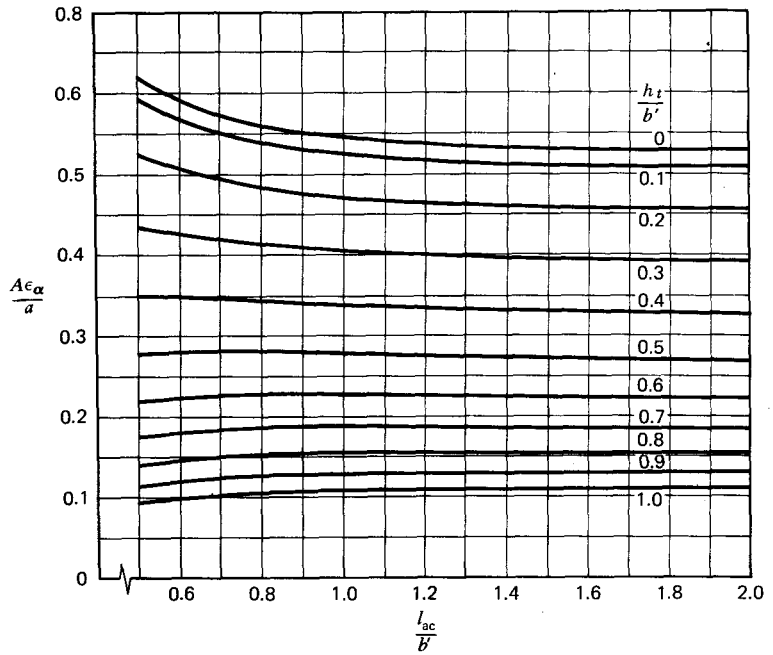

Figure 8.6a Downwash angle for $\Lambda = 0$.

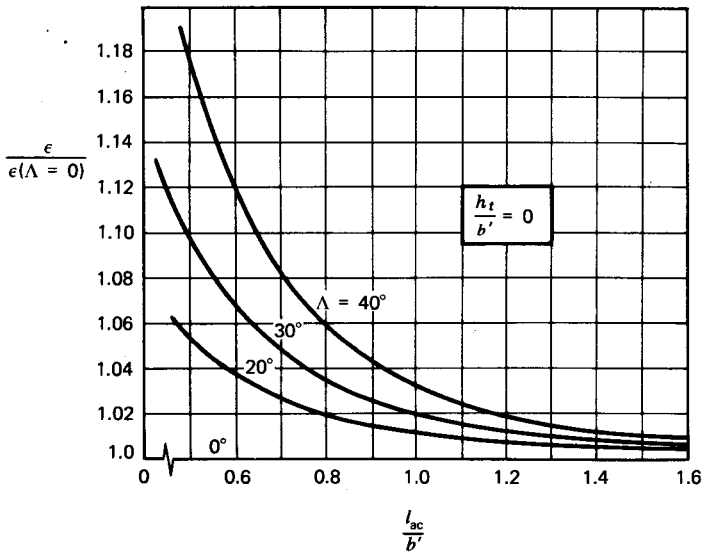

Figure 8.6b Correction to downwash angle for sweepback.

Thus,

$$\epsilon_\alpha = 0.447$$

LONGITUDINAL CONTROL

Control Position as a Function of Lift Coefficient

According to Equation 8.7, the pitching moment coefficient can be written as a linear function of α.

$$C_M = C_{M_0} + C_{M_\alpha}\alpha$$

From Equation 8.10,

$$C_L = C_{L_\alpha}\alpha + C_{L_i}i_t \tag{8.19}$$

where $C_{L_i} = -\eta_t a_t S_t/S$. Substituting for α in the equation for C_M and setting the result equal to zero gives

$$0 = C_{M_0} + \frac{C_{M_\alpha}}{C_{L_\alpha}}(C_L - C_{L_i}i_t) \tag{8.20}$$

C_{M_0} is given by Equation 8.5.

All-Movable Tail

If we now consider the tail incidence angle, i_t, to be a variable, we can write

$$C_{M_0} = C_{M_{ac}} + C_{M_i} i_t \tag{8.21}$$

where $C_{M_i} = \eta_t V_H a_t$.

Substitution of Equation 8.21 into Equation 8.20 results in the following equation for the trim tail incidence angle as a function of the lift coefficient.

$$i_t = -\frac{C_{M_\alpha} C_L + C_{L_\alpha} C_{M_{ac}}}{C_{M_i} C_{L_\alpha} - C_{M_\alpha} C_{L_i}} \tag{8.22}$$

C_{M_α} is negative for a statically stable airplane and C_{L_i} is always negative. $C_{M_{ac}}$ is usually negative and C_{L_α} is always positive. It therefore follows, if $l_t/\bar{c} > (h_n - h)$, that i_t as a function of C_L is of the form

$$i_t = AC_L + B$$

where A and B are positive constants.

Notice that

$$\frac{di_t}{dC_L} = -\frac{C_{M_\alpha}}{(C_{M_i} C_{L_\alpha} - C_{M_\alpha} C_{L_i})} \tag{8.23}$$

This allows one to determine experimentally the neutral point for a given airplane. This is done by measuring i_t as a function of C_L for different center-of-gravity locations. The slopes of the experimentally determined plots of i_t versus C_L are then plotted as a function of center of gravity and are extrapolated to the value of the center of gravity that gives a zero slope. From Equation 8.23, C_{M_α} for this center-of-gravity position is obviously zero. From Equation 8.13, it then follows that this center-of-gravity position corresponds to the neutral point.

The foregoing material applies strictly only to aircraft with all-movable tails. There are two variations on this configuration. The first is the fixed horizontal stabilizer-movable elevator configuration. The other is the movable horizontal stabilizer with a linked elevator (or trim tab). These three configurations are pictured in Figure 8.7. A variant on the configuration of Figure 8.7*c* is to input the control directly to the tab. Deflection of the tab produces a moment that rotates the rest of the tail. This configuration is referred to as a flying tail. Some persons refer to any all-movable tail as a flying tail.

Stabilizer-Elevator

Equations 8.19 to 8.23 apply to any of these configurations if i_t is taken to mean the incidence angle of the tail's zero lift line. To pursue this further, we know from Chapter Three that the lift coefficient for a flapped airfoil can be

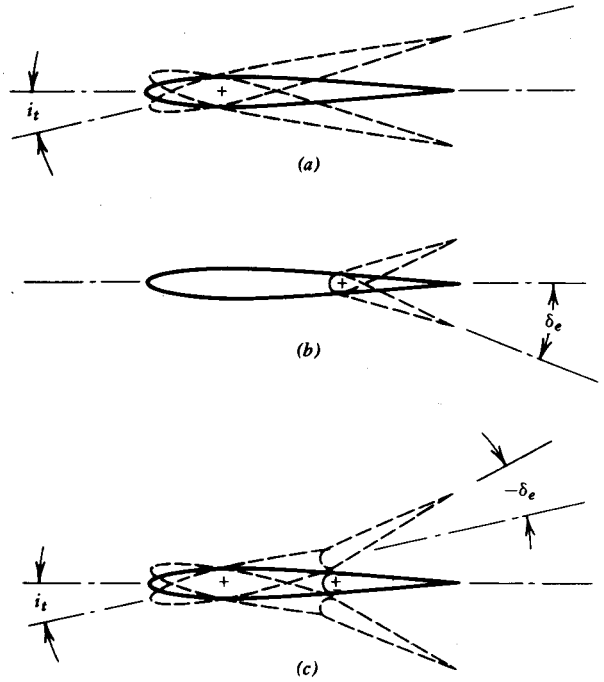

Figure 8.7 Horizontal tail configuration. (*a*) All-movable tail. (*b*) Horizontal stabilizer and elevator. (*c*) All-movable tail with linked tab.

expressed as

$$C_l = a(\alpha + \tau\,\delta)$$

Here, τ is the actual value of the flap effectiveness value and equals τ obtained from Figure 3.32 multiplied by η from Figure 3.33. Thus, referring to the tail configuration of Figure 8.7*b*, if the elevator is deflected downward through the angle δ_e, the incidence angle of the zero lift line is decreased by the amount $\tau\,\delta_e$. If i_{hs} denotes the incidence angle of the fixed horizontal stabilizer, then the incidence angle of the tail zero lift line will be

$$i_t = i_{hs} - \tau\,\delta_e \tag{8.24}$$

The coefficients C_{M_i} and C_{L_i} then become

$$\frac{\partial C_M}{\partial i_t} = \frac{\partial C_M}{\partial\,\delta_e}\frac{d\,\delta_e}{di_t}$$

or

$$C_{M_i} = -\frac{1}{\tau}\,C_{M_\delta}$$

Similarly,

$$C_{L_i} = -\frac{1}{\tau} C_{L_\delta}$$

Using Equations 8.22, 8.24, and the above expressions for C_{M_i} and C_{L_i} results in

$$\delta_e = -\frac{C_{M_\alpha} C_L + C_{L_\alpha} C_{M_{ac}}}{C_{M_\delta} C_{L_\alpha} - C_{M_\alpha} C_{L_\delta}} + \frac{i_{h_s}}{\tau} \tag{8.25}$$

Thus, as a function of C_L, δ_e has the same form as i_t, except that the slope of δ_e versus C_L will be negative, since the positive rotation of the elevator is opposite to that for the incidence angle.

Stabilator

Now consider the configuration in Figure 8.7*c*. Let i_{h_s} (which is now variable) and δ_e be related by

$$\delta_e = k_e i_{h_s}$$

Using Equation 8.24, i_t now becomes

$$i_t = i_{h_s}(1 - \tau k_e)$$

Thus, from Equation 8.22,

$$i_{h_s} = -\frac{C_{M_\alpha} C_L + C_{L_\alpha} C_{M_{ac}}}{C_{M_i} C_{L_\alpha} - C_{M_\alpha} C_{L_i}} \frac{1}{(1 - \tau k_e)} \tag{8.26}$$

This is identical to Equation 8.22, except for the factor $1/(1 - \tau k_3)$. By varying k_e, one is able to alter the rate of change of the tail incidence angle with C_L. Usually a negative value of k_e is used to make the tail more effective for a given displacement. This increases the tail lift curve slope since, for the linked elevator,

$$\frac{dC_l}{d\alpha} = a(1 - \tau k_e)$$

Control Forces

For obvious reasons, in the design of an airplane's control system, the stick or control wheel forces must lie within acceptable limits throughout the operating envelope (V-n diagram) of the airplane. In addition, the variation of these forces with airspeed about any trim point should be such as to give a proper "feel" to the pilot. Generally, this means that a push forward on the longitudinal control should be required to increase the airspeed, and a pull should be required to fly slower.

With regard to the longitudinal control forces, FAR Part 23 allows a maximum of 60 lb for a temporary application to a stick and 75 lb for a wheel.

A prolonged application is not allowed to exceed 10 lb for either type of control.

Gearing

The control force, P, is directly proportional to the control surface hinge moment, H.

$$P = GH \tag{8.27}$$

G is referred to as the gearing. To determine G, refer to the sketch in Figure 8.8. Here a schematic of a control linkage is shown between a stick and an elevator. If the system is in equilibrium,

$$PL = \left(\frac{H}{l_e}\right) l \tag{8.28}$$

where the stick force, P, and the hinge moment, H, are shown in their positive directions. Now allow the stick at the point of application of P to move a distance s in the direction of P. In so doing the elevator will rotate through an angle δ_e, given by

$$\delta_e = -\frac{s}{L}\frac{l}{l_e}$$

Substituting this into Equation 8.28 gives

$$P = \left(-\frac{\delta_e}{s}\right) H \tag{8.29}$$

Comparing Equation 8.29 to Equation 8.27 gives

$$G = -\frac{\delta_e}{s} \tag{8.30}$$

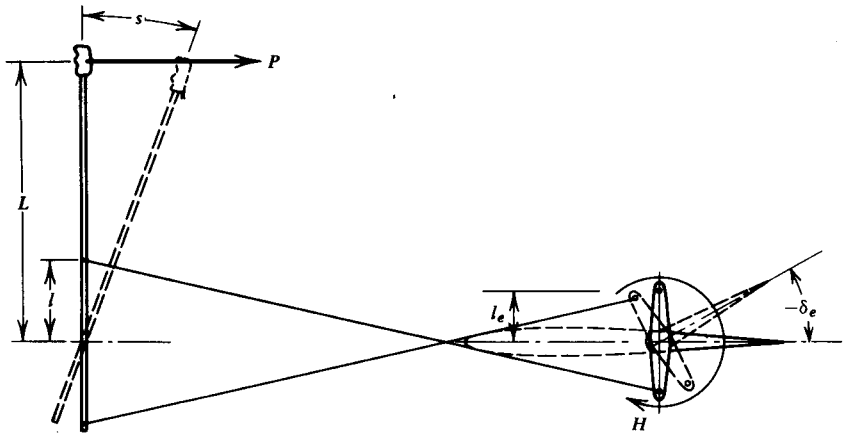

Figure 8.8 Schematic of a longitudinal control system.

This result is general and independent of the details of the linkage. Since δ_e is negative for a positive stick displacement, it follows that G is positive. It can also be obtained simply by noting that if the system is in equilibrium throughout its displacement, the net work done on the system is zero. Hence,

$$Ps + H\delta_e = 0$$

from which Equation 8.30 follows.

Stick Force for a Stabilator

In the case of an all-movable tail, the moment, H, can be expressed in terms of a moment coefficient, C_M, about the pivot. For a control surface that is hinged to a surface ahead of it, the "hinge" moment is usually expressed in terms of a hinge moment coefficient, C_h.

$$H = \tfrac{1}{2}\rho V^2 S\bar{c}C_H \tag{8.31}$$

S refers to the planform area of the *control surface* (such as the elevator), and $\bar{c}$ is the mean chord of the *control surface.*

Let us now consider the stick force ("stick" is used by most pilots and engineers as synonymous with control wheel) for a movable tail with a linked tab. For simplicity a symmetrical airfoil will be assumed, so that the moment coefficient can be written as

$$C_{M_t} = b_1\alpha_t + b_2\,\delta_e \tag{8.32}$$

The notation, b_1 and b_2, is borrowed from Reference 8.2 and avoids the use of triple subscripts in denoting the partial derivatives. Obviously,

$$b_1 = \left(\frac{\partial C_{M_t}}{\partial \alpha_t}\right)_{\delta_e=\text{constant}}$$

$$b_2 = \left(\frac{\partial C_{M_t}}{\partial\, \delta_e}\right)_{\alpha_t=\text{constant}}$$

The constant b_1 can be positive or negative, depending on the location of the pivot relative to the aerodynamic center. b_2, on the other hand, is usually negative.

To allow the stick force to be trimmed to zero, a constant term, δ_0, is added to the linked elevator angle so that

$$\delta_e = k_e i_{h_s} + \delta_0 \tag{8.33}$$

Substituting Equations 8.31, 8.32, and 8.33 into Equation 8.27 gives

$$\frac{P}{GqS_t\bar{c}_t} = -b_1 i_{h_s} + b_1\alpha(1-\epsilon_\alpha) + b_2 k_e i_{h_s} + b_2\,\delta_0$$

Replacing i_{h_t} by Equation 8.26 and using

$$q = \frac{W/S}{C_L}$$

results in

$$\frac{P}{GS_t\bar{c}_t} = \left(\frac{W}{S}\right)A + \frac{(B + b_2\,\delta_0)}{2}\rho V^2 \tag{8.34}$$

where

$$A = \left(\frac{b_1 - b_2 k_e}{1 - \tau k_e}\right)\left(\frac{C_{M_\alpha}}{C_{M_i}C_{L_\alpha} - C_{M_\alpha}C_{L_i}}\right) + \frac{b_1(1 - \epsilon_\alpha)}{C_{L_\alpha}}$$

$$B = \left(\frac{b_1 - b_2 k_e}{1 - \tau k_e}\right)\left(\frac{C_{L_\alpha}C_{M_{ac}}}{C_{M_i}C_{L_\alpha} - C_{M_\alpha}C_{L_i}}\right)$$

Regardless of the particular values of A and B, let us suppose that δ_0 is adjusted so that at a particular trim speed, V_{TR}, P equals zero. It then follows that

$$\frac{B + b_2\delta_0}{2}\rho V_{TR}^2 = -\left(\frac{W}{S}\right)A$$

We can then write

$$\frac{P}{GS_t\bar{c}_t} = \left(\frac{W}{S}\right)A\left[1 - \left(\frac{V}{V_{TR}}\right)^2\right] \tag{8.35}$$

The gradient of the stick force with velocity at a particular trim speed is found by differentiating Equation 8.35 with respect to V and letting $V = V_{TR}$.

$$\frac{dP}{dV_{TR}} = -\frac{2GS_t\bar{c}_t(W/S)A}{V_{TR}} \tag{8.36}$$

For a given trim speed a positive P, that is, a pull on the control, should result in a decrease in the speed. Thus, for the proper feel, the constant, A, in Equation 8.35 should be positive. This is referred to by FAR Part 23 as a stable stick force curve and is a requirement for all conditions of flight.

Stick Force for a Horizontal Stabilizer-Elevator Combination

The relationship for stick force and stick force gradient will now be developed for the horizontal tail configuration of Figure 8.7*b*. Such a configuration is trimmed either by changing the incidence of the horizontal stabilizer (so in a sense it is not fixed) or by deflecting a small flap, known as a trim tab, on the trailing edge of the elevator. The particular method of trim is not pertinent to the present development.

Assuming a symmetrical airfoil section, the elevator hinge moment coefficient will be written in the same form as Equation 8.32

$$C_H = b_1\alpha_t + b_2\,\delta_e + b_3\,\delta_t \tag{8.37}$$

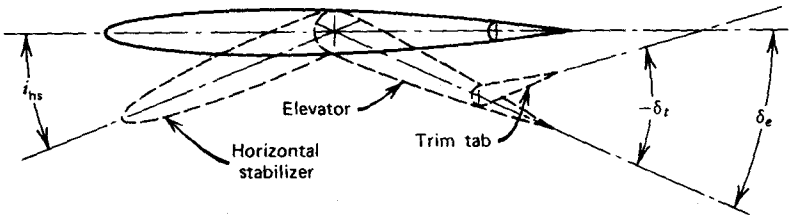

Figure 8.9 "Fixed" horizontal stabilizer-elevator-trim tab horizontal tail configuration. Note that in lieu of trim tab, incidence angle i_{hs} sometimes used to trim.

δ_t refers to the trim tab, as shown in Figure 8.9. Following the same procedure as for the all-movable tail, it can be shown that

$$\frac{P}{GS_e\bar{c}_e} = \left(\frac{W}{S}\right)A + \left[\left(\frac{b_2}{\tau} - b_1\right)i_{hs} + b_3\,\delta_t - B\right]\tfrac{1}{2}\rho V^2 \tag{8.38}$$

In this case A and B are given by

$$A = \frac{b_1(1-\epsilon_\alpha)}{C_{L_\alpha}} - \frac{b_2 C_{M_\alpha}}{(C_{M_\delta}C_{L_\alpha} - C_{M_\alpha}C_{L_\delta})}$$

$$B = \frac{b_2 C_{L_\alpha} C_{M_{ac}}}{C_{M_\delta}C_{L_\alpha} - C_{M_\alpha}C_{L_\delta}}$$

If i_{hs} or δ_t is adjusted to trim P to zero at a trim speed of V_{TR}, Equation 8.28 becomes

$$\frac{P}{GS_e\bar{c}_e} = \left(\frac{W}{S}\right)A\left[1 - \left(\frac{V}{V_{TR}}\right)^2\right] \tag{8.39}$$

The rate of change of stick force with speed will be

$$\frac{dP}{dV_{TR}} = -\frac{2GS_e\bar{c}_e(W/S)A}{V_{TR}} \tag{8.40}$$

Estimation of Aerodynamic Hinge Moments

Reference 8.3, similar to Reference 5.5, is a comprehensive collection of data relating to aerodynamics, structures, and performance. If one requires an extensive treatment of the effects of airfoil thickness, aerodynamic balance, trailing edge angle, and other geometric parameters on the hinge moment coefficient, this reference should be consulted. The many geometric features that affect the aerodynamic performance of an elevator are pictured in Figure 8.10. These are all considered to some extent by the reference.

For illustrative purposes, a limited amount of data is presented here in Figures 8.11 to 8.15, based on Reference 8.2 and also Reference 8.3. Figures

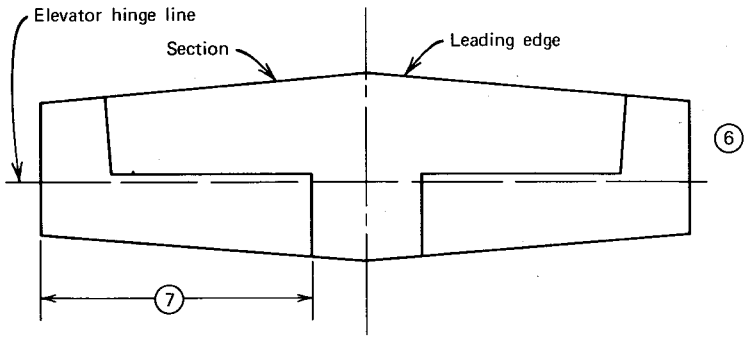

(a)

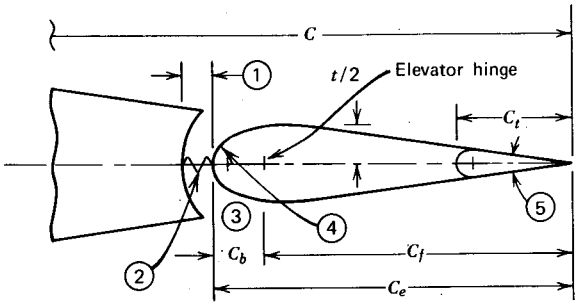

Factors affecting tail performance

1. Gap
2. Seal (or lack of)
3. Aerodynamic balance, balance ratio, BR
4. Nose shape
5. Trailing edge bevel
6. Control horn balance
7. Spanwise extent of elevator
8. Total tail aspect ratio and taper ratio
9. Ratio of c_e to c

(b)

Figure 8.10 Horizontal tail geometry. (a) Planform view, (b) Section view.

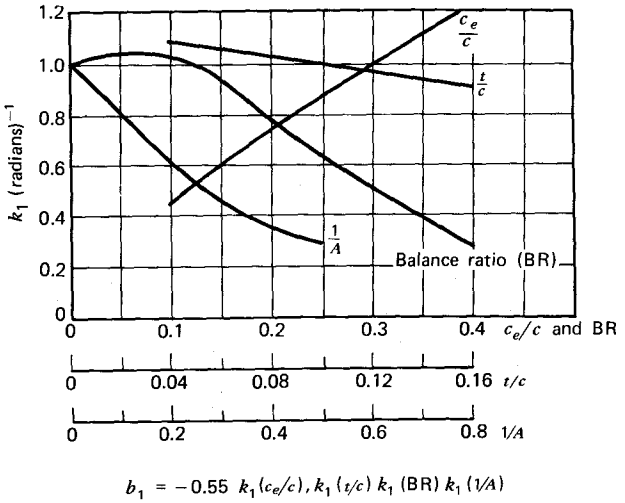

Figure 8.11 Factors determining the rate of change of elevator hinge moment with angle of attack. (BR = $[(C_b/C_t)^2 - (t/2C_t)^2]^{1/2}$

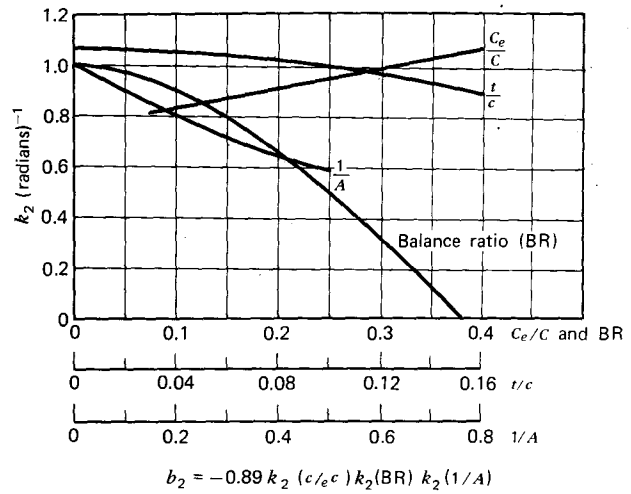

Figure 8.12 Factors for determining the rate of change of elevator hinge moment with elevator angle.

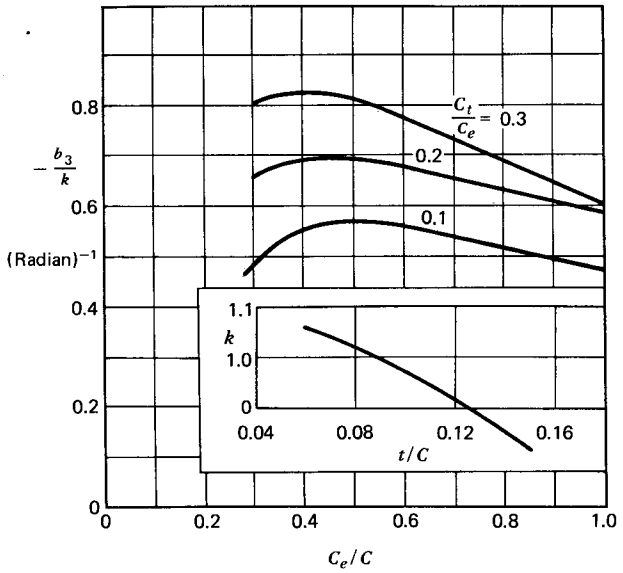

Figure 8.13 Rate of change of elevator hinge moment coefficient with trim tab angle.

8.11 and 8.12 present factors k_1 and k_2, from which b_1 and b_2 in Equation 8.37 can be obtained. These curves actually represent deviations from a norm defined by the following factors.

1. 10% thick, symmetrical 2-D airfoil.
2. The ratio of elevator chord-to-airfoil chord (c_e/c) equals 0.3.
3. No aerodynamic balance.
4. A round nose on the elevator.

Each curve in these figures represents the effect of varying one parameter while keeping the others at their nominal value. For the nominal case,

$$b_1 = -0.55$$

$$b_2 = -0.89$$

Thus,

$$b_1 = -0.55k_1\left(\frac{c_e}{c}\right)k_1\left(\frac{t}{c}\right)k_1(BR)k_1\left(\frac{1}{A}\right)$$

$$b_2 = -0.89k_2\left(\frac{c_e}{c}\right)k_2\left(\frac{t}{c}\right)k_2(BR)k_2\left(\frac{1}{A}\right)$$

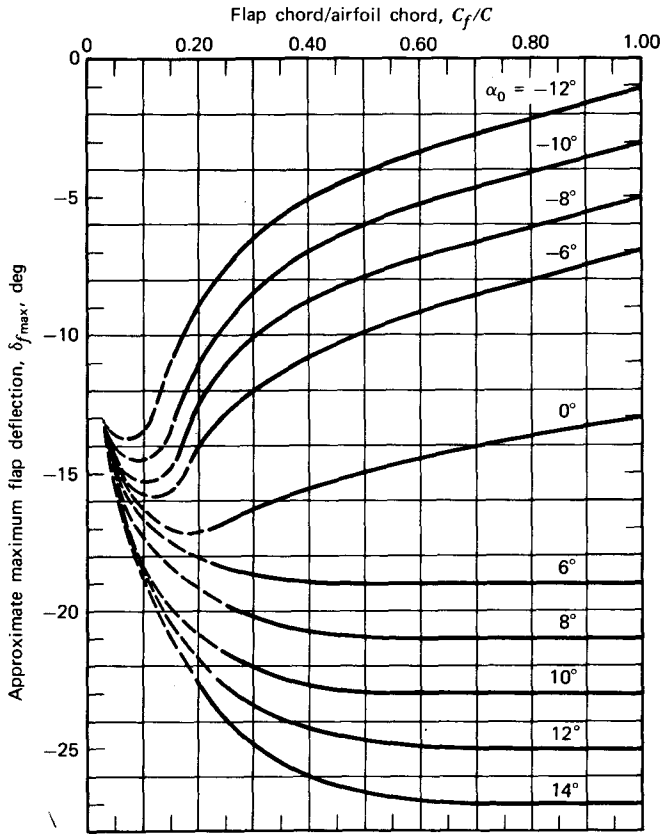

Figure 8.14 Approximate maximum allowable flap deflections for linear limits of airfoil characteristics at various angles of attack.

For example, suppose the following is given for a horizontal tail.

$$A = 3.60$$

$$\frac{c_e}{c} = 0.37$$

$$\frac{c_t}{c_e} = 0.30$$

$$\frac{t}{c} = 0.10$$

$$\frac{b_e}{b} = 1.0$$

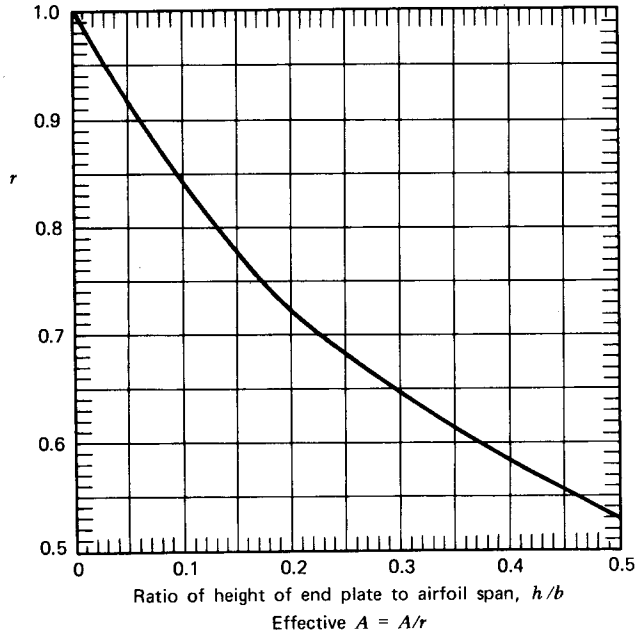

Figure 8.15 Correction factor to aspect ratio for effect of end plates.

$$\frac{b_t}{b} = 0.25$$

$$BR = 0$$

The notation is a little confusing, since the subscript t, denoting "tail," has been dropped but added again to denote "tab."

For this case, from Figure 8.11,

$$k_1\left(\frac{c_e}{c}\right) = 1.16$$

$$k_1\left(\frac{t}{c}\right) = 1.0$$

$$k_1(BR) = 1.0$$

$$k_1\left(\frac{1}{A}\right) = 0.49$$

From Figure 8.12,

$$k_2\left(\frac{c_e}{c}\right) = 1.05$$

$$k_2\left(\frac{t}{c}\right) = 1.0$$

$$k_2(BR) = 1.0$$

$$k_2\left(\frac{1}{A}\right) = 0.73$$

Thus, b_1 and b_2 are estimated to be

$$b_1 = -0.55(1.16)(0.49)$$
$$= -0.31$$

$$b_2 = -0.89(1.05)(0.73)$$
$$= -0.68$$

The effect of the tab on the hinge moment is obtained from Figure 8.13. For a two-dimensional airfoil,

$$\frac{b_3}{k} = -0.83$$

$$k = 0.97$$

Hence,

$$b_3 = -0.81$$

Since most trim tabs are located near the midspan of the elevator, the correction for aspect ratio is assumed to be negligible. However, since the tab extends over only 25% of the tailspan, the value of b_3 is reduced in proportion. Thus,

$$b_3 = -0.20$$

For this example, it follows that

$$C_H = -0.31\alpha - 0.68\delta_e - 0.20\delta_t$$

The angles α, δ_e and δ_t are in radians.

The foregoing relationships assume linear relationships between C_H and the angles α, δ_e, and δ_t. As the material relating to flaps in Chapter Three showed earlier, linear aerodynamics holds only up to some combination of flap angle and angle of attack, beyond which flow separation occurs. An estimate of these limits can be obtained from Figure 8.14 (taken from Ref. 8.4). This graph is for a NACA 0009 airfoil having a plain flap and operating at a Reynolds number of 3.41×10^6. This value of R is typical for the horizontal tail of a light to medium aircraft at landing speeds.

Figure 8.14 is not applicable to trim tabs. However, the reference notes on conventional control surfaces (elevator with trim tab), a satisfactory maximum for tab deflection exists between the angles of +/–15and +/–20° for

moderate flap deflections. Thus, for a constant tab chord, it is better to use a large-span tab deflected to a small angle than a short-span tab deflected to a large angle.

The combination of the vertical and horizontal tails on an airplane, that is, its complete tail assembly, is called the empennage. On some airplanes the empennage consists of a vertical tail mounted at each tip of the horizontal tail. These "twin tails" act as end plates to the horizontal tail and effectively increase its aspect ratio. An estimate of this increase can be obtained from Figure 8.15. The effective aspect ratio equals the geometric value of A divided by the factor r. For example, a tail with $A = 4.0$ would have a lift curve slope of approximately $0.06C_L$/deg. If end plates having a height-to-span ratio of 0.4 were put on this tail, its effective aspect ratio would increase to 6.7. Thus a_t would increase to approximately 0.073, an increase of 22%. Although possibly not as great, one would also expect a similar improvement in the effectiveness of the elevator.

Example Calculation of Stick Force

Again, the Cherokee 180 will be used as an example, and I emphasize that the numbers are in no way endorsed by the manufacturer. The tail dimensions and angular movements were measured by students during a course on techniques of flight testing for which the Cherokee 180 was used. Being an easy and forgiving airplane to fly, it is a good vehicle for such a course.

The horizontal tail of the Cherokee, shown in Figure 8.16, is of the type pictured in Figure 8.7*c*. This type of tail is sometimes called a "stabilator." The gain between the elevator and the horizontal stabilizer, k_e, as well as the gearing, G, can be determined from the graphs presented in Figure 8.16. The stick position and angles shown here are arbitrary. They were obtained by moving the control wheel to a given position and measuring the distance from an arbitrary reference point on the wheel to an arbitrary reference point on the instrument panel. At each position, a protractor with a bubble level was placed on the horizontal stabilizer and then on the elevator to obtain the angle of these surfaces relative to the horizontal. Using these graphs, you should be able to determine that

$$k_e = -1.50$$

$$G = +0.5 \text{ rad/ft.}$$

The following quantities are estimated from the tail geometry assuming the airfoil to be symmetrical with the aerodynamic center at $0.25c$ and a section lift curve slope equal to $0.106C_l$/deg.

$$a_t = 0.0642C_L/\text{deg} \qquad \text{(Equation 3.74)}$$

$$\tau = 0.55 \qquad \text{(Figure 3.32)}$$

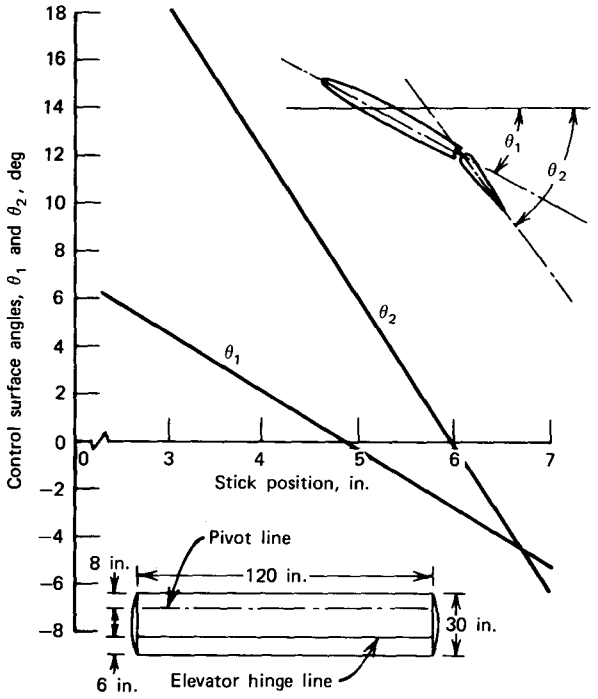

Figure 8.16 Geometry and linkage for the Cherokee 180 tail.

$$\eta = 0.80 \qquad \text{(Figure 3.33)}$$

$$\frac{\Delta C_M}{\Delta C_l} = -0.185 \qquad \text{(Figure 3.31)}$$

For the symmetrical airfoil with $\delta_e = 0$, $C_{M_{ac}} = 0$, so C_M at the pivot line, which is 1.7% of the chord behind the $C/4$ point, will be

$$C_M = 0.017 a_t \alpha_t$$

Thus,

$$b_1 = 0.0625/\text{rad}$$

The increment in C_{L_t} due to the elevator deflection will be

$$\Delta C_{L_t} = a_t \tau \eta \, \delta_e$$
$$= 1.616 \, \delta_e$$

with δ_e in radians.

The increment in C_M about the pivot line produced by δ_e will equal the sum of the increment in $C_{M_{ac}}$ and the moment produced by the increment in

C_L acting ahead of the pivot.

$$\Delta C_M = -0.185(1.616)\,\delta_e + 1.616(0.017)\delta_e$$
$$= 1.616\,\delta_e(-0.185 + 0.017)$$

Thus, it follows that

$$b_2 = -0.271/\text{rad}$$

The following numbers are typical of the Cherokee 180 with four passengers, full-fuel, but no baggage.

$W = 2255$ lb

$h = 0.197$ (dimensionless location of center of gravity)

For ϵ_α of 0.447, $h_n = 0.442$, so that

$$C_{M_\alpha} = C_{L_\alpha}(h - h_n)$$
$$= 4.50(0.197 - 0.442)$$
$$= -1.10/\text{rad}$$

Also,

$$C_{M_i} = \eta_t V_H a_t$$
$$= (1)(0.384)(3.68)$$
$$= 1.41$$

$$C_{L_i} = -a_t\left(\frac{S_t}{S}\right)$$
$$= -0.575$$

The constant, A, in Equation 8.34 becomes

$$A = 0.0476$$

The stick force, from Equation 8.35, becomes

$$P = GS_t\bar{c}_t\left(\frac{W}{S}\right)A\left[1 - \left(\frac{V}{V_{TR}}\right)^2\right]$$
$$= (0.5)(25)(2.5)(14.1)(0.0476)\left[1 - \left(\frac{V}{V_{TR}}\right)^2\right]$$
$$= 20.97\left[1 - \left(\frac{V}{V_{TR}}\right)^2\right]$$

The estimated stick force, P, is presented in Figure 8.17 as a function of airspeed for different trim speeds.

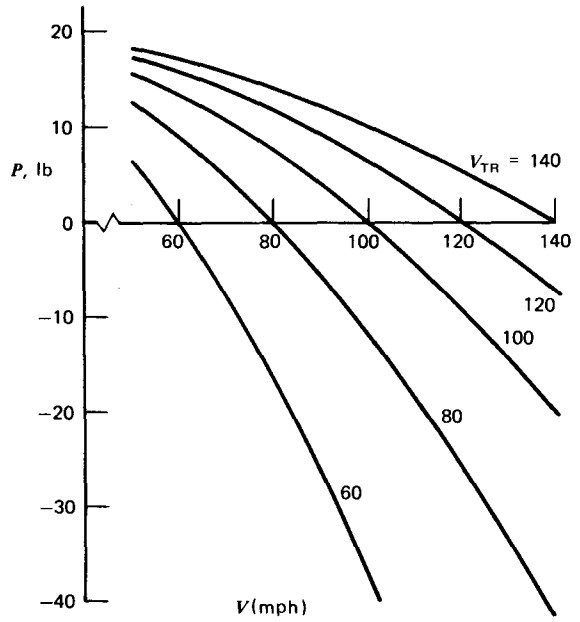

Figure 8.17 Calculated stick force versus velocity for a Cherokee 180.

Stick-Free Longitudinal Static Stability

Up to this point we have been concerned with "stick-fixed" longitudinal static stability. The pitching moment as a function of α has been determined assuming that the necessary force was applied to the control stick to hold the elevator (or other types of control surfaces) at its trimmed position. Suppose, however, that the pilot does not hold the stick fixed. Sometimes, in a cross-country flight, one likes to be able to trim the airplane and sit back and relax. The degree to which one can relax depends on the airplane's stick-free static stability.

As we will see shortly, freeing the stick has the effect of changing the slope of the tail lift curve. Thus, the results that have been obtained for the stick-fixed case will still hold if an effective a_t is used.

The stabilator and the stabilizer-elevator configuration will again be considered separately, since there are basic differences in the analyses. The final results from the two analyses will, however, be similar.

Elevator-Stabilizer Configuration

This is the easiest of the two tail configurations to treat. If the stick force is zero, it follows that the hinge moment of the elevator must be zero. From

Equation 8.37,

$$0 = b_1\alpha_t + b_2\,\delta_e + b_3\,\delta_t$$

Or δ_e, the floating elevator angle, is related to α_t and δ_t by

$$\delta_e = -\frac{b_1}{b_2}\alpha_t - \frac{b_3}{b_2}\delta_t$$

The lift coefficient of the tail is given by

$$C_{L_t} = a_t(\alpha_t + \tau\,\delta)$$

with the small contribution from δ_t being neglected. With δ_e related to α_t, C_{L_t} becomes

$$C_{L_t} = a_t\alpha_t\left(1 - \frac{\tau b_1}{b_2}\right) - a_t\frac{b_3}{b_2}\tau\,\delta_t$$

Thus,

$$\frac{dC_{L_t}}{d\alpha_t} = a_tF_e \tag{8.41}$$

where F_e is called the free elevator factor and is defined by

$$F_e = 1 - \frac{\tau b_1}{b_2} \tag{8.42}$$

Normally, as seen by a previous example, b_1 and b_2 are both negative for the stabilizer-elevator combination. Thus F_e is typically less than one. For the earlier example, $b_1 = -0.33$ and $b_2 = -0.69$. C_e/C was given as 0.37, so that τ would equal approximately 0.58. For this particular tail the value of F_e becomes 0.72.

Stabilator Configuration

The stabilator trim tab is mechanically linked to the fuselage, as shown schematically in Figure 8.18. The tail is trimmed by moving the attachment point of the link to the fuselage. With the stick free and the hinge moment trimmed to zero, the entire tail is floating around the pivot line. If the fuselage angle of attack is disturbed, the tail will tend to maintain a constant angle of attack. However, the tab, being linked to the fuselage, will deflect, thereby changing the aerodynamic moment about the pivot line. This, in turn, will cause the entire tail to float to a different position at which the moment is again zero. Thus, to determine the free elevator factor for a stabilator, the linkage to the fuselage must be taken into account. The tail cannot be treated as an entity, as was just done for the horizontal stabilizer-elevator configuration. We begin by setting Equation 8.32 equal to zero and substituting

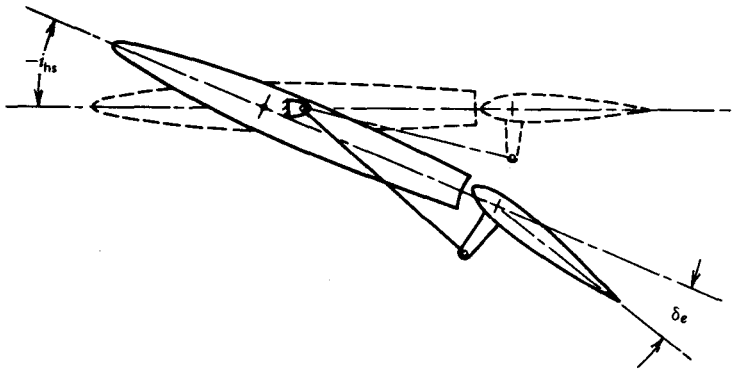

Figure 8.18 The linkage for the stabilator tail.

Equation 8.33 for δ_e. This leads to an expression for the *floating* incidence angle, i_{hs}.

$$i_{hs} = \frac{b_1(1-\epsilon_\alpha)}{b_1 - b_2 k_e}\alpha + \frac{b_2}{b_1 - b_2 k_e}\delta_0 \tag{8.43}$$

The tail lift coefficient can be written as

$$C_{L_t} = a_t[\alpha(1-\epsilon_\alpha) - i_{hs} + \tau(k_e i_{hs} + \delta_0)]$$

Substituting Equation 8.43 for i_{hs}:

$$C_{L_t} = a_t\left[\alpha(1-\epsilon_\alpha) - \frac{(1-\tau k_e)b_1(1-\epsilon_\alpha)}{b_1 - b_2 k_e}\alpha + \left(\tau - \frac{b_2}{b_1 - b_2 k_e}\right)\delta_0\right] \tag{8.44}$$

Thus the rate of change of tail lift coefficient with α will be

$$\frac{dC_{L_t}}{d\alpha} = a_t(1-\epsilon_\alpha)\left[1 - \frac{(1-\tau k_e)b_1}{b_1 - b_2 k_e}\right] \tag{8.45}$$

For the stick-fixed case, where the incidence angle is fixed, the tail lift curve slope in the downwash of the wing is simply

$$\frac{dC_{L_t}}{d\alpha} = a_t(1-\epsilon_\alpha)$$

By comparison to Equation 8.45, it follows that for the stabilator configuration, the free elevator factor is given by

$$F_e = 1 - \frac{(1-\tau k_e)b_1}{b_1 - b_2 k_e} \tag{8.46}$$

Using the numbers previously estimated for the Cherokee 180, the value for F_e is estimated to be

$$F_e = 1.30$$

Thus, the effectiveness of the stabilator in providing longitudinal static stability is not degraded by freeing the stick; indeed, it is actually improved!

Stick-Free Static Margin

The effect of freeing the elevator on the neutral point can be determined simply by multiplying a_t by the free elevator factor, F_e, and using this effective tail lift curve slope in the expressions previously derived for the stick-fixed case.

If F_e is less than 1.0 the neutral point shifts forward, thereby decreasing the static margin for a given center-of-gravity position.

Steady Maneuvering

A wing-tail combination is pictured in Figure 8.19 undergoing a steady pull-up maneuver. For clarity, the angle $\Delta\alpha_t$ is shown much larger than it

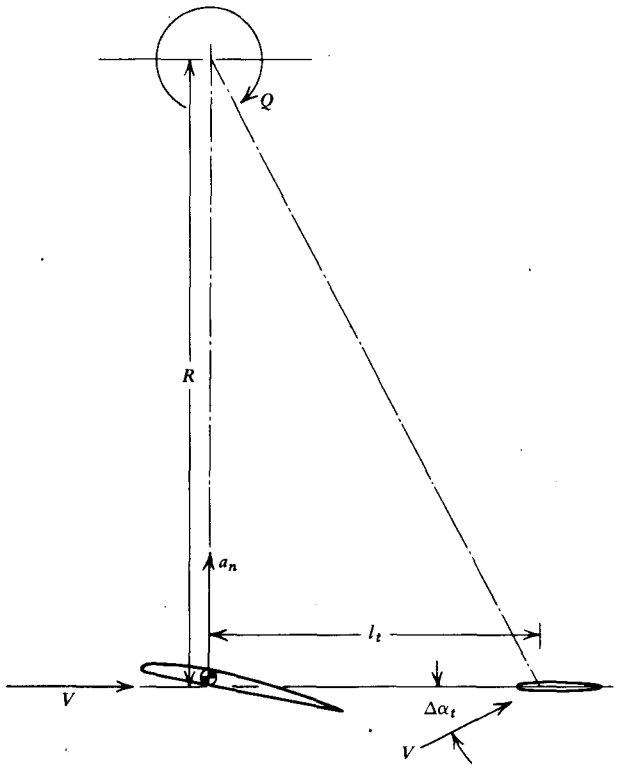

Figure 8.19 Wing-tail combination in a steady pull-up maneuver.

actually is; that is, the ratio of l_t to the radius of the flight path, R, is much less than one. The acceleration, a_n, of the airplane toward the center of curvature requires a lift in excess of the weight given by

$$L = W\left(1 + \frac{a_n}{g}\right) \tag{8.47}$$

The lift-to-weight ratio is known as the load factor, n.

$$n = 1 + \frac{a_n}{g} \tag{8.48}$$

The relationships derived thus far that relate C_M to C_L (or α) hold for the maneuvering case. However, an additional increment must be added to C_M as a result of the increment in α_t due to the angular velocity, Q.

$$\Delta M = -\tfrac{1}{2}\rho V^2 \eta_t S_t a_t \, \Delta\alpha_t l_t$$

But

$$\Delta\alpha_t = \frac{l_t}{R}$$

$$= \frac{Ql_t}{V} \tag{8.49}$$

Thus, in coefficient form,

$$\Delta C_M = \frac{\Delta M}{\tfrac{1}{2}\rho V^2 S\bar{c}}$$

or

$$\Delta C_M = -\eta_t a_t V_H \frac{l_t Q}{V} \tag{8.50}$$

Notice that we can also visualize the airplane as translating with a linear velocity of V while rotating about its center of gravity with an angular velocity of Q. The tail is then moving down with a velocity of l_tQ, which leads to Equation 8.49.

Horizontal Stabilizer-Elevator Configuration: Elevator Angle per g

Including the effect of Q, we can now write Equation 8.7 as

$$C_M = C_{M_0} + C_{M_\alpha}\alpha + C_{M_\delta}\delta_e + C_{M_Q}Q \tag{8.51}$$

However, neither Q nor C_{M_Q} is dimensionless (although their product is). Thus, it is sometimes desirable to write Equation 8.51 as

$$C_M = C_{M_0} + C_{M_\alpha}\alpha + C_{M_\delta}\delta_e + C_{M_q}\bar{q} \tag{8.52}$$

where $\bar{q}$ is a dimensionless pitch rate defined by

$$\bar{q} = \frac{Q\bar{c}}{2V} \tag{8.53}$$

The choice of $\bar{c}/2$ as a reference length is simply according to convention and has no physical significance.

From Equation 8.50, C_{M_q} is seen to equal approximately

$$C_{M_q} = -\eta_t a_t V_H \frac{2l_t}{\bar{c}} \tag{8.54}$$

C_{M_q} is referred to as "pitch damping," since it represents a negative moment proportional to the rotational velocity about the pitch axis.

In a steady pull-up maneuver, there is no angular acceleration, so C_M must be zero as it is in trimmed level flight. Assuming C_{M_0} to remain constant, we can therefore equate the increment C_M resulting from the steady maneuver to zero. Since C_M is assumed linear with α, δ, and $\bar{q}$, we can write

$$0 = C_{M_\alpha} \Delta\alpha + C_{M_\delta} \Delta\delta_e + C_{M_q}\bar{q}$$

or

$$\Delta \delta_e = -\left(\frac{C_{M_\alpha} \Delta\alpha + C_{M_q}\bar{q}}{C_{M_\delta}}\right) \tag{8.55}$$

Remember that $\bar{q}$ now represents the dimensionless pitch rate and *not* the dynamic pressure. Since

$$V = QR$$

and

$$a_n = \frac{V^2}{R}$$

it follows from Equation 8.53 that

$$\bar{q} = \frac{g\bar{c}}{2V^2}\left(\frac{a_n}{g}\right) \tag{8.56}$$

The quantity (a_n/g) is the acceleration expressed as the ratio to the acceleration due to gravity. When, for example, we speak about "pulling 4g's," we mean that $a_n/g = 4.0$.

$\Delta\alpha$ can be obtained from Equations 8.47 and 8.48.

$$\frac{L}{W} = 1 + \frac{a_n}{g}$$

or

$$\frac{C_L + \Delta C_L}{C_L} = 1 + \frac{a_n}{g}$$

Thus,

$$\Delta C_L = C_L \frac{a_n}{g}$$
$$= C_{L_\alpha} \Delta\alpha + C_{L_\delta} \Delta\delta_e$$

so that

$$\Delta\alpha = \frac{C_L}{C_{L_\alpha}}\frac{a_n}{g} - \frac{C_{L_\delta}}{C_{L_\alpha}}\Delta\,\delta_e \tag{8.57}$$

where C_L is calculated for $1g$ flight. Combining Equations 8.55, 8.56, and 8.57 results in an expression for the elevator angle per g of acceleration.

$$\frac{\Delta\,\delta_e}{(a_n/g)} = -\frac{C_{M_\alpha}C_L + g\bar{c}/2V^2 C_{M_q}C_{L_\alpha}}{C_{M_\delta}C_{L_\alpha} - C_{M_\alpha}C_{L_\delta}} \tag{8.58}$$

Substituting Equation 8.13 for C_{M_α}, Equation 8.58 becomes

$$\frac{\Delta\,\delta}{(a_n/g)} = -\frac{C_{L_\alpha}C_L}{C_{M_\delta}C_{L_\alpha} - C_{M_\alpha}C_{L_\delta}}\left(h - h_n + \frac{\rho\bar{c}S}{4m}C_{M_q}\right)$$

where m is the mass of the airplane. We now define a relative mass parameter, μ.

$$\mu = \frac{2m}{\rho\bar{c}S} \tag{8.59}$$

$\bar{c}/2$ is the same reference length used in the definition of $\bar{q}$ (Equation 8.53). This length multiplied by the wing area gives a reference volume. The parameter μ is then the ratio of the airplane mass to the air mass within this volume. Using the definition of μ, equation 8.58 becomes

$$\frac{\Delta\,\delta_e}{(a_n/g)} = \frac{C_{L_\alpha}C_L}{C_{M_\delta}C_{L_\alpha} - C_{M_\alpha}C_{L_\delta}}\left(h_n - h - \frac{1}{2\mu}C_{M_q}\right) \tag{8.60}$$

Similar to the neutral point, there is a particular value of h, known as the stick-fixed maneuver point, h_m, for which no elevator deflection is required to produce an acceleration. Indeed, if the center of gravity moves aft of this point, the effect of the elevator is reversed. From Equation 8.60,

$$h_m = h_n - \frac{1}{2\mu}C_{M_q} \tag{8.61}$$

Since C_{M_q} is negative, h_m lies aft of the neutral point.

In terms of the neutral point,

$$\frac{\Delta\,\delta_e}{(a_n/g)} = \frac{C_{L_\alpha}C_L}{C_{M_\delta}C_{L_\alpha} - C_{M_\alpha}C_{L_\delta}}(h_m - h) \tag{8.62}$$

The quantity $(h_m - h)$ is known as the stick-fixed maneuver margin. Again, it is emphasized that C_L is calculated for straight and level flight. It is not the total airplane C_L required during the steady pull-up maneuver.

Stabilator Angle per g

The preceding developments will apply to the stabilator configuration if $\Delta\,\delta_e$ is replaced by Δi_{hs}, C_{M_δ} by C_{M_i}, and C_{L_δ} by C_{L_i}. A separate analysis of the stabilator with regard to a steady maneuver is therefore unnecessary.

Stick Force per g

Stabilizer-Elevator Configuration In order to calculate the stick force required per g of normal acceleration, we again use Equations 8.27 and 8.37.

$$C_H = b_1\alpha_t + b_2\,\delta_e + b_3\,\delta_t$$

But, in the steady pull-up,

$$\alpha_t = \alpha(1-\epsilon_\alpha) - i_{hs} + 2\frac{l_t}{\bar{c}}\bar{q} \tag{8.63}$$

Thus,

$$\eta_T\frac{P}{GqS_e\bar{c}_e} = b_1\left[\alpha(1-\epsilon_\alpha) - i_{hs} + 2\frac{l_t}{\bar{c}}\bar{q}\right] + b_2\,\delta_e + b_3\,\delta_t$$

Now let δ_t be adjusted to trim P to zero for unaccelerated flight. For this condition let $\alpha = \alpha_0$ and $\delta_e = \delta_{e_0}$, such that $\alpha = \alpha_0 + \Delta\alpha$, $\delta_e = \delta_{e_0} + \Delta\delta_e$. It then follows that

$$\frac{P}{G\eta_t qS_e\bar{c}_e} = b_1\left[\Delta\alpha(1-\epsilon_\alpha) + 2\frac{l_t}{\bar{c}}\bar{q}\right] + b_2\,\Delta\,\delta_e$$

$\Delta\alpha$ is obtained from Equation 8.57 and $\Delta\delta_e$ from Equation 8.62. Also, from Equation 8.56,

$$2\frac{l_t}{\bar{c}}\bar{q} = g\frac{l_t}{V^2}\left(\frac{a_n}{g}\right)$$

Thus the stick force per g becomes

$$\frac{P}{a_n/g} = G\eta_t S_e\bar{c}_e\left(\frac{W}{S}\right)\left[b_1\left(\frac{(1-\epsilon_\alpha)}{C_{L_\alpha}} + \frac{1}{\mu}\frac{l_t}{\bar{c}}\right) + \left(\frac{b_2C_{L_\alpha} - b_1C_{L_\delta}(1-\epsilon_\alpha)}{C_{M_\delta}C_{L_\alpha} - C_{M_\alpha}C_{L_\delta}}\right)(h_m - h)\right] \tag{8.64}$$

The position of h for which P equals zero is known as the stick-free maneuvering point and is denoted by h'_m. In terms of h'_m, the stick force per g becomes

$$\frac{P}{a_n/g} = G\eta_t S_e\bar{c}_e\left(\frac{W}{S}\right)\left[\frac{b_2C_{L_\alpha} - b_1C_{L_\delta}(1-\epsilon_\alpha)}{C_{M_\delta}C_{L_\alpha} - C_{M_\alpha}C_{L_\delta}}\right](h'_m - h) \tag{8.65}$$

where

$$h'_m = h_m + b_1\left[\frac{(1-\epsilon_\alpha)}{C_{L_\alpha}} + \frac{1}{\mu}\frac{l_t}{\bar{c}}\right]\left(\frac{C_{M_\delta}C_{L_\alpha} - C_{M_\alpha}C_{L_\delta}}{b_2C_{L_\alpha} - b_1C_{L_\delta}(1-\epsilon_\alpha)}\right) \tag{8.66}$$

The quantity $(h'_m - h)$ is known as the stick-free maneuver margin.

Stabilator The stick force per g for the stabilator is obtained in a manner similar to that which was followed for the stabilizer-elevator configuration. The moment coefficient about the pivot line is once again given by Equation 8.32. Also, in the steady pull-up, Equation 8.63 again applies and δ is related to i_{hs} by Equation 8.33. Thus, for the stabilator,

$$\frac{P}{\eta_t G q S_t \bar{c}_t} = b_1\left[\alpha(1-\epsilon_\alpha) - i_{hs} + 2\frac{l_t}{\bar{c}}\bar{q}\right] + b_2(k_e i_{hs} + \delta_0)$$

Now let δ_0 be adjusted so that $P = 0$ for $\bar{q} = 0$. For this trim condition we again let $\alpha = \alpha_0$ and $i_{hs} = i_{hs_0}$, so that, generally, $\alpha = \alpha_0 + \Delta\alpha$ and $i_{hs} + i_{hs_0} + \Delta i_{hs}$. Thus,

$$\frac{P}{G\eta_t q S_t \bar{c}_t} = b_1\left[\Delta\alpha(1-\epsilon_\alpha) - \Delta i_{hs} + g\frac{l_t}{V^2}\left(\frac{a_n}{g}\right)\right] + b_2 k_e\,\Delta i_{hs}$$

or

$$\frac{P}{a_n/g} = G\eta_t S_t \bar{c}_t\left(\frac{W}{S}\right)\left[b_1\left(\frac{1-\epsilon_\alpha}{C_{L_\alpha}} + \frac{1}{\mu}\frac{l_t}{\bar{c}}\right) + \left(\frac{b_2 C_{L_\alpha} k_e - b_1 C_{L_i}(1-\epsilon_\alpha)}{C_{M_i} C_{L_\alpha} - C_{M_\alpha} C_{L_i}}\right)(h_m - h)\right] \quad (8.67)$$

The similarity of this relationship to the corresponding equation for the stabilizer-elevator tail configuration is obvious. Again, we can express the stick force per g in terms of the stick-free maneuvering point.

$$\frac{P}{a_n/g} = G\eta_t S_t \bar{c}_t\left(\frac{W}{S}\right)\left[\frac{b_2 C_{L_\alpha} k_e - b_1 C_{L_i}(1-\epsilon_\alpha)}{C_{M_i} C_{L_\alpha} - C_{M_\alpha} C_{L_i}}\right](h'_m - h) \quad (8.68)$$

where

$$h'_m = h_m + b_1\left(\frac{1-\epsilon_\alpha}{C_{L_\alpha}} + \frac{1}{\mu}\frac{l_t}{\bar{c}}\right)\left[\frac{C_{M_i} C_{L_\alpha} - C_{M_\alpha} C_{L_i}}{b_2 C_{L_\alpha} k_e - b_1 C_{L_i}(1-\epsilon_\alpha)}\right] \quad (8.69)$$

An airplane loaded so that the center of gravity is close to the stick-free maneuvering point presents a dangerous situation. The pilot can impose extreme inertia loads on the airplane with the application of little or no control force. Such a situation, however, is rarely encountered if an adequate static margin is maintained, since the stick-fixed and stick-free maneuver points are aft of the corresponding neutral points.

Effect of Fuselage and Nacelles

A body, such as a fuselage or nacelle, is not a very efficient producer of lift by comparison to a wing or tail surface. Thus, except for missilelike configurations, where the body is relatively large, the contribution of the fuselage or nacelles to the total airplane lift can be neglected. However, in the case of the moment, fuselage and nacelle contributions can be fairly significant and result in a measurable shift of the neutral point. Generally, the

increments to C_{M_α} are positive, resulting in a decrease in h_n. Depending on the incidence of the wing relative to the fuselage and nacelles, these components can also contribute to C_{M_0}. Thus, including the fuselage and/or nacelles, Equation 8.7 becomes

$$C_M = C_{M_0} + \Delta C_{M_0} + (C_{M_\alpha} + \Delta C_{M_\alpha})\alpha \tag{8.70}$$

The increments ΔC_{M_0} and ΔC_{M_α} result from the addition of the fuselage and/or nacelles to the basic wing-tail combination. Thus, the relationships derived thus far are unchanged if the total values for C_{M_0} and C_{M_α} are used. An increment to C_{L_α} can also be included.

It is somewhat futile to present either data or theoretical results for predicting ΔC_{M_0} or ΔC_{M_α} in view of the many possible fuselage-nacelle-wing-tail combinations. Real fluid effects and lifting surface-body interference effects severely limit any application of theoretical solutions of the body alone.

For approximate purposes, expressions for C_{L_α} and C_{M_α} for bodies alone are presented that are based on material from DATCOM (Ref. 5.5). The lift curve slope of an axisymmetric body, having a length of l and a diameter d, can be expressed in the form

$$C_{L_{\alpha B}} = 2\left[1 - 1.76\left(\frac{l}{d}\right)^{-1.5}\right] \text{/rad} \tag{8.71}$$

Here, C_L is based on a reference area, S_0, which is the body's cross-sectional area at a station X_0 back from the nose. X_0 is a function of a station X_1; X_1 is the station along the body where ds/dx has its minimum value. Usually this means the point of maximum cross-sectional area. In terms of the body length, X_0 and X_1 are related by

$$X_0 = 0.367 + 0.533X_1$$

The slope of the body moment curve can be estimated from

$$C_{M_{\alpha B}} = C_{L_{\alpha B}}(X_M - X_0 + \bar{l}_0) \tag{8.72}$$

C_{M_B} is based on a reference area of S_0 and the body length, l. X_m is the station for the moment center expressed as a fraction of l. $\bar{l}_0$ is an average length that, multiplied by S_0, gives the body volume ahead of the station X_0. Again, $\bar{l}_0$ is relative to the total body length.

Since $C_{L_{\alpha B}}$ and $C_{M_{\alpha B}}$ are based on the body geometry, their values must be corrected when they are applied to the total airplane. More specifically, $C_{L_{\alpha B}}$ must be multiplied by the ratio S_0/S before being added to Equation 8.11. Similarly, $C_{M_{\alpha B}}$ must be multiplied by $(S_0 l)/(S\bar{c})$ before being added to equations previously derived from C_{M_α}. It should be emphasized that the expression for the lift curve and moment curve slopes hold only for small angles of attack.

Effects of Propulsion System

Propellers

Both propellers and jets can affect longitudinal static stability. Consider first the case of a propeller-driven airplane, shown schematically in Figure 8.20. As illustrated in the figure, a propeller develops not only a thrust, T, directed along its axis of rotation, but also a force, P_N, directed normal to its axis. It will be shown that P_N is proportional to the propeller thrust, α, and the advance ratio, J, and is directed upward for a positive angle of attack.

Since the thrust is directed along the propeller axis and rotates with the rest of the airplane, its contribution to the moment about the center of gravity does not change with α. Hence C_{M_α} is not affected by T. On the other hand, C_{M_0} is affected by T since, generally, the thrust line will not pass through the center of gravity. If the thrust line lies a distance of Z_p above the center of gravity, then C_{M_0}, given by Equation 8.5, is decreased by the amount

$$\Delta C_{M_0} = -\left(\frac{T}{qS}\right)\left(\frac{Z_p}{\bar{c}}\right) \tag{8.73}$$

The normal force, P_N, affects both the trim, C_{M_0}, and the stability, C_{M_α}. C_{M_0} is increased by the amount

$$\Delta C_{M_0} = C_{N_p}\frac{l_p}{\bar{c}} \tag{8.74}$$

while C_{M_α} is increased by

$$\Delta C_{M_\alpha} = C_{N_{p\alpha}}\frac{l_p}{\bar{c}} \tag{8.75}$$

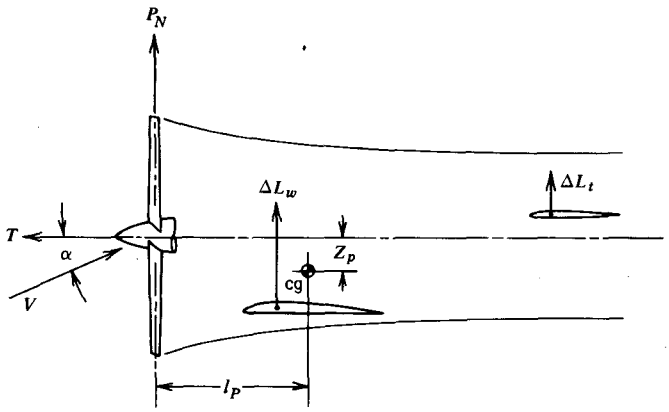

Figure 8.20 Effect of propeller forces and slipstream on longitudinal static stability.

where

$$C_{N_p} = \frac{P_N}{qS}$$

$$C_{N_{p\alpha}} = \frac{\partial C_{N_p}}{\partial \alpha}$$

In addition to contributing to the forces and moments affecting longitudinal motion, a propeller at an angle of attack produces a yawing moment that couples with the lateral-directional behavior of the airplane. Let us now examine the origin of both the normal force and yawing moment. Figure 8.21*a* shows a side view of a propeller at an angle of attack α. It is seen that a component of the free-stream velocity, $V\alpha$, lies in the plane of the propeller and is directed upward. Figure 8.21*b* is a view in the plane of rotation looking in the direction of flight. Measuring the displacement of a blade from the

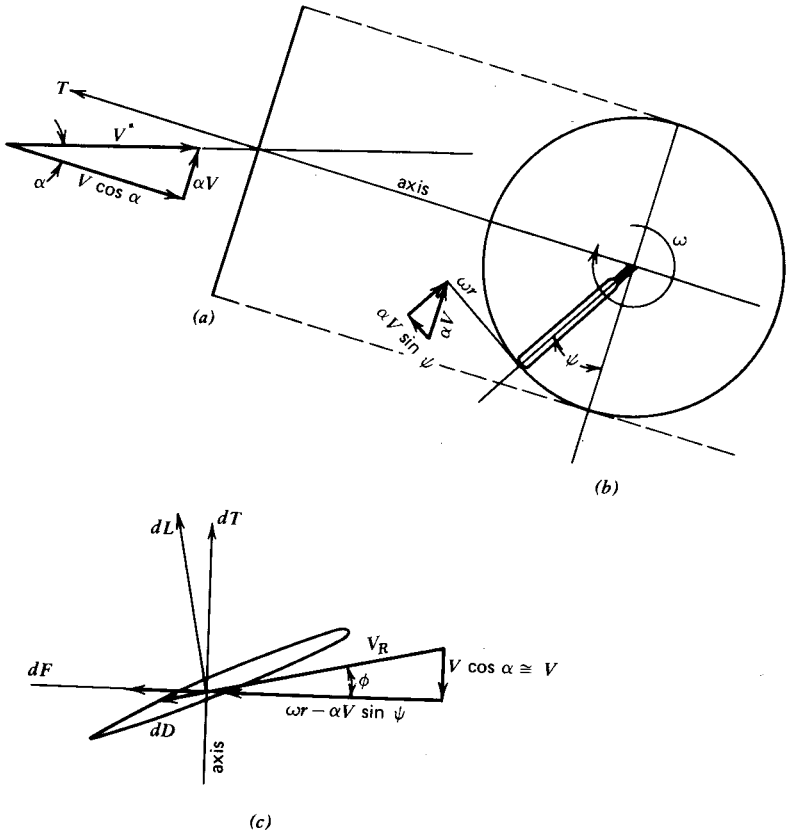

Figure 8.21 Forces on a propeller at an angle of attack.

vertical bottom line, it is seen that a blade section experiences a velocity normal to the blade given by the sum of ωr and $\alpha V \sin \psi$. In Figure 8.21*c* we view a section of the blade looking in toward the hub. The section lift and drag combine vectorially to produce a thrust per unit blade length of

$$\frac{dT}{dr} = \frac{dL}{dr}\cos\phi - \frac{dD}{dr}\sin\phi$$

Similarly, a differential force, dF/dr, lying in the plane of rotation is generated given by

$$\frac{dF}{dr} = \frac{dL}{dr}\sin\phi + \frac{dD}{dr}\cos\phi$$

dF/dr will have components of dP_N/dr directed upward and dY_p/dr directed to the right and given by

$$\frac{dP_N}{dr} = -\frac{dF}{dr}\sin\psi$$

$$\frac{dY_p}{dr} = \frac{dF}{dr}\cos\psi$$

Since all three of these force components vary with the blade position, ψ, average values are obtained by integrating each with respect to ψ from 0 to 2π and then dividing by 2π. For example,

$$T = \frac{B}{2\pi}\int_0^{2\pi}\int_0^R \frac{dT}{dr}\,dr\,d\psi \tag{8.76}$$

where B is the number of blades and R is the propeller radius.

In order to cast the equations in a tractable form, it is assumed that the angle ϕ is small so that

$$V_R \simeq \omega r - V\alpha \sin\psi$$

With this assumption dL/dr and dD/dr become

$$\frac{dL}{dr} = \tfrac{1}{2}\rho(\omega r - V\alpha\sin\psi)^2 c C_l \tag{8.77}$$

$$\frac{dD}{dr} = \tfrac{1}{2}\rho(\omega r - V\alpha\sin\psi) c C_d \tag{8.78}$$

C_l, as well as the local velocity, varies with ψ, whereas C_d is assumed to be constant. Using a quasisteady approximation (neglecting unsteady aerodynamics), C_l is written as

$$C_l = a(\beta - \phi) \simeq a\left(\beta - \tan^{-1}\frac{V}{\omega r - V\alpha\sin\psi}\right)$$

β the blade pitch angle defined in figure 6.9, will be chosen so as to give a constant C_l along the blade when α is zero.

$$C_l = a\left(\beta - \tan^{-1}\frac{V}{\omega r}\right) \tag{8.79}$$

Thus,

$$\beta = \frac{\bar{C}_l}{a} + \tan^{-1}\frac{V}{\omega r}$$

The differential, instantaneous pitching, and yawing moments about the y- and z-axes, respectively, will be given by

$$dM_p = \frac{dT}{dr} r\cos\psi\, dr$$

$$dN_p = \frac{dT}{dr} r\sin\psi\, dr$$

The foregoing relationships are combined and integrated over ψ from 0 to 2π and over r from 0 to R. The chords c and C_d are assumed constant, so they can be taken outside of the integration. The following results are obtained.

$$T = \frac{\sigma qA}{2}\left(\frac{\pi}{J}\right)\left(\frac{2\pi}{3J}\bar{C}_l - C_d\right) \tag{8.80}$$

$$P_N = \frac{\sigma qA}{2}\left\{\bar{C}_l + \frac{aJ}{2\pi}\ln\left[1+\left(\frac{\pi}{J}\right)^2\right] + \frac{\pi}{J}C_d\right\}\alpha \tag{8.81}$$

$$N_p = \frac{-\sigma qAR}{2}\left\{\frac{2\pi}{3J}\bar{C}_l + \frac{a}{2}\left[1-\left(\frac{J}{\pi}\right)^2\ln\left(1+\left[\frac{\pi}{J}\right]^2\right)\right] - \frac{\pi}{J}C_d\right\}\alpha \tag{8.82}$$

$M_p = 0$

$Y_p = 0$

σ = blade area/disc area

It is convenient to express P_N and N_p in terms of T and the product TR, respectively. Since the same assumptions are involved in calculating T, P_N, and N_p, the ratios of P_N and N_p to T are probably more accurate than the predicted absolute values of these quantities. Also, (σqA) cancels out, so that one needs only to estimate the average lift coefficient of the blades in order to obtain the force and moment ratios.

In steady, level flight, the thrust is equal to the airplane drag. Thus, knowing the drag, propeller geometry, advance ratio, and q, one can calculate the $\bar{C}_l$ from Equation 8.80. The result is relatively insensitive to C_d, so that a typical value of 0.01 can be assumed for this quantity.

Figure 8.22*a* and 8.22*b* presents the derivatives of P_N and N_p with respect to α in ratio form as a function of advance ratio for constant values of $\bar{C}_l$. If the propeller geometry is not known, a reasonable value of $\bar{C}_l$ would probably be around 0.8.

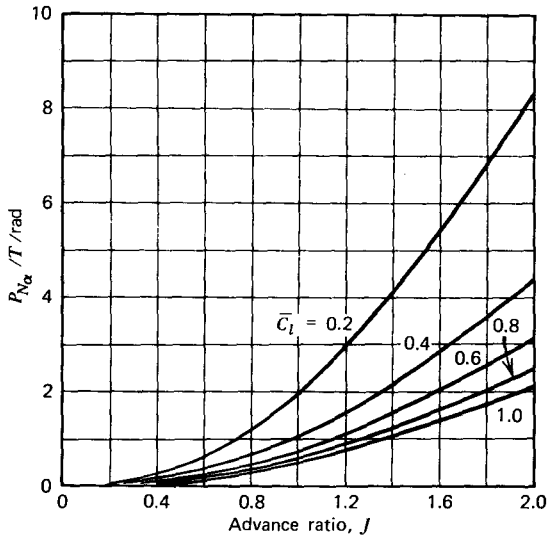

Figure 8.22a Ratio of propeller normal force derivative to thrust.

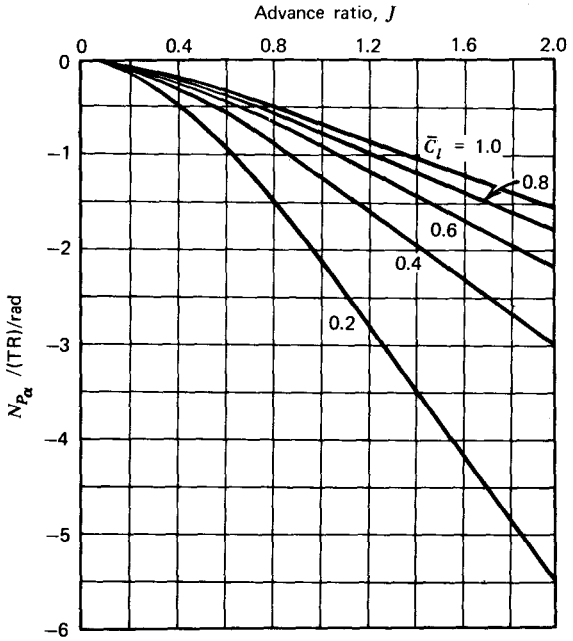

Figure 8.22b Ratio of propeller moment derivative to product of thrust and radius.

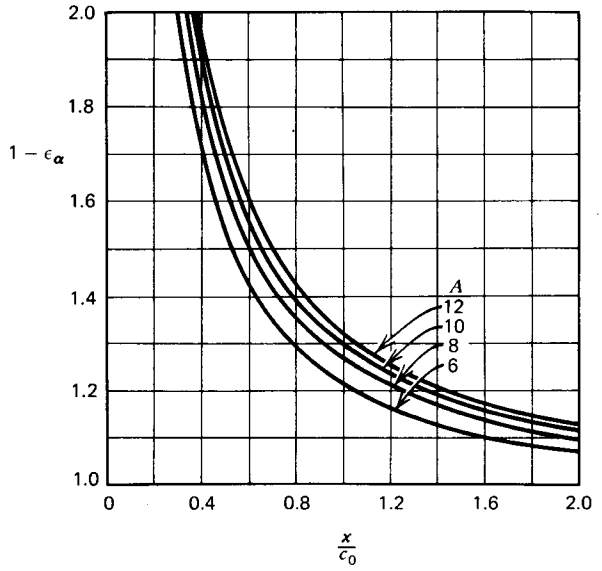

Figure 8.22c Correction for upwash ahead of a wing. Model of figure 8.5 assumed using an unswept elliptic wing. c_0 = root chord, x = distance ahead of quarter-chord line.

The direction of P_N is independent of the direction of the propeller rotation. However, the sign of the moment, N_p, is reversed if the propeller rotates opposite to that shown in Figure 8.21. As derived, all rotations and moments follow the right-handed coordinate system of Figure 8.1.

This method for predicting P_{N_α} and N_{p_α} is original with this text and is untested. Sufficiently complete systematic data against which to compare the predictions could not be found. An alternate method for predicting P_N and N_p is offered in Reference 8.13. Graphs based on this reference can be found in other sources, but they seem to be specific to particular propellers, and their general applicability appears questionable. The conclusions of Reference 8.13 may be applied, however, without these graphs. They state that a propeller behaves like a fin having the same area as the average projected side area of the propeller with an effective aspect ratio of approximately 8. The moment produced by the propeller is approximately equal to the lift on the fin multiplied by the propeller radius. "Average" side area means an average area projected in one revolution. This is given approximately by one-half the number of blades times the projected side area of one stationary blade.

In calculating the propeller normal force, one must account for the fact that there is an upwash ahead of the wing that effectively increases the angle

of attack. Thus Equation 8.75 becomes

$$\Delta C_{M_\alpha} = C_{N_{p_\alpha}} \frac{l_p}{\bar{c}}(1 - \epsilon_\alpha) \tag{8.83a}$$

This can also be written as

$$\Delta C_M = \left(\frac{P_{N_\alpha}}{T}\right) C_D \frac{l_p}{\bar{c}}(1 - \epsilon_\alpha) \tag{8.83b}$$

which assumes the thrust equal to the drag. Again, ϵ_α is the rate of change of *downwash* with α. Ahead of the wing, ϵ_α is negative so that $(1 - \epsilon_\alpha)$ is greater than unity. This factor is presented in Figure 8.21*c*. This graph was calculated using the vortex system shown in Figure 8.5. Again, in the final analysis, one should resort to wind tunnel testing of a powered model to determine these effects accurately.

The effect of the propeller slipstream on the wing and tail will not be treated here in any detail. At higher speeds, these effects are small and can usually be neglected. At the lower speeds, however, the increased q in the propeller slipstream can increase both the wing and tail lift. In addition, particularly for V/STOL (vertical/short takeoff and landing) applications, the propeller-induced velocity can become appreciable relative to the free-stream velocity, resulting in significant changes in the section angles of attack of both the wing and tail. For a detailed treatment of those effects, refer to Reference 3.3

Jets

The two principal effects of a jet propulsion system entail the forces developed internally on the jet ducts and the influence of the jet exhaust on the flow field of the tail. The following is based on material in Reference 8.2.

Figure 8.23 depicts schematically the flow through a jet propulsion system. The notation is similar to that of the reference. First, it is obvious that an increment to the trim moment results from the thrust, T, which is independent of α. This increment can be written as

$$\Delta C_M = \left(\frac{T}{qS}\right)\frac{Z_j}{\bar{c}} \tag{8.84}$$

Second, as in the case of the propeller, a normal force is developed by the jet. This force, N_j, is directed normal to the exhaust velocity $\mathbf{V}_j$ and acts at the intersection of lines parallel to $\mathbf{V}_i$ and $\mathbf{V}_j$ through the centers of the inlet and exhaust. This is usually close to the inlet. Applying momentum principles to the system, the magnitude of $\mathbf{N}_j$ is found to be

$$N_j = m_j V_i \theta$$

where m_j is the mass flow rate through the engine. The angle θ equals the

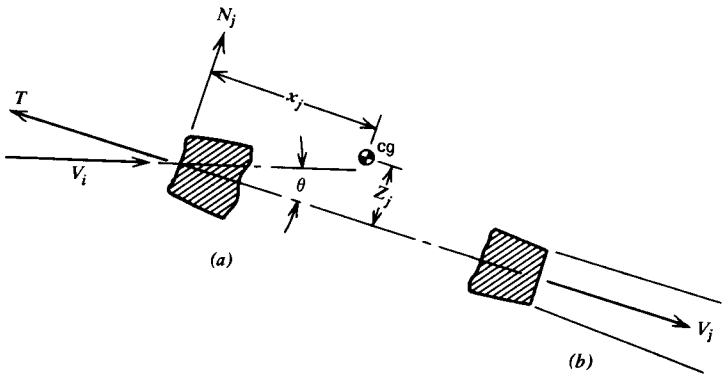

Figure 8.23 The normal force produced by a jet engine. (*a*) Intake. (*b*) Tail pipe.

angle of attack of the thrust line α minus the downwash angle ϵ_i at the inlet. If the inlet is ahead of the wing, ϵ_i will generally be negative.

$$\theta = \alpha - \epsilon_i$$

From this, it follows that the normal force, N_j, contributes an increment to C_{M_α}, given by

$$\Delta C_{M_\alpha} = \left(\frac{m_j V_i}{qS}\right)\frac{X_j}{c}(1 - \epsilon_{i_\alpha}) \tag{8.85}$$

Since

$$m_j = \rho_i A_i V_i$$

Equation 8.85 can be evaluated given the characteristics of the engine. The quantity $(1 - \epsilon_{i_\alpha})$ can be estimated using Figure 8.22 or Figure 8.6.

The influence of the jet exhaust on the flow field external to the jet is illustrated in Figure 8.24. Viscous shear along the edges of the jet produces an entrainment of the external flow into the jet. To the external flow, the jet appears somewhat like a distributed line of sinks. As shown in Figure 8.24, this jet-induced flow can produce a change in the local flow direction for a lifting surface in proximity to the jet.

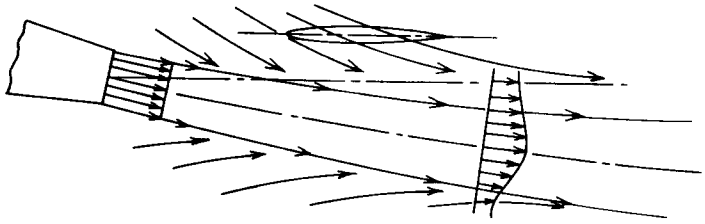

Figure 8.24 Flow inclination resulting from flow entrainment.

Again, the calculation of flow inclination and the effect on a lifting surface is a difficult task and is best determined from wind tunnel tests. The effect can be appreciable and generally should not be neglected. According to Reference 8.2, it may vary with α enough to reduce the stability significantly.

From material to be found in the appendix of Reference 8.2, an approximate estimate of the inclination angle due to jet entrainment can be calculated from

$$\epsilon = \frac{C_D}{n\left(\frac{x}{b}\right)\left(\frac{r}{b}\right)A} \tag{8.86}$$

where

C_D = airplane drag coefficient
n = number of engines
x = distance aft of exhaust exit plus 2.3 diameters of the jet at its exit
r = radial distance from jet centerline
b = wingspan
A = aspect ratio

Although α does not appear in Equation 8.86, the inclination of the jet itself varies with α, which causes the distance, r, to change. For more detailed information on this, see Reference 8.2 and the original sources on this topic, which are noted in the reference.

Ground Effect

Downwash velocities are decreased when the airplane is operating close to the ground. Since the ground is a solid boundary to which the normal component of velocity must vanish, its presence alters the streamline pattern that exists around the airplane out-of-ground effect. In order to determine ground effect, an image system representing the airplane's vortex system is placed below the airplane a distance equal to twice the height of the airplane above the ground. The vortex strength of the image system is of opposite sign to the original vortex system. Thus, midway between the two systems, their induced velocities in the vertical direction will cancel, satisfying the boundary condition along the ground.

An additional graph to estimate the effect of the ground on downwash is not needed in light of this information. Instead, one can again make use of Figure 8.6*a*. For example, suppose an airplane is operating a height above the ground, h, equal to half of its span. Also, let the distance $l_{t_{ac}}$ equal b and

$h_t/b = 0.05$. Relative to b',

$$h = 0.637b'$$
$$l_{ac} = 1.273b'$$
$$h_t = 0.0637b'$$

Relative to the image system the tail is located at,

$$l_{t_{ac}} = 1.273b'$$
$$h_t = (0.637 + 0.637 + .0637)b'$$
$$= 1.338b'$$

Thus, from Figure 8.6*a*, for the image system

$$\epsilon_\alpha = 0.06\frac{a}{A}$$

This downwash is subtracted from that for the airplane out-of-ground effect which, in this case, is

$$\epsilon_\alpha = 0.527Aa$$

Thus, the downwash in this case is decreased by 11% due to the ground effect. This decrease will, of course, improve the static stability and change the trim.

LATERAL AND DIRECTIONAL STATIC STABILITY AND CONTROL

We now turn our attention to the static forces and moments that tend to rotate the airplane about its x- and z-axes or translate it along its y-axis. First consider directional stability and control about the z-axis.

Directional Static Stability

Figure 8.25 illustrates an airplane undergoing a positive sideslip. In this case, the component of its velocity vector along the y-axis is nonzero and positive. The airplane is "slipping" to the right. This results in a positive sideslip angle, β, being defined as shown. As a result of the velocity vector no longer lying in the plane of symmetry, a yawing moment, N, is produced by the fuselage and by the side force on the vertical tail. The airplane will possess positive static directional stability (sometimes called weathercock stability, after the weathervane) if

$$\frac{\partial N}{\partial \beta} = N_\beta > 0 \tag{8.87}$$

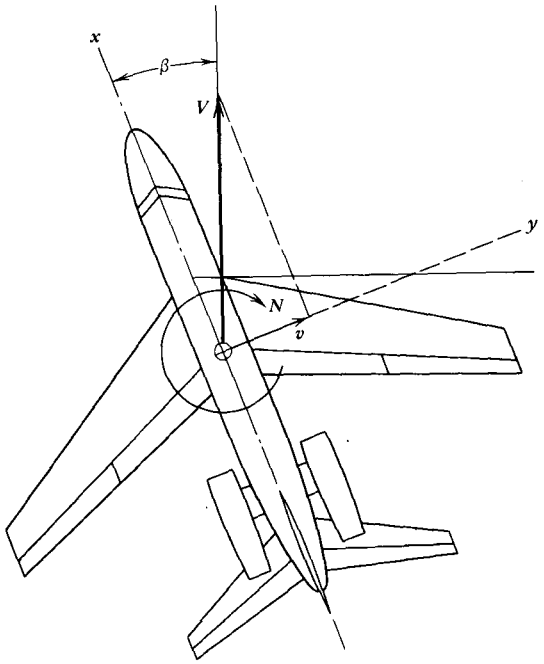

Figure 8.25 An airplane having a positive sideslip.

The criterion for longitudinal static stability required the slope of the moment curve to be negative. In this case, the sign is opposite because the yawing moment is opposite in direction to the angle β.

Generally, the yawing moment from the fuselage is destablizing. However, it is usually small and easily overridden by the stabilizing moment contributed by the vertical tail, so airplanes generally possess static directional stability. However, the vertical tail is not normally sized by any considerations of static directional stability. Instead, the minimum tail size is determined by controlability requirements in the event of an asymmetric engine failure or flying qualities requirements related to dynamic motion.

The yawing moment is expressed in coefficient form by

$$N = C_N q S b \tag{8.88}$$

The contribution to C_N from the fuselage can be estimated on the basis of Equation 8.72. However, in calculating $C_{N_{\beta B}}$ corresponding to $C_{M_{\alpha B}}$, the difference in signs and reference lengths must be remembered. $C_{y_{\beta B}}$ will also be of opposite sign to $C_{L_{\alpha B}}$.

The contribution of the vertical tail to the static directional stability is formulated in a manner similar to that followed in determining the horizontal

tail's effect on longitudinal stability. If the aerodynamic center of the vertical tail is located a distance of l_v behind the center of gravity, then

$$N_v = \eta_t q S_v l_v a_v [\beta(1 - \epsilon_\beta)]$$

or

$$C_{N_{v_\beta}} = \eta_t \frac{S_v}{S} \frac{l_v}{b} a_v (1 - \epsilon_\beta) \tag{8.89}$$

The vertical tail volume, V_v, is defined by

$$V_v = \frac{S_v}{S} \frac{l_v}{b}$$

so that Equation 8.89 becomes

$$C_{N_{v_\beta}} = \eta_t V_v a_v (1 - \epsilon_\beta) \tag{8.90}$$

a_v is the slope of the lift curve for the vertical tail. An estimate of this quantity is made more difficult by the presence of the fuselage and horizontal tail. If the vertical tail is completely above the horizontal tail, then it is recommended that an effective aspect ratio be calculated for the vertical tail equal to the geometric aspect ratio multiplied by a factor of 1.6. If the horizontal tail is mounted across the top of the vertical tail (the so-called T-tail configuration), this factor should be increased to approximately 1.9 to allow for the end-plate effect of the fuselage on the bottom of the vertical tail and the horizontal tail on the top. This latter factor of 1.9 is only typical of what one might expect for an average ratio of fuselage to tail size. For a more precise estimate of this factor, one should resort to wind tunnel tests or Reference 8.3 or 5.5.

The sidewash factor, ϵ_β, is extremely difficult to estimate with any precision. For preliminary estimates, it can be taken to be zero. However, one should be aware of its possible effects on N_v.

Directional Control

Control of the yawing moment about the z-axis is provided by means of the rudder. The rudder is a movable surface that is hinged to a fixed vertical stabilizer. The rudder is the vertical counterpart to the elevator, and its effectiveness is determined in the same way. Referring to Figure 8.26, the vertical tail is shown at zero sideslip angle with the rudder deflected positively through the angle δ_r. The rudder produces an increment in the vertical tail lift (or side force) that results in an increment in the yawing moment, given by

$$\Delta N = -l_v \Delta L_v$$

The increment in the tail lift is given by

$$\Delta L_v = \eta_t q S_v a_v \tau \delta_r$$

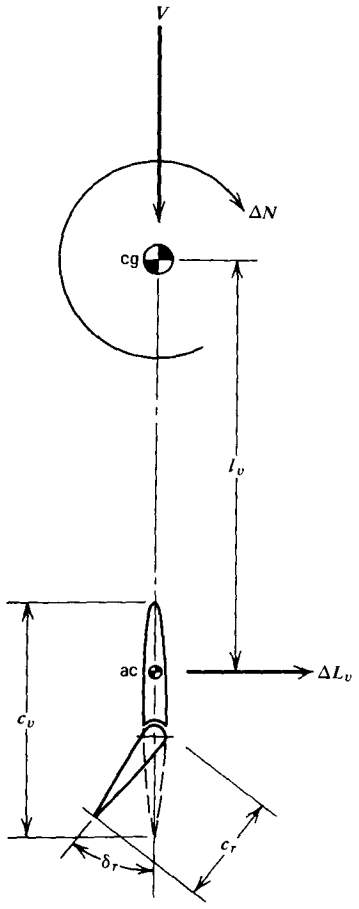

Figure 8.26 Rudder control.

so that in coefficient form, the rate of change of C_N with respect to the rudder angle becomes

$$C_{N_\delta} = -\eta_t V_v a_v \tau \tag{8.91}$$

The subscript r is dropped on δ, since it should be obvious that δ refers to the rudder when considering C_N. τ is the effective change in the angle of the zero lift line of the vertical tail per unit angular rotation of the rudder and is estimated in the same manner in which τ was obtained for the elevator.

As an example in the use of the rudder, suppose the airplane pictured in Figure 8.25 lost power on its right engine. If each engine is located a distance of Y_e from the fuselage centerline, the resulting asymmetric thrust would produce a yawing moment about the center of gravity equal to TY_e. In steady

trimmed flight the thrust, T, must equal the drag and N must be zero. Therefore,

$$DY_e + qSbC_{N_\delta}\,\delta_r = 0$$

or

$$\delta_r = \frac{C_D Y_e}{\eta_t V_v a_v \tau b}$$

Given the airplane and rudder geometry and C_D as a function of V, one can then calculate the vertical tail volume necessary to keep δ_r within prescribed limits, usually a linear operating range.

Lateral Control

In the engine-out example just presented, you may have noticed that the airplane was really not in trim. With the rudder deflected to balance the yawing moment of the engine, a side force is produced that must be counteracted by some means. This can be done by rolling the airplane around its x-axis to give a component of the weight along its y-axis. This is shown schematically in Figure 8.27. To carry the preceding engine-out example further, the sum of the forces along the y-axis must be zero for trim. Thus,

$$\Delta L_v + W\phi = 0$$

or

$$\phi = \frac{-\eta_t q S_v a_v \tau\,\delta_r}{W}$$

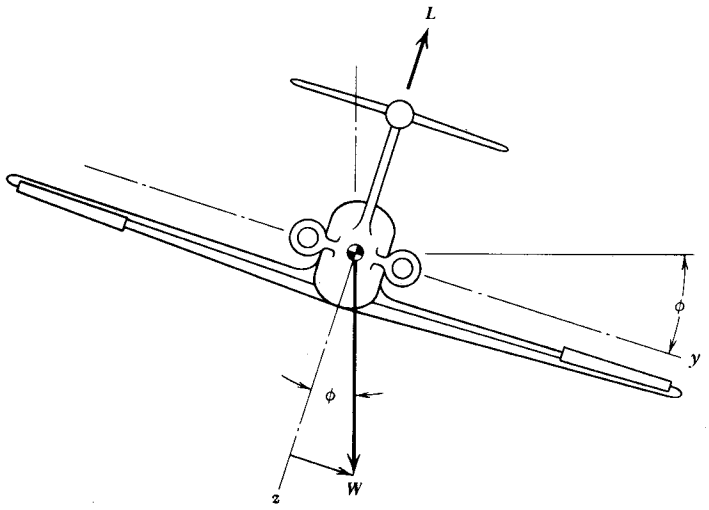

Figure 8.27 Rear view of an airplane with positive roll.

Substituting for δ_r gives

$$\phi = -\frac{C_D}{C_L}\frac{Y_e}{l_v} \tag{8.92}$$

Thus, to trim the engine-out situation completely, the pilot must have the capability to roll the airplane. This is accomplished by movable control surfaces that are hinged on the outer rear portion of each side of the wing, as shown in Figure 8.28. These surfaces, known as ailerons, move differentially: as one moves up, the other moves downward. Since the ailerons do not necessarily move the same amount, the aileron deflection is defined as the total angle between the two ailerons. For example, if the right aileron moves down 10° and the left aileron moves up 14°, the aileron deflection, δ_a, is equal to 24°. δ_a is defined to be positive when the right aileron rotates in a positive direction.

It was the incorporation of roll control that distinguished the efforts of the Wright Brothers from those of the other aviation pioneers of their day. Instead of ailerons, however, the Wright Brothers warped their box wing to provide a differential angle of attack from one wing tip to the other. This was improved on by Glenn Curtiss, who developed the hinged aileron, which was a considerable improvement over having to warp the wing. Since they had first recognized the need for complete lateral control and had devised the means to do so, the Wright Brothers brought a legal suit against Glenn Curtiss, claiming that his ailerons infringed on their patent rights. After a lengthy and bitter legal fight, the courts ruled in favor of the Wright Brothers. I have only the greatest respect and admiration for the Wright Brothers, but I question this particular legal decision, since it seems to me that Curtiss' development of the separate movable aileron control surface was, indeed, a

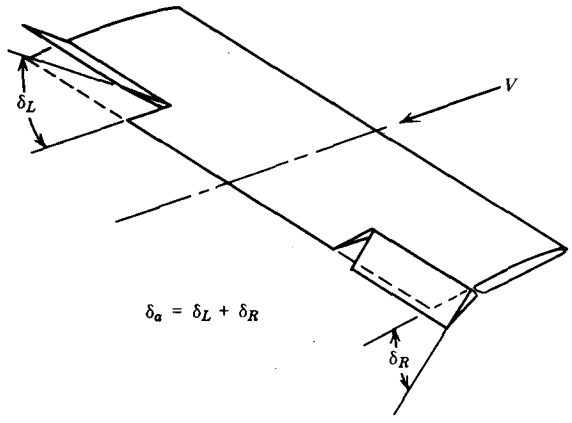

Figure 8.28 Aileron control surfaces for roll control.

control system distinct from the wing-warping system developed by the Wrights.

Leaving history and returning again to the technical aspect of roll control, observe that, when an airplane is rolled through an angle, ϕ, there is no mechanism present to generate an aerodynamic restoring moment. In the preceding cases involving angle of attack and sideslip angle, we encountered the derivatives C_{M_α} and C_{N_β}, respectively, that had nonzero values. In the case of the roll angle, however, the corresponding derivative C_{l_ϕ} is always zero. Because of this, the concept of roll stability, in the static sense, does not exist. At the most one could say that an airplane possesses neutral static stability in roll.

We define the rolling moment coefficient by reference to the wing area and wingspan, as with the yawing moment coefficient.

$$L = qSbC_l \tag{8.93}$$

Here we have a real problem with notation, since one tends to think of lift when the letters L or l are used. You will have to be careful and aware of the application of the coefficients in order to make a distinction. Generally, if the lowercase l is being used with reference to the entire airplane, it has reference to the rolling moment.

The rolling moment produced by the ailerons can be estimated by reference to Figure 8.29. As shown, the inboard end of the aileron is located a distance of y_1 from the wing centerline. The aileron extends from there out to a distance of y_2. As a result of the aileron deflection, an increment in the section lift per unit span is produced on the right side and is given by

$$d(\Delta L) = qca_0\tau\,\delta_{a_R}\,dy$$

This incremental lift results in a differential rolling moment.

$$dL = -yqca_0\tau\,\delta_{a_R}\,dy$$

Integrating this over the spanwise extent of the right aileron gives

$$L = -qa_0\tau\,\delta_{a_R}\int_{y_1}^{y_2} cy\,dy$$

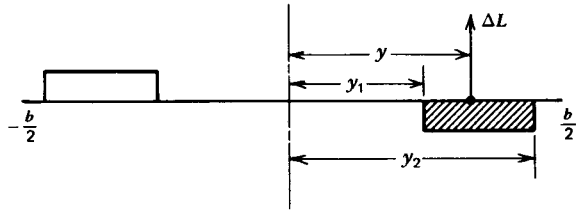

Figure 8.29 Rear view of wing with ailerons deflected.

Since the wing is symmetrical, it is easily shown that a similar contribution to the rolling moment is obtained from the left side, so the total rolling moment is given by

$$L = -qa_0\tau(\delta_{a_R} + \delta_{a_L}) \int_{y_1}^{y_2} cy\, dy$$

$$= -qa_0\tau\,\delta_a \int_{y_1}^{y_2} cy\, dy \tag{8.94}$$

In dimensionless form, C_l, becomes

$$C_l = -\tfrac{1}{4}a_0\tau\,\delta_a A \int_{x_1}^{x_2} \left(\frac{c}{b}\right) x\, dx \tag{8.95}$$

where $x = y/(b/2)$.

For a linearly tapered wing this can be integrated to give

$$C_l = -a_0\tau\,\delta_a \frac{[3(x_2^2 - x_1^2) - 2(1-\lambda)(x_2^3 - x_1^3)]}{12(1+\lambda)} \tag{8.96}$$

This relationship for C_l is only approximate, since the increment in the section C_l is assumed to be constant over the aileron. Induced effects associated with a finite lifting surface are neglected. By comparison with experimental measurements (Ref. 8.8), it is obvious that these induced effects are significant and cannot be neglected.

If the aspect ratio of the wing is fairly high, say approximately 6 or higher, then one can use a fairly simple model to correct Equation 8.96 for induced effects. Otherwise, a set of graphs, found in References 5.5 and 8.3, should be used.

When deflected, an outboard aileron will produce an incremental lift distribution something like that sketched in Figure 8.30*a*. Thus, on either end of the aileron, an incremental vortex system is shed in a manner similar to that shed at the tips of a wing. This incremental vortex system will induce an additional downwash over the aileron, thereby reducing its incremental lift. It is assumed that this reduction is in proportion to the reduction in lift that one would expect from a finite wing having an aspect ratio equal to the aspect ratio of that portion of the wing spanned by the aileron. If this ratio is denoted by A_a, Equation 8.96 is corrected by multiplying it by the correction to the lift curve slope for a wing.

$$\frac{A_a}{A_a + [2(A_a+4)]/(A_a+2)}$$

For the case where $x_2 = 1.0$, A_a, A, x_1, and λ are related by

$$A_a = \left[\frac{(1-x_1)(1+\lambda)}{1 - x_1 + \lambda(1+x_1)}\right]\frac{A}{2}$$

Figure 8.30*b* presents C_{l_δ} predicted on the basis of the foregoing rela-

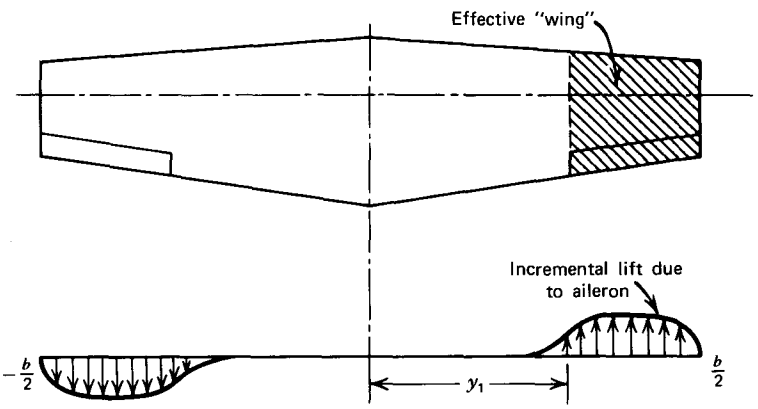

Figure 8.30a Simplified model of an aileron.

tionships. In preparing this figure, it was assumed that:

$a_0 \simeq 0.106 C_l$/deg

$\eta \simeq 0.80$ (correction to τ—see Equation 3.49 and Figure 3.33)

$x_2 = 1.0$

$\frac{c_a}{c} = 0.25$

For other aileron-wing chord ratios, this figure must be corrected for the effect on τ. This correction is provided as an insert in Figure 8.30*b*. In order to determine C_{l_δ} for a value of c_a/c different from 0.25, the value of C_{l_δ} read from the figure is multiplied by the factor k_a. It is interesting to note that Figure 3.33 for η results in extreme nonlinearities in τ for flap angles beyond about 15 or 20°. Yet aileron data appear linear with δ_a up to angles of approximately 30°. This is further evidence that, because of induced effects, the section angles of attack are reduced over the ailerons. Indeed, according to Reference 8.8, as the aspect ratio of the portion of the wing covered by the aileron decreases, the range of δ_a over which C_l is linear with δ_a increases.

If x_2 is less than unity, superposition can be used to calculate C_{l_δ}. For example, suppose $x_1 = 0.5$ and $x_2 = 0.9$. Then C_{l_δ} can be calculated from

$$C_{l_\delta}\begin{pmatrix} x_1 = 0.5 \\ x_2 = 0.9 \end{pmatrix} = C_{l_\delta}\begin{pmatrix} x_1 = 0.5 \\ x_2 = 1.0 \end{pmatrix} - C_{l_\delta}\begin{pmatrix} x_1 = 0.9 \\ x_2 = 1.0 \end{pmatrix}$$

Again, the subscript a is dropped on the δ in writing C_{l_δ}, since δ_a is the primary control for producing a rolling moment.

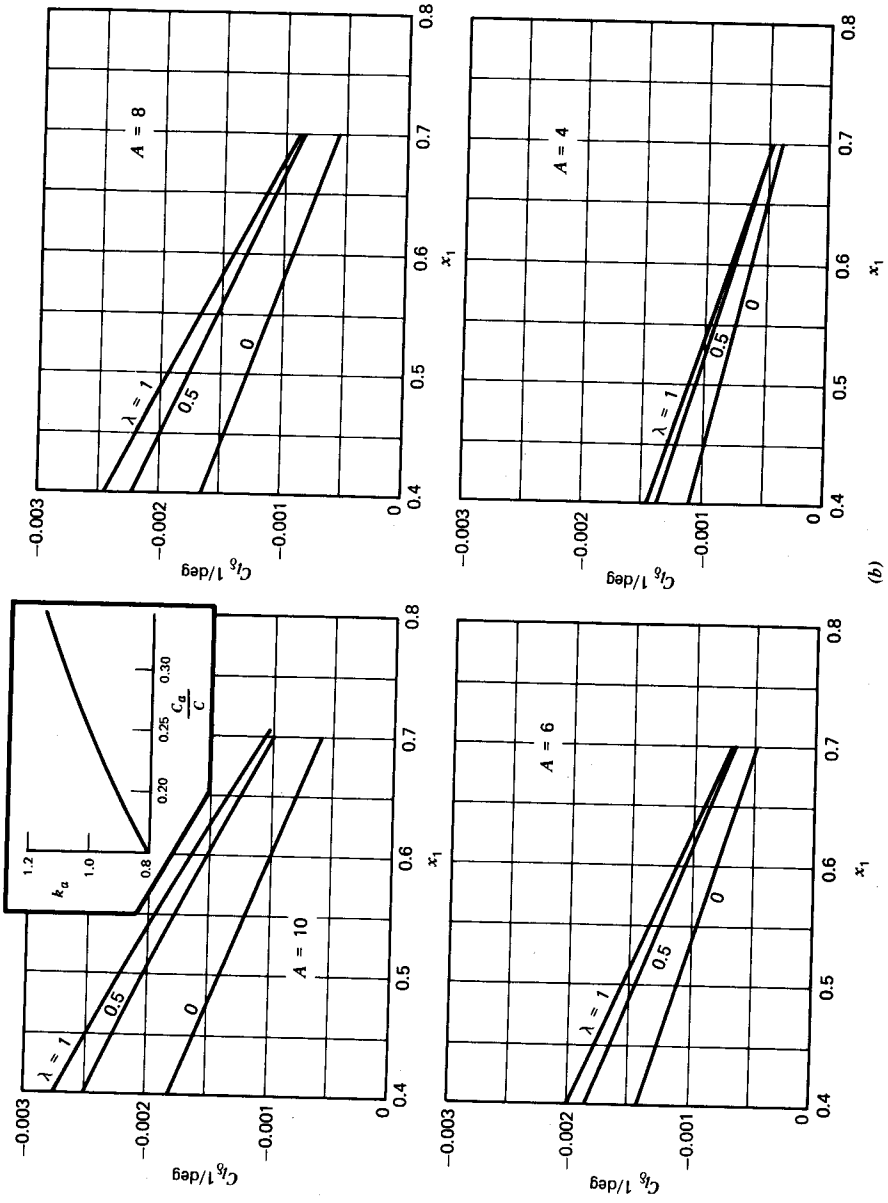

Figure 8.30b Aileron control as a function of wing and aileron geometry. $\Lambda = 0$, $x_2 = 1.0$.

Adverse Yaw

A pilot initiates a turn from straight flight by rolling the airplane in the desired direction of the turn while at the same time applying a little rudder in order to start the airplane yawing in the desired direction. If done properly, a so-called coordinated turn is achieved where the resultant of the gravitational and inertial forces remains perpendicular to the wing. The pilot may feel a little heavier in a coordinated turn but, at least, forces tending to throw him or her to one side or the other are not experienced. A full pitcher of beer will not slosh in a coordinated turn. (Note that FAA regulations forbid the consumption of alcohol by a pilot eight hours prior to fiying.)

A pair of aileron surfaces, which are simply plain flaps that travel symmetrically when deflected, will usually produce a motion known as adverse yaw. At an angle of attack, a flap deflected downward will produce a drag increment greater than that produced by the same deflection upward. Thus, for example, suppose the right aileron moves up and the left one moves down to initiate a turn to the right. The higher drag on the left aileron will produce a yawing moment that tends to yaw the airplane to the left, opposite to what was desired. This is known as adverse yaw due to ailerons, a characteristic that can make an airplane uncomfortable to fly.

To alleviate adverse yaw, the mechanical linkages are sometimes designed so that, for a given control movement, the upward movement on one aileron is greater than the downward movement on the opposite aileron. For example, on the Cherokee 180, the aileron moves up 30° but down only 15°.

Another means of alleviating the adverse yaw is in the design of the aileron. Figure 8.31 illustrates a possible way of accomplishing this. The configuration shown in Figure 8.31, known as a Frise aileron, has the hinge point below the aileron surface. As the aileron is raised, the nose projects down into the flow, thereby increasing the drag on the up aileron.

Roll Control by the Use of Spoilers

A spoiler is a device on the upper surface of an airfoil that, when extended into the flow, causes the flow to separate, resulting in a loss of lift. The effect is illustrated in Figure 8.32, which also illustrates several types of spoilers.

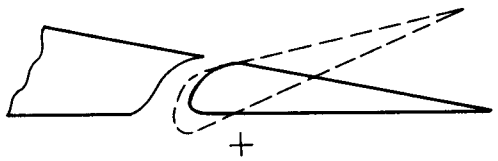

Figure 8.31 The Frise aileron designed to eliminate adverse yaw.

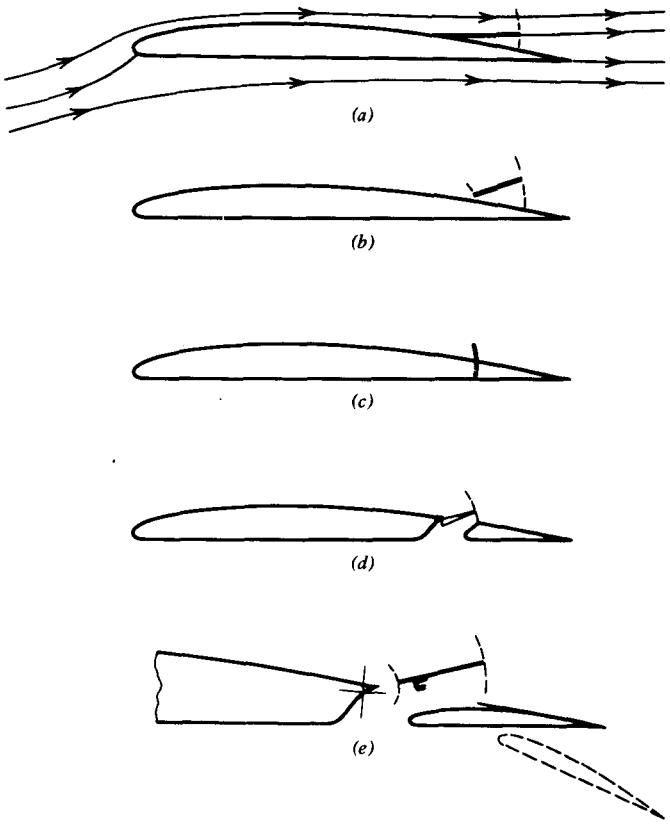

Figure 8.32 Types of spoiler ailerons. (*a*) Retractable aileron. (*b*) Gapped retractable aileron. (*c*) Plug aileron. (*d*) Slot-lip aileron. (*e*) Modified slot-lip aileron with gap and Fowler flap.

Roll control can be accomplished by the use of spoilers installed on the outboard extent of each wing in place of conventional ailerons. If a roll to the right is desired, the spoiler on that side is raised, reducing the lift on the right wing and causing a positive rolling moment. The drag will also be increased on the right wing, producing a favorable yawing moment.

Spoilers for roll control are currently used on several military airplanes and most jet transports to augment the primary aileron controls. They are also used on at least one general aviation airplane, the twin-turboprop Mitsubishi MU-2, as the sole means of roll control. In this case, the use of spoilers only for roll control permits the use of full-span Fowler flaps with a higher wing loading. According to Reference 8.10, "As the requirements increase for higher wing loading to improve ride and performance, better handling quali-

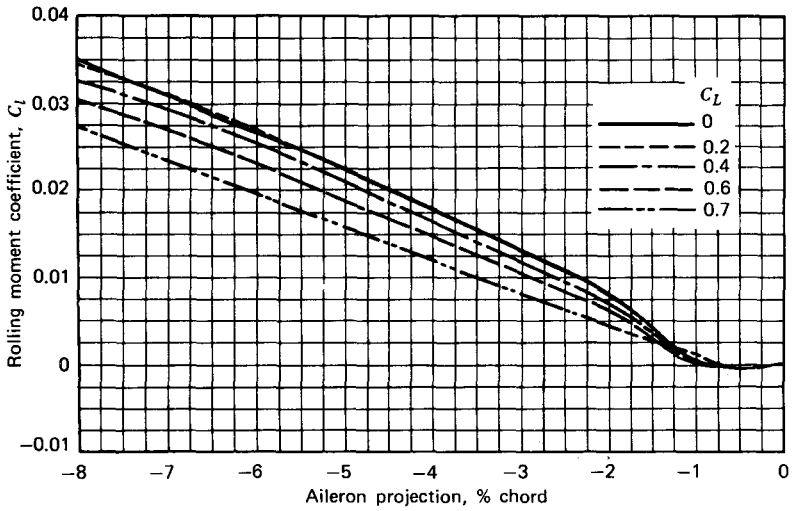

Figure 8.33 Performance of retractable spoiler ailerons. $A = 4.13$, $x_1 = 0.4$, $x_2 = 1.0$; rectangular planform.

ties, and improved high lift devices, spoilers will probably be applied more extensively to light aircraft in the future."

Figure 8.33 (taken from Ref. 8.8), presents some rolling moment data typical of the retractable spoiler aileron of the type pictured in Figure 8.32. Note that for aileron projections in excess of 2% of the chord, the variation of C_l with the projection is quite linear. However, for projections less than this amount, the graphs are highly nonlinear. In fact, little or no rolling moment is produced until the projection exceeds 1% of the chord. This "dead" region would not produce a very satisfactory feel to the pilot.

The configurations of Figure 8.32*b* and 8.32*e* are intended to remove the dead region at low spoiler deflections. As soon as the gap is opened, its influence is felt in producing separated flow. The configuration of Figure 8.32*e* is the type used on the MU-2.

In the past, spoilers have not been used as the sole primary source of roll control because of their nonlinear characteristics. At high angles of attack their effectiveness can be reduced or even reversed. This nonlinear behavior is also reflected in the control forces that result from nonlinear hinge moments. In addition, a lag can occur in reestablishing the attached flow pattern when the spoiler is retracted. Objections to spoiler ailerons have also been based on the fact that the rolling moment is produced by the loss of lift on one side of the wing. This results in an accompanying loss in altitude.

It appears that by careful design, these objections can be overcome. Also, actual flight experience and simulation studies indicate a negligible

difference in the roll dynamics between conventional and spoiler-type ailerons. Thus the loss in altitude associated with spoiler control does not seem to be a problem.

Aileron Reversal

Before leaving the subject of ailerons, mention should be made of a behavior known as aileron reversal. As the name suggests, it is a behavior whereby the action of an aileron, as related to its deflection, is opposite to what one would normally expect. This anomalous behavior is primarily associated with airplanes that have thin, flexible, sweptback wings that operate at high speeds. As a result of the aerodynamic moment, such a wing will tend to twist as the aileron is deflected. For example, an up aileron, which is intended to drop the wing, may instead twist the wing nose up sufficiently to cause a net increase in the wing lift.

To pursue this behavior, consider Figure 8.34, which illustrates the situation with a simplified model. A symmetrical airfoil section is shown mounted on a torsional spring with a spring constant of k_θ. When the flap is deflected through a positive angle δ, an aerodynamic moment is produced that causes the airfoil to rotate through an angle α (shown positively). This results in an opposing moment generated by the spring that, at some α, balances the aerodynamic moment. Thus,

$$k_\theta \alpha = qc^2 C_{m_\delta} \delta$$

and

$$C_l = (C_{l_\alpha} \alpha + C_{l_\delta} \delta)$$

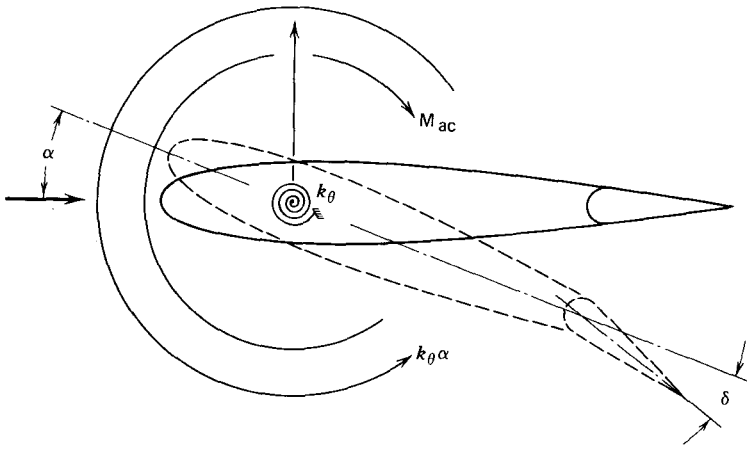

Figure 8.34 A wing section mounted on a torsional spring to illustrate aileron reversal.

Thus,

$$C_l = \left(\frac{C_{l_\alpha} C_{M_\delta} q c^2}{k_\theta} + C_{l_\delta}\right) \delta \tag{8.97}$$

Since C_{M_δ} is negative, it is obvious that, for a given k_θ, there is a q above which the flap deflection will produce a decrease in the lift.

Aileron reversal can be avoided by the obvious means of limiting the operational q or by stiffening the wing; either method can impose operational penalties on the airplane. A less obvious method is used to lock out conventional outboard ailerons at high speeds and employ spoiler control instead.

Steady Rolling Motion

A measure of aileron control power is afforded by the steady roll rate, P, produced by the aileron. This rate is such that the rolling moment from the ailerons equals the damping moment resulting from P. The origin of this damping moment can be seen from Figure 8.35.

A section of the right wing located a distance y from the centerline will experience an increment in its angle of attack because of P, given by

$$\Delta\alpha = \frac{Py}{V}$$

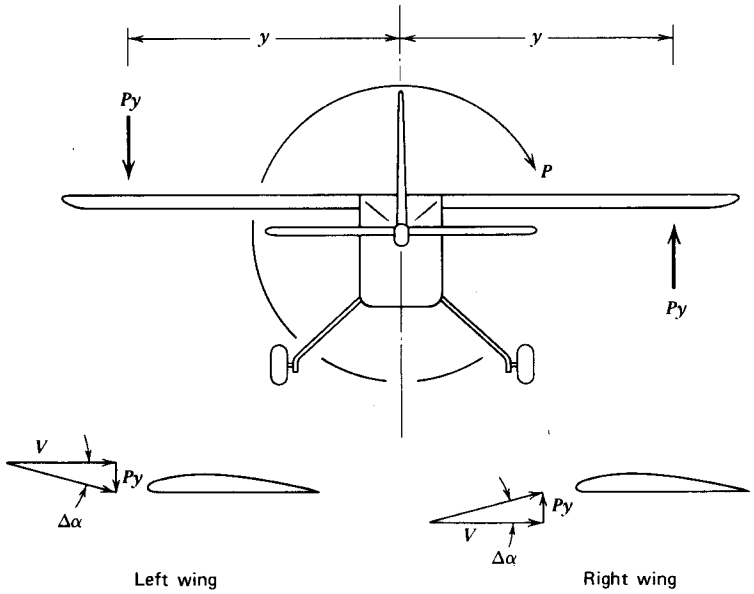

Figure 8.35 Origin of damping moment resulting from roll rate, P.

Neglecting induced effects, $\Delta\alpha$ results in a differential moment given by

$$dL = -yqca_0 \frac{Py}{V} dy$$

The total rolling moment is obtained by integrating this equation from 0 to $b/2$ and multiplying by two to account for the left wing. In coefficient form this becomes

$$C_l = -\frac{a_0 A}{2}\left(\frac{Pb}{2V}\right)\int_0^1 \left(\frac{c}{b}\right)x^2\, dx \tag{8.98}$$

The quantity $(Pb/2V)$ will be denoted by $\bar{p}$ and is comparable to the dimensionless pitch rate, $\bar{q}$. $\bar{p}$ can be interpreted geometrically as the tangent of the helix angle prescribed by the wing tip as the rolling airplane advances through the air.

For a linearly tapered wing, Equation 8.98 integrates to

$$C_l = -\frac{a_0 \bar{p}}{12}\frac{1+3\lambda}{1+\lambda}$$

or

$$C_{l_{\bar{p}}} = -\frac{a_0}{12}\frac{1+3\lambda}{1+\lambda} \tag{8.99}$$

The derivation of Equation 8.99 provides some insight into the origin of the roll damping but, otherwise, is of little value because of induced effects that were neglected. Correcting a_0 for aspect ratio improves the accuracy somewhat.

Calculated values of $C_{l_{\bar{p}}}$ based on lifting surface theory are presented in Figure 8.36 (taken from Ref. 8.11). The original source of these calculations is Reference 5.5. These graphs are all for zero sweep angle of the midchord line. Results for other sweep angles can be found in the references. Generally, $C_{l_{\bar{p}}}$ is insensitive to $\Lambda_{1/2}$ up to approximately $\pm 20°$. This range increases as the aspect ratio decreases.

Calculations of $C_{l_{\bar{p}}}$ for a complete airplane configuration must also include contributions from the horizontal and vertical tails. The horizontal tail's contribution can be determined on the basis of Figure 8.36 multiplied by $S_t b_t^2/Sb^2$. The vertical tail's contribution can also be determined on the same basis by visualizing the tail to be one-half of a wing. Thus the geometric aspect ratio of the vertical tail is doubled to enter Figure 8.36. The resulting value of $C_{l_{\bar{p}}}$ is multiplied by $S_v b_v^2/Sb^2$ and then halved. If the horizontal stabilizer is mounted on top of the vertical tail, the value of A_v must be increased, possibly by as much as 20%, to account for the end-plate effect of the horizontal tail on the vertical tail.

In a steady roll, the aileron-produced rolling moment and the damping moment will be equal in magnitude but of opposite sign. To find the steady

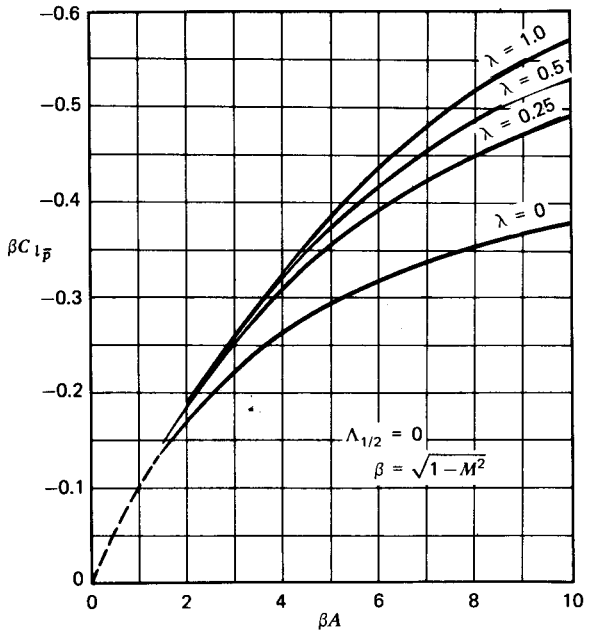

Figure 8.36 Roll damping coefficient derivative. Note that $C_{l_{\bar{p}}}$ should be corrected by ratio of section lift curve slope to 2π.

rolling velocity as a function of aileron angle, we set the sum of the aileron and damping moments to zero.

$$C_{l_\delta}\delta_a + C_{l_{\bar{p}}}\bar{p} = 0$$

or

$$\frac{Pb}{2V} = -\frac{C_{l_\delta}}{C_{l_{\bar{p}}}}\delta_a \tag{8.100}$$

Thus, the dimensionless roll rate is directly proportional to the aileron deflection angle. $Pb/2V$ will typically range from approximately 0.05 to 0.10, depending on the maneuverability requirements imposed on the airplane.

Past practice was to specify values of $\bar{p}$ but both civil and military requirements (Refs. 8.1 and 8.12) now state specific requirements on P or, to be more specific, on a displacement of ϕ in a given time. For example, FAR Part 23 requires that an airplane weighing less than 6000 lb on the approach must have sufficient lateral control to roll it from 30° in one direction to 30° in the other in 4 sec. In landing at 20% above the stalling speed, this number is increased to 5 sec. Mil-F-8785 B requires an air-to-air fighter to be rolled 360° in 2.8 sec, an interceptor aircraft 90° in 1.3 sec, a transport or heavy bomber 30° in 1.5 sec, and a light utility aircraft 60° in 1.4 sec.

Coupling Effects

There are several interactions or couplings involving lateral-directional controls and motions that are important considerations in providing satisfactory handling or riding qualities for an airplane. We have already seen one of these, a coupling between yaw and aileron displacement. Similarly, the rudder deflection can produce a rolling moment, since the center of pressure of the rudder-vertical fin combination generally lies above the center of gravity. These two control couplings are denoted in coefficient form by:

$$C_{n_{\delta_a}}$$

$$C_{l_{\delta_R}}$$

Other couplings include:

$$C_{l_r}$$

$$C_{N_p}$$

$$C_{l_\beta}$$

These represent, respectively, a rolling moment due to yawing, a yawing moment due to rolling, and a rolling moment resulting from sideslip. This last coupling is an important and well-known one that is called "dihedral effect."

Rolling Moment with Rudder

If the center of pressure of the fin-rudder combination lies a distance of Z_v above the longitudinal axis passing through the center of gravity, an increment, ΔL_v, in the lift (side force) will produce an increment in the rolling moment, given by

$$\Delta L = Z_v \, \Delta L_v$$

In coefficient form this becomes

$$\Delta C_l = \frac{Z_v}{b} \frac{\Delta L_v}{qS}$$

$$= \frac{Z_v}{b} C_{Y_\delta} \delta_r \tag{8.101}$$

The side force derivative C_{Y_δ} is obtained from

$$\Delta Y = \eta_t q S_v a_v \tau \, \delta_r$$

or

$$C_{Y_\delta} = \eta_t \frac{S_v}{S} a_v \tau \tag{8.102}$$

Rolling Moment with Yaw Rate

Figure 8.37 illustrates a wing having a tapered planform that is yawing at the rate of R rad/sec. The wing is operating at a lift coefficient of C_L. It will be assumed that the section lift coefficients are constant and equal to C_L. Because of the rotational velocity R, a section on the right side located at y experiences a local velocity equal to $V - Ry$ while the corresponding section on the left wing has a velocity of $V + Ry$. Thus a differential rolling moment is produced equal to

$$dL = y\tfrac{1}{2}\rho c C_L[(V + Ry)^2 - (V - Ry)^2]\, dy$$

Expanding and integrating from 0 to $b/2$ results in

$$L = \frac{\rho c C_L R V b^3}{12}$$
$$= \tfrac{1}{3} q S b \bar{r} C_L$$

Therefore,

$$C_{l_r} = \frac{C_L}{3}$$

As an exercise, show that, for a linearly tapered wing,

$$C_{l_r} = \frac{C_L}{6}\left(\frac{1+3\lambda}{1+\lambda}\right) \tag{8.103}$$

The vertical tail can also contribute to C_{l_r}. Because of the yaw rate, its angle of sideslip is decreased by Rl_v/V. Thus, an incremental side force on the tail is generated, given by

$$\Delta Y = \eta_t q S_v a_v \frac{l_v R}{V}$$

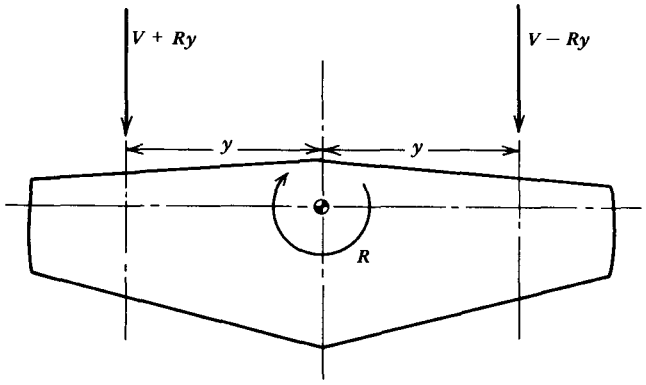

Figure 8.37 A wing yawing and translating.

In coefficient form,

$$C_Y = 2\eta_t a_v V_v \bar{r} \tag{8.104}$$

This incremental side force acting above the center of gravity produces an increment in the rolling moment, given by

$$\Delta L = \eta_t q S_v a_v \frac{l_v R}{V} Z_v$$

or, in coefficient form,

$$C_{l_r} = C_{y_r} \frac{Z_v}{b} \tag{8.105}$$

$$= 2\eta_t a_v V_v \left(\frac{Z_v}{b}\right)$$

The total C_{l_r} equals

$$C_{l_r} = \frac{C_L}{6}\left(\frac{1+3\lambda}{1+\lambda}\right) + C_{y_r}\frac{Z_v}{b} \tag{8.106}$$

Yawing Moment with Roll Rate

Referring again to Figure 8.35, it is seen that on the right wing, which is moving down, the lift vector is inclined forward through the angle Py/V. On the left wing, the inclination is to the rear. The components of these tilted lift vectors in the x direction give rise to a differential increment in the yawing moment equal to

$$dN = -2yqcC_L \frac{Py}{V} dy$$

Integrating from 0 to $b/2$, the total yawing moment increment in coefficient form for a linearly tapered wing becomes

$$C_N = -\frac{C_L \bar{p}}{12}\left(\frac{1+3\lambda}{1+\lambda}\right) \tag{8.107}$$

Rolling Moment with Sideslip Angle—Dihedral Effect

The rate of change of rolling moment with sideslip angle, C_{l_β}, is important to the handling qualities of an airplane. Generally, a small negative value of C_{l_β} is desirable, but too much dihedral effect makes an airplane uncomfortable to fly. The principal factors affecting C_{l_β} are sweepback, placement of the wing on the fuselage, and the dihedral angle of the wing, Γ.

The primary control over C_{l_β} is exercised through the dihedral angle, Γ, shown in Figure 8.38. Although the sweepback angle also affects C_{l_β} significantly, Λ is normally determined by considerations other than C_{l_β}. From Figure 8.38, it can be seen that a positive sideslip results in an upward velocity component along the right wing and a downward component along

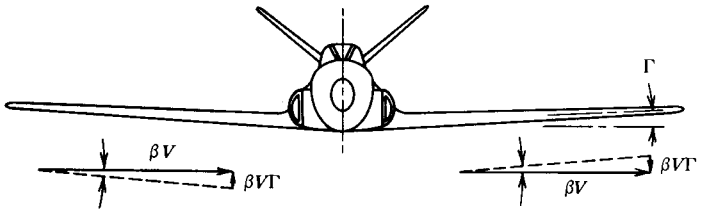

Figure 8.38 Definition of dihedral angle.

the left wing. Added to the free-stream velocity, this results in an increase in the angle of attack over the right wing equal to

$$\Delta\alpha = \beta\Gamma$$

Over the left wing, an opposite change in α occurs. This differential increment in α results in a differential rolling moment, given by

$$dl = 2qca\beta\Gamma y\, dy$$

or

$$C_l = 2a\beta\Gamma \frac{\int_0^{b/2} cy\, dy}{bS}$$

For a linearly tapered wing, this reduces to

$$C_l = \frac{a}{6}\left(\frac{1+2\lambda}{1+\lambda}\right)\beta\Gamma$$

or

$$C_{l_\beta} = \frac{a}{6}\left(\frac{1+2\lambda}{1+\lambda}\right)\Gamma \tag{8.108}$$

The derivation of Equation 8.108 has neglected induced effects that are appreciable for low aspect ratios. Its primary value lies in disclosing the linear relationship between Γ and C_{l_β}.

It is recommended that the contribution to C_{l_β} from Γ be estimated using Figure 8.39. This figure represents the departure of C_{l_β} from the following normal case and is based on graphs presented in Reference 8.11 or 5.5.

$$\lambda = 0.5$$

$$A = 6.0$$

$$\Lambda_{1/2} = 0$$

$$C_{l_\beta} = -0.00021\,\Gamma/\text{deg}(\Gamma \text{ in deg})$$

Thus,

$$C_{l_\beta} = -0.00021 k_\lambda k_A k_\Lambda \Gamma \tag{8.109}$$

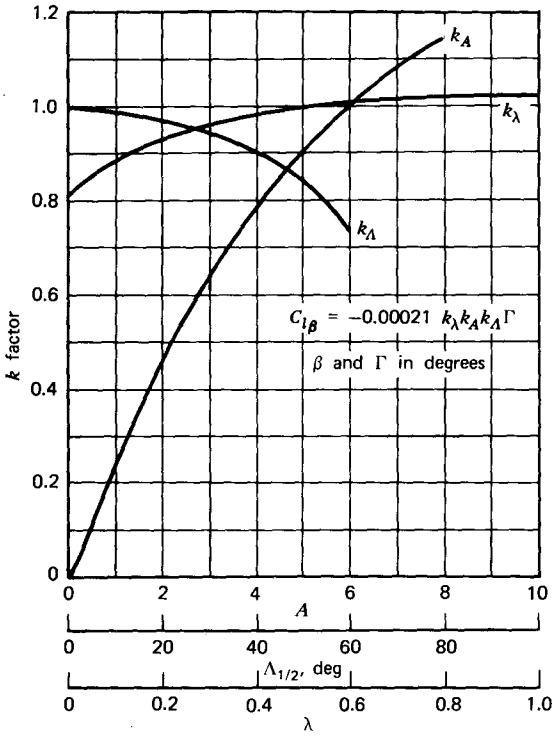

Figure 8.39 Effect of wing dihedral angle on C_{l_β}. Note that factors represent relative effects of varying each parameter independently from the normal case. $\lambda = 0.5$, $A = 6.0$, $\Lambda_{1/2} = 0$.

where the functions k_λ, k_A, and k_Λ are obtained from Figure 8.39 as functions of λ, A, and $\Lambda_{1/2}$, respectively.

The effect of sweepback on C_{l_β} is determined with the help of Figure 8.40. A swept wing is shown operating at a positive sideslip angle β. From the geometry, the velocity component normal to the leading edge of the right wing is given by

$$V \cos(\Lambda - \beta)$$

The corresponding velocity on the left wing is

$$V \cos(\Lambda + \beta)$$

If C_{l_n} is the section lift coefficient based on the normal velocity and "normal chord," then the differential lift on the right and left wings will be

$$dL_R = q \cos^2(\Lambda - \beta) c \cos \Lambda C_{l_n} ds$$

$$dL_L = q \cos^2(\Lambda + \beta) c \cos \Lambda C_{l_n} ds$$

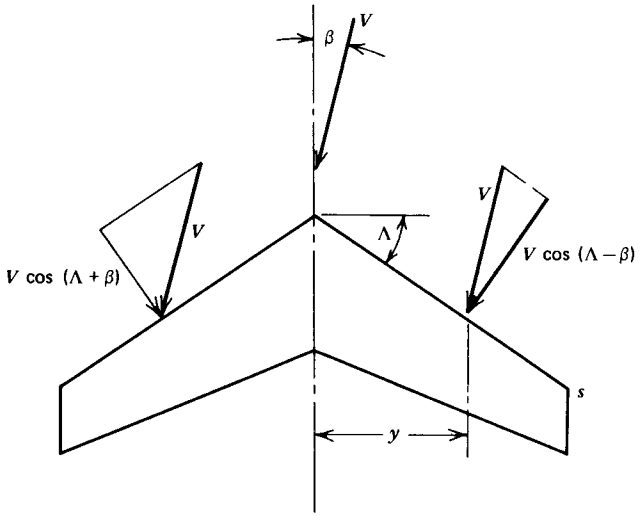

Figure 8.40 Effect of sweepback on dihedral effect.

The differential rolling moment is therefore

$$dl = qcC_{l_n} y[\cos^2(\Lambda + \beta) - \cos^2(\Lambda - \beta)] \cos \Lambda \, ds$$

But

$$y = s \cos \Lambda$$

$$dy = ds \cos \Lambda$$

Thus,

$$l = qC_{l_n}[\cos^2(\Lambda + \beta) - \cos^2(\Lambda - \beta)] \int_0^{b/2} cy \, dy$$

The total lift (for $\beta = 0$) is given by

$$L = 2q \cos^2 \Lambda C_{l_n} \int_0^{b/2} c \, dy$$

$$= qSC_{l_n} \cos^2 \Lambda$$

Thus the wing C_L and the normal section C_{l_n} are related by

$$C_L = C_{l_n} \cos^2 \Lambda$$

and the rolling moment coefficient becomes

$$C_l = \frac{C_L}{\cos^2 \Lambda}[\cos^2(\Lambda + \beta) - \cos^2(\Lambda - \beta)] \frac{\int_0^{b/2} cy \, dy}{Sb}$$

If this equation is differentiated with respect to β and evaluated at $\beta = 0$, the following results.

$$C_{l_\beta} = -4C_L \tan \Lambda \left[\frac{\int_0^{b/2} cy\, dy}{Sb} \right] \tag{8.110}$$

For a linearly tapered wing, Equation 8.110 reduces to

$$C_{l_\beta} = -\frac{1+2\lambda}{3(1+\lambda)} C_L \tan \Lambda \tag{8.111}$$

Again, this result is only qualitatively correct. Generally,

$$C_{l_\beta} = -f(A, \lambda) C_L \tan \Lambda \tag{8.112}$$

Figure 8.41 (based on Ref. 5.5) presents C_{l_β}/C_L as a function of Λ for a range of aspect ratios. The variation with tan Λ is seen to hold only for the higher aspect ratios. This figure can be used with Equation 8.111 to estimate C_{l_β} for other taper ratios.

Observe that wing sweep can contribute significantly to dihedral effect. In order to avoid an excessive dihedral effect on aircraft with highly swept wings, it is frequently necessary to employ a negative dihedral angle on the wing, particularly if the wing is mounted high on the fuselage.

The effect that the wing placement on the fuselage has on C_{l_β} is seen by reference to Figure 8.42. In a plane across the top of the fuselage, the cross-flow around the fuselage is seen to go up on the right side and down on the left. Thus, for a high wing, this flow increases the angle of attack of the right wing while decreasing α on the left wing. This results in a negative rolling moment comparable to a positive dihedral effect. For a low wing, the effect is just the opposite. This is the reason, as you may have observed, that

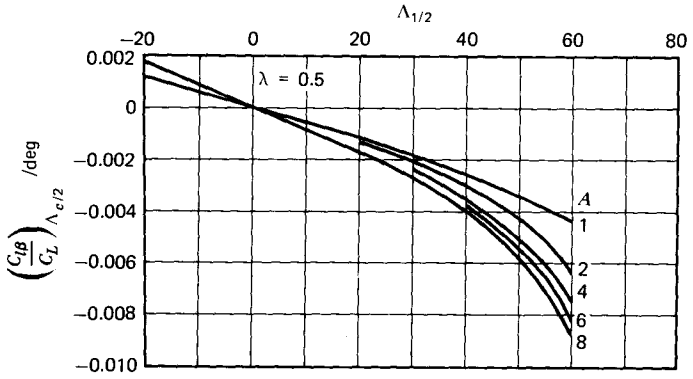

Figure 8.41 Effect of wing sweep on C_{l_β}.

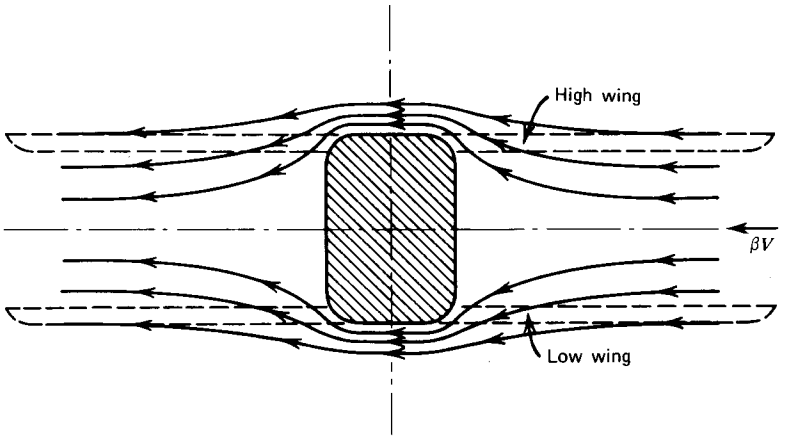

Figure 8.42 Rear view showing the cross-flow around a fuselage.

the dihedral angle for unswept low wings is generally greater than for high wings. Many high-wing airplanes do not have any dihedral angle at all.

As a rule, it is recommended that the following be added to C_{l_β} to account for the fuselage cross-flow (Ref. 8.6).

$$\text{High-wing } \Delta C_{l_\beta} = -0.00016/\text{deg}$$

$$\text{Midwing } \Delta C_{l_\beta} = 0$$

$$\text{Low-wing } \Delta C_{l_\beta} = 0.00016/\text{deg}$$

This information on C_{l_β} and the other stability derivatives is intended only as an introduction to the subject. For more complete information on these quantities, see Reference 5.5 and 8.3.

PROBLEMS

All questions refer to the airplane pictured in Figure 8.43.

8.1 Calculate the mean aerodynamic chord and location of the aerodynamic center of the wing.
8.2 Calculate the location of the stick-fixed neutral point.
8.3 What is the center-of-gravity location for a 10% stick-fixed static margin?
8.4 For a 10% stick-fixed static margin, calculate the tail incidence angle to trim at a cruise Mach number of 0.7 at a standard altitude of 8 km.

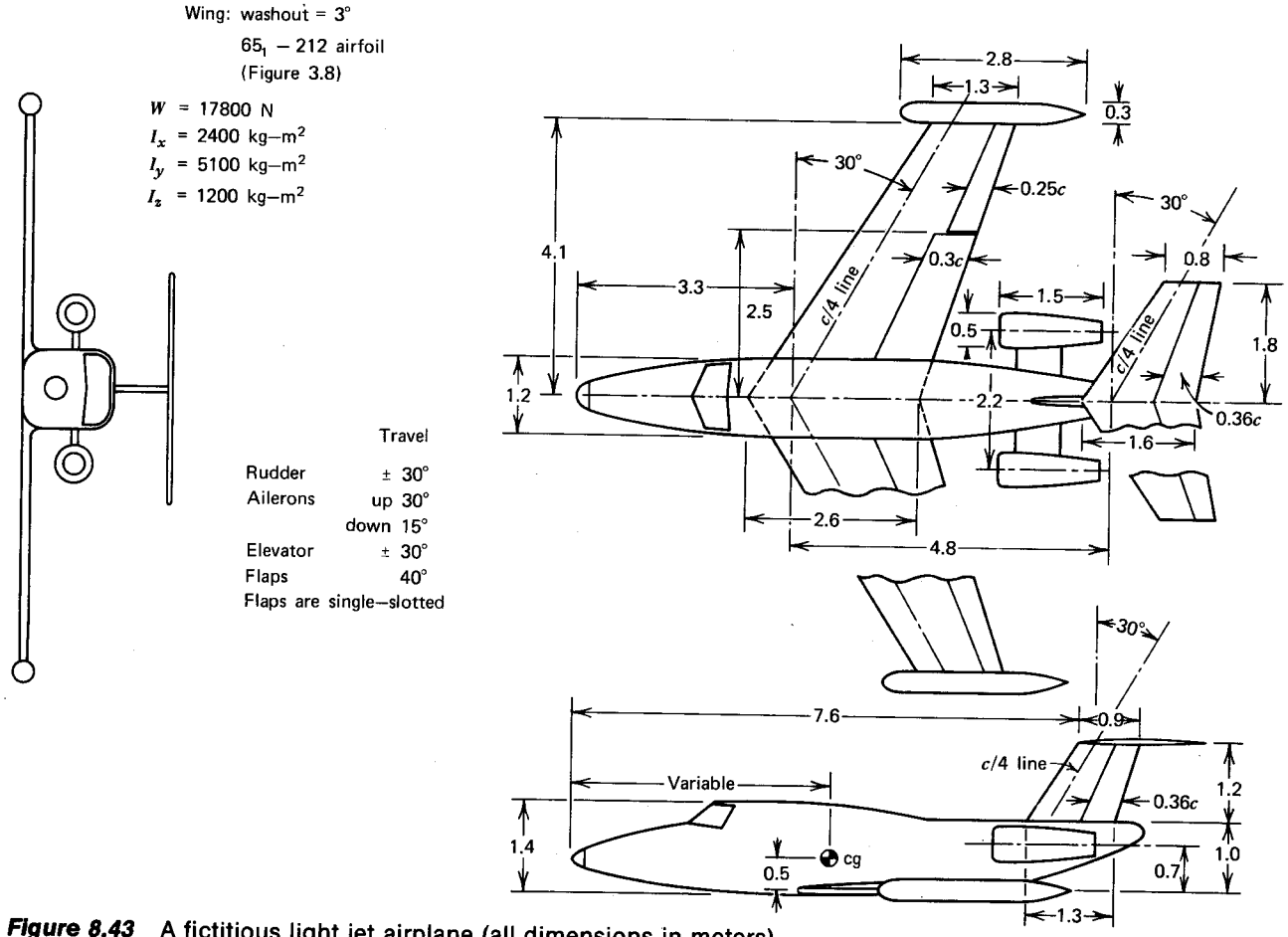

Figure 8.43 A fictitious light jet airplane (all dimensions in meters).

8.5 With the incidence angle of the tail set as calculated in Problem 8.4, determine if the elevator control is sufficient to trim the airplane at its stalling speed at SSL conditions.
8.6 Trim is accomplished by changing the incidence of the horizontal tail. With the airplane trimmed at 20% above the stalling speed, SSL, calculate the gearing to keep the push on the control wheel below 75 lb for a true airspeed of 150 kt SSL.
8.7 Calculate the stick-free neutral point.
8.8 What is the elevator angle required per g of acceleration at a true airspeed of 150 kt at SSL conditions? Use the center of gravity from Problem 8.3.
8.9 What is the stick force per g for the conditions of Problem 8.8 using the results from Problems 8.3 and 8.6?
8.10 Repeat Problem 8.2 with the wing 3 m above the ground.
8.11 Calculate $C_{N_{\dot{\beta}}}$ and C_{N_δ}, assuming the center-of-gravity location as found in Problem 8.3.
8.12 Calculate the aileron and rudder positions required to trim the airplane straight and level with the right engine out at 150 kt TAS at SSL conditions. Use the center of gravity from Problem 8.3.
8.13 At SSL conditions and 40% above the stalling speed, what is the maximum crosswind for which the fuselage could be kept aligned with the runway? Use the center of gravity from Problem 8.3.
8.14 In a steady rolling maneuver at 20% above the stalling speed SSL, what is the maximum attainable rate of roll?

REFERENCES

8.1 Anonymous, *Federal Air Regulations Part* 23—*Airworthiness Standards: Normal, Utility and Acrobatic Category Airplanes*, continuously revised.
8.2 Etkin, Bernard, *Dynamics of Flight*, John Wiley, New York and London, 1959.
8.3 Anonymous, *Royal Aeronautical Society Data Sheets*, continually updated.
8.4 Ames, M. B., and Sears, R. I. *Determination of Control Surface Characteristics from NACA Plain-Flap and Tab Data*, NACA R 721, 1941.
8.5 Roskam, J., *Flight Dynamics of Rigid and Elastic Airplanes*, published by author, Lawrence, Kan., 1973.
8.6 Perkins, C. D., and Hage, R. E., *Airplane Performance, Stability and Control*, John Wiley, New York and London. 1949.

8.7 Campbell, J. P., and McKinney, M. O., *Summary of Methods for Calculating Dynamic Lateral Stability and Response and for Estimating Lateral Stability Derivatives*, NACA R 1098, 1952.

8.8 Fischel, Jack, Rodger, L. N., Hagerman, J. R., and O'Hare, W. M., *Effect of Aspect Ratio on the Low-Speed Lateral Control Characteristics of Untapered Low-Aspect-Ratio Wings Equipped with Flap and with Retractable Ailerons*, NACA R 1091, 1952.

8.9 Fink, M. P., Freeman, D. C., Jr., and Greer, H. D. *Full-Scale Wind-Tunnel Investigation of the Static Longitudinal and Lateral Characteristics of a Light Single-Engine Airplane*, NASA TN D-5700, March 1970.

8.10 Roskam, J., and Kohlman, D. L., *Spoilers for Roll Control of Light Airplanes*, AIAA Paper No. 74–861, AIAA Mechanics and Control of Flight Conference, Anaheim, Calif., August 5–9, 1974.

8.11 Roskam, J., *Methods for Estimating Stability and Control Derivatives of Conventional Subsonic Airplanes*, published by author, Lawrence, Kans., 1971.

8.12 Anonymous, *Mil-F-8785 B Military Specification-Flying Qualities of Piloted Aircraft*, August 1969.

8.13 Ribner, H. A., *Propellers in Yaw*, NACA R 820, 1945.

NINE
LONGITUDINAL DYNAMIC STABILITY AND CONTROL

As an introduction to the subject of longitudinal dynamic stability and control, this chapter will treat the airplane as a rigid body having three degrees of freedom. These consist of rotation about the y-axis and translations in the x and z directions. In the general case, a rigid body will have six degrees of freedom: three rotations and three translations. However, because of the symmetry of an airplane, there is very little coupling between longitudinal and lateral motion, so that for most purposes the two motions can be considered independent of each other. A more formal proof of this statement can be found in advanced texts on the subject.

We cannot apply Newton's second law of motion directly to the airplane. The forces and velocities with which we are concerned are all related to a coordinate system that is fixed to the airplane and moving with it. This is a noninertial reference frame. It is therefore necessary to perform a transformation from this moving frame of reference to one that is fixed (for our purposes, relative to the Earth).

EQUATIONS OF MOTION

Consider Figure 9.1*a*, which depicts the airplane coordinate system at some instant of time, t. The x-axis is aligned with the wing zero lift line, as before, and passes through the center of gravity. The z-axis is normal to the x-axis and directed downward. The resultant linear velocity of the center of gravity is denoted by V, with components of U and W along the x- and z-axes, respectively. At this instant the x- and z-axes are aligned with another set of axes, x' and z', which are fixed axes. Generally, the airplane is pitching upward at a rate of $\dot{\Theta}$ and is accelerating both linearly and angularly.

At an increment of time, Δt, later, the picture will be as shown in Figure 9.1*b*. The $x - z$ axes have rotated through a pitch angle of $\dot{\Theta}\,\Delta t$ relative to the fixed $x' - z'$. Also, the velocity components have been incremented as shown. We now

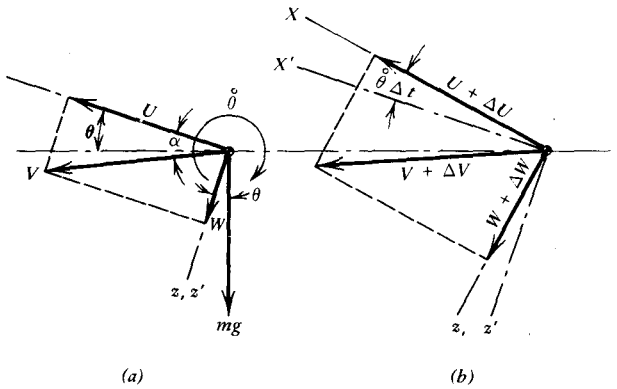

Figure 9.1 Transformation of velocity vectors between a fixed and moving reference system. (*a*) At time t. (*b*) At time $t + \Delta t$.

consider the change in the components of the momentum vectors in the inertial frame of reference that occurred during the time interval of Δt.

If m represents the mass of the airplane, then at time $t + \Delta t$, the momentum in the x' direction is given by

$$\text{mom}_x = m[(U + \Delta U)\cos(\dot{\Theta}\,\Delta t) + (W + \Delta W)\sin(\dot{\Theta}\,\Delta t)]$$

At time t, this momentum component is simply

$$\text{mom}_x = mU$$

Thus the time rate of change of momentum in the x' direction will equal

$$\lim_{\Delta t \to 0} \frac{\text{mom}_x\,(t + \Delta t) - \text{mom}_x\,(t)}{\Delta t}$$

From Newton's second law of motion, the sum of the forces acting in the x' direction, which coincides with x in the limit, is equal to this rate of momentum. Thus,

$$X - mg\sin\Theta = m(\dot{U} + W\dot{\Theta}) \tag{9.1}$$

Similarly, in the z direction,

$$Z + mg\cos\Theta = m(\dot{W} - U\dot{\Theta}) \tag{9.2}$$

X and Z represent the sum of the aerodynamic forces (including the thrust) in the x and z directions, respectively. A dot over a quantity indicates the derivative with respect to time.

The third equation of motion can be written directly as

$$M = I_y\ddot{\Theta} \tag{9.3}$$

where M is the sum of the aerodynamic moments. An alternate derivation of Equations 9.1, 9.2, and 9.3 is found at the beginning of Chapter Ten.

The right-hand sides of Equations 9.1 and 9.2 can also be obtained by use of vector calculus. It is shown in Reference 8.2 that the time derivative of a vector defined in a rotating reference frame is given by

$$\frac{d\mathbf{A}}{dt} = \frac{\delta \mathbf{A}}{\delta t} + \boldsymbol{\omega} \times \mathbf{A} \tag{9.4}$$

$\delta \mathbf{A}/\delta t$ is the apparent derivative as viewed in the moving reference system. $\boldsymbol{\omega}$ is the angular velocity vector for the moving reference system.

The velocity components U and W can be expressed in terms of the resultant velocity, V, and angle of attack, α.

$$U = V \cos \alpha$$
$$W = V \sin \alpha$$

Therefore,

$$\dot{U} = \dot{V} \cos \alpha - V\dot{\alpha} \sin \alpha$$
$$\dot{W} = \dot{V} \sin \alpha + V\dot{\alpha} \cos \alpha$$

In terms of V and α, Equations 9.1 and 9.2 become

$$X - mg \sin \Theta = m[\dot{V} \cos \alpha - V\dot{\alpha} \sin \alpha + V\dot{\Theta} \sin \alpha] \tag{9.5a}$$

$$Z + mg \cos \Theta = m[\dot{V} \sin \alpha + V\dot{\alpha} \cos \alpha - V\dot{\Theta} \cos \alpha] \tag{9.5b}$$

Generally, X is a function of V, α, $\dot{\Theta}$, and higher derivatives of these quantities. The same is true of Z and M. In addition, X, Z, and M also depend on a control angle and, possibly, its derivatives as a function of time. If δ is given as a function of time, and if X, Z, and M can be determined as a function of V, α, $\dot{\Theta}$, and δ, then the set of nonlinear, simultaneous differential Equations 9.3 and 9.5 can be integrated numerically to determine V, α, and Θ as a function of time. The position and orientation of the airplane relative to the fixed axes, x' and z', can then be determined from

$$x' = x'(t = 0) + \int_0^t V(\cos \alpha \cos \Theta + \sin \alpha \sin \Theta)\, dt \tag{9.6}$$

$$z' = z'(t = 0) + \int_0^t V(\sin \alpha \cos \Theta - \cos \alpha \sin \Theta)\, dt \tag{9.7}$$

$$\Theta = \Theta(t = 0) + \int_0^t \dot{\Theta}\, dt \tag{9.8}$$

The X and Z forces can be written in terms of the lift, drag, and thrust by reference to Figure 9.2.

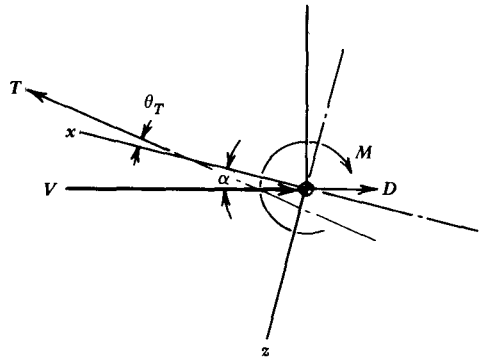

Figure 9.2 Resolution of forces along x- and z-axes.

$$X = L \sin \alpha + T \cos \Theta_T - D \cos \alpha \tag{9.9}$$

$$Z = -L \cos \alpha - T \sin \Theta_T - D \sin \alpha \tag{9.10}$$

Θ_T is the inclination of the thrust vector. The pitching moment resulting from the offset of the thrust line is included in the sum of the aerodynamic moments, M.

The lift can be written as

$$L = \tfrac{1}{2}\rho V^2 S(C_{L_\alpha}\alpha + C_{L_{\bar{q}}}\bar{q} + C_{L_\delta}\delta) \tag{9.11}$$

Similarly, the drag is calculated from

$$D = \tfrac{1}{2}\rho V^2 S C_D \tag{9.12}$$

where

$$C_D = C_D(C_L)$$

The moment is determined from

$$M = \tfrac{1}{2}\rho V^2 S\bar{c}(C_{M_\alpha}\alpha + C_{M_{\bar{q}}}\bar{q} + C_{M_\delta}\delta) + TZ_p \tag{9.13}$$

These relationships are approximate in several ways. First, in a strict sense, the airplane C_D is not a unique function of the airplane C_L. One must examine the division between the wing lift and the tail lift to determine the total C_D for a total C_L. For most purposes, however, it is sufficient to assume that the usual airplane drag polar holds for relating C_D to C_L. Second, unsteady aerodynamic effects are not included at this point. These will be incorporated in terms such as $C_{L_{\dot{\alpha}}}$ and $C_{M_{\dot{\alpha}}}$. Also, when the airplane accelerates, the air surrounding it accelerates; this leads to an effective increase in the mass of the airplane. So-called "added mass" effects are generally negligible when considering airplane motion, but become important for lighter-than-air (LTA) vehicles, where the mass of the displaced air is nearly equal to the mass of the

vehicle. This leads to terms such as $X_{\dot{V}}$ and $M_{\dot{\theta}}$, which will not be considered here.

Linearization of the Equations

As we will see, it is quite informative to linearize the foregoing equations about a trimmed condition. In this way, the factors affecting longitudinal dynamic stability are more easily identified than by means of a numerical solution. Also, the normal modes of motion can be examined more readily and their shapes determined.

The momentum relationships previously derived will hold for any orthogonal axis system with its origin at the center of gravity. Thus far we have used the zero lift line of the wing to define the x-axis. For linearizing the equations, it is considerably more convenient to choose an x-axis that is aligned with the free-stream velocity in the trimmed condition. The z-axis is again directed "downward," normal to the x-axis. As such, these axes are referred to as stability axes. Any other orthogonal sets through the center of gravity are known as body axes.

With the choice of stability axes, the U and W velocities will be denoted by

$$\begin{aligned} U &= U_0 + u \\ W &= w \end{aligned} \tag{9.14}$$

The lowercase letters indicate incremental velocities relative to their trimmed values. With the choice of axes the trimmed value of W is, of course, equal to zero. U_0 represents a steady free-stream velocity. It will be assumed that

$$\frac{u}{U_0} \ll 1$$

$$\frac{w}{U_0} \ll 1$$

so that orders higher than the first in these terms will be neglected.

The unsteady angle of attack, α, can now be written as

$$\begin{aligned} \alpha &= \tan^{-1} \frac{w}{U_0 + u} \\ &\simeq \frac{w}{U_0} \end{aligned} \tag{9.15}$$

Notice that α is the angle of attack of the x-axis, so the lift coefficient must now be written as

$$C_L = C_{L_0} + C_{L_\alpha}\alpha \tag{9.16}$$

From Equation 9.15, α is of the same order as u/U_0 and w/U_0. The X and Z forces and the moment M will be written as the sum of their trim values and small, unsteady increments.

$$\begin{aligned} X &= X_0 + \Delta X \\ Z &= Z_0 + \Delta Z \\ M &= \Delta M \end{aligned} \tag{9.17}$$

There is no M_0 in Equation 9.17 because M equals zero for trim.

Finally, the pitch angle is linearized by writing Θ as

$$\Theta = \Theta_0 + \theta \tag{9.18}$$

Here, θ is assumed small and of the same order as the other incremental values.

The sine and cosine of an angle and its increment can be written as

$$\begin{aligned} \sin(\Theta_0 + \theta) &\simeq \sin\Theta_0 + \theta\cos\Theta_0 \\ \cos(\Theta_0 + \theta) &\simeq \cos\Theta_0 - \theta\sin\Theta_0 \end{aligned}$$

Using these equations and substituting Equations 9.14 to 9.17 into Equations 9.1 to 9.3 results in a linearized form for the equations of motion.

$$\Delta X - mg\cos\Theta_0\theta = m\dot{u} \tag{9.19a}$$

$$\Delta Z - mg\sin\Theta_0\theta = mU_0(\dot{\alpha} - \dot{\theta}) \tag{9.19b}$$

$$\Delta M = I_y\ddot{\theta} \tag{9.19b}$$

Also, for the trimmed condition,

$$X_0 - mg\sin\Theta_0 = 0 \tag{9.20a}$$

$$Z_0 + mg\cos\Theta_0 = 0 \tag{9.20b}$$

$$M_0 = 0 \tag{9.20c}$$

Typically, let us consider the incremental force ΔZ. In coefficient form,

$$Z = \tfrac{1}{2}\rho[(U_0 + u)^2 + w^2]SC_Z$$

As a dimensionless coefficient C_Z would be expected to vary with α, $\bar{q}$, and the elevator control position, δ. Thus we will assume C_Z to be of the form

$$C_Z = C_{Z_0} + C_{Z_\alpha}\alpha + C_{Z_q}\bar{q} + C_{Z_\delta}\delta$$

Combining these two relationships results in

$$\begin{aligned} Z = {} & \tfrac{1}{2}\rho U_0^2 SC_{Z_0} + \rho U_0 SC_{Z_0}u \\ & + \tfrac{1}{2}\rho U_0^2 S(C_{Z_\alpha}\alpha + C_{Z_q}\bar{q} + C_{Z_\delta}\delta) + (\text{higher-order terms}) \end{aligned}$$

It follows that,

$$\frac{\Delta Z}{(1/2)\rho U_0^2 S} = 2C_{Z_0}\frac{u}{U_0} + C_{Z_\alpha}\alpha + C_{z_{\bar{q}}}\bar{q} + C_{Z_\delta}\delta \tag{9.21}$$

ΔX involves the thrust, so its development is slightly different. Assuming that T lies along the x-axis,

$$\begin{aligned} X &= T - D\cos\alpha + L\sin\alpha \\ &\simeq T_0 + \Delta T - \tfrac{1}{2}\rho[(U_0+u)^2 + w^2]S(C_D - C_L\alpha) \end{aligned}$$

C_D and C_L can be expressed as

$$C_D = C_{D_0} + C_{D_\alpha}\alpha \qquad C_L = C_{L_0} + C_L\alpha$$

For gliding flight or for a turbojet, one can assume T to be a constant. Thus, for these cases,

$$X = T_0 - \tfrac{1}{2}\rho U_0^2 S C_{D_0} - \rho U_0 u S C_{D_0} - \tfrac{1}{2}\rho U_0^2 S(C_{D_\alpha} - C_{L_0})\alpha$$

or

$$\frac{\Delta X}{(1/2)\rho U_0^2 S} = -2C_{D_0}\frac{u}{U_0} - (C_{D_\alpha} - C_{L_0})\alpha \tag{9.22}$$

For a piston engine airplane with constant speed propellers, we will assume that the propeller efficiency remains essentially constant as u changes. Thus, the thrust power remains constant, so

$$(T_0 + \Delta T)(U_0 + u) = T_0 U_0$$

or, approximately,

$$\Delta T = -T_0\frac{u}{U_0} \tag{9.23}$$

Thus, for this case,

$$\frac{\Delta X}{(1/2)\rho U_0^2 S} = -\frac{T_0}{(1/2)\rho U_0^2 S}\frac{u}{U_0} - 2C_{D_0}\frac{u}{U_0} - (C_{D_\alpha} - C_{L_0})\alpha$$

From Equation 9.20*a* and 9.20*b*,

$$\frac{T_0}{(1/2)\rho U_0^2 S} = C_{D_0} + C_{L_0}\tan\Theta_0$$

Therefore,

$$\frac{\Delta X}{(1/2)\rho U_0^2 S} = -(3C_{D_0} + C_{L_0}\tan\Theta_0)\frac{u}{U_0} - (C_{D_\alpha} - C_{L_0})\alpha \tag{9.24}$$

This equation of Equation 9.22 can be written in the form

$$\Delta C_X = C_{X_u}\frac{u}{U_0} + C_{X_\alpha}\alpha$$

where:

$$C_{X_u} = -2C_{D_0} \text{ for jets or gliding flight} \tag{9.25a}$$

$$C_{X_u} = -(3C_{D_0} + C_{L_0} \tan \Theta_0) \text{ for piston engine airplanes} \tag{9.25b}$$

$$C_{X_\alpha} = C_{L_0} - C_{D_\alpha} \tag{9.26}$$

In deriving these expressions $C_{x_{\bar{q}}}$ and C_{x_δ} are assumed to be negligible.

The expression for ΔM does not include a dependence on u, since $C_{M_0} = 0$.

$$\frac{\Delta M}{(1/2)\rho U_0^2 S\bar{c}} = C_{M_\alpha}\alpha + C_{M_{\bar{q}}}\bar{q} + C_{M_\delta}\delta \tag{9.27}$$

In order to nondimensionalize the linearized equations of motion, a time t^* is defined that is sometimes referred to as an "air second."

$$t^* = \frac{\bar{c}}{2U_0} \tag{9.28}$$

Real time is then referenced with respect to t^*.

$$\tau = \frac{t}{t^*} \tag{9.29}$$

Thus, for example,

$$\frac{du}{dt} = \frac{du}{d\tau}\frac{d\tau}{dt}$$

$$= \frac{2U_0}{\bar{c}}\frac{du}{d\tau}$$

Consistent with the earlier definition of $\bar{q}$, note that a reference length of $\bar{c}/2$ is used in the definition of t^*. A dimensionless velocity $\tilde{u}$ will also be used, defined by

$$\tilde{u} = \frac{u}{U_0} \tag{9.30}$$

The mass of the airplane will be expressed in a dimensionless form, μ, given by

$$m = \mu\rho S\left(\frac{\bar{c}}{2}\right) \tag{9.31}$$

Similarly, the mass moment of inertia is expressed in dimensionless form by

$$I_y = i_y\rho S\left(\frac{\bar{c}}{2}\right)^3 \tag{9.32}$$

Equations 9.21 to 9.32, when substituted into Equation 9.19, result in a set of linearized dimensionless equations defining the longitudinal dynamic motion of an airplane about a trimmed condition. In reducing these equa-

tions, it should be noted that, because of the use of stability axes,

$$C_{Z_0} = -C_{L_0}$$

Thus, from Equation 9.20*b*,

$$C_{L_0} = \frac{mg}{(1/2)\rho U_0^2 S} \cos \theta_0$$

and, from Equation 9.20*a*,

$$C_{X_0} = C_{L_0} \tan \theta_0$$

The nondimensional, linearized equations of motion can be written finally as:

$$2\mu\dot{\tilde{u}} - C_{X_u}\tilde{u} - C_{X_\alpha}\alpha + C_{L_0}\theta = 0 \tag{9.33a}$$

$$2C_{L_0}\tilde{u} + 2\mu\dot{\alpha} - C_{Z_\alpha}\alpha - (2\mu + C_{Z_{\dot{q}}})\dot{\Theta} + C_{L_0}\tan\Theta_0\theta = C_{Z_\delta}\delta \tag{9.33b}$$

$$-C_{M_\alpha}\alpha + i_y\ddot{\Theta} - C_{M_{\dot{q}}}\dot{\Theta} = C_{M_\delta}\delta \tag{9.33c}$$

It is emphasized that all derivatives in these equations are with respect to the dimensionless time τ. Thus, in Equation 9.33, $\dot{\Theta}$ is really the previously defined $\bar{q}$.

Terms like C_{Z_α}, C_{Z_q}, C_{X_α}, C_{M_α}, and $C_{M_{\dot{q}}}$ are referred to as stability derivatives. It may be necessary to include additional terms involving other stability derivatives in Equation 9.33, depending on the airplane configuration and its operating regime. For example, an airplane operating at transonic speeds will be sensitive to speed changes because of Mach number effects. Hence a term will have to be added to C_{X_u} to account for the increase in C_D with Mach number.

If the lift on a wing varies with time, a sheet of spanwise vorticity is shed downstream. If the rate at which the lift changes is sufficiently high, this shed vorticity can significantly change the lift, as a function of α, from the steady-state value. Except for the effect of the unsteady wing wake on the horizontal tail, the motion of an airplane is usually sufficiently slow, so that unsteady aerodynamic effects can be neglected.

One will find a fairly comprehensive discussion of stability derivatives in References 8.2 and 8.11. Following the earlier reference, an estimate of the unsteady effect of the wing on the tail can be made based on the fact that it takes a finite time for the wing wake to be convected downstream to the tail. Thus $\epsilon(t)$ at the tail is produced by the wing α at $t - \Delta t$. If α is increasing at a constant rate of $\dot{\alpha}$,

$$\epsilon(t) = \epsilon_\alpha\alpha - \epsilon_\alpha\dot{\alpha}\,\Delta t$$

where $\epsilon_\alpha\alpha$ would be the steady-state downwash. Δt is the time required for the wake to be transported from the wing to the tail. This is given ap-

proximately by $\Delta t = l_t/U_0$. Thus,

$$\epsilon(t) = \epsilon_\alpha \alpha - \epsilon_\alpha \dot{\alpha} \frac{l_t}{U_0}$$

or

$$\epsilon_{\dot{\alpha}} = -\epsilon_\alpha \frac{l_t}{U_0} \tag{9.34}$$

The product $\epsilon_{\dot{\alpha}}\dot{\alpha}$ represents a decrease in the tail angle of attack. Hence, both Z and M will vary with $\dot{\alpha}$, so terms $-C_{Z_{\dot{\alpha}}}\dot{\alpha}$ and $-C_{M_{\dot{\alpha}}}\dot{\alpha}$ can be added to Equations 9.33*b* and 9.33*c*, respectively. Normally, the effects embodied in $\epsilon_{\dot{\alpha}}$ are small, so they were neglected initially in formulating Equation 9.33.

A SUMMARY LOOK AT THE STABILITY DERIVATIVES AND OTHER PARAMETERS AFFECTING LONGITUDINAL DYNAMIC MOTION

X Derivatives and Parameters

Equation 9.33*a* contains the terms μ, C_{X_u}, $C_{X_{\dot{\alpha}}}$, and C_{L_0}. Given the wing area, mean aerodynamic chord, air mass density, and airplane mass, the dimensionless "mass," μ, can be calculated from Equation 9.31. C_{L_0} is simply the trim lift coefficient and can be determined from

$$C_{L_0} = \frac{mg}{q_0 S}$$

where $q_0 = \frac{1}{2}\rho U_0^2$.

Expressions for the derivative C_{X_u} are presented in Equation 9.25. These expressions involve the trim drag coefficient C_{D_0} and the trim pitch angle Θ_0. Since we are using stability axes, Θ_0 is simply the climb angle for the trim conditions. C_{D_0} is a function of C_{L_0} and is given by

$$C_{D_0} = \frac{f}{S} + \frac{C_{L_0}^2}{\pi A e}$$

We will again use the Cherokee 180 pictured in Figure 3.62 as an example. For the trim condition, straight and level flight at a true airspeed of 50 m/s (111.8 mph) at a standard altitude of 1500 m (4921 ft) is selected. For this airplane,

$$A = 5.625$$
$$I_y = 1693 \text{ kg} - \text{m}^2 \text{ (1249 slug-ft}^2\text{)}$$
$$W = 10{,}680.0 \text{ N (2400 lb)}$$
$$S = 14.86 \text{ m}^2 \text{ (160 ft}^2\text{)}$$
$$\bar{c} = 1.60 \text{ m (5.25 ft)}$$

An f of 0.5 m^2 (5.38 ft^2) (see discussion of Table 4.4) and an e of 0.6 (see discussion following Equation 4.33) will be assumed.

From Figure 2.3, the standard mass density at 1500 m equals 1.058 kg/m^2. Thus,

$$q_0 = \tfrac{1}{2}(1.058)(50)^2$$
$$= 1323.0 \text{ N/m}^2$$

Thus the trim lift and drag coefficients become

$$C_{L_0} = 0.543$$
$$C_{D_0} = 0.0615$$

Since Θ_0 is zero, C_{X_u} for this propeller-driven airplane becomes

$$C_{X_u} = -0.185$$

From Equation 9.26,

$$C_{X_\alpha} = C_{L_0} - C_{D_\alpha}$$
$$= C_{L_0} - C_{L_\alpha}\frac{dC_D}{dC_L}$$

or

$$C_{X_\alpha} = C_{L_0} - \frac{2C_{L_0}C_{L_\alpha}}{\pi Ae} \tag{9.35}$$

C_{L_α} was calculated previously for the Cherokee wing-tail combination as equal to 4.50/rad. Using Equation 8.71, an increment to C_{L_α} due to the fuselage is estimated to equal 0.13/rad. The propeller contribution to C_{L_α} can be estimated using Figure 8.22*a* together with the estimated C_{D_0}. Assuming a $\bar{C}_l$ of 0.6 and a J of 1.0,

$$\frac{P_{N_\alpha}}{T} \simeq 0.8/\text{rad}$$

Thus,

$$\Delta C_{l_\alpha} = 0.8C_{D_0}$$
$$= 0.05$$

The total C_{L_α} is equal to the sum of these separate contributions.

$$C_{L_\alpha} = 4.68/\text{rad}$$
$$C_{X_\alpha} = 0.0637/\text{rad}$$

The gross weight corresponds to a mass of 1089 kg. Thus, for the given gross weight and moment of inertia,

$$\mu = 86.6$$
$$i_y = 210.0$$

Using the foregoing numerical constants, Equation 9.33*a* becomes

$$173.0\dot{\tilde{u}} + 0.185\tilde{u} - 0.0637\alpha + 0.543\theta = 0 \tag{9.36}$$

Z Derivatives and Parameters

In addition to some of the terms just considered, Equation 9.33*b* contains the terms C_{Z_α}, $C_{Z_{\tilde{q}}}$, and C_{Z_δ}. To these we will add the derivative $C_{Z_{\dot{\alpha}}}$.

The derivative C_{Z_α}, because of the use of stability axes, is simply given by

$$C_{Z_\alpha} = -C_{L_\alpha} \tag{9.37}$$

$C_{Z_{\tilde{q}}}$ can be obtained by using Equation 8.49. At the trimmed condition,

$$\Delta Z = -\eta_t q_0 S_t a_t \frac{Ql_t}{V_0}$$

or

$$\frac{\Delta Z}{q_0 S} = -2\eta_t \frac{S_t}{S}\frac{l_t}{\bar{c}} a_t \frac{Q\bar{c}}{2V_0}$$

so that,

$$C_{Z_{\tilde{q}}} = -2\eta_t V_H a_t \tag{9.38}$$

Based on the experimental data of Reference 8.9, an η_t of 1.0 appears reasonable. At the cruise thrust coefficient, η_t is slightly greater than unity at low α values and less than unity at the higher α values. The horizontal tail volume for the Cherokee is approximately 0.392. Thus,

$$C_{Z_{\tilde{q}}} = -2.88$$

The increment in the Z force resulting from $\dot{\alpha}$ can be determined from Equation 9.34. At the trim condition,

$$\Delta Z = \eta_t q_0 S_T a_T \left(-\epsilon_\alpha \frac{l_t}{U_0}\right)\dot{\alpha}$$

or

$$C_{Z_{\dot{\alpha}}} = -2\eta_t V_H \epsilon_\alpha a_t \tag{9.39}$$

In Equation 9.39, $\dot{\alpha}$ is with respect to the dimensionless time τ, whereas in the preceding equation for ΔZ, the derivative is with respect to real time.

ϵ_α is estimated in Chapter Eight for the Cherokee to equal 0.447. Thus, $C_{Z_{\dot{\alpha}}}$ for the Cherokee is estimated to be

$$C_{Z_{\dot{\alpha}}} = -1.29/\text{rad-air sec}$$

The increment in Z resulting from an elevator deflection will be

$$\Delta Z = -\eta_t q_0 S_t a_t \tau\, \delta_e$$

or

$$C_{Z_\delta} = -\eta_t \frac{S_t}{S} a_t \tau \tag{9.40}$$

For a stabilator configuration, the effective lift curve slope is greater than a_t (with the tab fixed) because of the linked tab. This increased slope was given earlier as

$$\frac{dC_{L_T}}{d\alpha} = a_t(1 - \tau k_e)$$

Thus, Equation 9.40, for the stabilator configuration, becomes

$$C_{Z_\delta} = -\eta_t \frac{S_t}{S} a_t(1 - \tau k_e) \tag{9.41}$$

For the Cherokee, $k_e = -1.5$. The effective τ was estimated previously to equal 0.44. Thus,

$$C_{Z_\delta} = -0.934/\text{rad}$$

With the foregoing constants, Equation 9.33*b* for the Cherokee 180 becomes (including $\dot{\alpha}$ term)

$$1.09\tilde{u} + 175.0\dot{\alpha} + 4.68\alpha - 170.0\dot{\theta} = -0.934\delta \tag{9.42}$$

M Derivatives and Parameters

The equation of motion governing pitching, Equation 9.33*c*, requires the values of C_{M_α}, $C_{M_{\dot{q}}}$ and C_{M_δ}. In addition, we will include the term $C_{M_{\dot{\alpha}}}$.

C_{M_α} can be estimated on the basis of Equation 8.8 for a wing-tail combination. An increment to C_{M_α} for the fuselage is obtained from Equation 8.72 and for a propeller from Figure 8.22*a* and 8.22*c*.

For the Cherokee these components of C_{M_α} are estimated to equal:

$$\Delta C_{M_\alpha} = -0.963/\text{rad} \quad \text{(wing-tail)}$$
$$\Delta C_{M_\alpha} = +0.072/\text{rad} \quad \text{(propeller)}$$
$$\Delta C_{M_\alpha} = +0.150/\text{rad} \quad \text{(fuselage)}$$

Thus, for the total,

$$C_{M_\alpha} = -0.741/\text{rad}$$

The damping moment derivative, $C_{M_{\dot{q}}}$, is given by Equation 8.54. For the Cherokee 180,

$$C_{M_{\dot{q}}} = -7.42$$

$C_{M_{\dot{\alpha}}}$ is equal to $C_{Z_{\dot{\alpha}}}$ multiplied by the tail length referenced to $\bar{c}$.

$$C_{M_{\dot{\alpha}}} = -2\eta_t V_H \epsilon_\alpha \frac{l_t}{\bar{c}} a_t \tag{9.43}$$

For the Cherokee 180,

$$C_{M_{\dot{\alpha}}} = -3.32/\text{rad-air sec}$$

C_{M_δ} is equal to C_{Z_δ} multiplied by the dimensionless tail length. Thus, for

the stabilator configuration,

$$C_{M_\delta} = -\eta_t \frac{S_t}{S} a_t(1 - \tau k_e) \frac{l_t}{\bar{c}} \tag{9.44}$$

For the Cherokee 180,

$$C_{M_\delta} = -2.40/\text{rad}$$

Using the preceding stability derivatives for the Cherokee 180 results in the following for Equation 9.33*c*.

$$0.741\alpha + 3.32\dot{\alpha} + 210.0\ddot{\theta} + 7.42\dot{\theta} = -2.40\delta \tag{9.45}$$

EXAMINATION AND REDUCTION OF EQUATIONS OF LONGITUDINAL MOTION

Solution of nth-Order Linear Differential Equation with Constant Coefficients

The equations in Equation 9.33 are described as linear simultaneous differential equations with constant coefficients. The solution of these equations can be written as the sum of a transient solution and a steady-state solution. These are also referred to as homogeneous and particular solutions.

The steady state, or particular solution, is the part of the total solution that satisfies exactly the differential equation, including the forcing function. The transient solution satisfies the differential equation with the forcing function set equal to zero.

A linear differential equation of the nth order can be written in a general form as

$$C_n \frac{d^n x}{dt^n} + C_{n-1} \frac{d^{n-1} x}{dt^{n-1}} + \cdots + C_1 \frac{dx}{dt} + C_0 x = f(t) \tag{9.46}$$

To specify the problem completely, initial conditions equal in number to the order of the equation must be given. This usually means specifying x and its derivative up to order $n - 1$ at $t = 0$.

The solution to the homogeneous equation $[f(t) = 0]$ is of the form

$$x = Ae^{\sigma t} \tag{9.47}$$

The nth derivative will be

$$\frac{d^n x}{dt^n} = A\sigma^n e^{\sigma t}$$

This equation substituted into Equation 9.46 for $f(t)$ equal to zero leads to an nth degree polynomial for σ known as the characteristic equation.

$$C_n\sigma^n + C_{n-1}\sigma^{n-1} + \cdots + C_2\sigma^2 + C_1\sigma + C_0 = 0 \tag{9.48}$$

There are n roots or values of σ that will satisfy this polynomial. Thus, the general solution for x will be

$$x = A_1 e^{\sigma_1 t} + A_2 e^{\sigma_2 t} + \cdots + A_n e^{\sigma_n t} \tag{9.49}$$

where $\sigma_1, \sigma_2, \ldots \sigma_n$ are the roots of Equation 9.48. These roots may be positive or negative real numbers or complex numbers with positive or negative real parts. If a complex root exists, its conjugate must also exist. Complex roots always appear in pairs of the form

$$\sigma = a \pm ib$$

$A_1, A_2, \ldots, A_n$ are real or complex constants to be determined from the initial conditions.

Let us examine the behavior of a term containing a particular type of root. Consider the following items.

1. e^{at}.
2. e^{-at}.
3. $e^{(a+ib)t}$.
4. $e^{(-a+ib)t}$.

If a and b are positive real quantities, it is obvious that item 1 will become infinitely large as t approaches ∞. This is an unstable transient motion. Conversely, item 2 is stable. Item 3 can be written as

$$e^{at} e^{ibt}$$

Since

$$e^{ibt} = \cos bt + i \sin bt$$

the complex root with a positive real part represents an oscillatory motion having an amplitude that increases without limit as t approaches ∞. This situation is also unstable. Conversely, item 4 is a stable oscillatory root. Thus, to investigate the stability of the transient solution, one need only consider the roots of the polynomial given by Equation 9.57.

The particular solution is referred to as the steady-state solution since, for a stable system, it remains while the transient solution vanishes as t approaches ∞. The particular solution is of the same form as $f(t)$ if $f(t)$ can be expressed as a polynomial in t or in the form of

$$f(t) = Ae^{i\omega t}$$

or

$$f(t) = A \cos \omega t + B \sin \omega t$$

For example, suppose $f(t)$ were given by

$$f(t) = At^3 + Be^{i\omega t} + C \cos \omega t$$

Then the steady-state solution for x would take the form

$$x = at^3 + bt^2 + ct + d + fe^{i\omega t} + g\cos\omega t$$

Notice that when $f(t)$ is a polynomial, x must include all orders of t up to the highest in $f(t)$, even though some of the lower-order terms may be missing in $f(t)$.

As a fairly simple (and well-used) example of the foregoing, consider the second-order damped system governed by the equation

$$\ddot{x} + 2\zeta\omega_n\dot{x} + \omega_n^2 x = f(t) \tag{9.50}$$

The characteristic equation becomes

$$\sigma^2 + 2\zeta\omega_n\sigma + \omega_n^2 = 0$$

The roots of this equation are

$$\sigma_{1,2} = \omega_n(-\zeta \pm \sqrt{\zeta^2 - 1} \tag{9.51}$$

ζ is referred to as the critical damping ratio for reasons that are now obvious. When ζ is positive but less than unity, σ will be complex and x will be a damped oscillation. When ζ is greater than unity, σ will be a negative real number, and the motion will be aperiodic.

Suppose $f(t)$ is given by

$$f(t) = A + Be^{i\omega t} \tag{9.52}$$

The particular solution will be of this same form.

$$x = X_0 + X_1 e^{i\omega t}$$

Substituting this into the original equation gives

$$X_1(\omega_n^2 - \omega^2 + 2\zeta\omega\omega_n i)e^{i\omega t} + \omega_n^2 X_0 = A + Be^{i\omega t}$$

In order for this equation to be satisfied for all t, the coefficients of like terms involving t must identically satisfy the equation. Thus,

$$X_1 = \frac{B}{\omega_n^2 - \omega^2 + 2\zeta\omega\omega_n i}$$

$$X_0 = \frac{A}{\omega_n^2}$$

It is instructive to clear the denominator of X_1 of the complex number, so that

$$X_1 = B\,\frac{\omega_n^2 - \omega^2 - 2\zeta\omega\omega_n i}{(\omega_n^2 - \omega^2)^2 + 4\zeta^2\omega^2\omega_n^2}$$

If we further denote the frequency ratio ω/ω_n by r, X_1 can be written as

$$X_1 = \frac{B}{\omega_n^2}\frac{1-r^2-2\zeta ri}{(1-r^2)^2+4\zeta^2 r^2}$$

B/ω_n^2 is simply the static value of X_1 for $\omega = 0$. Thus the ratio of X_1 to its static value can be written as

$$\frac{\omega_n^2 X_1}{B} = \frac{1-r^2}{(1-r^2)^2+4\zeta^2 r^2} - i\frac{2\zeta r}{(1-r^2)^2+4\zeta^2 r^2} \tag{9.53}$$

The complete solution to Equation 9.50, forced in the manner given by Equation 9.52, is thus

$$x = e^{-\zeta\omega_n t}(x_1 e^{i\sqrt{1-\zeta^2}\omega_n t} + x_2 e^{-i\sqrt{1-\zeta^2}\omega_n t}) + \frac{A}{\omega_n^2} + \frac{B}{\omega_n^2}\frac{1-r^2-2\zeta ri}{(1-r^2)^2+4\zeta^2 r^2}e^{i\omega t} \tag{9.54}$$

x_1 and x_2 are constants to be determined by the values of x and $\dot{x}$ at $t = 0$.

The complex form for x and the forcing function may seem somewhat mysterious at first if one is not used to this type of mathematical treatment. Certainly there is nothing imaginary about the longitudinal motion of an airplane. The complex notation is simply a convenient mathematical device to show the amplitude and phase relationships between various terms in the system.

For example, consider Equation 9.53. This can be written in the form

$$\frac{\omega_n^2 X_1}{B} = C_1(r,\zeta) - iC_2(r,\zeta)$$

so that the steady-state solution becomes

$$x = \frac{A}{\omega_n^2} + \frac{B}{\omega_n^2}[C_1(r,\zeta) - iC_2(r,\zeta)]e^{i\omega t} \tag{9.55}$$

The complex quantity in the brackets can be further expressed as

$$[C_1(r,\zeta) - iC_2(r,\zeta)] = Re^{-i\phi}$$

where:

$$R = \sqrt{C_1^2 + C_2^2}$$

$$\phi = \tan^{-1}\frac{C_2}{C_1}$$

Thus Equation 9.55 becomes

$$x = \frac{A}{\omega_n^2} + \frac{B}{\omega_n^2}Re^{i(\omega t-\phi)} \tag{9.56}$$

If $Be^{i\omega t}$ is pictured as a force vector of magnitude B rotating around the origin in the complex plane, the time-dependent part of x, $x - A/\omega_n^2$, can be pictured as a displacement vector of magnitude BR/ω_n^2 rotating at the same

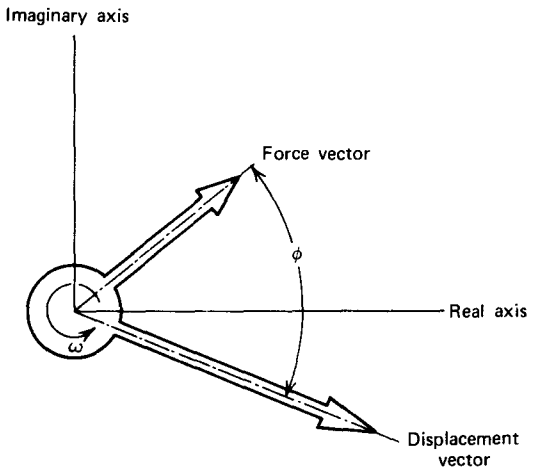

Figure 9.3 Significance of complex representation for oscillatory vectors.

rate of ω but lagging behind the force vector by an angle of ϕ. This is illustrated in Figure 9.3.

ω_n is known as the undamped natural frequency, since this is the frequency at which the force-free system will oscillate when perturbed and with $\zeta = 0$. It is interesting to examine Equation 9.56 when the system is forced at its natural frequency. For this case $r = 1.0$, so $C_1(r, \zeta) = 0$ and $C_2(r, \zeta) = (2\zeta)^{-1}$ and ϕ therefore equals $\pi/2$ or 90°. Thus the displacement of a second-order damped system, when forced at its natural frequency, will always lag the force by 90°, regardless of the damping.

Mode Shapes

Let us return to the longitudinal equations of motion for the Cherokee 180 (Equations 9.36, 9.42, and 9.45). The stability of the motion is determined from the transient solution. For this, it is assumed that $\tilde{u}$, α, and θ are of the form

$$\tilde{u} = u_1 e^{\sigma t} \tag{9.57a}$$

$$\alpha = \alpha_1 e^{\sigma t} \tag{9.57b}$$

$$\theta = \theta_1 e^{\sigma t}, \tag{9.57c}$$

The set of equations then become, after dividing out $e^{\sigma t}$,

$$(173\sigma + 0.185)u_1 + (-0.0637)\alpha_1 + 0.543\theta_1 = 0 \tag{9.58a}$$

$$1.09u_1 + (175\sigma + 4.68)\alpha_1 + (-170\sigma)\theta_1 = 0 \tag{9.58b}$$

$$(3.32\sigma + 0.741)\alpha_1 + (210\sigma^2 + 7.42\sigma)\theta_1 = 0 \tag{9.58c}$$

One could solve Equation 9.58*a* to 9.58*c* for each variable (u_1, α_1, and θ_1) in turn. However, to obtain σ, it is more direct to use the fact that for u_1, α_1, and θ_1 to have nonzero values, the determinant formed from the coefficients of these terms must vanish. This leads to the following quartic for σ. This is the characteristic equation for the system.

$$\sigma^4 + 7.84 \times 10^{-2}\sigma^3 + 4.80 \times 10^{-3}\sigma^2 + 5.40 \times 10^{-6}\sigma + 7.55 \times 10^{-8} = 0 \quad (9.59)$$

The problem is to extract the roots of this quartic. Since all of the coefficients are positive, there will be no positive real roots. However, there may be a positive real part of a complex root. This can be determined without actually finding the roots. We write the preceding polynomial in the following general form.

$$\sigma^4 + a_3\sigma^3 + a_2\sigma^2 + a_1\sigma + a_0 = 0 \quad (9.60)$$

It can be shown (Ref. 8.2) that the system for which this is the characteristic equation will be stable if a quantity R, known as Routh's discriminant, is positive. R is defined by

$$R = a_3a_2a_1 - a_1^2 - a_3^2a_0 \quad (9.61)$$

For a cubic, R takes the form (with $a_3 = 1$)

$$R = a_2a_1 - a_0 \quad (9.62)$$

In addition to satisfying the requirement that R be positive, it is emphasized that each of the coefficients must also be positive.

In the case of Equation 9.59, each of the coefficients is positive, and

$$R = 1.539 \times 10^{-9}$$

Hence we now know that the stick-fixed longitudinal dynamic motion of the Cherokee 180 is stable. Although this in itself is valuable, we need to know more before we can assess the flying qualities.

Unless one has a canned computer routine handy, the extraction of complex roots from a quartic can be formidable. One method, which involves some trial and error or graphical procedures, begins by writing Equation 9.60 as the product of two quadratics.

$$(\sigma^2 + B\sigma + C)(\sigma^2 + D\sigma + E) = 0 \quad (9.63)$$

Expanding Equation 9.63 and equating coefficients of like terms with Equation 9.60 gives

$$\begin{aligned} a_3 &= B + D \\ a_2 &= C + BD + E \\ a_1 &= DC + BE \\ a_0 &= CE \end{aligned} \quad (9.64)$$

These can be reduced to give

$$B = \frac{a_3}{2} \pm \left[\left(\frac{a_3}{2} \right)^2 - a_2 + C + \frac{a_0}{C} \right]^{1/2} \tag{9.65}$$

$$B = \frac{a_1 C - a_3 C^2}{a_0 - C^2} \tag{9.66}$$

Equations 9.65 and 9.66 are two implicit relationships involving B and C. They can be solved graphically by calculating B from each equation over a range of C values and noting the value of C graphically that results in the same B value from each equation. Numerically, one can subtract Equation 9.66 from Equation 9.65. Calling this difference $f(C)$, the problem reduces to finding the value of C for which $f(C) = 0$. Having C, B is obtained immediately from either Equation 9.65 or Equation 9.66. Because of the symmetry of the problem, D and E can then be calculated from

$$\begin{aligned} D &= a_3 - B \\ E &= \frac{a_0}{C} \end{aligned} \tag{9.67}$$

Using a programmable calculator, the foregoing procedure was applied to Equations 9.65 through 9.67 with the following result.

$$B = 0.0775 \tag{9.68a}$$

$$C = 0.00472 \tag{9.68b}$$

$$D = 8.84 \times 10^{-4} \tag{9.68c}$$

$$E = 1.60 \times 10^{-5} \tag{9.68d}$$

Substituting these values into Equation 9.63 and solving the two resulting quadratic equations gives the following four roots for σ.

$$\sigma = -0.0388 \pm 0.0567i \tag{9.69a}$$

$$\sigma = -0.000442 \pm 0.00397i \tag{9.69b}$$

As we concluded earlier, there are no real positive roots, so the motion is stable. Having these roots we can now write the transient solution for, say $\tilde{u}$, as

$$\tilde{u} = e^{-0.0388\tau}(u_1 e^{0.0567i\tau} + u_2 e^{-0.0567i\tau}) + e^{-4.42\times10^{-4}\tau}(u_3 e^{0.00397i\tau} + u_4 e^{-0.00397i\tau}) \tag{9.70}$$

This equation is in terms of the dimensionless time, τ. It can be expressed in terms of t by substituting Equation 9.29 for τ.

In this example, $t^* = 0.016$ sec. Hence, in terms of t, Equation 9.70 becomes

$$\tilde{u} = [e^{-2.43t}(u_1 e^{3.54it} + u_2 e^{-3.54it})] + [e^{-0.0265t}(u_3 e^{0.248it} + u_4 e^{-0.248it})] \tag{9.71}$$

The two separate functions of time within the brackets are referred to as normal modes. u_1, u_2, u_3, and u_4 are arbitrary complex constants to be determined by the initial conditions when the particular solution is included. It is generally true, as in this specific example, that the homogeneous solution can be expressed as the sum of the normal modes.

These two normal modes are typical of the stick-fixed longitudinal motion of most airplanes. The shapes of both modes are similar, but have different time constants. The real parts of these functions are presented graphically in Figure 9.4*a* and 9.4*b*. Notice the different time scales used in the two figures. The first mode, in Figure 9.4*a*, has a much shorter period than the other mode and is heavily damped. The damping of the amplitudes are shown by the dashed lines on each figure.

A measure of damping is provided by the time to damp to half-amplitude. The amplitude of either function is of the form

$$ue^{-at}$$

If the amplitude is A_1 at time t_1, the increment in time, $T_{1/2}$, to give an amplitude, A_2, equal to half of A_1 is found from

$$\frac{A_2}{A_1} = \frac{1}{2} = \frac{e^{-a(t+T_{1/2})}}{e^{-at}} = e^{-aT_{1/2}}$$

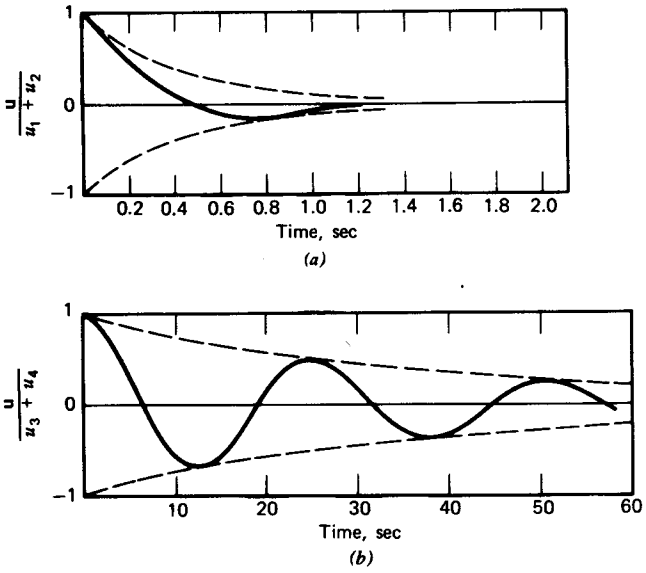

Figure 9.4 (*a*) The short-period longitudinal mode. (*b*) The long-period (phugoid) longitudinal mode.

or, the time to damp to half-amplitude, $T_{1/2}$, is calculated from

$$T_{1/2} = \frac{\ln 2}{a} \tag{9.72}$$

The period of the mode, T, is the time required to complete one cycle. Thus,

$$\omega T = 2\pi$$

or

$$T = \frac{2\pi}{\omega} \tag{9.73}$$

For the mode shown in Figure 9.4*a*,

$$a = 2.43$$
$$\omega = 3.54 \text{ rad/sec}$$

Thus,

$$T = 1.77 \text{ sec}$$
$$T_{1/2} = 0.285 \text{ sec}$$

For obvious reasons, this mode is referred to as the *short-period* mode. As noted, it is heavily damped. Because of its nature, this mode is not normally discernable to a pilot. For the other mode,

$$a = 0.0265$$
$$\omega = 0.248 \text{ rad/sec}$$

Thus, for this mode,

$$T = 25.3 \text{ sec}$$
$$T_{1/2} = 26.2 \text{ sec}$$

This more lightly damped mode is called the *long-period*, or *phugoid*, mode. It is easily discerned by the pilot.

The shapes of these modes, that is, the relative magnitudes and phase between the three displacements α, θ, and $\tilde{u}$, can be found from Equation 9.58 with the known values of σ. Using one of the displacements, say θ, as the reference, Equation 9.58 can be solved for the ratios u_1/θ_1 and α_1/θ_1.

From Equation 9.58*c*, which involves only α and θ, we can write

$$\frac{\alpha_1}{\theta_1} = \frac{210\sigma^2 + 7.42\sigma}{-3.32\sigma - 0.81} \tag{9.74}$$

For the real part of the phugoid, $\sigma = -0.000442 + 0.00397i$. Combining these relationships gives

$$\frac{\alpha_1}{\theta_1} = 0.0364e^{i\phi} \tag{9.75}$$

where $\phi = -78.1°$.

Substituting α_1/θ_1 into Equation 9.58*a* or 9.58*b* and solving for u_1/θ_1 gives

$$\frac{u_1}{\theta_1} = 0.78e^{i\phi} \tag{9.76}$$

where $\phi = 99.1°$.

For the short-period mode, $\sigma = -0.0388 + 0.0567i$. Substituting this root into Equation 9.74 gives

$$\frac{\alpha_1}{\theta_1} = 1.313e^{i\phi} \tag{9.77}$$

where $\theta = 2.18°$.

Substituting this into Equation 9.58*a* gives

$$\frac{u_1}{\theta_1} = 0.0407e^{i\phi} \tag{9.78}$$

where $\phi = 52.8°$.

Using θ as the reference, we are now in a position to describe the two modes by referring to Equations 9.75 to 9.78. For the phugoid, the amplitude of α is seen to be small compared to the amplitude of the velocity increment. The latter is seen to lead the pitch angle by approximately 99°, while the angle-of-attack increment lags θ by approximately 78°. For the short-period mode the velocity increment is small compared to the angle of attack. In this mode both α and u lead θ by angles less than 90°.

Phugoid (Long-Period Mode)

The phugoid represents motion at a nearly constant angle of attack. Although the pitch angle is varying periodically, the altitude is also changing so as to maintain a nearly constant α. This is depicted in Figure 9.5. The displacements are exaggerated for clarity. Beginning at the top of one cycle, the airplane has slowed down to its minimum airspeed, and its attitude is nearly level. It then begins to lose altitude. As it does so, its speed increases, followed by a nose-down attitude. At the bottom of the cycle its airspeed is a maximum and its attitude is again nearly level. It then begins to climb. The

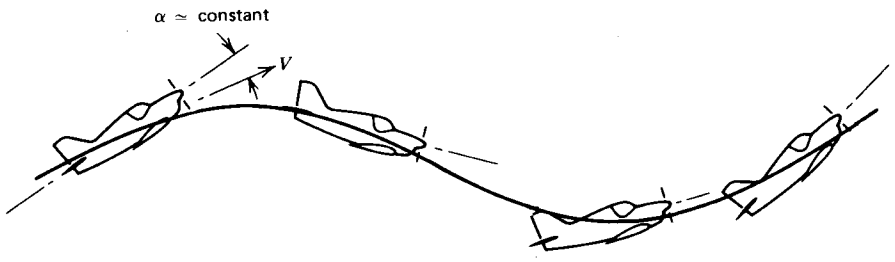

Figure 9.5 The phugoid mode; oscillating, longitudinal motion at a constant angle of attack.

airspeed begins to drop off, followed by a nose-up attitude, and the cycle is repeated.

Since α, and hence C_L, is approximately constant for the phugoid, an approximate value for the period of the mode can be obtained as follows. At any instant of time, the net force on the airplane in the vertical direction can be written approximately as

$$F_Z = W - \tfrac{1}{2}\rho(U_0^2 + 2U_0 u)C_{L_0}S$$

But

$$W = \tfrac{1}{2}\rho U_0^2 C_{L_0} S$$

Thus, the unsteady force accelerating the airplane vertically downward is

$$F_Z = -\rho U_0 C_{L_0} S u$$

The approximate equation of motion in this direction is

$$F_Z = m\ddot{Z}$$

Integrating this equation, assuming u to be of the form

$$u = u_{\max} \sin \omega t$$

gives

$$Z = \frac{\rho U_0 C_{L_0} S u_{\max}}{m\omega^2} \sin \omega t$$

Thus the maximum change in the potential energy (PE) of the airplane is

$$\Delta \text{PE} = \frac{2g\rho U_0 C_{L_0} S u_{\max}}{\omega^2}$$

This must equal the maximum change in the kinetic energy (KE) of the airplane, given by

$$\Delta \text{KE} = 2m U_0 u_{\max}$$

It follows that ω is given approximately by

$$\omega = \sqrt{2}\,\frac{g}{U_0} \text{ rad/sec} \tag{9.79}$$

This approximate result is seen to be independent of airplane geometry. It can be found in other references, but is frequently written in a somewhat disguised form as

$$\omega = \frac{C_{L_0}}{\sqrt{2}\mu} \text{ rad/air sec}$$

As written here, the units of ω are radians per air seconds. Expressed in real time, this equation reduces to Equation 9.79. For the example case of the Cherokee 180 at 50 m/s, Equation 9.79 predicts an ω of 0.278 rad/sec, or a

period of 22.6 sec. This period is 2.7 sec, or approximately 10%, shorter than the exact value calculated previously.

Short-Period Mode

A very close approximation to the short-period mode is obtained by assuming that u is constant for this mode. With this approximation, Equation 9.33 for the control-fixed case reduces to

$$(2\mu - C_{Z_{\dot\alpha}})\dot\alpha - C_{Z_\alpha}\alpha - (2\mu + C_{Z_q})\dot\theta + C_{L_0}\tan\theta_0\theta = 0 \qquad (9.80a)$$

$$-C_{M_{\dot\alpha}}\dot\alpha - C_{M_\alpha}\alpha + i_y\ddot\theta - C_{M_q}\theta = 0 \qquad (9.80b)$$

Both C_{Z_α} and C_{Z_q} are normally small compared to 2μ. These two terms will therefore be neglected. If we let $\theta_0 = 0$, the following quadratic is obtained for the characteristic equation.

$$2\mu i_y\sigma^2 - [C_{Z_\alpha}i_y + 2\mu(C_{M_q} + C_{M_{\dot\alpha}})]\sigma + C_{Z_\alpha}C_{M_q} - 2\mu C_{M_\alpha} = 0 \qquad (9.81)$$

or

$$\sigma = \frac{C_{Z_\alpha}}{4\mu} + \frac{C_{M_q} + C_{M_{\dot\alpha}}}{2i_y} \pm i\left[-\left(\frac{C_{Z_\alpha}}{4\mu} + \frac{C_{M_q} + C_{M_{\dot\alpha}}}{2i_y}\right)^2 - \left(\frac{2\mu C_{M_\alpha} - C_{Z_\alpha}C_{M_q}}{2\mu i_y}\right)\right]^{1/2} \qquad (9.82)$$

For the Cherokee 180 example, this approximation to σ becomes

$$\sigma = -0.0391 \pm 0.0544i$$

Thus, with this approximation, the damping is predicted within 1% and the frequency within 4% of the previously calculated values.

SOLUTION OF THE LONGITUDINAL EQUATIONS OF MOTION USING AN ANALOG COMPUTER

An analog computer is used primarily for solving differential equations. Although it is not as accurate as the digital computer, for certain applications it is more valuable. For example, one can examine the effect of varying a parameter on the solution of a differential equation simply by turning a potentiometer on the analog computer.

The heart of an analog computer is the operational amplifier, which is a high-gain, high-impedance amplifier. The symbol for such an amplifier is shown in Figure 9.6*a*. Consider what happens when this amplifier is connected into the circuit shown in Figure 9.6*b*. e_1, e_2, and e_3 represent three time-dependent input voltages, which are applied to resistance R_1, R_2, and R_3, respectively. The input resistors are tied to a feedback resistor, R_F, at a point SJ known as the summing junction. As shown, R_F is across the operational amplifier. All voltages are relative to ground. If i_x denotes current flow

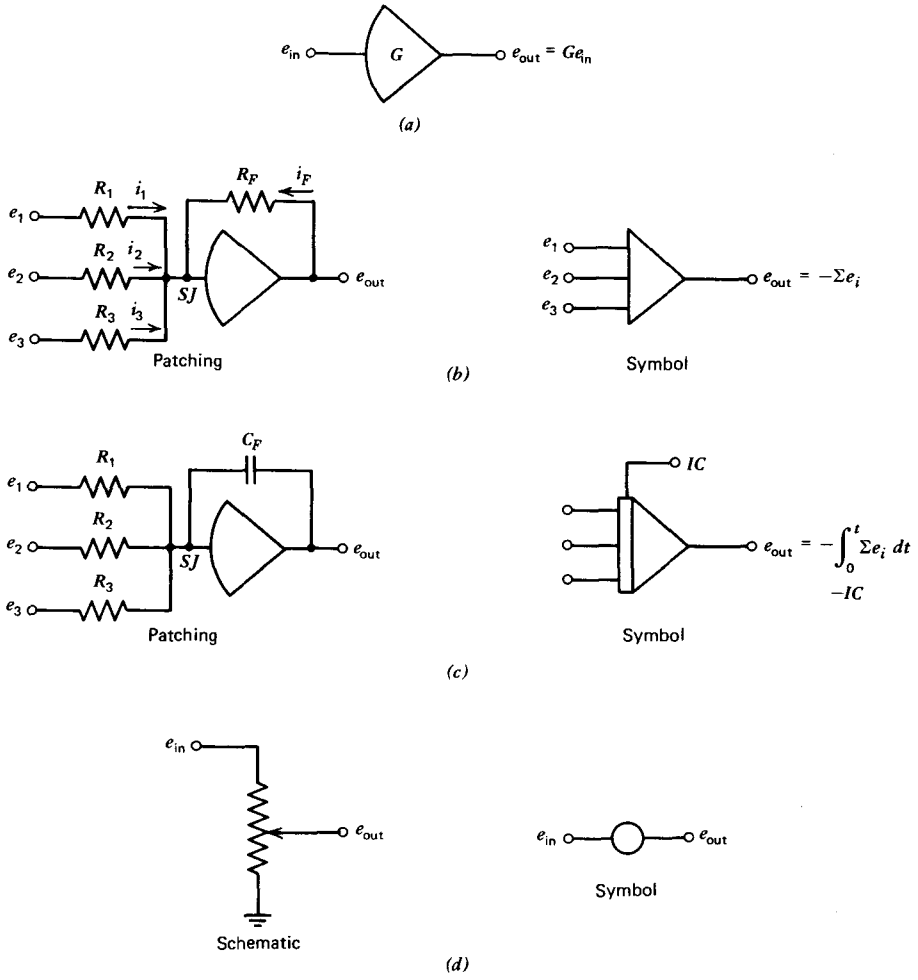

Figure 9.6 Analog computer elements. (*a*) Operational amplifier. (*b*) Summer. (*c*) Integrator. (*d*) Potentiometer.

through the x-circuit component then, from Kirchoff's theorem, the net flow into the junction SJ must equal zero.

$$i_1 + i_2 + i_3 + i_F = i_A \tag{9.83}$$

However,

$$i_A = \frac{e_{SJ} - e_0}{Z}$$

In this equation, Z is the impedance of the amplifier, which is assumed to be high. Since all voltages are limited in order to stay within the linear range of

the amplifier, it follows that

$$i_A \simeq 0 \tag{9.84}$$

e_{SJ} and e_0 are related by the gain of the amplifier.

$$e_0 = Ge_{SJ}$$

or

$$e_{SJ} = \frac{e_0}{G}$$

G is also assumed to be high, so that approximately

$$e_{SJ} \simeq 0 \tag{9.85}$$

SJ is referred to as a virtual ground point.

A good operational amplifier will have a DC gain of approximately 10^7 and an impedance of $10^{10}\,\Omega$. Its frequency response (gain versus frequency) will be flat from zero to 10^6 Hz with feedback. Obviously, the approximation, given by Equation 9.93, is a very good one.

The voltage drop across a resistance is given by Ohm's law.

$$e = iR \tag{9.86}$$

Combining Equations 9.83 to 9.86, it follows that

$$e_0 = -\left(\frac{R_F}{R_1}e_1 + \frac{R_F}{R_2}e_2 + \frac{R_F}{R_3}e_3\right) \tag{9.97}$$

Thus, the patching shown in Figure 9.6*b* results in an output voltage e_0 equal to the negative sum of the input voltages multiplied by the ratio of the input resistors to the feedback resistor. Most standard analog computers provide for ratios (referred to as gains) of 1.0 or 10.0. Taken as a whole, the combination of operational amplifier, input resistors, and feedback resistor is known as a *summer*. The symbol for a summer is shown in Figure 9.6*b*.

It is left to you to show that an *integrator* is formed by using a feedback capacitance, C_F, in place of R_F. In this case the patching shown in Figure 9.6*c* gives an output voltage equal to

$$e_0 = -\int_0^t \left(\frac{e_i}{C_F R_1} + \frac{e_2}{C_F R_2} + \frac{e_2}{C_F R_3}\right) dt \tag{9.88}$$

By putting an initial charge on the feedback capacitor, one is also able to allow for an initial condition on the quantity being represented by the output voltage.

The schematic for a potentiometer is also included in Figure 9.6. The input voltage is supplied to one end of a resistance coil, and the other end of the coil is grounded. The output voltage is taken from a wiper. When the wiper contacts the input end of the coil, the output voltage is equal to the

input voltage. As the "pot" is turned, the wiper moves toward the ground, so that the output voltage goes to zero. Thus, one can effectively multiply a voltage signal by a factor from zero to unity by feeding the voltage signal through a pot. Combined with an input gain of 10 into a summer or integrator, the pot allows a programmer to multiply a signal by a factor from 0 to 10. In practice one tries to avoid setting a pot below a value of 0.1, since accuracy is lost. There are times, however, when this is unavoidable if a term represents a small contribution to the solution.

Generally, problems to be solved with an analog computer have to be both time-scaled and magnitude-scaled. This is best explained by means of an example for which we refer to Equation 9.50. The example will also illustrate the general procedure that is followed to construct the patching diagram to solve a given differential equation. We begin by solving for the highest derivative. In this case,

$$\ddot{x} = f(t) - 2\zeta\omega_n\dot{x} - \omega_n^2 x \tag{9.89}$$

To be more specific, suppose x represents the displacement of a light mass supported on a stiff spring with a damping ratio less than critical. Let

$$\omega_n = 600 \text{ rad/sec}$$
$$\zeta = 0.5$$

Also, let

$$f(t) = 0$$
$$x(0) = 0.85 \text{ mm}$$
$$\dot{x}(0) = 0$$

Equation 9.89 becomes

$$\ddot{x} = -600\dot{x} - 360{,}000x \tag{9.90}$$

We now "guesstimate" the maximum values to be expected for x and $\dot{x}$. In this case, it is not too difficult. Since it is a damped oscillation, the initial value of x should be the maximum. We will therefore pick a convenient maximum value for x, known as a "rounded up maximum" (RUM), of 1.0 to which to reference x. RUM values should be higher than any expected values of a particular variable, but not too high, or accuracy will be lost.

The maximum value of $\dot{x}$ should equal approximately the maximum value of x multiplied by ω_n. A RUM value for $\dot{x}$ of 1000 should therefore suffice. We now rewrite Eqn 9.90 expressing x and $\dot{x}$ in terms of their RUM values.

$$\ddot{x} = -600{,}000\left(\frac{\dot{x}}{1000}\right) - 360{,}000\left(\frac{x}{1}\right) \tag{9.91}$$

If we now divide through by 1×10^6,

$$\left(\frac{\ddot{x}}{1 \times 10^6}\right) = -0.6\left(\frac{\dot{x}}{1000}\right) - 0.36\left(\frac{x}{1}\right) \tag{9.92}$$

The problem appears to be magnitude-scaled satisfactorily at this point, since the coefficients of the scaled values of x and $\dot{x}$ lie between 0.1 and 10. However, to integrate $\ddot{x}/(1 \times 10^6)$ and get $\dot{x}/1000$, we would need to multiply the former by 1000. Thus we need to time-scale the problem. In this case, we need to "slow down" the action in order to plot the motion. Denoting the problem time by τ and the real time with which the computer works as t, let

$$\tau = \beta t \tag{9.93}$$

Now consider

$$\begin{aligned} x &= 1000 \int \left(\frac{\dot{x}}{1000}\right) d\tau \\ &= 1000 \int \left(\frac{\dot{x}}{1000}\right) \frac{d}{dt}\, dt \\ &= 1000\beta \int \left(\frac{\dot{x}}{10{,}000}\right) dt \end{aligned}$$

Thus, multiplying $\dot{x}$ by β and integrating with respect to real time results in x as a function of τ.

The RUM values correspond to the rated voltage of the computer, which is referred to as the machine unit. Thus, for example, suppose the voltage signal at a given instant equals 3 V for a 10-V machine, or 0.3 of a machine unit. If this signal represents a variable having a RUM value of 1000, the value of the variable at that instant would be 300.

Now consider Figure 9.7*a*. To begin, it is assumed that the output from summer 1 equals $-(\ddot{x}/1 \times 10^6)$. This signal is fed through pot 1, which is set at 1000β, and then into integrator 2. The output of this integrator equals $(\dot{x}/1000)$. This output is fed through pot 2, which is set again at 1000β, and then into integrator 3. The output of this integrator is equal to $-(x/1)$. Thus we easily obtain $\dot{x}$ and x by simply integrating $\ddot{x}$ twice. Having these quantities we can now satisfy the differential equation, Equation 9.86, as illustrated in Figure 9.7*b*. Since $\ddot{x}/1 \times 10^6$ equals the sum of $-0.6\dot{x}/1000$ and $0.36x/1$, we take the voltage from amplifier 2, which is proportional to $\dot{x}/1000$, and run it through summer 4 to change the sign. The output of this summer is then fed into pot 3 set at 0.6 and from the pot into amplifier 1. Also, the voltage from amplifier 3 is fed into pot 4 set at 0.36 and from the pot into summer 1.

The initial condition on the problem is provided by patching from a +1 machine unit reference into pot 5. Since x is initially equal to 0.85 of its RUM value, this pot is set at 0.85. The output of this pot is then fed into the IC (initial condition) connection for the integrator module patched into amplifier 3.

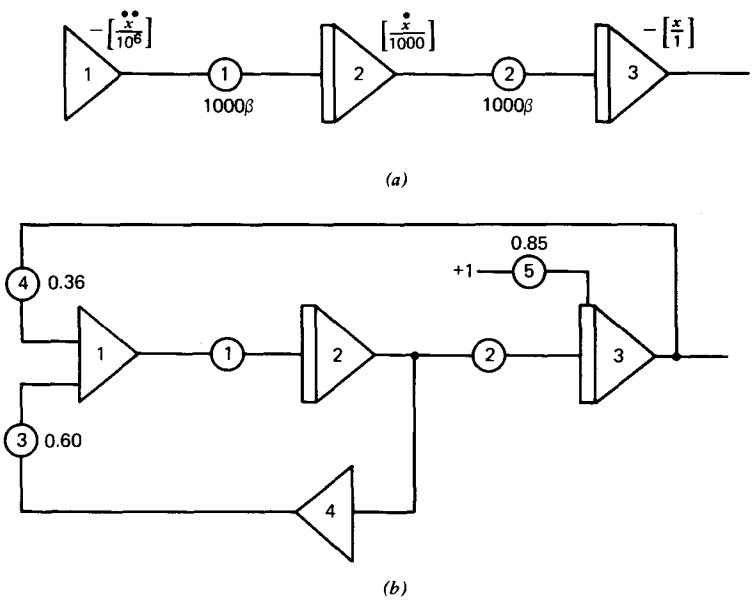

Figure 9.7 Patching for a damped oscillator.

For this relatively simple example, it is obvious that the RUM values chosen for x and $\dot{x}$ are sufficiently high to assure that the amplifier outputs will not exceed the rated machine voltage. However, if an amplifier overflows (as indicated by some kind of marker, usually a light), one simply rescales, choosing higher RUM values.

Let us now turn to the solution of the set of simultaneous, linear differential equations, Equations 9.36, 9.42, and 9.45. In particular consider the following experiment. At an altitude of 1500 m the airplane is trimmed to fly hands-off at a true airspeed of 50 m/s. Without changing the power setting, the stick is held back to a position that provides a steady speed of 40 m/s. Thus, relative to the trim airspeed, $\tilde{u} = -0.2$. Now return the stick suddenly to its trimmed position and hold it fixed (in the manner of a step function). Thus disturbed, the airplane will exhibit an unsteady longitudinal motion, which we will attempt to predict using the analog computer

Expressing all derivatives with respect to real time, all angles in degrees, and the incremental velocity, u, in meters per second, the governing equations become:

$$\dot{u} = -0.0668u + 0.0201\alpha - 0.171\theta \tag{9.94a}$$

$$\dot{\alpha} = -0.449u - 1.69\alpha + 0.983\dot{\theta} - 0.337\delta \tag{9.94b}$$

$$\ddot{\theta} = -0.988\dot{\alpha} - 15.1\alpha - 2.21\dot{\theta} - 44.6\delta \tag{9.94c}$$

Unsteady aerodynamic terms in $\dot{\alpha}$ are included in Equation 9.94

From the experiment we are given that u equals -10 m/s initially. Also, at $t = 0$, all derivatives are zero. Thus Equation 9.94 can be solved to give the following initial values.

$$\alpha(0) = 0.0570 \text{ rad} = 3.26°$$
$$\theta(0) = 0.0848 \text{ rad} = 4.86°$$
$$\delta(0) = -0.0193 \text{ rad} = -1.11°$$

Since δ is zero for $t > 0$, the problem can be run on the computer in one of two ways. First, δ can be patched into the problem and the airplane "flown" through the pot representing δ. This pot is adjusted until $u = -10$ m/s, at which condition the pot setting should correspond to the preceding $\delta(0)$ value. α and θ will also assume their correct initial values. A function switch can then be thrown to disconnect the δ input, simulating the return of the stick to its trimmed position. The ensuing analog behavior should represent the unsteady behavior of the airplane. The second, and simpler, way to run the problem is to impose the proper initial values on u, α, and θ, letting δ equal zero. In scaling this problem one might assume that the initial values of u, α, and θ represent maximum upper bounds on these variables. However, if one chooses the RUM values on this basis, the amplifier representing θ will overflow. By trial and error, a RUM value for θ of 20° was found to be satisfactory. Five degrees and 10 m/s were chosen for α and u, respectively, based on their initial values. Magnitude-scaled; Equation 9.94 becomes:

$$\left(\frac{\dot{u}}{5}\right) = -0.134\left(\frac{u}{10}\right) + 0.0201\left(\frac{\alpha}{5}\right) - 0.684\left(\frac{\theta}{20}\right) \tag{9.95a}$$

$$\left(\frac{\dot{\alpha}}{20}\right) = -0.420\left(\frac{\alpha}{5}\right) + 0.976\left(\frac{\dot{\theta}}{20}\right) - 0.223\left(\frac{u}{10}\right) - 0.335\left(\frac{\delta}{20}\right) \tag{9.95b}$$

$$\left(\frac{\dot{\theta}}{100}\right) = -0.442\left(\frac{\ddot{\theta}}{20}\right) - 0.775\left(\frac{\alpha}{5}\right) - 0.199\left(\frac{\dot{\alpha}}{20}\right) - 8.92\left(\frac{\delta}{20}\right) \tag{9.95c}$$

These equations do not have to be time-scaled in order to examine the phugoid mode. For the short-period mode, however, the action has to be slowed down. Figure 9.8 presents the patching diagram to solve these equations. The top row of amplifiers sums and integrates $\dot{U}$ to obtain u. The second row performs the same function for α. The third row of amplifiers sums and integrates $\ddot{\theta}$ twice to obtain $\dot{\theta}$ and θ.

Observe how the equations are tied together. For example, to satisfy the second term on the right-hand side of Equation 9.94*b*, the output from amplifier 6 is fed into pot 11 set at 0.976 and is then fed into amplifier 1, which is summing $\dot{\alpha}$. The numbering of the amplifiers and pots may seem somewhat haphazard, but it was chosen to be convenient for the analog computer that was available to me.

The outputs for amplifiers 2, 3, and 9, representing $(u/10)$, $(\alpha/5)$, and

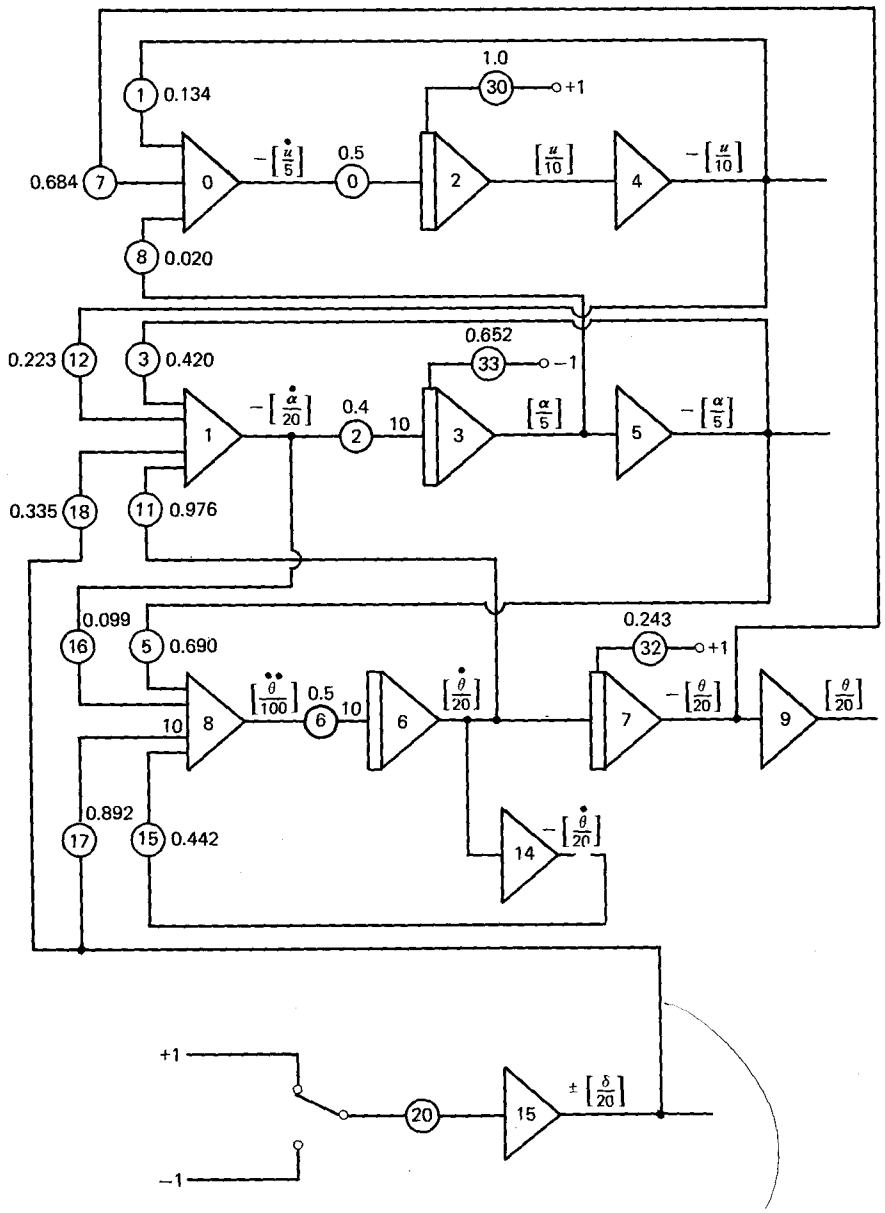

Figure 9.8 Patching diagram for the longitudinal equations of motion.

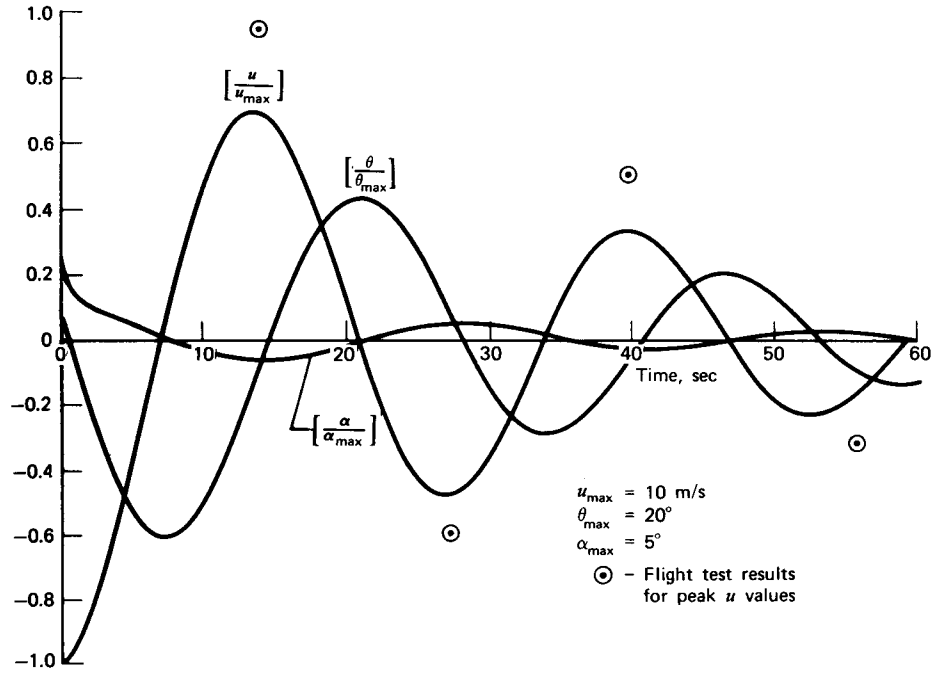

Figure 9.9 Longitudinal motion of a Cherokee 180 as predicted by an analog computer.

(θ/20) as a function of real time, are presented in Figure 9.9. These results were obtained directly from the traces of an x-y plotter with a built-in time base. As reflected by the trace, the short-period mode damps out quickly, leaving only the phugoid. You should satisfy yourself that the frequency, damping, and phase relationships shown here are close to those calculated previously for the phugoid.

This experiment, the results of which are predicted in Figure 9.9, was flown by me with some of my students using only the standard equipment in the airplane. Flying at a density altitude of 1500 m, the airplane was trimmed, hands-off, to fly straight and level at a true airspeed of 50 m/s. A small telescoping rod was then placed between the back of the control wheel and the instrument panel in order to reference the trim stick position. The wheel was pulled back and held at the position to maintain a steady true airspeed of 40 m/s. Simultaneously, the wheel was pushed forward and held fixed at its trim position, and a stopwatch was started. The times when the airspeed attained maximum and minimum values were then visually noted. The values themselves were also noted simply by reading the airspeed indicator. In this manner, the experimental points shown in Figure 9.9 were obtained. The

agreement between the analog results and the experimental points is good considering that the stick motion only approximates a step function, that there is some lag in the airspeed indicator, and the errors inherent in the simplistic manner in which the data were obtained.

Predictions of longitudinal dynamic motion for relatively simple configurations such as the Cherokee are not too difficult to accomplish and can be done so with some degree of confidence. This is not necessarily so, however, for high-performance aircraft operating at high Mach numbers or for V/STOL aircraft, in which the lift and propulsion systems may be integrated. Because this is an introductory textbook, the details of treating these types of aircraft are beyond its scope. In the case of high-speed aircraft, the aerodynamic stability derivatives must also include the dependence of the forces and moments on speed. For example, suppose an aircraft is operating just below its critical Mach number. If it is disturbed by some type of input, the perturbations in the aircraft's velocity and angle of attack can produce compressibility effects that drastically alter the lift, drag, and pitching moment coefficients.

LONGITUDINAL FLYING QUALITIES

The evaluation of an airplane's flying quality is one of subjectiveness. It is difficult to quantify how an airplane feels to a pilot. An airplane may even have an unstable mode (as we will see in the next chapter) and yet feel fine to the pilot if the time to double amplitude is sufficiently long.

Figure 9.10 (taken from Ref. 9.1) presents the latest revision of the so-called Cooper-Harper Scale for evaluating airplane flying qualities Obviously, with adjectives such as "excellent," "good," "fair," "moderate," "considerable," and "extensive," different pilots will give the same airplane different ratings. Nevertheless, this system does provide a rational and somewhat objective base for measuring an airplane's flying quality. Because of the subjective nature of the Cooper-Harper Scale, Reference 9.1 mainly emphasizes three levels within the scale.

Level 1: Cooper-Harper scale = $1 - 3.5$

Level 2: Cooper-Harper scale = $3.5 - 6.5$

Level 3: Cooper-Harper scale = $6.5 - 9+$

In order to assure that an airplane lies within one of these levels (level 3 is really undesirable but flyable), Reference 9.1 specifies definite dynamic characteristics that the airplane should possess.

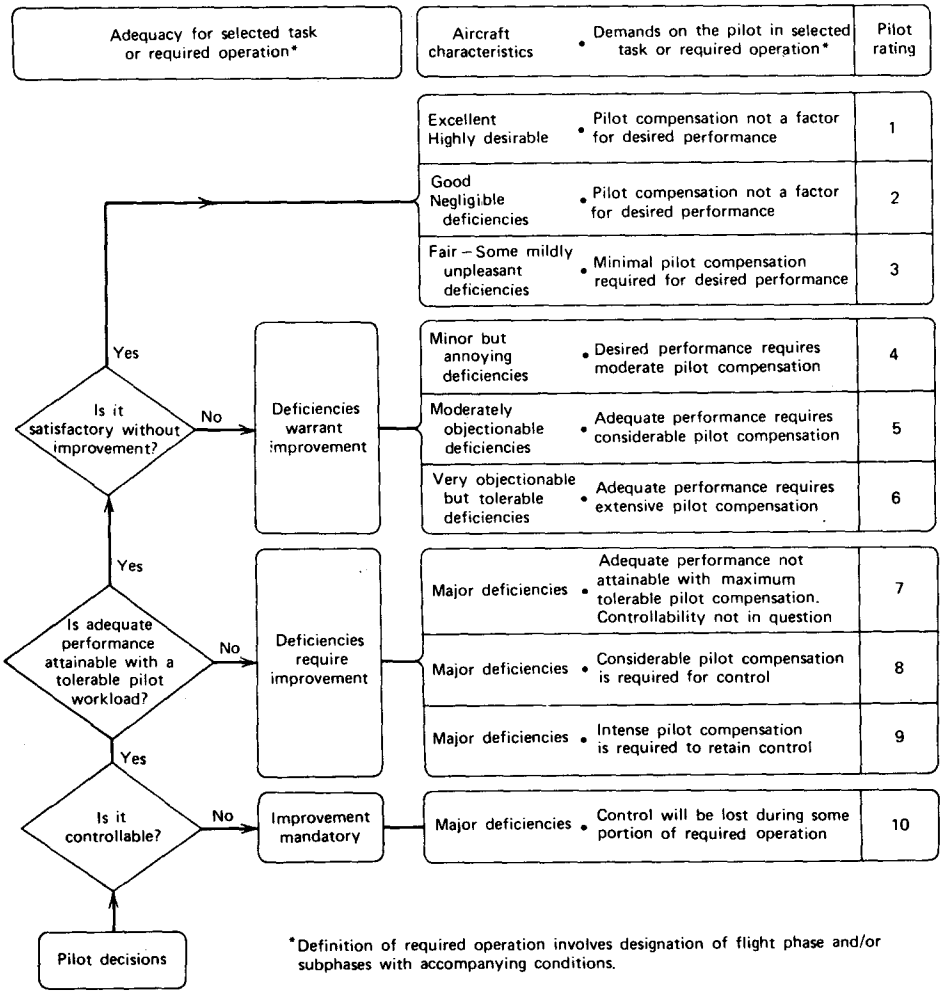

Figure 9.10 Cooper-Harper scale for rating airplane handling qualities.

Phugoid Mode

First, with regard to the *phugoid mode*,

$$\text{Level 1: } \zeta > 0.04 \tag{9.96a}$$

$$\text{Level 2: } \zeta > 0 \tag{9.96b}$$

$$\text{Level 3: } T_2 > 55 \text{ sec} \tag{9.96c}$$

ζ is the damping ratio, and T_2 is the time to double amplitude.

The damping ratio, ζ, for a particular mode, is related to the roots of the characteristic equation as follows. Let the roots defining an oscillatory mode be given by

$$\sigma_{1,2} = -a \pm i\omega$$

Now consider the product

$$(\sigma - \sigma_1)(\sigma - \sigma_2) = 0$$

Expanded, it is

$$\sigma^2 + 2a\sigma + a^2 + \omega^2 = 0 \tag{9.97}$$

Comparing Equation 9.97 to Equation 9.50, it is obvious that

$$\omega_n^2 = a^2 + \omega^2 \tag{9.98a}$$

$$\zeta = \frac{a}{\omega_n} \tag{9.98b}$$

For the example of the Cherokee 180, in real time, $a = 0.0265$ and $\omega = 0.248$ for the phugoid. Hence, the damping ratio, ζ, equals 0.106 and the undamped natural frequency, ω_n, equals 0.249 rad/sec. Thus, according to the criteria of Equation 9.96, the Cherokee falls within level 1.

Flight Path Stability

Another criterion relating to longitudinal motion discussed in Reference 9.1 is that of *flight path stability*. This refers to the flight-path-angle change effected by elevator control at a constant power setting. For the landing approach flight phase, this angle as a function of true airspeed should have a slope at the minimum operational speed, which is negative or less positive than:

$$\text{Level 1: } 0.06°/\text{kt} \tag{9.99a}$$

$$\text{Level 2: } 0.15°/\text{kt} \tag{9.99b}$$

$$\text{Level 3: } 0.24°/\text{kt} \tag{9.99c}$$

In effect, these are tantamount to stating that one should not design an airplane to operate too far into the backside of the power-required curve. In this region, the flight-path-angle (positive for climb) will increase as the speed is increased for a constant power setting.

Short-Period Mode

Both the short-period frequency and damping ratio are important to achieving satisfactory flying qualities. When the damping is too low, the short-period response can produce an annoying oscillation. When the damping

Table 9.1 Short-Period Damping Ratio Limits

	Categories A and C		Category B	
Level	Minimum	Maximum	Minimum	Maximum
1	0.35	1.30	0.3	2.00
2	0.25	2.00	0.2	2.00
3	0.15	—	0.15	—

is too high, the response to control input can be sluggish. Therefore, upper and lower limits to short-period damping are recommended in Reference 9.1 in order to achieve a given Cooper-Harper level. These limits are given in Table 9.1 according to the following flight categories.

Category A These are nonterminal flight phases that require rapid maneuvering, precision tracking, or precise flight path control such as air-to-air combat, in-flight refueling (receiver), terrain-following, and close formation flying.

Category B These are nonterminal flight phases that are normally accomplished using gradual maneuvers and no precision tracking, although accurate flight path control may be required. This category includes climb, cruise, and descent, in-flight refueling (tanker), and aerial delivery.

Category C These are terminal flight phases requiring gradual maneuvers but precise flight path control. These include takeoff, catapult takeoff, approach, wave-off/go-around, and landing.

Specifying the damping ratios alone, as in Table 9.1, is not necessarily sufficient to assure adequate flying qualities. As mentioned earlier, the short-period frequency is also important. Indeed, it appears as if the values of frequency and damping ratio for satisfying flying qualities are interdependent.

Reference 9.1 and other sources present a number of graphs similar to Figure 9.11. These are sometimes referred to as target plots. Since the establishment of these boundaries is subjective in nature, the contours defining the Cooper-Harper levels should not be taken as hard and fast. However, an airplane that falls to the left of level 3 in Figure 9.11 can be dangerous to fly.

For the Cherokee 180, the roots of the characteristic equation for the short-period mode were calculated previously. In real time these were

$$\sigma_{1,2} = -2.43 \pm 3.54i$$

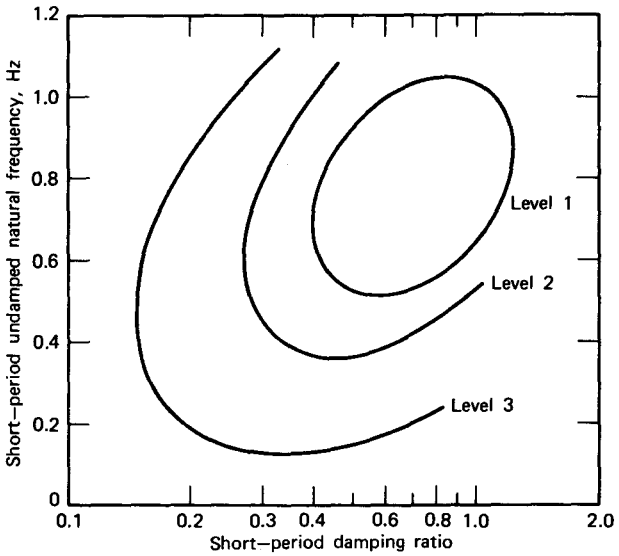

Figure 9.11 Short-period handling qualities criteria.

Thus, from Equation 9.97, for this mode

$$\zeta = 0.566$$
$$\omega_n = 4.29 \text{ rad/sec}$$
$$= 0.68 \text{ Hz}$$

These values are seen to lie well within the level 1 region of Figure 9.11.

PROBLEMS

9.1 The motion of a coupled system having two degrees of freedom (x, y) is governed by

$$\ddot{x} + 2x - y = 0$$
$$10x + \ddot{y} - 4\dot{y} = e^{i\omega t}$$

(a) Write the homogeneous or transient solution for x and y. (b) Write the particular solution. (c) Is the system stable? Why or why not? (d) Describe the shapes of each mode. (e) Sketch x versus t for each mode if $x = 1$ for $t = 0$.

9.2 In a wind tunnel, a wing having a mass of m is suspended from a spring having a constant of k. The wing can move vertically but is restrained from rotating. At rest, the wing is at a zero angle of attack. Derive an

expression for the vertical position of the wing as a function of time if the wing is displaced from its static position and released.

9.3 While undergoing phugoid motion, an airplane has a peak velocity of 150 m/s at some instant of time. Forty seconds later, it has a peak velocity of 134 m/s. As time progresses, the velocity approaches a steady value of 120 m/s. What is the undamped natural frequency and damping ratio for this motion?

9.4 Draw the patching diagram to solve Problem 9.1*a* with an analog computer.

9.5 For the Cherokee 180, calculate the criteria given by Equation 9.99 for airspeeds of 50, 60, and 70 kt at standard sea level conditions and a gross weight of 10.7 kN.

The following problems refer to the airplane pictured in Figure 8.43 with the center of gravity positioned to give a 10% stick-fixed static margin.

9.6 Calculate all of the longitudinal stability and control derivatives required to solve the longitudinal equations of motion.

9.7 Calculate the phugoid and short-period mode shapes for a Mach number of 0.5 at a standard altitude of 15,000 ft.

9.8 Calculate the flight path stability for an approach at 20% above the stall, SSL conditions.

9.9 Based on the results of Problems 9.7 and 9.8, assess the handling qualities of this airplane.

9.10 For the conditions of Problem 9.7, write a computer program to integrate numerically the longitudinal equations of motion, including a control input. Determine the answers to Problem 9.7 by means of the program.

REFERENCES

9.1 Chalk, C. R., Neal, T. P., Harris, T. M., and Pritchard, F. E., *Background Information and User Guide for MIL-F-8785B (ASG), "Military Specification—Flying Qualities of Piloted Airplanes,"* AFFDL-TR-69-72, August 1969.

TEN
LATERAL-DIRECTIONAL DYNAMIC STABILITY AND CONTROL

EQUATIONS OF MOTION

In the previous chapter we dealt with motion *in the plane* of symmetry. Motion *of the plane* of symmetry will now be considered. This motion consists of transition in the y direction called sideslip; rotation about the x-axis referred to as rolling; and rotation about the z-axis, or yawing. To begin, the equations of motion will once again be derived, but in a somewhat more basic and complete manner than that which was followed in Chapter Nine. The following derivation closely parallels a similar development presented by Seckel (Ref. 10.4).

Figure 10.1 illustrates a particle of mass of the airplane located at the point x, y, z, in the moving-body axis system. As shown, the axis system is translating with instantaneous velocity components of U, V, and W in the x, y, and z directions while rotating about these axes at angular rates of P, Q, and R.

The linear velocity components of ΔM in the x, y, and z directions are, obviously,

$$\dot{x} = U + Qz - Ry \tag{10.1a}$$

$$\dot{y} = V - Pz + Rx \tag{10.1b}$$

$$\dot{z} = W + Py - Qx \tag{10.1c}$$

The accelerations are obtained directly by differentiating the above velocities.

$$\ddot{x} = \dot{U} + \dot{Q}z + Q\dot{z} - \dot{R}y - R\dot{y} \tag{10.2a}$$

$$\ddot{y} = \dot{V} - \dot{P}z - P\dot{z} + \dot{R}x + R\dot{x} \tag{10.2b}$$

$$\ddot{z} = \dot{W} + \dot{P}y + P\dot{y} - \dot{Q}x - Q\dot{x} \tag{10.2c}$$

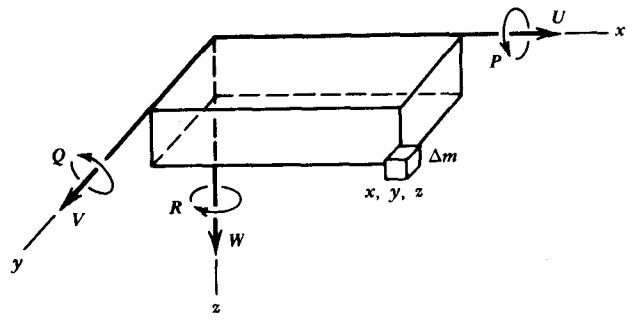

Figure 10.1 Motion of a particle of mass in a moving reference system.

$\dot{x}$, $\dot{y}$, and $\dot{z}$ are obtained from Equations 10.1, so Equation 10.2 becomes:

$$\ddot{x} = \dot{U} + QW + QPy - Q^2x - RV + RPz - R^2x + \dot{Q}z - \dot{R}y \qquad (10.3a)$$

$$\ddot{y} = \dot{V} - PW - P^2y - PQx + RU + RQz - R^2y - \dot{P}z + \dot{R}x \qquad (10.3b)$$

$$\ddot{z} = \dot{W} + PV - P^2z + PRx - QU - Q^2z + QRy + \dot{P}y - \dot{Q}x \qquad (10.3c)$$

It is convenient at this point to use the concept of inertia forces and moments. Briefly, this concept allows one to treat a dynamic system as a static one by employing pseudoforces acting on the system equal in magnitude to the product of each mass and its acceleration. The forces are directed opposite to the accelerations. As an example, consider Figure 10.2. The dynamic equation of motion is, obviously,

$$F = M\ddot{x} \qquad (10.4)$$

Now, however, add a force on the mass opposite in direction to $\ddot{x}$ equal to $M\ddot{x}$. As a problem in statics, the sum of the forces on the mass equals zero.

$$F - M\ddot{x} = 0$$

This, of course, is equal to Equation 10.4.

The inertia forces on the mass element can be written as

$$F_{x_i} = -m\ddot{x} \qquad (10.5a)$$

$$F_{y_i} = -m\ddot{y} \qquad (10.5b)$$

$$F_{z_i} = -m\ddot{z} \qquad (10.5c)$$

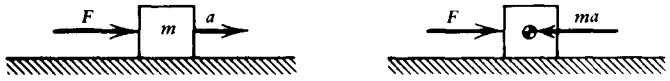

Figure 10.2 Concept of inertia force.

with $\ddot{x}$, $\ddot{y}$, and $\ddot{z}$ given by Equation 10.3. These inertia forces give rise to inertia moments. The moment arms can be seen in Figure 10.1. For example, an x force on Δm gives rise to a moment about the y-axis equal to $F_x Z$. Therefore, the three inertia moments become:

$$M_{x_i} = F_{z_i} y - F_{y_i} z \tag{10.6a}$$

$$M_{y_i} = F_{x_i} z - F_{z_i} x \tag{10.6b}$$

$$M_{z_i} = F_{y_i} x - F_{x_i} y \tag{10.6c}$$

This can be written in vector form as

$$\mathbf{M}_i = \mathbf{R} \times \mathbf{F}_i$$

The total inertia forces and moments acting on the airplane are obtained by summing Equations 10.5 and 10.6 over the total airplane mass. In evaluating these sums, the following sums vanish since the origin of the coordinate system is at the center of gravity

$$\sum \Delta m x = 0$$

$$\sum \Delta m y = 0$$

$$\sum \Delta m z = 0$$

Also, because of symmetry,

$$\sum \Delta m x y = 0$$

$$\sum \Delta m y z = 0$$

In addition, by definition,

$$I_x = \sum \Delta m (y^2 + z^2) \tag{10.7a}$$

$$I_y = \sum \Delta m (x^2 + z^2) \tag{10.7b}$$

$$I_z = \sum \Delta m (x^2 + y^2) \tag{10.7c}$$

$$I_{xz} = \sum \Delta m x z \tag{10.7d}$$

With these definitions, the total inertia forces and moments can be determined. From

$$\mathbf{F} + \mathbf{F}_i = 0$$

$$\mathbf{M} + \mathbf{M}_i = 0$$

it follows that

$$F_x = m(\dot{U} + QW - RV) \tag{10.8a}$$

$$F_y = m(\dot{V} - PW + RU) \tag{10.8b}$$

$$F_z = m(\dot{W} + PV - QU) \tag{10.8c}$$

$$L = I_x\dot{P} + QR(I_z - I_y) - I_{yz}(Q^2 - R^2) - I_{xz}(R + PQ) - I_{xy}(Q - PR) \tag{10.8d}$$

$$M = I_y\dot{Q} + PR(I_x - I_z) + I_{xz}(P^2 - R^2) - I_{yz}(R - PQ) - I_{xy}(P + QR) \tag{10.8e}$$

$$N = I_z\dot{R} + PQ(I_y - I_x) - I_{xy}(P^2 - Q^2) - I_{xz}(P - QR) - I_{yz}(Q + PR) \tag{10.8f}$$

Not included in these equations are angular momentum vectors that may be present because of rotors or other rotating components. If $\mathbf{h}$ denotes such an angular momentum vector, then $\boldsymbol{\omega} \times \mathbf{h}$ must be added to the above momentum equations. Thus Equation 10.8*d*, 10.8*e*, and 10.8*f* becomes,

$$L = I_x\dot{P} - I_{xz}\dot{R} + Qh_z - Rh_y \tag{10.9a}$$

$$M = I_y\dot{Q} - Ph_y + Rh_x \tag{10.9b}$$

$$N = I_z\dot{R} - I_{xz}\dot{P} + Ph_y - Rh_z \tag{10.9c}$$

Equations 10.8*a*, 10.8*c*, and 10.8*e* were derived previously in Chapter Nine and were used to examine longitudinal dynamic stability and control. Equations 10.8*b*, 10.8*d*, and 10.8*f* will be used for the analysis of lateral-directional stability and control.

EULER ANGLES

Although we will not be concerned with them to any extent, it might be well at this point to define the so-called Euler angles. Finite angular rotations of an airplane about its own body axes are not commutative. The final orientation of the airplane will depend on the order in which the rotations are performed. To illustrate this, hold a small model in front of you, heading directly away from you with wings level. Now rotate the model 90° about its x-axis, then 90° about its y-axis, and then 90° around its z-axis, all directions positive in accordance with the right-hand rule. The model will now be pointing nose-down with its top toward you. Now reverse the order. Rotate it 90° about its z-axis, then the y-axis, and then the x-axis. In this case, the model's final orientation will be nose-up with its top toward you.

The Euler angles, starting with a given airplane orientation, are rotations denoted by ϕ, θ, and ψ about the x, y, and z-axes, respectively. However, the order of rotation is *first* about the z-axis, then about the y-axis, and then about the x-axis. In other words, the airplane is first yawed, then pitched, and then rolled.

With this order of rotation, the components of the angular velocity vector, P, Q, and R, are related to $\dot{\phi}$, $\dot{\theta}$, and $\dot{\psi}$ by,

$$P = \dot{\phi} - \dot{\psi} \sin \theta \tag{10.10a}$$

$$Q = \dot{\theta} \cos \phi + \dot{\psi} \cos \theta \sin \phi \tag{10.10b}$$

$$R = \dot{\psi} \cos \theta \cos \phi - \dot{\theta} \sin \phi \tag{10.10c}$$

For small values of ϕ, θ, and ψ, these become

$$P \simeq \dot{\phi} \tag{10.11a}$$

$$Q \simeq \dot{\theta} \tag{10.11b}$$

$$R \simeq \dot{\psi} \tag{10.11c}$$

REDUCTION OF THE LATERAL-DIRECTIONAL EQUATIONS OF MOTION

The lateral-directional equations of motion are linearized and nondimensionalized in a manner similar to that followed for longitudinal motion. The resultant velocity is taken to be nearly constant and equal to U_0. V and W are assumed to be small by comparison to U_0. The angles ϕ, θ, and ψ and their derivatives are also taken to be small. Orders higher than the first for any of these small quantities are neglected. Also, the velocity V is replaced by $U_0\beta$. Hence the lateral-directional equations reduce to

$$y + mg\phi = mU_0(\dot{\beta} + R) \tag{10.12a}$$

$$L = I_x\ddot{\phi} - I_{xz}\dot{R} \tag{10.12b}$$

$$N = I_z\dot{R} - I_{xz}\ddot{\phi} \tag{10.12c}$$

The aerodynamic force, Y, and moments, L and N, are expressed in coefficient form using S as the reference area and b as the reference length. The coefficients are then expanded in a Taylor series, assuming them to be a function of β, $\bar{p}$, $\bar{r}$, δ_a, and δ_r. $\bar{p}$ and $\bar{r}$ are dimensionless rates similar to $\bar{q}$ and are defined by

$$\bar{p} = \frac{Pb}{2U_0} \tag{10.13a}$$

$$\bar{r} = \frac{Rb}{2U_0} \tag{10.13b}$$

Again a characteristic time t^* is defined. However, in the lateral-directional case, the reference length is taken as $b/2$.

$$t^* = \frac{b}{2U_0} \tag{10.14}$$

The dimensionless time τ is given by

$$\tau = \frac{t}{t^*} \tag{10.15}$$

The mass and moments of inertia are expressed by

$$I_x = i_x \rho S \left(\frac{b}{2}\right)^3 \tag{10.16a}$$

$$I_z = i_z \rho S \left(\frac{b}{2}\right)^3 \tag{10.16b}$$

$$I_{xz} = i_{xz} \rho S \left(\frac{b}{2}\right)^3 \tag{10.16c}$$

$$m = \mu \rho S \frac{b}{2} \tag{10.16d}$$

Substituting Equations 10.13 to 10.16 into Equation 10.12 results in the final nondimensional, linearized equations of motion governing lateral-directional motion.

$$C_{Y_\beta}\beta + C_{Y_{\dot\beta}}\dot\phi + C_{L_0}\phi + C_{Y_r}\bar r + C_{Y_{\delta_r}}\delta_r = 2\mu(\dot\beta + \bar r) \tag{10.17a}$$

$$C_{l_\beta}\beta + C_{l_{\dot\beta}}\dot\phi + C_{l_r}\bar r + C_{l_{\delta_a}}\delta_a + C_{l_{\delta_r}}\delta_r = i_x\ddot\phi - i_{xz}\dot{\bar r} \tag{10.17b}$$

$$C_{n_\beta}\beta + C_{n_{\dot\beta}}\dot\phi + C_{n_r}\bar r + C_{n_{\delta_a}}\delta_a + C_{n_{\delta_r}}\delta_r = i_z\dot{\bar r} - i_{xz}\ddot\phi \tag{10.17c}$$

In Equation 10.17, all derivatives indicated by a dot are with respect to the dimensionless time τ.

A SUMMARY LOOK AT THE STABILITY DERIVATIVES AND OTHER PARAMETERS AFFECTING LATERAL-DIRECTIONAL DYNAMIC MOTION

Y Derivatives

Equation 10.17*a* is the equation governing primarily the acceleration of the airplane's mass in the *y* direction. It contains the stability derivatives, C_{Y_β}, $C_{Y_{\dot\beta}}$, and C_{Y_r}, the control derivative $C_{Y_{\delta_r}}$, and the parameters, C_{L_0} and μ. C_{L_0} is the trim lift coefficient and needs no further explanation. The dimensionless mass μ is defined by Equation 10.16*d*. For the Cherokee 180 example used previously at an altitude of 1500 m,

$$\mu = \frac{2m}{\rho S b}$$

$$= 15.2$$

$$C_{L_0} = 0.543$$

C_{Y_β}

The side force derivative, C_{Y_β}, consists primarily of contributions from the fuselage, the vertical tail, and the normal force resulting from the propulsion system.

Referring to Figure 8.25, a positive sideslip angle of β results in a negative side force on the fuselage and vertical tail. The force on the fuselage can be estimated on the basis of Equation 8.71. The y force on the vertical tail will be given by

$$Y_v = -\eta_t q S_v a_v \beta (1 - \epsilon_\beta)$$

or

$$C_{Y_v} = -\eta_t \frac{S_v}{S} a_v \beta (1 - \epsilon_\beta) \tag{10.18}$$

For the Cherokee 180, the effective aspect ratio of the vertical tail (see discussion following Equation 8.90) is estimated to equal 2.84. This value of A substituted into Equation 3.70 gives an estimated lift curve slope of 3.04/rad. The ratio S_v/S equals 0.0713. ϵ_β is taken to be zero, and η_t to be unity so

$$C_{Y_{\beta_v}} = -0.216/\text{rad}$$

The fuselage and propeller contributions to C_{Y_β} are assumed to equal their contributions to C_{z_α} that were previously estimated to total -0.18/rad. Thus the total side force derivative for the Cherokee 180 is estimated to equal

$$C_{Y_\beta} = -0.396/\text{rad}$$

$C_{Y_{\bar{p}}}$

The side force resulting from the rolling velocity is normally small. It results primarily from the vertical tail lying above the longitudinal axis through the center of gravity. If the aerodynamic center of the vertical tail lies a distance of Z_v above the center of gravity, then it will experience, as shown in Figure 10.3, an angle of attack resulting from a roll rate, P, equal to

$$\Delta\alpha = \frac{PZ_v}{U_0}$$

The direction of $\Delta\alpha$ is such as to produce a negative Y force, given by

$$Y_v = -\eta_t q S_v a_v \frac{PZ_v}{U_0}$$

In coefficient form,

$$C_{Y_v} = -2\eta_t \frac{S_v}{S} \frac{Z_v}{b} a_v \bar{p} \tag{10.19}$$

where

$$\bar{p} = \frac{Pb}{2U_0}$$

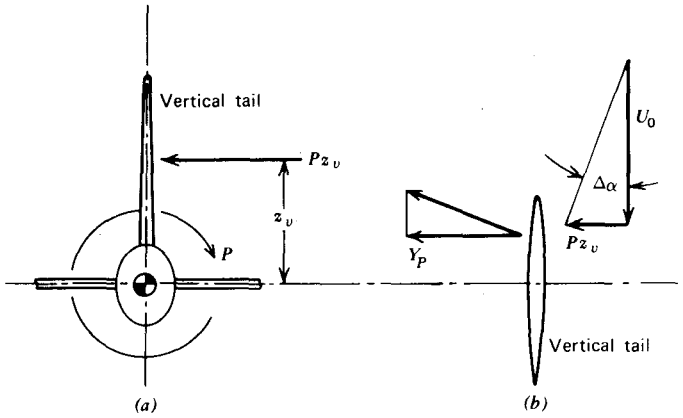

Figure 10.3 Angle-of-attack increment at vertical tail resulting from roll rate. (*a*) Rear view. (*b*) Top view.

For the Cherokee 180, $Z_v/b \simeq 0.09$. Thus,

$$C_{Y_{\bar{p}}} = -0.039$$

$C_{Y_{\bar{r}}}$

The side force due to yaw rate results from the damping force on the vertical tail and on the propulsor.

If the vertical tail is aft of the center of gravity a distance of l_v, a yaw rate of R will produce on increment in the angle of attack, as shown in Figure 10.4, equal to

$$\Delta\alpha = \frac{l_v R}{U_0}$$

A side force in the y direction results, given by

$$Y_v = \eta_t q S_v a_v \frac{R l_v}{U_0}$$

In coefficient form, this becomes

$$C_{Y_v} = 2\eta_t a_v V_v \bar{r} \tag{10.20}$$

V_v is the vertical tail volume defined previously, and $\bar{r}$ is the dimensionless yaw rate.

For the Cherokee 180, $V_v \simeq 0.031$. Thus,

$$C_{Y_{v_{\bar{r}}}} = 0.188$$

In a similar manner, a propeller experiences an angle-of-attack change

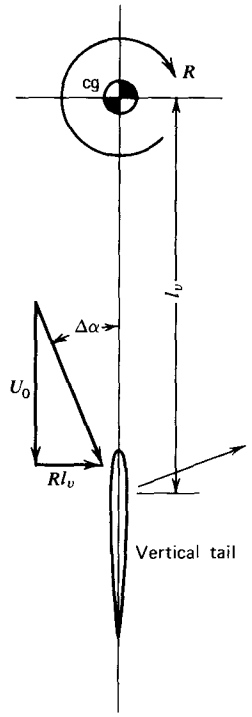

Figure 10.4 Angle-of-attack increment at vertical tail due to yaw rate. Top view.

due to R, given by

$$\Delta\alpha = \frac{Rl_p}{U_0}$$

where l_p represents the distance of the propeller ahead of the center of gravity. The direction of $\Delta\alpha$ is opposite to that shown in Figure 10.4, so the Y force on the propeller is

$$Y_{\text{prop}} = -P_{N_\alpha} \frac{Rl_p}{U_0}$$

In dimensionless form this becomes

$$C_{Y_{\text{prop}}} = -2 \frac{P_{N_\alpha}}{T} \frac{T}{qS} \frac{l_p}{b} \bar{r}$$

or

$$C_{Y_{\text{prop}}} = -2 \frac{P_{N_\alpha}}{T} C_{D_0} \frac{l_p}{b} \bar{r} \tag{10.21}$$

For the Cherokee 180, the following quantities were estimated previously for the trim condition of 50 m/s at an altitude of 1500 m and a gross weight of 10,680 N.

$$\frac{P_{N_\alpha}}{T} = 0.8/\text{rad}$$

$$C_{D_0} = 0.0615$$

l_p/b equals 0.236. Hence

$$C_{Y_{F_{\text{prop}}}} = -0.0232/\text{rad/air sec}$$

The total C_{Y_r} for the Cherokee is therefore estimated to be

$$C_{Y_r} = 0.165$$

$C_{Y_{\delta_r}}$

The control derivative giving the rate of change of side force with rudder deflection is found from

$$\Delta y = \eta_t q S_v a_v \tau_r \delta_r$$

or, in coefficient form,

$$C_{Y_{\delta_r}} = \eta_t a_v \tau_r \frac{S_v}{S} \tag{10.22}$$

For the Cherokee 180, τ_r is estimated, using Figures 3.32 and 3.33 to equal 0.54. Thus,

$$C_{Y_{\delta_r}} = 0.117/\text{rad}$$

l Derivatives

Equation 10.17*b* governs primarily the angular acceleration about the roll axis. The stability derivatives C_{l_β}, $C_{l_{\dot\beta}}$, C_{l_p}, the control derivatives $C_{l_{\delta_a}}$, $C_{l_{\delta_r}}$, and the parameters i_x and i_{xz} are needed to evaluate this equation.

From the definition of i_x given by Equation 10.16*a*, for the Cherokee 180,

$$i_x \simeq 24.6$$

The product of inertia I_{xz} is unavailable for the example airplane. If the x-axis is a principle axis, I_{xz} is equal to zero, so it is reasonable to assume that I_{xz} is small. Therefore, it will be assumed that

$$i_{xz} \simeq 0$$

C_{l_β}

This derivative, known as "dihedral effect," has been previously covered in some depth. C_{l_β} can be calculated on the basis of Equations 8.108 to 8.112. The Cherokee 180 is a low-wing airplane having a dihedral angle of 7.5°. The

wing is unswept, untapered, and has an aspect ratio of 5.625. From Figure 8.39, the contribution to C_{l_β} from the wing equals −0.0895/rad. To this we add 0.0092 to account for the presence of the fuselage. Thus, for the wing-fuselage combination,

$$C_{l_\beta} = -0.0803/\text{rad}$$

The vertical tail placed above the center of gravity also contributes to C_{l_β}. At a sideslip angle of β, the vertical tail develops a side force in the negative y direction equal to

$$\Delta y = -\eta_t q S_v a_v \beta$$

Acting at a height above the center of gravity of Z_v, this increment in the y force gives rise to a rolling moment equal to

$$\Delta l = -\eta_t q S_v a_v A_v \beta$$

Thus, in coefficient form,

$$C_{l_{\beta_v}} = -\eta_t \frac{S_v}{S} \frac{Z_v}{b} a_v \tag{10.23}$$

For the Cherokee 180,

$$C_{l_{\beta_v}} = -0.0195/\text{rad}$$

Adding the contribution of the vertical tail to that of the wing-fuselage combination gives a total dihedral effect of

$$C_{l_\beta} = -0.0998/\text{rad}$$

An effect that is not included here, but that can be important, particularly at low speeds with flaps down, is illustrated in Figure 10.5. As a propeller-driven airplane slips to the right, the slipstream trails to the left, causing an increased lift on the left wing. This can result in a significant increase in C_{l_β}. This interaction is difficult to predict in a general way. It is best obtained by means of wind tunnel testing with a powered model.

$C_{l_{\bar{p}}}$

The roll damping coefficient can be calculated on the basis of Figure 8.36 for both the wing and horizontal tail. For the Cherokee's wing, $C_{l_{\bar{p}}} = -0.420$. For the horizontal tail, $A_t = 4.10$ and $\lambda_t = 1.0$. Thus, from Figure 8.36, $C_{l_{\bar{p}_t}} = -0.335$. However, this value is based on the tail area and span. To base $C_{l_{p_t}}$ on the wing's dimension, we note that

$$l_t = \eta_t q S_t b_t \frac{p b_t}{2V} C_{l_{p_t}}$$

Thus,

$$\frac{l_t}{qSb\bar{p}} = \eta_t \frac{S_t}{S} \left(\frac{b_t}{b}\right)^2 C_{l_{p_t}} \tag{10.24}$$

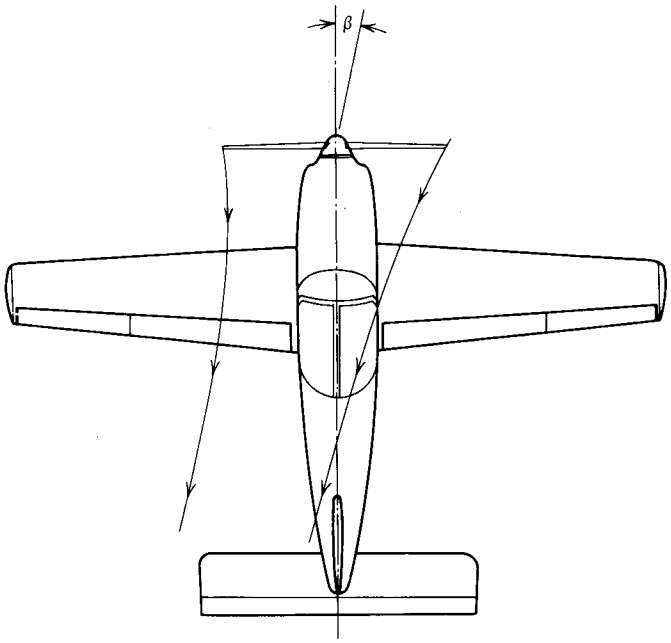

Figure 10.5 Effect of slipstream on dihedral effect.

For the Cherokee,

$$\frac{S_t}{S}\left(\frac{b_t}{b}\right)^2 = 0.017$$

Thus the total C_{l_β} due to the wing and horizontal tail is equal to -0.426.

The vertical tail also contributes to C_{l_β}. As recommended in Chapter Eight, Figure 8.36 can also be applied to the vertical tail as if it extended below the fuselage to the same extent as above. The value obtained is then halved and corrected according to Equation 10.24. For the Cherokee the increment to C_{l_β} from the vertical tail is approximately half of that from the horizontal tail. Thus, for the Cherokee 180,

$$C_{l_\beta} = -0.429$$

C_{l_r}

The rate of change of rolling moment with yawing velocity was considered in Chapter Eight. C_{l_r} is composed of two contributions, one from the wing and the other from the vertical tail. According to Equation 8.103 for the

Cherokee 180, the wing's contribution to C_{l_r} will equal

$$C_{l_r} = \frac{C_{L_0}}{6}\left(\frac{1+3\lambda}{1+\lambda}\right)$$
$$= 0.181$$

The contribution to C_{l_r} from the vertical tail is given by Equation 8.105.

$$C_{l_r} = C_{y_{v_r}}\frac{Z_v}{b}$$
$$= 0.017$$

Hence, the total C_{l_r} for the Cherokee 180 is estimated to equal

$$C_{l_r} = 0.198$$

$C_{l_{\delta_a}}$

Aileron roll control was covered in Chapter Eight. $C_{l_{\delta_a}}$ can be estimated on the basis of Figure 8.30*b*. For the Cherokee 180,

$$\lambda = 1.0$$
$$A = 5.625$$
$$x_1 = 0.603$$
$$x_2 = 1.0$$
$$\frac{c_a}{c} = 0.193$$

Using these equations and a linear interpolation for aspect ratio for values of A between 4 and 6 gives a value for $C_{l_{\delta_a}}$ from Figure 8.30*b* of

$$C_{l_{\delta_a}} = -0.0531/\text{rad}$$

Since the maximum aileron deflection for the Cherokee is 30° up and 15° down, the total δ_a of 45° gives a predicted

$$C_{l_{\delta_{max}}} = 0.0417$$

$C_{l_{\delta_r}}$

$C_{l_{\delta_r}}$ can be found from Equations 8.101 and 8.102. For the Cherokee 180, $C_{Y_{\delta_r}}$ was estimated to equal 0.117/rad. Therefore,

$$C_{l_{\delta_r}} = C_{Y_{\delta_r}}\frac{Z_v}{b}$$
$$= 0.0105/\text{rad}$$

N Derivatives

C_{N_β}

The change of yawing moment coefficient was covered in Chapter Eight. Equation 8.90 expresses the contribution from the vertical tail as

$$C_{N_{v_\beta}} = \eta_t V_v a_v (1 - \epsilon_\beta)$$
$$= 0.094/\text{rad}$$

for the Cherokee.

The contributions to C_{N_β} from both the propeller and fuselage are obtained from the values estimated in Chapter Nine for C_{M_α}. There, the total C_{M_α} from the fuselage and propeller was estimated to equal 0.153/rad. To obtain C_{N_β}, the sign must be reversed and C_{M_α} multiplied by $\bar{c}/b$. Thus, due to the fuselage and propeller,

$$C_{N_\beta} = -0.0268/\text{rad}$$

Thus, for the Cherokee 180,

$$C_{N_\beta} = 0.0672/\text{rad}$$

$C_{N_{\bar{p}}}$

$C_{N_{\bar{p}}}$ is given by Equation 8.107. For the Cherokee 180 at a trim lift coefficient of 0.543, this equation reduces to

$$C_{N_{\bar{p}}} = -0.0905$$

this contribution comes from the wing. There will also be a small contribution from the vertical tail, given by

$$C_{N_{\bar{p}_v}} = -C_{Y_{\bar{p}}} \frac{l_v}{b}$$

or, for the Cherokee,

$$C_{N_{\bar{p}_v}} = -0.017$$

Thus, the total becomes

$$C_{N_{\bar{p}}} = -0.0735$$

$C_{N_{\bar{r}}}$

$C_{N_{\bar{r}}}$ can be obtained directly from the vertical tail and propeller contributions to $C_{Y_{\bar{r}}}$. It is left to you to show that

$$C_{N_{\bar{r}}} = -C_{Y_{\bar{r}_v}} \frac{l_v}{b} + C_{Y_{\bar{r}_p}} \frac{l_p}{b} \tag{10.25}$$

or, for the Cherokee,

$$C_{N_{\bar{r}}} = -0.188(0.435) - 0.0232(0.236)$$
$$= -0.0873$$

$C_{N_{\delta_a}}$

The adverse aileron yaw is difficult to estimate. In view of the differential aileron deflections used on the Cherokee, it will be assumed that $C_{N_{\delta_a}} = 0$.

$C_{N_{\delta_r}}$

$C_{N_{\delta_r}}$ is given by

$$C_{N_{\delta_r}} = -C_{Y_{\delta_r}} \frac{l_v}{b} \tag{10.26}$$

Thus, for the Cherokee,

$$C_{N_{\delta_r}} = -0.0509/\text{rad}$$

In addition to the stability derivatives, the parameter i_Z is needed to evaluate Equation 10.17*c*. From Equation 10.16*b*, for the Cherokee 180,

$$i_Z \simeq 1.18$$

LATERAL-DIRECTIONAL EQUATIONS FOR THE CHEROKEE 180

The three equations governing the lateral-directional motion and control of the Cherokee 180 are obtained by substituting the calculated stability and control derivatives into Equation 10.17. This reduces to:

$$30.4\dot{\beta} + 0.396\beta + 0.039\dot{\phi} - 0.543\phi + 30.2\bar{r} = 0.117\,\delta_r \tag{10.27a}$$

$$0.0993\beta + 0.153\ddot{\phi} + 0.429\dot{\phi} - 0.198\bar{r} = 0.0531\,\delta_a + 0.0105\,\delta_r \tag{10.27b}$$

$$-0.0672\beta + 0.0735\dot{\phi} + 1.18\dot{\bar{r}} + 0.0873\bar{r} = -0.0509\,\delta_r \tag{10.27c}$$

The characteristic equation for this set of simultaneous, linear differential equations is obtained from the determinant.

$$\begin{vmatrix} (30.4\sigma + 0.396) & +(0.039\sigma - 0.543) & 30.2 \\ 0.0998 & (0.153\sigma^2 + 0.429\sigma) & -.198 \\ -0.0672 & +0.0735\sigma & (1.18\sigma + 0.08.73) \end{vmatrix} = 0$$

This determinant reduces to the following.

$$\sigma^4 + 2.90\sigma^3 + 0.381\sigma^2 + 0.215\sigma - 0.000454 = 0 \tag{10.28}$$

Since the constant is negative, it is obvious that Equation 10.28 will have a positive real root. Thus the Cherokee is predicted to possess at least one mode of the lateral-directional motion that is unstable.

Typical of lateral-directional motion, Equation 10.28 has two real roots and a pair of complex roots. The real roots can be found from trial and error,

by graphical means, or otherwise to equal

$$\sigma_1 = -2.79$$
$$\sigma_2 = 0.00210$$

$(\sigma - \sigma_1)$ can be divided into Equation 10.28 (simply follow the same procedure as is done in a long division problem) to obtain a cubic. The cubic is then divided by $(\sigma - \sigma_2)$ to obtain a quadratic, which can be solved for the pair of complex roots

$$\sigma_3 = -0.055 + 0.277i$$
$$\sigma_4 = -0.055 - 0.277i$$

Mode Shapes

The significance of these roots and the instability exhibited by the positive real root can be examined by looking at the shapes of each mode in the same manner that was followed for the longitudinal motion.

For the transient solution, δ_a and δ_r are zero. Using Equation 10.27*a* and 10.27*b*, we can eliminate $\bar{r}$ to solve for the ratio of ϕ to β. This result, which holds for any σ, is

$$\frac{\phi}{\beta} = -\frac{\sigma + 0.513}{0.766\sigma^2 + 2.15\sigma - 0.0180} \tag{10.29}$$

$\bar{r}/\beta$ can then be obtained from any one of the equations. Using Equation 10.27*a*

$$\frac{\bar{r}}{\beta} = -(1.007\sigma + 0.0131) - \frac{\phi}{\beta}(0.00129\sigma - 0.0180) \tag{10.30}$$

Roll Mode

For $\sigma = -2.79$, ϕ/β and $\bar{r}/\beta$ become

$$\frac{\phi}{\beta} = -42.3$$

$$\frac{\bar{r}}{\beta} = 1.88$$

Since $\bar{r} \simeq \dot{\psi}$, we can replace $\bar{r}$ by $\sigma\psi$, so that

$$\frac{\psi}{\beta} = -0.674$$

or

$$\frac{\phi}{\psi} = 62.8$$

For this mode, it is seen that both β and ψ are small compared to ϕ. Thus, this mode is predominantly a damped rolling motion. Indeed, if one neglects all but the ϕ terms in Equation 10.27*b*, a value for σ of -2.80 that is very close to the exact value is obtained immediately.

The time for the roll rate to damp to half of its initial value can be found from Equation 9.72 to be

$$T_{1/2} = -\frac{\ln 2}{\sigma}$$
$$= 0.248 \text{ air sec}$$

For the lateral motion, from Equation 10.14,

$$t^* = \frac{b}{2U_0}$$
$$= \frac{9.14}{2(50)}$$
$$= 0.0914 \text{ sec}$$

Thus,

$$T_{1/2} = 0.0227 \text{ sec}$$

Obviously, this is a heavily damped, stable mode.

Spiral Mode

Consider the positive real root, $\sigma = 0.00210$. In this case, from Equation 10.29,

$$\frac{\phi}{\beta} = 38.5$$
$$\frac{\bar{r}}{\beta} = 0.677$$

or, again replacing $\bar{r}$ by $\sigma\psi$,

$$\frac{\psi}{\beta} = 323$$

or

$$\frac{\phi}{\psi} = 0.119$$

For this mode, the motion is seen to be predominantly a heading change with a small roll angle and sideslip angle. With σ being positive, these angles increase with time, so the mode is actually unstable! With ψ increasing exponentially with time, the flight path of the airplane describes a spiral. Thus, this mode is referred to as the spiral mode. If it is unstable, as in this case, the motion is referred to as spiral divergence; otherwise, it is referred to as spiral convergence.

The time to double amplitude is found from

$$\tau_{\text{dbl}} = \frac{\ln 2}{\sigma}$$
$$= 330 \text{ air sec}$$

or

$$T_{\text{dbl}} = 30.2 \text{ sec}$$

This time is characteristic of many aircraft and is sufficiently long so that the pilot compensates for the divergence without realizing it. Although spiral divergence cannot be described as unsafe, it can result in extreme attitudes if the pilot should be studying a chart and forgets to fly the airplane for a few moments. It can prove catastrophic for the noninstrument-rated pilot who finds herself or himself in instrument conditions.

The root for the spiral mode is normally small, so it can be closely approximated by the constant term in the characteristic equation divided by the coefficient of σ to the first power. From Equation 10.17, the determinant defining the characteristic equation is:

$$\begin{vmatrix} (2\mu\sigma - C_{Y_\beta}) & -(C_{Y_{\hat{p}}}\sigma + C_{L_0}) & (2\mu - C_{Y_{\hat{r}}}) \\ -C_{l_\beta} & (i_x\sigma^2 - C_{l_{\hat{p}}}\sigma) & -(i_{xz}\sigma + C_{l_{\hat{r}}}) \\ -C_{N_\beta} & -(i_{xz}\sigma^2 + C_{N_{\hat{p}}}\sigma) & (i_z\sigma - C_{N_{\hat{r}}}) \end{vmatrix} = 0$$

When this determinant is expanded for typical values of the stability derivatives, one obtains approximately

$$2\mu(C_{l_\beta}C_{N_{\hat{p}}} - C_{N_\beta}C_{L_{\hat{p}}})\sigma = C_{L_0}(C_{N_\beta}C_{l_{\hat{r}}} - C_{l_\beta}C_{N_{\hat{r}}})$$

or

$$\sigma = \frac{C_{L_0}}{2\mu}\frac{C_{N_\beta}C_{l_{\hat{r}}} - C_{l_\beta}C_{N_{\hat{r}}}}{C_{l\beta}C_{N_{\hat{p}}} - C_{N_\beta}C_{l_{\hat{p}}}} \tag{10.31}$$

Equation 10.31 neglects terms in σ of order higher than the first. It also neglects some first-order terms in σ that are typically small. For the Cherokee, this approximation for the root of the spiral mode gives a value of 0.00227 that is 8% higher than the exact value.

The denominator of Equation 10.31 is usually positive, so the combination of terms in the numerator governs whether or not the spiral mode

is stable. For spiral convergence,

$$C_{N_\beta} C_{l_r} < C_{l_\beta} C_{N_r} \tag{10.32}$$

Since most of the contribution to C_{l_r} results from the wing, this derivative is not too easily adjusted. Varying the vertical tail size will change C_{N_β} and C_{N_r} approximately in the same proportion. Also, the vertical tail size is normally fixed by other considerations. Hence the primary control on the spiral mode is exercised through C_{l_β}, the dihedral. Increasing the dihedral effect will tend to make the spiral mode more stable. However, as stated previously, too much dihedral leads to an unpleasant feel to the airplane.

Oscillatory or "Dutch Roll" Mode

The pair of complex roots of the characteristic equation for the lateral-directional motion of the Cherokee was given previously as $-0.055 \pm 0.277i$. When substituted into Equation 10.29 (using $+0.277i$) and Equation 10.30, the following results are obtained.

$$\frac{\phi}{\beta} = -0.192 + 0.864i$$

or

$$\frac{\phi}{\beta} = 0.885 e^{i\gamma} \tag{10.33}$$

where $\gamma = 102.5°$.

Also,

$$\frac{\bar{r}}{\beta} = 0.0392 - 0.263i$$

Replacing $\bar{r}$ by $\sigma\psi$ gives

$$\frac{\psi}{\beta} = -0.940 + 0.045i$$

or

$$\frac{\psi}{\beta} = 0.941 e^{i\gamma} \tag{10.34}$$

where $\gamma = 177.3°$.

Relating ψ to ϕ,

$$\frac{\psi}{\phi} = 1.06 e^{i\gamma} \tag{10.35}$$

where $\gamma = 74.8°$.

This mode is a damped oscillation where the three angles ϕ, β, and ψ have approximately the same magnitudes. In the case of the Cherokee 180, the time to damp to half-amplitude equals 1.15 sec with a period of 2.07 sec.

The motion of the airplane for this mode can be described as follows. Imagine that the airplane begins to yaw to the right. As it does so, it slips to

the left, so that its path remains nearly a straight line. As it yaws to the right, it begins to roll in that direction. While still rolled to the right, the airplane begins to yaw to the left and slip to the right. This turning and rolling motion is somewhat mindful of the weaving and twisting that an ice skater undergoes in skating along the ice. Hence the mode has come to be called the "Dutch roll" after the country well known for its ice skating.

This mode, for the Cherokee 180, is barely discernable to the pilot. It can be excited by a step input to the rudder and is observable. However, as predicted, it damps rapidly. For some airplanes the Dutch roll mode is lightly damped, making them somewhat unpleasant to fly. One gets the feeling that the rear end is trying to pass the front end.

LATERAL-DIRECTIONAL FLYING QUALITIES

Requirements on the three lateral-directional modes to assure a desired level of flying quality can be found in Reference 9.1. Although specific to military aircraft, these criteria can obviously prove of use in the evaluation or design of civil aircraft. Tables 10.1, 10.2, and 10.3 present criteria for the three

Table 10.1 Maximum Roll Mode Constant

Flight Phase Category	Class[a]	Level 1	Level 2	Level 3
A	I, IV	1.0	1.4	
	II, III	1.4	3.0	
B	All	1.4	3.0	10
C	I, II-C, IV	1.0	1.4	
	II-L, III	1.4	3.0	

[a] C and L refer to carrier and land operations.

Table 10.2 Minimum Dutch Roll Frequency and Damping

Level	Flight Phase Category	Class	Min ζ	Min $\zeta\omega_n$, rad/sec	Min ω_n, rad/sec
	A	I, IV	0.19	0.35	1.0
		II, III	0.19	0.35	0.4
1	B	All	0.08	0.15	0.4
	C	I, II-C			
		IV	0.08	0.15	1.0
		II-L, III	0.08	0.15	0.4
2	All	All	0.02	0.05	0.4
3	All	All	0.02	—	0.4

Table 10.3 Spiral Stability—Minimum Time-to-Double Amplitude

Class	Flight Phase Category	Level 1, sec	Level 2, sec	Level 3, sec
I and IV	A	12	12	4
	B and C	20	12	4
II and III	All	20	12	4

modes as a function of the Cooper-Harper level, flight phase category, and class of airplane. Airplane class is defined according to:

Class I —Small, light airplanes.
Class II —Medium weight, low-to-medium maneuverability.
Class III—Large, heavy, low-to-medium maneuverability.
Class IV—High maneuverability.

Roll Mode

Table 10.1 presents the maximum roll mode time constants that should not be exceeded in order to achieve a given flying quality level. In order to interpret this table, one needs to understand the meaning of the term "time constant."

A first-order, linear system $x(t)$ obeys a differential equation, which can be written as

$$\dot{x} + \frac{1}{\tau}x = f(t) \tag{10.36}$$

where τ is defined as the time constant. For the homogeneous solution, x will be of the form

$$x = x_0 e^{\sigma t}$$

so Equation 10.36 becomes

$$\left(\sigma + \frac{1}{\tau}\right)x = 0$$

or

$$\sigma = -\frac{1}{\tau} \tag{10.37}$$

The homogeneous solution for x can therefore be written as

$$x = x_0 e^{-t/\tau} \tag{10.38}$$

Thus, the time constant, τ, is a measure of the damping in a first-order system.

The more heavily damped a system, the smaller will be its time constant. Given an initial displacement and released, the system will damp to $1/e$ or 0.368 of its initial displacement in a time equal to the time constant. The time to halve amplitude and the time constant, τ, are related by

$$T_{1/2} = 0.693\tau \tag{10.39}$$

For the Cherokee 180 example, for the roll mode, $\sigma = -2.79$, so

$$\tau = 0.350 \text{ air sec}$$

or, in real time,

$$\tau = 0.033 \text{ sec}$$

This value is well within the level 1 criteria for the class I airplane for all flight phases.

Dutch Roll Mode

Table 10.2 presents criteria for the frequency and damping ratio for the Dutch roll mode. Note that minimum values are specified for ζ, ω_n, and for the product $\zeta\omega_n$. The minimum value for ω_n is determined from the column labeled ω_n. However, the governing damping requirement equals the largest value of ζ obtained from either of the two columns labeled ζ and $\zeta\omega_n$.

For the Cherokee 180 example, in real time,

$$\sigma = -0.601 \pm 3.03i$$

Thus, from Equation 9.51,

$$\zeta = 0.194$$

$$\omega_n = 3.09 \text{ rad/sec}$$

With reference to Table 10.2, the Cherokee's damping in this mode is governed by the column labeled ζ and is seen to be nearly equal to the minimum value prescribed for a flying quality level of 1 in the flight phase category A. Thus one would not expect to encounter any problems from the Dutch roll mode with this airplane.

Spiral Stability

The use of Table 10.3 should be obvious and needs no explanation. For the Cherokee example, the "time to double" of 30.2 sec is seen to exceed all of the minimum times specified in this table.

SPINNING

When stalled an airplane has a tendency to "drop off" into a spin, particularly if the stall is asymmetrical or entered with power. A pilot can purposefully initiate a spin by kicking the rudder hard to one direction at the top of the stall.

In a spin, an airplane rotates around a vertical spin axis as it is descending rapidly in a nose-down attitude. The path of its center of gravity prescribes a helix around the spin axis. The airplane's motion and attitude result in a high angle of attack on the order of 45° or more.

The stall/spin is one of the major causes of light plane accidents today. In my opinion, the blame for this can be placed on pilot training instead of current airplane designs. On a landing approach, too many pilots fly too slow. Rarely is there a valid reason for dragging a light airplane in under power at a speed just above the stalling speed. Under such a condition, an unexpected gust or a maneuver on the part of the pilot can produce an asymmetrical stall. If this occurs on the approach, the altitude may be insufficient to recover from either the stall or ensuing spin, regardless of how well the airplane is designed.

FAR Part 23 requires, for the normal category, that a single-engine airplane be able to recover from a one-turn spin in not more than one additional turn, with the controls applied in the manner normally used for recovery. Normally, to recover from a spin, one uses forward stick and rudder opposite to the direction of the spin. Ailerons are generally ineffective for spin recovery, since the wing is fully stalled. FAR Part 23 also requires, for the normal category, that the positive limit maneuvering load factor and applicable airspeed limit not be exceeded in a spin. In addition, there may be no excessive back pressure (on the stick) during the spin or recovery, and it must be impossible to obtain uncontrollable spins with any use of the controls.

The analysis of spinning, in order to design for good spin-recovery characteristics, is difficult because of the nonlinear nature of the problem. However, one can understand the principal factors influencing spin recovery by reference to Figure 10.6. A side view of the spinning airplane is shown in Figure 10.6*a*. As the airplane descends, the aerodynamic forces on the aft fuselage and tail, F_F and F_T, tend to nose the airplane downward. However, in a nose-down attitude, because of the rotation, centrifugal forces are developed on the airplane's mass to either side of the center of gravity. These create a pitching moment about the center of gravity that opposes the nose-down aerodynamic moment.

The wing is completely stalled in a spin so that its resultant force, F_w, is approximately normal to the wing. In a nose-down altitude, the horizontal component of F_w points in toward the spin axis and balances the centrifugal force

while the vertical component of F_w balances the weight. If θ is the angle of the nose up from the vertical, as shown in figure 10.6 (*a*), then the angular velocity about the spin axis, Ω, the spin radius, R_s, and θ are related by,

$$R_s = g/\Omega^2 \tan \theta$$

For a typical light aircraft R_s, for a steep spin, is of the order of 0.2 of the wing span and decreases to .06 *b* for a flat spin. Corresponding θ values equal approximately 45° and 60°.

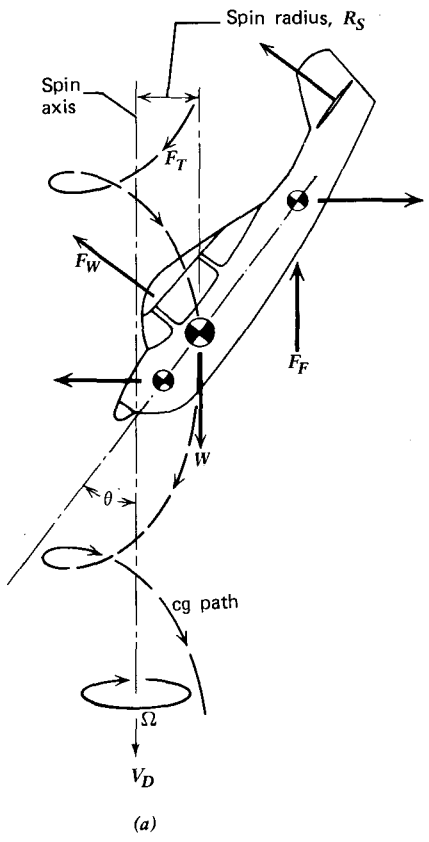

Figure 10.6 Aerodynamic and inertia forces influencing the spin behavior of an airplane (a) Side view. (*b*) Top view. (*c*) Autorotative forces.

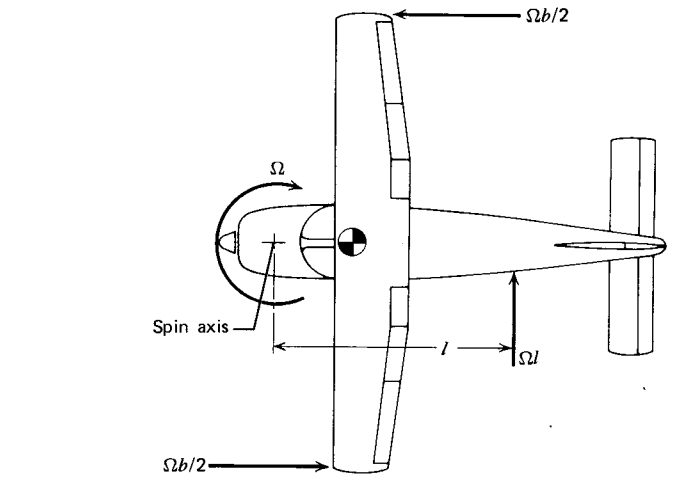

(b)

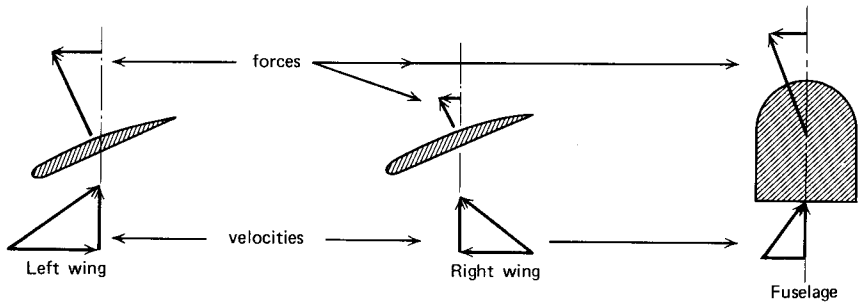

(c)

Figure 10.6 *(continued)*

Normally, the angle of roll, ϕ, is small in a spin. Using equations 10.8*d*, *e*, and *f*, it can be shown that the inertia moments about the spin axis and about the airplane's *y*-axis are proportional to Ω^2 and $(I_z - I_y)$. Thus, the spinning behavior of an airplane is determined as much, possibly more so, by its mass distribution as by its aerodynamic shape.

The pro-spin, autorotative forces can be produced by both the wing and the fuselage. Referring to figure 10.6 (*b*), consider the resultant velocities in a spin at each wing tip and at a typical fuselage section aft of the *cg*. Assume R_s to be small as in the case of a flat spin. The velocities at each of these locations combine vectorially with the descent velocity, V_D as shown in figure 10.6 (*c*) to produce extremely high angles of attack for the wing sections and a nearly vertical flow from beneath the fuselage. For the wing, particularly one with a well-rounded leading edge, a net moment in the direction of rotation results from the higher

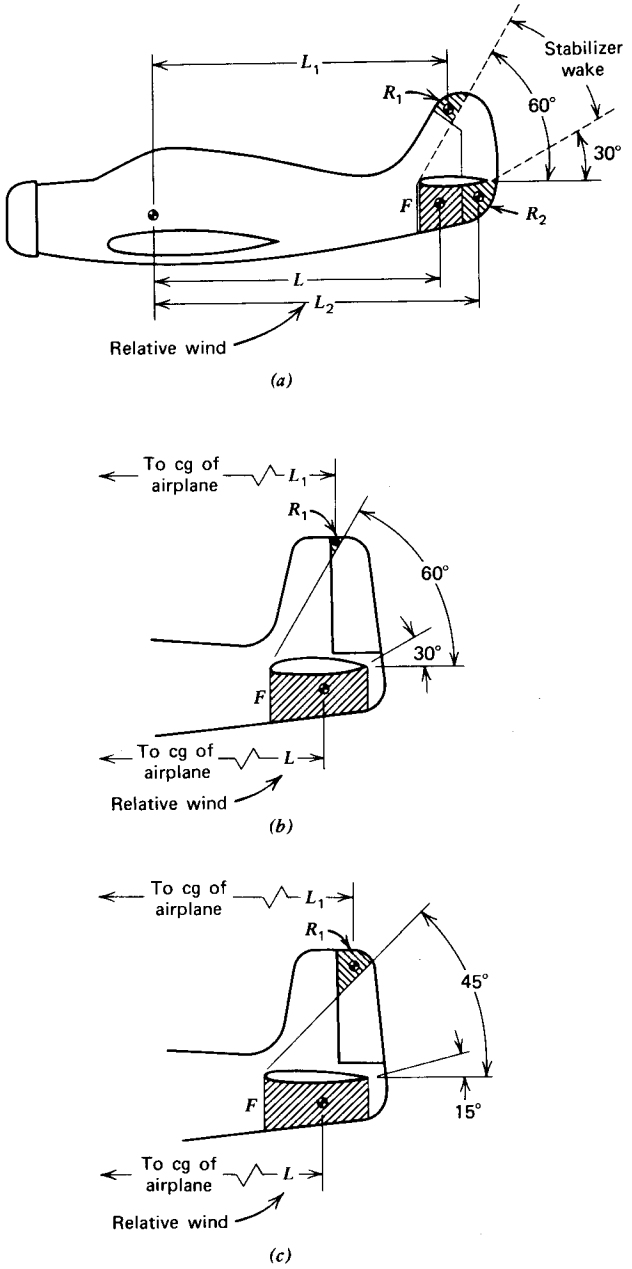

Figure 10.7 Definition of tail damping power factor. (*a*) Full-length rudder; α assumed to be 45°. (*b*) Partial length rudder; α assumed to be 45°, TDR < 0.019. (*c*) Partial-length rudder; α assumed to be 30°, TDR > 0.019.

angle of attack on the left side compared to the right side. The aft fuselage, depending upon its geometry, can develop a force also in the direction of rotation.

Rudder control is the principal means of recovering from a spin. Therefore, in designing the empennage, the placement of the horizontal tail relative to the rudder is important. If the horizontal tail is too far forward, in a spin its wake will blanket the rudder, making it ineffective.

An attempt to quantify the blanketing of the vertical tail by the horizontal tail is presented in Figure 10.7 (taken from Ref. 10.1). Referring to this figure, a term called the tail damping power factor (TDPF) is defined by

$$\text{TDPF} = \frac{FL^2}{S(b/2)^2}\frac{R_1L_1 + R_2L_2}{S(b/2)} \tag{10.40}$$

Equation 10.40 is given here only to acquaint you with its definition, since it is found in more recent references related to spinning (Refs. 10.2 and 10.3). I question its value in view of the arbitrary selection of α in the spin and the use of the projected area F underneath the horizontal tail. The cross-sectional

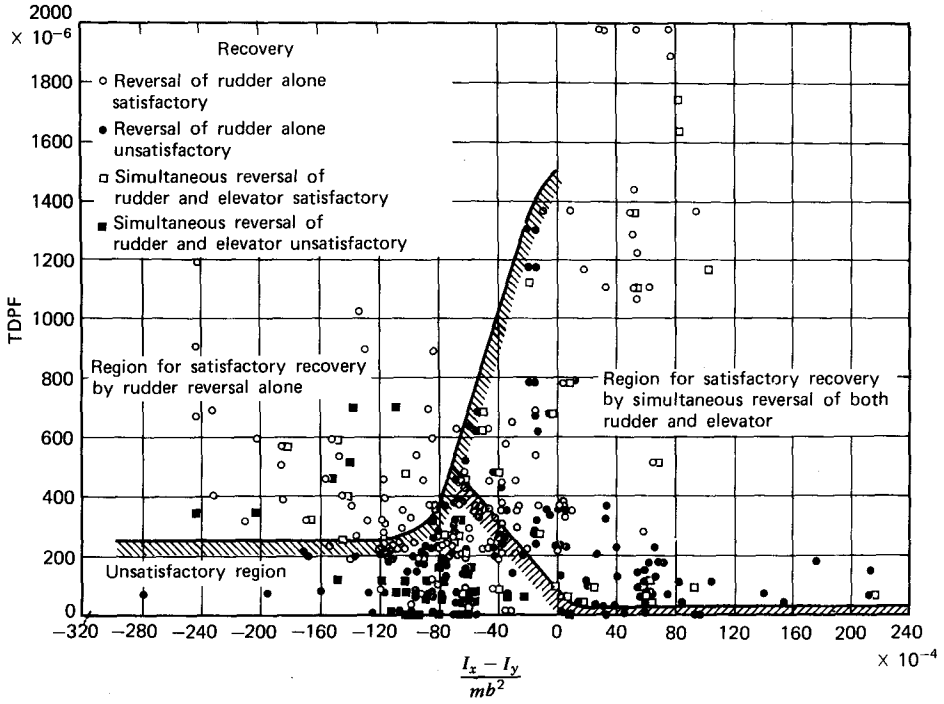

Figure 10.8 Spin recovery design requirements for airplanes with μ values less than 30.

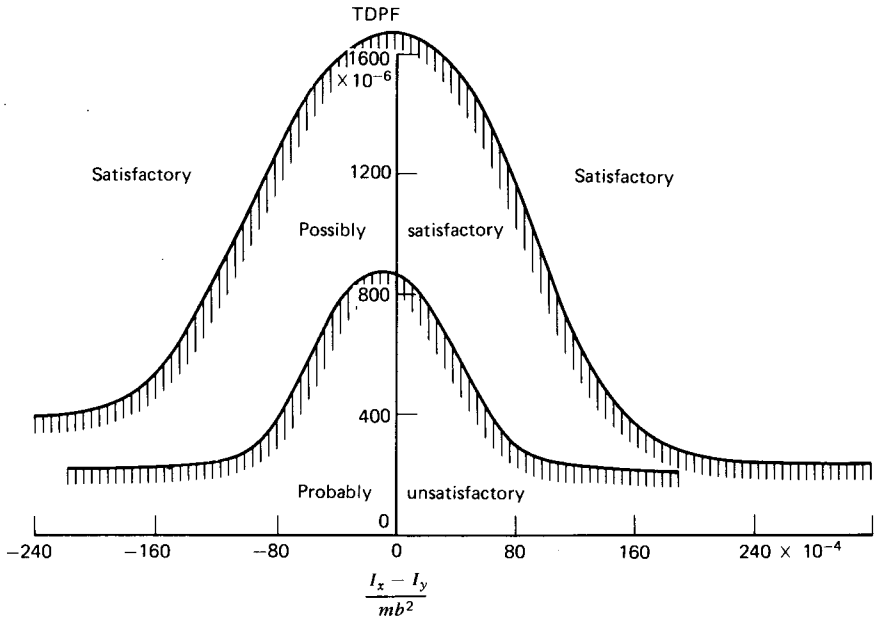

Figure 10.9 Criteria for spin recovery.

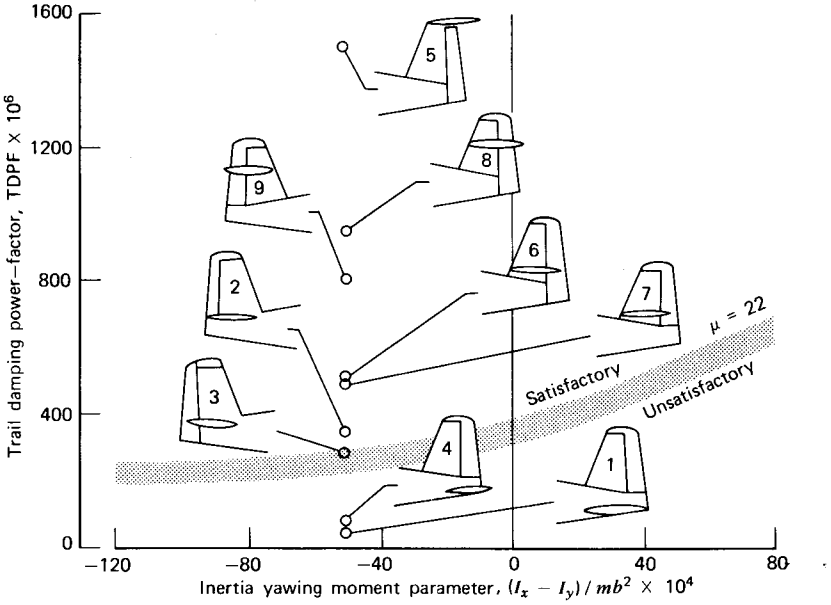

Figure 10.10 Spin recovery for a light airplane with different tail configurations.

shape of this area must certainly influence the damping effectiveness of this area.

According to Reference 10.1, the TDPF for satisfactory spin recovery is a function of an airplane's mass distribution. This is shown in Figure 10.8 (taken from Ref. 10.1). Boundaries are suggested on this figure that divide regions of satisfactory spin recovery characteristics from unsatisfactory regions. However, from the points included on the figure, it is obvious that these boundaries are not too well defined. Indeed, there are several unsatisfactory points lying well within the region denoted as being satisfactory. Similar graphs for μ values as high as 70 can be found in the reference.

The scatter and overlapping of the points in Reference 10.1 appear to rule out any valid definition of the criteria as a function of μ. Instead, the graph of Figure 10.9 is offered as representative of any μ value. In the region labeled "satisfactory," there were no unsatisfactory points to be found in the reference. For the region labeled "possibly satisfactory," there were approximately an equal number of satisfactory and unsatisfactory points. In the region labeled "probably unsatisfactory," the data points were predominantely unsatisfactory.

Despite the uncertainty associated with this figure, one point is obvious. For satisfactory spin recovery characteristics, the moments of inertia about the pitching and rolling axes should be significantly different.

Figure 10.10 is taken from Reference 10.3. Obviously, neither the shape of the curve dividing the satisfactory region from the unsatisfactory region nor the values of TDPF for satisfactory recovery agree with Figure 10.9. Tails 1, 3, and 4 were found to be unsatisfactory for spin recovery with ailerons neutral. With ailerons deflected, tails 2 and 7 were also unsatisfactory. This reference concludes that TDPF cannot be used to predict spin recovery. However, it is important to provide damping to the spin and very important to provide exposed rudder area for spin recovery. In modern aircraft, the T-tail is becoming very popular. The reason for this is twofold. First, from Figure 10.10, such a tail configuration provides excellent spin recovery characteristics. Second, the horizontal tail is removed from the wing wake, thereby minimizing downwash effects. For the same tail effectiveness, the T-tail will allow a smaller horizontal tail, thereby saving on weight and drag.

PROBLEMS

10.1 Assuming small angles, calculate the maximum deviation for the Cherokee example from a straight path if only the Dutch roll mode is excited with a maximum sideslip angle of 5°.

10.2 Estimate TDPF for the Cherokee 180 and determine where it lies on Figure 10.9. (Note: This aircraft is placarded against intentional spins.)

10.3 Draw the patching diagram to solve the lateral-directional equations of motion on an analog computer.
10.4 Dynamically scaled, radio-controlled models are frequently used for spin testing. Examine the scaling relationships involving size, mass, and mass distribution required for dynamic simulation of a full-scale airplane with a model.

The following problems refer to the airplane pictured in Figure 8.43 with the center of gravity positioned to give a 10% stick-fixed static margin.

10.5 Calculate all of the lateral-directional stability and control derivatives required to solve Equation 10.17.
10.6 Calculate the roll, spiral, and Dutch roll mode shapes for a Mach number of 0.5 at a standard altitude of 15,000 ft.
10.7 Discuss the lateral-directional handling qualities for flight phase category B for this aircraft based on the results of Problem 10.6.
10.8 Do you think the spin recovery would be satisfactory for this airplane?

REFERENCES

10.1 Neihouse, A. I., Lichtenstein, J. H., and Pepoon, P. W. *Tail-Design Requirements for Satisfactory Spin Recovery*, NACA TN 1045, April 1946.
10.2 Bowman, J. S., "Aircraft Spinning," *Aeronautics and Astronautics*, *4*(3), March 1966.
10.3 Bowman, J. S., and Burk, S. M., *Comparison to Results from Spin Tunnel and Radio Control Model Spin Tests with Full-Scale Airplane Results*, presented at General Aviation Technologyfest, AIAA, Wichita, Kans., November 18–19, 1977 (NASA TP 1009).
10.4 Seckel, Edward, *Stability and Control of Airplanes and Helicopters*, Academic Press, New York and London, 1964.

A.1
THE SI SYSTEM

SI is an abbreviation for Système International and is a metric system of units that is being adopted internationally for all scientific and engineering work. This brief presentation presents only the aspects of the system pertinent to this text.

Names of International Units

Physical Quanity	Name of Unit	Symbol	
Length	Meter	m	
Mass	Kilogram	kg	
Time	Second	s	
Electric current	Ampere	A	
Temperature	Kelvin	K	
	DERIVED UNITS		
Area	Square meter	m^2	
Volume	Cubic meter	m^3	
Frequency	Hertz	Hz	(s^{-1})
Density	Kilogram per cubic meter	kg/m^3	
Velocity	Meter per second	m/s	
Angular velocity	Radian per second	rad/s	
Acceleration	Meter per second squared	m/s^2	
Angular acceleration	Radian per second squared	rad/s^2	
Force	Newton	N	($kg \cdot m/s^2$)
Pressure	Newton per square meter[a]	N/m^2	
Kinematic viscosity	Square meter per second	m^2/s	
Dynamic viscosity	Newton-second per square meter	$N \cdot s/m^2$	
Work, energy, quantity of heat	Joule	J	($N \cdot m$)
Power	Watt	W	(J/s)
Entropy	Joule per kelvin	J/K	
Specific heat	Joule per kilogram kelvin	$Jkg^{-1}K^{-1}$	
Thermal conductivity	Watt per meter kelvin	$Wm^{-1}K^{-1}$	

[a] $1\ N/m^2 = 1$ Pascal, denoted by Pa.

DEFINITIONS

***newton* (*N*)** The newton is the force that gives a mass of 1 kg an acceleration of 1 m/s/s.

***joule* (*J*)** The joule is the work done when the point of application of 1 N is displaced a distance of 1 m in the direction of force.

***watt* (*W*)** The watt is the power that gives rise to the production of energy at the rate of 1 J/s.

Conversion Factors

Multiply	By	To Get
Pounds (lb)	4.448	Newtons (N)
Feet (ft)	0.3048	Meters (m)
Slugs	14.59	Kilograms (kg)
Slugs per cubic foot (slugs/ft^3)	515.4	Kilograms per cubic meter (kg/m^3)
Horsepower (hp)	0.7457	Kilowatts (kW)
Pounds per square inch (psi)	6895.0	Pascals (Pa)
Pounds per square foot (psf)	47.88	Pascals (Pa)
Miles per hour (mph)	0.4471	Meters per second (m/s)
Knots (kt)	0.5151	Meters per second (m/s)

MISCELLANEOUS

$g = 32.2 \text{ ft/sec}^2 = 9.81 \text{ m/s}^2$ at sea level

$°K = °C + 273.19$

$°R = °F + 459.7$

$°C = (°F - 32)(5/9)$

Universal Gas Constant ($p = \rho RT$)

$R = 1716 \text{ ft}^2/\text{s}^2/°R$

$= 287.0 \text{ m}^2/\text{s}^2/°K$

PREFIXES

The names of multiples and submultiples of SI units may be formed by application of the following prefixes.

Factor by which unit is multiplied	Prefix	Symbol
10^{12}	tera	T
10^{9}	giga	G
10^{6}	mega	M
10^{3}	kilo	k
10^{2}	hecto	h
10	deka	da
10^{-1}	deci	d
10^{-2}	centi	c
10^{-3}	milli	m
10^{-6}	micro	μ
10^{-9}	nano	n
10^{-12}	pico	p
10^{-15}	femto	f
10^{-18}	atto	a

A.2
STANDARD ATMOSPHERE

English Units

Altitude Z,* ft	Temperature T, °R	Pressure P, lb/ft^2	Density ρ, lb sec^2/ft^4	Speed of sound, ft/sec	Kinematic viscosity, ft^2/sec
0	518.69	2116.2	2.3769^{-3}	1116.4	1.5723^{-4}
1,000	515.12	2040.9	2.3081	1112.6	1.6105
2,000	511.56	1967.7	2.2409	1108.7	1.6499
3,000	507.99	1896.7	2.1752	1104.9	1.6905
4,000	504.43	1827.7	2.1110	1101.0	1.7324
5,000	500.86	1760.9	2.0482	1097.1	1.7755
6,000	497.30	1696.0	1.9869^{-3}	1093.2	1.8201^{-4}
7,000	493.73	1633.1	1.9270	1089.3	1.8661
8,000	490.17	1572.1	1.8685	1085.3	1.9136
9,000	486.61	1512.9	1.8113	1081.4	1.9626
10,000	483.04	1455.6	1.7556	1077.4	2.0132
11,000	479.48	1400.0	1.7011^{-3}	1073.4	2.0655^{-4}
12,000	475.92	1346.2	1.6480	1069.4	2.1196
13,000	472.36	1294.1	1.5961	1065.4	2.1754
14,000	468.80	1243.6	1.5455	1061.4	2.2331
15,000	465.23	1194.8	1.4962	1057.4	2.2927
16,000	461.67	1147.5	1.4480^{-3}	1053.3	2.3544^{-4}
17,000	458.11	1101.7	1.4011	1049.2	2.4183
18,000	454.55	1057.5	1.3553	1045.1	2.4843
19,000	450.99	1014.7	1.3107	1041.0	2.5526
20,000	447.43	973.27	1.2673	1036.9	2.6234
21,000	443.87	933.26	1.2249^{-3}	1032.8	2.6966^{-4}
22,000	440.32	894.59	1.1836	1028.6	2.7724
23,000	436.76	857.24	1.1435	1024.5	2.8510
24,000	433.20	821.16	1.1043	1020.3	2.9324
25,000	429.64	786.33	1.0663	1016.1	3.0168

English Units

Altitude Z,* ft	Temperature T, °R	Pressure P, lb/ft^2	Density ρ, lb sec^2/ft^4	Speed of sound, ft/sec	Kinematic viscosity, ft^2/sec
26,000	426.08	752.71	1.0292^{-3}	1011.9	3.1044^{-4}
27,000	422.53	720.26	9.9311^{-4}	1007.7	3.1951
28,000	418.97	688.96	9.5801	1003.4	3.2893
29,000	415.41	658.77	9.2387	000.13	3.3870
30,000	411.86	629.66	8.9068	994.85	3.4884
31,000	408.30	601.61	8.5841^{-4}	990.54	3.5937^{-4}
32,000	404.75	574.58	8.2704	986.22	3.7030
33,000	401.19	548.54	7.9656	981.88	3.8167
34,000	397.64	523.47	7.6696	977.52	3.9348
35,000	394.08	499.34	7.3820	973.14	4.0575
36,000	390.53	476.12	7.1028^{-4}	968.75	4.1852^{-4}
37,000	389.99	453.86	6.7800	968.08	4.3794
38,000	389.99	432.63	6.4629	968.08	4.5942
39,000	389.99	412.41	6.1608	968.08	4.8196
40,000	389.99	393.12	5.8727	968.08	5.0560
41,000	389.99	374.75	5.5982^{-4}	968.08	5.3039^{-4}
42,000	389.99	357.23	5.3365	968.08	5.5640
43,000	389.99	340.53	5.0871	968.08	5.8368
44,000	389.99	324.62	4.8493	968.08	6.1230
45,000	389.99	309.45	4.6227	968.08	6.4231
46,000	389.99	294.99	4.4067^{-4}	968.08	6.7380^{-4}
47,000	389.99	281.20	4.2008	968.08	7.0682
48,000	389.99	268.07	4.0045	968.08	7.4146
49,000	389.99	255.54	3.8175	968.08	7.7780
50,000	389.99	243.61	3.6391	968.08	8.1591
51,000	389.99	232.23	3.4692^{-4}	968.08	8.5588^{-4}
52,000	389.99	221.38	3.3072	968.08	8.9781
53,000	389.99	211.05	3.1527	968.08	9.4179
54,000	389.99	201.19	3.0055	968.08	9.8792
55,000	389.99	191.80	2.8652	968.08	1.0363^{-3}
56,000	389.99	182.84	2.7314^{-4}	968.08	1.0871^{-3}
57,000	389.99	174.31	2.6039	968.08	1.1403
58,000	389.99	166.17	2.4824	968.08	1.1961
59,000	389.99	158.42	2.3665	968.08	1.2547
60,000	389.99	151.03	2.2561	968.08	1.3161

English Units

Altitude Z,* ft	Temperature T, °R	Pressure P, lb/ft^2	Density ρ, lb sec^2/ft^4	Speed of sound, ft/sec	Kinematic viscosity, ft^2/sec
61,000	389.99	143.98	2.1508^{-4}	968.08	1.3805^{-3}
62,000	389.99	137.26	2.0505	968.08	1.4481
63,000	389.99	130.86	1.9548	968.08	1.5189
64,000	389.99	124.75	1.8636	968.08	1.5932
65,000	389.99	118.93	1.7767	968.08	1.6712
66,000	389.99	113.39	1.6938^{-4}	968.08	1.7530^{-3}
67,000	389.99	108.10	1.6148	968.08	1.8387
68,000	389.99	102.06	1.5395	968.08	1.9286
69,000	389.99	98.253	1.4678	968.08	2.0230
70,000	389.99	93.672	1.3993	968.08	2.1219
71,000	389.99	89.305	1.3341^{-4}	968.08	2.2257^{-3}
72,000	389.99	85.142	1.2719	968.08	2.3345
73,000	389.99	81.174	1.2126	968.08	2.4486
74,000	389.99	77.390	1.1561	968.08	2.5683
75,000	389.99	73.784	1.1022	968.08	2.6938

SI Units

Altitude Z, m	Temperature T, K	Pressure P N/m^2	Density ρ kg/m^3	Speed of sound m/s	Kinematic Viscosity, m^2/s
0	288.16	1.01325+5	1.2250	340.29	1.4607−5
300	286.21	9.7773+4	1.1901	339.14	1.4956
600	284.26	9.4322	1.1560	337.98	1.5316
900	282.31	9.0971	1.1226	336.82	1.5687
1,200	280.36	8.7718	1.0900	335.66	1.6069
1,500	278.41	8.4560	1.0581	334.49	1.6463
1,800	276.46	8.1494	1.0269	333.32	1.6869
2,100	274.51	7.8520	9.9649−1	332.14	1.7289
2,400	272.57	7.5634	9.6673	330.96	1.7721
2,700	270.62	7.2835	9.3765	329.77	1.8167
3,000	268.67	7.0121	9.0926	328.58	1.8628
3,300	266.72	6.7489	8.8153	327.39	1.9104
3,600	264.77	6.4939	8.5445	326.19	1.9595
3,900	262.83	6.2467	8.2802	324.99	2.0102

SI Units

Altitude Z, m	Temperature T, K	Pressure P N/m^2	Density ρ kg/m^3	Speed of sound m/s	Kinematic Viscosity, m^2/s
4,200	260.88	6.0072	8.0222	323.78	2.0626
4,500	258.93	5.7752	7.7704	322.57	2.1167
4,800	256.98	5.5506	7.5247	321.36	2.1727
5,100	255.04	5.3331	7.2851	320.14	2.2305
5,400	253.09	5.1226	7.0513	318.91	2.2903
5,700	251.14	4.9188+4	6.8234−1	317.69	2.3522−5
6,000	249.20	4.7217	6.6011	316.45	2.4161
6,300	247.25	4.5311	6.3845	315.21	2.4824
6,600	245.30	4.3468	6.1733	313.97	2.5509
6,900	243.36	4.1686	5.9676	312.72	2.6218
7,200	241.41	3.9963	5.7671	311.47	2.6953
7,500	239.47	3.8299	5.5719	310.21	2.7714
7,800	237.52	3.6692	5.3818	308.95	2.8503
8,100	235.58	3.5140	5.1967	307.68	2.9320
8,400	233.63	3.3642	5.0165	306.41	3.0167
8,700	231.69	3.2196	4.8412	305.13	3.1046
9,000	229.74	3.0800	4.6706	303.85	3.1957
9,300	227.80	2.9455	4.5047	302.56	3.2903
9,600	225.85	2.8157	4.3433	301.27	3.3884
9,900	223.91	2.6906	4.1864	299.97	3.4903
10,200	221.97	2.5701	4.0339	298.66	3.5961
10,500	220.02	2.4540	3.8857	297.35	3.7060
10,800	218.08	2.3422	3.7417	296.03	3.8202
11,100	216.66	2.2346	3.5932	295.07	3.9564
11,400	216.66	2.1317	3.4277	295.07	4.1474
11,700	216.66	2.0335+4	3.2699−1	295.07	4.3475−5
12,000	216.66	1.9399	3.1194	295.07	4.5574
12,300	216.66	1.8506	2.9758	295.07	4.7773
12,600	216.66	1.7654	2.8388	295.07	5.0078
12,900	216.66	1.6842	2.7081	295.07	5.2494
13,200	216.66	1.6067	2.5835	295.07	5.5026
13,500	216.66	1.5327	2.4646	295.07	5.7680
13,800	216.66	1.4622	2.3512	295.07	6.0462
14,100	216.66	1.3950	2.2430	295.07	6.3378
14,400	216.66	1.3308	2.1399	295.07	6.6434
14,700	216.66	1.2696	2.0414	295.07	6.9637
15,000	216.66	1.2112	1.9475	295.07	7.2995
15,300	216.66	1.1555	1.8580	295.07	7.6514
15,600	216.66	1.1023	1.7725	295.07	8.0202
15,900	216.66	1.0516	1.6910	295.07	8.4068
16,200	216.66	1.0033	1.6133	295.07	8.8119

SI Units

Altitude Z, m	Temperature T, K	Pressure P N/m^2	Density ρ kg/m^3	Speed of sound m/s	Kinematic Viscosity, m^2/s
16,500	215.66	9.5717+3	1.5391	295.07	9.2366
16,800	216.66	9.1317	1.4683	295.07	9.6816
17,100	216.66	8.7119	1.4009	295.07	1.0148−4
17,400	216.66	8.3115	1.3365	295.07	1.0637
17,700	216.66	7.9295+3	1.2751−1	295.07	1.1149−4
18,000	216.66	7.5652	1.2165	295.07	1.1686
18,300	216.66	7.2175	1.1606	295.07	1.2249
18,600	216.66	6.8859	1.1072	295.07	1.2839
18,900	216.66	6.5696	1.0564	295.07	1.3457

A.3
AIRPLANE DATA

The following samples of airplane data (Figures A.3.1 to A.3.20 and Table A.3.1) are taken from *Aircraft Handling Qualities Data*, by Robert K. Heffley and Wayne F. Jewell, NASA CR-2144, December 1972. The figures include:

- Flight envelope.
- C_L and C_D as a function of M and altitude.
- Weight and moments of inertia.
- Three-view sketches to scale.

In addition, stability derivatives are tabulated for the Convair 880. The following definitions apply to notations on the sketches.

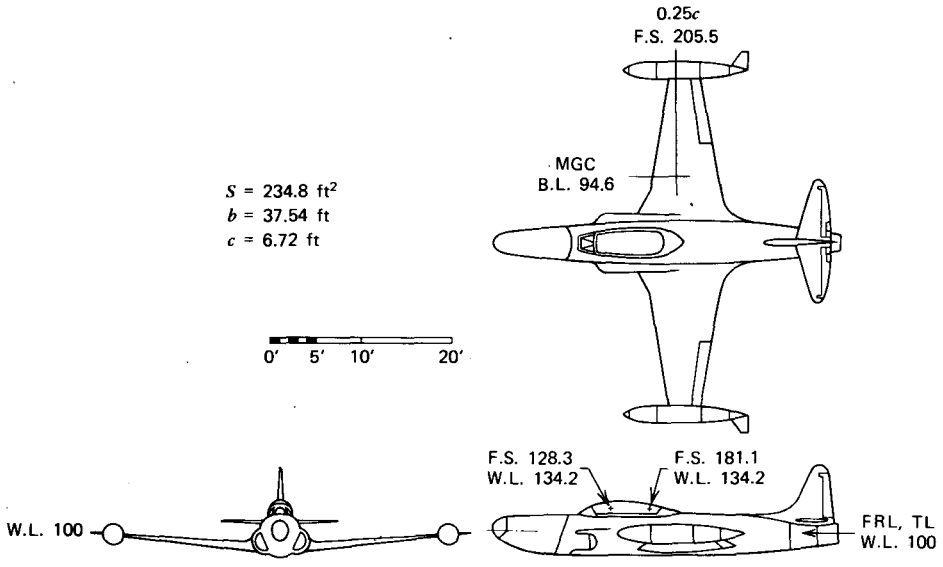

Figure A.3.1 NT-33; a general arrangement.

F.S. = fuselage station = inches aft of reference transverse plane near the nose.
W.L. = waterline = inches above horizontal reference plane.
B.L. = buttline = inches to right of vertical plane of symmetry.

Nominal Configuration

230-gal tip tanks
60% internal fuel
W = 13,700 lb
cg at 0.263$\bar{c}$, W.L. 100.2
I_x = 23,800 slug-ft^2
I_y = 21,100 slug-ft^2
i_z = 43,800 slug-ft^2
I_{xz} = 480 slug-ft^2
} body axis

Power Approach Configuration

230-gal tip tanks
25% internal fuel
Full flaps
Gear down
1.4 V_s
W = 11,800 lb
cg at 0.260$\bar{c}$, W.L. 100
I_x = 12,700 slug-ft^2
I_y = 20,700 slug-ft^2
I_z = 32,000 slug-ft^2
I_{xz} = 480 slug-ft^2
} body axis

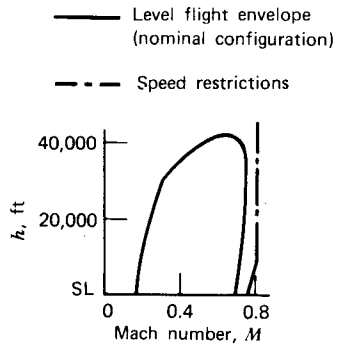

Figure A.3.2 NT-33A; flight envelope.

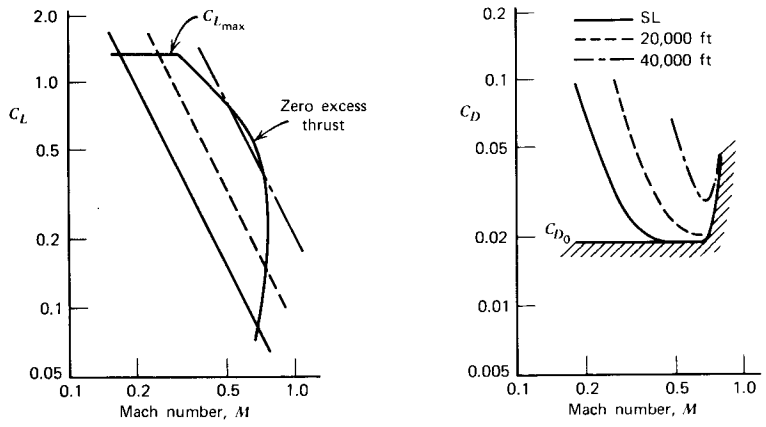

Figure A.3.3 NT-33A; 13,700 lb.

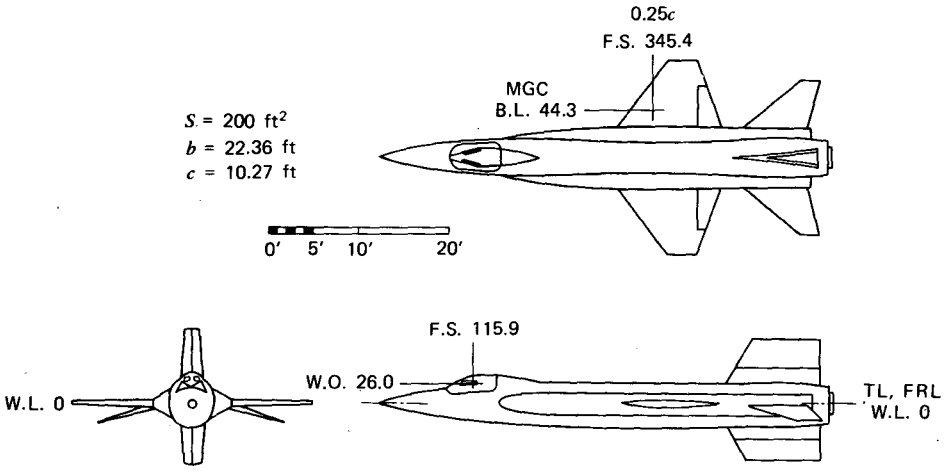

Figure A.3.4 X-15; a general arrangement.

Nominal Configuration

Zero fuel
Lower ventral on
Speed brakes retracted
$W = 15{,}560$ lb
cg at $0.22\bar{c}$
$i_x = 3650$ slug-ft^2
$I_y = 80{,}000$ slug-ft^2
$I_z = 82{,}000$ slug-ft^2
$I_{xz} = 590$ slug-ft^2

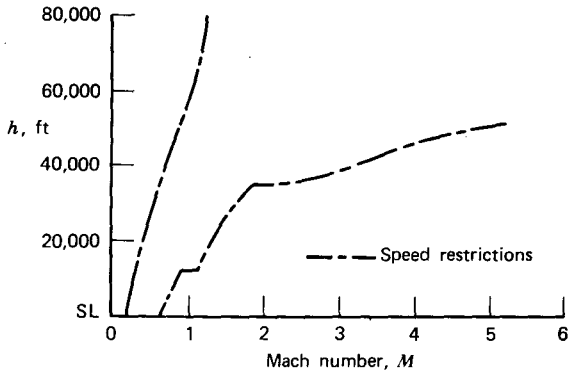

Figure A.3.5 X-15; flight envelope.

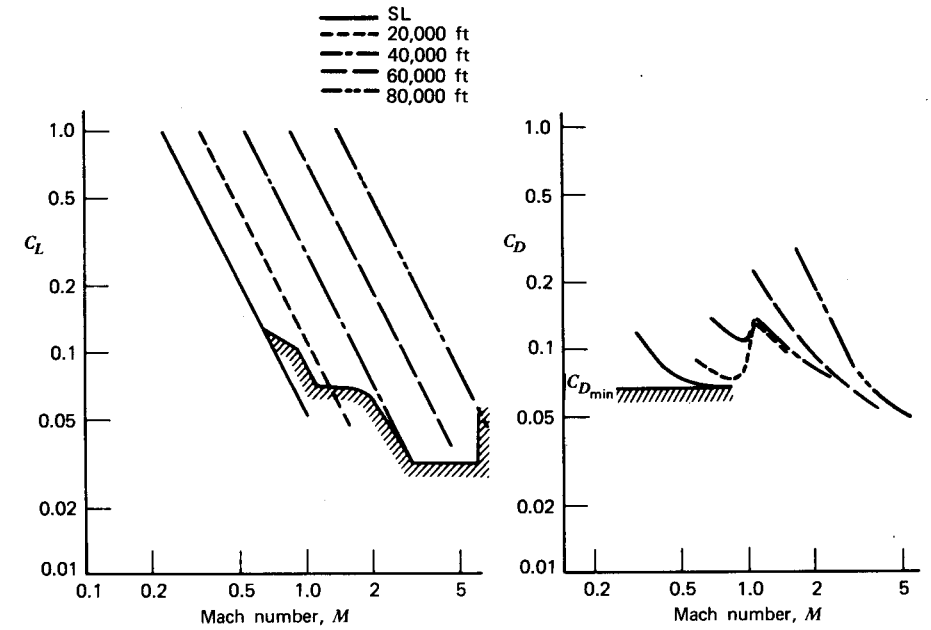

Figure A.3.6 X-15; 15,560 lb.

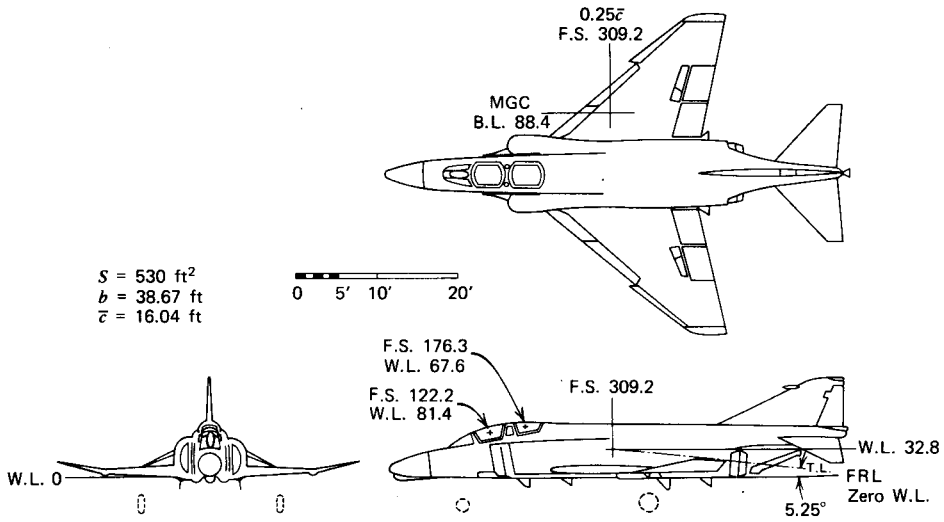

Figure A.3.7 F-4C; a general arrangement.

Nominal Configuration

4 AIM-7 missiles
60% internal fuel
$W = 38{,}924$ lb
cg at $0.289\bar{c}$, W.L. 27.65
$I_x = 25{,}001$ slug-ft^2
$I_y = 122{,}186$ slug-ft^2
$I_z = 139{,}759$ slug-ft^2
$I_{xz} = 2177$ slug-ft^2
} body axis

Power Approach Configuration

2 AIM-7 missiles aft
20% internal fuel
Full flaps, BLC
Gear down
19 units angle of attack
$W = 33{,}196$ lb
cg at $0.291\bar{c}$, W.L. 25.2
$I_x = 23{,}668$ slug-ft^2
$I_y = 117{,}500$ slug-ft^2
$I_z = 133{,}723$ slug-ft^2
$I_{xy} = 1573$ slug-ft^2
} body axis

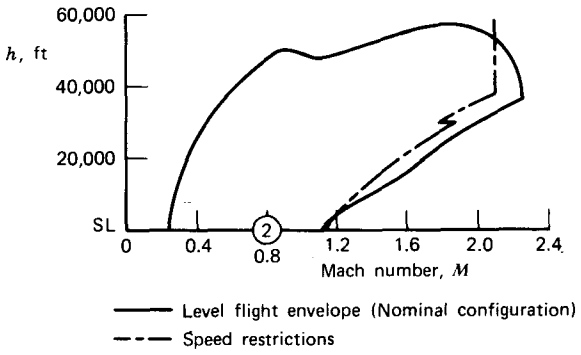

Figure A.3.8 F-4C; flight envelope.

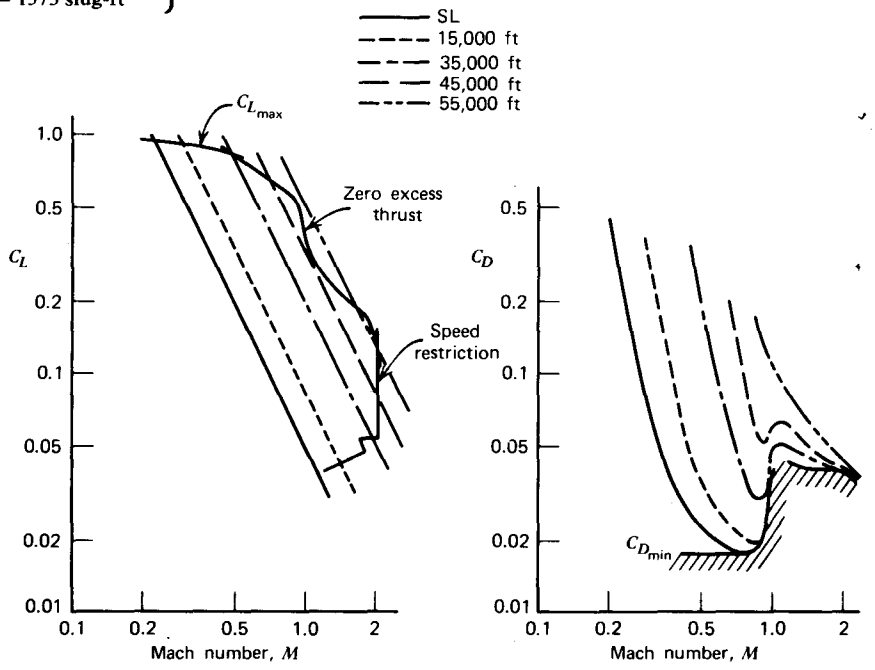

Figure A.3.9 F-4C; 38,942 lb.

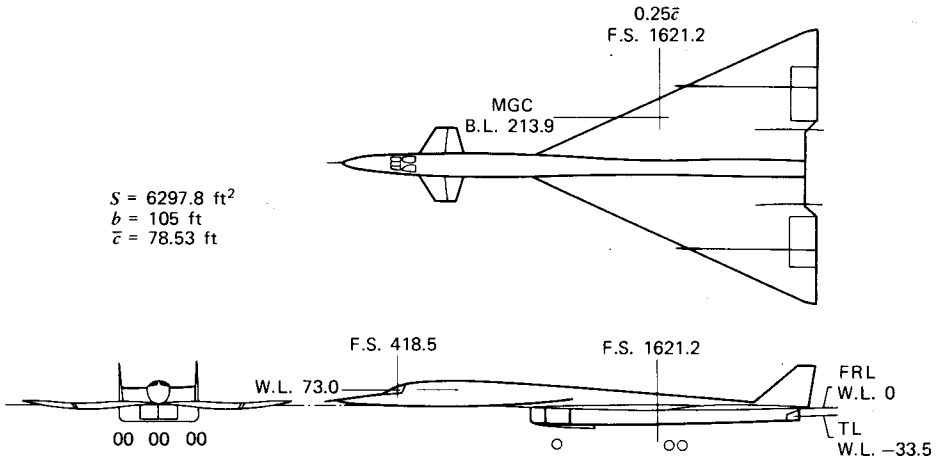

Figure A.3.10 XB-70A; a general arrangement.

Nominal Configuration

Tips folded according to flight condition
50% internal fuel
$W = 384{,}524$ lb
cg at $0.218\bar{c}$, W.L. −7.2
$I_x = 1.8 \times 10^6$ slug-ft^2
$I_y = 19.9 \times 10^6$ slug-ft^2
$I_z = 22.1 \times 10^6$ slug-ft^2
$I_{xz} = -0.88 \times 10^6$ slug-ft^2
} body axis

Power Approach Configuration

Tips extended
19% internal fuel
Canard flaps down
Gear down
$W = 300{,}000$ lb
cg at $0.235\bar{c}$
$I_x = 1.45 \times 10^6$ slug-ft^2
$I_y = 16 \times 10^6$ slug-ft^2
$I_z = 17.2 \times 10^6$ slug-ft^2
$I_{xz} = -0.6 \times 10^6$ slug-ft^2
} body axis

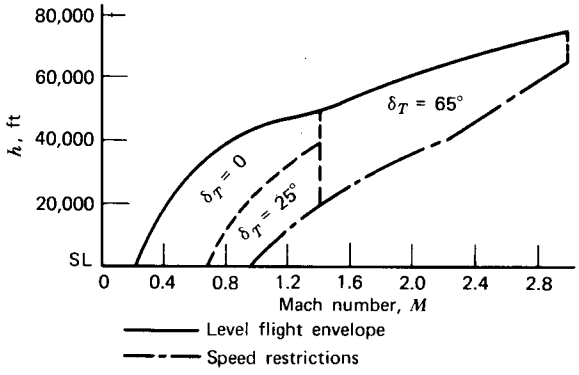

Figure A.3.11 XB-70A; flight envelope.

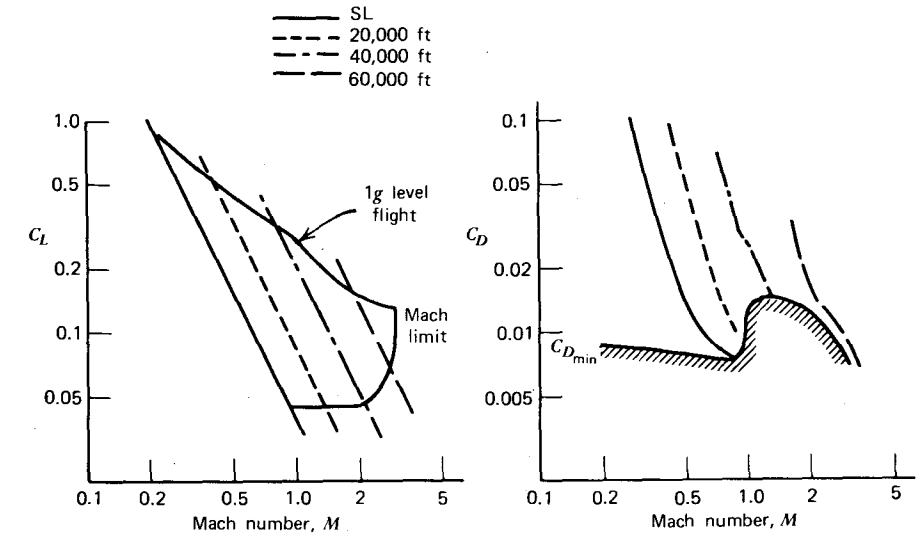

Figure A.3.12 XB-70A; 384,524 lb.

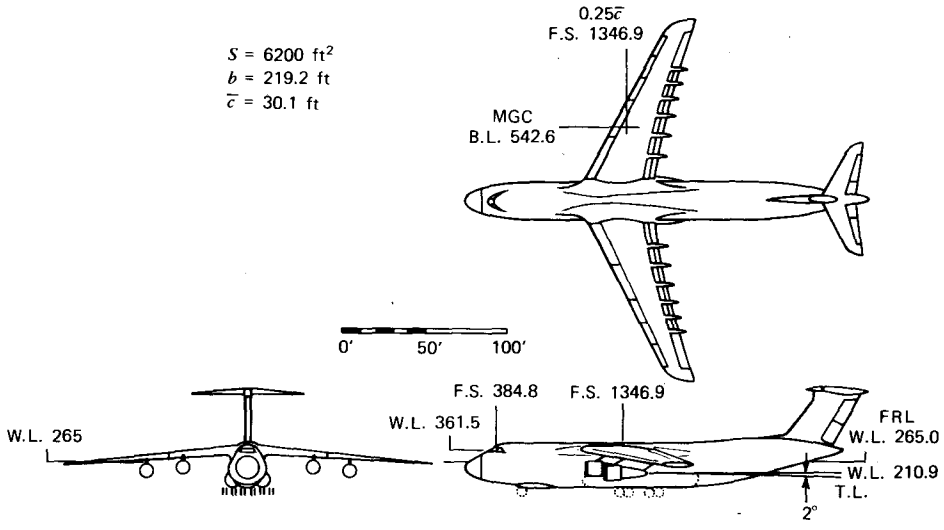

Figure A.3.13 C-5A; a general arrangement.

Nominal Configuration

220,000 lb cargo
TOGW less 40% fuel
$W = 654{,}362$ lb
cg at $0.30\bar{c}$, W.L. 265
$I_x = 27.8 \times 10^6$ slug-ft^2
$I_y = 31.8 \times 10^6$ slug-ft^2
$I_z = 56.2 \times 10^6$ slug-ft^2
$I_{xz} = 2.46 \times 10^6$ slug-ft^2
} body axis

Power Approach Configuration

220,000 lb cargo
TOGW less 80% fuel
30° flaps
Gear down
$1.4V_s$
$W = 580{,}723$ lb
cg at $0.30\bar{c}$, W.L. 265
$I_x = 19.1 \times 10^6$ slug-ft^2
$I_y = 31.3 \times 10^6$ slug-ft^2
$I_z = 47.0 \times 10^6$ slug-ft^2
$I_{xz} = 2.5 \times 10^6$ slug-ft^2
} body axis

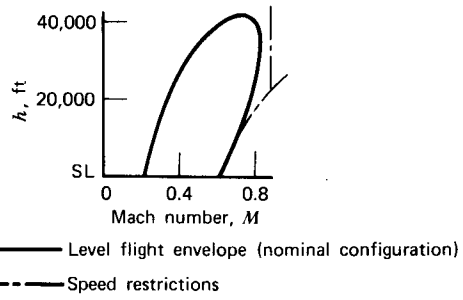

Figure A.3.14 C-5A; flight envelope.

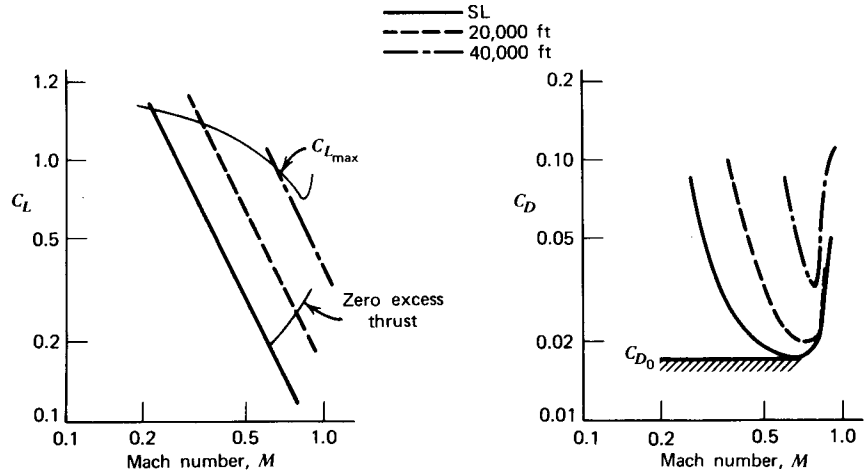

Figure A.3.15 C-5A; 654,362 lb.

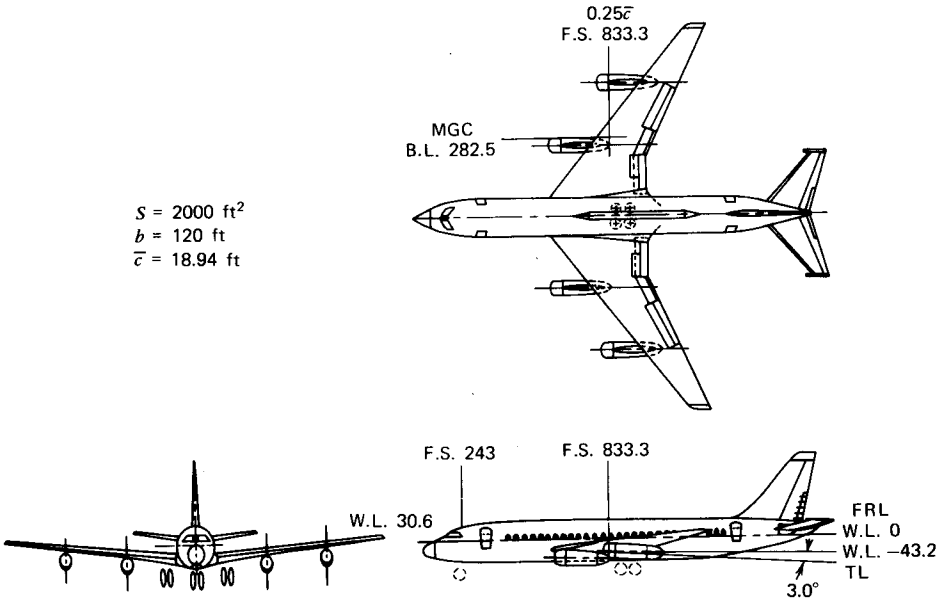

Figure A.3.16 CV-880M; a general arrangement.

Nominal Configuration

W = 155,000 lb
cg at 0.25$\bar{c}$, W.L. −19.2
I_x = 1,510,000 slug-ft^2
I_y = 2,510,000 slug-ft^2
I_z = 4,100,000 slug-ft^2

Power Approach Configuration

Flaps 30°
Gear up
W = 126,000 *lb*
cg at 0.195$\bar{c}$, W.L. −19.2
I_x = 1,150,000 slug-ft^2
I_y = 2,450,000 slug-ft^2
I_z = 4,070,000 slug-ft^2

Landing Configuration

Same as power approach except:
Flaps 50°
Speedbrakes 8°
Gear down

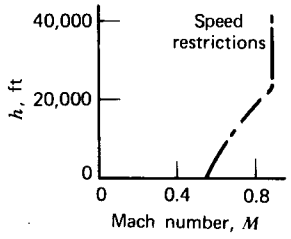

Figure A.3.17 CV-880M; flight envelope.

Table A.3.1 CV-880 M Longitudinal Nondimensional Stability Derivatives

Flight condition	1	2	3	4	5	6	7
Configuration	L	PA					
Speed	134 KTAS	165 KTAS	0.6M	0.86M	0.7M	0.8M	0.86M
Altitude	SL	SL	23K	23K	35K	35K	35K
α_0 (deg)	5.2	4.3	5.3	2.8	8.3	4.7	4.0
C_L	1.03	0.68	0.36	0.175	0.454	0.347	0.301
C_D	0.154	0.080	0.022	0.019	0.025	0.024	0.023
C_{L_α} (1/rad)	4.66	4.52	4.28	4.41	4.62	4.8	4.9
C_{D_α} (1/rad)	0.43	0.27	0.14	0.07	0.18	0.15	0.13
C_{m_α} (1/rad)	−0.381	−0.903	−0.522	−0.572	−0.568	−0.65	−0.74
$C_{L_{\dot\alpha}}$ (1/rad)	2.7	2.7	2.44	2.5	2.75	2.75	2.9
C_{L_q} (1/rad)	7.92	7.72	6.76	6.37	7.51	7.5	7.62
$C_{m_{\dot\alpha}}$ (1/rad)	−4.17	−4.13	−4.16	−4.66	−4.4	−4.5	−4.6
C_{m_q} (1/rad)	−12.2	−12.1	−11.5	−11.8	−12.0	−12.0	−12.0
$C_{L_{\delta_e}}$ (1/rad)	0.22	0.213	0.193	0.141	0.203	0.190	0.180
$C_{m_{\delta_e}}$ (1/rad)	−0.657	−0.637	−0.586	−0.438	−0.618	−0.57	−0.532
$C_{h_{\delta_e}}$ (1/rad)	−10.326	−0.328	−0.336	−0.278	−0.342	−0.31	−0.285
$C_{L_{\delta_{t_e}}}$ (1/rad)	0.055	0.0532	0.482	0.0352	0.0508	0.047	0.0450
$C_{m_{\delta_{t_e}}}$ (1/rad)	−0.164	−0.159	−0.146	−0.11	−0.155	−0.14	−0.134
$C_{h_{\delta_{t_e}}}$ (1/rad)	−0.287	−0.285	−0.297	−0.343	−0.312	−0.335	−0.352

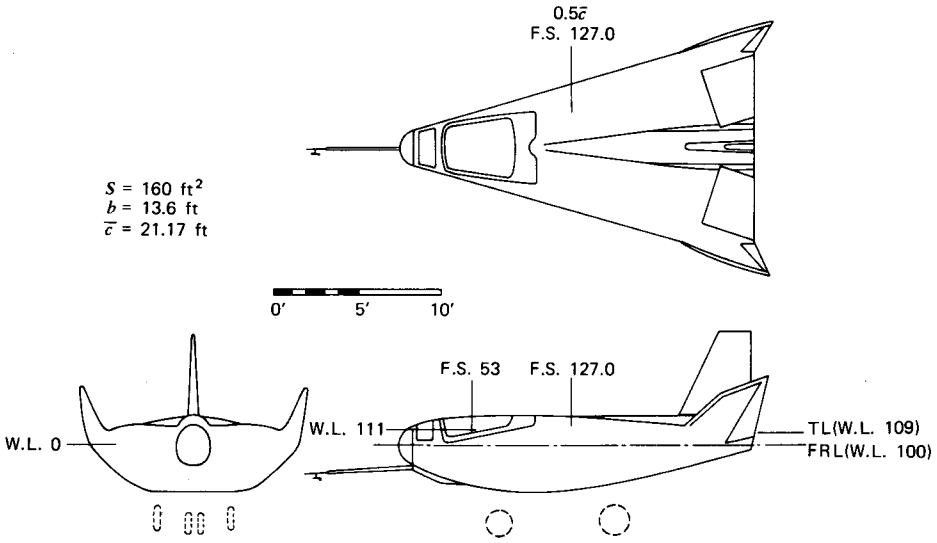

Figure A.3.18 HL-10; a general arrangement.

Nominal Configuration

Zero fuel (burnout)
Gear up
Transonic or subsonic configuration, depending on flight condition
$W = 6466$ lb
cg at $0.517\bar{c}$, W.L. 94.4
$I_x = 1353$ slug-ft^2
$I_y = 6413$ slug-ft^2
$I_z = 7407$ slug-ft^2
$I_{xz} = 399$ slug-ft^2
} body axis

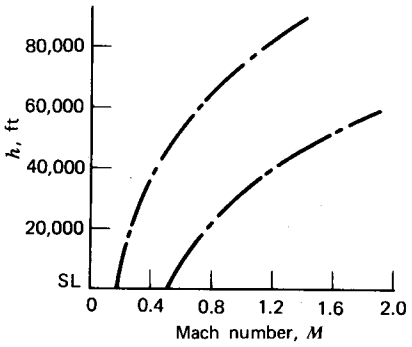

Figure A.3.19 HL-10; flight envelope; nominal envelope extremes.

Configuration	Speed Brakes	Elevon Flaps	Tip-Fin Flaps
Subsonic	Zero	Zero	Zero
Transonic	8°	30°	30.5°/32.5°

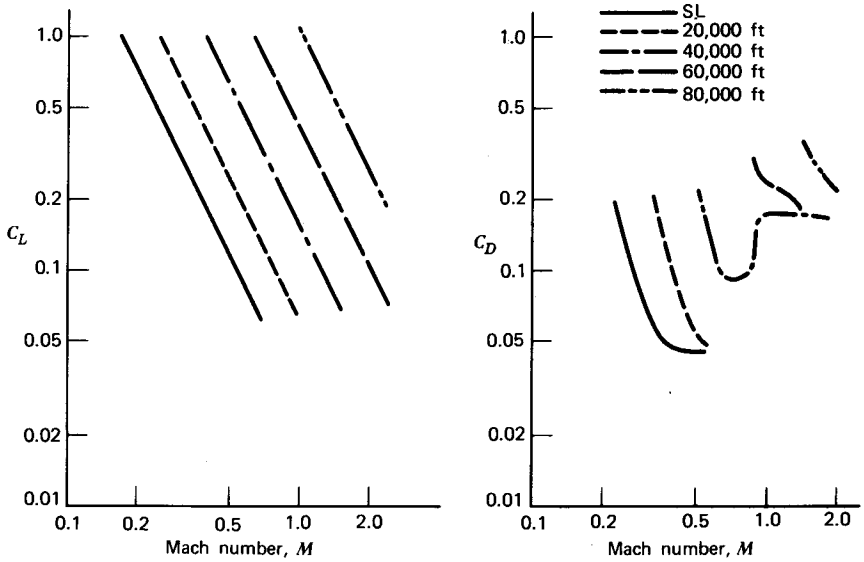

Figure A.3.20 HL-10; 6466 lb.

A.4
NOMENCLATURE AND ABBREVIATIONS

This listing includes only the symbols used throughout the text or a chapter. Symbols limited to a few pages are defined when used and are not listed here.

ENGLISH NOMENCLATURE

a	speed of sound; slope of lift curve, $dC_L/d\alpha$
a_n	acceleration normal to flight path
a_0	speed of sound at sea level; slope of lift curve, $dC_l/d\alpha$
a_t	slope of horizontal tail lift curve, $dC_{L_t}/d\alpha$
a_v	slope of vertical tail lift curve, $dC_{L_v}/d\alpha$
$\bar{a}$	average acceleration
A	projected frontal area; reference area; aspect ratio, b^2/S; disc area
A_B	cooling baffle area
b	wingspan; propeller section chord in Figure 6.11
b_1	constant (Equation 8.32)
b_2	constant (Equation 8.32)
b_3	constant (Equation 8.37)
b'	span between rolled-up vortices
B	$(M^2-1)^{1/2}$; number of propeller blades
c	chord length
c_f	flap chord
c_0	midspan chord
c_t	tip chord
$\bar{c}$	mean aerodynamic chord or geometric mean chord
C_d	section drag coefficient = D/qc
$\overline{C_d}$	average section drag coefficient for propeller
C_D	drag coefficient for finite wing or airplane = D/qS
C_{D_i}	induced drag coefficient

C_{D_0}	parasite drag coefficient = C_D for $C_L = 0$
C_{D_v}	drag coefficient for body based on volume to the two-thirds power
C_f	skin friction coefficient = D/qS_w
C_F	average skin friction coefficient for airplane
C_h	hinge moment coefficient = $H/qS\bar{c}$ (S and $\bar{c}$ for control surface)
C_l	section lift coefficient = L/qc; rolling moment coefficient = L/qSb
$\bar{C}_l$	average section lift coefficient for propeller
C_L	wing or airplane lift coefficient = L/aS
C_{L_A}	airplane lift coefficient at approach speed
C_{L_0}	trim C_L; C_L for zero angle of attack
C_m	section pitching moment coefficient = M/qc^2
C_M	airplane pitching moment coefficient = $M/qS\bar{c}$
C_{M_q}	$\partial C_M/\partial \bar{q}$
C_n	normal force coefficient = F_n/qc
C_N	yawing moment coefficient = N/qSb
C_p	pressure coefficient = $(p - p_\infty)/q$; specific heat at constant pressure
C_P	propeller power coefficient = $P/\rho n^3 D^5$
C_{P_i}	induced power coefficient
C_S	propeller speed-power coefficient = $(\rho V^5/Pn^2)^{1/5}$
C_T	propeller thrust coefficient = $T/\rho n^2 D^4$
C_V	specific heat at constant volume
C_X	X force coefficient = X/qS
C_Y	side force coefficient = Y/qS
C_Z	Z force coefficient = Z/qS
C_μ	jet momentum coefficient = m/qc or m/qS
D	drag; propeller diameter; body diameter
D_c	cooling drag
D_f	skin friction drag
D_i	induced drag
e	Oswald's wing efficiency factor (Equation 4.32); voltage
f	frequency, Hz; equivalent flat-plate area
f_s	rate of change of total energy with fuel weight, $\partial h_e/\partial W_f$
F	force, jet engine thrust; Prandtl's tip loss factor (Equation 6.37)
F_e	free elevator factor (Equations 8.42 and 8.46)
F_g	gross jet engine thrust
F_n	force normal to chord; net jet engine thrust
F_0	turbojet static thrust
g	acceleration due to gravity
G	gain of operational amplifier; gearing (Equations 8.27 and 8.30)
h	height; location of center of gravity aft of leading edge of $\bar{c}$ as a fraction of $\bar{c}$, height defined in Figure 2.16; propeller section thickness in Figure 6.11
h_{abs}	absolute ceiling

h_e total energy of airplane per unit weight
h_l location of horizontal tail aerodynamic center aft of leading edge of $\bar{c}$ as a fraction of $\bar{c}$
h_n location of airplane neutral point aft of leading edge of $\bar{c}$ as a fraction of $\bar{c}$
h_{nw} location of wing neutral point aft of leading edge of $\bar{c}$ as a fraction of $\bar{c}$
h_0 distance defined in Figure 2.2
H hinge moment
i current
i_{hs} incidence angle of horizontal stabilizer, positive nose down
i_t incidence angle of horizontal tail, positive nose down
i_x dimensionless mass moment of inertia about x-axis (Equation 10.16)
i_{xz} dimensionless mass product of inertia about x-z axes (Equation 10.16)
i_y dimensionless mass moment of inertia about y-axis (Equation 10.16)
i_z dimensionless mass moment of inertia about z-axis (Equation 10.16)
I_x mass moment of inertia about x-axis
I_{xz} mass product of inertia about x-z axes
I_y mass moment of inertia about y-axis
I_z mass moment of inertia about z-axis
J propeller advance ratio = V/nD
k_e constant (Equation 8.33)
K_c correction factor (Figure 6.34a)
K_p see Equation 5.97 and Figure 5.38
K_v see Equation 5.97 and Figure 5.38
l reference length
l_{ac} distance defined in Figure 8.5
l_t distance from center of gravity to horizontal tail aerodynamic center
l_v distance from center of gravity to vertical tail aerodynamic center
L lift; rolling moment
m airplane mass; mass flow rate; doublet strength
M pitching moment; Mach number
M_{cr} critical Mach number
n rotational speed, rps; load factor, L/W
N yawing moment, rpm
N_p propeller yawing moment
N_j jet normal force
N_1 low-pressure rotor rpm (forward compressor, aft turbine)
N_2 high-pressure rotor rpm (aft compressor, forward turbine)
p static pressure; distance from leading edge of airfoil to Z_{max}; propeller pitch
p_{t_2} total pressure at compressor inlet

p_{t_7}	total pressure in turbine exhaust
$\bar{p}$	dimensionless roll rate, $pb/2V$
p_∞	free-stream static pressure
p_a	atmospheric pressure
p_0	reservoir pressure; sea level atmosphere pressure
P	stick force; power; roll rate
P_a	power available
P_B	static pressure just ahead of cooling baffle
P_E	static pressure at engine cowling exit
P_i	propeller-induced power
P_{i_0}	static propeller-induced power
P_N	propeller normal force
P_r	power required
p_s	excess specific power, dh_e/dt (Equation 7.61)
P_{use}	useful power
P_{xs}	excess power $(P_a - P_r)$
q	dynamic pressure, $\rho V^2/2$; source strength, point or distributed
$\bar{q}$	dimensionless pitch rate, $Q\bar{c}/2V$
Q	volume flux; source strength; pitch rate; propeller torque
r	pressure ratio for the Brayton cycle (Equation 6.69)
r_0	sea level value of r
$\bar{r}$	dimensionless yaw rate, $Rb/2V$; radius vector from point P to vortex element in Biot-Savart law
R	universal gas constant, $p/\rho T$; Reynolds number, Vl/ν; yaw rate; electrical resistance; radius; radius of curvature; range
R_x	Reynold's number based on x distance from leading edge
R/C	rate of climb
s	stick travel
s_a	airborne distance for takeoff or landing
S	planform area; Strouhal number, fD/V; distance, reference area
S_w	wetted area
t	time; temperature, °C; airfoil thickness (sometimes denotes maximum value or ratio of maximum value to c)
t_e	endurance time
t^*	air seconds (Equations 9.28 and 10.14)
T	thrust, absolute temperature
T_B	temperature just ahead of cooling baffle
T_c	thrust coefficient (Equation 6.22)
T_0	static thrust
u	x component of velocity; increment in same component above U_0
$\tilde{u}$	dimensionless perturbation velocity in x direction, u/U_0
U_0	trimmed airplane velocity; free-stream velocity
v	y component of velocity

v_r	radial component of velocity
v_θ	tangentiai component of velocity
V	local velocity; free-stream velocity
V_A	approach velocity
V_c	velocity of climb
V_{cal}	calibrated airspeed
V_e	equivalent airspeed; resultant velocity (Figure 6.9)
V_E	velocity at engine cowling exit
V_G	ground speed
V_H	horizontal tail volume
V_i	indicated airspeed
V_{LOF}	liftoff speed
V_m	volume
V_{mc}	minimum control speed
V_{mu}	minimum unstick speed
V_0	free-stream velocity
V_r	resultant velocity (Figure 6.9)
V_R	takeoff rotation speed
V_s	stalling speed
V_{s_1}	stalling speed, one engine out
V_T	propeller tip speed, wR
V_{TR}	trim speed
V_v	vertical tail volume
V_w	wind velocity
V_1	critical engine failure calibrated airspeed
V_2	airspeed over takeoff obstacle
V_∞	free-stream velocity
w	z component of velocity; downwash; propeller-induced velocity
w_a	axial component of propeller-induced velocity
w_0	static value of propeller-induced velocity; impact velocity (Equation 6.60)
w_t	tangential component of propeller-induced velocity
W	airplane weight
W_a	airflow
W_E	airplane empty weight
W_f	fuel flow rate
W_F	total fuel weight
W_I	initial airplane weight
x	cartesian coordinate, directed forward; relative radius along propeller blade, r/R
x_h	relative hub radius for propeller, rh/R
x_j	distance of center of gravity aft of inlet (Figure 8.23)
x_p	x-coordinate of point at which induced velocity is to be calculated

X resultant aerodynamic force on airplane in x direction
y right-handed, orthogonal coordinate directed to the right, spanwise distance to right of airplane centerline
y_p y location of point at which induced velocity is to be calculated
Y resultant aerodynamic force on airplane in y direction
z cartesian coordinate directed downward; airfoil camber (sometimes denotes maximum value or ratio of maximum value to c)
z_p z location of point at which induced velocity is to be calculated
Z resultant aerodynamic force on airplane in z direction
Z_j distance of jet thrust line below center of gravity
Z_p distance of propeller thrust line above center of gravity

GREEK NOMENCLATURE

α angle of attack; angle defined in Biot-Savart law (Figure 2.16)
α_i induced angle of attack
α_{0l} angle of zero lift
β sideslip angle, angle defined in Biot-Savart law (Figure 2.16); Prandtl-Glauert compressibility correction factor $(1 - M^2)^{1/2}$; blade section pitch angle
γ ratio of specific heats (1.4 for air); vortex strength (point or distributed)
Γ wing dihedral angle; vortex strength
δ ratio of ambient pressure to sea level ambient pressure; flow deflection angle that causes oblique shock wave; fractional increase in C_{D_i} above elliptic case; boundary layer thickness
δ_a aileron deflection, sum of left and right aileron angles, positive for right aileron down, left aileron up
δ_e elevator angle, positive for down elevator
δ_f flap angle, positive down
δ_r rudder angle, positive to the left
δ_t trim tab angle, positive down
δ^* displacement thickness (Figure 4.2 and Equation 4.3)
Δ denotes an increment
ϵ wing twist (positive nose up); downwash angle; apex angle for delta wing; drag-to-lift ratio
ϵ_T wing twist at tip
ϵ_α $\partial\epsilon/\partial\alpha$ = rate of change of downwash angle with α
ϵ_β $\partial\epsilon/\partial\beta$ = rate of change of sidewash angle with β
ξ damping ratio
η propeller efficiency = TV/P; correction to τ (Figure 3.33)
η_i ideal propeller efficiency

η_t	ratio of dynamic pressure at tail to free-stream g
θ	pitch angle; oblique shock wave angle; angle between thrust line and horizontal; ratio of absolute ambient temperature to sea level value
θ_c	climb angle between velocity vector and horizontal
θ_D	descent angle between velocity vector and horizontal
λ	taper ratio, c_t/c_0; also function in Figure 5.42; propeller advance ratio, V/wR
Λ	angle of sweepback
μ	coefficient of viscosity; Mach wave angle; dimensionless airplane mass (Equations 9.31 and 10.16); coefficient of braking or rolling friction
ν	kinematic viscosity
ρ	mass density
σ	ratio of mass density to sea level value; root of characteristic equation; propeller section solidity, $Bc/\pi R$
τ	flap effectiveness factor (Equation 3.48 and Figure 3.32); dimensionless time, t/t^*; time constant (time for a damped system to reach $1/e$ of its initial displacement)
ϕ	roll angle; velocity potential; resultant flow angle for propeller blade section (Figure 6.9)
ϕ_c	compressible velocity potential
ϕ_i	incompressible velocity potential
ϕ_T	helix angle at tip of propeller trailing vortex system
ψ	stream function; yaw angle
ω	angular velocity or circular frequency, radians per second
$\boldsymbol{\omega}$	curl of velocity vector, $\nabla \times \mathbf{V}$
ω_n	undamped natural frequency, radians per second

SUBSCRIPTS

a	ailerons
ac	aerodynamic center
am	ambient
B	base; cooling baffle
c	compressible; corrected
CLB	climb
CR	cruise
DES	descent
e	elevator
f	flap
HLD	hold
i	incompressible; index, induced, initial

j	jet; index
k	index
l	lower
max	maximum
min	minimum
0	reservoir, sea level, free-stream
opt	optimum
t	horizontal tail
T	horizontal tail
V	vertical tail
w	winglet
W	wing
	Any quantity may indicate differentiation with respect to quantity, for example, $C_{l_\alpha} = dC_l/d\alpha$.
1/4	quarter chord
1/2	midchord
1	just upstream of shock wave
2	just downstream of shock wave
∞	conditions far removed from body (free stream)

SUPERSCRIPTS

*	throat conditions where $M = 1$
·	derivative with respect to time, t, or dimensionless time, τ

ABBREVIATIONS

ac	aerodynamic center
bhp	brake horsepower
BPR	bypass ratio
BSFC	brake specific fuel consumption
cp	center of pressure
cg	center of gravity
CHT	cylinder head temperature
EGT	exhaust gas temperature
EPR	engine pressure ratio, p_{t_7}/p_{t_2}
eshp	effective shaft horsepower
FAA	Federal Aviation Administration
FAR	Federal Air Regulations
gph	gallons per hour
IGE	in-ground effect

kt	knots
LE	leading edge
ln	natural logarithm
MAP	manifold absolute pressure
NACA	National Advisory Committee for Aeronautics
NASA	National Aeronautics and Space Administration
OGE	out-of-ground effect
rpm	revolutions per minute
rps	revolutions per second
SFC	specific fuel consumption
shp	shaft horsepower
TE	trailing edge
thp	thrust horsepower
TIT	turbine inlet temperature
TO	takeoff
TSFC	thrust specific fuel consumption

INDEX

Abbreviations, 647
Ackeret theory, 274
Acoustic velocity, 34
Adverse yaw, 534
Aerodynamic center, 66, 87, 91, 484
Afterburner, 376
Aileron, 62, 528
  reversal, 537
Airborne distance for takeoff, 427
Airfoil, families, 63, 72
  general aviation, 78
  low-Reynolds numbers, 151
  supercritical, 76, 261
  thin-airfoil analytical treatment, 89
  thin-airfoil numerical treatment, 84
  thin-airfoil theory, 82
Airplane data, Boeing 747, 421
  C-5A, 635
  CV-880M, 637
  Cherokee 180, 148, 359, 502, 503, 561-565, 584, 596-605
  Cherokee Arrow, 361, 362, 435
  Citation I, 453-460
  F-4C, 632
  HL-10, 638
  Learjet, 202
  NT-33, 629
  Piper Navajo, 340
  X-15, 631
  XB-70A, 634
Air second, 559, 595
Airspeed, calibrated, 38
  determination of, 36
  equivalent, 38
  indicated, 38
  true, 38
Analog computation, 576
Angle-of-attack, definition, 10
  induced, 134
Angle-of-zero lift, 138
Anttinello, John, 130
Area rule, 321
Aspect ratio, definition, 61
  effective, 194
Atmosphere, standard, 20, 624, 629

Bernoulli, Daniel and John, 5
Bernoulli's equation, compressible, 34
  incompressible, 34
Biot-Savart law, 45
Boundary layer, definition, 23
  thickness, 164
Brake specific fuel consumption, 338
Brayton cycle, 379
Breguet range equation, 441
Buffet, 460

Camber, 63, 69
Ceiling, absolute, 435
  service, 437
Center of pressure, 65
Chanute, Octave, 2, 4, 11, 72
Choked flow, 248
Chord, airfoil, 63
  mean, 61
Circular cylinder, 51, 57
Circulation, bound, 132
  definition, 44
  elliptic distribution, 135
Climb, angle of, 12
  rate of, 12, 432
  time to, 439
Compressible similarity transformations, 238
Compressor stall, 403
Conservation of mass, 26
Control forces, 491
Cooling of gas turbine blades, 402
Coordinate system, 478
Coupling effects on stability and control, 541
Critical attitude, 339
Critical Reynolds number, 170
Curl of velocity vector, 38
Curtiss, Glenn, 529

Damping pitching moment, 509

Damping rolling moment, 538
Delta wings, 294-314
Descent, 447
Differential equations, linear nth order, 565
Dihedral, 543
Directional control, 526
Directional static stability, 524
Divergence of velocity vector, 38
Downwash, 134, 486
Drag, base, 162, 315
  breakdown, 196, 199-203
  cooling, 162, 206-214
  count, 196
  divergence Mach number, 244, 262
  form, 162, 168
  induced, 162, 185, 293, 306, 420
  interference, 162, 181
  parasite, 162, 216
  pressure, 162
  profile, 162
  reduction, induced, 214
    skin-friction, 221
  skin-friction, 162, 163, 197, 221, 288, 319
  streamlined shapes, 176
  transonic, 321
  trim, 203-206
  wave, 162, 271, 277
Drag bucket, 76, 225
Drag coefficient, 24, 162
Dynamic stability, definition, 477

Elementary flow functions, 42
Elliptical wing, 136
Endurance, 446
Energy equation, 249
Engine date, Lycoming 0-360-A piston, 336, 337
  Lycoming TI0-540 supercharged piston, 341, 342
  P&W JT4A-3 turbojet, 385, 387-397
  P&W JT9D-7A turbofan, 399-402
  P&W of Canada JT15D turbofan, 406, 408
  P&W of Canada PT6A-27 turboprop, 409, 410
  Wright Brothers, 332
Engine ratings, 377
Engine weights, 334
Equivalent flat plate area, 196
Euler, Leonhard, 5
Euler angles, 594

Flaps, Anttinello, 130
  blown, 126
  definition, 63
  drag increment, 109
  jet, 122
  leading edge, 114
  linear range, effectiveness, 109
    efficiency, 112
    $C\ell_{max}$ increment, 112
  pitching moment, 102
  plain, 99
  Reynolds number effects, 100
  slotted, 100
  split, 99
  thickness effects, 102
Flat plate area, 196
Flight envelope, 460
Fluid dynamics, 22
Fluid statics, 16
Flying qualities, Dutch roll mode, 612
  flight path stability, 587
  lateral-directional, 610
  longitudinal, 585
  phugoid criteria, 586
  roll mode, 611
  short period mode, 587
  spiral stability, 612
Fuselage moment, 513

Gas dynamics, 244
Gas turbine engine, 371
Gearing, control, 492
Ground effect, 420, 523
Ground roll, 419, 423, 425

Harmonic function, 39
Helmholtz's theorem, 133
High lift devices, *see* Flaps, leading edge devices

Induced angle of attack, 134, 135
Installation losses, 411
Isentropic flow, 244

Jet flap, 122
Joukowski, Nikolai, 9

Karman vortex street, 171
Kutta condition, 66
Kutta-Joukowski theorem, 54, 84

Lanchester, F. W., 5
Landing distance, airborne, 448

flare, 450
ground roll, 451
Langley, S. P., 72
Lateral control, 528
Lateral-directional, equations of motion, 591
mode shapes, oscillatory (Dutch roll), 609
roll mode, 606
spiral mode, 607
stability derivatives, ℓ-derivatives, 600
N-derivatives, 604
Y-derivatives, 596
Laval nozzle, 245
Leading edge high lift devices, flaps, 114
Kruger flap, 114
slots and extensible slats, 113
Leading edge suction force, 296
Lift, maximum, *see* Flaps, leading edge devices
Lift, powered, 120
Lift coefficient, definition, 24, 64
fuselage effect, 144
maximum, delta wings, 302
prediction of, 81, 93, 120, 140
trim effect, 146
Lift curve, 69, 137, 239, 284, 288
Lift distribution, additional, 141
basic, 141
Schrenk's approximation, 141
spanwise, 140
vortex-lattice method, 140
Lilienthal, Otto, 4
Load factor, 464
Longitudinal, control, 488
dynamic stability and control, 552
equations of motion, formulation, 552
linearization, 556
mode shapes, 569
reduction, 565
stability derivatives, M, 564
X, 561
Z, 563
static stability, 479, 505

Mach number, critical, 240
definition, 25
limiting, 262
Mach waves, 258
Maneuvering, elevator angle per g, 509
Maneuvering envelope, 463
Maneuver point, 511, 512
Maneuver margin, 511, 512
Mass, conservation of, 26
Mass flux, 27
Mean aerodynamic chord, 485
Moment coefficient, aerodynamic center, 91
definition, 65
momentum flux, 27
momentum theorem, 29
motion, equations of fluid, 31

National Advisory Committee for Aeronautics (NACA), 63
National Aeronautics and Space Administration (NASA), 63
Neumann problem, 54
Neutral point, 481
Newton, Isaac, 5
Nomenclature, 640
Numerical solutions, potential flow, 54
thin airfoil, 82

Oswald's wing efficiency factor, 194
Otto cycle, 379

Phugoid, 572, 574
Pitot-static tube, 18, 35
Potential flow, incompressible, 38
linearized compressible, 271-279
Powered lift, 120
Power-required, 436, 438
Prandtl, Ludwig, 9
Prandtl-Glauert compressibility factor, 238
Pressure coefficient, critical, 263
definition, 50, 65
limiting, 263
Propeller, charts, 359
design, 368
moment, 516
normal force, 516
selection, 366
theory, momentum, 340
momentum-blade element, 349
vortex, 351
thrust vs. speed, 362
Prop fan, 413
Propulsion effects on stability, 515, 521

Quartic, extraction of roots, 570

Range, 440
Rankine oval, 47
Reynolds number, critical, 170
chart, 229

definition, 25
transition, 164
Roll control, 540
Roll damping, 538
Rosen, George, 411
Routh's discriminant, 570

St. Venant's equation, 248
Separation, definition, 24, 69
imminent, 117
Shear stress, 25
Shock waves, expansion waves, 258
normal, 248
oblique, 253
Short period mode, 572, 576
SI system of metric units, 621
Sound, speed of, 34
Source, 44
Spinning, 613
Spoilers, 534
Stabilator, 491
Stability, *see* Longitudinal and lateral
Stagnation point, 22
State, equation of, 17, 249
Static margin, 481, 508
Stratford, B. S., 117
Stream function, 39
Streamline, 22
Strouhal number, 171
Supercharging, 339
Supercritical airfoils, 261
Supersonic airfoils, 266
Supersonic wings, 304-314
Surge of turbojet engines, 403
Sweep angle, 62
Sweepback, definition, 281
effect on drag, 288-294
effect on lift, 283-290

Tail volume, 482, 526
Takeoff, definition of speeds, 418
distance, 418-431
balanced field length, 431
Taper ratio, 62
Thermodynamics of turbojet engines, 378
Thrust specific fuel consumption (TSFC), 382, 412
Transition point, 23, 164
Transonic airfoils, 261
Treffetz plane, 215
Turbofan performance, 385
Turbojet history, 370
Turbojet performance, 385
Turboprop performance, 405

Uniform flow, 41

Velocity potential, 39
V-n diagram, 463
Voisin Brothers, Charles and Gabriel, 5
von Ohain, Hans, 370
Vortex, bound, 132
continuity, 133
lift, 299
point, 43
street, 171
trailing, 131

Weissinger's approximation, 84
Whitcomb, Richard T., 78, 215, 321
Whittle, Sir Frank, 370
Wing, efficiency factor, 194
geometry, 61
Winglets, 215-221
Wortmann, F. X., 232
Wright Brothers, Orville and Wilbur, 72
first flight, 1
flyer, 3